BİNGÖL ÜNİVERSİTESİ

e-ISSN 2149-6366

Cilt 14, Sayı 2, Haziran 2025
Volume 14, Issue 2, June 2025

TDFD
TÜRK DOĞA ve FEN DERGİSİ

TURKISH JOURNAL OF NATURE AND SCIENCE

TJNS

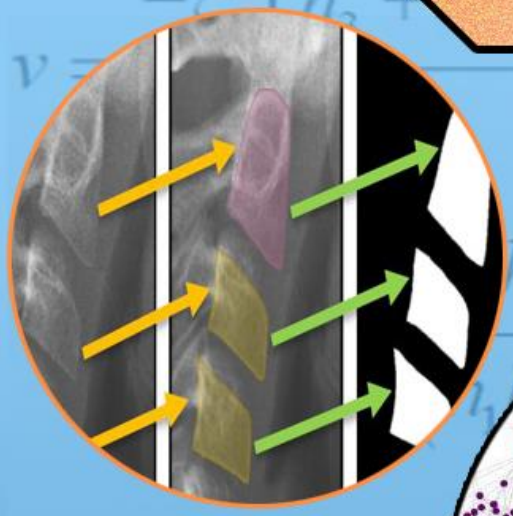

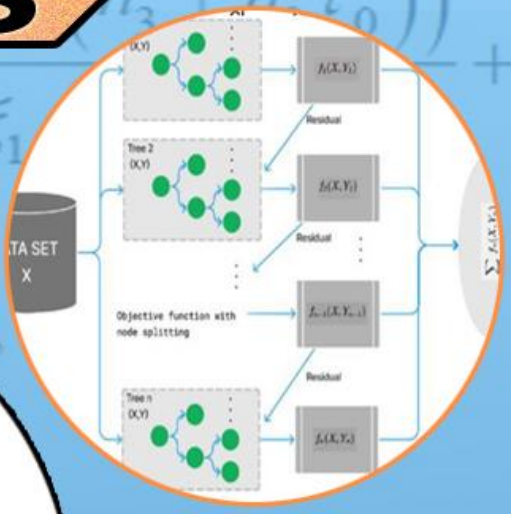

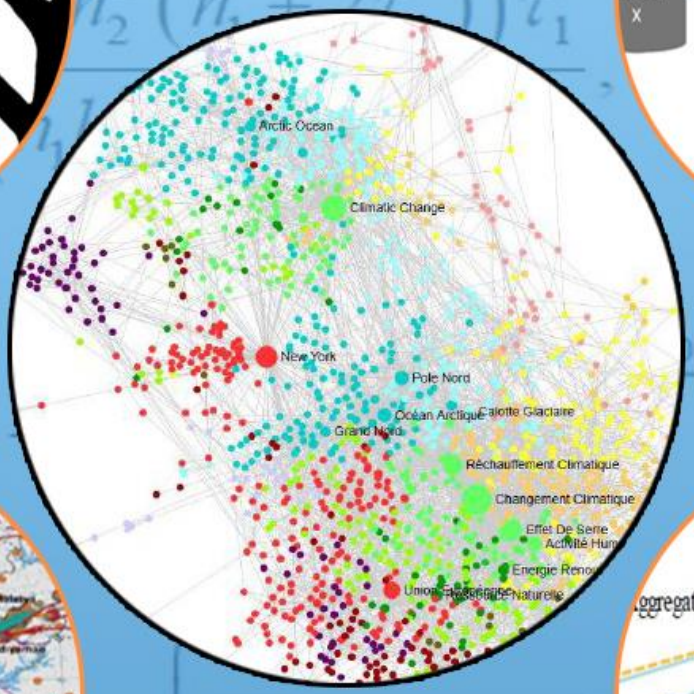

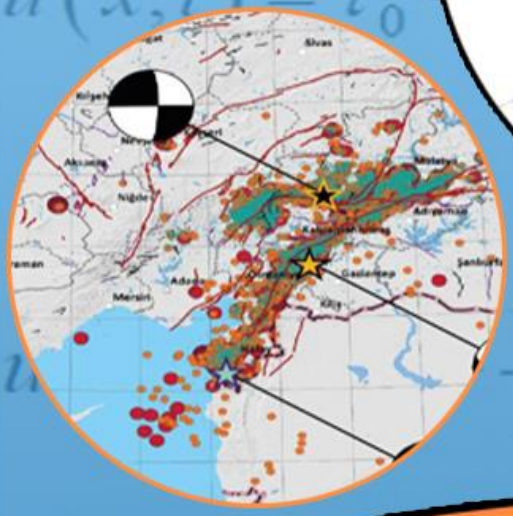

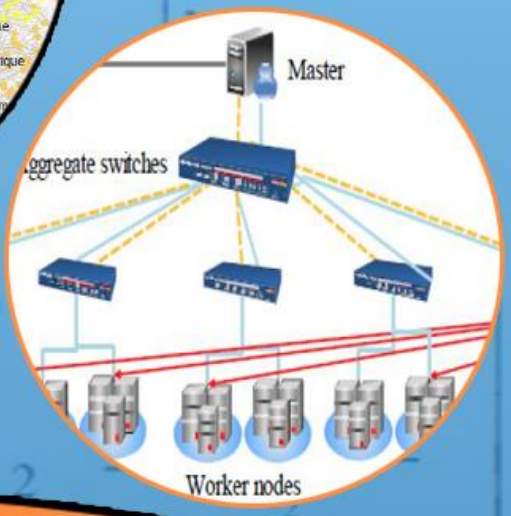

www.dergipark.gov.tr/tdfd

Bingöl Üniversitesi Fen Bilimleri Enstitüsü tarafından yayımlanmaktadır.
Published by Bingol University Institute of Science

ULAKBİM TR DİZİN

TÜRK DOĞA VE FEN DERGİSİ

Amaç

Türk Doğa ve Fen Dergisi, Dergipark tarafından yayınlanan Bingöl Üniversitesi Fen Bilimleri Enstitüsüne ait ulusal ve hakemli bir dergidir. Türk Doğa ve Fen Dergisi, Türkiye ve dünyanın her yerinden gelen doğa ve fen bilimlerinin her alanında özgün, yayımlanmamış, yayımlanmak üzere başka yere gönderilmemiş makale, derleme ve sempozyum değerlendirmesi gibi çalışmaların bilim alemine sunulması amacıyla kurulmuştur.

Kapsam

Türk Doğa ve Fen Dergisinde Mühendislik, Ziraat, Veterinerlik, Fen ve Doğa Bilimleri alanlarından olmak üzere Türkçe ve İngilizce hazırlanmış orijinal makale, derleme ve sempozyum değerlendirmesi gibi çalışmalar yayımlanır. Türk Doğa ve Fen Dergisi sadece online sistemde yayınlanmakta olup ayrıca kağıt baskısı bulunmamaktadır.

Merhaba…

Türk Doğa ve Fen Dergisi, Dergipark tarafından yayınlanmakta olup Bingöl Üniversitesi Fen Bilimleri Enstitüsüne aittir. Bahar ve güz dönemi olmak üzere yılda iki defa çıkarılan ulusal hakemli bir dergi olarak ilk sayısını 2012 bahar döneminde yayımlamıştır. Türk Doğa ve Fen Dergisi, Türkiye ve dünyanın her yerinden gelen doğa ve fen bilimlerinin her alanında özgün, yayımlanmamış, yayımlanmak üzere başka yere gönderilmemiş makale, derleme ve sempozyum değerlendirmesi gibi çalışmaların bilim alemine sunulması amacıyla kurulmuştur. İlk sayısından bugüne kesintisiz olarak faaliyetlerini sürdürmektedir.

Türk Doğa ve Fen Dergisi sadece online sistemde yayınlanmakta olup ayrıca kağıt baskısı bulunmamaktadır. Dergimize gelen her çalışma öncelikle Turnitin intihal programında taranmaktadır. Dergimizde editörlerin, hakemlerin ve yazarların, uluslararası yayım etik kurallarına uyması ve makalelerin yazım kurallarına uyumlu olması zorunluluğu vardır.

Yazarlar yayımlanmak üzere dergimize gönderdikleri çalışmaları ile ilgili telif haklarını zorunlu olarak Bingöl Üniversitesi Türk Doğa ve Fen Dergisi'ne devretmiş sayılırlar. Yazarlardan herhangi bir ücret talep edilmemektedir. Yazarların değerlendirmeleri, dergimizin resmi görüşü olarak kabul edilemez. Çalışmaların her türlü sorumluluğu yazarlarına aittir. Araştırma ürünleri için etik kurul raporu gerekli ise, çalışma üzerinde bu raporun alınmış olduğu belirtilmeli ve kurul raporu sisteme kaydedilmelidir. Araştırma ile ilgili intihal, atıf manipülasyonu, sahte veri uydurma vb. suistimallerin tespit edilmesi halinde yayım ve etik ilkelerine göre davranılır. Bu durumda çalışmanın yayımlanmasını önlemek, yayımdan kaldırmak ya da başka işlemler yapmak için gerekli işlemler takip edilmektedir.

Dergimizde, kaynak gösteriminde uluslararası Vancouver sistemine geçilmiştir. Ayrıca dergimiz, Creative Commons ile lisanslanmak suretiyle dergimizde yayımlanan makalelerin paylaşımı, kaynak gösterimi ve yayımlanmasında dergi ve yazar haklarını korumaya almıştır. 2018 yılı güz döneminden itibaren makaleler, uluslararası yazar kimlik numarası ORCID No'su ile yayımlanmaktadır.

Dergi ekibi, dergimizin ulusal ve uluslararası indekslerce taranan bir dergi olması yönünde çalışmalarını titizlikle sürdürmektedir. Dergimize gösterilen ilgi bu yönde bizleri teşvik etmeye devam edecektir.

Bingöl Üniversitesi Fen Bilimleri Enstitüsü tarafından yayımlanmaktadır

EDİTÖRLER (YAYIN) KURULU

Prof. Dr. Zafer ŞİAR

Bingöl Üniversitesi, Fen-Edebiyat Fakültesi, Matematik Bölümü
E-Mail: zsiar@bingol.edu.tr

Prof. Dr. Uğur ÇAKILCIOĞLU

Munzur Üniversitesi, Pertek Sakine Genç Meslek Yüksekokulu, Bitki Morfolojisi ve Anatomisi Bölümü
E-Mail: ucakilcioglu@yahoo.com

Doç. Dr. Kamuran DİLSİZ

Bingöl Üniversitesi, Fen-Edebiyat Fakültesi, Fizik Bölümü
E-Mail: kdilsiz@bingol.edu.tr

Doç. Dr. Şükran KONCA

Bakırçay Üniversitesi, Mühendislik ve Mimarlık Fakültesi, Temel Bilimler, Matematik Bölümü
E-Mail: sukran.konca@bakircay.edu.tr

Doç. Dr. İdris YAZGAN

Kastamonu Üniversitesi, Fen Edebiyat Fakültesi, Biyoloji

E-Mail: idrisyazgan@gmail.com

Doç. Dr. Abdulcabbar YAVUZ

Gaziantep Üniversitesi, Mühendislik Fakültesi, Metalurji ve Malzeme Mühendisliği
E-Mail: ayavuz@gantep.edu.tr

Doç. Dr. Bünyamin ALIM

Bayburt Üniversitesi, Teknik Bilimler Meslek Yüksekokulu, Elektrik ve Enerji Bölümü
E-Mail: balim@bayburt.edu.tr

Doç. Dr. Mustafa Şükrü KURT

Erzurum Teknik Üniversitesi, Fen Fakültesi, Temel Bilimler
E-Mail: mustafa.kurt@erzurum.edu.tr

Doç. Dr. Sinan SAĞIR

Karamanoğlu Mehmetbey Üniversitesi, Fizik

E-Mail: sinansagir@kmu.edu.tr / sinan.sagir@cern.ch

Doç. Dr. Murat AYDEMİR

Erzurum Teknik Üniversitesi, Fen Fakültesi, Temel Bilimler

E-Mail: murat.aydemir@erzurum.edu.tr

Mühendislik Bilimleri

Prof. Dr. Figen KOREL

İzmir Yüksek Teknoloji Enstitüsü, Gıda Mühendisliği Bölümü
E-Mail: figenkorel@iyte.edu.tr

Prof. Dr. Kubilay ASLANTAŞ

Afyon Kocatepe Üniversitesi, Teknoloji Fakültesi, Makine Mühendisliği Bölümü
E-Mail: aslantas@aku.edu.tr

Prof. Dr. Hamit Özkan GÜLSOY

Marmara Üniversitesi, Teknoloji Fakültesi, Metalurji ve Malzeme Mühendisliği Bölümü
E-Mail: ogulsoy@marmara.edu.tr

Prof. Dr. Ali Adnan HAYALOĞLU

İnönü Üniversitesi, Mühendislik Fakültesi, Gıda Mühendisliği Bölümü
E-Mail: adnan.hayaloglu@inonu.edu.tr

Prof. Dr. Barbara SAWICKA

University of Life Sciences in Lublin, Department of Plant Production Technology and Commodities Sciences
E-Mail: barbara.sawicka@gmail.com

Prof. Dr. İbrahim GÜNEŞ

Giresun Üniversitesi, Mühendislik Fakültesi, İnşaat Mühendisliği Bölümü
E-Mail: ibrahim.gunes@giresun.edu.tr

Doç. Dr. Serhat ŞAP

Bingöl Üniversitesi, Teknik Bilimler Meslek Yüksekokulu, Elektrik ve Enerji Bölümü
E-Mail: ssap@bingol.edu.tr

Doç. Dr. Sırma YEĞİN

Ege Üniversitesi, Mühendislik Fakültesi, Gıda Mühendisliği Bölümü
E-Mail: sirma.yegin@ege.edu.tr

Doç. Dr. Hasan OĞUL

Sinop Üniversitesi, Mimarlık ve Mühendislik Fakültesi, Nükleer Enerji Mühendisliği
E-Mail: hogul@sinop.edu.tr

Doç. Dr. Murat YILMAZTEKİN

İnönü Üniversitesi, Mühendislik Fakültesi, Gıda Mühendisliği Bölümü
E-Mail: murat.yilmaztekin@inonu.edu.tr

Doç. Dr. Ferhat AYDIN

Sakarya Uygulamalı Bilimler Üniversitesi, Teknoloji Fakültesi, İnşaat Mühendisliği Bölümü
E-Mail: ferhata@subu.edu.tr

Dr. Öğr. Üyesi Nurullah DEMİR

Bingöl Üniversitesi, Mühendislik ve Mimarlık Fakültesi, Gıda Mühendisliği Bölümü
E-Mail: ndemir@bingol.edu.tr

Doç. Dr. Ahmet GÜNER

Bingöl Üniversitesi, Mühendislik ve Mimarlık Fakültesi, Elektrik ve Elektronik Mühendisliği Bölümü
E-Mail: aguner@bingol.edu.tr

Dr. Öğr. Üyesi Tahir AKGÜL

Sakarya Uygulamalı Bilimler Üniversitesi, Teknoloji Fakültesi, İnşaat Mühendisliği Bölümü
E-Mail: tahirakgul@subu.edu.tr

Dr. Erhan Sulejmani

University of Tetova, Faculty of Food Technology and Nutrition
E-Mail: erhan.sulejmani@unite.edu.mk

Dr. Hacène Medjoudj

Larbi Ben M'Hidi University of Oum El Bouaghi, Food Science Department
E-Mail: medjoudjh@yahoo.com

Dr. Avinash Lakshmikanthan

Nitte Meenakshi Institute of Technology, Department of Mechanical Engineering, Karnataka, India
E-Mail: avinash.laks01@gmail.com

Dr. Manjunath Patel GC

PES Institute of Technology and Management, Department of Mechanical Engineering, Karnataka, India
E-Mail: manju09mpm05@gmail.com

Sağlık Bilimleri

Doç. Dr. Aydın Şükrü BENGÜ

Bingöl Üniversitesi, Sağlık Hizmetleri Meslek Yüksekokulu, Tıbbi Hizmetler ve Teknikler
E-Mail: abengu@bingol.edu.tr

Dr. Öğr. Üyesi Dilhun Keriman ARSERİM UÇAR

Bingöl Üniversitesi, Sağlık Bilimleri Fakültesi, Beslenme ve Diyetetik Bölümü
E-Mail: dkucar@bingol.edu.tr

Dr. Öğr. Üyesi Abdullah TUNÇ

Bingöl Üniversitesi, Sağlık Bilimleri Fakültesi, İş Sağlığı ve Güvenliği Bölümü
E-Mail: atunc@bingol.edu.tr

Dr. Öğr. Üyesi Ramazan GÜNDOĞDU

Bingöl Üniversitesi, Sağlık Hizmetleri Meslek Yüksekokulu, Eczane Hizmetleri
E-Mail: rgundogdu@bingol.edu.tr

Dr. Alexander HERGOVICH

UCL Cancer Institute, Faculty of Medical Sciences, Department of Cancer Biology, UCL, London, UK
E-Mail: a.hergovich@uc.ac.uk

Dr. Valenti GOMEZ

UCL Cancer Institute, Faculty of Medical Sciences, Department of Oncology, UCL, London, UK
E-Mail: valentin.gomez@ucl.ac.uk

Veterinerlik Bilimleri

Prof. Dr. Fatih Mehmet KANDEMİR

Atatürk Üniversitesi, Veteriner Fakültesi, Veteriner Hekimliği Temel Bilimler
E-Mail: fmehmet.kandemir@atauni.edu.tr

Doç. Dr. Akın KIRBAŞ

Bozok Üniversitesi, Veteriner Fakültesi, Klinik Bilimler Bölümü
E-Mail: akindahiliye55@yahoo.com

Doç. Dr. Emrah Hicazi AKSU

Atatürk Üniversitesi, Veteriner Fakültesi, Klinik Bilimler Bölümü
E-Mail: emrahaksu@atauni.edu.tr

Ziraat Bilimleri

Doç. Dr. Zeynep DUMANOĞLU

Bingöl Üniversitesi, Ziraat Fakültesi, Biyosistem Mühendisliği Bölümü
E-Mail: zdumanoglu@bingol.edu.tr

Prof. Dr. Kağan KÖKTEN

Bingöl Üniversitesi, Ziraat Fakültesi, Tarla Bitkileri Bölümü
E-Mail: kahafe1974@yahoo.com

Prof. Dr. Mustafa SÜRMEN

Adnan Menderes Üniversitesi, Ziraat Fakültesi, Tarla Bitkileri Bölümü
E-Mail: mustafa.surmen@adu.edu.tr

Prof. Dr. Banu YÜCEL

Ege Üniversitesi, Ziraat Fakültesi, Hayvan Yetiştirme Anabilim Dalı, Zootekni Bölümü
E-Mail: banu.yucel@ege.edu.tr

Prof. Dr. Hakan İNCİ

Bingöl Üniversitesi, Ziraat Fakültesi, Zootekni Bölümü
E-Mail: hinci@bingol.edu.tr

TEKNİK EDİTÖRLER

Dr. Nimetullah KORKUT

Bingöl Üniversitesi, BİNUZEM, Bilgisayar Teknolojileri
E-Mail: nkorkut@bingol.edu.tr

DİL EDİTÖRÜ

Dr. Öğr. Üyesi Ahmet KESMEZ
Bingöl Üniversitesi, Yabancı Diller Yüksekokulu, İngilizce Bölümü
E-Mail: akesmez@bingol.edu.tr

BİNGÖL ÜNİVERSİTESİ

Türk Doğa ve Fen Dergisi
Turkish Journal of Nature and Scienc
www.dergipark.gov.tr/tdfd

CONTENTS

Volume 14, Issue 2, Page 1-10, 2025 https://doi.org/10.46810/tdfd.1570735 Research Article

BİNGÖL UNIVERSITY

Türk Doğa ve Fen Dergisi
Turkish Journal of Nature and Science

www.dergipark.gov.tr/tdfd

Two Approaches For Solving Nonlinear Equation Systems: Newton Raphson and Red Fox

Bayram KÖSE [1], Bahar DEMİRTÜRK [2*], Şükran KONCA [3]

[1] Izmir Bakırçay University, Faculty of Engineering and Architecture, Department of Electrical and Electronics Engineering, 35660 Menemen, İzmir, Türkiye
[2,3] Izmir Bakırçay University, Faculty of Engineering and Architecture, Department of Fundamental Sciences, 35660 Menemen, İzmir, Türkiye
Bayram KÖSE ORCID No: 0000-0003-0256-5921
Bahar DEMİRTÜRK ORCID No: 0000-0002-5911-5190
Şükran KONCA ORCID No: 0000-0003-4019-958X

**Corresponding author: bahar.demirturk@bakircay.edu.tr*

(Received: 20.10.2024, Accepted: 27.02.2025, Online Publication: 27.06.2025)

Keywords
Root finding,
Nonlinear systems of equations,
Optimization algorithms,
Newton Raphson algorithm,
Red fox algorithm

Abstract: In this study, the results obtained by using the Red Fox method, a new metaheuristic optimization method, and the Newton Raphson method, which is one of the numerical methods, in finding the solutions of nonlinear systems of equations, are compared and these comparative analyses are evaluated and recommendations are presented.

Doğrusal Olmayan Denklem Sistemlerini Çözmek İçin İki Yaklaşım: Newton Raphson ve Kızıl Tilki

Anahtar Kelimeler
Kök bulma,
Doğrusal olmayan denklem sistemleri,
Optimizasyon algoritmaları,
Newton Raphson algoritması,
Kızıl tilki algoritması

Öz: Bu çalışmada, doğrusal olmayan denklem sistemlerinin çözümlerini bulmak için yeni bir meta sezgisel optimizasyon yöntemi olan kızıl tilki yöntemi ile sayısal yöntemlerden biri olan Newton Raphson yöntemi kullanılarak elde edilen sonuçlar karşılaştırılmış, bu karşılaştırmalı analizler değerlendirilmiş ve öneriler sunulmuştur.

1. INTRODUCTION

Many engineering problems cover a wide range of topics that require modelling and analysis of complex systems. These models involve many variables and the relationships between them. These relationships may not always be linear. Nonlinear systems of equations are quite common in engineering problems and appear in many fields such as experimental design, manufacturing optimization, materials science, heat transfer, fluid mechanics, control systems, etc.

The roots of these equations are critical for solving the problem. For example, to determine the optimum conditions of a chemical reaction, it is necessary to find the roots of a nonlinear system of equations representing the rate of reaction or the design of a heat exchanger requires the solution of a nonlinear system of equations modelling heat transfer [1].

Engineering problems often involve systems of nonlinear equations. In experimental design, production and development phases, the root of these equations gives important information for decision making. The methods used for solving engineering problems should be chosen depending on the specific nature and complexity of the problem.

Solutions of systems of nonlinear equations can be more complex than solutions of linear equations. This is because analytical solutions of nonlinear equations are not always possible and numerical methods or metaheuristic optimization techniques are needed to solve these problems. Analytical methods, graphical methods, numerical methods, simulation and optimization techniques, software and computational tools are widely used to solve such systems. Numerical methods, which are widely used for solving systems of nonlinear equations, are usually iterative techniques and are used to calculate approximate values of the solution when the

solution cannot be expressed by an exact formula. The most widely used of these numerical methods is the Newton Raphson method. Metaheuristics are also powerful approaches that can be very effective in solving systems of nonlinear equations. These methods are generally developed for optimization problems and are known for their ability to find global solutions in complex and multidimensional solution spaces. The most widely used metaheuristics are genetic algorithms, particle swarm optimization, simulated annealing, tabu search, differential growth algorithm, etc.

When simulating and analysing aircraft motion in flight, a nonlinear model with appropriate initial conditions is used. Millidere et al. [2] used classical Newton Raphson method to solve a nonlinear system of algebraic equations to find the trim condition, a point at which the aircraft flight conditions should not change abruptly.

Gower et al. [3] proposed a new randomised method for solving systems of nonlinear equations by taking the gradients of the component functions and using Bregman projections onto the solution space of a Newton equation, which can find sparse solutions or solutions under certain simple constraints.

Pourrajabian et al. [4] solved three different nonlinear algebraic equation systems, a single nonlinear equation, a simple set of nonlinear equations and a complex set of nonlinear equations by using genetic algorithms.

Kotsireas et al. [5] gave a synthesis of the literature on the solution of systems of nonlinear equations and they aimed to assist interested readers who wish to identify appropriate solution techniques for solving various systems of nonlinear equations that may be encountered in real-world applications. Moreover, Odan [6] investigates the effectiveness of Genetic Algorithms in solving both linear and nonlinear systems of equations and compares their performance with conventional methods such as Gaussian Elimination, Newton's Method and Levenberg-Marquardt. Verma and Parouha [7] presented an innovative hybrid algorithm of Particle Swarm Optimization Algorithm and Evolutionary Algorithms to find the solution of nonlinear equation systems.

There are many problems raised in Chapra's book that have attracted the attention of researchers from many different disciplines. For example, the torsional buckling problem of open constant bisymmetric cross section constrained thin-walled bars was solved by the Newton Raphson method in [8] and it attracted the attention of Kujawa [9]. Also, a problem given by Chapra and Canale in [8] given by the equation governing the L-C-R circuit in electrical engineering is considered by Sharma et al. in [10].

Chapra and Canale [8] found approximate solutions to a system of nonlinear equations using the fixed-point iteration method, a derivative-free root-finding method and the Newton Raphson method, a derivative root-finding method. From this point of view, in this study, the Red Fox method, a metaheuristic optimization method, is used to find the solutions of the given system of nonlinear equations and the results are compared with the Newton Raphson method. The original aspect of this study is the use of a new metaheuristic method, the Red Fox search algorithm, in solving a nonlinear system of equations and comparing it with a numerical method, the Newton Raphson method, and presenting the evaluated results and recommendations.

2. SYSTEMS OF NONLINEAR EQUATIONS

A linear equation, for $1 \le i \le n$ and with a_i, b constants, can be defined in general form $f(x) = a_1x_1 + a_2x_2 + ... + a_nx_n - b = 0$. The solution of this linear equation is $x = (x_1, x_2, ..., x_n)$. The solution of the system of equations,

$$\begin{aligned} f_1(x_1, x_2, ..., x_n) &= 0 \\ f_2(x_1, x_2, ..., x_n) &= 0 \\ &\vdots \\ f_n(x_1, x_2, ..., x_n) &= 0 \end{aligned} \tag{1}$$

consisting of *n* equations and *n* unknowns can be defined as finding the value $x = (x_1, x_2, ..., x_n)$ of all equations at the same time, which results in all equations being equal to zero [8].

Equations that do not obey the form $f(x) = a_1x_1 + a_2x_2 + ... + a_nx_n - b = 0$ are called nonlinear equations.

Example. The equations $x^2 + xy = 10$ and $y + 3xy^2 = 57$ are nonlinear equations with two unknowns. These equations can also be expressed in the form

$$\begin{aligned} u(x, y) &= x^2 + xy - 10 = 0 \\ v(x, y) &= y + 3xy^2 - 57 = 0. \end{aligned} \tag{2}$$

Therefore, the solution will be the values of *x* and *y* that set the functions *u(x, y)* and *v(x, y)* equal to zero. Most of the approaches used to find such solutions are extensions of explicit methods for solving single equations. In [8], Chapra and Canale considered two of these methods, fixed point iteration and Newton Raphson methods, to find the solution of the system of equations given in (1).

In this study, the solutions of the system of equations given by (1) are found by using the Newton Raphson method from numerical methods and the Red Fox optimization method from metaheuristics methods and the results obtained are compared.

3. METHODS

In this section, the Newton Raphson method, the most widely used numerical method, and the Red Fox Optimization algorithm, one of the metaheuristics, will be discussed.

Numerical methods are highly effective tools that are frequently used in solving systems of nonlinear equations. These methods combine mathematical and computer science tools to provide solutions to complex problems for which analytical solutions cannot be obtained. Numerical methods, which usually follow an iterative approach, aim to obtain approximate values by approaching the solution step by step. Powerful approaches such as metaheuristics are used to solve engineering problems that cannot be solved by analytical methods. Metaheuristic algorithms used in solving optimization problems aim to reach the best solution with heuristic approaches. These algorithms are used with mathematical optimization algorithms. While mathematical optimization algorithms aim to reach a solution by scanning the entire solution set, metaheuristic optimization algorithms aim to reach the best solution or a near-optimal solution through heuristic approaches. The performance of these algorithms can vary depending on the problem type and test functions. They usually consist of models inspired by nature and mimicking the behavior of biological systems.

3.1. Newton Raphson Algorithm

The Newton Raphson method, which has a very fast convergence rate, is one of the most popular numerical methods that iteratively approaches the solution using derivative information and provides an efficient solution. This method uses the values of the function and the derivative function to generate a new point closer to the solution at each iteration. Although the method has some limitations, it provides a practical and reliable solution to many problems in terms of computational efficiency.

Select an arbitrary value x_n and calculate the value of $f(x_n)$ corresponding to this point. After this point, a tangent is drawn to the function at the point $(x_n, f(x_n))$. The point where the tangent crosses the x-axis is taken as the new value x_{n+1} and the same procedure is applied for x_{n+1}.

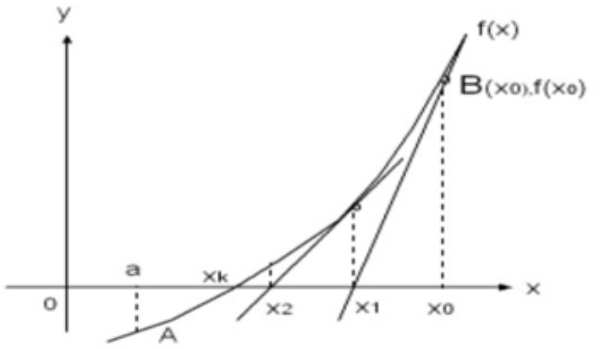

Figure 1. Newton Raphson method

The Newton Raphson method is based on the following iterative formula for algebraic equations in one variable:

$$x_{n+1} = x_n - \frac{f(x_n)}{f'(x_n)}.$$

The formula for systems of equations in two variables is given as follows:

$$\begin{bmatrix} x_1 \\ y_1 \end{bmatrix} = \begin{bmatrix} x_0 \\ y_0 \end{bmatrix} - \begin{bmatrix} \frac{\partial f_1}{\partial x} & \frac{\partial f_1}{\partial y} \\ \frac{\partial f_2}{\partial x} & \frac{\partial f_2}{\partial y} \end{bmatrix}^{-1}_{(x_0, y_0)} \cdot \begin{bmatrix} f_1 \\ f_2 \end{bmatrix}_{(x_0, y_0)}$$

The convergence rate of the Newton Raphson method shows a quadratic convergence rate. This means that with each iteration the distance to the solution decreases quadratically. This property makes the method very fast and efficient. This is also the reason why Newton Raphson is used in calculators that can perform solutions. Only one starting point needs to be chosen instead of an interval as in the bisection method. The success of the Newton Raphson method depends on the choice of this starting point. If the starting point is not chosen close enough to the solution, the method may not converge or may reach an incorrect solution. Therefore, it is important to determine a suitable starting point before applying the method.

The Newton Raphson method may not give the desired result in some cases, because of some limitations of the method. The function and derivative function must be continuous and differentiable. From the quotient expression in the denominator, division by zero can be a problem when the derivative is zero. This is since the tangent is parallel to the x-axis and does not intersect the x-axis at some point and cannot determine the new x-value. The starting point should be chosen close enough to the solution. If the solution has more than one root, the method may not always converge to the desired root or may only converge to a single root. In addition, the function may have problems such as oscillating around the root and accidentally missing the root [11]. The flowchart of Newton Raphson method can be given as follows:

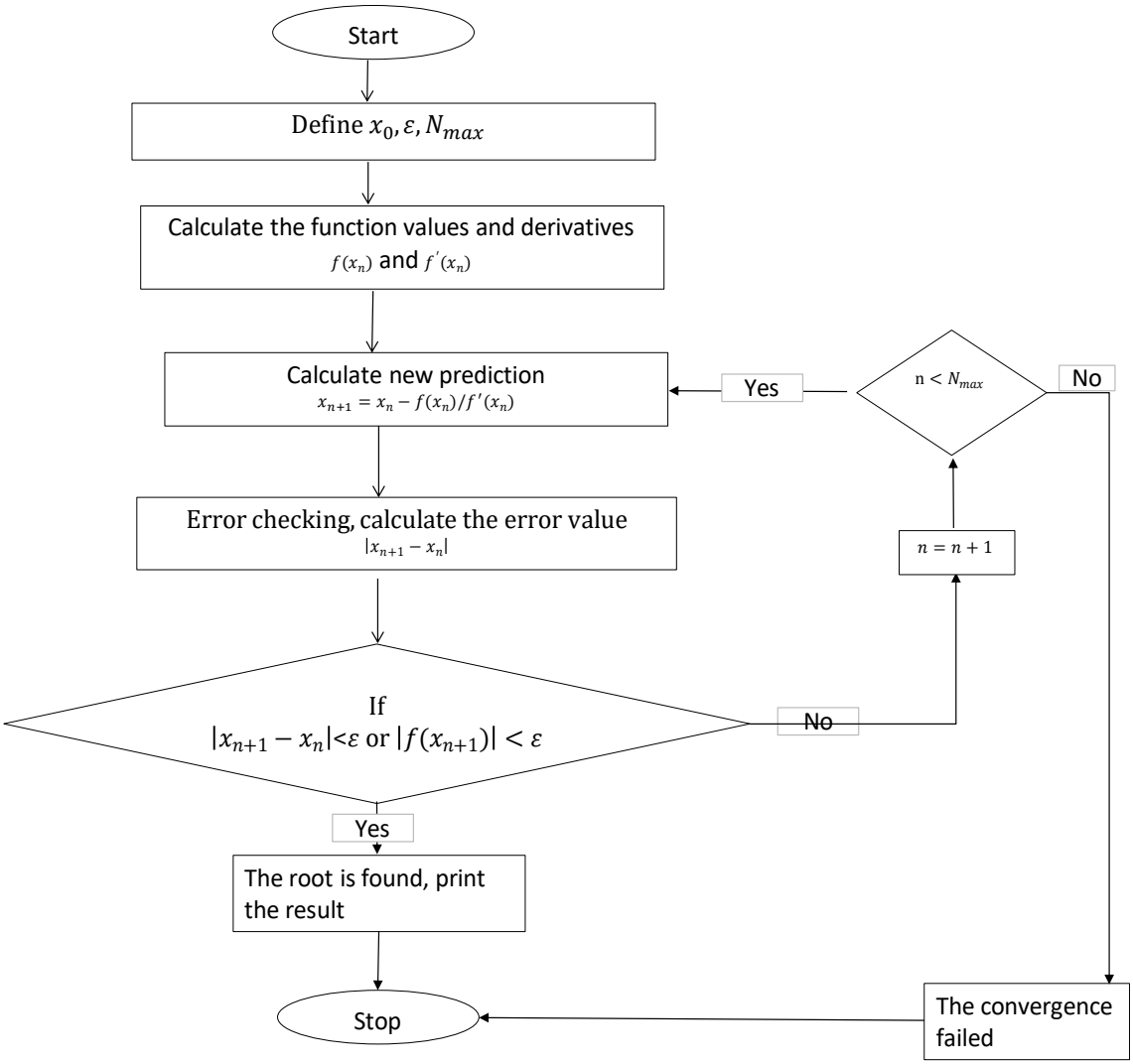

Figure 2. The flowchart of Newton Raphson method

3.2. Red Fox Optimization Algorithm

The advantages of metaheuristics include their applicability to complex and multidimensional problems where analytical methods are inadequate; their potential to find the global solution without getting stuck in the local optimum; and their stochastic nature, which allows them to produce different solutions in different runs. This can help to explore different aspects of the problem and increase the chances of finding the best solution. The Red Fox Algorithm is inspired by the hunting and herding behaviour of red foxes. The algorithm aims to find solutions to optimization problems by using concepts such as predator-prey relationship and within-pack hierarchy. In this section, the Red Fox Optimization Algorithm developed by Połap and Woźniak [12] based on the mathematical model of red fox habits, foraging, hunting and population is described in detail.

The Red Fox Algorithm is inspired by complex behaviours in nature. This gives the algorithm robustness and flexibility. The Red Fox Algorithm has the potential to find the global solution without getting stuck in the local optimum.

A population of red foxes consists of individuals living in specific territories and leading a nomadic life [13]. Each pack shares a single territory under the hierarchy of the alpha pair. When youngsters grow up, they can leave the pack and start their own pack if they have a good chance of taking over another territory. Otherwise, they stay in the family and one day take over the hunting grounds from their parents. The red fox is an effective predator of small animals, both domestic and wild animals. Foxes look for food at every opportunity as they roam the territory, sneaking up on their prey and hiding until they get close enough for an effective attack. This algorithm models foraging as global search, where foxes explore the area while their prey is away. In the second stage, roaming the habitat to get as close as possible before hunting is modelled as local search [14]. The conceptual model of this hunting behavior of the fox is shown in Figure 3.

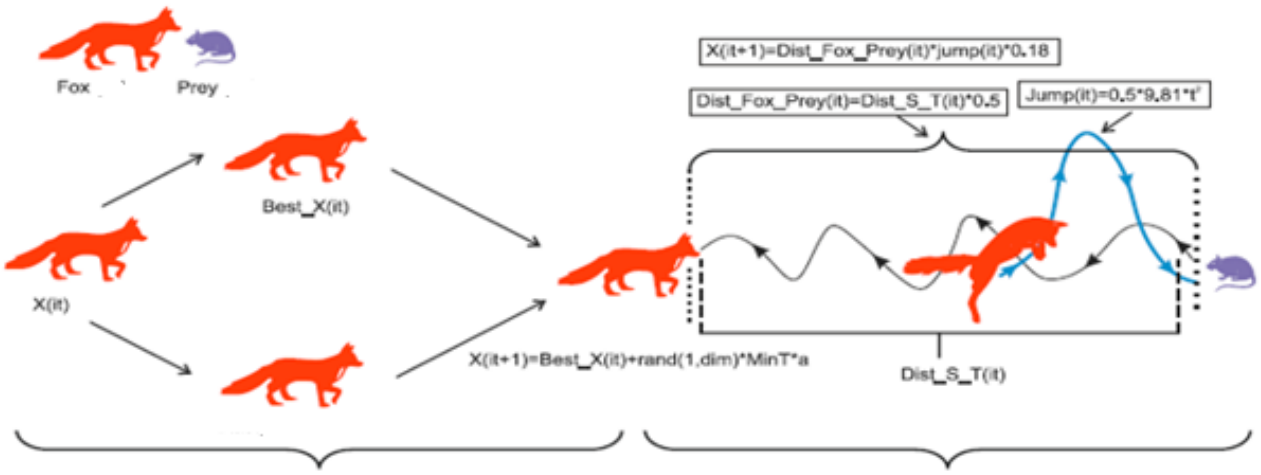

Figure 3. Red fox predation impact: reproduction and exploitation [14]

The red fox algorithm mimics the hunting behavior of the red fox as it dives under the snow to catch its prey. The basic techniques are based on the red fox trying to catch the best prey. The steps of red fox behavior are described below:

1. When snow covers the ground, the snow blocks the sight of the prey. The red fox tries to search for prey randomly.
2. The red fox finds the prey by hearing the ultrasound sound of the prey. However, it takes time for the fox to get close to the prey.
3. By listening to the sound of the prey and calculating the time difference, the red fox can determine the distance between itself and the prey.
4. After determining the distance, the red fox estimates the jumping distance needed to catch prey.
5. The walking process is randomized according to the minimum time and the best position.

Initially, the red fox moves randomly in the search space to discover the prey. This random movement is used to provide exploratory behavior. While searching, the red fox can hear the prey. Upon hearing the sound, the red fox enters the exploitation phase. It takes time for the sound of prey to reach the fox. The distance the sound travel can be calculated by multiplying the speed of sound in air by 343 m/s. The red fox tries to move forward to catch the prey according to the reception of the sound and decides to jump on the prey and tries to jump depending on the time it takes for the sound to be received. Červený et al. [15] showed that the fox prefers to jump in the northeast direction based on the magnetic alignment effect. In the study, it was found that the fox had an 82% chance of catching prey when jumping in the northeast direction, while it had an 18% chance of catching prey when jumping in the opposite direction.

The basic algorithm proposition assumes that at each iteration, individuals consist of a fixed number of foxes. Each is represented as a point with n coordinates $x = (x_0, x_1, \ldots, x_{n-1})$. Each fox is distinguished by the notation $((x_i^j)_t)$ at iteration t, where i is the number of foxes in the population and j is the coordinate with respect to the dimensions of the solution space. Foxes are assumed to search for solutions in the criterion function for optimal values.

In Search of Food - Global Search Phase: In a pack, each fox needs to play an important role for the survival of all family members. When food is not available in local habitats or to explore other territories, pack members travel to distant destinations. They share the knowledge they gain from this exploration with the family.

Roaming Local Habitat - Local Search Phase: The red fox roams its territory looking for potential prey. When it sees a possible prey, the fox begins to sneak up on it to get as close as possible without being noticed. Therefore, it circles and deceives the prey to trick it and convince it that the prey is not interested in it.

Reproduction and Pack Separation: In the wild, the red fox faces many dangers. There may be no food in the local habitat area, so it may be necessary to move elsewhere. Another danger comes from humans. If there are large losses in the pet population, people may hunt the fox.
To model these behaviors, in each iteration we select the worst 5% of the population according to the criterion function value. This is assumed to be foxes that leave the pack or are shot by hunters. To keep the number of individuals in the population constant, we replace them with new individuals using the habitat territory established by the alpha pair.

In this work, we define the number of foxes numFoxes = 40, maximum iterations numIterations = 100, lower limits lb = [0, 0], upper limits ub = [15, 15], size nVar = length(ub), to identify the worst 5% foxes alpha_fraction = 0.05, Alpha pair reproduction threshold is 0.44, $c_1 = 0.18$ and $c_2 = 0.82$, p variable is selected by the interval [0,1] randomly, and a random variable r is used to balance the exploration and exploitation phases.

The following parameters are taken and the steps below are followed in the flowchart of Red Fox Algorithm given by Figure 4.

$X_{(it+1)}$: The new position of the red fox after jumping,

$BestX_{it}$: The best solution ever found,

$rand(1,\text{dimension})$: Value used to allow the fox to discover prey by random walking,

$MinT$: Minimum time variable,

a : A value to reduce the search performance based on $BestX_{it}$ value,

$Dist\_Fox\_Prey_{it}$: Distance of the red fox from the prey,

$Jump_{it}$: The jumping value of red fox.

Th following parameters are taken and the steps below are followed in the flowchart of Red Fox Algorithm, given in Figure 4.

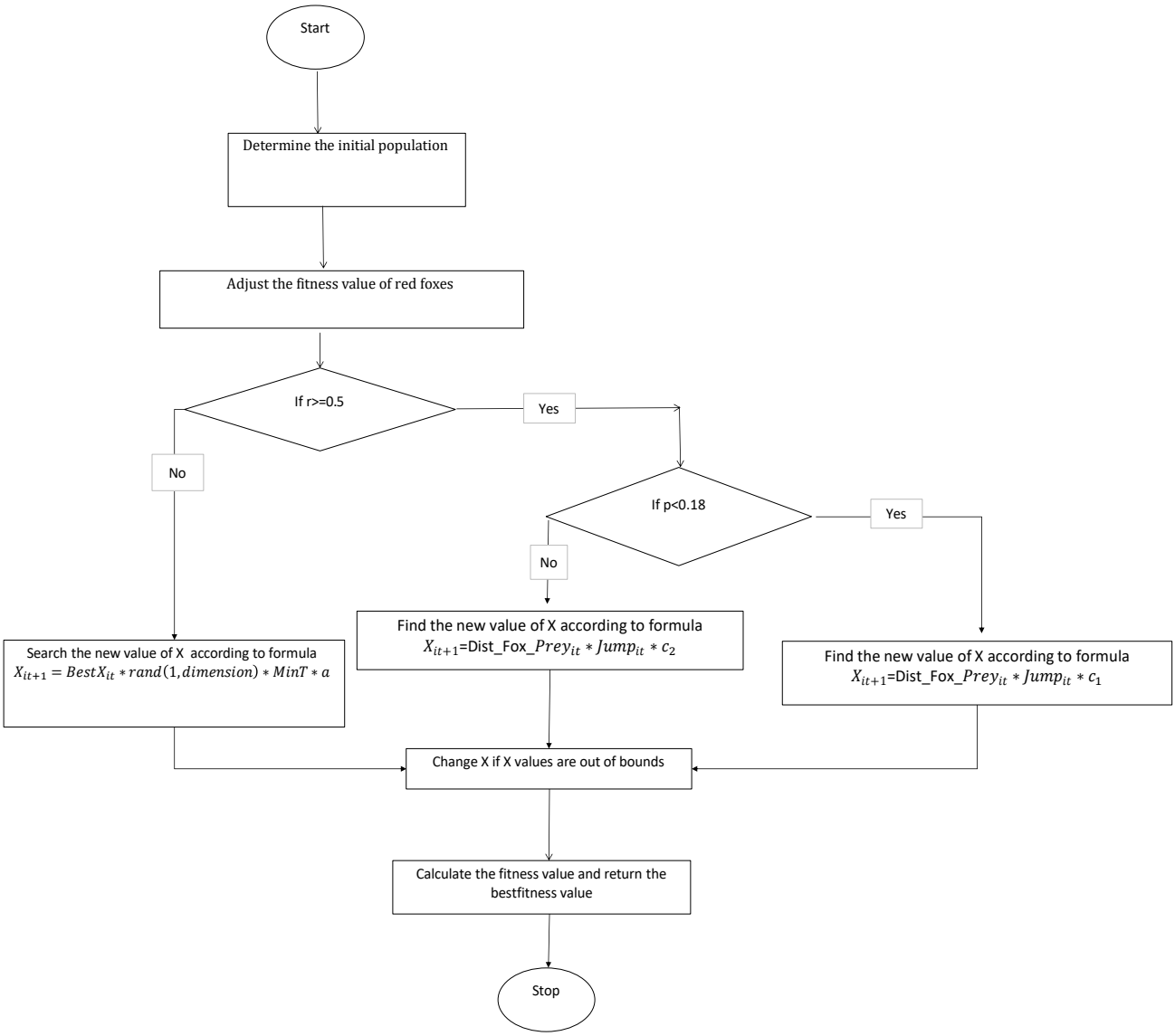

Figure 4. The flowchart of Red Fox Algorithm [16]

3.3. Optimization Approach for Finding the Roots

When the optimization process is used to find the roots of algebraic equations, the problem of finding the unknown values in each equation becomes an optimization problem to be solved by numerical methods. Optimization is the process of obtaining the best value of an objective function according to specified criteria. Since the numerical approach to finding roots in algebraic equations usually involves an iterative process, similarly, in finding roots with an optimization algorithm, starting from a given starting point, candidate root values are iteratively updated and reach a minimum or maximum value when the objective function is sufficiently close or a certain tolerance value is reached.

As an explicit consequence of Intermediate Value, Bolzano and Extreme Value Theorems which are known from classical Mathematical Analysis, we can give Theorem 3.3.1. Moreover, we will give Theorem 3.3.2 as a generalization of Theorem 3.3.1 for equations in one variable for finding roots in algebraic equations.

Theorem 3.3.1. (Root Search in Optimization Algorithm)

Let $I=[a,b]$ and $I\subset\square$. If the function $f:I\to R$ is continuous, then it has at least one minimum on this interval and if $|f(x_i)|=0$ then there exists at least one $x_i\in I,\ (i\in N)$ satisfying this equality (Köse et al., [17]).

Theorem 3.3.2. (Root Finding Algorithm for Nonlinear Equation Systems)

Let $I=[a,b]$ and $I\subset\square$. If the functions $f_i:I^n\to\square$ are continuous, then for each $1\le i\le n$ the functions f_i have at least one minimum value in this interval and have at least one point $x=(x_1,x_2,...,x_n)\in I$ that satisfies the equality $\sum_{i=1}^{n}\left|f_i(x_i)\right|=0$ (Köse et al., [17]).

4. PERFORMANCE EVALUATION AND ANALYSIS

In this section, the analysis of performance of two methods for approaching the roots is given. Firstly, we can examine the approximation graphics of Newton Raphson and Red Fox methods in Figure 5 for the first case.

As seen from Figure 5 (a), with Newton Raphson Method, in the initial iterations, large oscillations towards the solution point are observed. By the 15th iteration, the solution is quite close to the root, but the errors have not completely vanished. This case demonstrates that the Newton Raphson method is sensitive to the initial point and may not converge quickly if the starting value is far from the true root. Regardless of the number of iterations, it always finds the true root in the given nonlinear equation system. However, a poor initial guess can significantly increase the number of iterations required.

Unlike Newton Raphson Method, the Red Fox algorithm does not rely on the initial point and explores a wide search space. In the early iterations, a random search process is observed, while by the 85th iteration, it has approached the root significantly, as seen from Figure 5 (b). Also, it exhibits a more stable convergence pattern, which allows it to find a solution even in cases where the Newton Raphson method struggles. However, it requires more iterations and its convergence is irregular, which can be a disadvantage.

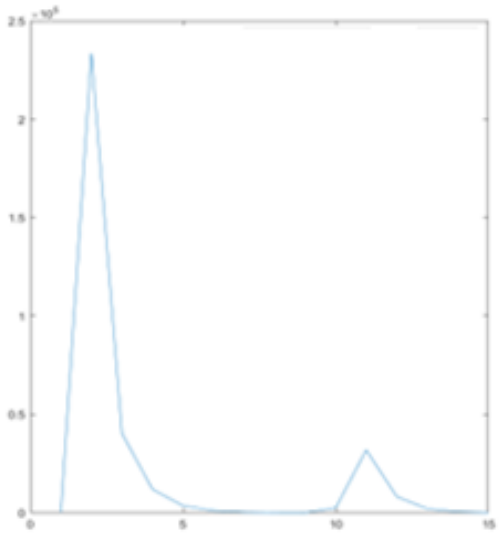

Figure 5. (a) The approximation graphic of Newton Raphson method for the initial values (x,y)=(8,0) case

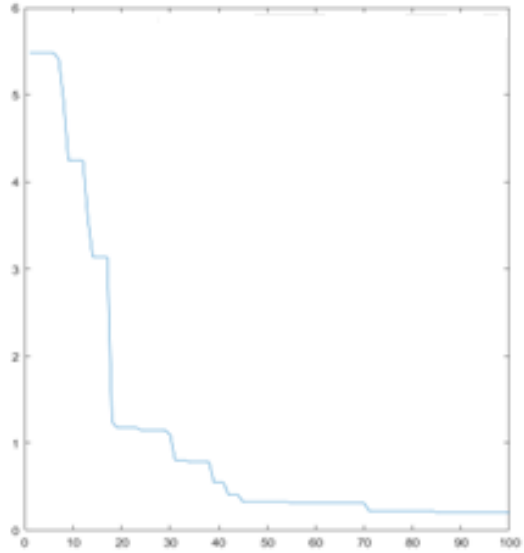

Figure 5. (b) The approximation graphics of Red Fox methods for (x-best,y-best)=(2.6963,2.6200) location case

Now we can give the approximation graphics of Newton Raphson and Red Fox methods in Figure 6 for the second case.

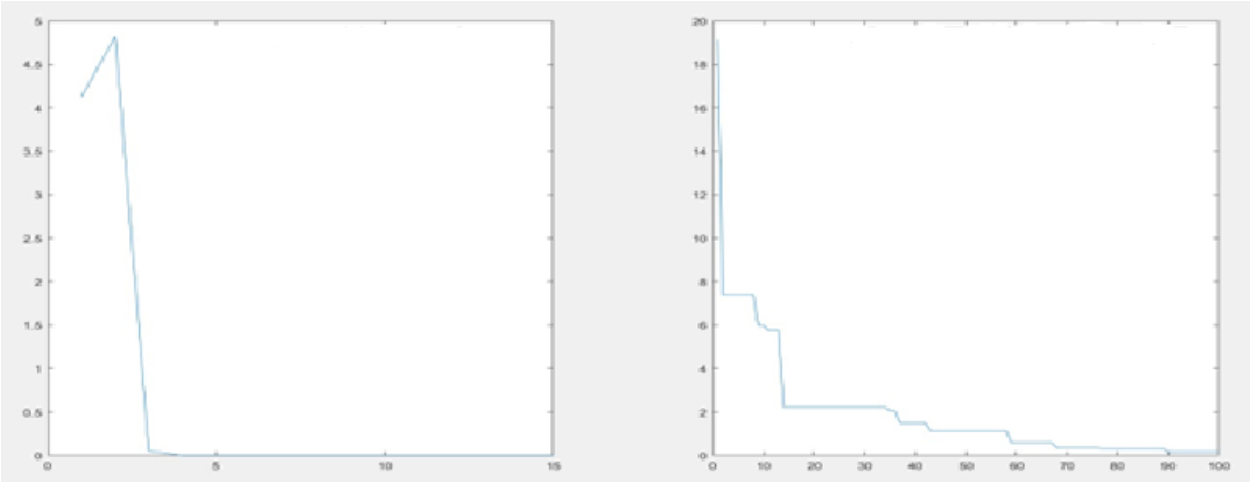

(a) **(b)**

Figure 6. (a) The approximation graphic of Newton Raphson method for the initial values *(x,y)=(1.5,3.5)* case
(b) The approximation graphic of Red Fox methods for (x-best,y-best)= (0.5,6.2403) location case.

In Case 2, given in Figure 6 (a), with the Newton Raphson Method, a more stable convergence is observed from the 3rd iteration. The errors are significantly reduced and in the 4th iteration, the root is found exactly. Since the initial point is close to the true root, the Newton Raphson method quickly reaches the solution. This case highlights the efficiency of Newton Raphson when a good initial guess is chosen, as it converges much faster than in Case 1.

As seen from Figure 6 (b), with the Red Fox Algorithm, a broad search process is observed in the initial iterations, but the solution is not fully reached until the 86th iteration. Although it eventually gets very close to the root, the convergence is much slower compared to Newton Raphson. In this case, Newton Raphson performs significantly better, as it reaches the solution in just four iterations. While the Red Fox algorithm has the advantage of not depending on the initial point, it requires more time to converge in this scenario.

Finally, we can give the approximation graphics of Newton Raphson and Red Fox methods in Figure 7 for the third case.

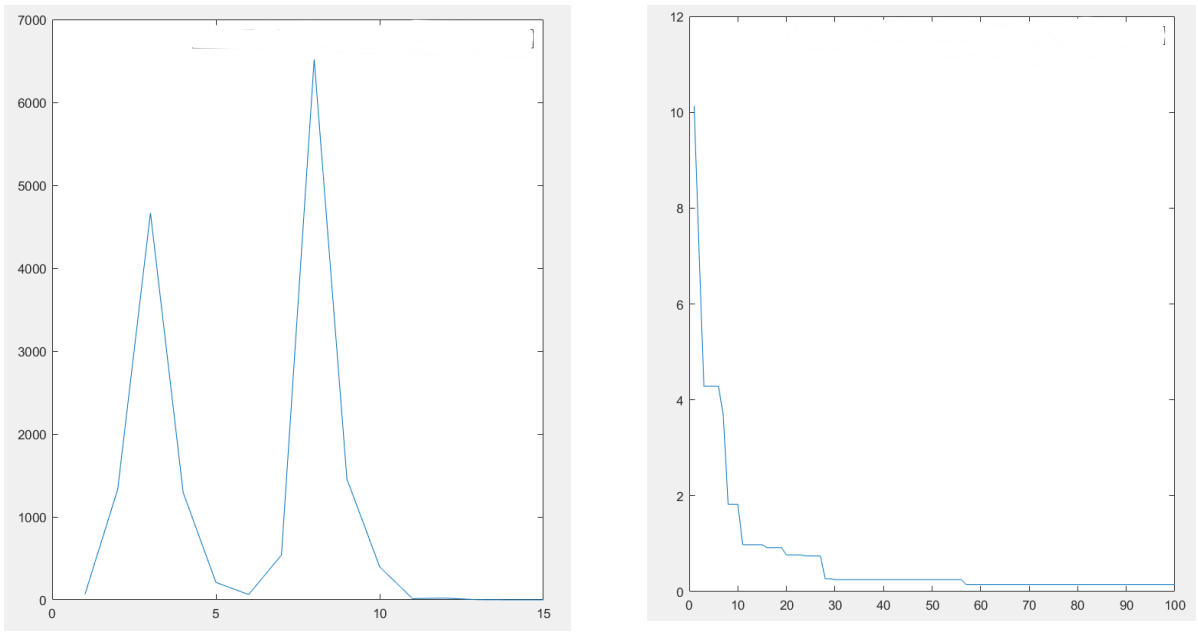

(a) **(b)**

Figure 7. (a) The approximation graphic of Newton Raphson method for the initial values (x,y)=(0.5,0.5) case
(b) The approximation graphic of and Red Fox methods for (x-best,y-best)= (0.5291, 5.3180) case.

In Case 3 given by Figure 7 (a), with the Newton Raphson Method, large errors and an unstable convergence process are observed in the first iterations. The true root is not fully reached until the 13th iteration, and only in the 15th iteration does it fully converge. Since the initial point is far from the root, the method requires more iterations to converge. The error rate is very high at the beginning, but as the iterations progress, it stabilizes and approaches the correct root.

In Case 3, given by Figure 7 (b), with the Red Fox Algorithm, a broad search process continues in the initial iterations, but by the 63rd iteration, the solution is significantly approached. The Red Fox method performs

better in cases where Newton Raphson struggles. However, it again requires more iterations than Newton Raphson and shows a slower convergence rate. In this case, Red Fox has an advantage because it does not require derivative information, but when Newton Raphson is applied correctly, it converges in fewer iterations and is more efficient.

Moreover, the roots and errors obtained by Newton Raphson and red Fox methods can be seen in Table 1, for three cases.

Table 1. The roots and errors of Newton Raphson and Red Fox Methods

Newton Raphson Method						Red Fox Method				
Initial Values (x, y)	**Iteration Number**	**x**	**y**	**Error of x**	**Error of y**	**(x-best, y-best) location**	**x-best**	**y-best**	**Error of x**	**Error of y**
(8,0) case	1	8.000	0.000	6.000	3.000	(2.6963, 2.6200)	2.6963	2.6200	0,6963	0,38
	5	3.500	4.200	2.500	1.800		2.5000	3.5000	0,5	0,5
	10	2.000	5.500	1.000	1.500		2.1000	3.9000	0,1	0,9
	15	**1.334**	**6.636**	**0.666**	**3.636**		2.0100	3.7500	0,01	0,75
	50	1.334	6.636	0.666	3.636		2.0000	3.2000	0	0,2
	85	1.334	6.636	0.666	3.636		**1.9639**	**3.0269**	**0,0361**	**0,0269**
(1.5,3.5) case	1	1.500	3.500	0.500	0.500	(0.5, 6.2403)	0.5000	6.2403	1,5	3,2403
	2	1.800	3.200	0.200	0.300		0.8000	5.5000	1,2	2,5
	3	1.9987	3.0023	0.0013	0.0023		1.2000	4.7000	0,8	1,7
	4	**2.000**	**3.000**	**0.000**	**0.000**		1.7500	2.7800	0,25	0,22
	50	2.000	3.000	0.000	0.000		1.9990	3.0010	0,001	0,001
	86	2.000	3.000	0.000	0.000		**1.9994**	**3.0003**	**0,0006**	**0,0003**
(0.5,0.5) case	1	0.500	0.500	1.500	2.500	(0.5291, 5.3180)	0.5291	5.3180	1,9999	2,318
	3	1.000	1.500	1.000	1.500		1.1000	4.0000	0,9	1
	6	1.400	0.500	0.600	2.500		1.5000	3.5000	0,5	0,5
	10	1.800	2.100	0.200	0.900		1.9000	3.2000	0,1	0,2
	13	2.000	3.100	0.000	0.100		1.9600	3.1250	0,04	0,125
	15	**2.000**	**3.000**	**0.000**	**0.000**		1.9100	3.100	0,09	2,69
	63	2.000	3.000	0.000	0.000		**2.0044**	**2.9967**	**0,0044**	**0,0033**

When these three graphs are analyzed, it is seen that in the Newton Raphson method, one of the numerical methods, when the starting point is far from the true root, the graphs oscillate a lot and almost find the true root around the 15th iteration. This supports the assertion that "the starting point should be chosen close enough to the solution", which is one of the constraints in the Newton Raphson method mentioned earlier. No matter how many iterations it takes, it always finds the true root in the nonlinear equation system we considered.

In the Red Fox method, it is observed that the approach to the true root occurs at different iteration numbers regardless of the initial positions. No regular relationship was observed between the initial position and the number of iterations to approach the true root. However, this metaheuristic shows that it is a preferable method as it produces results very close to the true root where the Newton Raphson method gets stuck. The problem was obtained by running the MATLAB program with the other parameters given above up to a maximum of 100 iterations with 40 foxes. It was observed that as the parameters such as the number of populations, maximum number of iterations, initial positions, etc. were changed, the number of steps we approached the true root varied.

5. CONCLUSIONS AND RECOMMENDATIONS

From the performance results obtained above, it can be said that metaheuristic methods as well as the Newton Raphson method, which is a mathematical optimization method, are powerful approaches that can be very effective in solving systems of nonlinear equations.

Since the Newton Raphson method relies on derivative information, it can provide rapid convergence. However, when the initial point is not chosen appropriately, significant oscillations may occur, leading to delays in convergence. Particularly, when the initial point is far from the true root, the convergence process slows down, and the number of iterations increases. Nevertheless, when an appropriate initial point is selected, the Newton Raphson method quickly finds the solution.

On the other hand, the Red Fox algorithm offers a global search capability as it does not depend on the initial point. This algorithm can find solutions in cases where Newton Raphson fails, particularly when derivative information is zero or when dealing with complex functions. However, it generally requires more iterations, and its convergence pattern is irregular.

Although there are studies similar to Chapra and Canale's work in the literature, the number of comparative studies focusing on different methods is noteworthy. We believe that these comparative studies will provide new perspectives for both practitioners and theoretical scientists. Depending on problem's nature, selecting the appropriate method is crucial for achieving efficient and reliable solutions. For problems requiring rapid convergence, where the initial point can be accurately chosen, the Newton Raphson method may be more effective. For problems where the effect of the initial point is uncertain or where derivative information is ambiguous, the Red Fox algorithm can be considered as an alternative approach. Hybrid approaches combining the advantages of both Newton Raphson and Red Fox algorithms can be developed for complex systems. Systematic optimization of the Red Fox algorithm's parameters such as population size and maximum number of iterations can improve convergence speed and stability.

REFERENCES

[1] Victor YP. Root-Finding and Root-Refining for a Polynomial Equation. Computer Science Technical Reports: City University of New York (CUNY); 2012.

[2] Millidere M, Karaman U, Uslu S, Kasnakoğlu C, Çimen T. Newton Raphson methods in aircraft trim: A comparative study. In: AIAA AVIATION 2020 Forum. American Institute of Aeronautics and Astronautics; 2020. p. 3198.

[3] Gower R, Lorenz DA, Winkler M. A Bregman–Kaczmarz method for nonlinear systems of equations. Comput Optim Appl. 2023;87(3):1059–1098.

[4] Pourrajabian A, Ebrahimi R, Mirzaei M, Shams M. Applying genetic algorithms for solving nonlinear algebraic equations. Appl Math Comput. 2013;219(24):11483–11494.

[5] Kotsireas IS, Pardalos PM, Semenov A, Trevena WT, Vrahatis MN. Survey of methods for solving systems of nonlinear equations, Part II: Optimization based approaches. arXiv. 2022. Available from: https://arxiv.org/abs/2208.08532

[6] Odan S. Metaheuristic method for solving systems of equations. arXiv. 2024. Available from: https://arxiv.org/abs/2409.16958

[7] Verma P, Parouha RP. Solving systems of nonlinear equations using an innovative hybrid algorithm. Iranian J Sci Technol Trans Electr Eng. 2022; 46:1005–1027.

[8] Chapra RP, Canale SC. Numerical Methods for Engineers. New York: McGraw-Hill Higher Education; 2002.

[9] Kujawa MA. Torsional buckling of restrained thin-walled bars of open bisymmetric cross-section. TASK Quarterly. Scientific Bulletin of Academic Computer Centre in Gdansk. 2012;16(3-4).

[10] Sharma JR, Kumar S, Cesarano C. An efficient derivative free one-point method with memory for solving nonlinear equations. Mathematics. 2019;7(7):604.

[11] Burden RL, Faires JD, Burden AM. Numerical Analysis. 10th ed. Canada: Cengage Learning; 2015.

[12] Połap D, Woźniak M. Red fox optimization algorithm. Expert Syst Appl. 2021; 166:1-21.

[13] Larivière S, Pasitschniak AM. Vulpes vulpes. Mammal Species. 1996; 537:1–11.

[14] Mohammed H, Rashid T. FOX: a FOX-inspired optimization algorithm. Appl Intell. 2023;53(1):1030–1050.

[15] Červený J, Begall S, Koubek P, Nováková P, Burda H. Directional preference may enhance hunting accuracy in foraging foxes. Biol Lett. 2011;7(3):355–357.

[16] Bektaş Y. Kızıl Tilki Optimizasyon Algoritması. Teknobilim 2023: Optimizasyon Modelleme ve Yapay Zeka Optimizasyon Algoritmaları. İstanbul: Efe Akademi; 2023.

[17] Köse B, Demirtürk B, Konca Ş. Application of Search Algorithms to Root-Finding Problems in Algebraic and Transcendental Contexts. 2025. (accepted in European Journal of Pure and Applied Mathematics)

Volume 14, Issue 2, Page 11-25, 2025 https://doi.org/10.46810/tdfd.1529139 Research Article

BİNGÖL UNIVERSITY

Türk Doğa ve Fen Dergisi
Turkish Journal of Nature and Science
www.dergipark.gov.tr/tdfd

Comparative Analysis of XAI Techniques on Telecom Churn Prediction Using SHAP and Interpreted ML Partial Dependence

Cem ÖZKURT[1*]

[1*]Sakarya University of Applied Sciences, Computer Engineering, Sakarya, Türkiye
Cem ÖZKURT ORCID No: 0000-0002-1251-7715

**Corresponding author: cemozkurt@subu.edu.tr*

(Received: 06.08.2024, Accepted: 24.03.2025, Online Publication: 27.06.2025)

Keywords
Explainable artificial ıntelligence,
SHAP,
Interpreted ML Partial Dependence,
Transparency and interpretability

Abstract: A comparative analysis of two prominent Explainable Artificial Intelligence (XAI) techniques, SHAP (SHapley Additive exPlanations) and Interpreted ML Partial Dependence, was conducted on a real-world Telecom Churn dataset consisting of 7,043 customer records. The objective of this study was to evaluate and compare the effectiveness of these techniques in enhancing the transparency and interpretability of machine learning models, specifically in telecom churn prediction. The study leveraged an XGBoost model, which achieved an accuracy of 94.12%, outperforming other machine learning models in the dataset. The methodology outlined the steps of data preprocessing and model training. Two separate analyses using SHAP and Interpreted ML Partial Dependence were conducted to evaluate their effectiveness in explaining model decisions and uncovering feature importance. The results of both techniques were discussed, highlighting their strengths and weaknesses, and providing valuable insights into interpretability and robustness. The SHAP analysis demonstrated that it is a powerful tool for identifying which features influence churn, particularly highlighting Contract type, Monthly Charges, and Tech Support as key drivers of customer churn. For instance, SHAP values revealed that customers with short-term contracts and no tech support were significantly more likely to churn, with SHAP values exceeding 0.6 in impact. This fine-grained analysis provided precise insights into individual predictions. On the other hand, the Interpreted ML Partial Dependence method showed the general effects of features, allowing for a broader perspective on model behavior. It illustrated how changes in Monthly Charges and Tenure affected churn probability across the dataset, showing that customers with longer tenure had lower churn probabilities on average. These results enhanced the transparency of model decisions, instilling trust in users and helping them understand how the model works. The key contribution of this study is the comparative evaluation of SHAP and Interpreted ML Partial Dependence in telecom churn prediction, offering a structured framework for selecting appropriate XAI techniques based on interpretability needs. SHAP provided instance-specific explanations, crucial for personalized customer retention strategies, while Partial Dependence offered a macroscopic view, useful for high-level decision-making and policy adjustments.This comparative analysis contributes to a deeper understanding of XAI methods and emphasizes the importance of selecting appropriate techniques to enhance transparency in telecom churn prediction models.

SHAP ve Interpreted ML Kısmi Bağımlılık Kullanarak Telekom İşten Ayrılma Tahmininde XAI Tekniklerinin Karşılaştırmalı Analizi

Anahtar Kelimeler
Açıklanabilir Yapay Zeka,
SHAP,
Yorumlanabilir ML'de Kısmi Bağımlılık,
Şeffaflık ve Yorumlanabilirlik

Öz: Önde gelen iki Açıklanabilir Yapay Zeka (XAI) tekniği olan SHAP (SHapley Additive exPlanations) ve Interpreted ML Kısmi Bağımlılık, 7.043 müşteri kaydından oluşan gerçek bir Telekom Churn veri kümesi üzerinde karşılaştırmalı bir analizle değerlendirildi. Bu çalışmanın amacı, bu tekniklerin makine öğrenimi modellerinin şeffaflığını ve yorumlanabilirliğini artırmadaki etkinliğini, özellikle telekom abonelik iptali (churn) tahmini bağlamında karşılaştırmaktır. Çalışmada, %94,12 doğruluk oranına ulaşarak diğer makine öğrenimi modellerinden üstün performans gösteren XGBoost modeli kullanılmıştır. Metodoloji kapsamında veri ön işleme ve model eğitimi adımları açıklanmış, SHAP ve Interpreted ML Kısmi Bağımlılık yöntemleriyle yapılan iki ayrı analiz karşılaştırılmıştır. Elde edilen sonuçlar, bu tekniklerin güçlü ve zayıf yönlerini ortaya koyarak model yorumlanabilirliği ve dayanıklılığı hakkında önemli içgörüler sunmuştur. SHAP analizi, Sözleşme Türü (Contract), Aylık Ücretler (Monthly Charges) ve Teknik Destek (Tech Support) gibi özelliklerin müşteri kaybı üzerindeki etkisini güçlü bir şekilde belirleyerek, modelin belirli tahminlerde bulunma nedenlerini açıklamada etkili bir yöntem olduğunu göstermiştir. Örneğin, SHAP değerleri, kısa vadeli sözleşmelere sahip ve teknik destek hizmeti almayan müşterilerin, 0,6'nın üzerinde SHAP etkisine sahip olarak, churn olasılığının önemli ölçüde yüksek olduğunu göstermiştir. Bu detaylı analiz, bireysel müşteri tahminlerini anlamak için kritik bilgiler sağlamıştır. Öte yandan, Interpreted ML Kısmi Bağımlılık yöntemi, Aylık Ücretler ve Abonelik Süresi (Tenure) gibi değişkenlerin churn olasılığı üzerindeki genel etkilerini göstererek daha geniş bir bakış açısı sunmuştur. Analiz sonuçları, özellikle uzun süreli abonelik süresine sahip müşterilerin daha düşük churn olasılığına sahip olduğunu ortaya koymuştur. Bu çalışmanın temel katkısı, telekom sektörü için SHAP ve Interpreted ML Kısmi Bağımlılık yöntemlerinin karşılaştırmalı bir değerlendirmesini sunarak, yorumlanabilirlik ihtiyaçlarına göre uygun XAI tekniklerinin seçilmesine yönelik yapılandırılmış bir çerçeve sunmasıdır. SHAP, bireysel tahminleri açıklamak için güçlü bir araç sunarken, Kısmi Bağımlılık yöntemi makro düzeyde analizler yapmak ve yüksek seviyeli kararlar almak için faydalıdır. Bu karşılaştırmalı analiz, XAI yöntemlerinin daha iyi anlaşılmasına katkı sağlamakta ve telekom abonelik iptali tahmin modellerinde şeffaflığı artırmak için uygun tekniklerin seçilmesinin önemini vurgulamaktadır.

1. INTRODUCTION

This study provides a comprehensive comparison of SHAP (SHapley Additive exPlanations) and Interpreted ML Partial Dependence for explainability in telecom churn prediction. By applying these techniques to a real-world dataset of 7,043 telecom customers, the research identifies Contract type, Monthly Charges, and Tech Support as key churn predictors, with SHAP values exceeding 0.6 in impact. The study demonstrates that SHAP is highly effective for customer-specific explanations, making it valuable for personalized retention strategies, while Partial Dependence Plots offer a broader understanding of feature influence, aiding in strategic decision-making. The XGBoost model, which achieved 94.12% accuracy, serves as the foundation for this analysis, highlighting the balance between performance and interpretability. The findings emphasize that SHAP excels in detailed, instance-based explanations, whereas Partial Dependence is more suitable for high-level business insights. By bridging the gap between model accuracy and transparency, this study offers practical guidance on selecting the most appropriate XAI technique for telecom churn analysis, contributing to more explainable and trustworthy AI-driven decision-making [25,27]. In today's data-driven world, where machine learning models increasingly dictate decision-making, the need for transparency and interpretability has reached unprecedented importance [25,27]. Nowhere is this more critical than in telecommunications, where accurate churn prediction is not just a technical goal but a strategic necessity for customer retention and service optimization [6,10]. This paper undertakes a comparative analysis of SHAP and Interpreted ML Partial Dependence, assessing their effectiveness in enhancing model transparency and interpretability in the context of telecom churn prediction [7,31]. The Methodology section details the dataset preprocessing and model training steps, focusing on XGBoost, a widely recognized model in this domain [10,17]. Recursive Feature Elimination (RFE) is applied to identify and retain only the most influential features, ensuring improved model performance and interpretability [31,19]. The Evaluation section provides a detailed comparison of SHAP and Partial Dependence, illustrating how each technique unveils feature importance and enhances interpretability in different ways [31,33]. The discussion highlights their respective strengths and weaknesses, offering insights into their applicability for various analytical needs [8,32]. Finally, this study contributes practical recommendations on selecting appropriate XAI techniques based on business

objectives and interpretability needs. The Conclusion and Future Works section summarizes key findings and discusses their broader implications, emphasizing the importance of choosing the right XAI approach in telecom churn prediction models [25,26]. Additionally, avenues for future research are outlined, focusing on further refinement of interpretability techniques and their integration into real-world telecom decision-making frameworks [33,32].

2. RELATED WORKS

The surge of machine learning applications across various sectors has been nothing short of transformative. Noteworthy contributions span diverse domains, showcasing the versatility and impact of these intelligent systems. In the realm of marketing, groundbreaking strides have been made with a coupon recommendation method, marrying machine learning prowess with simulated annealing algorithms [1]. This innovative approach not only enhances the order conversion rate but also fuels revenue growth. A parallel breakthrough emerges in the banking sector with DeepAFM, a sophisticated deep learning model tailored for precision marketing to predict potential credit card users [3].

Agriculture witnesses the fusion of technology and cultivation as machine learning techniques intricately map rice growth phases and bare land using Landsat-8 OLI imagery [2]. This not only demonstrates the accuracy of classification but also opens avenues for resource management applications. Analytical sciences delve into the intricacies of Raman and surface-enhanced Raman scattering experiments, where machine learning methods unravel chemical information from complex datasets [4].

Machine learning has made significant contributions in healthcare, such as disease classification developed a Support Vector Machine (SVM) classifier for diagnosing diabetes, showcasing the successful use of machine learning in medical datasets [5].

In the dynamic landscape of telecom, machine learning algorithms such as Prophet and XGBoost emerge as pivotal tools for forecasting network traffic [6]. The industry witnesses' cost and time reductions through automated test case generation, a testament to the efficiency brought by machine learning [7]. Anomaly detection in telecom operations sees a change in basic assumptions, resulting in a remarkable 90 percent reduction in team workload [9].

Within telecom, customer churn prediction stands out as a vital application, with machine learning models operating on big data platforms [10]. It is intriguing to note that non-machine learning AI approaches, such as propositional logic, find their place in certain tasks within telecom data analysis [8].

The literature extends its explorations into the constructive collaboration of machine learning across diverse domains. In the context of Cyber Manufacturing Systems, machine learning proves invaluable in detecting cyber-physical attacks [11]. The manufacturing industry witnesses a convergence of machine learning and optimization methods, capitalizing on advances in digitalization [12]. In radiological imaging, machine learning exhibits potential for recognizing and classifying complex patterns [14].

Furthermore, recent studies have delved into the integration of machine learning into the evaluation of physical security for cryptographic chips [15], the analysis of online transaction data [16], and its potential in medical imaging for disease detection at an early stage [18]. In the context of fault diagnosis, provided a survey of various machine learning algorithms applied in elevator systems [19]. Also specifically compared the performance of machine learning and deep learning algorithms in breast cancer prediction and diagnosis [17].

The literature reviewed demonstrates the wide-ranging applications of machine learning in diverse domains. This paper contributes to this body of knowledge by conducting a comparative analysis of Explainable Artificial Intelligence (XAI) techniques on telecom churn prediction, using SHAP and interpreted ML partial dependence.

3. MATERIAL AND METHOD

In this section, the procedures involved in data acquisition, pre-processing, and the implementation of our proposed methodology are outlined. The study commences with an explanation of the dataset used, followed by a description of the steps taken to preprocess the data. Subsequently, the proposed method is introduced, entailing the application of an XGBoost model for telecom churn prediction, augmented by Explainable AI techniques.

3.1. Dataset

The telecom churn dataset provides valuable insights into customer behaviour within the telecommunications sector, where customer loyalty plays a pivotal role. Understanding and mitigating customer subscription cancellations is critical for telecommunications companies to enhance decision-making processes. This dataset encompasses various customer attributes, including contract type, technical support status, and monthly charges, along with a binary "Churn" label indicating whether a customer terminated their subscription. It serves as a valuable resource for telecom companies seeking to analyse customer attrition patterns and formulate strategies to retain subscribers and improve overall service quality. Initially, all features of the available data set were not taken, but Recursive Feature Elimination (RFE) method was applied on the data set and the parameters obtained as output were used. Table 1 shows us the parameter ranking obtained as a result of RFE. MontlyCharges and tenure columns are reduced to values between 0-1 using Minmax Normalizer. TechSupport, Contract and OnlineSecurity columns were encoded as strings using the Label Encoding method. The churn value already contains the values 0 and 1 and shows

whether the telecom service continues or not depending on the current parameters. "1" indicates that he left the service and "0" indicates that he did not leave the service.

Table 1. Feature Selection and Ranking Table

Feature	Selected	Ranking
gender	FALSE	4
Partner	FALSE	6
Dependents	FALSE	tab
tenure	TRUE	1
PhoneService	FALSE	12
InternetService	FALSE	5
OnlineSecurity	TRUE	1
OnlineBackup	FALSE	3
DeviceProtection	FALSE	8
TechSupport	TRUE	1
StreamingTV	FALSE	11
StreamingMovies	FALSE	10
Contract	TRUE	1
PaperlessBilling	FALSE	7
PaymentMethod	FALSE	2
MonthlyCharges	TRUE	1

Table 2. A piece of example from dataset

Monthly Charges	Tech Support	Contract	OnlineSecurity	tenure	Churn
0.115423	0	0	0	0.013889	0
0.385075	0	1	1	0.472222	0
0.354229	0	0	0	0.027778	1
0.239303	2	2	1	0.625	0
0.521891	0	0	0	0.027778	1

3.2. Proposed Model

Following the training of the Telecom Churn dataset using the XGBoost model predictions for customer churn were obtained. To gain deeper insights into the "why" and "how" behind these predictions leveraging interpretable artificial intelligence tools, namely InterpretML and SHAP were proposed. This article aims to explore and compare the explanations provided by these tools, shedding light on the factors influencing the model's decisions.

InterpretML and SHAP are chosen for their effectiveness in offering interpretability to complex machine learning models. InterpretML employs various interpretability techniques to provide a global understanding of model behaviour, while SHAP (SHapley Additive exPlanations) values offer a nuanced view of feature contributions for individual predictions.

In the proposed methodology, interpretability results obtained from InterpretML and SHAP will be analysed and contrasted to unravel the underlying dynamics of the XGBoost model. By addressing the "why" and "how" aspects of predictions, an aim is set to enhance the transparency and trustworthiness of the predictive model. This is expected to contribute to a more informed decision-making process in the context of telecom churn prediction.

In addition, this data set was created with data from 7043 people. An example of the data set is given in Table 2.

To enhance the reliability of the results obtained from SHAP and InterpretML, the performance and methodologies of these tools have been carefully evaluated and independently analysed. These analyses are crucial in ensuring the accuracy and reliability of the model's predictions.

3.2.1. Machine learning

Machine learning, a subset of artificial intelligence, has significantly transformed data analysis methodologies across various domains [20, 23]. This changes in basic assumptions is evident in the telecommunications industry, where machine learning plays a pivotal role, particularly in the prediction of customer churn. The application of machine learning algorithms empowers telecom companies to navigate vast datasets, discern intricate patterns, and make highly accurate predictions. Amidst the diverse array of machine learning algorithms, XGBoost emerges as a preferred choice due to its adaptability and robust performance [21].

XGBoost, denoting eXtreme Gradient Boosting, has evolved into a cornerstone within the realm of machine learning. Tailored to overcome the limitations of traditional gradient boosting algorithms, XGBoost excels in both classification and regression tasks. Its effectiveness stems from its adeptness in handling diverse data types, managing missing values, and mitigating overfitting. These attributes render XGBoost particularly well-suited for intricate prediction scenarios, such as telecom churn prediction. In the specific context of telecom churn prediction, XGBoost has emerged as a go-to solution for telecom companies. Leveraging its analytical prowess across various customer attributes, including contract type, technical support status, and monthly charges, XGBoost provides accurate forecasts regarding customer subscription cancellations. As the subsequent sections of this article are explored, focus will be shifted towards the interpretation of the predictions generated by the XGBoost model. This interpretative process involves the utilization of tools such as InterpretML and SHAP, enhancing the transparency of the model. The interpretability of the XGBoost model is deemed crucial for gaining profound insights into the factors influencing telecom churn. Ultimately, this knowledge assists businesses in making well-informed decisions aimed at customer retention and the enhancement of service quality. This narrative builds upon the foundation laid by various scholarly works in the field of machine learning [23,24], among others. The integration of insights from these works contributes to a comprehensive understanding of the intersection between machine learning and telecommunications, enriching the discourse on predictive analytics in this dynamic industry. Figure 1 gives a working example of machine learning.

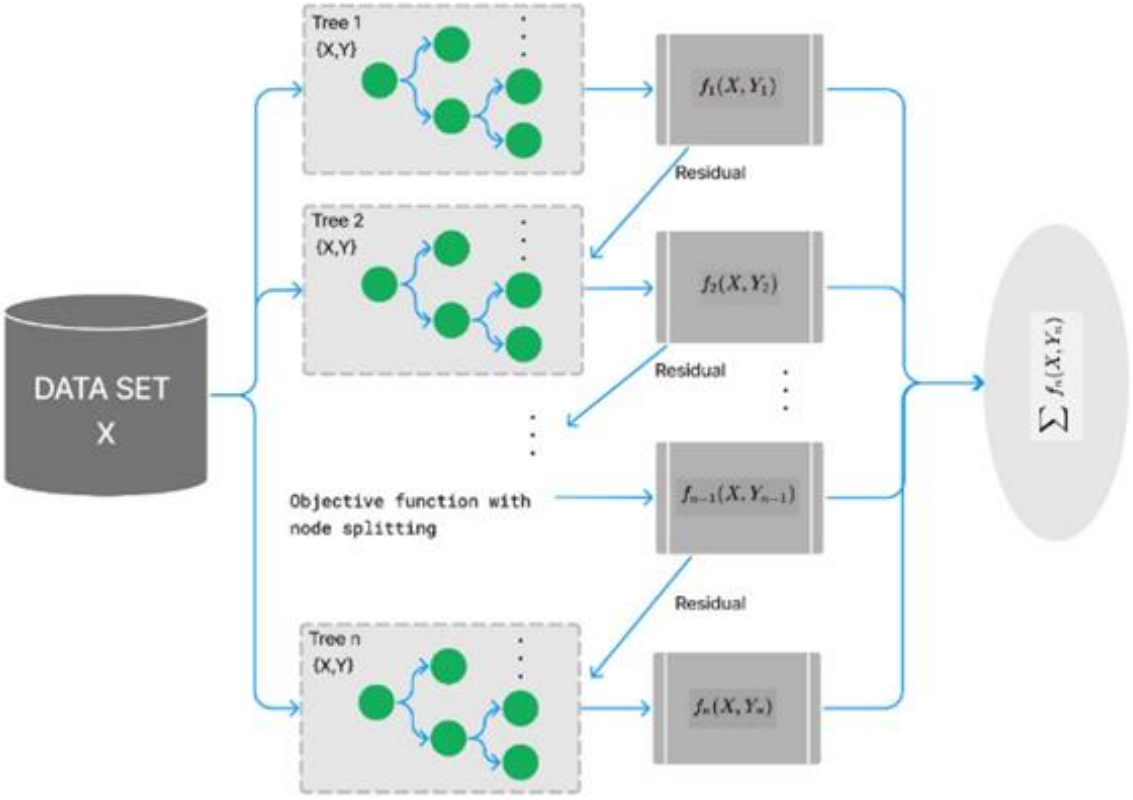

Figure 1. Working of machine learning

3.2.2. Explainable AI

Explainable AI, often abbreviated as XAI, represents a paradigm shift in artificial intelligence, emphasizing the transparency and interpretability of machine learning models [25]. As AI systems become increasingly intricate, understanding their decision-making processes becomes paramount. Explainable AI aims to demystify the inner workings of these models, providing comprehensible insights into how and why specific predictions are made [26]. In the realm of telecom churn prediction, where the stakes are high, Explainable AI plays a pivotal role [27]. Identifying the key parameters influencing churn is crucial for telecom companies seeking to retain customers effectively. With the application of machine learning models, particularly XGBoost in our case, a plethora of features contribute to predicting churn [28]. However, discerning which factors carry the most weight can be challenging without the aid of Explainable AI [29]. In the telecom churn landscape, parameters such as contract type, technical support status, and monthly charges emerge as influential factors [27]. Machine learning models analyse these features, but the "why" behind a prediction remains a black box [29]. A schematic visual presenting the Explainable AI method is given in Figure 2 also Figure 3 shows a comparative XAI method with machine learning algorithms.

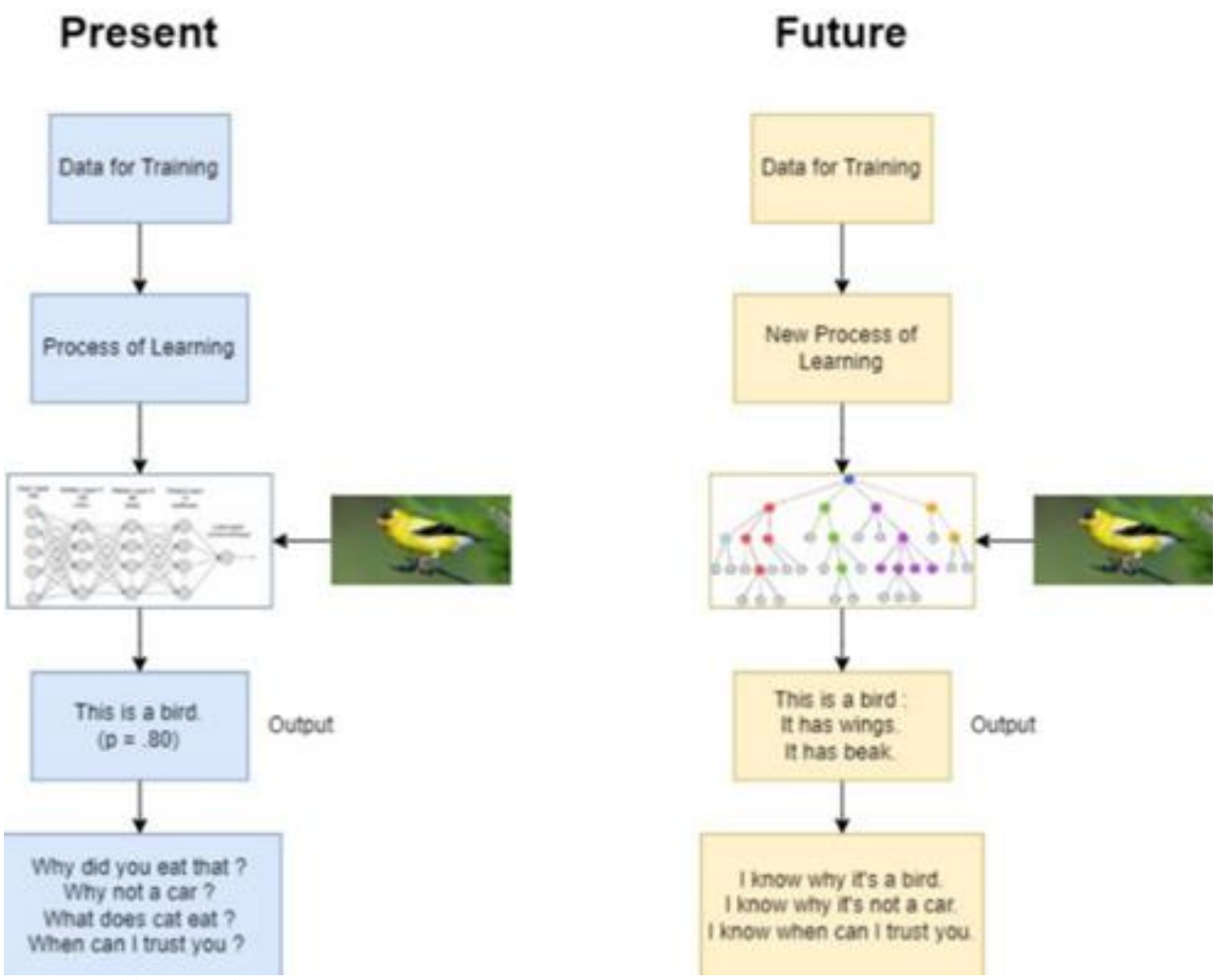

Figure 2. Explainable AI schema

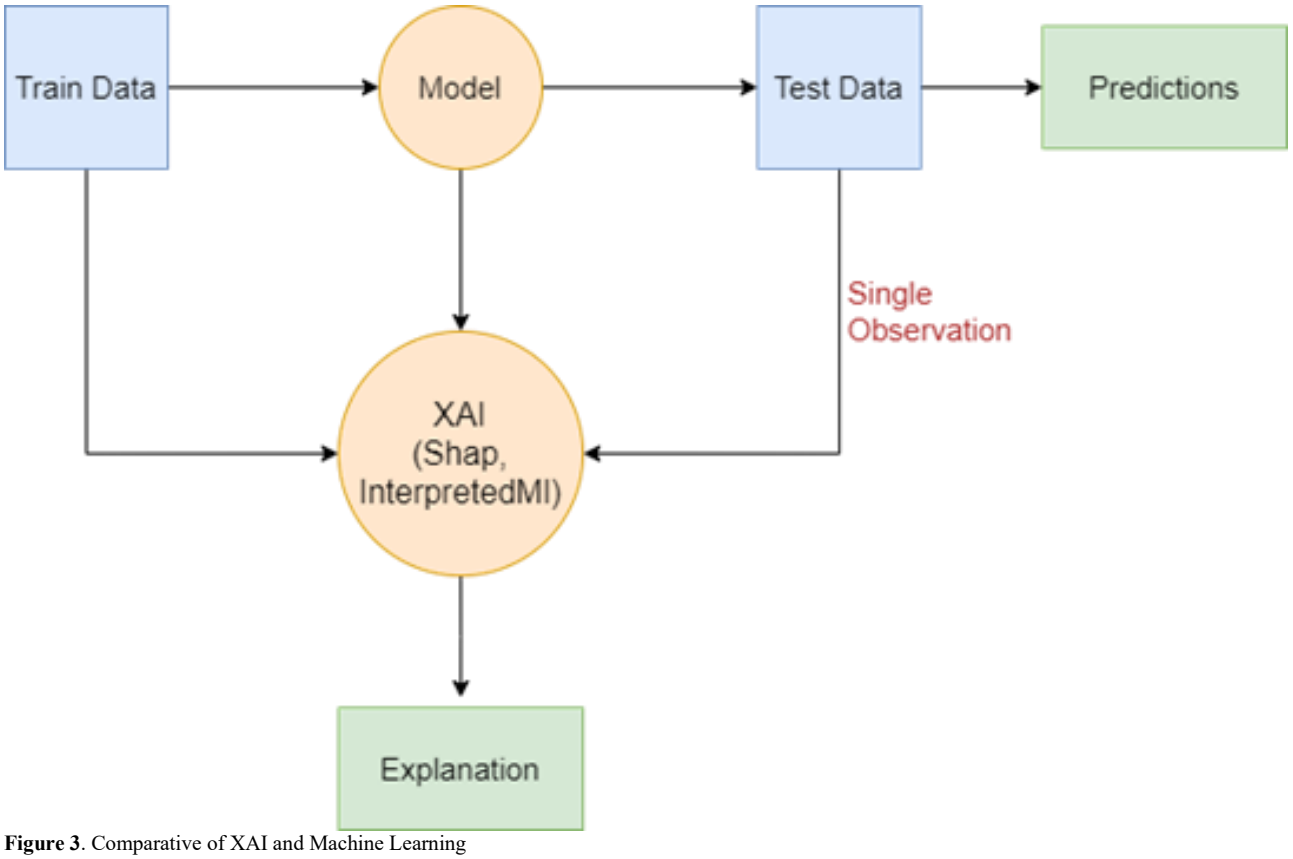

Figure 3. Comparative of XAI and Machine Learning

Explainable AI tools, such as InterpretML and SHAP, step in to shed light on the decision rationale, offering a transparent view of how these parameters contribute to the prediction of churn. After employing machine learning techniques like XGBoost to predict telecom churn, the next logical step is to leverage Explainable AI. InterpretML and SHAP, for instance, provide methodologies for interpreting and visualizing complex model outputs. By applying these tools, businesses can uncover the significance of each feature in the churn prediction process. This not only enhances the credibility of the predictions but also empowers telecom companies with actionable insights. Decision-makers can now understand not only that a customer is likely to churn but also the specific reasons driving that prediction, enabling them to implement targeted retention strategies and improve overall customer satisfaction.

3.3. SHAP (Shapley Additive exPlanations)

SHAP values are derived from cooperative game theory, specifically Shapley values, which distribute the contribution of each player in a coalition [32]. Applied to machine learning, SHAP values quantify the impact of each feature on a model's output [31]. For a given prediction f(x) of the model, the SHAP value ϕ_i for feature i can be expressed as:

$$\phi_i(f) = \sum_{S \subseteq N\{i\}} \frac{|S|!\,(|N| - |S| - 1)!}{|N|!} [f(S \cup \{i\}) - f(S)] \quad (1)$$

Here, N is the set of all features, and S represents a subset of features excluding [31]. This formula computes the contribution of feature by considering all possible subsets of features.

$$f_x(S) = E[f(x)|X_s] \quad (2)$$

$f_x(S)$ is the conditional expectation of f(x) given the information set X_s,

E[.] denotes the expectation operator,

f(x) is a random variable, and

X_s is an information set.

In Equation 2, the conditional expectation $f_x(S)$ is determined by the expected value of the random variable f(x) given the information set X_s. The information set X_s conditions the expectation, indicating that the anticipated value of f(x) is contingent upon the knowledge encapsulated in X_s. This formulation is a standard representation in probability theory and statistics, where the conditional expectation provides a way to model the expected outcome of a random variable in the presence of specific information or conditions specified by the information set. The equation serves as a concise expression encapsulating the relationship between the conditional expectation and the underlying random variable in a given informational context.
In the equation,

$$M + \sum_{i=1}^{n} \beta_i z_i = bias + \sum_{i=1}^{n} \beta_i \cdot Feature\ Contribution \mid x_i \quad (3)$$

where M represents an intercept term, and β_i denotes the coefficients associated with the variables z_i and x_i. The variables z_i and x_i are the features used in the model. The left side of the equation is the sum of the intercept $z_i$and the product of each coefficient $\beta_i$with its corresponding variable z_i.

The right side of the equation consists of the bias term and the sum of the product of each coefficient β_i with its corresponding feature x_i. This can be interpreted as the sum of the individual contributions of each feature x_i to the overall prediction.

Overall, the equation represents a linear relationship between the features and the predicted outcome, with each feature's contribution weighted by its respective coefficient.

The XAI output in Figure 4 is a SHAP (SHapley Additive exPlanations) value plot, which is a way of explaining the predictions of a machine learning model by looking at how much each feature contributes to the output. In this case, the model is predicting revenue, and the XAI output shows how much each of the features in the plot contributes to the predicted revenue [30]. Also Figure 5 shows the average impact of our features on model output.

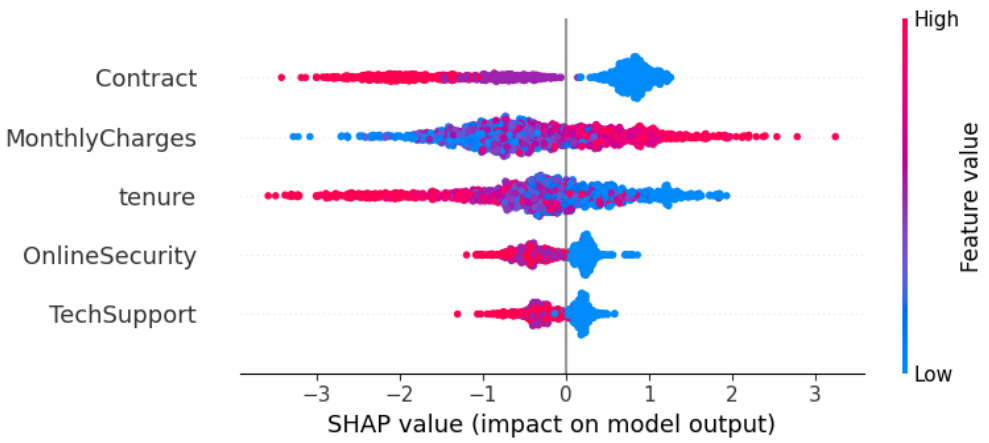

Figure 4. SHAP results for dataset

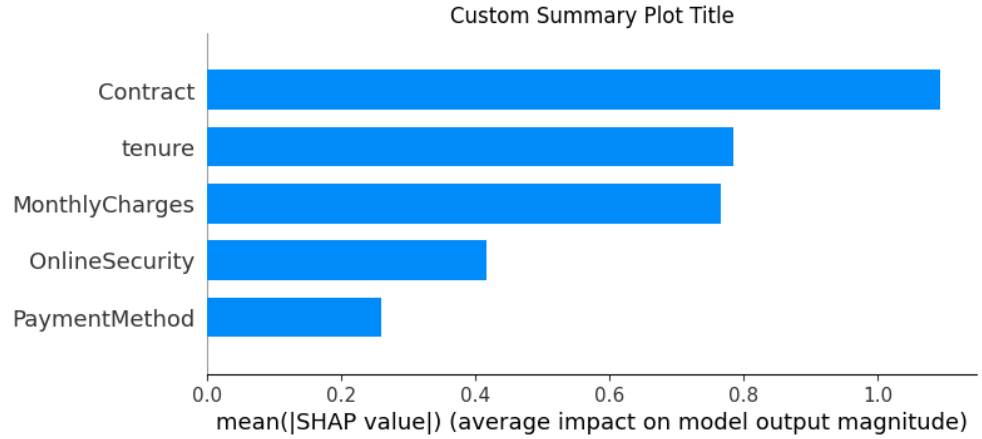

Figure 5. SHAP results for our data set shows average impact for each feature

The features in the plot are contract, monthlyCharges, tenure, onlineSecurity, and techSupport .The SHAP value for each feature is shown on the y-axis, and the features are arranged on the x-axis from lowest to highest SHAP value. The SHAP value for a feature tells you how much the model's prediction would change if the value of that feature were to change. For example, the SHAP value for contract is positive, which means that increasing the value of contract will increase the predicted revenue. Conversely, the SHAP value for tenure is negative, which means that increasing the value of tenure will decrease the predicted revenue [33].

The absolute value of the SHAP value tells you how important the feature is to the model's prediction. The features with the largest absolute SHAP values are the most important to the model. In this case, the most important features are contract, monthlyCharges, and onlineSecurity. The XAI output also shows how the SHAP values are distributed across different data points. The grey line in the plot shows the average SHAP value for each feature and the blue and red dots show the SHAP values for individual data points. The spread of the blue and red dots shows how much the SHAP values can vary for different data points. Overall, the XAI output tells you that the value of a contract, monthly charges, online security, and tech support has a significant impact on the predicted revenue. The higher the value of these features, the higher the predicted revenue. Tenure also has an impact on the predicted revenue, but it is a negative impact. The higher the value of tenure, the lower the predicted revenue.

3.4. Interpreted ML Partial Dependence

Partial dependence plots offer insights into the relationship between a specific feature and the model's predictions while holding other features constant. Interpreted ML Partial Dependence extends this concept to make partial dependence more accessible for interpretation. For a model M with input features X and output Y, the partial dependence $PDx_i(x_i)$ for a specific feature X_i at a certain value x_i is calculated as follows:

$$PDx_i(x_i) = E_{X\sim p(X)}[M(x)|X_i = x_i] \quad (4)$$

This equation represents the expected prediction of the model M given a fixed value x_i for the feature X_i. It provides a more intuitive understanding of how changes in a single feature influence the model's output.

Partial dependence plots (PDPs) are invaluable tools in the realm of interpretability for machine learning models. As illustrated in Figure 6 of the InterpretML framework the nuanced changes in the average response value of the model as we vary the tenure feature across the 0-1 range on both the x and y axes were observed. These plots provide a visual representation of how the feature's values influence the model predictions.

$$fs(s) = Exc[f(xs, Xc)] = \int f(xs, Xc)dP(Xc) \quad (5)$$

The function fs is defined as the expected value, denoted as Exc, of the conditional function $f(x_s, X_C)$, where x_s represents the features of interest and X_c denotes the remaining features treated as random variables in the machine learning model f. This expectation is obtained by integrating the function $f(x_s, X_C)$ with respect to the probability distribution $P(X_c)$.

In simpler terms, $f_s(s)$ signifies the average predicted outcome based on the features x_s of interest, considering the variability in the remaining features X_c according to their probability distribution $P(X_c)$. The integral reflects the process of taking into account the contribution of each combination of x_s and X_c values weighted by their respective probabilities in the overall prediction.

$$f_s(x_S) = \frac{1}{n}\sum_{i=1}^{n} f\hat{}(x_S, x_C^{(i)}) \quad (6)$$

Equation (7) expresses the partial dependence function $f_s(x_s)$, which is determined by calculating the average of the predicted values from the machine learning model $f\hat{}$ for the features of interest x_S. This average is obtained by summing the predicted values for each instance i and then dividing the sum by the total number of instances n. The feature values $x_C^{(i)}$ represent the actual features from the dataset that are not of interest, emphasizing the marginalization over these features in the calculation of the partial dependence. In passive voice, the equation conveys that the partial dependence function is computed by summing the predicted values for each instance and subsequently dividing the sum by the total number of instances.

$$I(x_S) = \sqrt{\frac{1}{K-1}\sum_{k=1}^{K}((f\hat{}(x_S^{(k)}) - \frac{1}{K}\sum_{k=1}^{K}(f\hat{}(x_S^{(k)}))^2} \quad (7)$$

The equation $I(x_S)$ is formulated to calculate a measure of variability or dispersion associated with the partial dependence estimates $f\hat{}(x_S^{(k)})$ for a set of feature values x_S. This measure is expressed as the square root of the average squared difference between each individual estimate and the overall average estimate.

In more detail, the expression involves obtaining K partial dependence estimates for the features in set S, denoted as $f\hat{}(x_S^{(k)})$ for $k = 1$ to K. The quantity inside the square root signifies the average squared deviation of each individual estimate from the mean estimate, which is the average of all K estimates. The fraction $\frac{1}{K-1}$ scales the summation to provide an unbiased estimate of the variance.

The resulting value $I(x_S)$ represents the standard deviation of the partial dependence estimates, offering insights into the spread or consistency of the model's predictions for different instances of x_S. This measure can be useful in assessing the stability and reliability of the partial dependence estimates for the specified set of features.

$$(x_S) = \frac{max_k\left(Sf\left(x_s^{(k)}\right)\right) - min_k\left(Sf\left(x_s^{(k)}\right)\right)}{4} \quad (8)$$

The formulation of the expression (x_S) provides a standardized representation for the features of interest x_S, achieved by calculating the difference between the maximum and minimum values of the partial dependence function Sf evaluated at different instances $x_s^{(k)}$, and subsequently dividing this difference by four. This normalization step ensures that the range of values resulting from the partial dependence function is adjusted, facilitating a more interpretable understanding of the features' impact on the model's predictions.

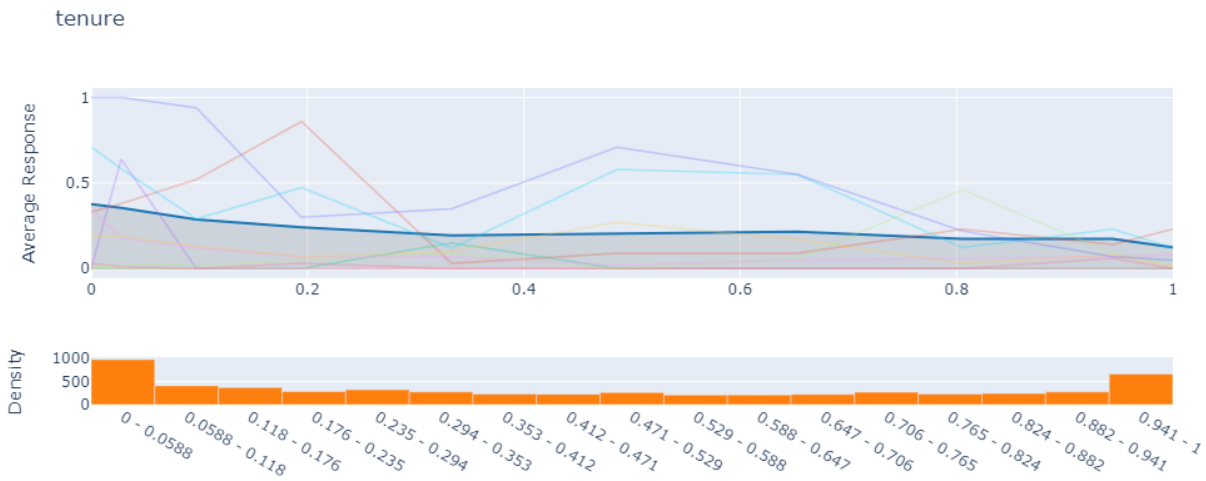

Figure 6. Tenure results InterpretML from dataset

In transitioning to the subsequent paragraph, the focus shifts to Figure 6, which specifically examines the tenure feature. Within the specified range, this figure elucidates the average response values, with the x and y axes capturing variations in the feature and its impact on the model's output, respectively. The plot's density visually encapsulates the concentration of the tenure feature's influence on the overall model.

In summary, these Partial Dependence plots serve as powerful tools for model interpretation, providing a clear and intuitive understanding of how individual features contribute to the model's behaviour. The visualizations not only depict the average response values but also convey the intensity of the feature's impact, enhancing our grasp of the model's inner workings. Incorporating such visual aids in high-level articles and discussions can significantly contribute to the accessibility and interpretability of complex machine learning models.
In our implementation, these Explainable AI techniques are applied post-training the XGBoost model. SHAP values provide a detailed breakdown of feature contributions, while Interpreted ML Partial Dependence offers insightful plots illustrating the impact of individual features on predictions.

4. RESULTS

Table 3 presents the results of experiments conducted with various machine learning models on the same dataset. Upon careful examination of the table, it becomes evident that the XGBoost model outperforms other machine learning models, exhibiting higher accuracy, precision, recall and F1 score. The superior performance of the XGBoost model underscores its effectiveness in capturing and generalizing patterns within the given dataset. This heightened accuracy, precision, recall, and F1 score not only emphasize the model's predictive prowess but also its robustness in consistently delivering reliable and high-quality predictions compared to alternative machine learning approaches. The model's capacity to adapt to intricate patterns and make accurate predictions contributes to its superior performance metrics across multiple evaluation criteria. The nuanced evaluation metrics, including precision, recall, and F1 score, shed light on the model's ability to strike a balance between correctly identifying positive instances and minimizing false positives and false negatives.

Table 3. Machine learning algorithm results

Machine Learning Methods	Accuracy	Precision	Recall	F1-Score
XGBoost	0.94125	0.94	1	0.97
Adaboost	0.93933	0.94	1	0.97
KNN	0.93933	0.94	1	0.97
CatBoost	0.93933	0.94	1	0.97
Logistic Regression	0.93933	0.94	1	0.97
SVM	0.93933	0.94	1	0.97
TFX	0.93835	0.94	1	0.97
Tensorflow Extends BBO	0.93835	0.94	1	0.97
Extra Trees	0.93737	0.94	1	0.97
Decision Tree	0.93542	0.94	0.99	0.97
Random Forest	0.93542	0.94	0.99	0.97
LightGBM	0.93346	0.94	1	0.97
NaiveBayes	0.43639	1	0.4	0.57

In this study, interpretable artificial intelligence tools, namely Shap and InterpretML-Partial Dependence, were employed to elucidate the XGBoost model trained on the telecom churn dataset. The primary goal was to explain the predictions made by the model, with a particular focus on two selected customers—one continuing with the service (churn=0) and the other leaving the company (churn=1). By comparing Shap outputs for these customers, it was observed that the 734th customer had a longer tenure than the 544th customer, as depicted in Figure 7. Additionally, Figure 7 revealed that the MonthlyCharges for the 544th customer were lower than those for the 734th customer.


```
Churn 1 Example Features:
     MonthlyCharges  TechSupport  Contract  OnlineSecurity    tenure
544        0.271642            2         0               2  0.180556

Churn 0 Example Features:
     MonthlyCharges  TechSupport  Contract  OnlineSecurity  tenure
734        0.715423            0         0               0   0.375
```

Figure 7. Customers parameters

Examining Figure 8 and Figure 9, the feature distributions influencing predictions for these selected customers were illustrated. These visualizations supported the interpretation that the 734th customer did not churn, while the 544th customer did. Notably, Figure 11 and Figure 12 indicated that the Contract feature played a crucial role in predicting churn for both customers. However, a discrepancy arose between Monthly Charges and tenure, with Figure 9 showing higher values for the non-churning customer, whereas Figure 8 revealed a significant impact of these features, both exceeding 0.6.

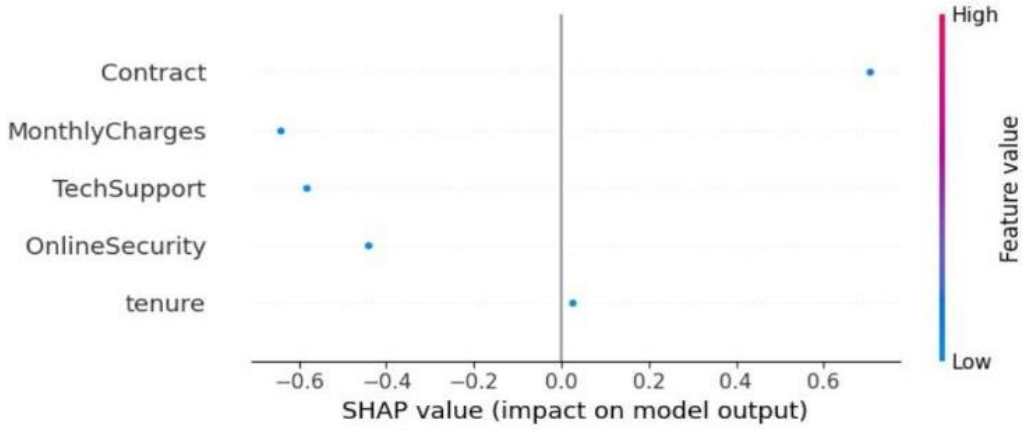

Figure 8. 544'th Customers SHAP values

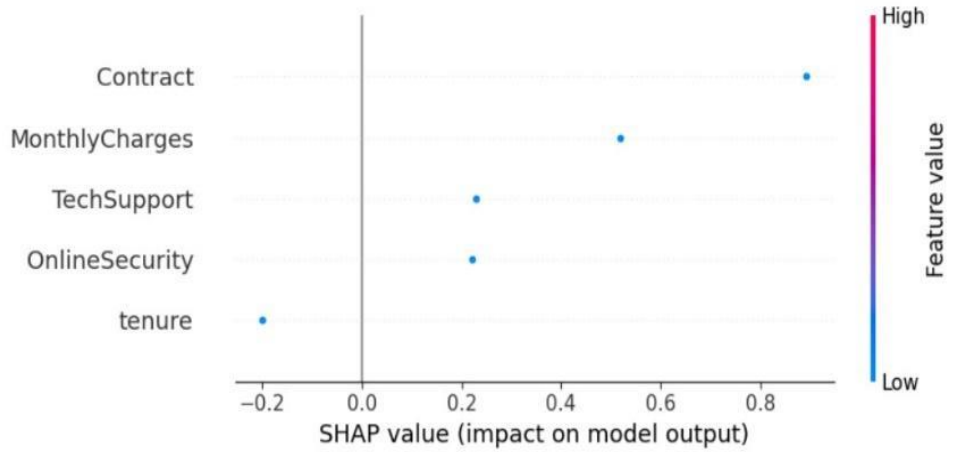

Figure 9. 734'th Customers SHAP values

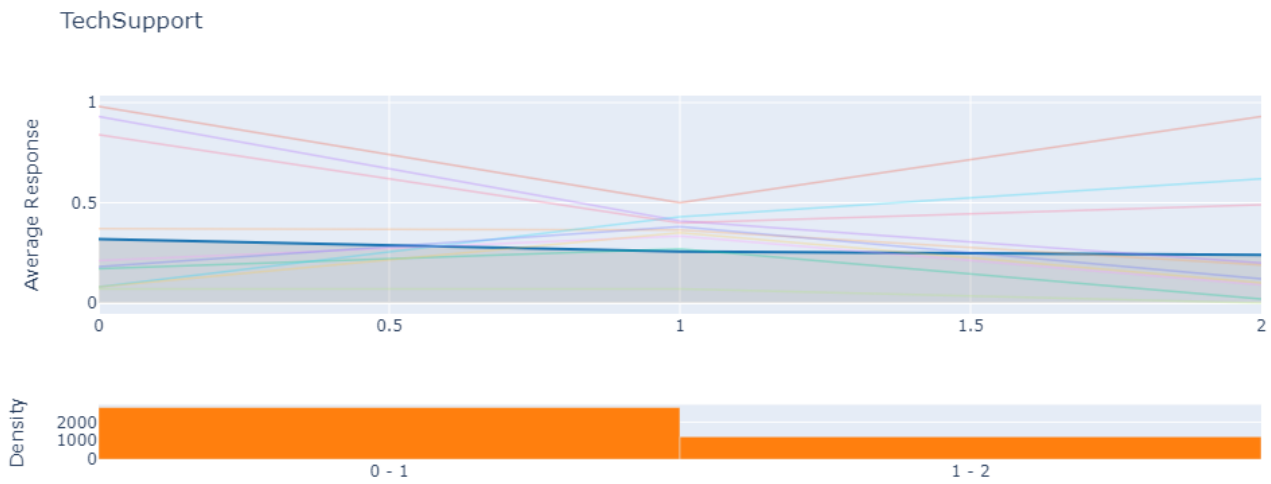

Figure 10. InterpretML results for TechSupport

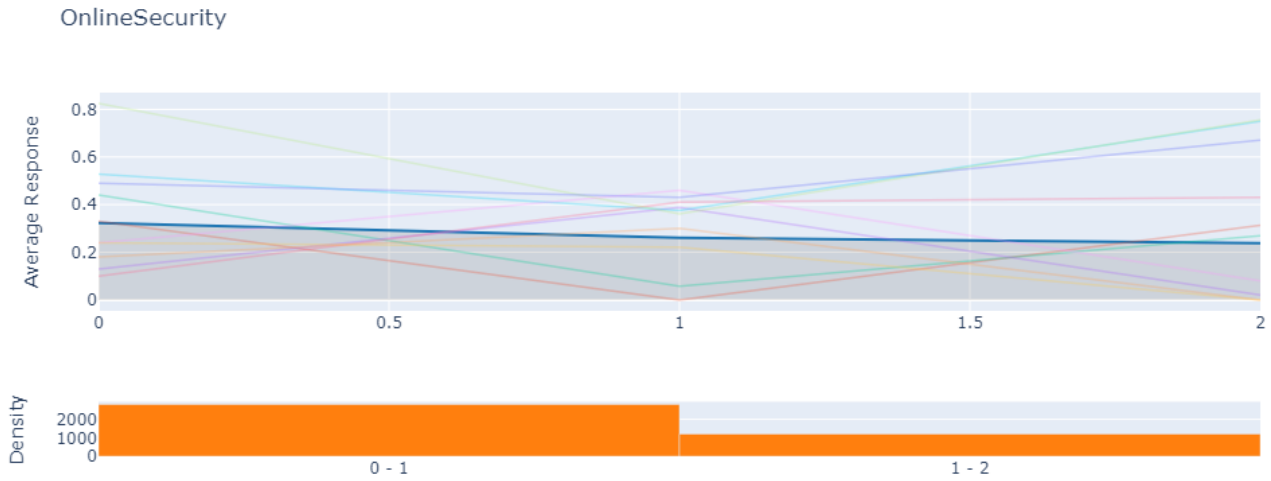

Figure 11. InterpretML results for OnlineSecurity

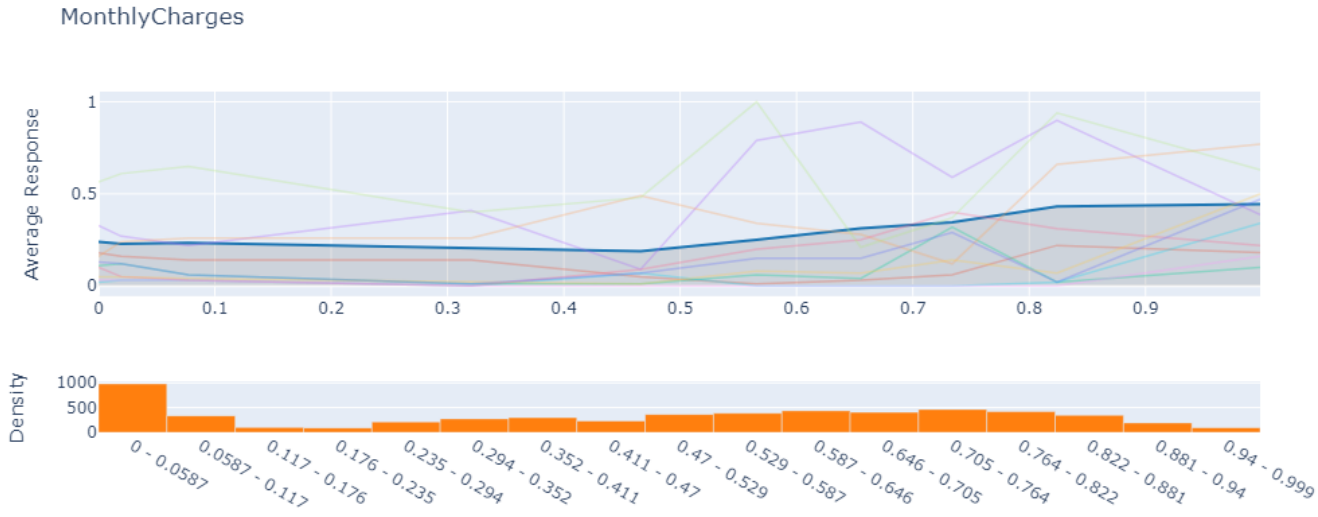

Figure 12. InterpretML results for MontlyCharges

Furthermore, limitations were encountered in delivering detailed explanations for the reasons behind specific customer churn or retention when employing InterpretML-Partial Dependence. Unlike Shap, InterpretML-Partial Dependence offers insights into how the model's prediction changes as a single feature varies while keeping all other features constant. It provides a partial dependence plot highlighting the average response of the prediction and the density of these features' influence on the prediction, as depicted in Figure 10.

The InterpretML partial dependence graphics shown at Figure 10,11 and 12 for the monthly charges, contract type, and tech support features offer a nuanced understanding of how these variables collectively influence the predictions, particularly in the context of OnlineSecurity. These graphics provide insightful visualizations that depict the relationship between the mentioned features and the predicted outcomes. By examining the partial dependence plots, one can discern the impact of monthly charges, contract type, and the availability of tech support on the likelihood of having OnlineSecurity services. The partial dependence graphics illustrate how changes in the values of monthly charges, various contract types, and the presence of tech support correlate with shifts in the model's predictions regarding the probability of having OnlineSecurity. This visual representation aids in identifying trends, patterns, and potential nonlinear relationships between these features and the target variable. Consequently, stakeholders can glean valuable insights into the factors that significantly contribute to the presence or absence of OnlineSecurity services, enabling informed decision-making and a deeper understanding of the model's behaviour in relation to these key predictors.

5. DISCUSSION AND CONCLUSION

The results obtained from this study highlight the effectiveness of SHAP and Interpreted ML Partial Dependence in enhancing the interpretability of telecom churn prediction models. The findings indicate that SHAP is particularly effective in identifying key features that influence individual customer churn decisions, whereas Interpreted ML Partial Dependence provides a more global perspective on feature importance and trends. Several previous studies have explored Explainable AI techniques in the context of customer churn prediction, primarily focusing on improving predictive accuracy rather than model interpretability. While prior research demonstrated the effectiveness of machine learning models such as XGBoost in telecom forecasting, they often lacked a comparative evaluation of explainability techniques. Our study builds on this by integrating SHAP and Interpreted ML Partial Dependence to bridge the gap between model performance and transparency. One of the key advantages of the proposed approach is its ability to provide improved transparency, enabling telecom companies to understand and trust AI-driven predictions. The SHAP analysis offers actionable insights by pinpointing individual-level risk factors, allowing for more personalized retention strategies. At the same time, Interpreted ML Partial Dependence presents a high-level overview of feature importance, which is useful for strategic decision-making. Additionally, the XGBoost model used in this study achieved a high predictive accuracy of 94.12%, reinforcing its reliability in telecom churn prediction. However, there are some limitations to consider. SHAP computations can be computationally expensive, especially for large datasets, making real-time analysis challenging. Moreover, Partial Dependence Plots do not fully capture feature interactions, limiting their ability to reflect complex dependencies within the data. There is also a trade-off between interpretability and performance, as the use of interpretability techniques sometimes necessitates a compromise on model complexity and predictive power. Despite these limitations, the study provides a valuable framework for applying and evaluating Explainable AI techniques in telecom churn prediction. Future research should focus on integrating additional interpretability methods, such as counterfactual explanations or LIME, to further enhance the transparency and usability of machine learning models in the telecom sector.

This study presents a comparative analysis of SHAP (SHapley Additive exPlanations) and Interpreted ML Partial Dependence to enhance the interpretability of telecom churn prediction models. By analyzing a real-world telecom dataset of 7,043 customers, the findings reveal that Contract type, Monthly Charges, and Tech Support are the most significant factors affecting customer churn, with SHAP values exceeding 0.6 in impact. The XGBoost model, achieving 94.12% accuracy, demonstrated high predictive performance, while the applied explainability techniques provided valuable insights into customer retention strategies. SHAP proved particularly effective in offering individual-level explanations, making it an ideal tool for personalized churn intervention strategies, highlighting that customers on short-term contracts and those without tech support are at higher risk of leaving. Conversely, Interpreted ML Partial Dependence offered a macroscopic view of feature impact, illustrating general trends such as the inverse relationship between tenure and churn, making it more suitable for strategic decision-making at a higher level. These insights suggest that telecom companies should focus on contract renewal incentives, enhanced customer support, competitive pricing strategies, and loyalty programs to mitigate churn risk. Future research should explore advanced feature engineering to refine customer behavior insights, hyperparameter tuning for improved model accuracy, and integration of additional behavioral metrics such as customer service interactions, payment history, and network usage patterns to strengthen predictive capabilities. Additionally, evaluating the real-world impact of XAI techniques in telecom operations and incorporating other interpretability methods like counterfactual explanations or LIME could provide a more comprehensive understanding of churn drivers. By applying context-specific XAI approaches, telecom providers can make data-driven decisions to enhance customer retention, improve pricing strategies, and optimize service offerings, ultimately ensuring greater transparency and trust in AI-driven predictive models.

Data Availability

The kaggle link of dataset is "https://www.kaggle.com/datasets/moe5998/telecom-customer-churn".

Conflict of Interest

The author declare that he has no known competing financial interests or personal relationships that could have appeared to influence the work reported in this paper.

Ethical Considerations

This research adheres to ethical principles and guidelines in conducting the comparative analysis of Explainable Artificial Intelligence (XAI) techniques, specifically SHAP (SHapley Additive exPlanations) and Interpreted ML Partial Dependence, on a Telecom Churn dataset.

REFERENCES

[1] Y. Qi, Jun Wang, Xin Ma, Na Dong, Hong-Mei Yuan, "Coupon Recommendation System Based on Machine Learning and Simulated Annealing Algorithm," Other Conferences, 2023.

[2] Fadhlullah Ramadhani, Reddy Pullanagari, Gabor Kereszturi, Jonathan Procter, "Mapping of Rice Growth Phases and Bare Land Using Landsat-8 OLI with Machine Learning," International Journal of Remote Sensing, 2020.

[3] Yue Qiu, Jianan Fang, "Prediction of Potential Credit Card Users of Bank Based on Deep Learning," Neural Networks, Information and Communication Engineering, 2022.

[4] Félix Lussier, Vincent Thibault, Benjamin Charron, Gregory Q. Wallace, Jean-Francois Masson, "Deep Learning and Artificial Intelligence Methods for Raman and Surface-enhanced Raman Scattering," Trends in Analytical Chemistry, 2020.

[5] V Kirankumar, Somula Ramasubbareddy, G Kannayaram, K Nikhil Kumar, "Classification Of Diabetes Disease Using Support Vector Machine," Journal of Computational and Theoretical Nanoscience, 2019.

[6] Garima Jain, Rajeev Ranjan Prasad, "Machine Learning, Prophet and XGBoost Algorithm: Analysis of Traffic Forecasting in Telecom Networks with Time Series Data," 2020 8th International Conference on Reliability, Infocom ..., 2020.

[7] K. Kikuma, Takeshi Yamada, Koki Sato, K. Ueda, "Preparation Method in Automated Test Case Generation Using Machine Learning," Proceedings of the 10th International Symposium on ..., 2019.

[8] Sandro Skansi, Kristina Sekrst, Marko Kardum, "A Different Approach for Clique and Household Analysis in Synthetic Telecom Data Using Propositional Logic," 2020 43rd International Convention on Information, ..., 2020.

[9] Ryan Mukai, Zaid Towfic, Monika Danos, Mazen Shihabi, David Bell, "MSL Telecom Automated Anomaly Detection," 2020 IEEE Aerospace Conference, 2020.

[10] Abdelrahim Kasem Ahmad, Assef Jafar, Kadan Aljoumaa, "Customer Churn Prediction in Telecom Using Machine Learning in Big Data Platform," Journal of Big Data, 2019.

[11] Mingtao Wu, Zhengyi Song, Young B. Moon, "Detecting Cyber-physical Attacks in CyberManufacturing Systems with Machine Learning Methods," Journal of Intelligent Manufacturing, 2019.

[12] Dorina Weichert, Patrick Link, Anke Stoll, Stefan Rüping, Steffen Ihlenfeldt, Stefan Wrobel, "A Review of Machine Learning for The Optimization of Production Processes," The International Journal of Advanced Manufacturing ..., 2019.

[13] Raffaele Cioffi, Marta Travaglioni, Giuseppina Piscitelli, Antonella Petrillo, Fabio De Felice, "Artificial Intelligence and Machine Learning Applications in Smart Production: Progress, Trends, and Directions," Sustainability, 2020.

[14] Zhenwei Zhang, Ervin Sejdic, "Radiological Images And Machine Learning: Trends, Perspectives, And Prospects," arXiveess.IV, 2019.

[15] Jiajing Liu, Congming Wei, Shengjun Wen, An Wang, "Design and Implementation of A Physical Security Evaluation System for Cryptographic Chips Based on Machine Learning," Conference on Intelligent Computing and Human-Computer, 2023.

[16] Kailai Chen, "On A Machine Learning Based Analysis of Online Transaction," Conference on Machine Learning and Computer Application, 2023.

[17] W. A. W. A. Bakar, M. Zuhairi, M. Man, J. A. Jusoh, N. L. N. Josdi, "Deep Learning Algorithm Vs XGBoost Using Wisconsin Breast Cancer Diagnosis," Conference on Computer Science and Communication Technology, 2022.

[18] Angona Biswas, MD Abdullah Al Nasim, Md Shahin Ali, Ismail Hossain, Dr. Md Azim Ullah, Sajedul Talukder, "Active Learning on Medical Image," arXiv-eess.IV, 2023.

[19] Jun Gong, Yueyi Zhang, Siji Chen, Jingnan Liu, "Survey on The Application of Machine Learning in Elevator Fault Diagnosis," International Conference on Applied Mathematics, Modelling, 2023.

[20] Johnson, J. M. (2019). Survey on Deep Learning with Class Imbalance.

[21] Guo, Y., Wang, H., Hu, Q., Liu, H., Liu, L., Bennamoun, M. (2019). Deep Learning For 3D Point Clouds: A Survey.

[22] Chen, J., Ran, X. (2019). Deep Learning With Edge Computing: A Review.

[23] Hüllermeier, E., Waegeman, W. (2019). Aleatoric And Epistemic Uncertainty In Machine Learning: An Introduction To Concepts And Methods.

[24] Dargan, S., Kumar, M., Ayyagari, M. R., Kumar, G. (2019). A Survey of Deep Learning and Its Applications: A New Paradigm to Machine Learning.

[25] Duan, Y., Edwards, J. S., Dwivedi, Y. K. (2019). Artificial Intelligence for Decision Making in The Era of Big Data - Evolution, Challenges and Research Agenda. International Journal of Information Management, IF: 7.

[26] Long, D., Magerko, B. (2020). What Is AI Literacy? Competencies and Design Considerations. Proceedings of the 2020 CHI Conference on Human Factors in..., IF: 6.

[27] Shrestha, Y. R., Ben-Menahem, S. M., von Krogh, G. (2019). Organizational Decision-Making Structures in The Age of Artificial Intelligence. California Management Review, IF: 5.

[28] Shen, Y., Song, K., Tan, X., Li, D., Lu, W., Zhuang, Y. (2023). HuggingGPT: Solving AI Tasks with ChatGPT and Its Friends in Hugging Face. arXiv-CS.CL, IF: 5.

[29] Ma, S., Lei, Y., Wang, X., Zheng, C., Shi, C., Yin, M., Ma, X. (2023). Who Should I Trust: AI or Myself? Leveraging Human and AI Correctness Likelihood to Promote Appropriate Trust in AI-Assisted Decision-Making. arXiv-CS.HC, IF: 3.

[30] Carlos Fernández-Loría; Foster Provost; Xintian Han; "Explaining Data-Driven Decisions Made By AI Systems: The Counterfactual Approach", ARXIV-CS.LG, 2020.

[31] Remah Younisse; Ashraf Ahmad; Q. A. Al-Haija; "Explaining Intrusion Detection-Based Convolutional Neural Networks Using Shapley Additive Explanations (SHAP)", BIG DATA COGN. COMPUT., 2022.

[32] Heewoo Jun; Alex Nichol; "Shap-E: Generating Conditional 3D Implicit Functions", ARXIV-CS.CV, 2023.

[33] T. Pianpanit; Sermkiat Lolak; Phattarapong Sawangjai; Thapanun Sudhawiyangkul; Theerawit Wilaiprasitporn; "Parkinson's Disease Recognition Using SPECT Image and Interpretable AI: A Tutorial", IEEE SENSORS JOURNAL, 2021.

Volume 14, Issue 2, Page 26-36, 2025 https://doi.org/10.46810/tdfd.1594252 Research Article

BİNGÖL UNIVERSITY

Türk Doğa ve Fen Dergisi
Turkish Journal of Nature and Science

www.dergipark.gov.tr/tdfd

Detection of Cervical Vertebrae Using Object Detection and Semantic Segmentation Methods in Lateral Cephalometric Radiographs

Mazhar KAYAOĞLU[1*], Abdulkadir ŞENGÜR[2], Saadet ÇINARSOY CİĞERİM[3], Sabahattin BOR[4]

[1] Bingöl University, Department of Informatics, Bingöl, Türkiye
[2] Fırat University, Faculty of Technology, Department of Electrical and Electronics Engineering, Elazığ, Türkiye
[3] Van Yüzüncü Yıl University, Faculty of Dentistry, Department of Clinical Sciences, Van, Türkiye
[4] İnönü University, Faculty of Dentistry, Department of Clinical Sciences, Malatya, Türkiye
Mazhar KAYAOĞU ORCID No: 0000-0002-5807-9781
Abdulkadir ŞENGÜR ORCID No: 0000-0003-1614-2639
Saadet ÇINARSOY CİĞERİM ORCID No: 0000-0002-4384-0929
Sabahattin BOR ORCID No: 0000-0001-5463-0057

**Corresponding author: mkayaoglu@bingol.edu.tr*

(Received: 30.11.2024, Accepted: 04.04.2025, Online Publication: 27.06.2025)

Keywords
Object detection, Semantic segmentation, Classification

Abstract: This study proposes an artificial intelligence-based method for the detection and semantic segmentation of C2, C3, and C4 cervical vertebrae in lateral cephalometric radiographs. The dataset used in the research consists of 3,085 lateral cephalometric radiographs provided by the Department of Orthodontics, Faculty of Dentistry, Van Yüzüncü Yıl University. Following evaluations by expert clinicians, 2,520 radiographs that met the criteria for diagnostic accuracy and clinical suitability were included in the study. In the initial stage, vertebral regions were identified using YOLOv8 and YOLOv11 object detection models, and these areas were meticulously annotated using QuPath software. The labelled data were then subjected to segmentation using advanced deep learning models such as Attention-UNet, Attention-ResUNet, SEEA-UNet, and ResAt-UNet.The study revealed that the object detection models achieved a high performance with an accuracy of 99.8%. Among the segmentation models, Attention-ResUNet demonstrated the best performance with an accuracy of 99.25%, while the ResAt-UNet model stood out with its balanced generalization capacity. The generated binary masks provided a reliable dataset for bone age estimation and skeletal maturity analysis. This study aims to reduce radiation exposure and streamline clinical workflows by eliminating the need for additional imaging. The findings indicate that AI-supported methods minimize errors caused by manual assessments and ensure standardization in skeletal analysis. It is anticipated that these methods could be widely utilized in orthodontic and pediatric medical applications in the future.

Nesne Algılama ve Semantik Bölütleme Yontemleri Kullanılarak Lateral Sefalometrik Radyografilerde Servikal Vertebra Analizi

Anahtar Kelimeler
Nesne tespiti, Semantik segmentasyon, Sınıflandırma

Öz: Bu çalışmada, lateral sefalometrik radyografilerde C2, C3 ve C4 servikal vertebralarının tespiti ve semantik segmentasyonu için yapay zeka tabanlı bir yöntem önerilmektedir. Araştırmada kullanılan veri seti, Van Yüzüncü Yıl Üniversitesi Diş Hekimliği Fakültesi Ortodonti Anabilim Dalı tarafından sağlanan 3085 lateral sefalometrik radyografiden oluşmaktadır. Uzman hekimler tarafından yapılan değerlendirme sonucunda, tanısal doğruluk ve klinik uygunluk kriterlerini karşılayan 2520 radyografi seçilerek çalışmaya dahil edilmiştir. İlk aşamada YOLOv8 ve YOLOv11 nesne algılama modelleri kullanılarak vertebra bölgeleri tespit edilmiş ve ardından bu alanlar QuPath yazılımı ile detaylı şekilde anotasyonlanmıştır. Etiketlenen veriler, Attention-UNet, Attention-ResUNet, SEEA-UNet ve ResAt-UNet gibi ileri seviye derin öğrenme modelleri kullanılarak segmentasyon işlemlerine tabi tutulmuştur. Çalışma, nesne algılama modellerinin %99,8 doğruluk oranıyla yüksek performans sergilediğini ortaya koymuştur. Segmentasyon modelleri arasında en iyi performansı %99,25 doğruluk oranı ile Attention-ResUNet gösterirken, ResAt-UNet modeli genelleme kapasitesindeki dengesiyle

dikkat çekmiştir. Elde edilen ikili maskeler, kemik yaşı tahmini ve iskeletsel olgunluk analizi için güvenilir bir veri seti oluşturmuştur. Bu çalışma, ek görüntüleme ihtiyacını ortadan kaldırarak radyasyon maruziyetini azaltmayı ve klinik süreçleri hızlandırmayı amaçlamaktadır. Sonuçlar, yapay zeka destekli yöntemlerin manuel değerlendirme kaynaklı hataları en aza indirdiğini ve iskeletsel analizde standardizasyon sağladığını göstermektedir. Gelecekte, bu yöntemlerin ortodonti ve pediatrik tıbbi uygulamalarda yaygın olarak kullanılabileceği öngörülmektedir.

1. INTRODUCTION

Bone age estimation is critically important for evaluating growth and development in children and adolescents. These estimations play a vital role in orthodontic treatment planning, diagnosing skeletal anomalies, and monitoring individual growth processes. Traditionally, hand-wrist radiographs have been one of the standard methods for this evaluation. However, hand-wrist radiographs require an additional imaging procedure, which may increase radiation exposure and prolong clinical workflows. As an alternative, the cervical vertebrae (C2, C3, C4) in lateral cephalometric radiographs offer an effective method for simultaneous bone age estimation and skeletal maturity assessment without the need for extra imaging.

To establish a foundation for bone age estimation, the detection and segmentation of the C2, C3, and C4 cervical vertebrae were addressed in this study. The morphological characteristics of cervical vertebrae serve as strong biological markers for determining skeletal maturity stages, and analyzing this region provides reliable results for bone age estimation. However, manual evaluations can be time-consuming and prone to subjective errors. Therefore, developing artificial intelligence-based automated methods enables a faster, more consistent, and highly accurate analysis process.

Lateral cephalometric radiographs obtained from the Orthodontics Department of Van Yüzüncü Yıl University Faculty of Dentistry were utilized for the detection and segmentation of C2, C3, and C4 cervical vertebrae. Specifically, YOLOv8 and YOLOv11 models were employed for object detection tasks, while segmentation was carried out using advanced deep learning models such as Attention-UNet, Attention-ResUNet, SEEA-UNet, and ResAt-UNet. Initial labeling of the cervical vertebral regions in the images was performed on the Roboflow platform, followed by detailed annotations using QuPath software. As a result of these processes, a high-quality dataset was created for use in bone age estimation and other clinical analyses.

The primary aim of this study is to propose a method for the detection and segmentation of C2, C3, and C4 cervical vertebrae in lateral cephalometric radiographs and to demonstrate the potential of artificial intelligence-based approaches in this field. The study seeks to eliminate the need for additional diagnostic methods, such as hand-wrist radiographs, in clinical workflows, providing a solution that saves time for orthodontists and minimizes human error. In the future, the segmentation outputs obtained through this study could serve as a reference for bone age estimation processes, establishing a new standard for skeletal maturity analysis. Cervical vertebra analysis is not only useful for growth and development predictions but also has broader clinical applications, such as diagnosing skeletal anomalies and planning surgeries. The integration of artificial intelligence-supported methods into this domain minimizes subjective errors in manual evaluations, enabling faster and more precise analyses. This enhances patient care quality while reducing the workload of clinicians. Therefore, cervical vertebra analysis is becoming an increasingly common method for skeletal evaluation in modern medical practices.

2. RELATED STUDIES

Makaremi et al. (2019) developed a deep learning-based method to classify cervical vertebral maturation (CVM) stages in lateral cephalometric images. The study proposed a custom-designed deep convolutional neural network (CNN) model for classifying CVM stages across six categories extracted from X-ray images. Tests conducted with various image preprocessing techniques and datasets demonstrated accuracy rates exceeding 95%. The results highlighted the potential of the proposed method to classify CVM stages accurately and efficiently, emphasizing its utility as a significant tool in orthodontic treatment planning. The study also underscored the importance of tailored network architectures in small and balanced datasets [1].

Masuzawa et al. (2020) introduced a multi-stage deep learning model for vertebral segmentation, localization, and identification in 3D CT images. In the first stage, vertebral classes (cervical, thoracic, lumbar) were segmented using 3D Fully Convolutional Networks, followed by individual vertebra identification through an iterative network in the second stage. The proposed method achieved a 96% segmentation accuracy with a Dice score, 8.3 mm localization error, and an 84% identification rate, surpassing existing methods. This study presented an integrated framework for automated vertebral analysis in 3D CT images [2].

Demirel and Sonuç (2021) developed a semi-automatic method for bone age estimation to monitor children's growth and for forensic applications. The method combined the areas of carpal bones and the distal epiphyseal region of the radius with an artificial neural network model. Applied to a dataset of radiographs from children aged 1–7 years, the model achieved 87% training accuracy and 85% test accuracy, offering effective results. This method aimed to support physicians by reducing observational errors and enhancing prediction accuracy in age determination [3].

Chen et al. (2022) proposed a method combining U-Net and Mask R-CNN models for the segmentation and identification of cervical and lumbar vertebrae. The method achieved accuracy rates above 90% in lateral X-ray images of patients with ankylosing spondylitis (AS). The study aimed to enhance automation and precision in clinical assessments, even under pathological conditions [4].

Khazaei et al. (2023) developed a deep convolutional neural network (CNN) model to classify adolescent growth spurts based on CVM stages. The study utilized 1,846 lateral cephalograms from an Iranian subpopulation, focusing on the C2, C3, and C4 vertebrae. The model achieved an accuracy of 82% in three-class scenarios and 93% in two-class scenarios. The ConvNeXtBase-296-based CNN model was optimized through transfer learning, achieving high accuracy with limited data. This work highlighted the potential of deep learning-based tools for automated growth stage assessment in orthodontic treatment planning [5].

Li et al. (2023) developed a fully automated deep learning-based system called psc-CVM for evaluating cervical vertebral maturation (CVM) stages. Trained on a dataset of 10,200 lateral cephalograms, the system operated in three stages: detection of C2, C3, and C4 vertebrae positions, shape extraction, and CVM assessment based on the extracted shapes. Tests showed an average AUC value of 0.94, an accuracy rate of 70.42%, a Cohen's Kappa value of 0.645, a weighted Kappa value of 0.844, and an intraclass correlation coefficient of 0.946, indicating high consistency with expert evaluations. The study demonstrated the system's potential as an accurate, reliable, and efficient tool for clinicians in assessing growth and developmental stages [6].

Kresnadhi et al. (2023) compared ResNet-101, InceptionV3, and InceptionResNetV2 architectures for classifying CVM stages using deep learning methods. Images from the CVM-900 dataset were processed with a focus on C2–C4 and C2–C6 regions, supported by data augmentation techniques. InceptionResNetV2 performed best with 54.1% accuracy in the C2–C6 region. However, issues such as overfitting and insufficient multi-scale feature extraction limited performance gains, emphasizing the need for more advanced approaches to address these challenges [7].

Akay et al. (2023) aimed to automatically determine CVM stages in lateral cephalometric radiographs using a deep learning-based CNN model. Data from 588 radiographs were divided into six stages, and the model achieved a 58.66% accuracy rate after 40 epochs of training. While high F1 scores were obtained in CVM Stage 1, classification errors occurred in transitional stages due to similarities. The results suggested the model could serve as a fast and suitable tool for clinical use, with potential for improved performance through larger datasets [8].

Atıcı et al. (2023) developed a two-stage deep learning-based model for evaluating CVM stages using a continuous classification system. Trained on 1,398 lateral cephalometric radiographs, the model combined images with chronological age, achieving an accuracy of 81.17%. The continuous classification method represented growth and development processes more accurately than traditional discrete classifications, with a Pearson correlation coefficient exceeding 0.9, demonstrating high reliability. This study provided a more precise and clinically applicable method for skeletal maturity assessment [9].

Motie et al. (2024) introduced a three-stage deep learning model to classify CVM stages. Using 2,325 lateral cephalograms, the method involved region detection with Faster R-CNN and classification through two ResNet101 models. The first model categorized images into two main groups (C1–C3 and C4–C6), while the second model further classified these into subcategories. The proposed method achieved an overall accuracy of 82.96%, outperforming previous single-stage models and offering high accuracy in classification processes. This study provided an effective approach for automated CVM evaluation in clinical applications [10].

Mohammed et al. (2024) developed a CNN-based method for estimating skeletal growth maturity based on CVM and lower second molar calcification levels. Using 1,200 lateral cephalograms and 1,200 panoramic images, the method achieved six-class classification accuracy rates of 98% for CVM prediction in males and 97% for second molar calcification prediction in females. The study demonstrated the efficacy of AI-based approaches in assessing growth and development stages with high accuracy, aligning with traditional orthodontic imaging methods [11].

In light of the reviewed studies, AI-based methods in cervical vertebra analysis and bone age estimation provide significant advantages in terms of accuracy and reliability. Accordingly, this study develops a method for the automatic detection, segmentation, and classification of cervical vertebrae (C2, C3, and C4). The goal is to establish an AI-supported framework for lateral cephalometric radiographs, reducing dependency on manual evaluations and automating the bone age estimation process. Details of the datasets, algorithms, and workflows used in this study are comprehensively explained in the materials and methods section.

3. MATERİALS AND METHODS

In this study, a method was developed for analyzing cervical vertebrae (C2, C3, and C4) from raw radiographic images. In the first stage, the regions containing the C2–C4 vertebrae were identified on lateral cephalometric radiographs and then annotated in detail to prepare them for analysis. The detected regions provide the necessary data for semantic segmentation and classification processes of the C2, C3, and C4 vertebrae.

3.1. Data Collection

The dataset used in this study consists of lateral cephalometric radiographs obtained from the Department of Orthodontics, Faculty of Dentistry, Van Yüzüncü Yıl University **(Decision No: 2023/09-12)**, and serves as the primary data source for the research. Initially, all images underwent a comprehensive evaluation by expert clinicians and were assessed for diagnostic adequacy, visibility of anatomical structures, and technical suitability. Following these evaluations, a total of 2,520 radiographs from patients aged 7 to 22 were selected. This dataset includes images from 1,302 female and 1,218 male patients and supports the reliability of the study and the accuracy of analytical processes due to its high-quality standards. The selection criteria were based on the technical characteristics of the images and their adequacy for clinical analyses.

3.2. Dataset Preparation

Figure 1 shows an example of a raw cephalometric image used in the study, obtained from the hospital. These images were annotated on the Roboflow platform for training YOLOv8 and YOLOv11 models, with regions containing C2, C3, and C4 vertebrae meticulously labeled. Adopting a top-down approach, the study first ensured the general localization of the vertebrae, followed by a more detailed detection of the specific vertebral regions. This method aims to increase the analytical accuracy of the images and ensure a more precise detection process in the selected regions.

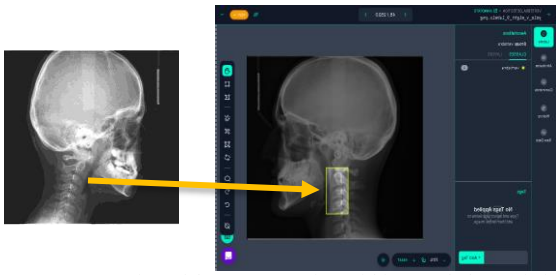

Figure 1. Annotation of the C2–C4 region within a cephalometric image

Figure 1 presents the labeling results of C2-C4 vertebra regions determined by YOLOv8 and YOLOv11 models. These areas underwent further analysis, and precise annotations for each vertebra (C2, C3, and C4) were made using the QuPath software. The flexibility offered by QuPath enabled accurate labeling of complex anatomical structures. During the annotation process, the boundaries of each vertebra were manually marked, taking into account their morphological features. This process contributed both to enriching the dataset for segmentation models and to obtaining a more detailed dataset for subsequent analysis phases. Figure 2 illustrates a visual example of this process performed using QuPath, detailing the annotation procedure for vertebra regions. This step is a critical part of model training, aiming to enhance segmentation and classification accuracy.

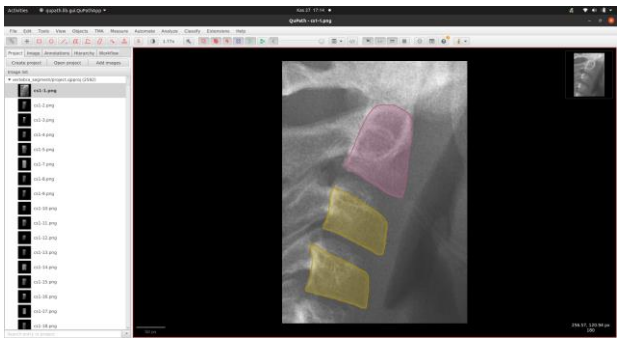

Figure 2. Annotation process for C2-C4 vertebrae

As a result of this process, a dataset containing input data for the deep learning-based U-Net models previously used in our study was created. Following the completion of the labeling and annotation processes, the obtained input images were prepared in RGB format and saved as PNG files, each with a resolution of 512x512 pixels. This process aimed to ensure the consistency and quality standards of the input data to optimize the model's segmentation capabilities.

Additionally, binary masks of the designated regions for each vertebra (C2, C3, C4) were generated as output images using QuPath. These masks were created in black-and-white format to emphasize only the relevant anatomical regions in the images and were also saved in PNG format with a resolution of 512x512 pixels. Defining the masks as black (background) and white (region of interest) facilitated the models' learning process by enabling a clearer distinction of target regions, thereby enhancing segmentation accuracy.

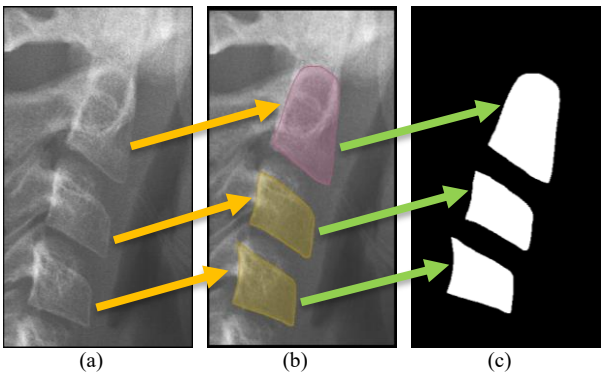

(a) (b) (c)

Figure 3. Segmentation process of C2-C4 vertebrae:
(a) Raw cephalometric image,
(b) Annotations of vertebra regions using QuPath,
(c) Binary masks created for the respective vertebrae.

Figure 3 presents a sample visual of the output images generated at the end of this process, providing a visual explanation of how the outputs are structured. These steps are crucial for ensuring the homogeneity of the dataset prepared for model training and enhancing the effectiveness of deep learning models. The dataset prepared in this manner offers a high standard to improve model performance and ensure suitability for future applications.

3.3. Object Detection

YOLOv8 and YOLOv11 models were employed for the automatic detection and segmentation of C2-C4 vertebra regions, forming a pivotal stage in the research methodology due to their rapid and accurate detection capabilities. YOLOv8 (You Only Look Once, Version 8) is a deep learning model that provides fast and effective results for object detection and classification tasks. As the latest version in the YOLO series, YOLOv8 introduces various improvements built upon previous models. The network architecture has been optimized to achieve more precise and faster object detection performance. YOLOv8 stands out with adaptive bounding box headers, better feature map extraction, and dynamic data augmentation techniques. The model is designed to be trained on large datasets and is preferred for real-time applications due to its low latency. Specifically, it provides an optimal balance between speed and accuracy [12].

YOLOv11 is one of the most up-to-date object detection models and offers significant improvements compared to earlier YOLO versions. This model utilizes deep learning techniques more efficiently, providing high accuracy in detecting both small and large objects. YOLOv11 uses multi-scale feature maps to improve performance across a wide range of scales and incorporates advanced regularization techniques that enhance the model's generalization ability. Additionally, the model is equipped with attention mechanisms, enabling more effective object detection, especially in complex scenes. YOLOv11 is a preferred model for both academic and industrial applications due to its real-time performance [13][14].

In this study, YOLOv8 was selected as the primary model for the automated, accurate, and rapid detection of C2, C3, and C4 vertebrae. YOLOv8 has demonstrated exceptional performance in object detection tasks, particularly excelling in mAP50 and mAP50-95 metrics. This capability ensures high accuracy, even in complex datasets such as lateral cephalometric radiographs with intricate anatomical structures. Additionally, the model's low latency facilitates efficient detection, enabling faster processing and minimizing potential diagnostic errors in clinical workflows. The advanced architecture of YOLOv8 effectively balances detection accuracy and computational efficiency. Its capacity to handle diverse and complex data structures provides a robust foundation for segmentation processes, where precision is critical. Moreover, the model simplifies the detection phase, reducing reliance on manual interventions and promoting a standardized, reproducible workflow. In contrast, YOLOv11, while being a lightweight model with lower hardware requirements, was not chosen as it could not match the high accuracy and rapid detection performance offered by YOLOv8. Based on these technical advantages, YOLOv8 was deemed the most suitable model for achieving the objectives of this study.

Figure 4 shows the workflow used for detecting the C2-C4 vertebra regions with the YOLOv8 architecture. In the input stage, cephalometric images were provided to the model. In the backbone section, image features were processed through convolutional layers, and key features were extracted. In the neck section, feature maps of different scales were merged and upscaled to enable multi-scale detection. In the prediction stage, the detected regions were identified, and outputs were generated. As a result, the C2-C4 vertebra regions were accurately detected, and the model's outputs were displayed.

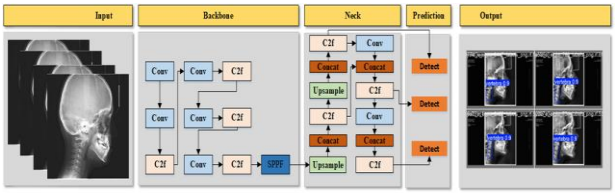

Figure 4. Workflow used for detecting the C2-C4 vertebra regions with the YOLOv8 architecture [15]

3.4. Semantic Segmentation

Semantic segmentation is a computer vision technique aimed at assigning a class to each pixel in an image. This method not only detects objects in an image but also defines the spatial boundaries of these objects in detail. Semantic segmentation is widely used in various fields, including medical image analysis, autonomous vehicles, satellite imaging, and augmented reality, where there is a need to distinguish objects or regions belonging to different classes, especially in complex scenes. It relies on deep learning models to classify pixels. The model extracts both low-level features (e.g., color and edges) and high-level features (e.g., shape and object meaning) from the input image. Each pixel is then assigned a class. Models such as U-Net, Fully Convolutional Networks (FCN), SegNet, and DeepLab are commonly used for this purpose. Semantic segmentation is frequently preferred in applications requiring high accuracy, such as medical image analysis. For instance, segmenting specific anatomical structures (e.g., organs or tissues) in X-ray or MRI images helps support diagnosis and treatment processes. Additionally, automatic and rapid segmentation reduces the time loss and human error associated with manual labeling. This method typically relies on an encoder-decoder architecture. The encoder extracts features from the input image, while the decoder uses these features to perform pixel-level classification. The model is often optimized using loss functions such as cross-entropy or dice loss in segmentation processes.

Semantic segmentation enables the precise identification of object or region boundaries by classifying pixels in detail, offering time savings and accuracy improvements compared to manual labeling. It is widely used in areas such as medical image analysis (organ and tumor segmentation), autonomous vehicles (road and pedestrian detection), satellite imaging (land classification), and industrial quality control [16] [17] [18].

Attention-UNet is a model that adds attention mechanisms to the classic U-Net architecture, highlighting important regions in the image. This model is particularly used to segment target regions more accurately in complex medical images. The attention mechanisms filter out irrelevant areas in the image while

improving classification and segmentation accuracy. Additionally, with attention gates, the model reduces unnecessary information overload by focusing only on the necessary features. This provides a significant advantage, especially in cases with limited datasets and low-contrast images [19].

Attention-ResUNet enhances the U-Net architecture by adding residual connections and attention mechanisms, which both simplify the learning process and improve segmentation performance. Residual connections speed up learning by reducing gradient loss encountered during training of deeper layers of the model. The attention modules ensure that critical regions in the image are emphasized more effectively. This model provides high accuracy in delicate tasks like tissue or organ segmentation in medical images, especially for low-contrast and complex structures [20].

SEEA-UNet integrates Squeeze-and-Excitation (SE) blocks into the U-Net architecture, enabling more effective emphasis on important features. SE blocks dynamically adjust the importance of each feature map, highlighting areas the model needs to focus on. This feature offers a significant advantage in medical image segmentation, especially when working with limited data. SEEA-UNet delivers high precision and enhances overall performance, particularly in areas like organ segmentation or distinguishing bone structures [21].

ResAt-UNet is a deep learning model that stands out in the field of medical image segmentation. This model combines the ResNet-based encoder structure with the U-Net architecture to provide effective segmentation performance. The model aims to improve segmentation accuracy with attention mechanisms and residual connections. Attention mechanisms allow the model to focus on important areas during segmentation, while residual connections prevent information loss and enable effective learning in deeper layers of the model. The main advantage of ResAt-UNet is that it provides more precise segmentation, especially when working with low-contrast and complex structures in medical images. This model is typically evaluated using metrics like Dice Similarity Coefficient (DSC) and Intersection over Union (IoU), where it yields higher results compared to the traditional U-Net architecture. ResAt-UNet is applied in various medical tasks such as brain tumor segmentation, lung lesion detection, and organ delineation. By combining ResNet and attention mechanisms, the model ensures both efficient feature extraction and the ability to focus on critical regions. These features make ResAt-UNet a strong choice for medical segmentation problems [22].

4. EXPERIMENTAL STUDIES

In our study, a powerful hardware infrastructure was preferred for processing large volumes of data and training deep learning models. In this context, a system with 100 GB of RAM capacity was used, and a dual GPU configuration from the NVIDIA RTX A4000 model, which is known for providing high performance in artificial intelligence applications, was specifically chosen. These GPUs played a critical role in accelerating deep learning algorithms and processing large datasets. The stages of dataset preparation, labeling, and image processing were carried out using the Python programming language. Thanks to Python's flexible structure and extensive library support, image processing and the implementation of deep learning models were efficiently completed. Popular libraries such as TensorFlow and NumPy were used during model training and validation stages. Additionally, tools like Pandas and Matplotlib were preferred to enhance the accuracy of data preprocessing and analytical processes.

With this robust hardware and software infrastructure, model training and testing processes were completed quickly, and it was also possible to optimize complex models and work with large datasets. The provided infrastructure contributed to the efficiency of the study and enhanced the reliability of the results.

As shown in Figure 5, the main workflow of our study is systematically visualized. This process encompasses all steps, starting from raw data processing and leading to the final output.

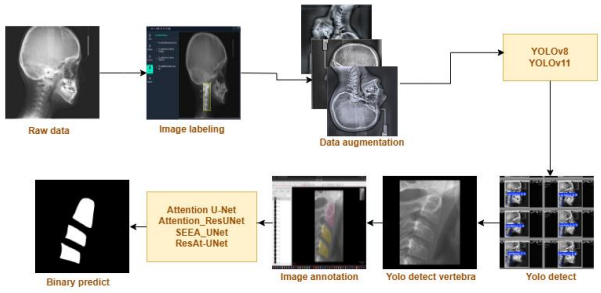

Figure 5. Flow diagram of the study

The study begins with the collection of raw lateral cephalometric X-ray images. On these images, the vertebra regions were highlighted and labeled. During the labeling process, particular focus was placed on the C2, C3, and C4 vertebrae, ensuring that these regions were clearly defined. Following the labeling process, the dataset was augmented with techniques such as rotation and scaling, as well as methods like Gaussian noise and contrast adjustments. These steps aimed to improve the models' generalizability under varying imaging conditions and to evaluate their robustness to noise. This comprehensive data augmentation strategy significantly contributed to assessing model performance in a broader context and adapting them for clinical applications.

Before segmentation, vertebra regions were automatically detected using YOLOv8 and YOLOv11 models. The speed and accuracy provided by these models effectively isolated critical vertebra regions, after which the necessary annotations for segmentation were performed. In the segmentation phase, various deep learning models with attention mechanisms were used. These included Attention-UNet, Attention-ResUNet, SEEA-UNet, and ResAt-UNet models, each aimed at more accurately differentiating the vertebra regions. The binary prediction

masks obtained from the application of these models clearly delineated the vertebral structures.

In this study, the cervical vertebra regions were detected using the YOLOv8 and YOLOv11 models. Both models were trained on a total of 2520 lateral cephalometric X-ray images. The data was divided into 70% for training, 20% for validation, and 10% for testing. During the training process, the batch size was set to 16 and the image size to 640 pixels. The training continued for a total of 100 epochs. The results for the models are listed in Table 1, and the outcome metrics are visually presented in Figure 6.

Table 1. Comparative results of YOLOv8 and YOLOv11 models

Metrik	Yolov8	Yolov11
Precision (P)	0.998	0.998
Recall (R)	0.998	0.998
Map50	0.995	0.994
Map50-95	0.783	0.782
Inference Time	1.8 Ms	1.9 Ms
Preprocess Time	0.3 Ms	0.3 Ms
Postprocess Time	0.3 Ms	0.3 Ms
Total Number of Layers	168	238
Number of Parameters	3,005,843	2,582,347
Gflops	8.1	6.3

When the results of both models were examined, it was observed that both YOLOv8 and YOLOv11 performed exceptionally well in object detection tasks. Both models detected the vertebra regions with high accuracy, achieving precision and recall values of 99.8%. YOLOv8 exhibited a slight advantage over YOLOv11 in mAP50 (99.5%) and mAP50-95 (78.3%) metrics. Additionally, YOLOv8 was observed to provide faster inference with a time of 1.8 ms. On the other hand, the YOLOv11 model operates with fewer parameters (2,582,347) and lower computational power requirements (6.3 GFLOPs). This indicates that YOLOv11 is a lighter model and offers a suitable alternative for applications that need to run on lower hardware resources. In terms of preprocessing and postprocessing times, both models provided similar results (0.3 ms).

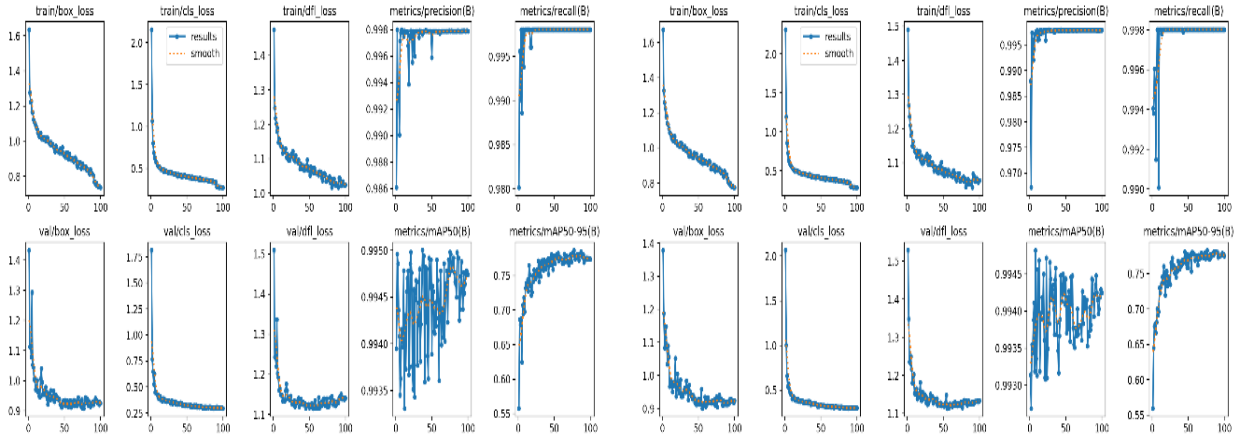

(a) (b)

Figure 6. Graphical representation of the results for the YOLOv8 (a) and YOLOv11 (b) models.

As a result, the graphs show a consistent decrease in the loss values during the training process for both models. In both YOLOv8 and YOLOv11 models, the metrics of train/box_loss, train/cls_loss, and train/dfl_loss steadily decreased after 100 epochs. Similarly, a significant reduction was observed in validation losses, and the models showed an increased generalization capacity throughout the training process. Looking at the Precision and Recall graphs, both models reached levels of 99.8%, with a rapid improvement early in the training process. For the mAP50 metric, YOLOv8 reached 99.5%, while YOLOv11 showed a similar result of 99.4%. In the mAP50-95 values, YOLOv8 slightly outperformed with 78.3%, while YOLOv11 showed 78.2%. YOLOv8 demonstrated superior performance in terms of accuracy and speed, while YOLOv11 stands out with its lower computational load. Both models offer effective and reliable options for cervical vertebra detection. These detections were used as input data for segmentation models, enabling a detailed analysis of the vertebra regions. During the segmentation phase, the aim was to reveal finer details and classify the detected regions more accurately. This approach provided a solid foundation for subsequent analysis and model accuracy by clearly differentiating the vertebral structures. The results for the models used in this context are shown in Table 2.

Table 2. Accuracy/loss graphs and confusion matrix of segmentation models' performance results

	Accuracy & Loss Graphs		Confusion Matrix
Attention-UNet	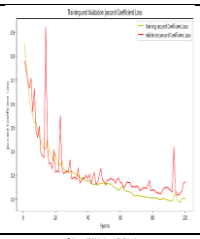	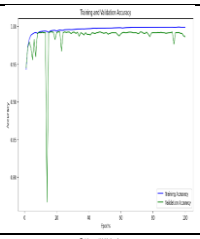	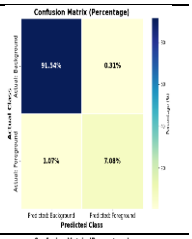
Attention-ResUNet	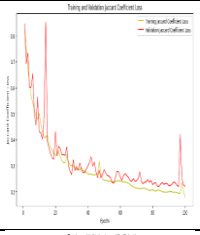	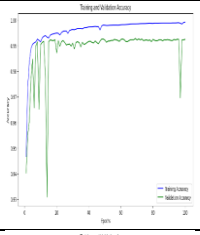	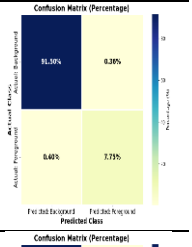
Seea-UNet	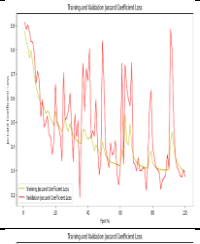	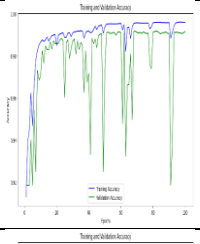	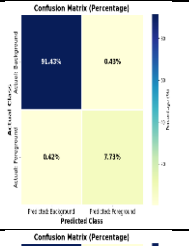
ResAt-UNet	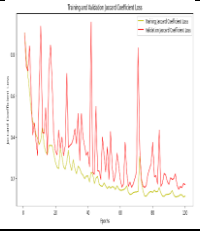	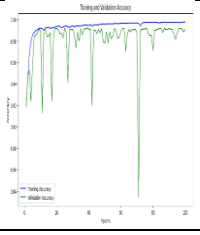	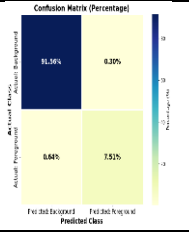

In Table 2, where the performance results of the segmentation models are examined, various findings have been obtained based on accuracy and loss graphs, as well as confusion matrices. The four different models used in the study Attention-UNet, Attention-ResUNet, SEEA-UNet, and ResAt-UNet demonstrated different performances during the training and validation phases. The Attention-UNet model achieved 99.88% training accuracy and 98.62% validation accuracy. However, fluctuations in the validation loss indicate that the model showed signs of overfitting in some cases and that its generalization ability might be limited. The Attention-ResUNet model, on the other hand, performed the best, with 99.92% training accuracy and 99.25% validation accuracy. The consistency between the training and validation losses suggests that the model has a strong generalization capacity. In the SEEA-UNet model, training accuracy was 99.59% and validation accuracy was 99.16%. The increase in validation loss suggests that the generalization ability of this model might be slightly more limited compared to the other models. The ResAt-UNet model achieved 99.78% training accuracy and 99.87% validation accuracy, obtaining a balanced result between training and validation performance. Low validation loss and Jaccard index loss indicate that the model has a high generalization capacity. When performance results based on the confusion matrix are evaluated, it is observed that the models show varying success levels in the "background" and "foreground" classes. The Attention-UNet model achieved high accuracy in the background class (99.25% F1-score), but drew attention to a lower recall value in the foreground class (86.86%), indicating difficulty in detecting some true positive examples. The Attention-ResUNet model reached 95.35% F1-score in the foreground class, demonstrating a balanced performance in both precision and recall. This shows that the model has a high detection rate and accurately identifies most of the true positive examples. The SEEA-UNet model also achieved high precision and recall values, but the recall value in the foreground class was slightly lower. The ResAt-UNet model stands out with a balanced result between training and validation accuracy and low loss values. It achieved 94.14% F1-score in the foreground class, but the recall value was slightly lower compared to the other models (92.16%), indicating that the model has strong generalization ability but may miss some true positives. Overall, the highest accuracy rate of 99.24% was achieved by the Attention-ResUNet model. The ResAt-UNet model, however, demonstrated strong generalization capacity with a balanced performance between training and validation and low loss values. The SEEA-UNet model stands out with its fast learning ability, while the Attention-UNet model, despite high training accuracy, lags behind other models in terms of generalization due to fluctuations in validation loss.

The Attention-ResUNet model demonstrated the highest inter-class agreement with a Cohen's Kappa value of 94.9%, exhibiting superior performance in segmentation accuracy. Statistical power analysis conducted for this model indicated that the dataset provided 100% power, confirming that the results are highly generalizable. SEEA-UNet achieved a Cohen's Kappa value of 94.4%, displaying high agreement and particularly excelling in small and detailed regions. Similarly, the statistical power for this model was calculated as 100%, establishing the reliability of its outcomes. The ResAt-UNet model, with a Cohen's Kappa value of 93.6%, stood out for its balanced generalization capacity, and power analysis demonstrated that this model also operated with 100% power, reinforcing the statistical significance of its results. The Attention-UNet model achieved a strong agreement with a Cohen's Kappa value of 90.4%, and power analysis revealed that the dataset used for this model also had 100% power. The power analyses conducted for each model demonstrated that the dataset, consisting of 2,520 images, is more than sufficient for ensuring the generalizability and reliability of the results. These findings confirm that the models provide effective and standardized methods suitable for clinical applications.

Table 3. Contains visuals of the predictions made by the segmentation models.

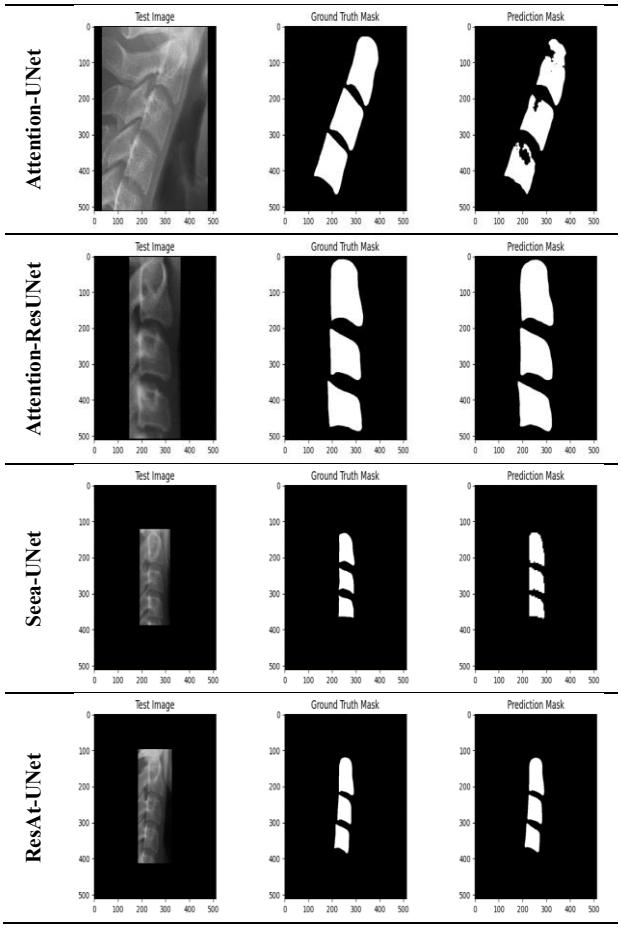

When the visuals of the segmentation model predictions in Table 3 are evaluated alongside the performance results of the models in Table 2, it can be observed that the Attention-UNet model provided very accurate predictions for the segmentation masks, especially in large and distinct vertebra regions. However, some deficiencies in the predicted masks were observed in smaller and boundary areas. This is consistent with the recall value of 86.86% in the foreground class. The model's precision value is at 95.74%, indicating a high true positive prediction rate, but some true positives have been missed. The Attention-ResUNet model demonstrated a more balanced performance in the segmentation masks, both in the background and foreground classes. The precision value for the foreground class was recorded at 95.61%, and the recall value at 95.10%. The segmentation masks showed that the vertebra boundaries were accurately segmented. Especially in complex boundary structures, the predicted masks closely matched the ground truth masks. The SEEA-UNet model stood out for its fast learning ability and low loss values. The segmentation masks in the visuals produced accurate results in large vertebra areas. However, the model's recall value is at 94.81%, and some deficiencies were observed in smaller vertebra regions. The precision value of 94.76% indicates a high accuracy rate. The ResAt-UNet model, especially with its segmentation accuracy in boundary areas, stood out. The segmentation masks showed that the vertebra boundaries were largely accurately segmented in both the background and foreground classes. The precision value for the foreground class was 96.20%, and the recall value was 92.16%. This shows that the model's accuracy is high, but some small vertebra areas were missed. Overall, the visual analysis of the segmentation masks indicates consistency with the models' classification metrics. The Attention-ResUNet model stands out in terms of overall accuracy and balance of the segmentation masks. The SEEA-UNet and ResAt-UNet models provided effective predictions in prominent vertebra areas but showed slight deficiencies in smaller areas. The Attention-UNet model, despite its high accuracy, made more errors in smaller and complex areas compared to the other models.

Table 4. IoU results of segmentation models

Model	IoU
Attention-ResUNet	0.9506
SEEA-UNet	0.9419
ResAt-UNet	0.9405
Attention-UNet	0.9219

Table 4 presents the Intersection over Union (IoU) values of the four different models used in this study. IoU is a critical metric for evaluating the performance of semantic segmentation models, quantitatively expressing the overlap ratio between the predicted and actual regions. According to Table 4, the highest IoU value, 95.06%, was achieved by the Attention-ResUNet model, which stands out with its superior segmentation accuracy. SEEA-UNet and ResAt-UNet demonstrated balanced and high accuracy, with IoU values of 94.19% and 94.05%, respectively. The Attention-UNet model, on the other hand, showed a comparatively lower performance with an IoU value of 92.19%. These differences in IoU values clearly highlight the sensitivity and generalization capacities of the models on the dataset. Particularly, Attention-ResUNet is considered a strong candidate for clinical applications in terms of segmentation accuracy. These findings demonstrate that AI-based approaches can achieve high levels of accuracy in semantic segmentation processes, significantly contributing to clinical decision-making workflows.

5. RESULTS AND FUTURE WORK

In this study, an artificial intelligence-based method was developed for the detection and semantic segmentation of the C2, C3, and C4 cervical vertebrae on lateral cephalometric radiographs. Our goal was to create a reliable infrastructure that will lay the groundwork for bone age prediction and skeletal maturity analysis, while also evaluating the potential of artificial intelligence technologies in this field.

In the study, the YOLOv8 and YOLOv11 models were used for object detection tasks, with both models achieving a 99.8% accuracy rate, enabling the rapid and effective detection of cervical vertebra regions. For the segmentation tasks, detailed annotations were performed using QuPath software, and the data were subsequently analyzed using deep learning models such as Attention-UNet, Attention-ResUNet, SEEA-UNet, and ResAt-UNet. In the comparative evaluation of these models, the Attention-ResUNet model stood out with a segmentation performance of 99.25% accuracy, while ResAt-UNet

drew attention with its superior generalization capacity. The resulting segmentation masks were prepared with high precision and created a suitable dataset for bone age prediction and related analyses. This work contributes to accelerating clinical processes and obtaining more reliable results, particularly in fields such as orthodontics and pediatric medicine. The developed method eliminates the need for additional imaging, reduces radiation exposure, and prevents subjective errors in manual evaluations. With these features, it offers an alternative approach to traditional methods such as hand-wrist radiographs. Additionally, this method has the potential to create a standardized framework for skeletal maturity analysis and bone age prediction processes.

This study demonstrates that the methods developed for the automatic detection and segmentation of C2, C3, and C4 vertebrae provide an innovative contribution by minimizing the subjective errors encountered in manual analyses in the literature and reducing radiation exposure. While similar studies in the literature have made significant contributions to advancements in this field, the proposed methods stand out due to the use of YOLO models and detailed segmentation stages. In this study, the original improvements made in model configurations have enhanced segmentation accuracy, offering a more efficient application in clinical processes.

In future studies, it is planned to perform automatic bone age prediction using the binary datasets obtained in this study. To improve the accuracy of these predictions, the existing dataset will be enriched, and analyses for different age groups will be conducted. The goal in this process is to enhance model performance using advanced artificial intelligence algorithms. It is expected that the results will allow for a more precise assessment of individuals' growth and development processes. Additionally, it is anticipated that these methods will also be used in the diagnosis of skeletal anomalies and in surgical planning processes.

In conclusion, this study represents an important step in the integration of artificial intelligence-based methods in medical image analysis. The developed method not only accelerates clinical processes and reduces error rates but also contributes to the digital transformation of modern medicine. In future studies, it is hoped that these approaches will be integrated into different medical application areas, providing more comprehensive and widely applicable solutions.

Notice

This study is derived from the doctoral dissertation entitled “Bone Age Assessment through the Analysis of Cervical Vertebrae in Lateral Cephalometric Radiographs Using Semantic and Instance Segmentation Methods,” conducted by Mazhar Kayaoğlu under the academic supervision of Abdulkadir Şengür.

REFERENCES

[1] M. Makaremi, C. Lacaule, and A. Mohammad-Djafari, “Deep learning and artificial intelligence for the determination of the cervical vertebra maturation degree from lateral radiography,” Entropy, vol. 21, no. 12, p. 1222, 2019.

[2] N. Masuzawa et al., “Automatic segmentation, localization, and identification of vertebrae in 3D CT images using cascaded convolutional neural networks,” in Medical Image Computing and Computer-Assisted Intervention–MICCAI 2020, LNCS 12261. Springer, 2020.

[3] O. Demirel and E. Sonuç, “Yapay Zeka Teknikleri Kullanılarak Kemik Yaşı Tespiti,” Türkiye Sağlık Enstitüleri Başkanlığı Dergisi, vol. 4, no. 3, pp. 17–30, 2021.

[4] Y. Chen et al., “Vertxnet: Automatic segmentation and identification of lumbar and cervical vertebrae from spinal x-ray images,” arXiv preprint, arXiv:2207.05476, 2022.

[5] M. Khazaei et al., “Automatic determination of pubertal growth spurts based on the cervical vertebral maturation staging using deep convolutional neural networks,” J. World Fed. Orthod., vol. 12, no. 2, pp. 56–63, 2023.

[6] H. Li et al., “The psc-CVM assessment system: A three-stage type system for CVM assessment based on deep learning,” BMC Oral Health, vol. 23, no. 1, p. 557, 2023.

[7] G. A. Kresnadhi et al., “Comparative Analysis of ResNet101, InceptionV3, and InceptionResnetV2 Architectures for Cervical Vertebrae Maturation Stage Classification,” in Proc. 2023 Int. Conf. on Electrical Engineering and Informatics (ICE), 2023.

[8] G. Akay et al., “Deep convolutional neural network—The evaluation of cervical vertebrae maturation,” Oral Radiol., vol. 39, no. 4, pp. 629–638, 2023.

[9] S. F. Atici et al., “A Novel Continuous Classification System for the Cervical Vertebrae Maturation (CVM) Stages Using Convolutional Neural Networks,” 2023.

[10] P. Motie et al., “Improving cervical maturation degree classification accuracy using a multi-stage deep learning approach,” 2024.

[11] M. H. Mohammed et al., “Convolutional Neural Network-Based Deep Learning Methods for Skeletal Growth Prediction in Dental Patients,” J. Imaging, vol. 10, no. 11, p. 278, 2024.

[12] J. Redmon and A. Farhadi, “YOLOv3: An incremental improvement,” arXiv preprint, arXiv:1804.02767, 2018.

[13] Z. Ge, “Yolox: Exceeding yolo series in 2021,” arXiv preprint, arXiv:2107.08430, 2021.

[14] A. Bochkovskiy, C.-Y. Wang, and H.-Y. M. Liao, “Yolov4: Optimal speed and accuracy of object detection,” arXiv preprint, arXiv:2004.10934, 2020.

[15] H. Herfandi et al., “Real-Time Patient Indoor Health Monitoring and Location Tracking with Optical Camera Communications on the Internet of Medical Things,” Appl. Sci., vol. 14, no. 3, p. 1153, 2024.

[16] J. Long, E. Shelhamer, and T. Darrell, "Fully convolutional networks for semantic segmentation," in Proc. IEEE Conf. on Computer Vision and Pattern Recognition, 2015, pp. 3431–3440.
[17] O. Ronneberger, P. Fischer, and T. Brox, "U-net: Convolutional networks for biomedical image segmentation," in Medical Image Computing and Computer-Assisted Intervention–MICCAI 2015: 18th International Conference, 2015, pp. 5–9.
[18] A. Garcia-Garcia et al., "A review on deep learning techniques applied to semantic segmentation," arXiv preprint, arXiv:1704.06857, 2017.
[19] O. Oktay et al., "Attention u-net: Learning where to look for the pancreas," arXiv preprint, arXiv:1804.03999, 2018.
[20] J. Schlemper et al., "Attention-gated networks for improving ultrasound scan plane detection," arXiv preprint, arXiv:1804.05338, 2018.
[21] J. Hu, L. Shen, and G. Sun, "Squeeze-and-excitation networks," in Proc. IEEE Conf. on Computer Vision and Pattern Recognition, 2018, pp. 7132–7141.
[22] Z. Fan et al., "ResAt-UNet: a U-shaped network using ResNet and attention module for image segmentation of urban buildings," IEEE J. Sel. Top. Appl. Earth Obs. Remote Sens., vol. 16, pp. 2094–2111, 2023.

Volume 14, Issue 2, Page 37-51, 2025 https://doi.org/10.46810/tdfd.1605168 Research Article

BİNGÖL UNIVERSITY

Türk Doğa ve Fen Dergisi
Turkish Journal of Nature and Science

www.dergipark.gov.tr/tdfd

Multiple Regression-Based Prediction Method to Assess the Impact of PGA and Distance on Post-Earthquake Structural Damage Levels

Ömer Faruk NEMUTLU[1*]

[1] Bingol University, Engineering and Architecture Faculty, Civil Engineering Department, Bingöl, Türkiye
Ömer Faruk NEMUTLU ORCID No: 0000-0001-7841-3911

**Corresponding author: ofnemutlu@bingol.edu.tr*

(Received: 23.12.2024, Accepted: 08.04.2025, Online Publication: 27.06.2025)

Keywords
Multiple regression, Artificial intelligence, Damage distribution, Earthquake observation, Kahramanmaraş earthquakes

Abstract: This study was carried out to evaluate the accuracy of the damage assessments made after the 06 February 2023 Kahramanmaras earthquakes and to ensure that these data are a guide for future studies in the field of earthquake engineering. The relationship between damage levels, peak ground acceleration (PGA) values measured by Disaster and Emergency Management Affair (DEMA) stations and distances to earthquake-affected cities were analyzed. Unlike the studies in literature, evaluation was made on multiple input and multiple output parameters, and a separate regression model was used for each output data. As a result of regression analysis, a significant relationship was found between damage levels and PGA-distance parameters. The R^2 scores for the "No damage" and "Heavy damage" levels were found to be 0.75 and 0.71, respectively. In the analyzes made by reducing the damage levels to two main categories (damaged and undamaged), the R^2 scores were calculated as 0.63 and 0.6, respectively. These results show that there is a sufficient level of agreement between the input and output parameters, but they reveal that the dataset should be expanded, and the positional details of the structures should be obtained separately for higher accuracy. Within the scope of the study, linear regression, polynomial regression, random forest and gradient boosting models were used and their performances were compared. According to the results obtained, gradient boosting and random forest models were the models that exhibited the best compatibility according to damage levels (0.75 and 0.71 R^2 scores for No damage and Heavy damage, respectively). In particular, the fact that the random forest model gives the best results in 5 out of 6 damage levels shows that the model is a method that produces fast and reliable results in such complex analyses. As a result, it was determined that model performance at low conforming damage levels could be improved by expanding the data set and increasing the available data details. These findings make important contributions to the accuracy analysis of damage assessments after earthquakes and provide a scientific basis for similar studies.

PGA ve Mesafenin Deprem Sonrası Yapısal Hasar Seviyeleri Üzerindeki Etkisini Değerlendirmek için Çoklu Regresyon Tabanlı Tahmin Yöntemi

Anahtar Kelimeler
Çoklu regresyon, Yapay zeka, Hasar dağılımı, Deprem gözlemi, Kahramanmaraş depremleri

Öz: Bu çalışma, 06 Şubat Kahramanmaras depremleri sonrasında yapılan hasar tespitlerinin doğruluğunu değerlendirmek ve bu verilerin deprem mühendisliği alanındaki gelecekteki çalışmalar için rehber olmasını sağlamak amacıyla gerçekleştirilmiştir. Hasar seviyeleri, Afet ve Acil Durum Yönetimi Başkanlığı (AFAD) istasyonlarının ölçtüğü en büyük yer ivmesi (PGA) değerleri ve depremden etkilenen şehirlere olan mesafeleri arasındaki ilişki analiz edilmiştir. Literatürdeki çalışmalardan farklı olarak, çoklu giriş ve çoklu çıkış parametreleri üzerinden değerlendirme yapılmış ve her bir çıkış verisi için ayrı regresyon modeli kullanılmıştır. Regresyon analizleri sonucunda, hasar seviyeleri ile PGA-mesafe parametreleri arasında anlamlı bir ilişki tespit edilmiştir. "Hasar yok" ve "Ağır hasar" seviyeleri için R^2 skorları sırasıyla 0.75 ve 0.71 olarak bulunmuştur. Hasar seviyeleri iki ana kategoriye (hasarlı ve hasarsız) indirgenerek yapılan analizlerde ise R^2 skorları sırasıyla 0.63 ve 0.6 olarak hesaplanmıştır. Bu sonuçlar, giriş ve çıkış parametreleri arasında yeterli düzeyde uyum olduğunu göstermekle birlikte, daha yüksek doğruluk için veri setinin genişletilmesi ve

yapıların konumsal detaylarının ayrı ayrı elde edilmesi gerektiğini ortaya koymaktadır. Çalışma kapsamında lineer regresyon, polinomal regresyon, random forest ve gradient boosting modelleri kullanılmış ve performansları karşılaştırılmıştır. Elde edilen sonuçlara göre gradient boosting ve random forest modelleri, hasar seviyelerine göre en iyi uyumu sergileyen modeller olmuştur. Bu modeller Hasarsız ve Ağır hasarlı durum için sırasıyla 0.75 ve 0.71 R^2 değerleri almıştır. Özellikle random forest modelinin 6 hasar seviyesinden 5'inde en iyi sonuçları vermesi, bu tür karmaşık analizlerde modelin hızlı ve güvenilir sonuçlar üreten bir yöntem olduğunu göstermektedir. Sonuç olarak, düşük uyum gösteren hasar seviyelerinde model performansının, veri setinin genişletilmesi ve mevcut veri detaylarının artırılmasıyla iyileştirilebileceği belirlenmiştir. Bu bulgular, depremler sonrası hasar tespitlerinin doğruluk analizine önemli katkılar sağlamakta ve benzer çalışmalar için bilimsel bir temel oluşturmaktadır.

1. INTRODUCTION

Earthquakes are one of the most important natural disasters within the borders of Turkiye in recent years. Because it contains the world's most active fault zones within its borders. The North Anatolian Fault Zone (NAFZ), the East Anatolian Fault Zone (EAFZ) and the West Anatolian Fault Zone (WAFZ) in the west of the country are faults that have the potential to produce significant earthquakes. In the past years, important earthquakes have occurred in these fault zones [1]. The 2003 Bingol Earthquake, the 2011 Van Earthquake, the 2020 Elazig Earthquake, the 2020 Izmir Earthquake, the 2023 Kahramanmaras Earthquakes are important destructive earthquakes that have occurred in Turkiye in the last quarter century [2]. These earthquakes caused significant loss of life and property. The Kahramanmaras earthquakes, which have passed for a very short time, are among the most important of these destructive earthquakes. The occurrence of two earthquakes with a magnitude of 7.7 M_w and 7.6 M_w only 9 hours apart has greatly increased the level of destruction and losses [3–6]. The first earthquake was an earthquake with an epicenter in Pazarcik. The earthquake, which occurred on February 06, 2023, at 04:17 local time, occurred on the EAFZ. When the surface fractures are examined, they are broken together with the EAFZ and the Oludeniz Fault Zone, which is the continuation of this fault zone. The surface deformation caused by this earthquake is about 300 km [7]. It continued the broken Amanos segment and proceeded to the city center of Hatay province. On the same day, after the first earthquake, the earthquake with the epicenter of Elbistan, which occurred at 13.24 local time, occurred on the Cardak Fault zone, one of the branches of the EAFZ [8].

The M_w 7.7 and M_w 7.6 magnitude earthquakes that occurred in Kahramanmaras on February 6, 2023 caused extensive loss of life and property. Field observations reveal that serious damage occurs due to design and construction errors, especially in reinforced concrete buildings. Among the main structural deficiencies, factors such as strong beam-weak column effect, short column formation, soft floor irregularities, errors in reinforcement placement and inadequate concrete quality stand out. In addition, the damage causes determined by field observations were also confirmed by nonlinear finite element analyses. This situation once again demonstrates the importance of evaluating the existing building stock in terms of compliance with earthquake regulations and carrying out the necessary retrofitting works [10]. The earthquakes of magnitude 7.8 and 7.6 and the Hatay earthquake of magnitude 6.4 that occurred on February 6, 2023 caused serious damage to various structures and critical infrastructures. Field observations and analyses evaluated the damage to residential, commercial and industrial structures, roads, bridges and energy systems [11]. Avğın et al. examines the acceleration records, spectral analyses and structural and geotechnical damage causes of earthquakes in their study. It was determined that 57% of the buildings in Kahramanmaras were damaged, and the most severe damage was concentrated in Dulkadiroğlu, Onikişubat and Göksun districts. The soft story effect, strong beam-weak column formation, inadequate shear wall use, low material quality and weak soil conditions are prominent among the damage causes [12]. Işık et al., in their study, examined the damages in 20 settlements located directly on the fault line and compared the PGA estimates in Turkey's current earthquake hazard maps with the actual measurements. In addition, reinforced concrete structures were evaluated in terms of earthquake engineering and pushover analyses were performed on a sample building model. The results showed that the target displacements were exceeded in some settlements and not in others. It was concluded that a more realistic representation of the earthquake hazard would increase the accuracy of building performance estimates [13].

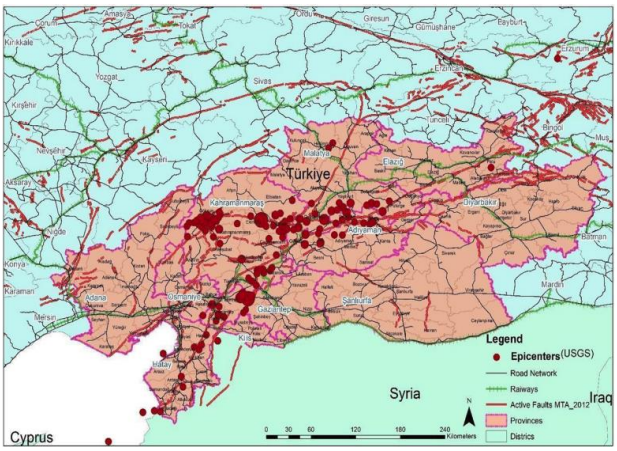

Figure 1. Cities affected by the Kahramanmaras earthquakes[9]

Research has shown that indicators such as ground motion parameters, PGA, play a critical role in determining the level of structural damage during earthquakes. For

example, Tao & Cai investigated the relationship between ground motion parameters and simulated structural damage and emphasized the importance of PGA in terms of damage estimation [14]. In addition, Zhou & Sun stated that a number of factors should be considered in post-earthquake damage assessments and emphasized the importance of ground motion characteristics among these factors [15]. Similarly, Liang et al. examined the effect of epicenteral distance on structural damage and showed that increasing distances were generally associated with less damage [16]. In the context of the Kahramanmaras earthquakes, Karaşin emphasized the unique factors contributing to structural damage in these events, especially addressing the effects of the duration and intensity of shaking. The study found that local geological conditions and material quality caused the diversity of damage [17]. In addition, Zengin & Aydin study emphasized that the observed damage is particularly attributed to the inadequacy of construction practices and poor material quality in the region, which increases the vulnerability of buildings to earthquakes [18]. Research supports the development of a multi-dimensional approach to understand structural weaknesses and solve the problems we face. Such methods allow for the development of strategies for improving construction materials and construction practices. Therefore, careful examination of factors such as PGA, epicenter distance and construction quality enables engineers and policy makers to develop more effective building codes and disaster response strategies [19].

In this study, the effects of PGA and distance to the earthquake epicenter on the post-earthquake damage levels of structures were investigated using a multiple regression model. The February 6, 2023 Kahramanmaras earthquake was used to create and validate the model. These earthquakes, which caused great destruction in Kahramanmaras and its surroundings, affected a wide area with different ground properties and building types. The 7.7 and 7.6 magnitude main shocks and the aftershocks following these main shocks seriously tested the resistance capacities of structures in the region and caused extensive damage. Therefore, the Kahramanmaras earthquakes provide a comprehensive data set to analyze the effects of variables such as PGA and distance on building damage.

Although the attenuation relationships in the literature show a relationship between PGA and distance, this relationship is not combined with damage. This combination can be achieved with multiple regression-based approaches. Some studies in this field examine how high ground accelerations change the damage level [20]. Multiple regression-based approaches allow for fast and low-cost large-scale damage analyses in this field.

Artificial intelligence has become an important part of our lives today. Multiple regression analyses, which are needed in such studies, can now be easily performed with artificial intelligence tools. Linear regression is the simplest regression technique for determining the linear relationship between the dependent variable and the independent variables. The resulting model expresses the relationship between the variables with a linear equation. The analysis of this model is easy and its results can be interpreted clearly. However, linear regression only gives effective results in cases where linear relationships exist. Polynomial regression is used when the relationships between the dependent variable and the independent variables are not linear. Therefore, it makes it possible to capture nonlinear relationships by adding second or higher order terms to model the more complex structure of the data [21]. However, polynomial regression is more susceptible to the problem of overfitting, especially when high-degree polynomials are used [22]. Gradient boosting and random forest are powerful machine learning methods based on decision trees. Random forest combines the predictions of each tree by creating multiple decision trees. This model provides high accuracy and low variance, and is more resistant to overfitting [23]. Studies have shown that gradient boosting generally provides better prediction performance than random forest. For example, gradient boosting models have been shown to provide mean squared error (MSE) compared to random forest [23]. However, random forest may be a more easily implemented option due to the flexibility of the model [24]. In another study, comparisons between gradient boosting and random forest showed that although gradient boosting provides higher accuracy, random forest requires less processing time [25]. In such a case, the integration of researchers into the fields they work in has become inevitable[26–28]. As part of this study, it is aimed to be used in studies in the field of earthquakes with artificial intelligence tools. Studies between artificial intelligence tools and earthquakes are available in the literature. Artificial intelligence tools are used in the classification of damage that occurs after earthquakes and earthquake risk analysis studies[29,30]. It is also used in damage assessment studies from satellite images. In his study, Nemutlu 2024[31] made an assessment on the level of damage in the earthquake-affected regions using satellite images of the Kahramanmaras earthquakes. In the study, satellite images taken before February 6 and satellite images after February 6 were evaluated through image processing techniques and deep learning models, and examinations were made on the determination of areas where the number of damaged structures is intense. On the other hand, there are studies on the detection of damage with damaged building visuals[32,33].

In the context of this research, the relationship between earthquake parameters and damages will be examined by using artificial intelligence tools. In the study, the parameters of the earthquakes were obtained from the earthquake stations, and the relationship between the damaged levels of the damaged structures collected by field work was analyzed by regression models and machine learning methods. The maximum ground acceleration (PGA) caused by the earthquake and the distance of the earthquake stations to the cities affected by the earthquake were used as input data, and the level of damage to the buildings after the earthquake was evaluated by accepting the output data as a dependent variable. The analyzes and analysis processes are explained in detail in the following sections. The results obtained were examined with their justifications.

2. MATERIAL AND METHOD

2.1. Kahramanmaras Earthquakes and Seismicity of the Region

Two destructive earthquakes caused significant loss of life and property at the 06 February 2023. Over 250000 buildings collapsed or severely damaged. 11 cities were directly affected by the earthquake. These cities are Adiyaman, Malatya, Kahramanmaras, Hatay, Elazig, Sanliurfa, Kilis, Gaziantep, Diyarbakir, Adana and Osmaniye. Most of the destruction is concentrated in the provinces of Adiyaman, Kahramanmaras, Hatay and Malatya [34,35]. In total, more than 14 million people living in 11 provinces were directly affected by the earthquake, and more than 50000 people lost their lives because of the collapsed buildings caused by the earthquake[36]. Figure 1 shows the 11 cities affected by the earthquake on a map of Turkiye. Figure 2 shows the fault lines where the earthquake occurred and the fractures that occurred.

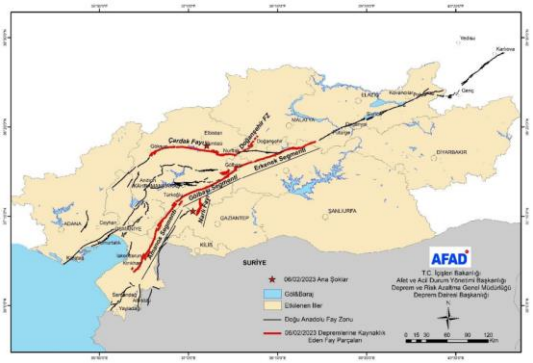

Figure 2. Map showing fault parts of the East Anatolian Fault[8]

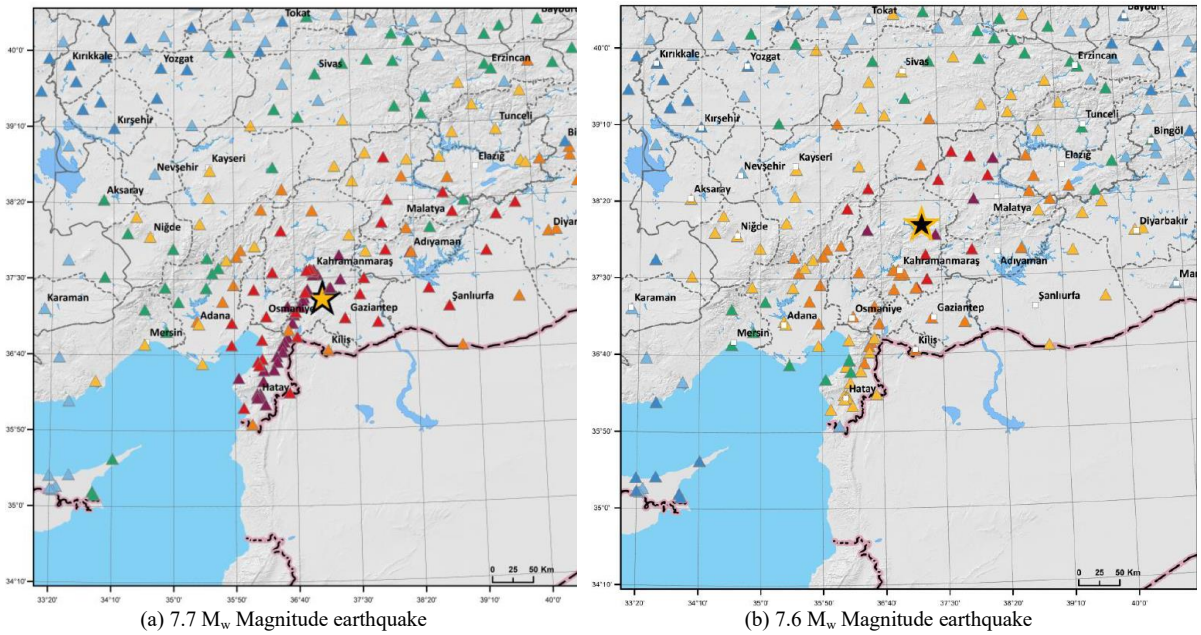

(a) 7.7 M_w Magnitude earthquake (b) 7.6 M_w Magnitude earthquake

Figure 3. Distribution of accelerometer stations in the area that recorded the 7.7 M_w and 7.6 M_w Magnitude earthquake[37]

After the earthquakes, many institutions, especially the Disaster and Emergency Management Affairs (DEMA), took measures related to the earthquake. The distribution of DEMA stations, which have a widespread station network in Turkiye, is given in Figure 3. Figure 3 shows the epicenters of the two earthquakes and the stations and locations that took records because of the earthquakes[38]. Aftershocks occurred after the earthquakes. The most important aftershock of these was the 6.4 M_w magnitude earthquake centered in Hatay on February 20. Figure 4 shows aftershock activity from 6 February to 6 May.

Table 1 and Table 2 show the distances from the epicenters of the earthquake to the nearest settlements according to DEMA information. [38]

2.2. Artificial Intelligence Tools and Machine Learning Process

Today, the analysis of data with artificial intelligence has started to be included in the subjects of researchers. Artificial intelligence can be classified in general terms as methods and problems. When looking at the methods of artificial intelligence, one of the most widely used methods is machine learning[39,40]. Commonly used methods besides machine learning are given in Figure 5. Machine learning, on the other hand, is divided into two sub-headings as traditional methods and deep learning according to the evaluation made by researchers in the most general sense. Traditional methods are methods such as regression, support vector machines, decision trees, artificial neural networks[41,42]. Although deep learning is an artificial intelligence approach based on artificial neural networks, its usage area and the applied process distinguish it from other machine learning methods. On the other hand, the applicability of these methods is related to how the data will be evaluated. To evaluate the available data with artificial intelligence tools, it is necessary to determine the problem. Artificial intelligence evaluates data through two different problems. These problems are regression and classification problems. How the data will be analyzed and which problem definition it conforms to affects the success rate of artificial

intelligence. In machine learning, the input data we have is trained by a model and obtained as output data. These models, which are located between the input and output data, vary according to the problem at hand and the data contained in this problem. Machine learning methods will be applied within the scope of the study. The main topic of study is regression problems. To evaluate regression problems, many regression models are within the scope of machine learning. Figure 6 provides the subheadings of machine learning and the details of these headings. The general concept of machine learning is given in Figure 7.

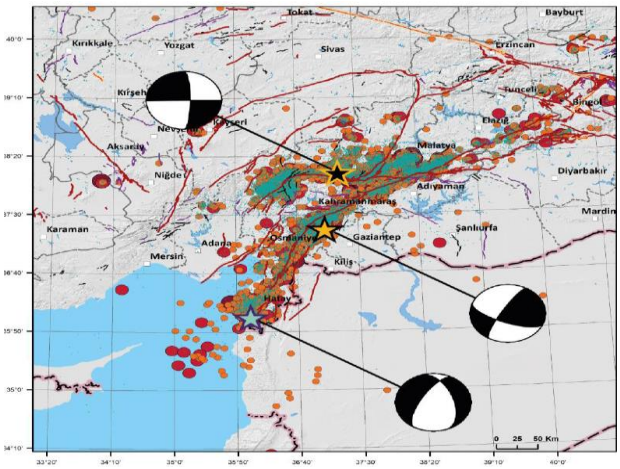

Figure 4. Distribution of aftershock activity from the 7.7 and 7.6 earthquakes (6 February to 6 May)[37]

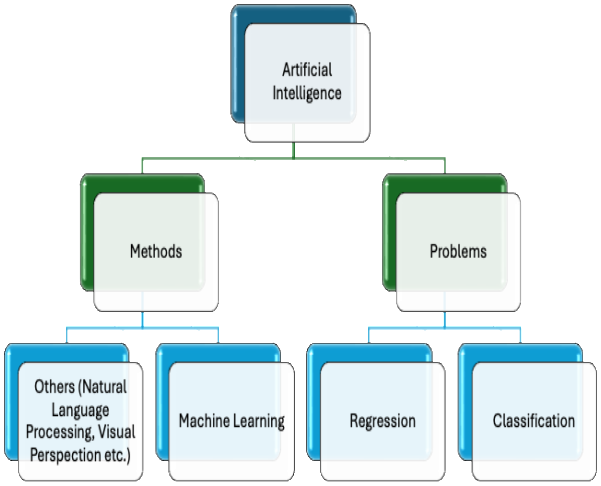

Figure 5. Methods and problems in the use of artificial intelligence

Table 1. Settlements near the epicenter affected by the M_w 7.7 earthquake

Country	City	County	Site	Distance (km)
Turkiye	Kahramanmaras	Pazarcik	Akdemir	2.72
Turkiye	Kahramanmaras	Pazarcik	Karahuyuk	2.84
Turkiye	Kahramanmaras	Turkoglu	Cennetpinari	3.75
Turkiye	Kahramanmaras	Pazarcik	Evri	4.48
Turkiye	Kahramanmaras	Pazarcik	Emiroglu	4.94

Table 2. Settlements near the epicenter affected by the M_w 7.6 earthquake[38]

Country	City	County	Site	Distance (km)
Turkiye	Kahramanmaras	Elbistan	Gumusdoven	1.70
Turkiye	Kahramanmaras	Ekinozu	Akpinar	2.09
Turkiye	Kahramanmaras	Elbistan	Ozcanli	4.90
Turkiye	Kahramanmaras	Ekinozu	Maarif	5.47
Turkiye	Kahramanmaras	Ekinozu	Ekinozu	5.72

Classification and regression are the two main problems in machine learning. What distinguishes these two problems from each other is the solution methods and the dataset in question. Should the data available is an uninterrupted continuous data set, the problem is considered as a regression problem. However, if the existing data is categorical, this problem is a classification problem. The output obtained in the classification problem is labels, while the outputs in the regression problem are numerical values. Classification algorithms; Logistic Regression, Support Vector Machines, Decision Trees, Bayesian, Random Forest, Gradient Boosting, Neural Networks. The algorithms used in the regression problem are linear regression, support vector regression, lasso, elastic net, random forest, decision trees, gradient boosting regression and neural networks. As can be seen, although the methods applied are similar, the versions differ according to the problems. The purpose of the classification problem is to increase the rate at which the model makes an accurate class prediction. The goal of the regression problem is to minimize the error between the actual values and the predicted value. For this reason, evaluation in regression problems is made with metrics such as R^2 score, mean absolute error (MAE), mean square error (MSE), root mean square error (RMSE)[39].

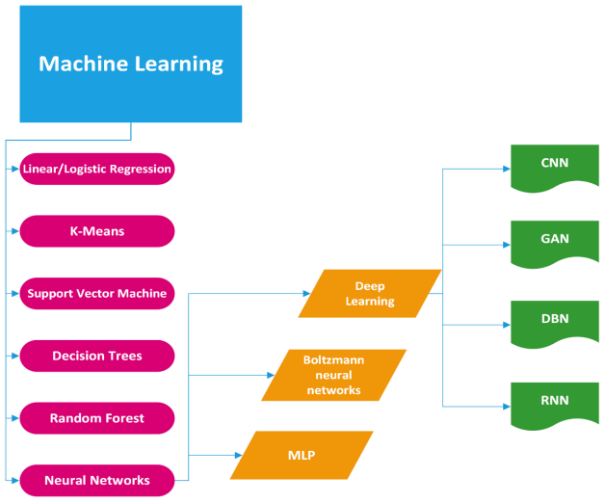

Figure 6. Methods of machine learning

The methods given in Figure 6 aim to model the relationship between an input variable and a target output variable. The purpose of regression models is to predict a continuous output after appropriate modeling. One of the most well-known models is linear regression. Looking at linear regression, it aims to directly reflect the relationship between the independent variable and the dependent variable. It is quick and easy to apply. But in general, it gives good results between variables that have a linear relationship. It is weak in modeling complex relationships. In polynomial regression [43], curves are obtained by adding polynomial terms of independent variables. These curves aim to reflect the relationship between dependent and independent variables. Support vector machines generalize by modeling data that lies between hyperplanes. In decision tree and random forest methods [44], it divides data into sections through simple rules. It aims to obtain stronger results by combining the results of the separated sections in the random forest method. Methods such as Gradient Boosting Regression [45], Neural Networks, K-Nearest Neighbors exhibit different approaches to minimize the distance between data. There are some things to consider when choosing one of these methods. The appropriate regression methods should be determined by considering the amount of data and the relevant dataset, the complexity of the model and the specific conditions of the features to be used in the study. Choices made without taking these situations into account will cause the results to be incompatible and incorrect. In contrast, models that seem to work in harmony do not give accurate results due to overfitting. Although the results obtained look good, overfitting is limited to the accuracy of the model and the dataset used.

Figure 7. Basic concept demonstration in machine learning

2.3. Relationship Between Damaged Structures and Earthquake Records

As outlined in this study, regression methods, random forest and gradient boosting methods were applied to the models. The random forest method is based on the decision tree method. The segmented data is trained on different subsets of the dataset. Estimates are made by averaging all tree estimates. As the name suggests, in this method, sub-datasets are created based on random samples in the training data set. Because the segmented data is trained with different data sets, diversity increases, and this randomness makes the model resistant to overfitting. In a nutshell, each decision tree makes an independent prediction, and these predictions are averaged for regression. Therefore, it is suitable for use in complex datasets due to its ability to overcome complexity in large data sets more easily and its overfitting resistance. Conversely, when looking at the gradient boosting regression method, it focuses on each tree correcting the errors of the previous model by creating decision trees, that is, weak estimators. In contrast to the random forest method, the final estimate is considered as the weighted sum of all decision trees. Due to its gradual approach to minimizing errors, it has high applicability in complex data sets. As part of this research, the damage data obtained from the field studies carried out after the Kahramanmaras earthquakes, the acceleration values related to the earthquake from DEMA's station network and the distances to the city centers will be evaluated. As it is known in the Kahramanmaras earthquakes, 11 cities in Turkiye were directly affected and structures were damaged. Table 3 gives the distribution of damage levels according to cities obtained from the damage assessment reports made by the Ministry of Environment, Urbanization and Climate Change in the field [46]. Buildings are classified according to 6 different damage levels: No Damage, Low Damaged, Medium Damaged, Heavy Damaged, Requiring Urgent Demolition and Collapsed. Until the date of obtaining this data, a total of 38330 buildings collapsed due to the earthquake. Moreover, Table 4 gives the PGA values taken from DEMA's data stations after the Kahramanmaras earthquakes and the distance of the stations to the city center. Table 4 also shows the city where the stations are located and the station code. Together with the information given in Table 3 and Table 4, the relationship between damage levels and PGA values produced by the earthquake will be evaluated over distance with artificial intelligence methods. In the study, PGA values obtained from the stations and the distance to the city center will be used as independent variables. Looking at the station data, since there are PGA values for two different directions, east-west and north-south, the PGA value, which is larger than these two directions, was used as the PGA value. The other independent variable, the distance parameter, is the distance of the stations to the city center. To be used in the study, the distance between the coordinates of the stations and the coordinates of 11 city centers affected by the earthquake was calculated. This variable is given as the calculated distance in Table 4. The dependent variables are the damage levels obtained from the damage assessment results of the cities. The damaged building data given in Table 3 was used as output data in models where PGA and calculated distance expressions obtained from earthquake stations were used as input data. In summary, how does the PGA value produced by the earthquake and the distance to the study area change the damage level after

the earthquake? This is the general concept of the study. The change in damage levels was examined by evaluating the increase or decrease of PGA and the approach or decrease of the distance together.

When the data from the study were assessed, it was determined that the problem was a regression problem. Therefore, regression methods were used. However, since there is no study to examine the relationship between these direct dependent and independent variables, multiple regression models will be used. In this study, input and output data are multiple variables. Maximum PGA and calculated distance data to be used as input data and damage levels will be evaluated through multiple regression models. Figure 8 shows the stages of applying the multiple regression model with different variables.

Table 3. Distribution of building damage in earthquake-affected cities according to damage levels [46]

Cities/Damage States	Number of Building	No Damage	Low Damage	Medium Damage	Heavy Damage	Urgently Demolished	Collapsed
Adana	324345	276691	39541	5118	2923	37	35
Adiyaman	110354	38666	38576	4629	20201	2329	5953
Diyarbakir	183730	129986	45602	3355	4708	59	20
Elazig	27760	11767	7945	506	7441	48	53
Gaziantep	282693	188639	68429	5524	14047	1994	4060
Hatay	342531	140337	103549	12874	64283	8038	13450
Kahramanmaras	225230	93168	79027	5987	35229	4423	7396
Kilis	34346	20188	11191	486	1867	151	463
Malatya	155204	60825	48690	2783	36046	1810	5050
Osmaniye	133992	87674	35006	1094	9010	530	678
Sanliurfa	321065	195565	112690	3192	7706	740	1172
Total	2141250	1243506	590246	45548	203461	20159	38330

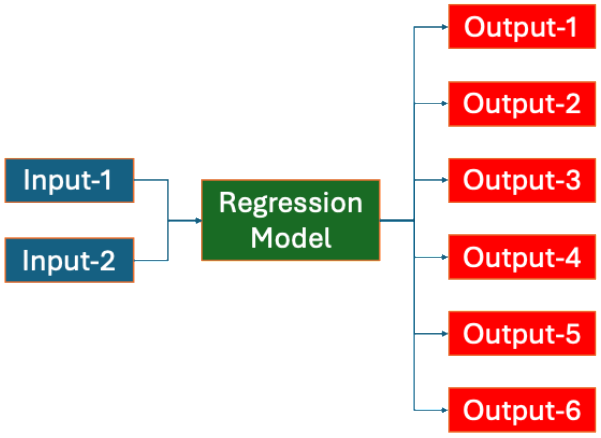

Figure 8. Machine learning process of multiple dependent and independent variables

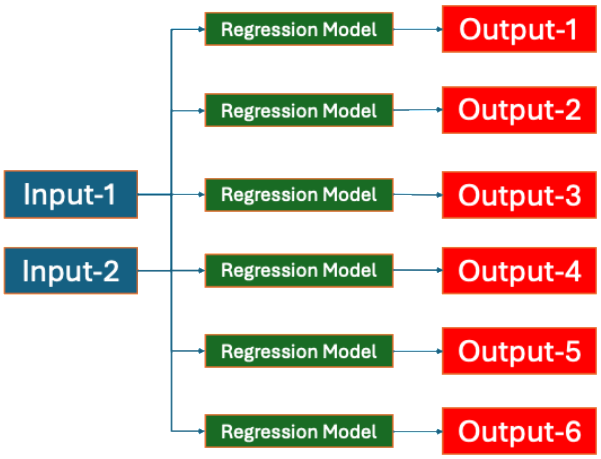

Figure 9. Machine learning process using multiple regression model within the scope of the study

Figure 8 illustrates the stages of machine learning for multiple dependent and independent variables. However, the multiple regression model to be applied within the scope of the study has a different approach from this process. Since a single regression model and multivariate status will not give appropriate results in the study, while multiple regression is applied in this study, model approaches also diversify. As can be seen in Figure 9, in the machine learning model used within the scope of the study, more than one independent variable aims to predict different dependent variables by training with different regression models. Even though the damage levels directly reflect the degree of damage, since the building entering each damage level does not enter the other damage levels, it reveals the necessity of evaluating the dependent variables through a separate regression model with the independent variables. This situation can be given as an example for a clearer understanding. When the distance calculated with PGA is evaluated directly through a single regression model, it will not be able to classify between damage levels. In other words, the PGA value and the calculated distance variables cannot determine the degree of damage. Whether it is a slightly damaged structure, or a heavily damaged structure is independent of PGA and distance parameters. However, it is thought that there is a relationship between the obtained PGA value, and the distance value calculated with the number of damaged structures obtained because of damage detection. Therefore, it is not intended to estimate the level of damage to the damaged structure. The aim of this study is to evaluate the relationship between the number of structures belonging to the damage levels and the PGA value of the earthquake and the distance to the area where the damage occurred. This is the purpose of using different regression models for

different levels of damage. Multiple variation, which is generally accepted, is differentiated in this study. The regression analyses and results obtained according to this approach are given in the following sections of the study. In the study, more than one regression method was tried, and the most appropriate regression model was determined for the relevant damage level. The regression analyses performed within the scope of the study were carried out using the code prepared on Phyton. The libraries and models used in the preparation of the code are as follows [47]:

- import pandas as pd
- import numpy as np
- import matplotlib.pyplot as plt
- import seaborn as sns
- from sklearn.model_selection import train_test_split
- from sklearn.preprocessing import PolynomialFeatures
- from sklearn.linear_model import LinearRegression
- from sklearn.ensemble import RandomForestRegressor, GradientBoostingRegressor
- from sklearn.tree import DecisionTreeRegressor
- from sklearn.metrics import mean_squared_error, r2_score
- from sklearn.preprocessing import StandardScaler

The stations used within the scope of the study include stations in cities affected by the earthquake that took records of 7.6 and 7.7 M_w magnitudes. The data were taken for two earthquakes and are given together in Table 4. Therefore, Table 4 contains values for two different stations with the same name. This situation is broken down according to the earthquakes given in the last column.

Table 4. Acceleration values from the stations and the distance of the stations to the city center

Code*	Province	PGA_NS** (cm/s^2)	PGA_EW** (cm/s^2)	MaksPGA** (cm/s^2)	Calculated Distance(km)	Earthquake***
0122	Adana	57.34304	52.33138	57.34304	258.024439	Pazarcik
0125	Adana	128.551	83.12265	128.551	217.6078245	Pazarcik
0127	Adana	54.98741	50.81184	54.98741	294.1709142	Pazarcik
0130	Adana	81.09731	68.23101	81.09731	245.943058	Pazarcik
0120	Adana	112.4618	115.9806	115.9806	194.8052095	Pazarcik
0129	Adana	49.91854	42.1567	49.91854	334.647704	Pazarcik
0123	Adana	41.42038	39.65318	41.42038	239.3306136	Pazarcik
0118	Adana	50.09951	38.23767	50.09951	243.5799995	Pazarcik
0119	Adana	43.46264	47.31035	47.31035	200.9083487	Pazarcik
0128	Adana	11.68445	14.22345	14.22345	276.3505367	Pazarcik
0124	Adana	8.571593	8.76492	8.76492	300.2768086	Pazarcik
0129	Adana	154.462	172.1792	172.1792	334.647704	Pazarcik
0127	Adana	56.0935	62.72347	62.72347	294.1709142	Pazarcik
0122	Adana	48.44631	67.45694	67.45694	258.024439	Elbistan
0130	Adana	79.31747	79.89938	79.89938	245.943058	Elbistan
0125	Adana	70.09405	50.6768	70.09405	217.6078245	Elbistan
0120	Adana	20.67546	25.01525	25.01525	194.8052095	Elbistan
0118	Adana	27.48687	24.4715	27.48687	243.5799995	Elbistan
0123	Adana	17.93101	27.66621	27.66621	239.3306136	Elbistan
0128	Adana	19.07407	19.72894	19.72894	276.3505367	Elbistan
0124	Adana	15.07867	20.11232	20.11232	300.2768086	Elbistan
0119	Adana	10.10975	11.75999	11.75999	200.9083487	Elbistan
0208	Adiyaman	30.19949	14.00124	30.19949	55.44248446	Pazarcik
0213	Adiyaman	242.2791	171.6946	242.2791	55.43172643	Pazarcik
0201	Adiyaman	474.1206	879.9495	879.9495	72.42297102	Pazarcik
0210	Adiyaman	65.90985	61.3746	65.90985	72.93748504	Pazarcik
0214	Adiyaman	61.67553	54.38109	61.67553	49.00909816	Pazarcik
0213	Adiyaman	121.297	126.6186	126.6186	55.43172643	Elbistan
0205	Adiyaman	44.87774	54.6579	54.6579	92.13885028	Elbistan
2107	Diyarbakir	74.75684	112.2655	112.2655	269.106092	Pazarcik
2104	Diyarbakir	72.83684	116.4655	116.4655	270.9526975	Pazarcik
2101	Diyarbakir	77.07944	71.42427	77.07944	323.8146848	Pazarcik
2103	Diyarbakir	53.7313	43.12138	53.7313	328.5451819	Pazarcik
2106	Diyarbakir	72.30118	61.69453	72.30118	307.0785457	Pazarcik
2108	Diyarbakir	20.65492	20.26613	20.65492	329.2730899	Pazarcik
2107	Diyarbakir	28.64484	47.6136	47.6136	269.106092	Pazarcik
2104	Diyarbakir	27.52314	21.22324	27.52314	270.9526975	Elbistan
2101	Diyarbakir	25.76558	21.59068	25.76558	323.8146848	Elbistan
2103	Diyarbakir	19.86305	23.82505	23.82505	328.5451819	Elbistan
2106	Diyarbakir	9.178418	8.270238	9.178418	307.0785457	Elbistan
2108	Diyarbakir	7.947267	5.894371	7.947267	329.2730899	Elbistan
2310	Elazig	60.45616	51.19656	60.45616	72.68669944	Pazarcik
2309	Elazig	38.26139	35.33888	38.26139	46.62227564	Pazarcik
2304	Elazig	32.68223	49.40283	49.40283	115.9637753	Pazarcik
2307	Elazig	33.62553	38.10754	38.10754	122.5618978	Pazarcik
2305	Elazig	58.1771	53.67463	58.1771	136.4866903	Pazarcik
2310	Elazig	41.466	55.23522	55.23522	72.68669944	Elbistan

2309	Elazig	62.65357	38.65393	62.65357	46.62227564	Elbistan
2308	Elazig	69.7981	48.52414	69.7981	101.0596715	Elbistan
2302	Elazig	12.35801	16.33764	16.33764	125.7133286	Elbistan
2307	Elazig	12.95982	15.56112	15.56112	122.5618978	Elbistan
2305	Elazig	5.356134	5.302636	5.356134	136.4866903	Elbistan
2712	Gaziantep	555.5879	592.3544	592.3544	36.92711957	Pazarcik
2703	Gaziantep	156.6342	165.0642	165.0642	44.01870845	Pazarcik
2709	Gaziantep	154.0308	127.0069	154.0308	45.0806162	Pazarcik
2711	Gaziantep	142.6439	119.6102	142.6439	44.24795116	Pazarcik
2718	Gaziantep	654.4308	630.312	654.4308	57.1246742	Pazarcik
2707	Gaziantep	98.64927	89.27893	98.64927	66.62504841	Pazarcik
2704	Gaziantep	102.235	160.6396	160.6396	77.31523048	Pazarcik
2703	Gaziantep	93.68232	63.4492	93.68232	44.01870845	Elbistan
2704	Gaziantep	34.59009	63.62961	63.62961	77.31523048	Elbistan
2718	Gaziantep	34.47282	50.5759	50.5759	57.1246742	Elbistan
3143	Hatay	381.0936	351.3809	381.0936	84.01575389	Pazarcik
3138	Hatay	888.7299	746.6645	888.7299	77.71924355	Pazarcik
3144	Hatay	611.2695	763.3625	763.3625	72.16215953	Pazarcik
3137	Hatay	428.373	670.1654	670.1654	65.65887763	Pazarcik
3134	Hatay	246.1068	203.9094	246.1068	75.35026556	Pazarcik
3145	Hatay	591.8801	692.2899	692.2899	58.09676004	Pazarcik
3139	Hatay	577.1307	504.8208	577.1307	51.91871923	Pazarcik
3116	Hatay	164.2769	168.8629	168.8629	51.84022805	Pazarcik
3142	Hatay	651.6892	739.2937	739.2937	41.45588121	Pazarcik
3112	Hatay	171.8594	83.63697	171.8594	48.92942351	Pazarcik
3115	Hatay	286.7226	241.5	286.7226	44.18495112	Pazarcik
3146	Hatay	483.8456	346.9315	483.8456	37.96742306	Pazarcik
3133	Hatay	221.4053	147.2227	221.4053	35.08977603	Pazarcik
3141	Hatay	961.1165	868.8192	961.1165	24.8151231	Pazarcik
3124	Hatay	572.6323	638.3214	638.3214	10.17359091	Pazarcik
3125	Hatay	822.616	1121.948	1121.948	11.50918597	Pazarcik
3135	Hatay	740.9707	1372.071	1372.071	40.44057724	Pazarcik
3123	Hatay	655.5713	593.9404	655.5713	8.00447787	Pazarcik
3132	Hatay	515.3094	514.6342	515.3094	6.803978332	Pazarcik
3126	Hatay	1178.116	999.3831	1178.116	9.612220001	Pazarcik
3131	Hatay	363.0329	366.0505	366.0505	5.644666684	Pazarcik
3129	Hatay	1351.5	1198.743	1351.5	7.465738456	Pazarcik
3136	Hatay	534.2245	401.9692	534.2245	5.686417693	Pazarcik
3140	Hatay	194.6867	218.7093	218.7093	23.72669254	Pazarcik
3147	Hatay	56.44854	47.51172	56.44854	30.11693011	Pazarcik
3143	Hatay	42.89935	39.84327	42.89935	84.01575389	Elbistan
3138	Hatay	49.2678	68.71472	68.71472	77.71924355	Elbistan
3144	Hatay	59.115	78.10838	78.10838	72.16215953	Elbistan
3134	Hatay	30.57111	40.03998	40.03998	75.35026556	Elbistan
3137	Hatay	23.03817	25.60015	25.60015	65.65887763	Elbistan
3139	Hatay	43.35793	57.54239	57.54239	51.91871923	Elbistan
3116	Hatay	17.08	19.196	19.196	51.84022805	Elbistan
3142	Hatay	10.38088	21.28696	21.28696	41.45588121	Elbistan
3115	Hatay	25.77447	27.45891	27.45891	44.18495112	Elbistan
3146	Hatay	17.67443	18.28782	18.28782	37.96742306	Elbistan
3141	Hatay	25.71274	23.11699	25.71274	24.8151231	Elbistan
3133	Hatay	19.90386	18.1046	19.90386	35.08977603	Elbistan
3135	Hatay	18.14687	15.50154	18.14687	40.44057724	Elbistan
3124	Hatay	21.75652	32.18029	32.18029	10.17359091	Elbistan
3125	Hatay	25.62747	21.04758	25.62747	11.50918597	Elbistan
3123	Hatay	23.0113	24.32187	24.32187	8.00447787	Elbistan
3132	Hatay	17.45727	22.97341	22.97341	6.803978332	Elbistan
3129	Hatay	22.78477	26.62058	26.62058	7.465738456	Elbistan
3136	Hatay	18.60377	22.79383	22.79383	5.686417693	Elbistan
3140	Hatay	29.10271	30.20007	30.20007	23.72669254	Elbistan
3147	Hatay	5.370752	7.258578	7.258578	30.11693011	Elbistan
4615	Kahramanmaras	584.6534	556.6476	584.6534	64.0362702	Pazarcik
NAR	Kahramanmaras	784.5689	619.7074	784.5689	63.45176373	Pazarcik
4616	Kahramanmaras	610.3447	428.5635	610.3447	82.31432921	Pazarcik
4630	Kahramanmaras	178.5622	124.0367	178.5622	82.71060379	Pazarcik
4629	Kahramanmaras	338.9347	248.1954	338.9347	80.70715678	Pazarcik
4632	Kahramanmaras	359.4571	299.2487	359.4571	80.26537483	Pazarcik
4625	Kahramanmaras	447.0017	466.3326	466.3326	85.83923916	Pazarcik
4624	Kahramanmaras	357.252	310.8946	357.252	89.25660956	Pazarcik
4614	Kahramanmaras	2165.615	2178.72	2178.72	66.38797756	Pazarcik
4626	Kahramanmaras	108.8081	223.0931	223.0931	92.71471793	Pazarcik
4621	Kahramanmaras	363.8016	295.5592	363.8016	93.49970259	Pazarcik
4620	Kahramanmaras	300.4047	320.9304	320.9304	94.53707107	Pazarcik
4619	Kahramanmaras	302.0343	194.7355	302.0343	96.50513536	Pazarcik
4618	Kahramanmaras	125.6644	159.4222	159.4222	97.25026352	Pazarcik

4617	Kahramanmaras	145.3257	115.1562	145.3257	98.49700167	Pazarcik
4611	Kahramanmaras	349.7206	321.1143	349.7206	94.30820604	Pazarcik
4613	Kahramanmaras	146.9338	153.5201	153.5201	129.5609468	Pazarcik
4631	Kahramanmaras	22.20652	19.33552	22.20652	115.7158986	Pazarcik
4612	Kahramanmaras	140.97	122.222	140.97	155.4221265	Pazarcik
4628	Kahramanmaras	91.09563	82.54909	91.09563	156.6641583	Pazarcik
4631	Kahramanmaras	337.3846	388.6079	388.6079	115.7158986	Pazarcik
4611	Kahramanmaras	194.4007	139.037	194.4007	94.30820604	Pazarcik
4620	Kahramanmaras	66.82375	81.33087	81.33087	94.53707107	Pazarcik
4625	Kahramanmaras	73.45961	50.68318	73.45961	85.83923916	Pazarcik
4617	Kahramanmaras	55.97399	82.69461	82.69461	98.49700167	Pazarcik
4612	Kahramanmaras	635.4467	523.2124	635.4467	155.4221265	Pazarcik
4614	Kahramanmaras	160.8168	206.0473	206.0473	66.38797756	Pazarcik
4624	Kahramanmaras	65.00184	79.7458	79.7458	89.25660956	Pazarcik
NAR	Kahramanmaras	126.5214	110.4217	126.5214	63.45176373	Elbistan
4615	Kahramanmaras	44.47337	73.751	73.751	64.0362702	Elbistan
4616	Kahramanmaras	57.54619	53.50307	57.54619	82.31432921	Elbistan
4613	Kahramanmaras	80.61347	78.2478	80.61347	129.5609468	Elbistan
7901	Kilis	53.11445	16.55168	53.11445	57.27891365	Pazarcik
7901	Kilis	50.9099	49.81428	50.9099	57.27891365	Elbistan
4408	Malatya	100.0891	137.1811	137.1811	47.30044778	Pazarcik
4406	Malatya	108.7379	131.3439	131.3439	32.95217427	Pazarcik
4409	Malatya	38.00886	28.49102	38.00886	79.5883046	Pazarcik
4412	Malatya	63.57863	68.89719	68.89719	34.31656851	Pazarcik
4410	Malatya	33.70423	45.49616	45.49616	84.48601049	Pazarcik
4405	Malatya	91.11829	126.4967	126.4967	65.47416203	Pazarcik
4404	Malatya	136.2437	137.4162	137.4162	47.68172015	Pazarcik
4414	Malatya	106.6179	163.844	163.844	36.62772173	Pazarcik
4407	Malatya	43.36136	33.08422	43.36136	52.09549835	Pazarcik
4413	Malatya	13.15253	10.18892	13.15253	60.14259075	Pazarcik
4409	Malatya	287.0381	218.0397	287.0381	79.5883046	Elbistan
4406	Malatya	467.2015	409.3123	467.2015	32.95217427	Elbistan
4410	Malatya	112.0973	127.2469	127.2469	84.48601049	Elbistan
4412	Malatya	159.0325	126.3764	159.0325	34.31656851	Elbistan
4405	Malatya	155.4112	158.0522	158.0522	65.47416203	Elbistan
4414	Malatya	81.40928	63.00617	81.40928	36.62772173	Elbistan
4404	Malatya	45.36233	48.54014	48.54014	47.68172015	Elbistan
4413	Malatya	36.78609	50.93417	50.93417	60.14259075	Elbistan
8002	Osmaniye	242.9514	202.8933	242.9514	101.8297877	Pazarcik
8003	Osmaniye	141.5669	185.7379	185.7379	111.5543084	Pazarcik
8004	Osmaniye	168.4261	181.8594	181.8594	144.7633524	Pazarcik
8002	Osmaniye	65.87371	45.50682	65.87371	101.8297877	Elbistan
8003	Osmaniye	48.69694	66.60214	66.60214	111.5543084	Elbistan
6304	Sanliurfa	210.8972	238.2282	238.2282	198.0535956	Pazarcik
6305	Sanliurfa	126.6591	104.0897	126.6591	230.8136543	Pazarcik
6306	Sanliurfa	65.89738	55.98942	65.89738	278.1915873	Pazarcik
6303	Sanliurfa	117.4226	114.4394	117.4226	221.9514892	Pazarcik
6302	Sanliurfa	59.94751	51.16346	59.94751	285.6036786	Pazarcik
6303	Sanliurfa	29.4311	21.68857	29.4311	221.9514892	Elbistan
6306	Sanliurfa	35.99724	27.16897	35.99724	278.1915873	Elbistan
6302	Sanliurfa	27.00732	19.33995	27.00732	285.6036786	Elbistan

*: DEMA Station Number for the cities.
**: Direction of recorded station.
***: Epicenter of earthquake.

3. RESULTS

As part of this research, the data were evaluated by multi-regression method. Linear regression, polynomial regression, gradient boosting and random forest regression models were used as regression methods. The models used are shown in Table 5. These regression models were analyzed with the code prepared on Phyton software[47].

Table 5. Model used in the study

Models
Linear Regression
Polynomial Regression
Gradient Boosting
Random Forest

All the regression models used were used for each damage level. Among the models, the model that is the most compatible, that is, the one that gives the highest R^2 value, was determined. When the models with the highest agreement for damage levels are examined, it is seen that the highest agreement is achieved in 5 out of 6 damage levels in the random forest regression model. The most compatible model for the heavy damage level was gradient boosting regression. The distribution of the selected regression models according to their damage levels is given in Table 6.

Table 6. Regression models selected for damage levels

Damage Level	Best Fitting Model
No Damage	Random Forest
Low Damage	Random Forest
Medium Damage	Random Forest
Heavy Damage	Gradient Boosting
Urgently Demolished	Random Forest
Collapsed	Random Forest

Table 7 shows the distribution of R^2 scores for damage levels and the predictive power results based on interpretation. R^2 values reflect the relationship between damage levels and PGA values of stations and station distance. When the data are examined, it is seen that there is a good level of harmony between the earthquake parameters of the undamaged and heavily damaged structures. The R^2 scores of no damage and heavy damage structures are 0.75 and 0.71, respectively. Damage levels, including low damage, medium damage, urgent demolition and collapsed buildings, are 50% compatible. It is expected that the R^2 scores of moderately damaged structures will be low. The determination of moderately damaged structures in the damage assessments made in the field is a subjective situation based on interpretation. The level of knowledge of the technical staff that determines the level of damage in the field, the approach of the damage assessment forms, and the inability to determine the damage of the structure make the concept of a moderately damaged building variable. In field observations, one expert's low damage can be detected as moderate damage by another expert. Likewise, this situation exists between medium damage and heavy damage. Therefore, high compliance in the prediction of moderate damage is not technically expected. Predictive power values based on interpretation were determined by the researcher. This evaluation shows the level of compliance of the number of structures belonging to the damage levels and the PGA and distance parameters of the earthquake. Even if the values between 0.4-0.5 are considered low in regression models, it is thought that higher predictive power will be achieved by increasing the number of data and the number of stations in this study.

Table 7. R^2 scores of damage levels and interpretive predictive power

Damage Levels	R^2 Score	Predictive Power
No Damage	0.75	Good
Low Damage	0.45	Medium
Medium Damage	0.46	Medium
Heavy Damage	0.71	Good
Urgently Demolished	0.56	Medium
Collapsed	0.61	Medium

With this study, it is seen that the number and quality of data will increase the consistency between them. The levels of damaged buildings examined within the scope of the study are the total numbers in the cities where the buildings damaged by the earthquake are located. Therefore, the calculated distances are a single value calculated based on the coordinates of the city center. If the distribution of the damaged structure is coordinate-oriented, the relationship between the damage level and the station data will be seen more clearly, as the distance of the evaluated station to the structure entering the relevant damage level can be better determined. Studies show that the effects of the structures affected by earthquakes, the damage mechanism and the causes of damage can be better reflected with the data at the stations close to the building. This shows that there is a relationship between damage levels and the location of the station and the earthquake parameters it takes measurements. This study shows that the relationship described can be revealed by regression models. The fact that the number of less damaged and heavily damaged structures is higher in number compared to other damage levels increases the success rate of compliance. When we separated the R^2 scores obtained in the study as damaged and undamaged, the R^2 scores were calculated as 0.63 and 0.6, respectively. These ratios show that if the number of data is increased and the coordinates of the damaged structure data used in the study are determined, they will reflect the relationship very well.

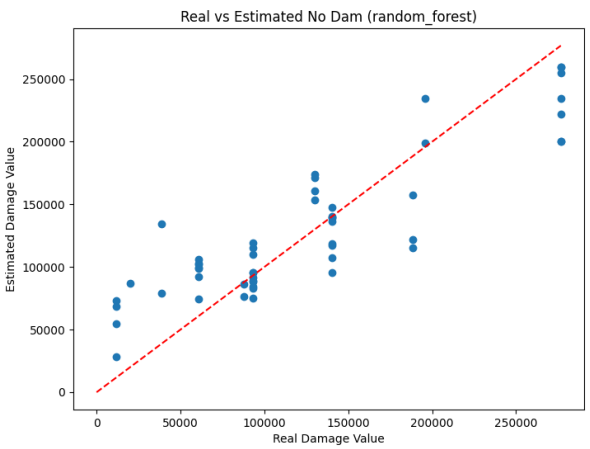

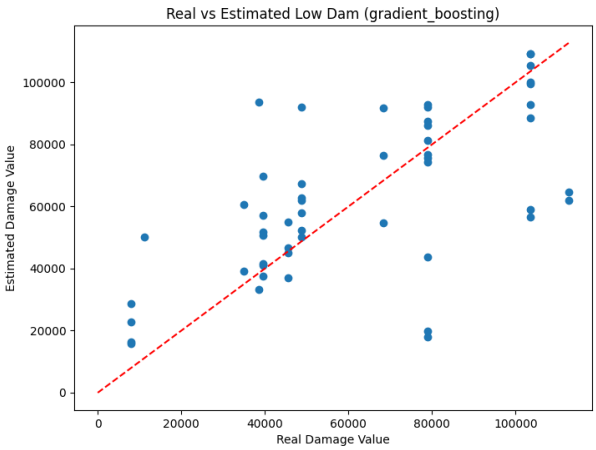

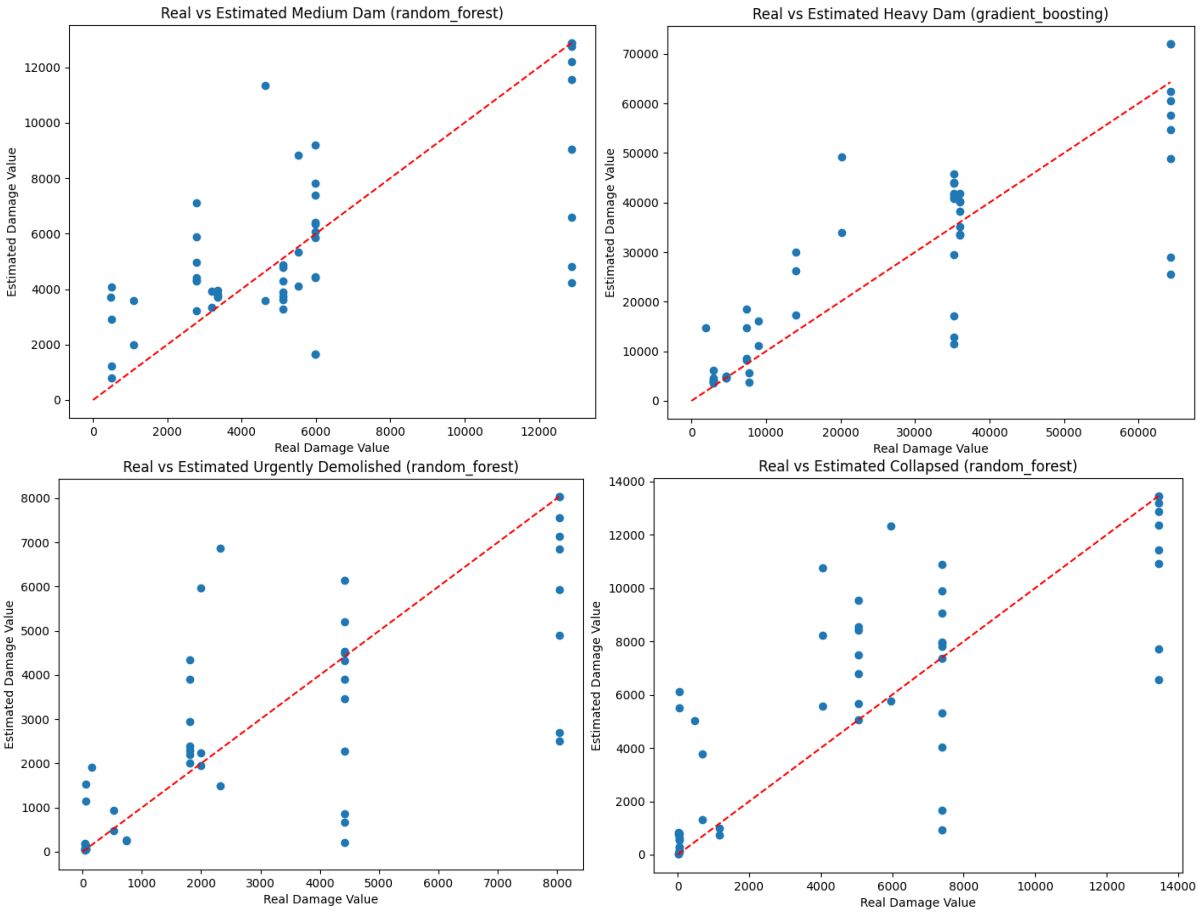

Figure 10. Damaged building values and predicted damaged building values based on damage levels

Figure 10 shows the distribution of actual and estimated values for damage levels. As can be seen at damage levels with high R^2 scores, scattering is lower. Damage levels of No Damage and Heavy Damaged structures are concentrated close to the trend line. In addition, when the values were examined, the actual and estimated values were collected in some value ranges due to the evaluation of the city-based damage distribution. Figure 10 supports the R^2 scores in Table 7. In such studies, the presence of coordinated information of damaged structures shows that it will increase the prediction power.

Table 8. Comparison of Random Forests and Gradient Boosting Regression Models [24,25]

Characteristics	Random Forest	Gradient Boosting
Model Structure	Trees trained in parallel	Sequentially trained trees
Performance	It's faster	Provides higher accuracy
Overfitting Risks	Less	Higher
Forecast Merge	Average of the forecasts of the trees	Focused on error correction
Hyperparameter Setting	Less sensitive	Requires more careful tuning

Table 8 shows the comparison between the two regression models that showed the highest agreement with the damage levels in the study. When the characteristics of random forest and gradient boosting regression models are examined, the model structure, model performance, overfitting risk, and hyperparameter settings used to combine predictions differ. As used in the study, random forest is more suitable for solving regression problems of complex data[48,49]. As can be seen in Table 6, 5 of the 6 damage levels used in the study give the best fit in the random forest model. The fact that the predictions in the decision trees are averaged, fast, have a low risk of overfitting, and have low precision in hyperparameter settings provides an advantage in the evaluation of complex data sets. Within the scope of this study, the random forest regression model showed high compatibility.

4. DISCUSSION AND CONCLUSION

Verification and evaluation of the damage assessment made after earthquakes will guide the evaluations to be made in future earthquakes. As outlined in this study, the relationship between the damage levels obtained because of the damage assessments made after the February 6, 2023 Kahramanmaras earthquakes and the maximum ground acceleration (PGA) of DEMA stations recorded in the Kahramanmaras earthquakes and their distances to the cities affected by the earthquake were examined. The results obtained after the evaluations are given below.

- In the study, unlike the literature, multiple input and multiple output parameters were evaluated in the multi regression model.
- A separate regression model was used for each output data in the regression problem in the study. In this way, the multiple regression approach is completely different compared to other studies.

- After the regression analysis, R^2 scores between damage levels and PGA-distance parameters and adaptive strength values based on interpretation were obtained. When the results are examined, there is a high agreement between the number of buildings that enter the heavy damage and no damage levels, and the values measured by the stations. The R^2 scores for the "No damage" and "Heavy damage" damage levels are 0.75 and 0.71, respectively. When the evaluation was reduced from 6 damage levels to 2 damage levels, damaged and undamaged, the R^2 scores were obtained as 0.63 and 0.6, respectively. This indicates that there is a sufficient level of harmony between the input and output parameters. However, it has been concluded that in case of higher success, the data set should be expanded, and the coordinate data of the damaged structures should be obtained separately.
- In regression analysis, more than one regression model (linear regression, polynomial regression, random forest and gradient boosting) was used to determine the best fit models among these models. Considering the results obtained according to the damage levels, the regression models that showed the best fit were the gradient boosting and random forest models.
- It is seen that the random forest regression model is a preferable model in terms of being the best compatible model in 5 out of 6 damage levels, and in complex analyzes such as damage-earthquake parameter relationship, hyperparameter sensitivity is low, fast and minimizes the risk of overfitting.
- It has been seen by the results of the study that low compliance levels of damage can be increased by increasing the number of data and detailing the level of information about the data.
- In such multiple regression analysis studies, all input data are analyzed and evaluated with a single regression model. In this study, the model that fits best was used for each input data. While this can be used in cases with independent input data as in this study, it would not be correct to use it on input data that is directly related to each other. Therefore, in the continuation of these studies, researchers can examine the relationship between damage and earthquake characteristics with a single regression model with high data sets.

REFERENCES

[1] Nemutlu ÖF, Balun B, Sari A. Damage assessment of buildings after 24 January 2020 Elazig-Sivrice earthquake. Earthquakes and Structures. 25 Mart 2021;20(3):325-35.

[2] Balun B, Nemutlu OF, Benli A, Sari A. Estimation of probabilistic hazard for Bingol province, Turkey. Earthquakes and Structures. 25 Şubat 2020;18(2):223-31.

[3] Avcil F, Işık E, İzol R, Büyüksaraç A, Arkan E, Arslan MH, vd. Effects of the February 6, 2023, Kahramanmaraş earthquake on structures in Kahramanmaraş city. Nat Hazards. Şubat 2024;120(3):2953-91.

[4] Altunsu E, Güneş O, Öztürk S, Sorosh S, Sarı A, Beeson ST. Investigating the structural damage in Hatay province after Kahramanmaraş-Türkiye earthquake sequences. Engineering Failure Analysis. 2024;157:107857.

[5] Öztürk S, Altunsu E, Güneş O, Sarı A. Investigation of industrial structure performances in the Hatay and Gaziantep provinces during the Türkiye earthquakes on February 6, 2023. Soil Dynamics and Earthquake Engineering. Nisan 2024;179:108569.

[6] Nemutlu ÖF, Balun B, Sarı A. 06 Şubat 2023 Kahramanmaraş Depremleri Kaynaklı Yapısal Hasarların Adıyaman İli Özelinde İncelenmesi. İçinde Konya; 2023.

[7] Hussain E, Kalaycıoğlu S, Milliner CW, Çakir Z. Preconditioning the 2023 Kahramanmaraş (Türkiye) earthquake disaster. Nature Reviews Earth & Environment. 2023;4(5):287-9.

[8] AFAD. 06 Şubat Kahramanmaraş(Pazarcık ve Elbistan) Depremleri Saha Çalışmaları Ön Değerlendirme Raporu. AFAD; 2023.

[9] Şenol Balaban M, Doğulu C, Akdede N, Akoğlu H, Karakayalı O, Yılmaz S, vd. Emergency response, and community impact after February 6, 2023 Kahramanmaraş Pazarcık and Elbistan Earthquakes: reconnaissance findings and observations on affected region in Türkiye. Bulletin of Earthquake Engineering. 01 Şubat 2025;23(3):1053-81.

[10] Altunişik AC, Arslan ME, Kahya V, Aslan B, Sezdirmez T, Dok G, vd. Field Observations and Damage Evaluation in Reinforced Concrete Buildings After the February 6th, 2023, Kahramanmaraş–Türkiye Earthquakes. J Earthquake and Tsunami. 01 Aralık 2023;17(06):2350024.

[11] Yuzbasi J. Post-Earthquake Damage Assessment: Field Observations and Recent Developments with Recommendations from the Kahramanmaraş Earthquakes in Türkiye on February 6th, 2023 (Pazarcık M7.8 and Elbistan M7.6). Journal of Earthquake Engineering. :1-26.

[12] Avğın S, Köse MM, Özbek A. Damage assessment of structural and geotechnical damages in Kahramanmaraş during the February 6, 2023 earthquakes. Engineering Science and Technology, an International Journal. 01 Eylül 2024;57:101811.

[13] Işık E, Hadzima-Nyarko M, Avcil F, Büyüksaraç A, Arkan E, Alkan H, vd. Comparison of Seismic and Structural Parameters of Settlements in the East Anatolian Fault Zone in Light of the 6 February Kahramanmaraş Earthquakes. Infrastructures. 2024;9(12).

[14] Tao D, Cai Y. Study on the Relation Between Ground Motion Parameters and Simulated Earthquake Damage of Simplified Masonry Structures. 2018.

[15] Zhou Q, Sun B. Study on Earthquake Damage Distribution of Multistory Masonry Buildings. The Open Civil Engineering Journal. 2015;9(1):435-41.

[16] Liang H, Li J, Yang Z, Li YQ. Effects of Epicentral Distance and Seismogenic Fault Distance on Seismic Damage of Dams in Wenchuan Earthquake.

Applied Mechanics and Materials. 2013;353-356:2187-90.
[17] Karaşin İB. Comparative Analysis of the 2023 Pazarcık and Elbistan Earthquakes in Diyarbakır. Buildings. 2023;13(10):2474.
[18] Zengin B, Aydin F. The Effect of Material Quality on Buildings Moderately and Heavily Damaged by the Kahramanmaraş Earthquakes. Applied Sciences. 2023;13(19):10668.
[19] Choi H, Sanada Y, KASHIWA H, Watanabe Y, Tanjung J, Jiang H. Seismic Response Estimation Method for Earthquake-damaged RC buildings. Earthquake Engineering & Structural Dynamics. 2016;45(6):999-1018.
[20] Huang HC. Characteristics of earthquake ground motions and the H/V of microtremors in the southwestern part of Taiwan. Earthquake Engineering and Structural Dynamics. 2002;31(10):1815-29.
[21] Bilen A, Özer AB. Regresyon Yöntemlerine Dayalı Suç Tespit Analizi Karşılaştırması Elazığ İli Örneği. Fırat Üniversitesi Mühendislik Bilimleri Dergisi. 2022;34(1):115-21.
[22] Shen Y, Wang L, Jian W, Shang J, Wang X, Ju L, vd. Big-Data and Artificial-Intelligence-Assisted Vault Prediction and EVO-ICL Size Selection for Myopia Correction. British Journal of Ophthalmology. 2021;107(2):201-6.
[23] Suparwito H, Polina AM. Prediction of Tobacco Leave Grades With Ensemble Machine Learning Methods. 2019;1-6.
[24] Liou L, Mostofsky E, Lehman LL, Salia S, Barrera FJ, Ying W, vd. Survival Machine Learning Methods for Mortality Prediction After Heart Transplantation in the Contemporary Era. Plos One. 2025;20(1):e0313600.
[25] Pahno S, Yang J, Kim SS. Use of Machine Learning Algorithms to Predict Subgrade Resilient Modulus. Infrastructures. 2021;6(6):78.
[26] Özçelik STA, Üzen H, Şengür A, Çelebi A. Derin öğrenme ile panoramik radyografi görüntülerinden diş segmentasyonu: UNet, FPN ve PSPNet karşılaştırması. Niğde Ömer Halisdemir Üniversitesi Mühendislik Bilimleri Dergisi. 2024;13(4):1347-54.
[27] Yusufoğlu E, Fırat H, Üzen H, Özçelik STA, Çiçek İB, Şengür A, vd. A Comprehensive CNN Model for Age-Related Macular Degeneration Classification Using OCT: Integrating Inception Modules, SE Blocks, and ConvMixer. Diagnostics. 2024;14(24):2836.
[28] Üzen H. İmalat Sistemlerinde Derin Öğrenme Tabanlı Doku Hata Tespiti [Doktora]. [Fen Bilimleri Enstitüsü]: İnönü Üniversitesi; 2022.
[29] Mangalathu S, Sun H, Nweke CC, Yi Z, Burton HV. Classifying earthquake damage to buildings using machine learning. Earthquake Spectra. 01 Şubat 2020;36(1):183-208.
[30] Xia H, Wu J, Yao J, Zhu H, Gong A, Yang J, vd. A Deep Learning Application for Building Damage Assessment Using Ultra-High-Resolution Remote Sensing Imagery in Turkey Earthquake. International Journal of Disaster Risk Science. 01 Aralık 2023;14(6):947-62.
[31] Nemutlu ÖF. Detection of earthquake damage using pre and past-earthquake satellite data. İçinde Tashkent, Uzbekistan; 2024. s. 256-66.
[32] Aloisio A, Rosso MM, De Leo AM, Fragiacomo M, Basi M. Damage classification after the 2009 L'Aquila earthquake using multinomial logistic regression and neural networks. International Journal of Disaster Risk Reduction. Ekim 2023;96:103959.
[33] Sheibani M, Ou G. The development of Gaussian process regression for effective regional post-earthquake building damage inference. Computer-Aided Civil and Infrastructure Engineering. 01 Mart 2021;36(3):264-88.
[34] Adanur S, Altunişik AC, Bayraktar A, Akköse M. Comparison of near-fault and far-fault ground motion effects on geometrically nonlinear earthquake behavior of suspension bridges. Natural Hazards. 2012;64(1):593-614.
[35] Işık E, Avcil F, Büyüksaraç A, İzol R, Arslan MH, Aksoylu C, vd. Structural damages in masonry buildings in Adıyaman during the Kahramanmaraş (Turkiye) earthquakes (Mw 7.7 and Mw 7.6) on 06 February 2023. Engineering Failure Analysis. 2023;151(May).
[36] Nemutlu ÖF, Sari A, Balun B. 06 Şubat 2023 Kahramanmaraş Depremlerinde (Mw 7.7-Mw 7.6) Meydana Gelen Gerçek Can Kayıpları Ve Yapısal Hasar Değerlerinin Tahmin Edilen Değerler İle Karşılaştırılması. Afyon Kocatepe University Journal of Sciences and Engineering. 27 Ekim 2023;23(5):1222-34.
[37] AFAD. 06 Şubat 2023 Pazarcık-Elibstan Kahramanmaraş(Mw:7.7-Mw:7.6) Depremleri Raporu. AFAD: AFAD; 2023 Haz s. 140.
[38] AFAD. tadas.afad.gov.tr. 2023.
[39] Mahesh B. Machine Learning Algorithms -A Review. C. 9, International Journal of Science and Research (IJSR). 2019.
[40] Sarker IH. Machine Learning: Algorithms, Real-World Applications and Research Directions. SN Computer Science. 22 Mart 2021;2(3):160.
[41] Alzubaidi L, Zhang J, Humaidi AJ, Al-Dujaili A, Duan Y, Al-Shamma O, vd. Review of deep learning: concepts, CNN architectures, challenges, applications, future directions. Journal of Big Data. 31 Mart 2021;8(1):53.
[42] Mishra C, Gupta D. Deep Machine Learning and Neural Networks: An Overview. IAES International Journal of Artificial Intelligence (IJ-AI). 01 Haziran 2017;6:66.
[43] Ostertagova E. Modelling Using Polynomial Regression. Procedia Engineering. 31 Aralık 2012;48:500-6.
[44] Breiman L. Random Forests. Machine Learning. 01 Ekim 2001;45(1):5-32.
[45] Zemel RS, Pitassi T. A Gradient-Based Boosting Algorithm for Regression Problems.
[46] Çevre Şehircilik ve İklim Değişikliği Bakanlığı. csb.gov.tr. Basın Bülteni. 2023.
[47] Python [Internet]. Python.org. 2024 [a.yer 21 Aralık 2024]. Erişim adresi: https://www.python.org/

[48] Nadkarni SB, Vijay GS, Kamath RC. Comparative Study of Random Forest and Gradient Boosting Algorithms to Predict Airfoil Self-Noise. Engineering Proceedings. 2023;59(1).

[49] Sousa M, Sant'Ana R, Fernandes R, Duarte J, Aploinário J, Thomä R. Comparison of Random Forest and Gradient Boosting Fingerprints to Enhance an Outdoor Radio-frequency Localization System. 2020.

Volume 14, Issue 2, Page 52-63, 2025 https://doi.org/10.46810/tdfd.1545596 Research Article

BİNGÖL UNIVERSITY

Türk Doğa ve Fen Dergisi
Turkish Journal of Nature and Science
www.dergipark.gov.tr/tdfd

HealthCraft: A Precision Model for Smart Resource Optimisation in Dynamic Big Data Healthcare Environments

Ümit DEMİRBAGA[1*]

[1] Bartın University, Engineering, Architecture and Design Faculty, Computer Engineering Department, Bartın, Türkiye
Ümit DEMİRBAGA ORCID No: 0000-0001-5159-0723

**Corresponding author: udemirbaga@bartin.edu.tr*

(Received: 10.09.2024, Accepted: 12.04.2025, Online Publication: 27.06.2025)

Keywords
Big data, Cloud computing, Machine learning, Resource utilisation, Prediction

Abstract: Cloud computing offers scalable computing and storage capabilities to handle massive healthcare data. When processing large-scale data, keeping the resource cost reasonable is crucial. Nonetheless, resource utilisation is frequently inefficient because of the inherent complexity and heterogeneity of distributed computing frameworks. In addition, it is challenging to model resource utilisation from real fault-occurring cloud systems. This study proposes an automated online resource utilisation prediction model that combines machine learning (ML) methods with automated log data preprocessing to predict future resource consumption. It allows smart and adaptable allocation of resources in large cloud-based data infrastructures suffering from typical failures like CPU, memory, network, and data locality problems. Using the Hadoop framework on a cloud cluster of 30 worker nodes, our model predicts resource utilisation with up to 97.3% accuracy - outperforming the other baseline models evaluated. In addition, our system accurately recognises resource bottlenecks. It reduces execution time by up to 30%, even in fault-injected environments, implying that it is robust enough for real-time big data analytics.

HealthCraft: Dinamik Büyük Veri Sağlık Hizmetleri Ortamlarında Akıllı Kaynak Optimizasyonu için Hassas Bir Model

Anahtar Kelimeler
Büyük veri, Bulut bilişim, Makine öğrenimi, Kaynak kullanımı, Tahmin

Öz: Bulut bilişim, büyük ölçekli sağlık verilerini işlemek için ölçeklenebilir hesaplama ve depolama yetenekleri sunar. Büyük ölçekli verilerin işlenmesi sırasında, kaynak maliyetini makul seviyede tutmak kritik öneme sahiptir. Bununla birlikte, dağıtık bilişim çerçevelerinin doğasında bulunan karmaşıklık ve heterojenlik nedeniyle kaynak kullanımı sıklıkla verimsiz olmaktadır. Ayrıca, gerçek hata oluşan bulut sistemlerinden kaynak kullanımını modellemek zorlu bir süreçtir. Bu çalışma, otomatik bir çevrimiçi kaynak kullanım tahmin modeli önererek, makine öğrenimi (ML) yöntemlerini otomatik günlük veri ön işleme ile birleştirerek gelecekteki kaynak tüketimini tahmin etmektedir. Önerilen model, CPU, bellek, ağ ve veri yerelliği sorunları gibi tipik arızalardan etkilenen büyük ölçekli bulut tabanlı veri altyapılarında akıllı ve uyarlanabilir kaynak tahsisini mümkün kılmaktadır. Hadoop çerçevesini kullanarak 30 çalışan düğümden oluşan bir bulut kümesinde, modelimiz kaynak kullanımını %97,3'e varan doğruluk oranıyla tahmin etmektedir ve karşılaştırılan diğer temel modellerden daha üstün performans göstermektedir. Ayrıca, sistemimiz kaynak darboğazlarını doğru bir şekilde tespit etmekte ve hata enjekte edilmiş ortamlar dahil olmak üzere çalışma süresini %30'a kadar azaltmaktadır, bu da onu gerçek zamanlı büyük veri analitiği için yeterince sağlam bir çözüm haline getirmektedir.

1. INTRODUCTION

With the increasing data and high internet speed, industries are using cloud computing more widely to meet their data analysis demands. The development of omics sciences like genomics, proteomics, and metabolomics has led to the collection of enormous volumes of data [1]. Data expansion is facilitated by the transition from paper medical records to electronic health records (EHR) [2]. Using such detailed and extensive data, doctors,

epidemiologists, and health policy experts seek to enhance population health and patient care. To properly exploit the created big data within a reasonable time, it is necessary to utilise the system resources efficiently. However, the dependent structure of cloud-based big data frameworks and the complex infrastructure of cloud computing consisting of servers, storage devices, networks, cloud management software and virtualisation result in inefficient use of system resources and loss of time and energy.

Resource utilisation prediction in big data systems estimates the resource requirement required for the successful completion of the application under current conditions, which improves resource utilisation, reduces costs and enhances performance. Statistical techniques and ML methods are the most common to estimate resource utilisation. In statistical methods (e.g. Automatic Regression Modelling), the relationship between variables is determined, and probability distributions are used for assumptions. However, these methods are very general because they make predictions for certain intervals and cannot be estimated accurately [3]. ML models, such as Support Vector Machine (SVM) [4], Genetic Algorithm (GA) [5], and Neural Network (NN) [6], are more widely adopted by researchers to perform a more accurate prediction. Researchers perform resource utilisation predictions of big data systems in simulators and online systems. The simulation models [7-9] create a virtual model by modelling the computer system mathematically and revealing the system controls. Online performance analysis systems [10-12] enable the collection of performance metrics through system logs, providing much more accurate and precise information. However, these technologies cannot offer predictive support for resource usage in environments with different failures. Moreover, most of these studies employ ML techniques to forecast future resource consumption using the historical traces of a data centre as their input. Despite the impressive outcomes of ML-based models, there are still certain limitations. Most models lack a precise method for handling workload non-stationarity. The interactions between characteristics of various sizes should be taken into account. For example, Feedforward Neural Networks (FNN), a part of a multi-layer perceptron, can be used as an efficient approach for dealing with complicated nonlinear systems since they inherit the learning capabilities of neural network models and the inference capabilities of fuzzy systems [13]. As a result, several researchers have built sophisticated controllers and represented complex plants using FNN techniques [14-15].

Considering the above analysis, we propose a novel, robust resource utilisation prediction model for cloud-based big data systems that simultaneously handles multiple resource sources under different fault conditions. Unlike existing models focusing primarily on CPU or memory usage, our approach integrates a multi-resource machine learning framework that simultaneously considers CPU, memory, network, and data locality constraints, enabling more accurate and adaptable resource provisioning. Our approach combines an automated log data preprocessing module, a feature extraction pipeline, and multi-resource machine learning models to predict future resource consumption accurately. We introduce a fault injection-based training mechanism to enhance its adaptability to real-world conditions, allowing the model to learn and generalise from system anomalies.

As a first step, an automated data-driven pipeline is proposed to move the raw data of multiple runs into a form suitable for predicting the resource utilisation of the big data cluster. Finally, the fine-tuned ML Models are used to predict upcoming resource utilisation based on historical system logs and injected fault conditions. We evaluate our model under realistic conditions by injecting four representative faults (CPU, memory, network and data locality) that frequently happen in big data systems. That way, we can test its performance when the environment changes dynamically.

The contributions of this paper can be summarised as follows:

- We introduce a fully automated pipeline to preprocess log data that improves data quality and minimises manual feature engineering.
- We design a multi-resource prediction model, jointly considering CPU, memory, network and data locality factors for more adaptive provisioning of cloud resources.
- We also introduce a fault injection mechanism, which allows the model to be trained and evaluated during real-world faults, greatly improving robustness and accuracy.
- We achieve a 97.3% prediction accuracy, considerably outperforming traditional ML-based resource utilisation models.

2. BACKGROUND

2.1. Navigating EHR Datasets

Significant developments have fuelled the ongoing evolution of data in the dynamic landscape of omics domains, such as proteomics, metabolomics, and genomics [16]. The transition from traditional paper medical records to Electronic Health Records (EHR) highlights this change even more [17]. Due to the ensuing explosion of large-scale healthcare data, healthcare professionals—from doctors and epidemiologists to specialists in health policy—have a critical chance to make well-informed decisions that will eventually improve population health and enhance patient care [18]. Therefore, building strong tools, infrastructure, and methodologies is imperative to fully utilise big data's promise. To this end, the National Early Warning Score (NEWS) was developed in the United Kingdom to identify and treat patients with acute diseases when their clinical condition worsens [19] [20].

2.1.1. Overview of the NEWS dataset

Patients with acute illnesses have seven physiological parameters measured during clinical evaluation: respiration rate, oxygen saturation, temperature, systolic blood pressure, heart rate, consciousness, and oxygen. The NEWS, ranging from 1 to 8 and representing the severity of the illness, is calculated through the following steps: Step 1: Acquiring the patient's score on each of the seven physiological parameters. Step 2: Adding together all of the physiological parameter scores to calculate the NEWS. Step 3: Checking if a single parameter has reached the trigger threshold. We use the NEWS data[*] generated based on the structure and values taken from South Tees Hospitals NHS Foundation Trust[†] . This allows us to confirm the effectiveness and dependability of the proposed system. In addition to the seven distinct physiological indicators, the dataset includes 52 other factors about the health state of the patients, such as weight, dates of admission, duration of hospital stay, pain score, nausea, vomiting, and pulse. An urgent clinical review should be triggered by an aggregate NEWS of 5 or 6, and a NEWS of 7 or above should trigger a high-level clinical alert or emergency clinical review. An "Urgent or emergency reaction" response is appropriate for NEWS values more than 7, indicating "High clinical risk".

2.2. MapReduce Paradigm for Big Healthcare Data

Big data in the healthcare industry refers to heterogeneous, multi-spectral, incomplete, and uncertain observations from primary sources that are presented in structured, semi-structured, and unstructured formats and include observations related to diagnosis, illness, injury, treatment, physical and mental disorders, demography, and disease prevention [21]. Unstructured data comprises medical imaging, notes, environmental, clinical, lifestyle, medication, and health economics data. Structured data contains ICD codes, phenotype, genotype, and genomic information [22]. In addition, the Internet of Things (IoT) has spurred the development of data-driven applications in industries, including transportation, networking, smart cities, and healthcare. Various sensors and devices to track a patient's health have been widely used in the health sector. MapReduce, a distributed programming model, is implemented in Apache Hadoop[‡] and Apache Spark[§] frameworks to analyse petabyte-scale datasets in a parallel manner on computer clusters [23]. The data is divided into smaller chunks using MapReduce, which then turns each piece into a set of tuples known as key-value pairs before eventually reducing these tuples. MapReduce consists of two main phases, namely Map and Reduce, which are carried out by the workers and generate key-value pairs. During the shuffle phase, these pairs are grouped by key and sent to the appropriate Reducer. Subsequently, Reducer groups the key-value pairs and constructs a smaller collection of data tuples from these tuples. The final outputs are ultimately produced and stored in the Hadoop Distributed File System (HDFS). Fig. 1 depicts the working principle of the MapReduce paradigm.

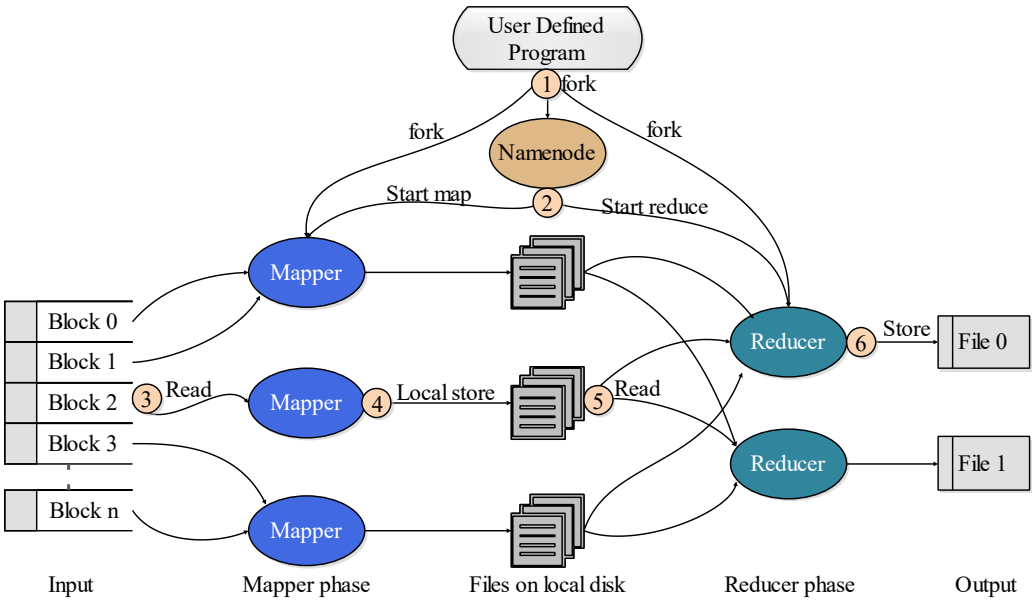

Figure 1. Overview of the MapReduce paradigm: Data processing workflow

2.3. Resource Utilisation Prediction

A resource utilisation prediction model estimates how much resource the system will require in the future to evaluate the system's performance and assess whether the system has adequate resources for users' demands. Resource utilisation prediction is adopted in diverse applications [24-26]. Demand and resource consumption estimates for large-scale data analysis are used to customise workload predictive resource management systems. The workloads, especially streaming data, are dynamic and constantly changing for big data systems [27]. Consequently, a robust and scalable resource

[*] https://github.com/umitdemirbaga/NEWS
[†] https://www.southtees.nhs.uk/
[‡] https://hadoop.apache.org/
[§] https://spark.apache.org/

utilisation prediction model is required to provide reasonable prediction accuracy. Conversely, resource utilisation prediction enables access to free resources and analyses the effects of allocating them to specific workloads [28]. Resource utilisation for predicting the system performance was first used in [29]. A few research studies then created a framework for measuring system performance based on usage patterns and evolution trends in large-scale datasets. Mean Field Theory (MFT), which studies the behaviour of high-dimensional complex systems, has been used to successfully predict and evaluate the performance of highly complex structures such as Hadoop applications [30].

3. PROPOSED SYSTEM

This section introduces our novel resource utilisation prediction model for big data systems. Fig. 2 presents the high-level architecture of the proposed approach for big healthcare data processing, which fundamentally consists of three main components: a big data monitoring system, a fault injection module, and a resource utilisation prediction system.

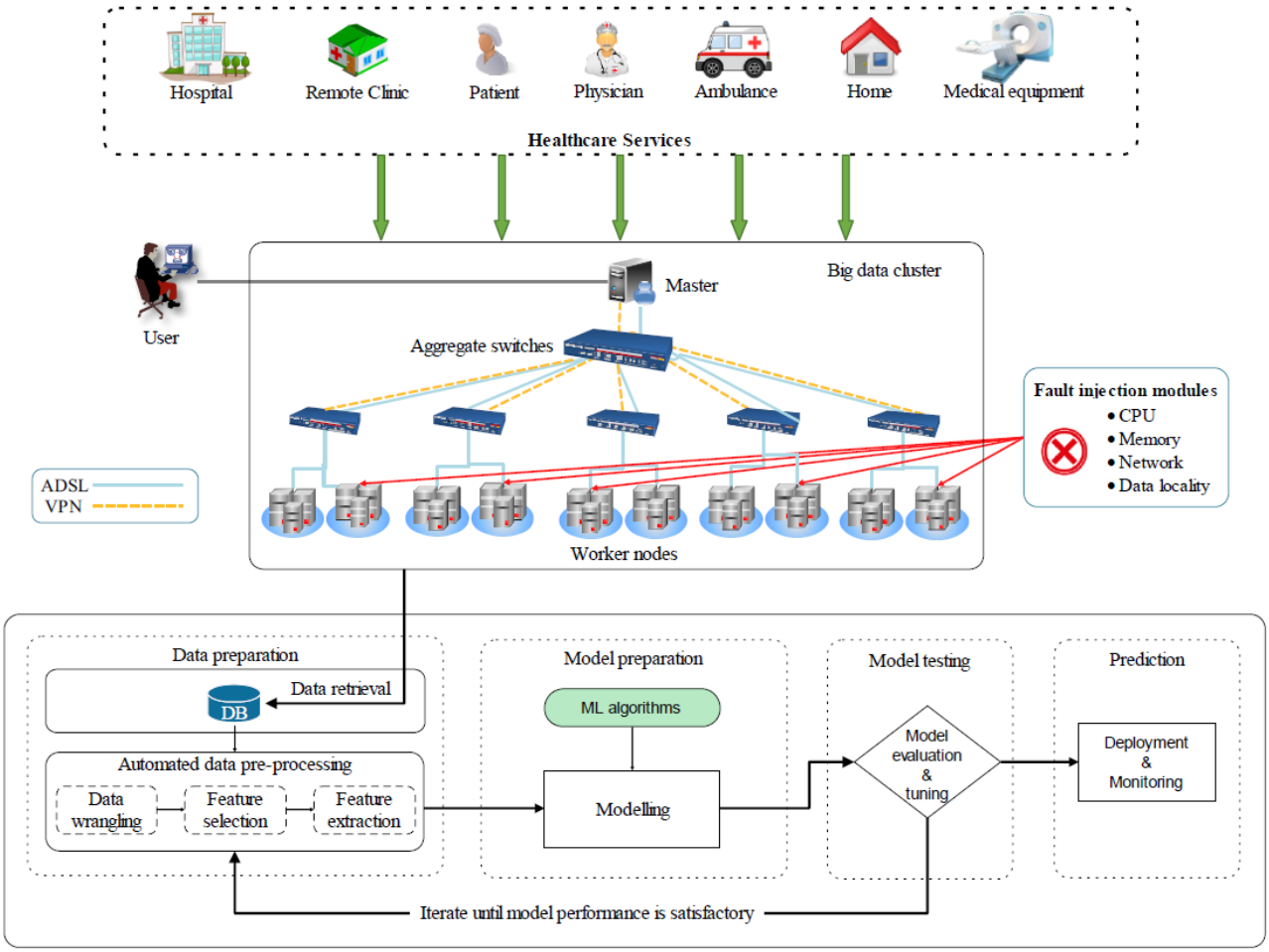

Figure 2. The overview of the proposed system's architecture

3.1. Monitoring Big Data Cluster for Log Collection

In this work, the Apache Hadoop framework is deployed on AWS (Amazon Web Services) EC2 instances, and MapReduce is used as a programming model for processing big healthcare data. We deployed SmartMonit [31], a real-time big data monitoring system, to collect tasks and infrastructure information from the Hadoop cluster in real-time. As shown in Fig. 3, SmartMonit has two sub-agents, TaskAgent and SystemAgent, managed by SmartAgent. TaskAgent employs the ResourceManager REST API[**] to collect the execution status of each task, and SystemAgent employs the Sigar API[††] to gather computing resource metrics, such as CPU/memory utilisation, network throughput, and disk I/O speeds. SmartAgent is responsible for receiving raw data from these two agents and storing it in a time-series database, InfluxDB[‡‡], via RabbitMQ[§§], a message broker system, for further processing.

[**] https://hadoop.apache.org/docs/r3.2.4/hadoop-yarn
[††] https://github.com/hyperic/sigar
[‡‡] https://www.influxdata.com
[§§] https://www.rabbitmq.com/

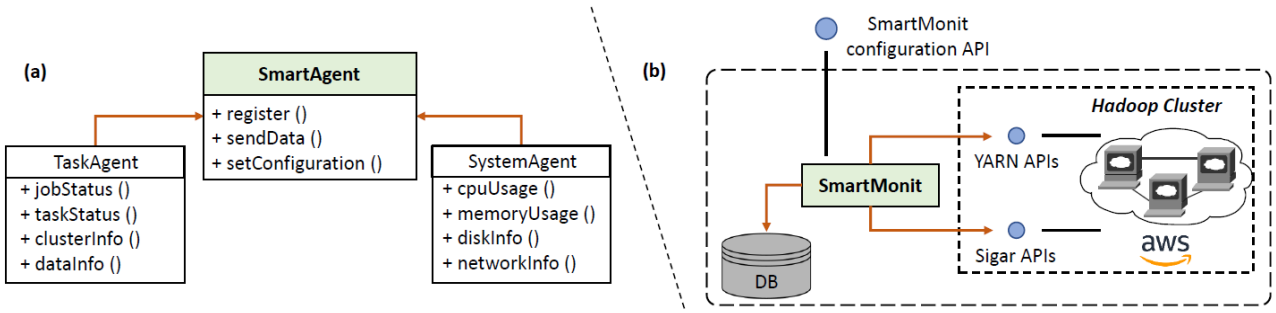

Figure 3. Model of monitoring agents (a); SmartMonit deployment in the proposed system (b)

3.2. Automated Data Pre-Processing

This data analysis pipeline module retrieves time-stamped raw logs stored in a time series database and prepares them for the next phase, implementing ML algorithms. The automated data pre-processing module conceptually consists of three main sections: data wrangling, feature extraction, and feature selection.

3.2.1. Data wrangling

This module includes a comprehensive set of data processing procedures to convert raw data collected from the cloud-based big data cluster into more readily used formats, including cleaning, organising, structuring, and enriching.

- **Regression imputation method for automatic missing value imputation:** The log collector forwards the collected data simultaneously from different APIs to the database or the next step for processing. Due to network congestion, a temporary outage of the Application Programming Interface (API), or an issue with the API itself, API response timeouts occur, in which the log collection process is interrupted. In addition, missing values occur in data sets for other reasons, such as storage limitations, security filters, data loss during data collection or the impossibility of measuring. Missing values in the dataset affect the analysis results, making it difficult to draw meaningful conclusions. To handle this, we propose an automatic missing value imputation to estimate and complete the missing values using the regression imputation method due to collecting large amounts of logs and the strong relationships between the variables. We implemented the regression imputation method by deploying the scikit-learn library in Python.

- **Automatic data encoding:** In this module, we combine one-hot encoding and label encoding techniques to convert categorical or serial data into numerical data that ML algorithms can easily process. Extensive logs are collected from the cloud-based Hadoop cluster deployed on AWS, including numeric and label data (e.g. configuration parameters). Therefore, using the label encoding technique, these parameters are converted into digital forms and made understandable by the machine.

3.2.2. Feature selection

Most of the relevant features are selected in this module to help improve the performance of our ML models. To this end, we implement the correlation analysis method, which measures the linear relationship between each pair of features. The implementation details are discussed in §4.4. Evaluation of Resource Utilisation Prediction.

3.2.3. Feature extraction

This module generates new features based on input data to identify the most significant linear combinations of features. The main objective is to reduce the dimensionality of feature vectors and categorise raw data into distinct groups by facilitating the interpretability and management of the data by ML models. To achieve this, we employ Principal Component Analysis (PCA) in Python, which helps create a new feature to specify the resource utilisation levels, ranging from 0 to 2. These steps are performed by following the steps below:

- **PCA implementation:** PCA is a dimensionality reduction technique that transforms the original set of features into a new set of orthogonal components, known as principal components. In our implementation, PCA efficiently captures the variance within the log data, which enables us to pinpoint the essential features that contribute significantly to the overall resource utilisation patterns. By retaining the principal components that capture the maximum variance, we effectively reduce the dimensionality of the data while preserving the crucial information necessary for accurate resource utilisation prediction.

- **Creation of new feature:** Based on the outcomes of PCA, a new feature is constructed to encapsulate the resource utilisation levels. The determination of these levels is as follows:

  - 0: Low Resource Utilisation
  - 1: Average Resource Utilisation
  - 2: Highest Resource Utilisation

These explicit explanations aim to comprehensively understand the methodology employed in setting and labelling the resource utilisation levels for subsequent predictions.

3.3. Fault Injection Modules

We have developed four fault injection models to experience real design problems in big data systems, which helps to test and improve the reliability and resilience of our proposed system in highly possible fault conditions, such as insufficient CPU and memory resources, network congestion or low bandwidth, and data locality issue in distributed systems, as indicated in our previous work [12].

The fault injection process involves generating realistic workloads and injecting faults into the VMs within a cluster. The algorithm takes into account various parameters, including VM ID (V_m), cluster (C), fault type (F), list of faults (F_l), injection duration (T_m), time interval (T_i), and workload (W_l).

3.3.1. CPU fault injection module

This module dynamically generates workload for the CPU. A set of computations is executed in parallel to increase the number of MIPS (million instructions per second) in the selected VMs. This model creates a high-dimensional Pascal's triangle, where each number is the sum of the two numbers just above it.

3.3.2. Memory fault injection module

It is designed to intentionally induce memory occupancy in the nodes of a computer cluster by creating vector objects in the memory, which enables monitoring the execution times of applications and making accurate and robust resource usage predictions when out-of-memory conditions occur.

3.3.3. Network fault injection module

Intermediate key-value pairs generated during the Map phase are distributed to the relevant nodes to be combined in the Reduce phase. At this stage, the network is overloaded, and delays occur. To improve data flow in MapReduce, Hadoop employs several strategies, including data compression, speculative execution, and pipelining. However, none of these can prevent the transfer of large data sets over the network. Since speculative applications cause data blocks to be transferred entirely to other nodes, delays are experienced. To experience this, the network fault injection module reduces bandwidth by transferring data between nodes, which creates delays similar to those seen in the Hadoop system.

3.3.4. Data locality fault injection module

The ability of a MapReduce job to process data on the same node where the data is stored is known as data locality. Moving data over the network imposes some overheads that lead to delays if a task is assigned to the node where the task's input data is not stored. To create a data locality issue, this module deletes the data blocks of the selected nodes, which causes data transfer from the other nodes that have a copy of the deleted blocks.

Algorithm 1: Fault injection into big data clusters

Input: - V_m: VM id,
- C: cluster,
- $\mathcal{G}$: fault type,
- F_l: list of faults,
- T_m: injection duration,
- T_i: time interval,
- W_l: workload.

```
1   // Initiate the process of fault injection
2   for selected V_m in C do
3       // Generate W_l
4       GenerateWorkload(W_l)
5       // Execute injection method
6       inj ← Assignn(G, T_m)
7       // Inject into the C
8       C ← Inject(inj)
9       // Interrupt the fault injection
10      sleep(T_i)
11  end for
```

Algorithm 1 demonstrates the pseudocode of the fault injection modules for big data clusters deployed on cloud environments. First, the user identifies V_m and F; then, based on the fault type, the workload is generated (see Algorithm 1, Line 4). Afterwards, the fault is injected for a predetermined time (T_m) (see Algorithm 1, Line 6). The generated workload is finally loaded into the selected VM (see Algorithm 1, Line 8). This process is suspended once the resource utilisation reaches 90%.

3.4. Resource Utilisation Prediction for Big Data Systems

To forecast the resource utilisation of big data systems, we implement six well-known ML algorithms, namely Support Vector Classifier (SVC), Gaussian Naïve Bayes, Logistic Regression, K-Nearest Neighbors (KNN), Decision Tree, and Random Forest. All these algorithms are evaluated and compared, considering accuracy rates, both online and offline analysis.

We propose an ML-based model with a pipeline that includes automated log data preprocessing, feature extraction, and multi-resource predictive modelling. This model is trained on labelled resource utilisation logs with supervised learning methods such as Decision Trees, k-nearest Neighbors (k-NN), and Random Forest classifiers. This is done so that the fault injection module can help the model learn from real-world failure scenarios and try to make the model robust to rare, unpredictable system anomalies. In contrast to traditional models that consider resource consumption in isolation, we model inter-relations between CPU, memory, network, and data locality constraints to allow for more adaptive and accurate resource provisioning.

3.5. Fault Injection and Testing

The four fault scenarios (CPU, memory, network, and data locality) were chosen because they are commonly encountered in real-world cloud computing and big data systems [12]. CPU overload failures are common in distributed computing workloads, where tasks surpass processing capacity due to high demand and end up degrading system performance or forcing tasks to fail. Memory leaks or too much memory usage can be a

common problem across long-running big data applications, leading to system slowdowns or crashes. Network congestion or packet loss impacts data-intensive applications, and the momentum is even higher in distributed computing frameworks like Apache Spark and Hadoop. Data locality in cloud computing refers to when a task is scheduled on a compute node that is remote from the data it needs to consume, which can greatly increase the cost of I/O and result in a waste of compute resources. These types of failures are well-known in other real-world failures of cloud and big data systems, which are incorporated into our model to ensure our approach is not formulated against a trivial model but rather in facing real-world challenges in large-scale computing environments.

4. RESULTS AND DISCUSSION

This section presents a comprehensive evaluation of the proposed system, including experimental setup and evaluation of resource utilisation prediction.

4.1. Experimental Setup

4.1.1. Environments

To evaluate our system, we set up a Hadoop cluster on AWS, consisting of 1 master and 30 worker nodes, each with 4 cores, 16 GB of memory, and 1TB of SSD storage. We chose Ubuntu Server[***] 20.04 LTS and SSD Volume Type as an operating system, and deployed Apache Hadoop 3.2.4[†††] and Apache Hive[‡‡‡] 3.1.3 versions.

4.1.2. Benchmarks and workload

We use the NEWS data detailed in §2.1. Navigating EHR datasets to evaluate the proposed system, taken from South Tees Hospitals NHS Foundation Trust[§§§] . The data includes 1M patients' healthcare data, including 552 different features, such as pulse, age, sex, nausea, given drugs, weight, length of stay, discharged deceased, etc. The data size for bencmarking the proposed system is 35 GB of healthcare data.

4.1.3. Methodology

Our experiments aim to evaluate the performance and accuracy of the proposed system. To this end, we inject four common faults separately, enabling data analysis under possible scenarios. We perform Hive queries in parallel over the dataset with five repetitions, comprising 25 experiments, including data processing without any faults.

4.2. Hyperparameter Tuning

We train the ML models using default or initial hyperparameters to establish a baseline performance. Following this, we employ a systematic Grid Search approach to optimise hyperparameters for each model, such as maximum depth (*max_depth*) and minimum samples split (*min_samples_split*) in Decision Trees, and the regularisation parameter (*C*) and kernel in SVC while the number of trees (*n_trees*), maximum depth (*max_depth*), and minimum samples split (*min_samples_split*) parameters are tuned for Random Forest model. Once the optimal hyperparameters are identified, the models are re-trained to enhance their capabilities in predicting resource utilisation within cloud-based big data systems.

After conducting hyperparameter tuning, the optimal values for each model were selected based on validation performance. The final hyperparameter values used in our experiments are summarised in Table 1.

Following this, we used Grid Search tuning[****] related to hyperparameters using the various data partitions from the cloud-based big data system logs to assess the tuned hyperparameters' generalisability. Subsets of varying workload patterns were used to train and validate the models to determine their adaptability. We found that optimal hyperparameter values were more or less stable across datasets. Still, some small variations were found in tuning parameters because models like Random Forest and KNN are sensitive to dataset distribution. The models remained highly predictive despite the changes, confirming our hyperparameter selection's stability and performance.

Although the Grid Search optimisation process makes improving our model performance in our study possible, it also applies to many other cloud computing scenarios. Hyperparameter tuning can be performed in real-time big data analytics using online learning approaches that continuously update model parameters as new data is received. Hyperparameter search strategies such as Bayesian Optimisation or Reinforcement Learning-based tuning could be adopted in edge-computing environments to reduce the overhead of exhaustive search methods, as edge devices do not possess unlimited computational resources. On the other hand, in heterogeneous workload scenarios, transfer learning methods can help provision previously optimised hyperparameters across workloads without starting the model training process from scratch. Such emphasises the wider relevance of hyperparameter optimisation beyond the narrative of this paper and leaves space for further research on adaptive tuning techniques.

[***] https://ubuntu.com/
[†††] https://hadoop.apache.org/release/3.2.4.html
[‡‡‡] https://hive.apache.org/
[§§§] https://www.southtees.nhs.uk/
[****] https://scikit-learn.org/stable/modules/grid_search.html

Table 1. Final hyperparameter values after tuning

Model	Hyperparameter	Value
Support Vector Classifier (SVC)	Kernel	RBF
	Regularization (C)	1.0
Gaussian Naïve Bayes	Smoothing factor	1e-9
Logistic Regression	Regularization (C)	0.01
	Solver	Lbfgs
KNN	Number of neighbors (K)	5
	Distance metric	Euclidean
Decision Tree	Max depth	10
	Minimum samples split	2
	Criterion	Gini
Random Forest	Number of trees	100
	Max depth	15
	Minimum samples split	4
	Criterion	Entropy

4.3. Cross-Validation

We conduct a 10-fold cross-validation process to ensure robust and unbiased performance assessment for the developed models. This process divides the dataset into ten equal-sized folds, where nine are used for training and one for validation in each iteration. The process is repeated for all ten folds, and the final reported results represent the average performance metrics (accuracy, precision, recall, F1-score) across all folds to ensure robustness and mitigate bias. In this way, we guarantee to provide more reliable and generalised ML models in predicting resource utilisation within cloud-based big data systems.

4.4. Evaluation of Resource Utilisation Prediction

This section provides a detailed explanation of the experimental evaluation conducted to assess the performance and reliability of the proposed system within real-world cloud computing environments. To this end, we processed the big healthcare dataset over a Hadoop cluster in AWS. We gather different log datasets with and without injection faults. With the help of the automated preprocessing system, logs are labelled, ranging from 0 to 2, based on resource utilisation levels. Fig. 4 demonstrates the data distribution of each stage for resource utilisation.

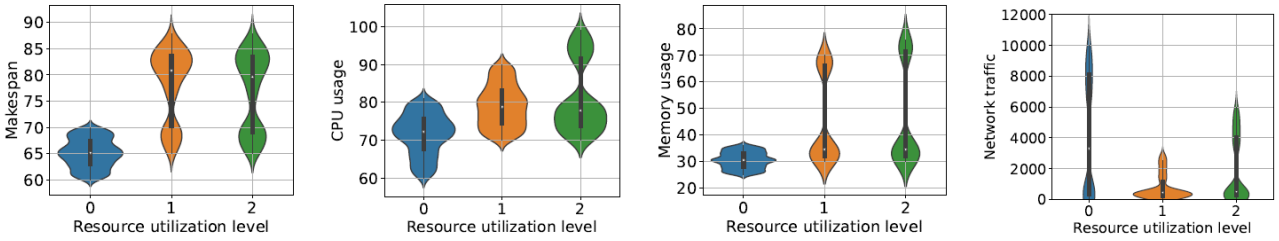

Figure 4. Training data distribution over the features based on resource utilisation levels

In the Hadoop ecosystem, tasks are distributed equally to all compute nodes by default, resulting in less powerful nodes (in terms of resources) needing more time to complete their tasks. To simulate the results of these issues in a heterogeneous big data system, we perform data processing under different scenarios, namely with and without faults. Fig. 5 shows the resource utilisation results for CPU, memory, and network over total execution time (makespan). As seen in Fig. 5(a), CPU utilisation is between 70% and 82%, and makespan varies from 60 to 66 seconds when there are no faults in the system. However, insufficient computation power of the node reaches 100%, increasing the makespan by around 30% (see Fig. 5(b)). Moreover, the data locality issue suspends data processing until the data transfer is complete, reducing CPU usage by 20% and increasing the makespan by 10% as seen in Fig. 6(c). The nodes with less memory resources than others in a heterogeneous big data cluster perform similarly. On nodes with insufficient memory, memory usage and makespan are inversely proportional (Fig. 5(d) and Fig. 5(e)). Moreover, Fig. 5(f) data locality issue decreases memory usage but increases makespan. Compared to Fig. 5(g) (under healthy conditions), Fig. 5(h) and Fig. 5(i) show that the makespan increases when the network usage increases and the number of executions increases dramatically when there is a data locality problem and network fault is injected to simulate the nodes with low bandwidth connections.

For a detailed analysis of our predictive system, we also apply accuracy, precision, recall, and F1-score as performance metrics (as shown in Fig. 6), which bring individual aspects to model assessment. Accuracy is the percentage of correctly classified instances concerning the total number of cases, giving us a descriptor of overall performance. In resource utilisation datasets, imbalanced classes are commonplace, so accuracy is not necessarily a good indicator. Precision is defined as the number of true positives divided by the sum of true positives and false positives, which helps to minimise false alarms. Recall (sensitivity), on the other hand, quantifies the precision of positive classification by determining the fraction of correctly identified adverse cases, which is

important for high-utilisation or failure-prone cases. That is where the F1-score, the harmonic mean of precision and recall, come into play, where a distinct balance is necessary between false positives and false negatives, which serve as a powerful metric in dynamic cloud-based big data environments.

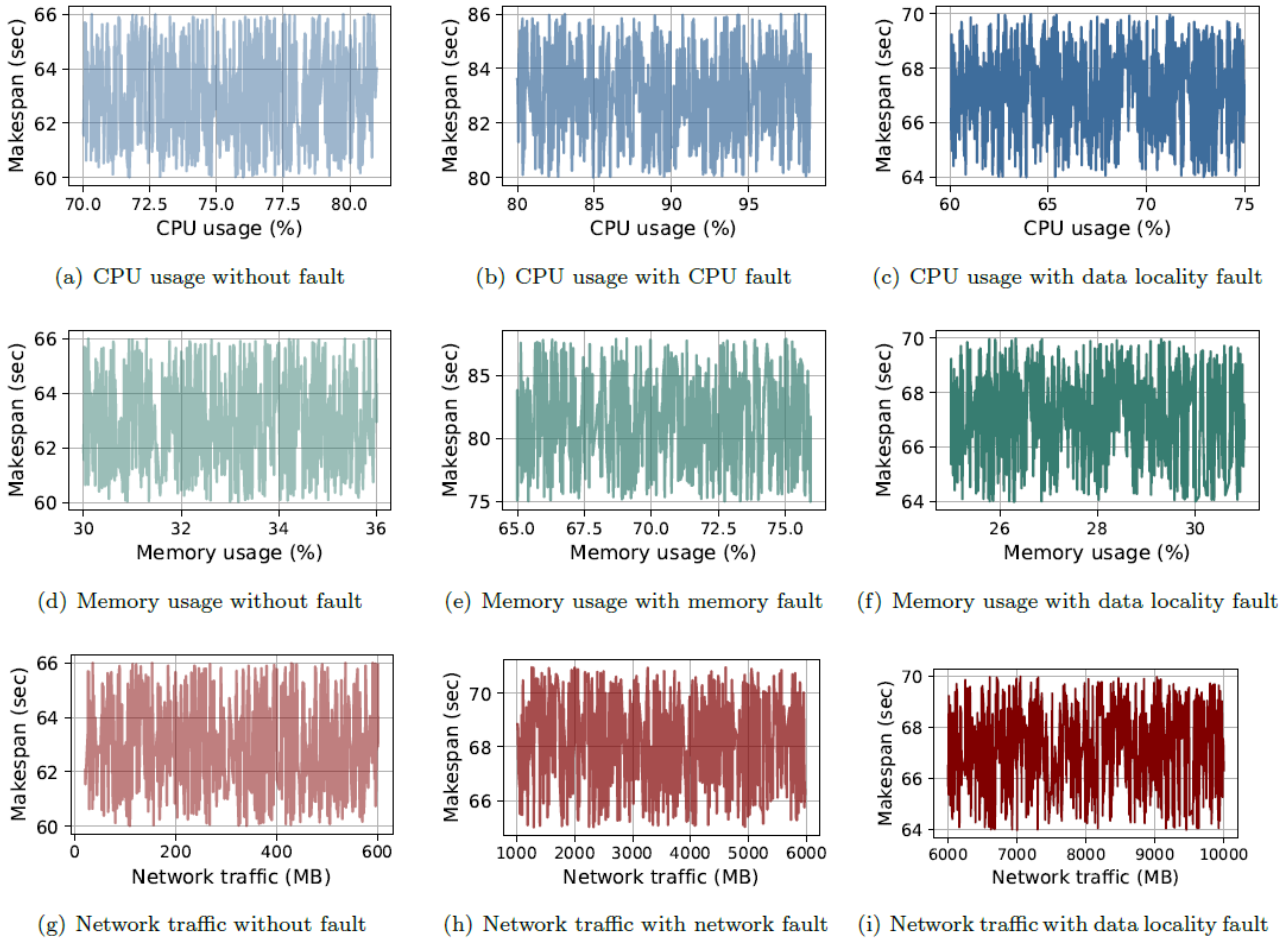

(a) CPU usage without fault (b) CPU usage with CPU fault (c) CPU usage with data locality fault

(d) Memory usage without fault (e) Memory usage with memory fault (f) Memory usage with data locality fault

(g) Network traffic without fault (h) Network traffic with network fault (i) Network traffic with data locality fault

Figure 5. Makespan vs resource utilisation under different scenarios

The proposed algorithms show a high performance in the energy prediction per resource under several online and offline failure situations. Now, we get the most accurate model, k-NN at 97.30%, followed by the random forest at 95.10%. K-NN is relatively successful as it can detect complex patterns and associations in the dataset by evaluating the closeness of examples in the feature space. The degree of sample closeness in this approach is an effective way of presenting how the k-NN structure succeeds in defining nuanced relations. In contrast, it operates using an ensemble of decision trees, merging predictions of the multiple trees to form a comprehensive insight into feature-target connections. Although the accuracy is the same, both these models manage to learn muscle patterns relevant enough to be captured in the prediction, making them appropriate candidates for dependency to ensure the success of our predictive framework. Generally, accuracy is not always the appropriate metric to assess a model's performance, especially when the classes are unbalanced. Metrics like accuracy, recall, or F1 score, which offer a more complex understanding of a model's performance, are better suited to these circumstances. Hence, the reviewed dataset is probably properly balanced if the F1 score, recall, and accuracy are equal.

Our ML-based model provides a 97.3% accuracy rate and does much better than baseline approaches. Incorporating fault injection modules renders the model more resilient, automatically adapting to maintain a high prediction performance level in dynamic workload fluctuations. Our results show the effectiveness of our approach in a real cloud-based big data environment, efficiently handling resource fluctuations, and maintaining high prediction performance across different execution scenarios.

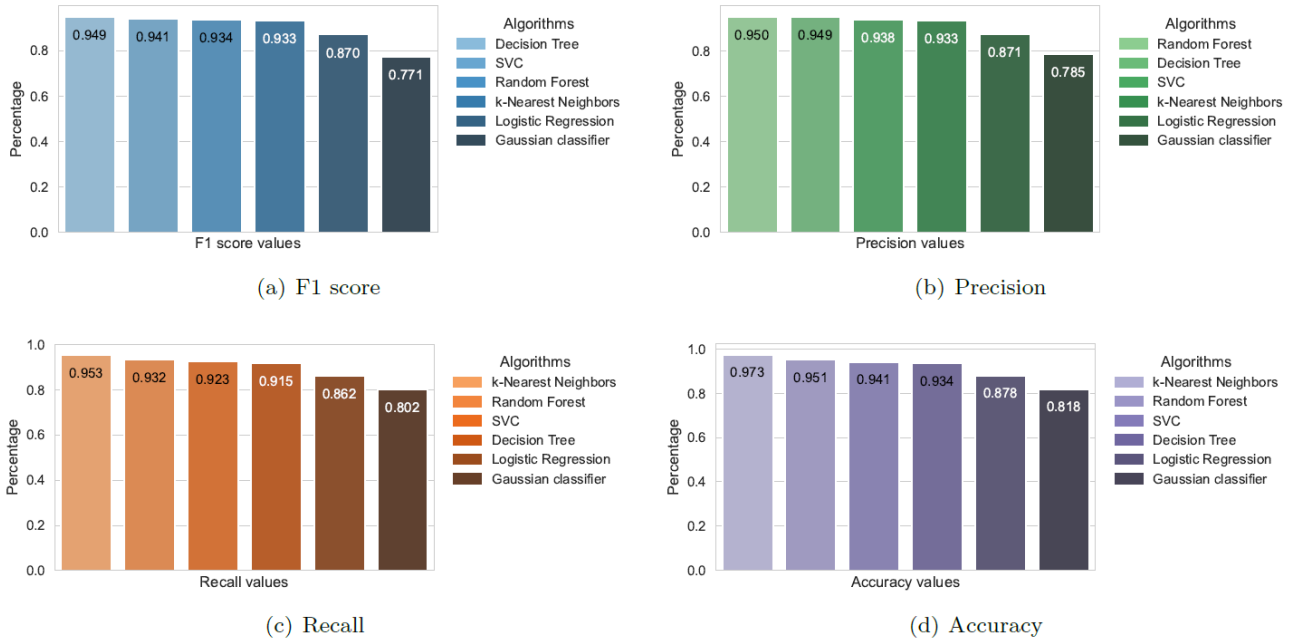

Figure 6 Comparison of performance evaluation metrics for ML algorithms.

5. RELATED WORK

In recent years, researchers have extensively studied resource utilisation prediction for cloud-based big data systems with different aspects, aims, and applications.

5.1. Resource Utilisation Prediction in Cloud Computing

Several recent works have engaged ML models to predict resource utilisation in cloud computing systems. Mehmood et al. developed a hybrid resource utilisation prediction model based on KNN and Decision Trees, resulting in better accuracy for workload prediction [32]. However, this model does not cater to fast-evolving cloud scenarios. Al-Asaly et al. developed a deep learning-based model for autonomic cloud computing environments, intentionally aiming to predict workload. Although their model outperformed traditional approaches, it is not based on real-time system monitoring and, therefore, was not as effective in dynamic cloud-based big data systems [33]. RL algorithms have recently been proposed to better provision cloud resources. For instance, Nguyen et al. developed an RL-based model for decentralised IoMT (Internet of Medical Things) networks that outperforms alternative solutions regarding resource allocation efficiency and reduced latency [38]. Gao et al. introduced a dynamic simulation budget allocation method, and an optimal computing budget allocation (OCBA) strategy was proposed to maximise resource utilisation efficiency [35]; however, this method is designed for passing in cloud environments.

5.2. Fault-Tolerant Resource Management in Big Data Systems

In recent years, fault-tolerant cloud computing strategies have gained much attention in the literature. Rahmanian et al. proposed an ensemble-based resource utilisation prediction model using Learning Automata, which uses the Single and Multiple Window concepts to train a resource utilisation prediction model. Nonetheless, this technique does not provide a real-time adjustment, as it is not accompanied by any live system observant [34]. Khan et al. surveyed blockchain-based edge computing frameworks, which can be applied in IoT applications, pointing out the benefits of using blockchain, including security protection and decentralised resource management [36]. Akbari Zarkesh et al. proposed EdgeLinker, a blockchain-based security mechanism designed for healthcare fog applications to ensure secure data transmission in distributed edge computing networks [39]. Byzantine Fault Tolerance (BFT) techniques have also been employed to maintain reliability in cloud environments. This also addresses the problem of having faulty nodes in a system using these methods, which is common for consensus in blockchain networks [40].

5.3. How Our Model Differs from Prior Work

Our enhanced model, however, is based on an automated structured analysis log data preprocessing pipeline that processes logs in real-time, automating feature extraction and transformation activities before ML model input, allowing for strong input into these models. The second branch is inspired by the characteristics of real-world errors, which are often omitted in prior studies, and we present four fault injection modules (CPU, memory, network, and data locality faults) to assess the system's performance under real-world errors. While most previous work tends to consider only CPU or memory prediction separately, we build a model that can predict multiple usages under changing workloads. Our model outperforms existing methods, achieving up to 97.3% prediction accuracy using hyperparameter-optimised fine-tuned ML algorithms. To clarify these comparisons, we summarise our model and related works in Table 2 below:

Table 2. Comparison of Related Studies

Study	Resource Type	Fault Tolerance	Real-Time Adaptability	Method Used	Accuracy (%)
[32]	CPU & Memory	No	Moderate	KNN & Decision Tree	91.5
[33]	CPU, Memory	No	No	Deep Learning-Based Workload Forecasting	95.4
[34]	CPU & Memory	No	No	Learning Automata	93.0
[36]	Edge/IoT	Yes	Moderate	Blockchain-Based Secure Resource Management	N/A
[39]	Edge Computing & Healthcare	Yes	Yes	Blockchain-Based Secure Communication	N/A
Our Proposed Model	CPU, Memory, Network, Data Locality	Yes	Yes	ML-Based Prediction & Fault Injection	97.3

6. CONCLUSION

Effective resource utilisation is the most critical aspect of processing large amounts of data in an acceptable amount of time. Inefficient resource utilisation is a common problem in cloud-based big data systems due to system heterogeneity, complexity, and unexpected errors, making it challenging to predict resource utilisation for provision resources. This article proposes an automated log data preprocessing-based online resource usage forecasting model using ML algorithms for big data systems. The experiments conducted under different fault scenarios show that our system predicts resource utilisation with a high accuracy rate and can identify the bottlenecks that lead to ineffective resource utilisation in big data systems.

The prediction of resource utilisation plays a crucial role in big data systems regarding time and cost management and provides the necessary provision of resources in case of need. Our system can help predict resource utilisation to embrace this matter for big data systems.

Acknowledgement

The author would like to express their sincere gratitude to South Tees Hospitals NHS Foundation Trust (United Kingdom) for their valuable support in providing access to anonymised healthcare data, which significantly contributed to the development of this study.

REFERENCES

[1] Koppad S, Gkoutos GV, Acharjee A. Cloud computing enabled big multi-omics data analytics. Bioinform Biol Insights. 2021;15.

[2] Wu PY, Cheng CW, Kaddi CD, Venugopalan J, Hoffman R, Wang MD. –omic and electronic health record big data analytics for precision medicine. IEEE Trans Biomed Eng. 2016;64(2):263–73.

[3] Kumar J, Singh AK. Workload prediction in cloud using artificial neural network and adaptive differential evolution. Future Gener Comput Syst. 2018;81:41–52.

[4] Gui B, Wei X, Shen Q, Qi J, Guo L. Financial time series forecasting using support vector machine. In: 2014 Tenth International Conference on Computational Intelligence and Security. IEEE; 2014. p. 39–43.

[5] Kim KJ, Han I. Genetic algorithms approach to feature discretization in artificial neural networks for the prediction of stock price index. Expert Syst Appl. 2000;19(2):125–32.

[6] Ullrich M, Lässig J. Current challenges and approaches for resource demand estimation in the cloud. In: 2013 International Conference on Cloud Computing and Big Data. IEEE; 2013. p. 387–94.

[7] Alwasel K, Calheiros RN, Garg S, Buyya R, Pathan M, Georgakopoulos D, et al. Bigdatasdnsim: A simulator for analyzing big data applications in software-defined cloud data centers. Softw Pract Exp. 2021;51(5):893–920.

[8] Jung J, Kim H. Mr-cloudsim: Designing and implementing mapreduce computing model on cloudsim. In: 2012 International Conference on ICT Convergence (ICTC). IEEE; 2012. p. 504–9.

[9] Calcaterra C, Carmenini A, Marotta A, Bucci U, Cassioli D. Maxhadoop: an efficient scalable emulation tool to test sdn protocols in emulated hadoop environments. J Netw Syst Manage. 2020;28(4):1610–38.

[10] Datadog [Internet]. New York: Datadog Inc.; [cited 2020 Jul 13]. Available from: https://www.datadoghq.com/

[11] Apache Chukwa [Internet]. [cited 2020 Jul 14]. Available from: https://chukwa.apache.org/

[12] Demirbaga U, Wen Z, Noor A, Mitra K, Alwasel K, Garg S, et al. Autodiagn: An automated real-time diagnosis framework for big data systems. IEEE Trans Comput. 2021;71(5):1035–48.

[13] Zhao K, Li S, Kang Z. Takagi-sugeno fuzzy modeling and control of nonlinear system with adaptive clustering algorithms. In: 2018 10th International Conference on Modelling, Identification and Control (ICMIC). IEEE; 2018. p. 1–6.

[14] Er MJ, Deng C. Obstacle avoidance of a mobile robot using hybrid learning approach. IEEE Trans Ind Electron. 2005;52(3):898–905.

[15] Al-Asaly MS, Bencherif MA, Alsanad A, Hassan MM. A deep learning-based resource usage prediction model for resource provisioning in an autonomic cloud computing environment. Neural Comput Appl. 2021;1–18.

[16] Royal College of Physicians. National early warning score (NEWS): standardising the assessment of acute-illness severity in the NHS. London: Report of working party; 2012.

[17] Ross M, Wei W, Ohno-Machado L. “Big data” and the electronic health record. Yearb Med Inform. 2014;23(1):97–104.

[18] Li S, Kang L, Zhao XM, et al. A survey on evolutionary algorithm based hybrid intelligence in bioinformatics. Biomed Res Int. 2014;2014:1–12.
[19] World Health Organization. Partnering for health early warning systems [Internet]. [cited 2025 Jun 21]. Available from: https://public-old.wmo.int/en/bulletin/partnering-health-early-warning-systems
[20] McGinley A, Pearse RM. A national early warning score for acutely ill patients: A new standard should help identify patients in need of critical care. BMJ. 2012;345(7869):9–9.
[21] Aujla GS, Jindal A. A decoupled blockchain approach for edge-envisioned IoT-based healthcare monitoring. IEEE J Sel Areas Commun. 2021;39(2):491–9.
[22] Mehta N, Pandit A. Concurrence of big data analytics and healthcare: A systematic review. Int J Med Inform. 2018;114:57–65.
[23] Dean J, Ghemawat S. Mapreduce: simplified data processing on large clusters. Commun ACM. 2008;51(1):107–13.
[24] Sun X, Ansari N, Wang R. Optimizing resource utilization of a data center. IEEE Commun Surv Tutor. 2016;18(4):2822–46.
[25] Ikhlasse H, Benjamin D, Vincent C, Hicham M. Multimodal cloud resources utilization forecasting using a bidirectional gated recurrent unit predictor based on a power efficient stacked denoising autoencoders. Alex Eng J. 2022;61(12):11565–77.
[26] Meng Y, Rao R, Zhang X, Hong P. Crupa: A container resource utilization prediction algorithm for autoscaling based on time series analysis. In: 2016 International Conference on Progress in Informatics and Computing (PIC). IEEE; 2016. p. 468–72.
[27] Margara A, Urbani J, Van Harmelen F, Bal H. Streaming the web: Reasoning over dynamic data. J Web Semant. 2014;25:24–44.
[28] Hameed A, Khoshkbarforoushha A, Ranjan R, Jayaraman PP, Kolodziej J, Balaji P, et al. A survey and taxonomy on energy efficient resource allocation techniques for cloud computing systems. Comput. 2016;98:751–74.
[29] Armstrong B, Eigenmann R. Performance forecasting: Towards a methodology for characterizing large computational applications. In: Proceedings of 1998 International Conference on Parallel Processing (Cat. No. 98EX205). IEEE; 1998. p. 518–25.
[30] Benaim M, Le Boudec JY. A class of mean field interaction models for computer and communication systems. Perform Eval. 2008;65(11–12):823–38.
[31] Demirbaga U, Noor A, Wen Z, James P, Mitra K, Ranjan R. Smartmonit: Real-time big data monitoring system. In: 2019 38th Symposium on Reliable Distributed Systems (SRDS). IEEE; 2019. p. 357–72.
[32] Mehmood T, Latif S, Malik S. Prediction of cloud computing resource utilization. In: 2018 15th International Conference on Smart Cities: Improving Quality of Life Using ICT & IoT (HONET-ICT). IEEE; 2018. p. 38–42.
[33] Al-Asaly MS, Bencherif MA, Alsanad A, Hassan MM. A deep learning-based resource usage prediction model for resource provisioning in an autonomic cloud computing environment. Neural Comput Appl. 2021;1–18.
[34] Rahmanian AA, Ghobaei-Arani M, Tofighy S. A learning automata-based ensemble resource usage prediction algorithm for cloud computing environment. Future Gener Comput Syst. 2018;79:54–71.
[35] Gao S, Xiao H, Zhou E, Chen W. Robust ranking and selection with optimal computing budget allocation. Automatica. 2017;81:30–6.
[36] Khan MA, Jan MA, He X. Blockchain-based edge computing frameworks for IoT applications: A comprehensive survey. IEEE Internet Things J. 2021;8(1):22–39.
[37] Aujla M, Jindal R. Blockchain-based healthcare monitoring for edge computing environments: Performance evaluation and analysis. IEEE Trans Ind Inform. 2020;16(3):2204–13.
[38] Nguyen DC, Pathirana PN, Ding M, Seneviratne A. BEdgeHealth: A decentralized architecture for edge-based IoMT networks using blockchain. arXiv. 2021;arXiv:2109.14295.
[39] Akbari Zarkesh M, Dastani E, Safaei B, Movaghar A. EdgeLinker: Practical blockchain-based framework for healthcare fog applications to enhance security in edge-IoT data communications. arXiv. 2024;arXiv:2408.15838.
[40] Cheikhrouhou O, Mershad K, Jamil F, Mahmud R, Koubaa A, Moosavi SR. A lightweight blockchain and fog-enabled secure remote patient monitoring system. arXiv. 2023;arXiv:2301.03551.

Volume 14, Issue 2, Page 64-72, 2025 https://doi.org/10.46810/tdfd.1619709 Research Article

BİNGÖL UNIVERSITY

Türk Doğa ve Fen Dergisi
Turkish Journal of Nature and Science
www.dergipark.gov.tr/tdfd

Alpha-Amylase Activity of Lactic Acid Bacteria Isolated from Different Fermented Products: Characterization of *Latilactobacillus Curvatus* Y2-1B Amylase

Şeyda Nur TÜRKAY RİFAİOĞLU[1,2], Kevser KARAMAN[2,3*], Hatice BEKİROĞLU[4]

[1]Erciyes University, Graduate School of Natural and Applied Sciences, Kayseri, Türkiye
[2]Erciyes University, Genome and Stem Cell Research Center, Kayseri, Türkiye
[3]Erciyes University, Faculty of Agriculture, Department of Agricultural Biotechnology, Kayseri, Türkiye
[4]Şırnak University, Faculty of Agriculture, Department of Food Engineering, Şırnak, Türkiye
Şeyda Nur TÜRKAY RİFAİOĞLU ORCID No: 0000-0002-6605-0989
Kevser KARAMAN ORCID No: 0000-0003-0729-6185
Hatice BEKİROĞLU ORCID No: 0000-0003-3328-1550

**Corresponding author: kevserkaraman@erciyes.edu.tr*

(Received: 14.01.2025, Accepted: 14.04.2025, Online Publication: 27.06.2025)

Keywords
Latilactobacillus curvatus,
Amylase,
Specific activity,
Thermostable

Abstract: In this study, ninety-one lactic acid bacteria isolates (LAB) were obtained from different fermented products and their ability to produce α-amylase was qualitatively examined using starch added medium. Of the LAB isolates, 75 LABs were qualitatively confirmed to be amylase positive, and 20 LABs in total were found to exhibit significant α-amylase production ability. Quantitative tests of α-amylase enzyme activity were then conducted and enzyme activity values for LABs were found in the range of 1.283 U/mL to 13.670 U/mL. Then, 3 LAB isolates (P4-2B, Y2-1B, S1-2B) were selected and identified by genotypic methods. The enzyme from the *Latilactobacillus curvatus* Y2-1B isolate was partially purified, and activity tests were conducted to ascertain the impact of pH, temperature, and cations. The lowest enzyme activity was found to be 0.554 U/mL at pH 9 and 0.694 U/mL at pH 6 as the highest value ($p<0.05$). On the other hand, the purified enzyme formed a band of approximately 40 kDa in SDS-PAGE while the presence of the genes *amy* was examined and approved. It was concluded that selected LAB isolates may be useful in industrial biotechnology and microbial enzyme industry due to their α-amylase enzyme activity.

Farklı Fermente Ürünlerden İzole Edilen Laktik Asit Bakterilerinin Alfa-Amilaz Aktivitesi: *Latilactobacillus Curvatus* Y2-1B Amilazının Karakterizasyonu

Anahtar Kelimeler
Latilactobacillus curvatus,
Amilaz,
Spesifik aktivite,
Termostabil

Öz: Bu çalışmada, farklı fermente ürünlerden doksan bir laktik asit bakterisi izolatı (LAB) elde edilmiş ve α-amilaz üretme yetenekleri nişasta eklenmiş ortam kullanılarak kalitatif olarak incelenmiştir. LAB izolatlarından 75 LAB'nin kalitatif olarak amilaz pozitif olduğu doğrulanmış ve toplamda 20 LAB'nin önemli α-amilaz üretim yeteneğine sahip olduğu bulunmuştur. Daha sonra α-amilaz enzim aktivitesinin kantitatif testleri yapılmış ve LAB'lar için kantitatif enzim aktivite değerleri 1.283 U/mL ile 13.670 U/mL arasında bulunmuştur. Daha sonra, 3 LAB izolatı (P4-2B, Y2-1B, S1-2B) seçilerek genotipik yöntemlerle tanımlanmıştır. Tanımlamadan sonra, *Latilactobacillus curvatus* Y2-1B izolasyonundan elde edilen enzim kısmen saflaştırılarak pH, sıcaklık ve katyonların etkisini belirlemek için aktivite testleri yapılmıştır. Enzim aktivitesinin en düşük değeri pH 9'da 0.554 U/mL ve en yüksek değeri pH 6'da 0.694 U/mL olarak bulunmuştur ($p<0.05$). Öte yandan, saflaştırılmış enzim SDS-PAGE'de yaklaşık 40 kDa'lık bir bant oluştururken, *amy* genlerinin varlığı incelenmiş ve doğrulanmıştır. Sonuç olarak seçilen LAB izolatlarının α-amilaz enzim aktivitesi nedeniyle endüstriyel biyoteknoloji ve mikrobiyal enzim endüstrisinde faydalı olabileceği değerlendirilmiştir.

1. INTRODUCTION

Enzymes have specialized catalytic functions that are formed by living organisms and catalyze biological and chemical reactions [1]. They are involved in many biochemical reactions necessary for all living organisms to perform their vital activities. In order to maintain homeostasis, energy production, and cellular function, metabolic enzymes are essential for controlling biochemical reactions. These enzymes fall into two general categories: anabolic enzymes, which help create complex molecules from simpler ones (like DNA polymerase and fatty acid synthase), and catabolic enzymes, which break down macromolecules to liberate energy (like amylase, lipase, and proteases) [2-4]. Sources of enzymes can be plant, animal or microbial. Enzymes obtained from microorganisms have many advantages compared to those of other sources. The use of enzymes derived from microorganisms, especially in the detergent industry, which is the most important field of use, in paper production, leather processing, textile industry, production of bakery products, alcohol production, cheese making, production of agrochemicals, etc. dates back to ancient Greece [5-7]. Many enzymes used in industry today are of microbial origin, selected on the basis of their high catalytic activity, non-toxicity and non-pathogenicity compared to plant- and animal-derived enzymes [8]. Amylases are one of the most widely used enzymes in industry. These enzymes hydrolyze starch molecules into polymers composed of glucose units [9]. Starch-degrading amylolytic enzymes are of great importance in biotechnological applications ranging from food, fermentation and textiles to paper industries. Most of the amylases used in industry originate from microbial sources due to various factors, for example the great microbial genetic diversity found in the environment. α-amylase is a key enzyme in the metabolism of a wide variety of living organisms that utilize starch as a carbon and energy source [10].

Fermented items are those made naturally or with the aid of starting cultures from plant and animal sources [11]. They are produced by microorganisms such as bacteria, yeasts and fungi [12]. During the fermentation process, lactic acid bacteria produce various organic acids and metabolites such as flavoring alcohols, aldehydes and esters [13]. LABs are Gram-positive, non-spore-forming, catalase-negative, facultative anaerobic, non-reducingnitrate, acid-resistant and form lactic acid as the main end product of carbohydrate fermentation [14-16]. Lactic acid bacteria used in traditional fermented foods are *Lactobacillus, Lactococcus, Tetragonococcus, Vagococcus, Weissella, Streptococcus, Leuconostoc, Aerococcus, Oenococcus and Pediococcus* [17].

The aim of this study was to isolate LAB from different fermented products and to investigate their ability to produce qualitative and quantitative α-amylase. In this direction, LABs with high activity were identified at molecular level and the effects of different parameters on enzyme activity were characterized.

2. MATERIAL AND METHOD

A total of 94 fermented samples were obtained from Hatay province (Türkiye) and were shown in Table 1 with the codes given. The samples were placed in sterile containers after collection and kept at +4 °C until analyses.

Table 1. Fermented samples from which LAB were isolated within the scope of the study (Ş: turnip, P: cheese, Y: pickled leaf, Z: pickled olive, T: pickle, S: vinegar, Sü: sürk cheese, Ty: salted yogurt, Yo: homemade yogurt)

Samples Provided						
Ş1	Y3	Z7	T6	S1	Sü4	TY8
Ş2	Y4	Z8	T7	S2	Sü5	Yo1
Ş3	Y5	Z9	T8	S3	Sü6	Yo2
Ş4	Y6	Z10	T9	S4	Sü7	Yo3
Ş5	Y7	Z11	T10	S5	Sü8	Yo4
Ş6	Y8	Z12	T11	S6	Sü9	Yo5
Ş7	Y9	Z13	T12	S7	Sü10	Yo6
P1	Y10	Z14	T13	S8	TY1	Yo7
P2	Z1	Z15	T14	S9	TY2	Yo8
P3	Z2	T1	T15	S10	TY3	Yo9
P4	Z3	T2	T16	S11	TY4	
P5	Z4	T3	T17	Sü1	TY5	
Y1	Z5	T4	T18	Sü2	TY6	
Y2	Z6	T5	T19	Sü3	TY7	

2.1 Isolation of Lactic Acid Bacteria

Ten g of sample was taken under sterile conditions and homogenized with 90 mL of Maximum Recovery Diluent (Merck) solution for 5 min. Detailed dilutions up to 10-3-10-5 were then prepared. The prepared dilutions were inoculated on MRS agar for lactic acid bacteria isolation and the inoculated plates were incubated at 30 ºC in anaerobic environment. After the shape and color characteristics of the microorganism colonies were examined, the colonies were purified. The isolates obtained were stored in 20% glycerol added MRS Broth at -80 ºC.

2.2 Qualitative α-Amylase Activity of the Isolates

The methodology described by Sudharhsan et al. [18] was followed to determine the qualitative α-amylase activity of the isoaltes after minor modification. The α-amylase activity of the isolates was first determined qualitatively on starch-MRS medium. The cultures were first inoculated into MRS broth containing 0.25% starch and activated overnight. Then, the cultures were inoculated into solid MRS media containing 0.25% starch. Certain areas of the solid medium were punctured with an agar piercer of approximately 5 mm and 50 µl of samples grown in liquid medium were placed in the cavity and incubated at 30 ºC. After incubation, iodine solution was dripped onto the medium and left for 15-30 minutes and then the formation of a zone around the colonies was considered positive (+) and the absence of a zone was considered as negative (-). The diameter of the zone was measured from different regions and quantitative α-

amylase enzyme activity determination was performed with the selected isolates.

2.3 Quantitative α-Amylase Activity of Selected Isolates

Among the isolates showing qualitative α-amylase activity, quantitative amylase activity of twenty LAB with high zone diameter were detected by DNS method described by Bernfeld [19]. For the test, the isolates were grown overnight in 1% of starch medium. After centrifugation, 100 µl of supernatant was mixed with 200 µl of 0.5% starch (dissolved in pH 7 buffer) solution and incubated at 37 ºC for 30 min. A 400 µl of DNS solution was added to the incubated samples and kept in a boiling water bath for 5 min. Then, 3 mL of distilled water was added to the samples and absorbances were measured at 540 nm using a spectrophotometer. Analyses were performed in three replicates. The different concentrations of maltose were used to prepare a calibration curve used to determine the released sugar concentration and enzyme activity was calculated using the following formula:

$$\text{Enzyme Activity U/mL} = \text{released sugar concentration (mg/mL)} \times \text{RVb (mL)} / (362.32) \times 103 \times (1/t) \times (1/EV) \quad (1)$$

Where RVb is reaction volume, t is duration (min), EV is enzyme volume and 362.32g/mol is the molecular weight of maltose and U/mL is the amount of enzyme releasing 1 µmol of reducing sugar per minute.

2.4 Identification of Isolates by Genotypic Methods and PCR Amplification

Phenol chloroform method was used for genomic DNA isolation of lactic acid bacteria [20]. 16S PEU7 (GCA AAC AGG ATT AGA TAC CC) and 16S DG74 (AGG AGG TGA TCC AAC CGC A) were used as primers for PCR amplification of 16S rRNA region of LAB isolates [21]. The final volume of the PCR mixture was 25 µL consisting of 2 µL buffer, 2 µL dNTP, 0.5 µL Taq polymerase, 17.5 µL nuclease-free water, 1 µL each primer and 1 µL template DNA. PCR reaction conditions were 95 °C for 10 min, 94 °C for 40 s, Tm °C for 1 min, 72 °C for 35 s, 35 cycles and final extension at 72 °C for 10 min. To test for amplification, a 2% agarose gel was run in 1xTBE buffer. The bands formed after the running process were analyzed by taking an image of the gel with an imaging device.

For sequence analysis, the PCR samples were sent to Sentebiolab Co. and the results were compared with the sequences obtained in FASTA format using the BLAST program with the sequences registered in the NCBI (National Center for Biotechnology Information) database and the genetically closest species were determined.

2.5 Determination of α-Amylase Gene Region

PCR amplification was performed with primer α-amy F' (AGATCAGGCGCAAGTTCAGT), R' (TTTTTATGGGCACACCACTCA) [22]. belonging to the α-amylase gene region in the identified isolates. The final volume of the PCR mixture was 25 µL using 2 µL buffer, 2 µL dNTP, 0.5 µL Taq polymerase, 17.5 µL nuclease-free water, 1 µL each primer and 2 µL template DNA. PCR reaction conditions were 94 °C for 30 s, 94 °C for 15 s, Tm °C for 30 s, 72 °C for 90 s, 35 cycles and final extension at 72 °C for 10 min. To test for amplification, a 2% agarose gel was run in 1xTBE buffer. The bands formed after running were analyzed by taking an image of the gel with an imaging device.

2.6 Partial Purification of α -Amylase from İsolates

Among the identified samples, *L. curvatus* Y2-1B isolate showing high α-amylase enzyme activity was partially purified. For purification, 1000 µl of activated *L. curvatus* Y2-1B isolate was added to 9 mL of liquid medium containing 1% starch in MRS broth and incubated at 30 ºC and 80 rpm for 24 hours for enzyme production. It was then centrifuged at 10000 rpm for 10 min at 4 ºC. The supernatant was filtered through a 0.22 µm filter and cold acetone (80%) was added to the filtrate and the sample-acetone mixture was incubated at -20 ºC for one night. Then, the supernatant was centrifuged at 10000 rpm for 10 min and 10 mL of sodium phosphate buffer (pH 5.5) was added to the precipitated enzyme. The acetone-purified α-amylase was stored at +4 ºC for analyses.

2.7 Molecular Weight of *L. Curvatus* Y2-1B α -Amylase

The molecular weight of α-amylase enzyme produced by partially purified *L. curvatus* Y2-1B was calculated by SDS-PAGE. SDS-PAGE analysis was performed according to the method described by LaemmLi [23] using 7.5% and 20% separating gel. The samples in powder form (10 mg/mL) were dissolved in distilled water and mixed (1:3 v/v) with the sample buffer (0.5 M Tris–HCl pH 6.8, 40% glycerol, 2% SDS, 0.2% bromophenol blue, 5% (w/v), β-mercaptoethanol). Then, the samples, which were kept in boiling water for 5 minutes, cooled and made ready for analysis. 5 µL of marker and 20 µL of prepared sample solutions were loaded in loading wells and a vertical electrophoresis system (Mini-PROTEAN®System, Bio-Rad) was run with a constant current of 20 mA/gel. After the running process was completed, the bands stained with the staining solution (25% Coomassie brilliant blue, 50% methanol, 50% acetic acid) were then kept in the destaining solution (50% methanol, 10%acetic acid) to remove excess dye. The bands were stained with staining solution (25% Coomassie brilliant blue, 50% methanol, 50% acetic acid) and then washed with destaining solution (50%methanol, 10%acetic acid) to remove excess dye. Biorad Gel Doc EZ imaging system was used to image the bands.

2.8 Effect of pH, Temperature and Cations on α-Amylase Enzyme Activity

The α-amylase activity of the purified *L. curvatus* Y2-1B isolate was examined at different buffer pHs, different temperatures and different ratios of cation ions ($CaCl_2$ and $CoCl_2$). For pH test; 0.5% starch solution was prepared using KH_2PO_4-Na_2HPO_4 as buffer at pH 3.0, 4.0, 5.0, 6.0, 7.0, 8.0 and 9.0. Then, the α-amylase activity of the isolates was measured according to the Bernfeld method [19]. For different temperature experiments, the α-amylase enzyme activity of *L. curvatus* isolate at 30 °C, 40 °C, 50 °C, 60 °C, 70 °C was measured according to the Bernfeld method. For different cations; 10 mM and 1 mM $CoCl_2$, 10 mM and 1 mM $CaCl_2$ stock solutions were prepared. The final concentration of the enzyme and solution mixture was 1 mM (1 µL solution and 99 µL enzyme) and pre-incubated at 37 °C for 1 h. After incubation, α-amylase enzyme activity was measured according to the Bernfeld method [19].

2.9 Protein Determination

The protein content of the partially purified enzyme was determined according to the Lowry method using bovine serum albumin (BSA) as a standard [24]. The analyses were carried out in three replicates.

3. RESULTS

A total of 91 LAB isolates were obtained from the fermented products. The morphologically different isolates were selected and purified (Figure 1). Qualitative enzyme activity of isolates was tested, and positive ones included to next steps. (Figure 2). Among the isolates showing α-amylase activity, twenty LAB with high zone diameter were selected and their extracellular α-amylase activities were determined spectrophotometrically (Figure 3). The lowest enzyme activity was determined as to be 1.28 U/mL and the highest activity was 13.67 U/mL.

tgr

Figure 1. LAB colonies

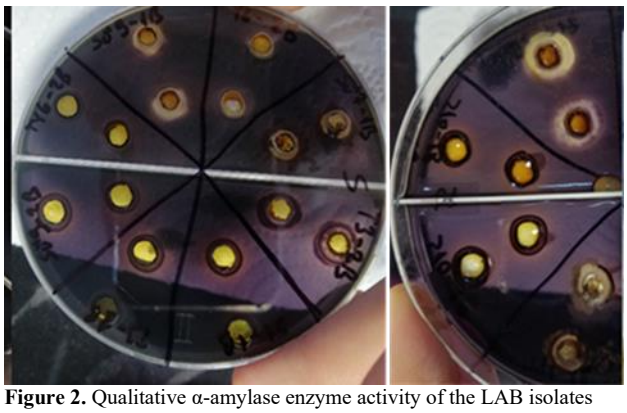

Figure 2. Qualitative α-amylase enzyme activity of the LAB isolates

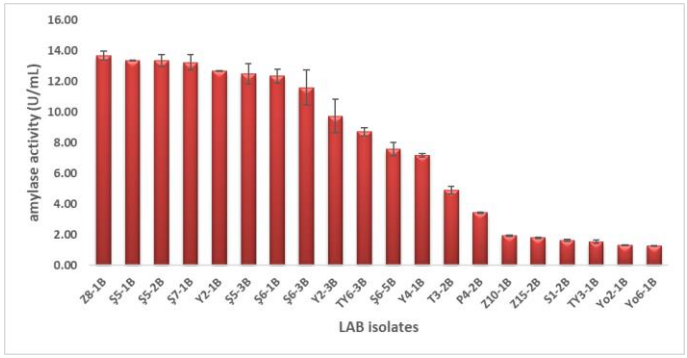

Figure 3. Quantitative α-amylase activity of the selected LAB isolates

Three selected LAB isolates of gel images of PCR products are shown in Figure 4 and three the isolates (P4-2B, Y2-1B, S1-2B) were identified (Table 2). The agarose gel image of the PCR amplification performed with the α-amy primer belonging to the α-amylase gene region in the identified isolates is shown in Figure 5. In the positive strains, 500 bp for *Lactiplantibacillus plantarum* S2-1B and approximaetley 350 bp for *Leuconostoc mesenteroides* P4-2B *Latilactobacillus curvatus* Y2-1B amplicon sizes were detected for amylase.

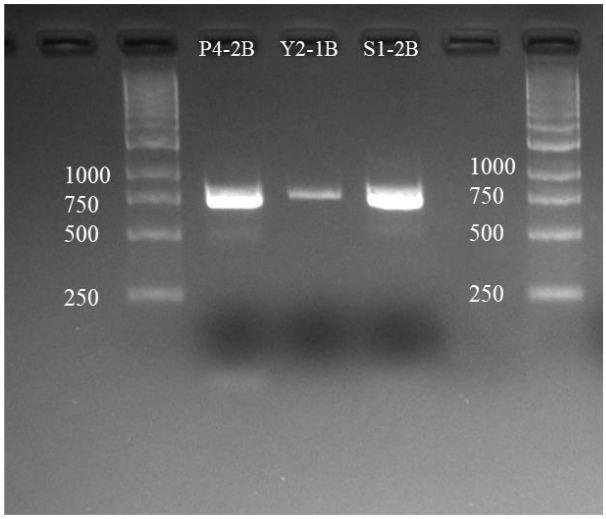

Figure 4. PCR image of the LAB isolates (*Leuconostoc mesenteroides* P4-2B *Latilactobacillus curvatus* Y2-1B, *Lactiplantibacillus plantarum* S2-1B)

Table 2. Information about the identified isolates

Isolates	Samples	Description	Percent homology with GenBank sequence	GenBank Accession No.
P4-2B	Cheese	*Leuconostoc mesenteroides*	99.31%	AB362705.1
Y2-1B	Pickled Leaf	*Latilactobacillus curvatus*	95.96%	MG031203.1
S1-2B	Vinegar	*Lactiplantibacillus plantarum*	99.86%	HG798398.1

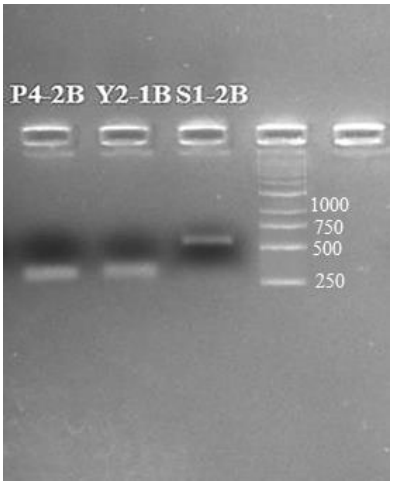

Figure 5. PCR image of *α-amy* gene region of the LAB isolates (*Leuconostoc mesenteroides* P4-2B, *Latilactobacillus curvatus* Y2-1B, *Lactiplantibacillus plantarum* S2-1B)

L. curvatus, which showed α-amylase enzyme activity and had a high zone diameter among the identified isolates, was selected and partial purification was performed and the effect of pH, temperature and cation on extracellular α-amylase activity was determined spectrophotometrically (Figure 6). The lowest enzyme activity in *L. curvatus* was found to be 0.554 U/mL at the pH 9 and 0.694 U/mL at pH 6 as a highest value. Regarding the temperature data of the enzyme activity, the lowest activity was 0.591 U/mL at 70 °C and the highest activity was 0.735 U/mL at 30 °C for *L. curvatus.* In cation effect, the lowest enzyme activity in *L. curvatus* was 0.662 U/mL at 10 mM $CaCl_2$ and the highest was 0.779 U/mL at 1 mM $CoCl_2$. Specific enzyme activity calculations were made upon determination of protein amount, and these values were determined as 1.354 U/mg at pH 6 and 1.082 U/mg at pH 9. On the effect of temperature, *L. curvatus* was determined as 1.154 U/mg at 70 °C and 1.434 U/mg at 30 °C. These values were determined as 1.291 U/mg at 10 mM $CaCl_2$ and 1.520 U/mg at 1 mM $CoCl_2$ (Figure 7). The relative activity value of the extracellular α-amylase enzyme of *L. curvatus* isolate was determined by incubation in KH_2PO_4-Na_2HPO_4 buffer at 37 °C for 30 min. It was found that *L. curvatus* had the highest enzyme activity at pH 6 (100%) (Figure 8). *L. curvatus* had the highest enzyme activity at 30 °C (100%), while *L. curvatus* had the highest enzyme activity at 1 mM $CaCl_2$ and 1 mM $CoCl_2$ (100%). The relative enzyme activity at pH 9 and 8 were 80 % and 86 %, respectively.

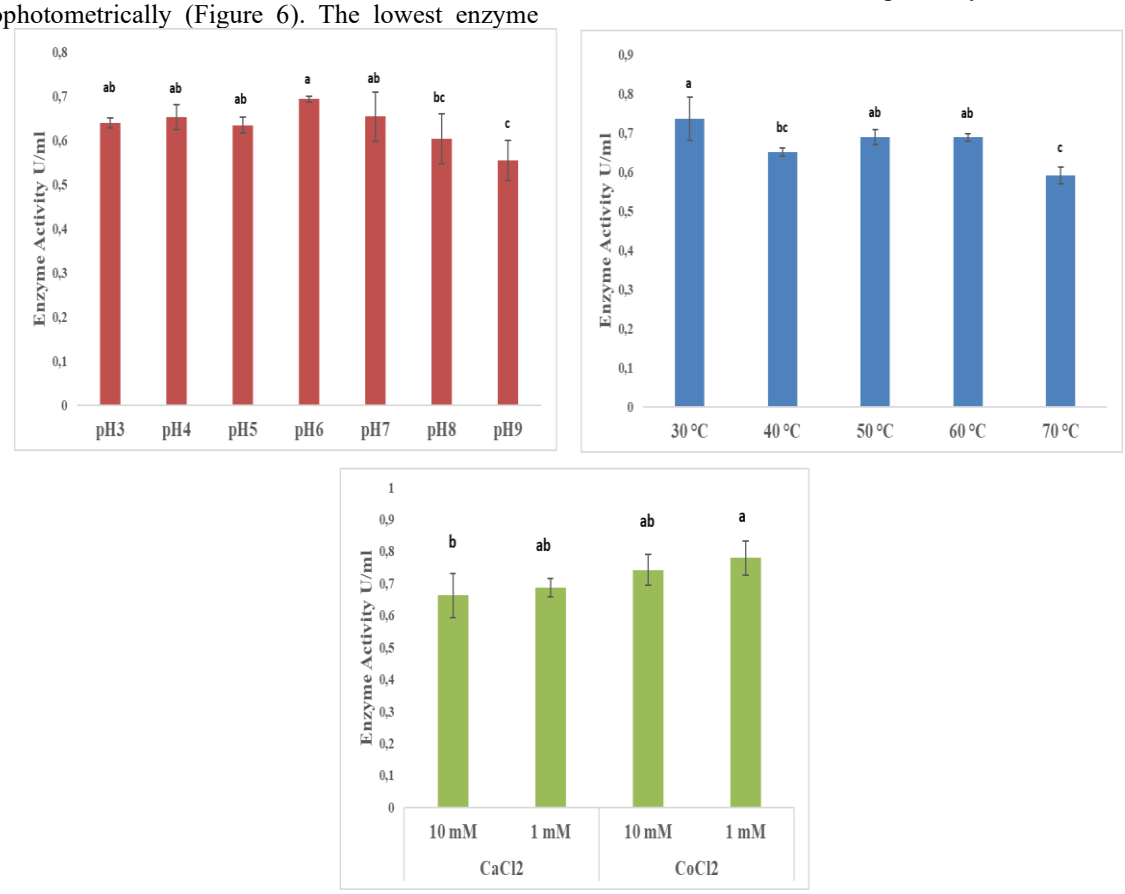

Figure 6. Effect of pH, temperature and different cations on α-amylase activity of *L. curvatus* Y2-1B isolate

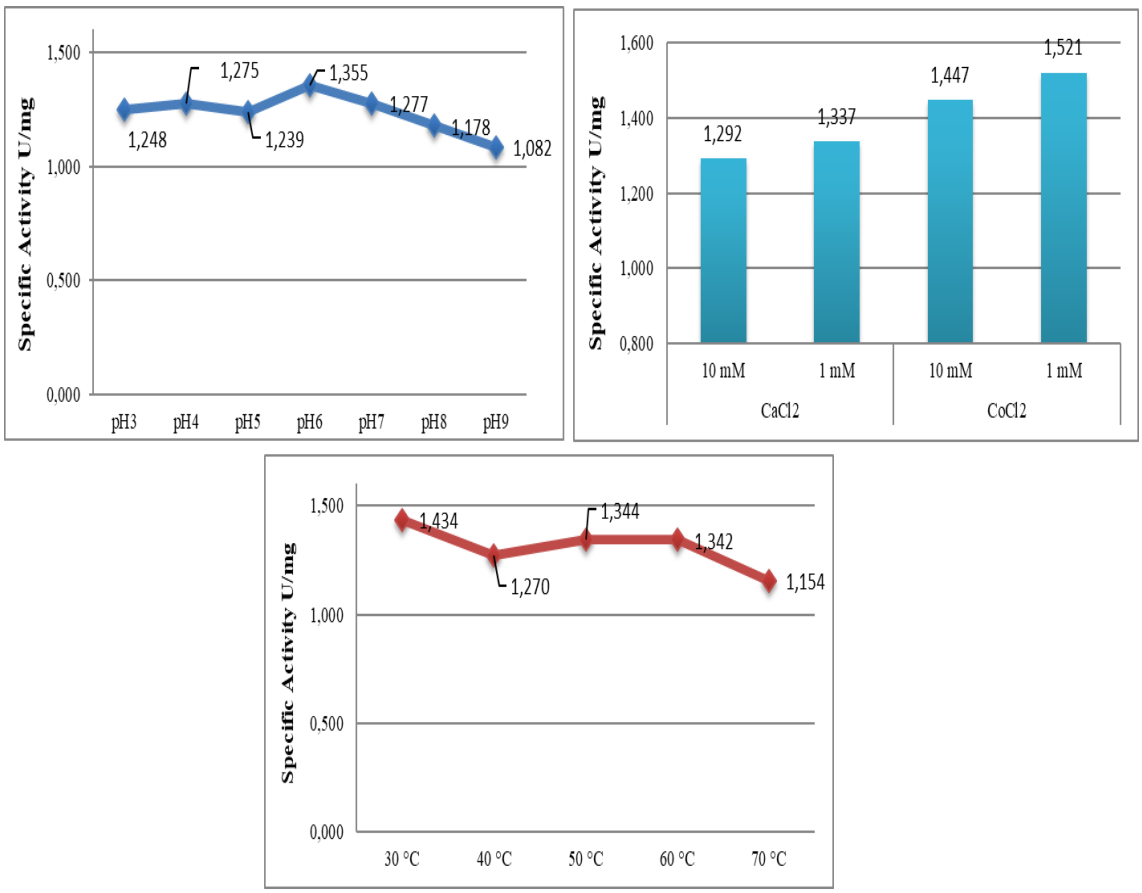

Figure 7. Specific α-amylase activity values of *L. curvatus* Y2-1B at different conditions

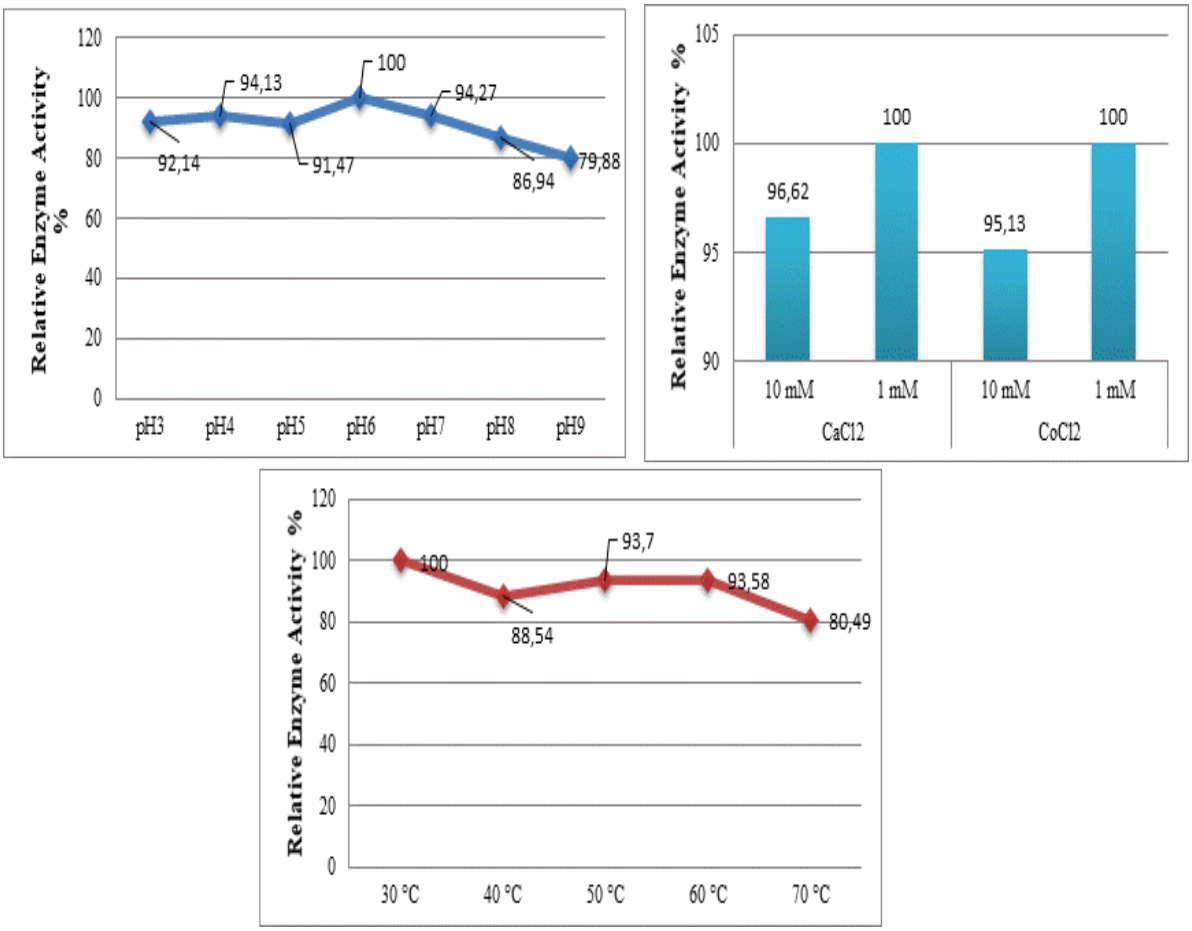

Figure 8. Relative enzyme activity for extracellular α-amylase of *L. curvatus* Y2-1B strain

It was determined that the purified enzyme formed a band of approximately 40 kDa in SDS-PAGE (Figure 9).

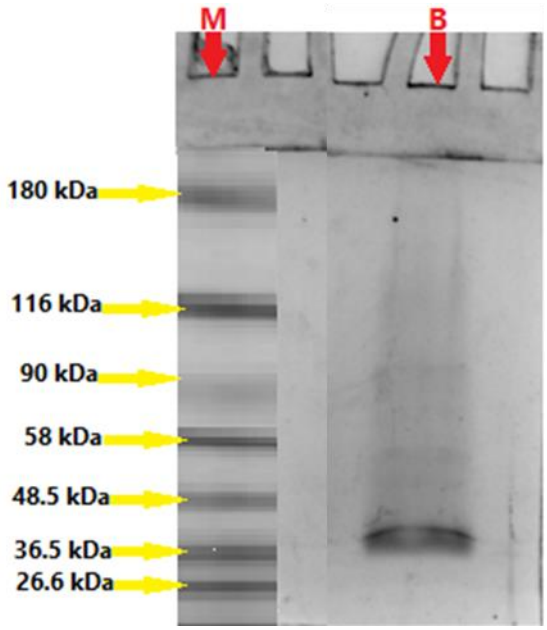

Figure 9. SDS-PAGE electrophoresis image of α-amylase isolated from *L. curvatus* Y2-1B. M: Marker, B: *L. curvatus*, Arrows are ordered by the molecular weight of the standard protein. (Sigma Marker TM wide range 26,6-180,000 Da)

4. DISCUSSION AND CONCLUSION

In this study, LAB were isolated from different fermented products, and their ability to produce α-amylase was investigated. LABs with high α-amylase activity were identified, characterized, and their effects on enzyme activities under different conditions were characterized. Vishnu et al. [25] determined the total amylase activity of *Lactobacillus amylophilus* strain as to be 0.59 U/mL. Orhan [26] found that *Lb. plantarum* ssp. *plantarum*, *Lb. casei, Lb. coryniformis* ssp. *tourquens, Pediococcus pentosaceus* ve *L. mesenteroides* ssp. *dextranicum* species showed amylase activity on starchy medium. In another study by Songré-Ouattara et al. [27], 30 LAB were selected for production of amylase, phytase and α-galactosidase were characterized. Two *L. plantarum* and three *L. fermentum* isolates that could produce one or more of these enzymes were selected and they found that the amylase activities of these isolates were lower than 0.05 Ceralpha Units/mL. These values were found to be low compared to our data.

Velikova et al. [28] stated that the strong expression of amy1 conformed to the presence of extracellular amylase activity (7–8 U/mL) as similar to our study.

Kanpiengjai et al. [29] reported that the amount of extracellular amylolytic enzyme was between 0.04-2.5 U/mL and *L. plantarum* isolate showed the highest activity. In their study about *L. plantarum* isolate, they found that the optimum temperature was between 40-60 oC and the optimum pH value was between 3.5-8, showing a wide pH stability, similar to our results. In another study, it was reported that the optimum pH range of amylase activity of *Enterococcus faecium* isolate was pH 6-7. The authors stated that the enzyme was significantly sensitive to pH and amylase activity was unstable at high temperatures and high pH values. In the same study, they found that Ca^{+2}, Na^{+} and Sr^{+2} metal ions increased amylase activity [30]. Abiodun Onilude et al. [31] reported that the highest amylase enzyme activity of *L. plantarum* isolate was at pH 7, gradually increased from pH 3 to pH 7 and the optimum temperature value was 40 ºC. In the study on the amylase ability of *Geobacillus thermoleovorans*, it was determined that the optimum temperature was 80 ºC and the optimum pH was 6 [32]. In a study conducted to obtain the optimum culture conditions of thermostable α-amylase produced by *Bacillus licheniformis* SO-B3 isolate, it was reported that the optimum temperature was at 70 °C and the optimum pH was in the range of 5.0-6.0 [33]. Pan [34] determined that the optimum enzyme activity value was 3.7 U/mL at pH 7.5 and the total protein amount was 7.0 mg and the specific activity value was 31.62 U/mg for *Bacillus subtilis* amylase enzyme isolated from soil. In the study conducted by Zhao et al. [35], it was determined that $CaCl_2$ played an important role in the production of amylase enzyme of *Bacillus amyloliquefaciens* isolate in addition to carbon and nitrogen sources. In another study, the amylase enzyme ability of *Pleurotus tuberregium* isolate was examined and it was found that the optimum activity was at pH 5, the optimum temperature was 70 ºC and $CaCl_2$ increased the activity [36].

It was informed that *L. curvatus* strain is a candidate probiotic and has several genes associated with carbohydrate utilization and bacteriocin production, and these genes can provide strong carbohydrate fermentative ability and antibacterial capacity [37]. In addition, carbohydrate metabolism enzymes such α-amylase and α-glucosidase enzymes are the subject of research on probiotic isolates. In the study conducted by Ragavan and Das [38], α-amylase and α-glucosidase enzyme of probiotic yeasts *Yarrowia lipolytica, Kluyveromyces lactis, Lipomyces starkeyi, Saccharomycopsis fibuligera* and *Brettanomyces custersianus* isolates were examined and it was determined that *L. starkeyi* showed the highest α-glucosidase enzyme activity of 66% and *K. lactis* showed the highest α-amylase enzyme activity of 75%. Jo et al. [39] examined the properties of *Limosilactobacillus fermentum* strain as an amylase and phytase producing starter for the preparation of rice-based probiotic beverages and stated that it is suitable for fermentation in terms of rapid growth rate, pH and metabolite changes in rice solution, amylase and phytase activities and optimal viscosity changes for beverage as starting properties for rice fermentation. In the same study, the cultivation status of *Limosylactobacillus fermentum* strain in different media was examined and it was reported that α-amylase enzyme showed an enzyme activity of 0.11 U in 0.5% rice added medium, α-amylase enzyme activity in the range of 0.08-0.02 U in MRS medium and phytase enzyme production was 17.65 U, indicating that this isolate can produce α-amylase and phytase enzymes.

Molecular weight of α-amylase expressed in *B. subtilis* WB800 was deterimined as 58.4 kDa [40], in *Bacillus amyloliquefaciens* FW2 was 55 kDa [37], in *Lactobacillus*

sp G3_4_1TO2 was 95 kDa, in *Anoxybacillus ayderensis* FMB1 isolate was found to be 58.5 kDa [32] and in *Bacillus subtilis* was indicated as 50 kDa [41]. It was informed that most microorganisms produce thermostable α-amylase with a molecular weight in the range of 21–160 kDa and most work well on acidic pH [30]. Tallapragada et al. [42] stated that the majority of α-amylases produced by lactic acid bacteria are near to 100 kDa. Supprtingly, Giraud and Cuny [43] informed that the amino acid sequences deduced show that both *amyA* genes encode a long polypeptide with a molecular weight of around 100 kDa. However, in different studies related to lactobacillus amylases, a well-defined band was obtained as 50 kDa [35]. The authors also informed that discrepancies in the estimation of the size can been explained either by migration artefacts of the proteins in SDS-PAGE or by glycosylation of the protein.

Enzyme studies have a crucial role in many industries such as food, textiles, cosmetics, detergents and amylases are one of the industrially important hydrolytic enzymes. Lactic acid bacteria are industrial microorganisms in terms of extracellular enzyme production. In this study, LABs with the ability to produce α-amylase enzyme using different fermented products were identified and it is thought to be important in terms of creating starter cultures for future studies and using them in different microbiology studies. *Latilactobacillus curvatus* Y2-1B isolate can be employed in thermophilic amylase enzyme production investigations since it demonstrated α-amylase enzyme activity at high temperatures.

Acknowledgement
This study was financially supported by Erciyes University Scientific Research Projects Coordination Unit under Grant number of FYL-2021-11216.

REFERENCES

[1] Abiodun Onilude A, Solomon Ayinla G, Eluehike C. Properties of Alpha-amylase of *Lactobacillus plantarum* Isolated from Cassava Waste Samples. Biotechnol J Int 2017; 19: 1–14.

[2] Temel Y, Ayna A, Hamdi Shafeeq I, Ciftci M. In vitro effects of some antibiotics on glucose-6-phosphate dehydrogenase from rat (Rattus norvegicus) erythrocyte. Drug Chem Toxicol 2020; 43: 219–223.

[3] Bayindir S, Ayna A, Temel Y, Ciftci M. The synthesis of new oxindoles as analogs of natural product 3,3″-bis(indolyl)oxindole and in vitro evaluation of the enzyme activity of G6PD and 6PGD. Turk J Chem 2018; 42: 332–345.

[4] Bayindir S, Temel Y, Ayna A, Ciftci M. The synthesis of N-benzoylindoles as inhibitors of rat erythrocyte glucose-6-phosphate dehydrogenase and 6-phosphogluconate dehydrogenase. J Biochem Mol Toxicol 2018; 32: e22193.

[5] Ataallahi E, Naderi-Manesh H, Roostaazad R, Yeganeh S. A simple 2-step purification process of α-amylase from *Bacillus subtilis*: Optimization by response surface methodology. Int J Biol Macromol 2021; 192: 64–71.

[6] Axelsson LT. Lactic acid bacteria: classification and physiology. In: Salmina S, Wright AV, eds. Lactic Acid Bacteria. USA: Marcel Dekker Inc; 1993. p.1–63.

[7] Bamigboye CO, Okonji RE, Oluremi IO, James V. Stain removing, juice-clarifying, and starch-liquefying potentials of amylase from Pleurotus tuberregium in submerged fermentation system. J Genet Eng Biotechnol 2022; 20: 23.

[8] Bernfeld P. Enzymes Carbohydrate Metabolism. Methods Enzymol 1955; 17: 149–158.

[9] Bilgehan H. Basic Microbiology and Immunology. İzmir: Faculties Bookstore Peace Publications; 1999. p.622.

[10] Bilgin H. Antimicrobial activity of a bacteriocinogenic bacterium isolated from a fermented milk product. Master's Thesis, Gaziosmanpaşa University, Tokat; 2008. p.55.

[11] Bulut Ç. Isolation and characterization of lactic acid bacteria from cheese. Master's Thesis, İzmir Institute of Technology, İzmir; 2003. p.112.

[12] Chen J, Chen X, Dai J, Xie G, Yan L, Lu L, Chen J. Cloning, enhanced expression and characterization of an α-amylase gene from a wild strain in Bacillus subtilis WB800. Int J Biol Macromol 2015; 80: 200–207.

[13] Chen Y, Yu L, Qiao N, Xiao Y, Tian F, Zhao J, Zhang H, Chen W, Zhai Q. *Latilactobacillus curvatus*: A candidate probiotic with excellent fermentation properties and health benefits. Foods 2020; 9: 1366.

[14] De Angelis M, Gallo G, Corbo MR, McSweeney PLH, Faccia M, Giovine M, Gobbetti M. Phytase activity in sourdough lactic acid bacteria: purification and characterization of a phytase from *Lactobacillus sanfrancisensis* CB1. Int J Food Microbiol 2003; 87: 259–270.

[15] Demain AL, Solomon NA. Manual of Industrial Microbiology & Biotechnology. Washington, DC: American Society for Microbiology; 1981. p.108.

[16] Durak MZ, Fromm HI, Huck JR, Zadoks RN, Boor KJ. Development of molecular typing methods for *Bacillus* spp. and *Paenibacillus* spp. isolated from fluid milk products. J Food Sci 2006; 71.

[17] Fincan SA, Özdemir S, Karakaya A, Enez B, Demiroğlu Mustafov S, Ulutaş MS, Şen F. Purification and characterization of thermostable α-amylase produced from *Bacillus licheniformis* So-B3 and its potential in hydrolyzing raw starch. Life Sci 2021; 264: 118639.

[18] Sudharhsan S, Senthilkumar S, Ranjith K. Physical and nutritional factors affecting the production of amylase from species of *Bacillus* isolated from spoiled food waste. Afr J Biotechnol 2007; 6: 430–435.

[19] Bernfeld P. Amylases, α and β. In: Colowick SP, Kaplan NO, eds. Methods in Enzymology, Vol 1. New York, NY: Academic Press; 1955. p.149–158.

[20] İspirli H. Tulum Peynirinden Laktik Asit Bakterilerinin (LAB) İzolasyonu, Moleküler Metotlarla TanımLanması ve Ekzopolisakkarit

(EPS) Üretim Potansiyelinin Genetik Olarak Belirlenmesi. Master's Thesis, Bayburt University, Bayburt; 2016. p.104.
[21] Durak MZ, Fromm HI, Huck JR, Zadoks RN, Boor KJ. Development of molecular typing methods for *Bacillus* spp. and *Paenibacillus* spp. isolated from fluid milk products. J Food Sci 2006; 71.
[22] Gänzle M, Ripari V. Composition and function of sourdough microbiota: From ecological theory to bread quality. Int J Food Microbiol 2016; 239: 19–25.
[23] LaemmLi UK. Cleavage of structural proteins during the assembly of the head of bacteriophage T4. Nature 1970; 227: 680–685.
[24] Lowry OH, Rosebrough NJ, Farr AL, Randall RJ. Protein measurement with the folin phenol reagent. J Biol Chem 1951; 193: 265–275.
[25] Vishnu C, Seenayya G, Reddy G. Direct conversion of starch to L(+) lactic acid by amylase producing *Lactobacillus amylophilus* GV6. Bioprocess Eng 2000; 23: 155–158.
[26] Orhan E. Enzyme activities of lactic bacteria and streptococci isolated from milk. Master's Thesis, Gazi University Institute of Science and Technology, Ankara; 2013. p.118.
[27] Songré-Ouattara LT, Mouquet-Rivier C, Icard-Vernière C, et al. Enzyme activities of lactic acid bacteria from a pearl millet fermented gruel (ben-saalga) of functional interest in nutrition. Int J Food Microbiol 2008; 128: 395–400.
[28] Velikova P, Stoyanov A, Blagoeva G, Popova L, Petrov K, Gotcheva V, Petrova P. Starch utilization routes in lactic acid bacteria: New insight by gene expression assay. Starch/Stärke 2016; 68: 953–960.
[29] Kanpiengjai A, Rieantrakoonchai W, Pratanaphon R, et al. High efficacy bioconversion of starch to lactic acid using an amylolytic lactic acid bacterium isolated from Thai indigenous fermented rice noodles. Food Sci Biotechnol 2014; 23: 1541–1550.
[30] Unban K, Kanpiengjai A, Takata G, et al. Amylolytic enzymes acquired from L-lactic acid producing *Enterococcus faecium* K-1 and improvement of direct lactic acid production from cassava starch. Appl Biochem Biotechnol 2017; 183: 155–170.
[31] Abiodun Onilude A, Solomon Ayinla G, Eluehike C. Properties of alpha amylase of *Lactobacillus plantarum* isolated from cassava waste samples. Biotechnol J Int 2017; 19: 1–14.
[32] Sudan SK, Kumar N, Kaur I, Sahni G. Production, purification and characterization of raw starch hydrolyzing thermostable acidic α-amylase from hot springs, India. Int J Biol Macromol 2018; 117: 831–839.
[33] Matpan Bekler F, Güven K, Gül Güven R. Purification and characterization of novel α-amylase from *Anoxybacillus ayderensis* FMB1. Biocatal Biotransform 2021;39:322–332.
[34] Pan I. Exploration for thermostable β-amylase of a *Bacillus* sp. isolated from compost soil to degrade bacterial biofilm. Microbiol Spectr 2021; 9:e 0064721.
[35] Zhao W, Zheng J, Wang YG, Zhou HB. A marked enhancement in production of amylase by *Bacillus amyloliquefaciens* in flask fermentation using statistical methods. J Cent South Univ Technol 2011; 18: 1054–1062.
[36] Pandey A, Nigam P, Soccol CR, Soccol VT, Singh D, Mohan R. Advances in microbial amylases. J Biotechnol Appl Biochem 2000; 31: 135–152.
[37] Pham VHT, Kim J, Shim J, Chang S, Chung W. Purification and characterization of strong simultaneous enzyme production of protease and α-amylase from an extremophile *Bacillus* sp. FW2 and its possibility in food waste degradation. Fermentation 2022; 8: 12.
[38] Ragavan ML, Das N. In vitro studies on therapeutic potential of probiotic yeasts isolated from various sources. Curr Microbiol 2020; 77: 2821–2830.
[39] Jo YM, Kim GY, Kim SA, Cheon SW, Kang CH, Han NS. *Limosilactobacillus fermentum* MG7011: An amylase and phytase producing starter for the preparation of rice-based probiotic beverages. Front Microbiol 2021; 12: 745952.
[40] Stiles ME, Holzapfel WH. Lactic acid bacteria of foods and their current taxonomy. Int J Food Microbiol 1997; 36: 1–29.
[41] Turpin W, Humblot C, Guyot JP. Genetic screening of functional properties of lactic acid bacteria in a fermented pearl millet slurry and in the metagenome of fermented starchy foods. Appl Environ Microbiol 2011; 77: 8722–8734.
[42] Tallapragada P, Rayavarapu B, Purushothama RP, Naige RN, Pogakul VP. Screening of potential probiotic lactic acid bacteria and production of amylase and its partial purification. J Genet Eng Biotechnol 2018; 16: 357–362.
[43] Giraud E, Gosselin L, Marin B, Parada JL, Raimbault M. Purification and characterization of an extracellular amylase from *Lactobacillus plantarum* strain A6. J Appl Bacteriol 1993; 75: 276–282.

Volume 14, Issue 2, Page 73-81, 2025 https://doi.org/10.46810/tdfd.1639048 Research Article

BİNGÖL UNIVERSITY

Türk Doğa ve Fen Dergisi
Turkish Journal of Nature and Science
www.dergipark.gov.tr/tdfd

Investigation of Hydrological Droughts in the Eastern Mediterranean Basin Using Hybrid Trend Analysis Methods

Sadık ALASHAN[1], Enes GÜL[2], Ahmet TOPRAK[3], Erdinç İKİNCİOĞULLARI[1*]

[1] Bingol University, Engineering and Architecture Faculty, Civil Engineering Department, Bingöl, Türkiye
[2] Inonu University, Engineering Faculty, Civil Engineering Department, Malatya, Türkiye
[3] Firat University, Humanities and Social Sciences Faculty, Geography Department, Elazığ, Türkiye

Sadık ALASHAN ORCID No: 0000-0003-1769-4590
Enes GÜL ORCID No: 0000-0001-9364-9738
Ahmet TOPRAK ORCID No: 0000-0001-6790-1856
Erdinç İKİNCİOĞULLARI ORCID No: 0000-0003-2518-980X

**Corresponding author: eikinciogullari@bingol.edu.tr*

(Received: 13.02.2025, Accepted: 15.04.2025, Online Publication: 27.06.2025)

Keywords
Trend, Mann-Kendall Test, Sen's Slope Estimator, Şen's Innovative Trend Analysis, Eastern Mediterranean Basin, Streamflow

Abstract: This study investigates the impact of climate change on river systems within the Eastern Mediterranean Basin (EMB), utilizing the Mann-Kendall (MK) test, enhanced by Sen's slope estimator (SSE) and Şen's Innovative Trend Analysis (ITA) methods. The research focuses on hydrological changes, particularly in streamflow trends, and examines their implications in the context of climate change and anthropogenic activities. The methodology involves a detailed analysis of hydro-meteorological series, including streamflow data from different observation stations. The research enhances the robustness of trend detection by applying advanced methodologies such as trend-preserving pre-whitening, which satisfies the serial independence requirement of the MK test. The study area comprises 10 sub-basins in the EMB, with a particular attention to the Göksu River and its tributaries. The results reveal significant declines in the annual streamflow values at several stations, demonstrating the considerable influence of climate and environmental changes on the basin's hydrology. These findings are further evaluated using ITA graphs, which offer a detailed analysis of the spatial and temporal variability in streamflow patterns. This research contributes to a better understanding of hydrological responses to climatic variability, providing vital information for water resource management and policies in regions undergoing significant environmental changes.

Hibrit Trend Analiz Yöntemleri Kullanılarak Doğu Akdeniz Havzasındaki Hidrolojik Kuraklıkların İncelenmesi

Anahtar Kelimeler
Trend, Mann-Kendall yöntemi, Şen'in eğim tahmini, Şen'in yenilikçi trend analizi, Doğu Akdeniz havzası, Akış

Öz: Bu çalışma, Şen eğim tahmincisi (SSE) ve Şen'in Yenilikçi Trend Analizi (ITA) yöntemleriyle geliştirilen Mann-Kendall (MK) yöntemini kullanarak, Doğu Akdeniz Havzası'ndaki (DAH) nehir sistemleri üzerindeki iklim değişikliğinin etkisini araştırmaktadır. Araştırma, özellikle akış eğilimlerindeki hidrolojik değişikliklere odaklanmakta ve bunların iklim değişikliği ve antropojenik faaliyetler bağlamındaki etkilerini incelemektedir. Metodoloji, farklı gözlem istasyonlarından gelen akış verileri de dahil olmak üzere hidro-meteorolojik serilerin ayrıntılı bir analizini içermektedir. Araştırma, MK testinin seri bağımsızlık gereksinimini karşılayan gelişmiş metodolojileri uygulayarak eğilim tespitinin sağlamlığını artırmaktadır. Çalışma alanı, DAH'daki 10 alt havzayı kapsamakta olup özellikle Göksu Nehri ve kollarını içermektedir. Sonuçlar, birkaç istasyonda yıllık akış değerlerinde önemli düşüşler olduğunu ortaya koyarak, iklim ve çevresel değişikliklerin havzanın hidrolojisi üzerindeki önemli etkisini göstermektedir. Bu bulgular, akış desenlerindeki mekansal ve zamansal değişkenliğin ayrıntılı bir analizini sunan ITA grafikleri kullanılarak değerlendirilmiştir. Bu araştırma, iklim değişkenliğine karşı hidrolojik tepkilerin daha iyi anlaşılmasına katkıda bulunarak, önemli çevresel değişiklikler geçiren bölgelerdeki su kaynakları yönetimi ve politikaları için önemli bilgiler sağlamaktadır.

1. INTRODUCTION

The evolving dynamics of climate change pose major challenges and opportunities for hydrological research focusing on studying drainage basin systems. Global climate changes, driven by increased greenhouse gas (GHG) emissions. These changes have profound impacts on the hydrological cycle, particularly on river flow and sediment transport. Historical data suggest that the concept of stationarity, which implies temporally invariant statistical characteristics, may no longer be applicable under these changing conditions [1]. This paradigm shift calls for a re-evaluation of conventional hydrological models. It underlines the need for robust trend analysis methods, such as the Mann-Kendall (MK) test, to detect and interpret these changes [2]. The MK test is known for its robustness in identifying trends in hydrological time series, and it is widely employed in various hydro-meteorological analyses. Wu et al. [3] noted the role of streamflow in examining drought characteristics by providing information on the frequency, duration, and severity of drought events. The application of these methods extends beyond drought analysis and covers a wide range of hydrological events.

Yue et al. [4] proposed the trend-preserving pre-whitening technique to eliminate serial correlation effects on time series, noting that the conventional pre-whitening techniques can remove portions of the trends along with the serial correlations. The authors used the Theil-Sen approach [5,6] to calculate trend slopes and hybridized it with the classical Mann-Kendall method, called MK-SSE. The Theil-Sen approach, known as the Sen slope estimator (SSE) in literature, calculates trend slopes using median slope values. However, with the increasing occurrence of extreme values (both low and high) are more frequent with the climate change phenomenon. Therefore, Alashan [7] was the first to hybridize the Mann-Kendal method with Şen's ITA approach (MK-ITA) to include the effects of the extremum events in trend analysis calculations. This hybridization highlighted how combining these methods improves our understanding of trends in hydro-meteorological variables. The classical MK test is effectively hybridized with Sen's slope estimator and Şen's ITA approach. These enhancements address the limitations of the MK test, especially regarding extreme values and serial autocorrelation in hydro-meteorological time series. Applying these methods has revealed significant trends in Oxford City River systems that are vital for understanding the regional impacts of climate change [7]. Furthermore, Bayazit and Önöz [8] and Şen [9] emphasized the crucial role of advanced methodologies in hydrological trend analyses, particularly in addressing the issue of serial correlation a common feature in hydro-meteorological records that can often distort trend analysis results. The innovative approaches, including over-whitening procedures and Şen's ITA, not only enhance the detection of trends in hydrological data but also ensure the preservation of key trend components essential for understanding the hydrological responses to climatic variability. These methodologies have played an important role in deciphering complex patterns in river flow time series records, providing essential data for water resource management and policies. This is especially critical in regions like the Eastern Mediterranean Basin (EMB), where hydrological changes are intricately linked with environmental and socio-economic factors.

Streamflow trend analysis is critical in river basins, where shifts in streamflow have significant consequences for water resource management. Cultivated areas and decreased rainfall are the main reasons for decreasing trends in watershed streamflow [10,11]. Gumus et al., [12] clarified that understanding streamflow trends is essential for designing dams and hydroelectric power plants and effectively managing flood and drought events. The MK test, alongside other methods such as Şen's ITA method, has been applied to various basins worldwide, providing valuable insights into spatial and temporal changes in river systems. Hydrological variability across different timescales is often assessed using standardized indices for both streamflow and precipitation [13]. Comparisons often reveal that innovative trend methods can offer different sensitivities compared to classical methods such as MK test [14]. Furthermore, robust methods are also needed to specifically address seasonal patterns or regional behaviors in hydro-meteorological data [15]. For example, the trend analyses conducted in the Tigris and Euphrates River basins have revealed significant trends in streamflow, emphasizing the effects of climatic and environmental changes [16–18]. These studies underscore the significance of trend analysis in river systems as a critical tool for policy-making and sustainable water resource management.

The trends detected in the EMB highlight the need for further research to ensure holistic water resources management and environmental protection. For instance, the study of the Upper Jhelum River Basin by Ougahi et al. [19] showed how climate change significantly affects vegetation productivity. Similarly, research in the Upper Awash River Basin by Emiru et al. [20] emphasized the future implications of climate change on hydrological conditions, impacting agricultural activities and human water demands. The observed trend in streamflow and sediment in the River Ganga was investigated by Zakwan and Ahmad [21]. In the study, MK, and hybridized versions with the Sen's slope, and Şen's ITA were conducted using annual maximum and minimum flow data in the Ganga River. In another study, where the river flows in the Western Mediterranean Basin of Turkey were analyzed monthly and annually, the Mann-Kendall trend test was applied to observe changes [22].

The Eastern Mediterranean and the Middle East (EMME) regions are particularly vulnerable to the impacts of climate change. The region is characterized by diverse climates, ranging from temperate in the north to arid desert conditions in the south [23]. This climatic diversity, combined with complex topography and varying socio-economic conditions, contributes to the region's unique vulnerability to climate change impacts [24]. The region has already experienced notable shifts in temperature and precipitation patterns, with increasing temperatures and a

general drought observed in recent decades [23,25]. These changes have significant implications for the region's water resources, agriculture, and human well-being. Drought events, characterized by prolonged periods of below-average precipitation, have become more frequent and intense, particularly in the southern and eastern parts of the EMME [24,26]. The Standardized Precipitation Index (SPI), a widely used drought index, has been instrumental in quantifying these changes, revealing a trend toward drier conditions in many areas [24,26]. In addition to drought, the EMME has also experienced an increase in the frequency and intensity of heat waves, especially in the northern regions [27]. These extreme weather events have far-reaching consequences for human health, energy consumption, and agricultural productivity. The complex interplay of climatic and anthropogenic factors in the EMME necessitates a comprehensive and nuanced approach to hydrological trend analysis. By understanding the historical context of climate variability and employing advanced statistical methods, researchers can better assess the region's vulnerability to climate change and develop effective adaptation and mitigation strategies.

In efforts to understand hydrological responses to climatic changes, the classical methodologies, while robust, often exhibit limitations in handling non-stationary and extreme conditions prevalent in river systems of regions such as those in the EMB. The development of hybrid trend analysis techniques, such as the Mann-Kendall test enhanced by Sen's slope estimator and Şen's ITA, represents a significant advancement. However, a clear research gap remains, largely because conventional methods are static and struggle to fully capture the dynamic and complex interactions driven by both climatic variability and anthropogenic activities. This study makes a substantial significantly advances hydrological trend analysis by deploying a hybrid methodology that combines the MK test, Sen's slope estimator, and Şen's ITA, overcoming the limitations of classical methods in capturing non-stationary conditions and providing a deeper understanding of the impacts of climate change on the hydrology of the EMB. The urgency of this research is underscored by the observed consistent decrease in streamflow, which has profound implications for water resource management and regional ecological balance, highlighting an imperative need for more dynamic and responsive analytical frameworks in hydrological sciences. In the context of hydrological trend analysis, particularly in the Eastern Mediterranean Basin, the MK test, enhancement by Sen's slope estimator and Şen's ITA, has provided comprehensive insights into the changing patterns of river systems. The aim of this paper is to extend these results by focusing on the Eastern Mediterranean basin and using the MK trend test and other statistical methods to analyze the hydrological changes in river systems and their impacts under the current conditions of climate change and human activities.

2. METHODOLOGY

Mann-Kendall (MK) test is the commonly used method for trend detection. However, it does not provide trend slope values for the examined time series. Trend slopes are calculated through a linear regression, Şen's slope estimator, and Şen's ITA methods. MK method is based on the possible existence of a trend in each time series. If a value in the series is bigger (smaller) than the previous value, then a sign function is 1 (-1). If the data values are equal, then the sign function takes 0 value (Eq. 1). The sum of the sign function gives an S test parameter (Eq.2). The S parameter is accepted to fit a Normal (Gaussian) probability distribution function (PDF), which has zero mean, and a variance value as expressed in Eq. 3 and 4. The normal distribution test statistics values are calculated according to Eq.5. If the values are greater (or smaller) than the tabulated values, then there are increasing (decreasing) trends in the time series. The tabulated values are selected through significance levels such as %99 (2.57), %95 (1.96), and %90 (1.65).

$$sign(z_j - z_i) = \begin{cases} 1 & if\ \ z_j > z_i \\ 0 & if\ \ z_j = z_i \\ -1 & if\ \ z_j < z_i \end{cases} \quad (1)$$

$$S = \sum_{i=1}^{n-1} \sum_{j=i+1}^{n} sign(z_j - z_i) \quad (2)$$

$$E(S) = 0 \quad (3)$$

$$Var(S) = \frac{n(n-1)(2n+5)}{18} \quad (4)$$

$$z = \begin{cases} \frac{S-1}{Var(S)} & if\ S > 0 \\ 0 & if\ S = 0 \\ \frac{S+1}{Var(S)} & if\ S < 0 \end{cases} \quad (5)$$

Another assumption of the MK method is that the time series must be serially independent. Most of the time, hydro-meteorological series have serially dependent structures, which give rise to a Type-2 error (the MK result gives a trend, although there is no trend in the time series). To use the MK in a serially dependent series, pre-whitening [28], over-whitening [9], trend-free Sen's slope [29], and hybrid Mann-Kendall methods with the SSE approach [4], and Şen's ITA [7] are used in the literature. The pre-whitening (PW) method removes correlation before using the MK method, but sometimes, it might remove a portion of the trend [8,30–32]. To conserve the trend in a time series, hybrid Mann-Kendall methods with Sen's slope (MK-SSE) and Şen's ITA (MK-ITA) method are applied to a dependent series. The MK-SSE calculates all possible trend slopes in the time series and uses the median trend slope value. Climate change affects hydro-meteorological events on low and high values. To consider the effects of low and high values on trend slope calculations, Alashan [7] proposed the MK-ITA method in the literature.

Let Z be a time series (Eq. 6) for which the trend slope is calculated by Eq. 7, where n is the data length, z_j and z_i are the next and previous data values. The SSE trend slope value is subtracted from the original time series to obtain a trendless time series (Z_{SSE}^{d}, Eq. 8). Correlation effects are removed from the trendless time series, and an

independent series with a trend is achieved by adding the SSE trend slope value to the trendless serially independent time series (Z_{SSE}^{t}, Eq. 9).

$$Z = \{z_1,\ z_2,\ z_3, \dots\dots\dots\dots\dots\dots\dots, z_n\} \quad (6)$$

$$s_{SSE} = median\left(\frac{z_j - z_i}{j-i}\right) \quad (7)$$

$$for \quad \forall \quad j > i; \quad i\ from\ 1\ to\ n - 1 \quad and \quad j\ from\ 2\ to\ n$$

$$Z_{SSE}^{d} = z_k - s_{SSE}.k; \qquad for\ k\ from\ to\ n; \quad (8)$$

$$Z_{SSE}^{t} = z_k^i + s_{SSE}.k \quad (9)$$

Şen [33] proposed a methodology to detect trends on a time series, which also has dependence and skewness. His method, ITA, is applied by dividing the time series into two equal parts and comparing these two halves after sorting on a square graph. Şen's ITA trend slope values are calculated by Eq. 10, where n is the data length, $\bar{x}$ and $\bar{y}$ are the mean of the first and second half sub-series. As mentioned in the MK-SSE method, the trend slope is subtracted from an original time series to conserve the trend slope on the time series (Z_{ITA}^{d}, Eq. 11) before removing correlation effects on the trendless time series (Z^{i}, Eq. 12). The trend slope values calculated by Şen's ITA adding to the independent series to achieve an independent and trendy series (Z_{ITA}^{t}, Eq.13).

$$s_{ITA} = \frac{2(\bar{x} - \bar{y})}{n} \quad (10)$$

$$Z_{ITA}^{d} = z_k - s_{ITA}.k \quad (11)$$

$$Z^{i} = z_k - \rho_1.z_{k-1} \quad (12)$$

$$Z_{ITA}^{t} = z_k^i + s_{ITA}.k \quad (13)$$

2.1. Study Area and Data

The EMB region lies in the south of Türkiye, within the Mediterranean climatic zone, (Figure 1). The Göksu River, the most important watercourse in the basin, is fed by numerous tributaries. Although the basin's first and second biggest streams are the Göksu River and Tarsus Stream, they are short and have a high channel slope. The Eastern Mediterranean Basin consists of 10 sub-basins, and its total area is 21,807 km2. The flow data located in the sub-basins of the Eastern Mediterranean Basin are shown in Figure 1. The flow data used in this study were provided by the General Directorate of State Hydraulic Works.

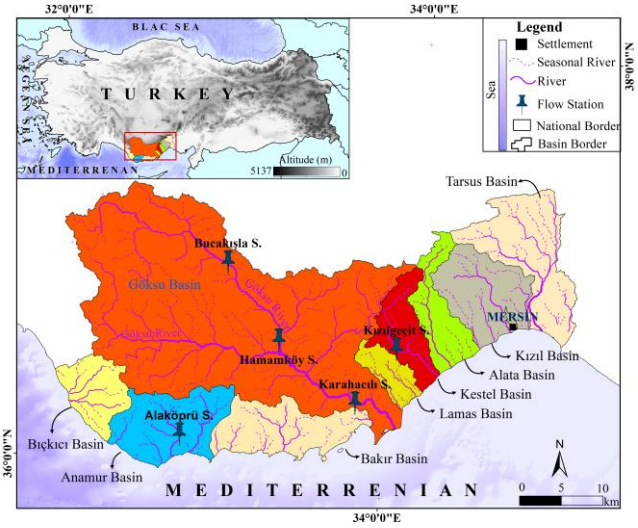

Figure 1. The location and general view of Eastern Mediterranean Basin.

The main branches are E17A017 Kızılgeçit-Lamas Stream, E17A014 Göksu River, E17A020 Hamamköy-Göksu River, E17A021 Alaköprü-Anamur Stream, and E17A012 Bucakkışla-Göksu River. The aim of the selection of this basin has been due to an increase in temperature values in recent years and a slight decrease in the total annual precipitation trend [34]. For this reason, the flow data are analyzed to determine the effect of precipitation on flow.

Statistics about stations with long streamflow values are given in Table 1. Göksu is mainstream on the EMB and has potential with 104.79 m^3/s annual flow on average at the Karahacılı station. The annual minimum average streamflow value is 1.80 m^3/s annual flow at Kızılgeçit station. The maximum skewness was calculated as 1.57 at Bucakkışla station, and the stream dries up in spring and summer. The basin has maximum flows in the spring season, with 339.3 m^3/s at the Karahacılı station. Only the Lamas stream at Bucakkışla station has negative skewness equal to -0.59 in the summer season. Minimum flows in the basin are observed in the summer months, ranging from 0 to 23.4 m^3/s.

Table 1. Statistical parameters of the streamflow gaging stations of East Mediterranean Basin.

	Stations	Stream	Observed Years	Minimum (m^3/s)	Mean (m^3/s)	Maximum (m^3/s)	Standard deviation (m^3/s)	Skew
Annual	Karahacılı	Göksu	1962-2021	49.66	104.79	194.96	35.79	0.30
	Hamam	Göksu	1966-2021	20.00	48.92	84.70	13.50	0.56
	Kızılgeçit	Göksu	1967-2022	1.80	5.06	13.50	2.30	1.18
	Alaköprü	Anamur	1968-2021	9.30	23.34	39.40	8.02	0.21
	Bucakkışla	Lamas	1962-2013	4.70	27.14	46.40	9.21	0.04
Autumn	Karahacılı	Göksu	1962-2021	27.6	51.0	96.5	14.78	0.55
	Hamam	Göksu	1966-2021	13.0	19.8	33.2	4.67	0.93
	Kızılgeçit	Göksu	1967-2022	1.3	3.08	6.5	1.14	0.85
	Alaköprü	Anamur	1968-2021	4.6	10.0	24.7	5.08	1.35
	Bucakkışla	Lamas	1962-2013	4.1	10.18	21.3	2.81	1.57
Winter	Karahacılı	Göksu	1962-2021	37.2	130.0	320.3	63.63	1.01
	Hamam	Göksu	1966-2021	21.4	50.04	135.3	22.40	1.28
	Kızılgeçit	Göksu	1967-2022	1.6	3.88	9.1	1.70	1.21
	Alaköprü	Anamur	1968-2021	7.8	31.24	64.7	15.38	0.43
	Bucakkışla	Lamas	1962-2013	11.3	31.40	78.3	15.51	0.96
Spring	Karahacılı	Göksu	1962-2021	39.2	184.82	339.3	78.29	0.21
	Hamam	Göksu	1966-2021	23.7	76.92	141.7	31.26	0.26
	Kızılgeçit	Göksu	1967-2022	2.1	9.44	27.4	5.38	1.17
	Alaköprü	Anamur	1968-2021	17.9	40.5	67.8	12.97	0.15
	Bucakkışla	Lamas	1962-2013	0	56.28	100.9	23.18	0.12
Summer	Karahacılı	Göksu	1962-2021	23.4	53.28	111.0	19.51	0.84
	Hamam	Göksu	1966-2021	11.7	20.38	34.6	5.65	0.44
	Kızılgeçit	Göksu	1967-2022	1.0	3.87	11.2	1.95	1.16
	Alaköprü	Anamur	1968-2021	4.2	11.6	32.9	6.03	1.24
	Bucakkışla	Lamas	1962-2013	0	10.7	16.0	2.88	-0.59

3. RESULTS

In this study, the original MK test, along with its hybrid versions combined with Sen's slope estimator (MK-SSE) and Şen's ITA (MK-ITA), is applied to detect trends in the streamflow values of the EMB. The MK method requires a serially independent time series; therefore, autocorrelation coefficients were calculated for the EMB streamflow are calculated to detect dependencies at each station. Except for the Bucakkışla station, all the EMB streamflow stations (Karahacılı, Alaköprü, Hamam, and Kızılgeçit) are serially dependent according to a 95% significance level (Figure 2). The maximum autocorrelation coefficient is calculated at the Kızılgeçit streamflow station located on the Göksu River.

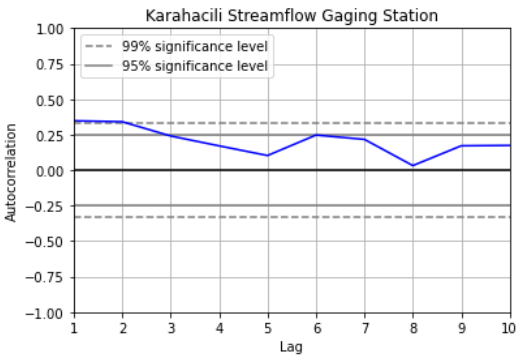

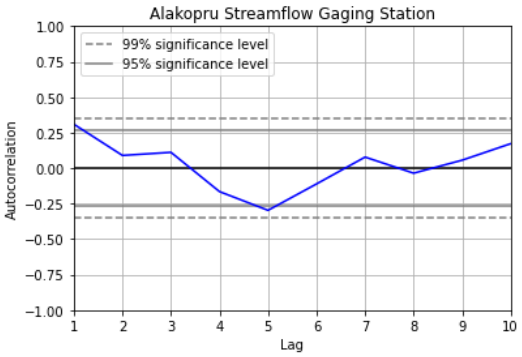

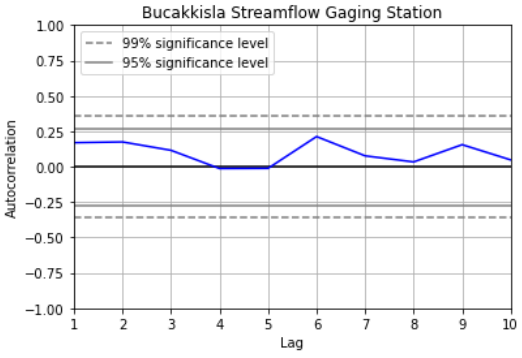

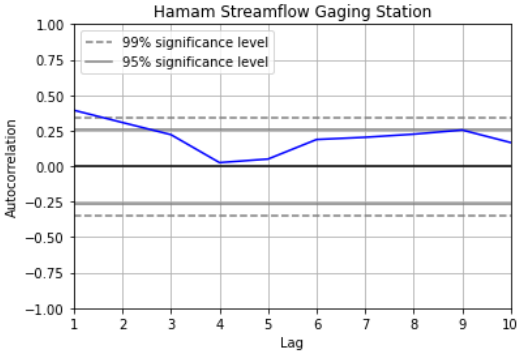

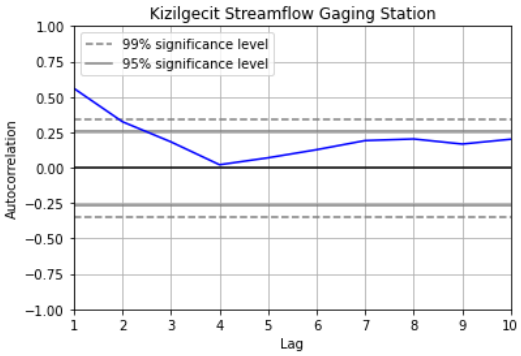

Figure 2. The autocorrelation coefficients of the streamflow gaging stations of the East Mediterranean Basin, Türkiye.

For annual streamflow values, Karahacılı, Hamam, Kızılgeçit, and Bucakkışla stations exhibit crucial decreasing trends. The absolute z values calculated by MK, MK-SSE, and MK-ITA exceed 2.57, indicating significance at the 99% confidence level (see Table 2). The Alaköprü station has important decreasing trends (z=-2.36 and z=-2.49) on annual streamflow values using MK and MK-ITA methods, although there is a crucial decreasing trend detected by MK-SSE (z=-2.87).

For autumn streamflow values, no significant trends are observed at the Karahacılı, Alaköprü, and Bucakkışla stations, whereas the Hamam and Kızılgeçit stations exhibit significant decreasing trends based on the MK, MK-SSE, and MK-ITA methods.

For winter streamflow values, crucial decreasing trends are observed at the Karahacılı, Hamam, and Kızılgeçit stations based on the MK, MK-SSE, and MK-ITA methods. At the Alaköprü station, a decreasing trend have been identified (z<-1.65), whereas the Bucakkışla station showed an important decreasing trend (z < -2.17) confirmed by all three methods: MK, MK-SSE, and MK-ITA.

For spring streamflow values, crucial decreasing trends are evident at Karahacılı, Hamam, Kızılgeçit, and Bucakkışla stations (z < -2.58), while an important decreasing trend is also observed at the Alaköprü stations (z < -2.17), based on the MK, MK-SSE, and MK-ITA methods.

For summer streamflow values, crucial decreasing trends are observed at the Hamam, Kızılgeçit, and Bucakkışla stations, as indicated by the MK, MK-SSE, and MK-ITA methods. At Karahacılı station, the MK and MK-ITA methods reveal decreasing trends (z < -1.74), while the MK-SSE indicates an important decreasing trend (z < -2.11). At the Alaköprü station, significant decreasing trends are detected by the MK-SSE and MK-ITA methods (z < -2.69), whereas the MK method shows an important decreasing trend (z = -2.50).

Table 2. The application of the MK, MK with Şen's slope, and MK with Şen's ITA to the East Mediterranean Basin, Türkiye.

	Stations	Mann-Kendall		Mann-Kendall with Sen's slope			Mann-Kendall with Şen's ITA		
		Z_{MK} (Eq.5)	Decision	S_{SSE} (Eq. 7)	Z_{SSE} (Eq. 9)	Decision	S_{ITA} (Eq.10)	Z_{ITA} (Eq. 13)	Decision
Annual	Karahacılı	-4.16	Crucial decreasing trend (CDT)	-1.212	-4.32	Crucial decreasing trend (CDT)	-1.206	-4.32	Crucial decreasing trend (CDT)
	Hamam	-4.50	CDT	-0.506	-4.60	CDT	-0.473	-4.59	CDT
	Kızılgeçit	-4.24	CDT	-0.080	-4.67	CDT	-0.073	-4.63	CDT
	Alaköprü	-2.36	Important decreasing trend (IDT)	-0.200	-2.87	CDT	-0.120	-2.49	Important decreasing trend (IDT)
	Bucakkışla	-3.15	CDT	-0.300	-3.20	CDT	-0.288	-3.16	CDT
Autumn	Karahacılı	-0.91	No trend	-0.106	-0.91	No trend	-0.303	-1.23	No trend
	Hamam	-5.59	CDT	-0.182	-5.55	CDT	-0.200	-5.58	CDT
	Kızılgeçit	-6.06	CDT	-0.054	-7.24	CDT	-0.052	-7.21	CDT
	Alaköprü	-1.05	No trend	-0.031	-1.01	No trend	-0.006	-1.13	No trend
	Bucakkışla	-1.47	No trend	-0.029	-1.49	No trend	-0.042	-1.49	No trend
Winter	Karahacılı	-2.96	CDT	-1.343	-2.99	CDT	-1.562	-2.98	CDT
	Hamam	-2.88	CDT	-0.456	-2.93	CDT	-0.436	-2.90	CDT
	Kızılgeçit	-3.71	CDT	-0.045	-4.09	CDT	-0.041	-3.97	CDT
	Alaköprü	-1.83	Decreasing trend (DT)	-0.242	-1.88	Decreasing trend (DT)	-0.136	-1.67	Decreasing trend (DT)
	Bucakkışla	-2.14	IDT	-0.294	-2.24	IDT	-0.400	-2.17	IDT
Spring	Karahacılı	-4.57	CDT	-2.730	-4.60	CDT	-2.730	-4.60	CDT
	Hamam	-3.63	CDT	-0.962	-3.79	CDT	-0.974	-3.81	CDT
	Kızılgeçit	-2.87	CDT	-0.125	-2.83	CDT	-0.124	-2.83	CDT
	Alaköprü	-2.17	IDT	-0.282	-2.34	IDT	-0.204	-2.28	IDT
	Bucakkışla	-2.58	CDT	-0.610	-2.58	CDT	-0.602	-2.58	CDT
Summer	Karahacılı	-1.74	DT	-0.297	-2.11	IDT	-0.231	-1.91	DT
	Hamam	-5.98	CDT	-0.263	-6.13	CDT	-0.282	-6.16	CDT
	Kızılgeçit	-5.04	CDT	-0.075	-5.30	CDT	-0.073	-5.25	CDT
	Alaköprü	-2.50	IDT	-0.126	-2.69	CDT	-0.134	-2.74	CDT
	Bucakkışla	-4.49	CDT	-0.100	-4.42	CDT	-0.108	-4.46	CDT

4. DISCUSSION

Annual, winter, spring, and summer streamflow values exhibit decreasing trends accros all stations within the East Mediterranean Basin. The MK, MK-SSE, and MK-ITA methods cannot detect any trend in autumn streamflow values at Karahacılı, Alaköprü, and Bucakkışla stations. ITA graphics for these streamflow values are plotted, where the red and green lines represent a -10% decreasing and +10% increasing trend lines (see Figure 3). The black line represents a trendless case, and the yellow line is the trend slope line for the scatter points (blue dots). The scatter points for Karahacılı and Bucakkışla stations' autumn streamflow values are under the trendless line, which represents a monotonically decreasing trend. However, Alaköprü station autumn flow values, represented by blue scattering points, are distributed over the trendless line, and thus, there is no monotonic trend on these values.

Berhail et al. [35] analyzed rainfall trends in the Macta basin using Sen's slope estimator, Şen's ITA, and MK methods. They found severe drought conditions in the northern part of the Mediterranean basin, and their findings are consistent with the results of this study. Dabanli et al., [36] also found positive trends in seawater temperatures on the Mediterranean coasts. There are gradually increasing meteorological and agricultural droughts in the Macta watershed near the Mediterranean Sea [37].

This study identified a decline in streamflow trends within the EMB, particularly during the spring and summer months. These results reflect broader hydrological concerns on a regional scale. The observed decline in flows may be indicative of more severe or protracted drought events, a finding that aligns with the observations made in the adjacent Euphrates Basin, where a strong correlation was identified between drought duration and severity [38]. However, it should be noted that drought characteristics can vary significantly between regions. Index-based studies in the Yeşilırmak Basin identified substantial trends, primarily at shorter 1- and 3-month timescales, contrasting with the showed annual and seasonal streamflow declines observed in the EMB [13]. While the hybrid MK methods detected clear trends, other research suggests that innovative graphical methods such as ITA/IPTA may be more sensitive than standard MK tests, potentially revealing additional nuances in the data [14]. It is evident that the outcomes of trend analysis for streamflow can vary depending on the analytical method applied. Conversely, consistent regional increases in temperature have been identified as a contributing factor to the hydrological shifts observed across the EMB [15]..

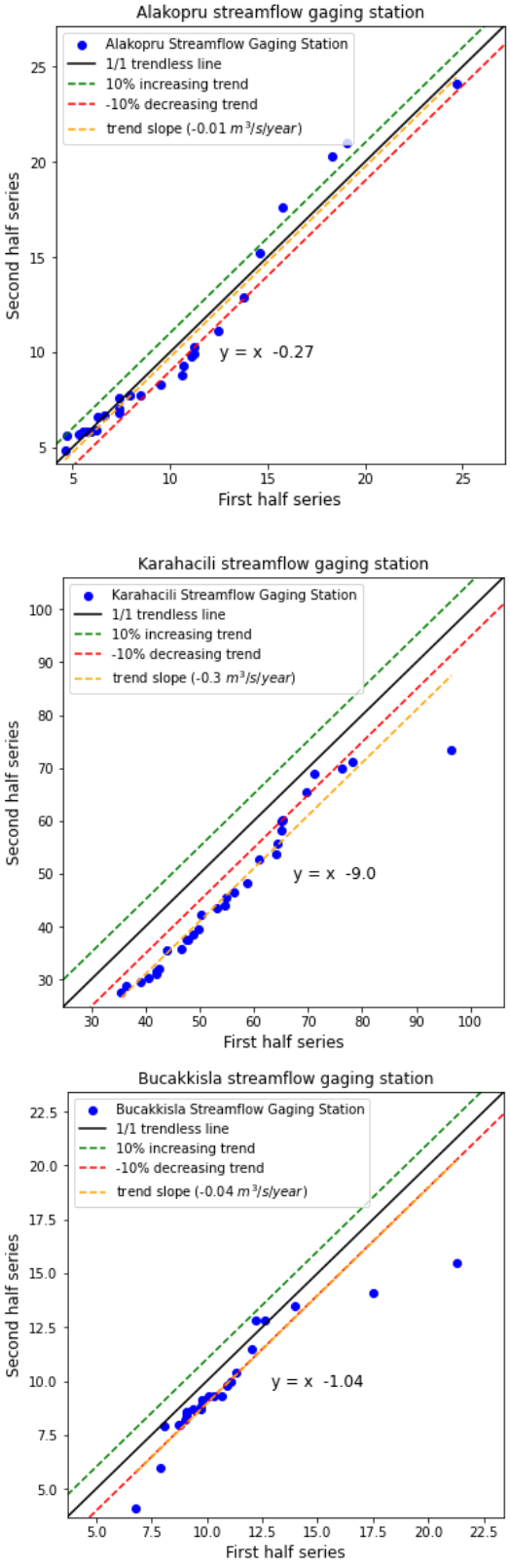

Figure 3. ITA graphs of autumn flow values at Eastern Mediterranean Basin stations, Türkiye.

5. CONCLUSION

The results were derived from carefully examining streamflow data from ten sub-basins in the EMB, considering the importance of serial dependence in hydro-meteorological series.

- The MK method yields consistent results with Şen's ITA and Sen's slope estimator.
- The comprehensive application of the MK test, along with Sen's Slope Estimator and Şen's ITA, has successfully demonstrated a uniformity in identifying decreasing streamflow trends, with annual reductions at critical stations like Karahacılı and Hamam, where trend z-scores of -4.16 and -4.50 respectively underscore the severity of hydrological decline.
- During the spring and summer seasons, which are critical for agricultural activities, the methods have detected significant decreases in streamflow at various stations.
- At Karahacılı, for instance the streamflow exhibited a z-score drop as severe as -4.57, reflecting the considerable seasonal impact on water resources.
- Consistently across the EMB, our enhanced trend analysis methods have highlighted a notable consistency in results, with significant declines in both the spring and summer seasons at stations like Hamam, where z-scores reached -6.16,
- Although no decreasing trends in spring flow values at Karahacılı, Alaköprü, and Bucakkışla stations have been detected employing the MK, hybrid MK-SSE, and MK-ITA methods, visual inspection reveals decreasing trends at Karahacılı and Bucakkışla stations.
- Consequently, the streamflow values in the EMB generally exhibit crucial declining trends. Therefore, future policymakers and designers in the same study area should consider the results of this paper in their planning and decision-making processes.

Acknowledgement

The flow data used in this study were taken from the General Directorate of State Hydraulic Works. The authors would like to thank the General Directorate of State Hydraulic Works (DSİ) for their contributions.

Conflict of Interest

The author declared no potential conflicts of interest with respect to the research, authorship, and/or publication of this article.

Ethics

There are no ethical issues with the publication of this manuscript.

REFERENCES

[1] Mouris K, Schwindt S, Pesci MH, Wieprecht S, Haun S. An interdisciplinary model chain quantifies the footprint of global change on reservoir sedimentation. Sci Reports 2023 131 2023;13:1–16. https://doi.org/10.1038/s41598-023-47501-1.

[2] Sigalla OZ, Valimba P, Selemani JR, Kashaigili JJ, Tumbo M. Analysis of spatial and temporal trend of hydro-climatic parameters in the Kilombero River Catchment, Tanzania. Sci Reports 2023 131 2023;13:1–17. https://doi.org/10.1038/s41598-023-35105-8.

[3] Wu H, Soh LK, Samal A, Chen XH. Trend analysis of streamflow drought events in Nebraska. Water Resour Manag 2008;22:145–64. https://doi.org/10.1007/S11269-006-9148-6.

[4] Yue S, Pilon P, Phinney B, Cavadias G. The influence of autocorrelation on the ability to detect trend in hydrological series. Hydrol Process 2002. https://doi.org/10.1002/hyp.1095.

[5] Theil H. A rank-invariant method of linear and polynomial regression analysis, Part I. Proc R Netherlands Acad Sci 1950.

[6] Sen PK. Estimates of the Regression Coefficient Based on Kendall's Tau. J Am Stat Assoc 1968;63:1379–89. https://doi.org/10.1080/01621459.1968.10480934.

[7] Alashan S. Combination of modified Mann-Kendall method and Şen innovative trend analysis. Eng Reports 2020;2:e12131. https://doi.org/10.1002/ENG2.12131.

[8] Bayazit M, Önöz B. To prewhiten or not to prewhiten in trend analysis? Hydrol Sci J 2007;52:611–24. https://doi.org/10.1623/HYSJ.52.4.611.

[9] Şen Z. Hydrological trend analysis with innovative and over-whitening procedures. Hydrol Sci J 2017;62:294–305. https://doi.org/10.1080/02626667.2016.1222533.

[10] İkincioğulları, E., Gül, E., Toprak A. Comparison of Flow Trends of The Eastern Mediterranean Basin with Mann Kendall and Innovative Trend Analysis Methods. 2. Int. Conf. Adv. Innov. Eng., Elazığ: Fırat University; 2023.

[11] Khemiri K, Jebari S, Berndtsson R, Maalel K. Is Climate or Direct Human Influence Responsible for Discharge Decrease in the Tunisian Merguellil Basin? Water 2021, Vol 13, Page 2748 2021;13:2748. https://doi.org/10.3390/W13192748.

[12] Gumus V, Avsaroglu Y, Simsek O. Streamflow trends in the Tigris river basin using Mann−Kendall and innovative trend analysis methods. J Earth Syst Sci 2022;131:1–17. https://doi.org/10.1007/S12040-021-01770-4.

[13] Yuce, M. I., Aytek, A., Esit, M., Deger, I. H., Yasa, I., Simsek, A., & Ugur F. Investigation of the meteorological and hydrological drought characteristics in yeşilirmak basin, Türkiye. Theor Appl Climatol 2025;156:1–16. https://doi.org/https://doi.org/10.1007/s00704-025-05437-8.

[14] Esit M. Investigation of innovative trend approaches

(ITA with significance test and IPTA) comparing to the classical trend method of monthly and annual hydrometeorological variables: a case study of Ankara region, Turkey. J Water Clim Chang 2023;14:305–29. https://doi.org/https://doi.org/10.2166/wcc.2022.356.

[15] Şan M. Combined innovative trend analysis methods for seasonal trend testing. J Hydrol 2025;649. https://doi.org/https://doi.org/10.1016/j.jhydrol.2024.132418.

[16] Buyukyildiz M. Evaluation of annual total precipitation in the transboundary Euphrates–Tigris River Basin of Türkiye using innovative graphical and statistical trend approaches. Appl Water Sci 2023;13:1–15. https://doi.org/10.1007/S13201-022-01845-7.

[17] Yurekli K. Identification of possible risks to hydrological design under non-stationary climate conditions. Nat Hazards 2023;116:517–36. https://doi.org/10.1007/S11069-022-05686-0.

[18] Terzioğlu ZÖ, Kankal M, Yüksek Ö, Nemli MÖ, Akçay F. Analysis of The Precipitation Intensity Values of Various Durations In Trabzon Province of Turkey By Şen's Innovative Trend Method. Sigma J Eng Nat Sci 2019;37:241–50.

[19] Ougahi JH, Cutler MEJ, Cook SJ. Assessment of climate change effects on vegetation and river hydrology in a semi-arid river basin. PLoS One 2022;17:e0271991. https://doi.org/10.1371/JOURNAL.PONE.0271991.

[20] Emiru NC, Recha JW, Thompson JR, Belay A, Aynekulu E, Manyevere A, et al. Impact of Climate Change on the Hydrology of the Upper Awash River Basin, Ethiopia. Hydrol 2022, Vol 9, Page 3 2021;9:3. https://doi.org/10.3390/HYDROLOGY9010003.

[21] Zakwan M, Ahmad Z. Trend analysis of hydrological parameters of Ganga River. Arab J Geosci 2021;14:1–15. https://doi.org/10.1007/S12517-021-06453-4.

[22] Saplıoğlu, K., Kilit, M., & Yavuz BK. Trend Analysis of Streams in The Western Mediterranean Basin of Turkey. Fresenius Environ Bull 2014;23:313–27.

[23] Lelieveld J, Hadjinicolaou P, Kostopoulou E, Chenoweth J, El Maayar M, Giannakopoulos C, et al. Climate change and impacts in the Eastern Mediterranean and the Middle East. Clim Change 2012;114:667–87. https://doi.org/10.1007/S10584-012-0418-4/.

[24] Tsesmelis DE, Leveidioti I, Karavitis CA, Kalogeropoulos K, Vasilakou CG, Tsatsaris A, et al. Spatiotemporal Application of the Standardized Precipitation Index (SPI) in the Eastern Mediterranean. Clim 2023, Vol 11, Page 95 2023;11:95. https://doi.org/10.3390/CLI11050095.

[25] Kostopoulou E, Jones PD. Assessment of climate extremes in the Eastern Mediterranean. Meteorol Atmos Phys 2005;89:69–85. https://doi.org/10.1007/S00703-005-0122-2/METRICS.

[26] Kesgin E, Genar Yaldiz S, Güçlü YS. Spatiotemporal variability and trends of droughts in the Mediterranean coastal region of Türkiye. Artic Int J Climatol 2024. https://doi.org/10.1002/joc.8370.

[27] Kuglitsch FG, Toreti A, Xoplaki E, Della-Marta PM, Zerefos CS, Trke M, et al. Heat wave changes in the eastern Mediterranean since 1960. Geophys Res Lett 2010;37:4802. https://doi.org/10.1029/2009GL041841.

[28] Von Storch H. Misuses of statistical analysis in climate research. Analysis of climate variability: applications of statistical techniques. HV Storch, A Navarra (Eds), 11-26 1995.

[29] Hamed KH, Ramachandra Rao A. A modified Mann-Kendall trend test for autocorrelated data. J Hydrol 1998;204:182–96. https://doi.org/10.1016/S0022-1694(97)00125-X.

[30] Chowdhury RK, Beecham S. Australian rainfall trends and their relation to the southern oscillation index. Hydrol Process 2010;24:504–14. https://doi.org/10.1002/HYP.7504.

[31] Douglas EM, Vogel RM, Kroll CN. Trends in floods and low flows in the United States: impact of spatial correlation. J Hydrol 2000;240:90–105. https://doi.org/10.1016/S0022-1694(00)00336-X.

[32] Yue S, Pilon P, Phinney B. Canadian streamflow trend detection: Impacts of serial and cross-correlation. Hydrol Sci J 2003;48:51–63. https://doi.org/10.1623/HYSJ.48.1.51.43478.

[33] Şen Z. Innovative Trend Analysis Methodology. J Hydrol Eng 2012;17:1042–6. https://doi.org/10.1061/(ASCE)HE.1943-5584.0000556.

[34] Oğuz K, AKIN S. Doğu Akdeniz Havzasında Sıcaklık, Yağış ve Aerosol Değişiminin İncelenmesi. Mühendislik Bilim ve Tasarım Derg 2019;7:244–53. https://doi.org/10.21923/JESD.464737.

[35] Berhail S, Tourki M, Merrouche I, Bendekiche H. Geo-statistical assessment of meteorological drought in the context of climate change: case of the Macta basin (Northwest of Algeria). Model Earth Syst Environ 2022;8:81–101. https://doi.org/10.1007/S40808-020-01055-7.

[36] Dabanli I, Şişman E, Güçlü YS, Birpınar ME, Şen Z. Climate change impacts on sea surface temperature (SST) trend around Turkey seashores. Acta Geophys 2021;69:295–305. https://doi.org/10.1007/S11600-021-00544-2.

[37] Elouissi A, Benzater B, Dabanli I, Habi M, Harizia A, Hamimed A. Drought investigation and trend assessment in Macta watershed (Algeria) by SPI and ITA methodology. Arab J Geosci 2021;14:1–13. https://doi.org/10.1007/S12517-021-07670-7/.

[38] Deger, I. H., Esıt, M., & Yuce MI. Univariate and bivariate hydrological drought frequency analysis by copula functions. Water Resour Manag 2023;37:4881–907. https://doi.org/https://doi.org/10.1007/s11269-023-03586-x.

Volume 14, Issue 2, Page 82-91, 2025 https://doi.org/10.46810/tdfd.1481031 Research Article

BİNGÖL UNIVERSITY

Türk Doğa ve Fen Dergisi
Turkish Journal of Nature and Science
www.dergipark.gov.tr/tdfd

Macro and Micro Nutritional Content and Physiochemical Soil Properties of Some Naturel Medicinal and Aromatic Plants

Banu KADIOĞLU[1]*

[1]Eastern Anatolia Agricultural Research Institute Management Soil and Water Resources Campus, Erzurum, Türkiye
Banu KADIOĞLU ORCID No: 0000-0002-9041-5992

Corresponding author: banu250@hotmail.com.tr

(Received: 09.05.2024, Accepted: 16.04.2025, Online Publication: 27.06.2025)

Keywords
Burnetrose, Darkplantain, Patience dock, Sea-buckthorn, Natural, Physical-chemical soil properties

Abstract: Medicinal and aromatic plants have been consumed for food and health. In the research; it is aimed to determine the micro and macro plant nutrient content and physicochemical soil properties of the fruits and leaves of some plants that are naturally found in the Kop Pass region and are generally consumed as medicinal plants. According to the results of the physicochemical analysis of the soil samples taken from the root depths of the plants (0-40 cm), the soils are generally mildly acid to slightly alkaline, unsalted, clayey to heavy clayey soils, medium to good organic matter, medium to high in lime content, very high in phosphorus and potassium was found to be high and sufficient. According to the results of fruit and leaf analyzes of the plants (*Elaeagnus rhamnoides*, *Rosa spinosissima*, *Plantago atrata* and *Rumex patientia*) samples taken from their natural habitats, the highest NPK content is 0.34%-0.59%-1.44% in the leaves of the plantain and the lowest NPK content is % in the rosehip leaves. It was determined as 0.14-0.19%-0.67%. Regarding the plant's nutrient content, the leaf parts valued higher than the fruit parts in terms of macro (Ca, Mg) and micro (Fe, Cu, Mn, Zn) plant nutrients.

Bazı Doğal Tıbbi ve Aromatik Bitkilerin Makro ve Mikro Besin İçerikleri ve Fizyokimyasal Toprak Özellikleri

Anahtar Kelimeler
Kuşburnu, Yabani İğde, Sinir otu, Labada, Doğal, Fiziksel-kimyasal toprak özellikleri

Öz: Tıbbi ve aromatik bitkiler gıda ve sağlık amacıyla tüketilmektedir. Araştırmada; Kop Geçidi bölgesinde doğal olarak bulunan ve genellikle tıbbi bitki olarak tüketilen bazı bitkilerin meyve ve yapraklarının mikro ve makro bitki besin maddesi içeriği ile fizikokimyasal toprak özelliklerinin belirlenmesi amaçlanmaktadır. Bitkilerin kök derinliklerinden (0-40 cm) alınan toprak örneklerinin fizikokimyasal analiz sonuçlarına göre topraklar genel olarak hafif asitli-hafif alkali, tuzsuz, killi-ağır killi topraklar, orta-iyi organik madde içerikli topraklardır, kireç içeriğinin orta ila yüksek, fosfor ve potasyum içeriğinin çok yüksek ve yeterli olduğu tespit edilmiştir. Doğal ortamlarından alınan bitki (*Elaeagnus rhamnoides*, *Rosa spinosissima*, *Plantago atrata* ve *Rumex Patientia*) örneklerinin meyve ve yaprak analizleri sonuçlarına göre en yüksek NPK içeriğini %0.,34-%0.59-%1.44 ile sinirotu, en düşük NPK içeriğini ise %0.14-0.19-%0.67 ile kuşburnu yaprakları almıştır. Besin maddeleri içeriğine bakıldığında makro (Ca, Mg) ve mikro (Fe, Cu, Mn, Zn) bitki besin maddeleri açısından yaprak kısımlarının meyve kısımlarından daha yüksek değere sahip olduğu belirlenmiştir.

1. INTRODUCTION

Located in three phytogeographic zones and fauna variety, Türkiye has an important place in different climatic and ecological conditions and rich in natural flora diversity used for food and health purposes. Natural plants found in the vegetation of the North East Anatolia Region in the Iran-Turan (Irano-Turanian) flora group constitute the vegetation of the Eastern Anatolia and the Black Sea Passage [1; 2]. Erzurum and Bayburt provinces that make up our study area are rich in biological diversity and medicinal plants. According to WHO, the number of medicinal and aromatic plants used globally is around 20 thousand, and four thousand of these are widely used. A significant portion of the medication used for treatment is naturally sourced medicine. While the increasing world population's food deficit is attempted to be met by carrying out alternative agricultural activities such as

traditional or organic agriculture, mountain plants are also used for health purposes. The demand for herbal products has significantly increased over the past few decades, with a variety of end uses including flavours, colourants, essential oils, sweeteners, antioxidants, and nutraceuticals [3].

The value chain for medicinal and aromatic plants is complex, involving numerous industries in both primary and secondary processing of products and services. Native medicinal and aromatic plants have been utilised in the Mediterranean region for nutritional purposes or for the treatment of various illnesses and disorders in both people and animals since antiquity due to their complex phytochemical components and associated therapeutic characteristics. Ex situ conservation of medicinal and aromatic plants currently offers documented plant material for genetic advancement and comparative chemodiversity studies, enables the sustainable use of medicinal and aromatic plants for low-input multipurpose cultivation schemes in arid lands and challenging soils, permits their exploitation for human use and/or for animal feeds, and ensures the potential to meet the needs and aspirations of both present and future generations [4].

The development and production of aromatic and medicinal plants are closely tied to changes in the surrounding climate. Abiotic stressors, such as dryness, higher salt concentrations, temperature, ozone, UV rays, and heavy metal exposure, commonly limit the development and productivity of plants globally. Abiotic stresses change many metabolic processes and decrease CO2 uptake and diffusion, further inhibiting photosynthesis. Macro and micro plant nutrients make plants more beneficial for human health by changing plant morphology, anatomy, and chemical composition and increasing or decreasing plants' resistance and tolerance to diseases and pests [5]. The use of natural herbs for food and health purposes has necessitated identifying the differences in these plants' nutrient content in different locations and differences in their physical and chemical properties in the environment in which they grow.

This study was carried out to evaluate the nutritional elements of some natural plants consumed for health and food purposes in Erzurum and Bayburt provinces and the physico-chemical properties of the soils they grow. Physical and chemical soil analyzes were performed on soil samples taken from plant root depths. At the same time, macro and micro plant nutrient contents were investigated in fruit and leaf parts of plants taken from their natural habitats.

2. MATERIAL AND METHOD

The study was carried out between the years 2022-2023 in order to determine the differences between the physicochemical soil properties and the amount of macro and micro plant nutrients of some plants that are naturally found in Erzurum and Bayburt and consumed as health and food. Plant soils were taken from their natural habitat in triplicate. Plants used in the study are sea buckthorn (*Elaeagnus rhamnoides* L. A. Nelson), burnetrose (*Rosa spinosissima* L.), darkplantain (*Plantago atrata* Hoppe) and patiencedock (*Rumex patientia* L.). Soil samples were taken from plant root depths (0-40 cm) and brought to the laboratory by numbering. After the soil samples were air-dried, they were sieved through a 2mm sieve and made ready for analysis. In soil samples; in suspensions prepared for texture with the Bower method [6], 1 (example): 2.5 (water) ratio, soil reaction with a glass electrode pH meter [7], organic carbon determined by the modified Walkey Black method. The amount of organic matter was calculated by multiplying the content with a coefficient of 1.724 [8]. The lime content of the soil sample (mineral CO_2) was determined by Scheibler calcimeter, and from the obtained mineral CO_2 results, lime ($CaCO_3$) was determined as calcium carbonate equivalent by volumetric method [9]. The electrical conductivity values from the saturation paste extract were found to be mmhos cm-1 [10]. Total phosphorus content of soil samples was determined by ICP OES spectrophotometer (Perkin-Elmer, 2100 DV, ICP/OES, Shelton, CT 06484-4794, USA) in filters extracted with sodium bicarbonate, and potassium content was determined by flame photometer in filters extracted with ammonium easetate [11].

Plant samples were taken from their natural habitat in eightylicate (for each plants twentylicate), depending on the usage period (leaves in April, fruits in September-October). Plant samples were first dried at room temperature and then in an oven at 70 °C until they reached constant weight. Afterwards, the dried samples were ground in a Teflon blade mill with a thickness of approximately 2 mm and made ready for analysis [12]. The plant samples' total nitrogen content was determined by the micro Kjeldahl method after wet combustion with a mixture of sulfuric acid. After the plant samples were wet burned with a mixture of sulfuric acid, the total nitrogen content was determined by the Mikrokjeldahl method [13]. After wet burning with nitric perchloric acid mixture, macro and micro plant nutrients were determined by Perkin Elmer (Optima 2100) Model ICP – OES device [14]. Statistical analysis was performed in the JMP 5.0.1 program, with each subject separately according to the factorial arrangement in the random blocks. Soil and plant (fruit/leaf) were subjected to analysis of variance according to factorial experimental design in randomized blocks depending on locations, and differences between means were determined according to LSD (5%) multiple comparison test. The relationship between traits were visually demonstrated with graphics obtained from Genstat 12th Edition [15] and JumpPro-13 software.

3. RESULTS AND DISCUSSION

3.1. Physical and chemical properties of soil

The analysis of soils from the natural habitats of *E. rhamnoides, R. spinosissima, P. atrata and R. patientia* show that between the locations, lime, P and K were significant at 1%, the pH, EC, texture and OM were nonsignificant. It has been determined that lime and potassium have the highest value in Bayburt, and phosphorus in Erzurum. It was determined that EC,

texture, lime contents were important at 1% and K content at 5% for plants, and pH and P averages were insignificant. In addition, the highest values for EC, lime, texture and K were determined by *P.atrata, E.rhamnoides and R.patientia*, respectively. When the location x plant interaction was examined, the EC, lime, and K values were significant at 1%, pH, soil texture, OM, and P values were insignificant (Table 1).

At the Erzurum location, the soils of *Elaeagnus rhamnoides* had highest EC (1.60 mmhos cm-1). In comparison, in the Bayburt location given by Rosa spinosissima with the lowest value of 0.60 mmhos cm-1. While the lime content in Erzurum location was 1.51% (*E. rhamnoides*), 1.00% (*P. atrata*), 0.70% (*R. spinosissima*) and 0.33% (R.patientia) the lime content was 42.23% (*P.atrata*), 40.87% (*R. patientia*), 11.14% (*E. rhamnoides*) and 2.32% (*R. spinosissima*) for the Bayburt location (Table 1). In terms of potassium values, E.rhamnoides, R.spinosissima, P.atrata and R.patientia in Erzurum location were at "sufficient" level, while for the Bayburt location, the potassium amount of E.rhamnoides and R.patientia was in the "excess" class, while the R.spinosissima and P.atrata soils were at the "sufficient" level (Table 2).

Table 1. Varyans analysis for soil properties according to mean of square

Sources of variation	pH	EC (mmhos cm-1)	Texture	OM (%)	Lime (%)	Salt (%)	P (%)	K (%)	N (%)
Location	1.5	0.0004	1.5	0.0338	3265.73**	0.0145**	2561**	8177.04**	0.00667*
Error-1	3.5783	0.3454	362.5	0.2463	0.0144	4.176	0.00042	5.20833	0.00042
Species	2.5456**	0.7671**	2242	2.7738**	619.901**	0.0073**	51**	650.863**	0.12645**
Location* Species	1.3611	0.5704**	205.5	0.8538**	645.143**	0.0089**	34.0704**	1243.72**	0.02963**
ERROR	0.4067	0.0071	62.5	0.0596	0.018	4.1676	0.000417	5.21	0.0004

Table 2. Physical and chemical properties of soils

Location	Plants	pH	OM (%)	P (%)	K (%)	EC (mmhos cm^{-1})	Clay (%)	Silt (%)	Sand (%)	Lime (%)
Erzurum	*E.rhamnoides*	5.30	2.30	0.030	0.011	1.60	46	30	24	1.5
	R.spinosissima	6.60	4.40	0.026	0.010	1.30	42	25	33	0.7
	P.atrata	7.40	3.70	0.019	0.008	1.47	48	32	20	1.0
	R.patientia	7.77	2.50	0.020	0.011	1.40	45	23	32	0.3
Bayburt	*E.rhamnoides*	7.20	2.80	0.032	0.263	1.30	45	30	25	11.1
	R.spinosissima	6.90	3.40	0.028	0.014	0.60	54	28	18	2.3
	P.atrata	7.27	4.30	0.019	0.017	2.10	60	25	15	42.2
	R.patientia	7.70	3.10	0.022	0.031	1.80	43	32	25	40.9

Soil texture, which determines the soil water and nutrient holding capacity, affec the rate of soil formation. Clay soils have high water and nutrient holding capacity, slow movement of water in the soil, and less aeration. This type of soil structure is resistant to water and wind erosion [16]. Since the structure of the plant soils that are the subject of the research is clayey, it is thought that they are rich in plant nutrients and resistant to water and wind erosion. It was stated that R.spinosissima, known as gara guşburni in the region,

grows on limestone or volcanic rocks on arid, rocky slopes at an altitude of 1200-2700 and has 7-11 oval leaflets. E.rhamnoides is a 10 m tall, thorny tree from the oleaster family, also known as sandthorn, sea-buckthorn, or xinjiang, used for anti-inflammatory intestinal diseases Erzurum and Bayburt [17]. It grows in sandy and rocky areas on wetlands in mountainous regions.

With its spinach-like structure, patience dock, or sorrel, a short plant rich in vitamins and minerals, the most known and used in the region, grows naturally in wetlands, on the edges of fields, and pastures. It has been stated that the plant is generally consumed as an anti-inflammatory and as food in the regions of this research [17; 18]. Plantago, known as broadleaf plantain, which grows in wetlands, compacted, degraded soil structure, is used as an anti-inflammatory and for wound treatments and nourishment purposes [19].

Soil pH affects the availability of nutrients and microorganism activities in the soil. The optimum pH value for plant growth is around 6.5-7.0. When the soil reaction (pH) rises from 7.5 to 8.0, the presence of elements such as Fe, Mn and Zn in the soil decreases and the plant cannot take up nutrients. When the pH value falls below 5.5-5.0, iron, manganese and aluminum elements accumulate in the soil in such a way that they have a toxic effect on the plant [20; 21]. As a result of the research, it is thought that the plant soils are between 5.30 and 7.70 and it is among the suitable values for plant growth, and therefore the availability of plant nutrients is not a problem.

Organic matter, which helps to increase the water holding capacity of the soil, ensures that the soil gains a good structure and that the plant nutrients become useful [16]. The results of the research determined that the amount of organic matter supports plant growth. In a study conducted on the extreme spreading area of the sea- buckthorns plant, it was stated that the plant grows in calcareous soil with a content of 164 mM - 520 mM EC, 0.66% - 3% organic matter, sandy-loam, and loam texture, 6.6-7.1 pH [22].

At the end of the examination of the natural environment soils of E.rhamnoides, R.spinosissima, P.atrata and R.patientia plants, the amount of organic matter was found between 2.30 and 4.40, and the electrical conductivity was between 0.60 and 2.10 (Figure 1).

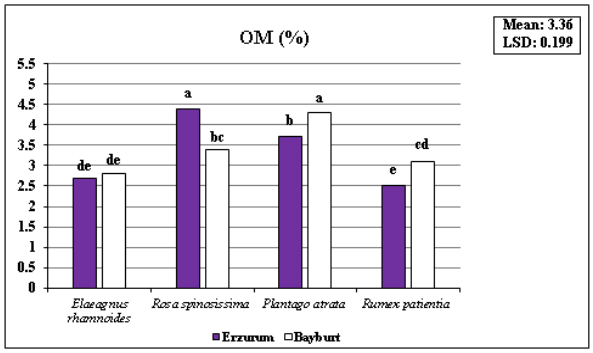

Figure 1. Interaction of location and species for OM (%)

According to Ramesh and colleagues [23], soil organic carbon is essential for the health of agro-ecosystems and is at the heart of the idea of sustainable soil health management. The amount of carbon stored in soils (in SOM) is at least three times that of the atmosphere or live plants. This substantial reservoir of organic carbon is sensitive to changes in the surrounding environment or climate. The ability of organic matter to endure is not due to the fundamental characteristics of the organic material itself, but rather to physicochemical and biological factors from the environment that lower the probability (and hence speed) of decomposition. In other words, the ability of soil organic carbon to persist is essentially an ecosystem feature rather than a molecular one. It is challenging to include the complexity of the soil system into a single conceptual model or to transform it into a manageable yet precise numerical model. The range of spatial patterns in soil spans many orders of magnitude (from nanometer minerals to football-sized soil clods), and there is interaction between solid, liquid, gas, and biological ones. The new information is still largely qualitative in nature. In many cases, it provides vital information and novel model structures, but does not provide information on how to parameterize them [24].

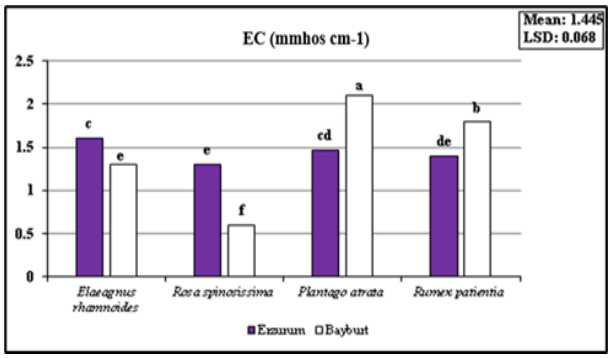

Figure 2. Interaction of location and species for EC (mmhos cm-1).

An important link between plants and soil can be seen in the interaction of location and species for EC (Figure 2), which may be partially sourced through rhizosphere respiration and biogeochemical processes. Rhizospheric microorganisms influence plant physiology by producing secondary metabolites in medicinal and aromatic plants, nitrogen fixation, nutrition uptake, and other beneficial outcomes [25]. Terpenes, alkaloids, flavonoids, carotenoids, plant hormones, carboxylic/organic acids, and fatty acids are just a few of the diverse group of compounds (phytochemicals) found in root exudates and extracts that play a crucial role in the development of plants as well as the control of the rhizosphere microbiota and soil characteristics [26]. These exudates and extracts may be sourcing from the studied medicinal and aromatic plant and/or neighbouring other native species exsisting in proximate location. Calcareous soil is a soil that contains free calcium carbonate. This type of soil is common in humid and semihumid regions as well as in arid and semiarid regions, especially if their parent material is $CaCO_3$-rich. The presence of $CaCO_3$ influences the availability of N, P, K, Mg, Zn, Cu, and Fe to plants as well as the induction of alkaline reactions in calcareous soils (Figure 3). Carbonates in soil assist in buffering the pH between 7.5 and 8.5. Apart from chemical influence, $CaCO_3$ in calcareous soil influences its physical properties as well [27].

The geographic variation is one element that is far from human control, because of different climatic conditions and edaphic factors that exist in each region [28]. Numerous medicinal plant species' chemical compositions are impacted by poorly drained soils [29]. Lychnophora ericoides [30] and Cryptomeria fortunei [31] of various origins can be used as examples of medicinal plant species where geographic variations in chemical compositions' quantity and quality as well as the existence of distinct chemotypes have been reported.

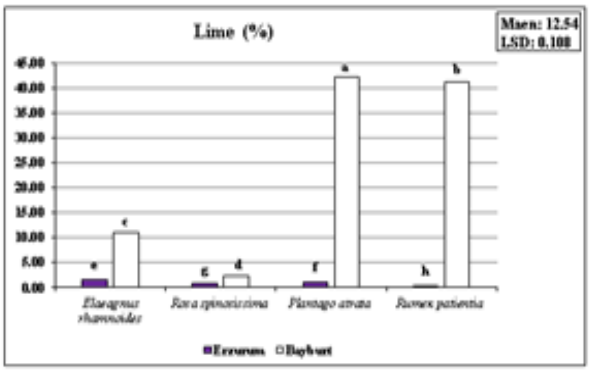

Figure 3. Interaction of location and species for lime (%)

3.2. Macro and micro nutrient contents of the plants

The effect of mineral substances on plant growth has been known for two thousand years. The amount of mineral substances that plants need to grow and develop is very limited. They take the necessary elements as well as the minerals that should not be taken. Fruit and leaf analysis of E.rhamnoides and R.spinosissima, show that P, Fe and Mn were significant at 1%, and K, Ca, Mg and Zn at 5%. At the same time, N and Cu were insignificant, and in plants, N, K, Ca, Mg, Fe, Cu, Mn, and Zn were found to be significant at 1%, whereas P was found to be insignificant. When the location x plant interaction

was examined, it was found that Mn values were important at 1%, while N, P, K, Ca, Mg, Fe, Cu and Zn values were insignificant (Table 3; Table 4).

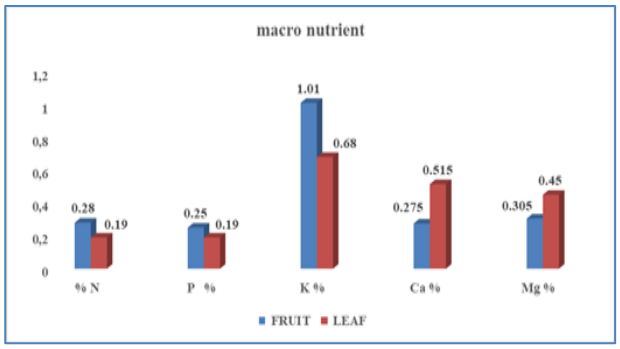

Figure 4. Average macronutrient content of *E. rhamnoides* and *R .spinosissima*

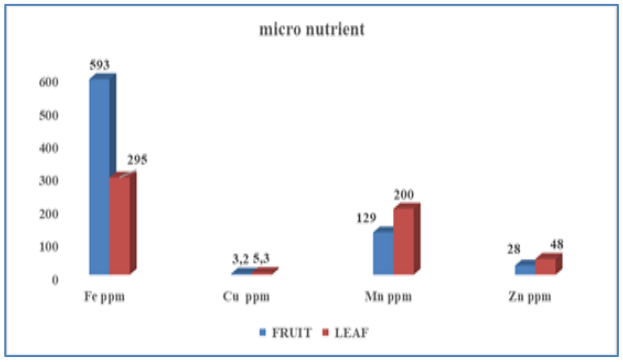

Figure 5. Average micronutrient content in *E. rhamnoides* and *R. spinosissima*

In the study, it was determined that Erzurum location gave better results, N (0.28%), P (0.25%), K (1.01%) and Fe (593 ppm) values were higher in fruits (Figure 4) and Ca (0.525%), Mg (0.465%), Cu (5.3 ppm), Mn (200 ppm), and Zn (45 ppm) nutrient contents in leaves (Figure 5). N, P, K are plant nutrients necessary for regular fruit formation and development and increase fruit quality among the plant nutrients. The researchers reported that the N% P% and K% contents differ in plants depending on the plant species, variety, age, and the plant sample taken [32]. In the study, nitrogen content in fruits and leaves was found to be between 0.33 and 0.13 the values (Figure 6). Nitrogen is the building block of protein and is the structural element of nucleic acid and chlorophyll molecule [20].

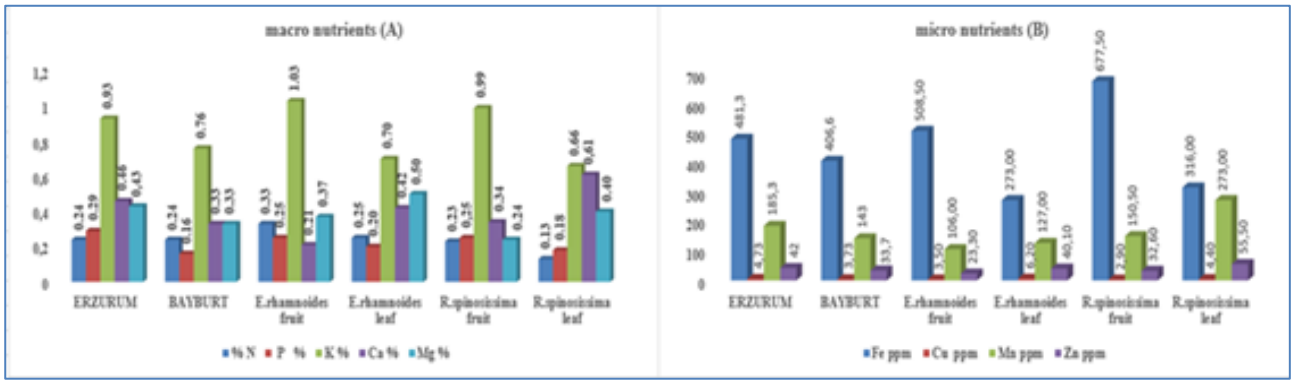

Figure 6. Plant macro and micronutrient contents

Table 3. Varyans analysis for fruit and leaf samples according to mean of square

	Sources of variation	N (%)	P (%)	K (%)	Ca (%)	Mg (%)	Fe (ppm)	Cu (ppm)	Mn (ppm)	Zn (ppm)
Fruit	Location	0.00282**	0.11801**	0.0867*	0.07207**	0.0192**	15123**	0.0075**	660.083*	74.5008**
	Error-1	2.415	3.3355	0.01002	0.00099	0.00025	200	0.000	33.3333	0.58333
	Species	0.02466**	7.5455	0.00333	0.06601**	0.04813**	85683**	0.9075**	5084.08**	63.0208**
	Location*Species	0.00034*	0.00021	0.08333*	0.00908*	0.02803**	4800**	0.0675**	2494.08**	81.6408**
	ERROR	0.0025	0.00006	0.010008	0.000992	0.000333	100.0	1.1214	33.33	0.5833
Leaf	Location	0.00175*	0.0075**	0.1121*	0.07521**	0.0675*	18723**	11.4075**	12545.3**	1793.41*
	Error-1	0.00011	0.0001	0.0011	0.00333	0.00727	0.0000	1.1225	44.3333	146.417
	Species	0.0426*	0.0027**	0.0027	0.10268**	0.08333**	5547**	10.2675**	62496.3**	323.441*
	Location*Species	0.0001	2.634	0.0027	7.555**	0.02083	3	1.6875**	8965.33**	532.001
	ERROR	0.0001	4.257	0.0027	0.0008	0.002933	200.00	0.00250	74.3	138.083

Table 4. Results of analysis properties of fruit and leaf samples

	Species	N (%)	P (%)	K (%)	Ca (%)	Mg (%)	Fe (ppm)	Cu (ppm)	Mn (ppm)	Zn (ppm)
Fruit	*Elaeagnus rhamnoides*	0.33 a	0.25	1.03	0.21 b	0.39 a	508.5 b	3.45 a	111.00 b	28.30 b
	Rosa spinosissima	0.23 b	0.24	0.99	0.35 a	0.27 b	677.5 a	2.90 b	152.16 a	32.33 a
	Mean	0.275	0.0245	1.01	0.28	0.33	5.93.00	3.17	131.58	30.50
	LSD $_{(0.05)}$	0.002**	-	-	0.018**	0.010**	5.773**	6.118**	3.333**	0.440**
	Location									
	Erzurum	0.30 a	0.35 a	1.10 a	0.36 a	0.37 a	628.50 a	3.20 a	139.00 a	28.10 b
	Bayburt	0.26 b	0.15 b	0.93 b	0.20 b	0.29 b	557.50 b	3.15 b	124.16 b	33.08 a
	Mean	0.28	0.25	1.01	0.28	0.33	593.00	3.17	131.58	30.50
	LSD $_{(0.05)}$	0.002**	0.003**	0.057*	0.018**	0.009**	8.164**	1.115**	3.333*	0.440**
	CV (%)	**16.66**	3.22	9.90	10.71	3.03	1.68	3.31	4.38	2.48
Leaf	*Plantago atrata*	0.25 a	0.21 a	0.71	0.43 b	0.55 a	273.00 b	6.20 a	127.00 b	40.06 b
	Rumex patientia	0.13 b	0.18 b	0.68	0.62 a	0.38 b	316.00 a	4.35 b	271.33 a	50.45 a
	Mean	0.19	0.195	0.69	0.525	0.465	294.5	5.27	199.16	45.25
	LSD $_{(0.05)}$	0.006*	3.779**	-	5.756**	0.031**	8.164**	0.028**	4.977**	6.78*
	Location									
	Erzurum	0.18 b	0.22 a	0.79 a	0.60 a	0.54 a	334.00 a	6.25 a	231.50 a	57.48 a
	Bayburt	0.20 a	0.17 b	0.60 b	0.45 b	0.39 b	255.00 b	4.30 b	166.83 b	33.03 b
	Mean	0.19	0.195	0.69	0.525	0.465	294.50	5.27	199.16	45.25
	LSD $_{(0.05)}$	0.006*	0.005**	0.018**	0.028**	0.049*	0.149**	0.251**	3.844**	
	CV (%)	5.26	3.26	7.24	3.77	10.86	4.80	0.19	4.32	2.85

Increasing soil pH affects phosphorus availability. Phosphorus is an ATP building element and energy component. It accelerates plant root development, growth and maturation, renews plant cells and increases resistance against diseases [20; 32]. Phosphorus and Calcium play a role in the formation of bones and teeth in the human body and fulfill important functions for the body by participating in the structure of sugar phosphates, nucleotides, phosphoproteins and phospholipids [33]. Phosphorus content is transferred from leaves to seed and fruit towards vegetative development and accumulates in these parts. Potassium provides plant root development, plant health and resistance. Potassium is a mineral substance that takes part in important metabolic and physiological events such as maintaining osmotic pressure in our body, ensuring acid-base balance, muscle functions and transmission of nerve impulses [34]. At the same time, the potassium content of the plant leaves is higher. However, the amount of potassium in phloem is relatively high. The potassium content of young leaves, meristematic tissues, and fleshy fruits, where phloem is transported more, is higher because the substances dissolved in the phloem sap are carried up and down in the plant [32]. For these reasons, one can assume that the N, P and K contents are relatively higher in the plants fruit parts. In our study, phosphorus ratios in fruit were found between 0.25%-0.25% and potassium ratios between 1.03%-0.99% (Figure 4). Phosphorus ratios were found between 0.18%-0.20% in the leaves, while potassium ratios were found as 0.66%-0.70% (Figure 6). A study conducted on cornelian cherry fruits stated that K and P contents were high [35]. Magnesium is effective in metabolic events such as photosynthetic energy storage, protein synthesis, nucleotide formation and hydrolysis of many organic compounds in plants [36]. During the growth period of the plants, the ratio of K, Ca and Mg is high and the plant nutrients in the plant are at the highest rate at the beginning of growth [37]. It was stated that the Mg limit values were between 0.15-1.00% [32]. In light of the data obtained from our study, in the fruit-leaf analysis of burnetrose and sea-buckthorn, it was determined that % Mg values were 0.50-0.40 in leaves and 0.37-0.24 in fruits (Figure 4; Figure 5). Zinc plays a vital role in the plant's development and taste, being an extraordinary micronutrient element and a trace element found in all enzyme classes, even in trace amounts [38]. In the study, it was determined that Cu and Mn values gave the highest value in E.rhamnoides (6.2 ppm) and R.spinosissima (273 ppm) in location x plant interaction (Figure 8, Figure 9). Studies have shown that rosehip is a very important food rich in vitamins and minerals, and contains macro and micro minerals [39; 40]. In addition, there are potassium, calcium, magnesium, iron and phosphorus minerals in the content of sea buckthorn.

According to the leaf analysis results in Plantago atrata and Rumex patientia, where leaf parts are used extensively, it was determined that while K, Fe, and Zn were essential at 1% in the locations, other elements were insignificant. In terms of plants, N, P, Fe, Mn, and Zn were significant at 1%, Cu at 5%, and non-significant K, Ca, and Mg. When the location x plant interaction was examined, it was found that Fe and Zn were found to be 1%, Mg 5% significant N, P, K, Ca, Cu, and Mn non-significant.

According to the study results, it was determined that the plant nutrients were between the limit values (Figure 6). It was determined that Erzurum location gives better results than Bayburt location. It was determined that N (0.34%), P (0.59%), K (1.44%), Ca (0.53%), Mg (0.45%), Cu (13 ppm) and Zn (33.4 ppm) mineral values highest were found in P.atrata, while Fe (1340 ppm) and Mn (82 ppm) values were highest in R.patientia (Figure 7; Figure 8). The high Fe content of R.patientia indicates that it can be recommended as a consumable food source in terms of eliminating Fe deficiency, which is common in the region. Iron is an indispensable mineral substance for life, used in electron transport, oxygen transport and storage, oxidative metabolism, cell growth and division, and catalysis of reactions essential for the body [41]. Iron is vital for the production of dry matter in the plant and is the main ingredient that makes up chlorophyll. It

is involved in photosynthesis and related enzymatic reactions occurring in chlorophylls, so the development of young parts of the plant and dry matter production are closely related to the amount of iron [42].

In a study conducted in Sivas, the macro and micronutrients of the leaf parts of the naturally grown evelik / labada plant were examined, the nutrients in the leaves were determined as 2.59% for N, 0.360 for P, 6.85% and 0.66% for K. % for Mg and 0.48% for Ca, 225.8 mg/kg for Fe, 27.5 mg/kg for Zn, 30.4 mg/kg for Mn and 8.9 mg/kg for Cu [43]. When the plant x location interaction was examined, it was found that Mg (0.48%), Fe ppm (895 ppm), and Zn ppm (365 ppm) values were high in P.atrata in Erzurum location, while % Mg (0.42%) and Fe ppm (1805 ppm) values were high in R.patientia. Zn ppm (302 ppm) value was high in P.atrata in the Bayburt location (Figure 7; Figure 8; Figure 9; Figure 10). Fe limit values were10-1000 [32] and Zn limit values were 2-240 ppm [20].

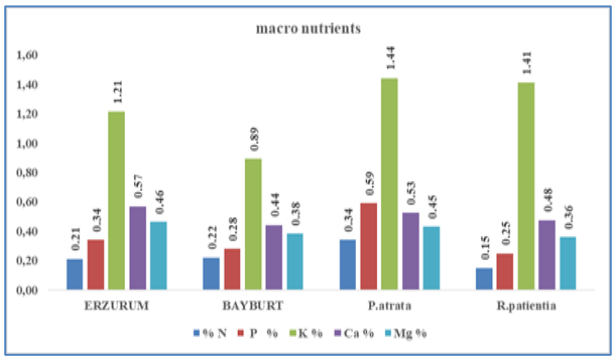

Figure 7. Macro nutrient content of leafy plants (*P. atrata* and R. *patientia*)

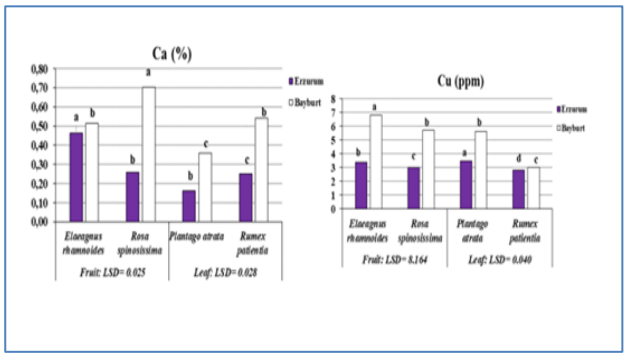

Figure 8. Interaction of location and species of fruit and leaf for Ca (%), Cu (ppm). Error bars indicate significant differences according to the LSD test at P≤0.05

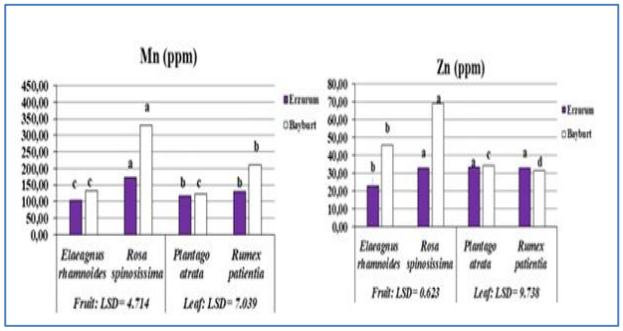

Figure 9. Interaction of location and species of fruit and leaf for Mn and Zn (ppm). Error bars indicate significant differences according to the LSD test at P≤0.05

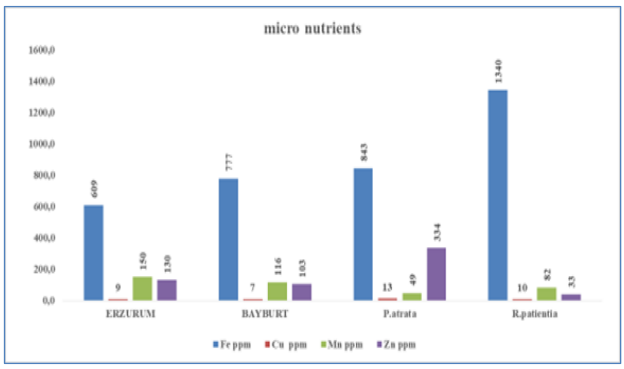

Figure 10. Micronutrient content of leafy plants (*P. atrata* and *R. patientia*)

Mg, Fe and Zn are nutritional elements effective in chlorophyll synthesis, plant water transmission, and leaf development, and their contents vary in the plant depending on the soil structure. In order to determine the mineral concentrations of Evelik/labada plants, 1.7% for N, 22.33 mg/100 g for P, 624 mg/100 g for K, 82.84 mg/100 g for Ca, in the study collected from natural areas in the Eastern Anatolia Region, It is stated that it is found as 36.47 mg/100 gr for Mg, 1.45 mg/100 gr for Na, 75.70 mg/100 gr for S [19]. Another study conducted with trees and shrubes in Nigeria stated that the Fe content was between 10.24 and 30.01 ppm [44]. In another study conducted on wild plants consumed as vegetables in the Aegean region, it was stated that the amounts of Fe and Zn were higher in plants in the wild form [45]. As a result of another study, it was stated by the researchers that the Zn amount was higher in spinach [46]. Ezeagu et al. [44], reported that the Zn content ranged from 9.9-67.2 ppm Cu content to between 6.6 and 20.7 ppm in a study conducted with trees and shrubs Mn content between 202-592 ppm. The results of our study show parallelism with other studies.

According to the data obtained in the study, it was determined that Erzurum soils had slightly acid, salt-free, clayey, organic matter content at good, the lime content of the soils were very low, phosphorus and potassium content was medium and sufficient and that Bayburt soils were slightly alkaline, salt-free, clayey, good in organic matter, high lime content, high phosphorus content and sufficient potassium content. It was determined that macro-micro plant nutrients are on the border in Erzurum and Bayburt locations, but Zn (P. atrata / leaf) in Erzurum location is higher than the limit value of Zn (*P. atrata* / leaf) and Fe (*R. patientia* / leaf) in Bayburt location (Figure 8; Figure 9).

3.3. Principal component analysis for species

Principle component analysis in properties of Elaeagnus rhamnoides and Rosa spinosissima explained that PC-1 and PC-2 the diagonal line between PC-1 and PC-2 separates this species in terms of some traits. PC1 and PC2 showed variation in levels that 58.13% and 31.05%, respectively (Figure 11). Toncer et al. [47], repoted that total variation of Lippia citriodora of content of leaves and flowers was 80.39%.

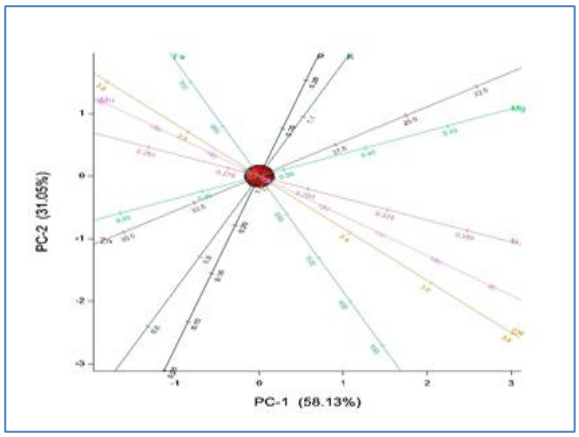

Figure 11. Principle component analysis for *E. rhamnoides* and *R. spinosissima*

The total variation in components was 89.18%. The diagonal indices form two groups; Group-1 had five indices: P, K, Mg, N and Cu. They formed narrow angles and were positively correlated each other. Group-2 included four indices: Ca, Fe, Mn and Zn. Ca, Fe and Mn formed narrow angles. These traits were negatively correlated with traits of other group (Figure 11). Principle component analysis in properties of Plantago atrata and Rumex patientia explained that PC-1 and PC-2 the diagonal line between PC-1 and PC-2 separates this species in terms of some traits. PC-1 and PC-2 showed variation in levels that 58.56% and 37.66%, respectively (Figure 12).

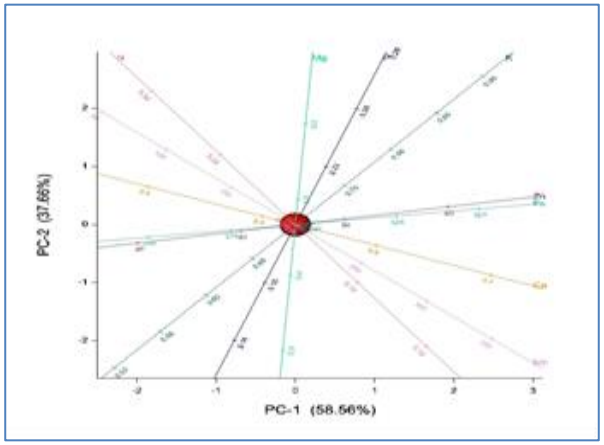

Figure 12. Principle component analysis for *P. atrata* and *R. patientia*

The total variation in components was 96.22%. The diagonal indices form two groups; Group-1 had eight indices: Mg, Cu, P, K, Zn, Fe, Ca and Mn. They formed narrow angles and were positively correlated each other. Group-2 included one indices (N). N value was negatively correlated with traits of other group (Figure 12). Principle component analysis are widely used to facilitate compare of traits among huge data populations [48]. Keefover Ring [49], stated that variation of component in aromatic plants was 91.00% (PC-1:79.1%, PC-2: 11.1%).

4. CONCLUSION

It was determined that the plant's mineral content leaves that the leaf parts valued higher than the fruit parts in terms of macro and micro plant nutrients. According to the results of the physicochemical analysis of the soil samples taken from the root depths of the plants (0-40 cm), the soils are generally mildly acid to slightly alkaline, unsalted, clayey to heavy clayey soils, medium to good organic matter, medium to high in lime content, very high in phosphorus and potassium was found to be high and sufficient.

Acknowledgement

Support was received from Karabük University Forest Engineering Department of Botany for the identification of plant species. Soil analyzes were carried out at the Erzincan Horticultural Research Institute, and plant analyzes were carried out at the East Anatolian High Tecnology Application and Research Center.

REFERENCES

[1] Genckan MS. Meadow-Pasture examination on Turkey's vegetation zones as the source of flora. Ege University Faculty of Agriculture Journal. 1984;21:231-260.

[2] Gumus I. A research on the floristic structure of Eleşkirt (Ağrı) plain grain fields and its surroundings. Atatürk University Faculty of Agriculture Journal. 1993;24 (1):14-31.

[3] Murthy, HN, Georgiev MI, Park SY, Dandin VS, Paek KY. The safety assessment of food ingredients derived from plant cell, tissue and organ cultures: a review. Food Chemistry 2015;176:426-432.

[4] Grigoriadou K, Krigas N, Maloupa E. Sustainable use of mediterranean medicinal-aromatic plants. Academic Press; 2020.

[5] Yıldız N. Principles of plant nutrition and symptoms of nutritional disorders in plants. Turkey: Eser Ofset Printing; 2012.

[6] Bower CA, Wilcox LV. Soluble Salts Black CA (Ed) Methods of Soil Analysis. 2nd ed. Medisenwisconsin, USA; 1965.

[7] Mc Lean EO. Soil pH and lime requirement. methods of soil analysis part 2. chemical and microbiological properties second edition. Agronomy 1982;9(2):199-224.

[8] Walkey A. Critical examination of a rapid method for determining organic carbon in soils. Soil Sciences. 1946;63:251-263.

[9] Nelson RE. Carbonate and gypsum. In: Methods of soil analysis, Part 2. Chemical and microbiological properties. Madison Wisconsin: Soil Sci Soc of Amer Inc; 1982.

[10] Richards LA. Diagnosis and ımprovement saline and alcaline soil. 3ed. US Dep. Agr. Handbook; 1954.

[11] Olsen SR, Cole CV, Watanable FS, Dean LA. Estimation of Available Phosphorus in Soils by Extraction with Sodium. Washington DC: US Government Printing Office; 1954.

[12] Kacar B, Inal A. Plant Analysis. 3rd Edition. Istanbul, Turkey: Nobel Publishing; 2008.

[13] AOAC. Official methods of analysis of the association of official analytical chemists. The Association, Arlington, VA, Washington, DC; 1990.
[14] Genstat. Genstat for windows introduction. VSN International, Hemel Hempstead. 2009.
[15] Ergene, A. Fundamentals of Soil Science. Erzurum/Türkiye: Ataturk Univ. 1987.
[16] Kadioglu B, Kadioglu S. Erzurum's wıld rose (Rose sp.). 4th.International Symposium of Medicinal and Aromatic Plants, 2-4 October, 2018 Çeşme-İzmir/Türkiye.
[17] Kadioglu B, Kadioglu S, Tasgin G. Evaluation of medicinal and aromatic plant consumption in Erzurum province according to the seasons. Journal of Muş Alparslan Unniversity Agricultural Productıon and Technologies. 2021a;1(1):73-83.
[18] Yıldız N. Deficiency and toxicity symptoms of plant nutrients. Turkey: Eser Ofset Printing; 2004.
[19] Kadioglu B, Kadioglu S, Tasgin G. Determination of the habits of medicinal and aromatic plant consumers in Erzurum province. Bahçe. 2021;50(1):7-15.
[20] Yıldız N. Fundamentals of plant nutrition and symptoms of nutritional disorder in plants. Turkey: Eser Ofset Printing; 2008.
[21] Dizdaroglu T, Onal. M. Some extreme range traits of Hippophae rhomnoid L. III. International Non-Wood Forest Products Symposium, 2014. 8-10 May, 2014. Kahramanmaraş.
[22] Ramesh T, Bolan NS, Kirkham MB, Wijesekara H, Kanchikerimath M, Rao CS. et al. Soil organic carbon dynamics: Impact of land use changes and management practices: A review. Advances in Agronomy. 2019;156:1-107.
[23] Schmidt MW, Torn MS, Abiven S, Dittmar T, Guggenberger G, Janssens IA, Trumbore S. E. Persistence of soil organic matter as an ecosystem property. Nature. 2011;478(7367):49-56.
[24] Shaikh MN, Mokat DN. Role of rhizosphere fungi associated with commercially explored medicinal and aromatic plants: a review. Curr Agr Res J. 2018;6 (1):72-77.
[25] Kushwaha A, Hans N, Giri BS, Rene ER, Rani R. Uncovering the phytochemicals of root exudates and extracts of lead (Pb) tolerant Chrysopogon zizanioides (L.) Roberty in response to lead contamination and their effect on the chemotactic behavior of rhizospheric bacteria. Environmental Science and Pollution Research. 2022;29(29):44998-45012.
[26] Lambers, H, Chapin FS, Pons TL, Lambers H, Chapin FS, Pons TL. Ecosystem and global processes: ecophysiological controls. Plant Physiological Ecology. 2008;18:555-571.
[27] Moghaddam M, Farhadi N. Influence of environmental and genetic factors on resin yield, essential oil content and chemical composition of Ferula assa-foetida L. populations. Journal of Applied Research on Medicinal and Aromatic Plants. 2015;2(3):69-76.
[28] Figueiredo AC, Barroso JG, Pedro LG, Scheffer JJC. Physiological aspects of essential oil production. Essential oils: Basic and applied research. 1997;95-107. DOI: 10.1016/j.foodchem.2006.06.049.
[29] Curado P, Malafronte R, Duarte AMRC, Kirchgatter K, Branquinho MS, Galati EAB. Malaria epidemiology in low-endemicity areas of the atlantic forest in the vale do ribeira, são paulo, brazilacta tropica. 2006;100(1–2):54-62.
[30] Xie Y, Huang Q, Yang F, Lei C. Chemical variation in essential oil of Cryptomeria fortunei from various areas of China. Industrial Crops and Products. 2012;36(1):308-312.
[31] [Kacar B, Katkat AV. Plant nutrition. 5th Edition. Ankara, Turkey: Nobel Publishing; 2010.
[32] Otle S, Ozdestan Ocak O, Nakilcioğlu TA, Kartal E, Ozyurt VH. Food Chemistry. Izmir: Ege University Press; 2016.
[33] Gozlekcı S, Esrıngu A, Ercıslı S, Eyduran SP, Akın M, Bozovıc D, Negreanu-Pırjo T, et al. Mıneral content of cornelıan cherry (Cornus mas L.) fruıts. Oxidation Communications 2017;1(I):301–308.
[34] Nakilcioğlu TA. Omer Halisdemir University Journal of Engineering Sciences. 2019;8(2): 863-874.
[35] Jezek M, Geilfus CM, Bayer A, Mühling KH. Photosynthetic capacity, nutrient status, and growth of maize (Zea mays L.) upon mgso4 leaf-application. Front. Plant Sci. 2014;5;781.
[36] Mayland HF. Factors affecting yield and nutritional quality of crestedwheat-grass. In: Johnson, K. L. (Ed.), Crested Wheatgrass its Values, Problem sand Myths: Symposium Proceedings. Utah State University, Logan. 1986. P. 215-216.
[37] Broadley MR, White PJ, Hammond JP, Zelko I, Lux A. Zinc in plants. New Phytologist. 2007;173(4):677–702.
[38] Çınar İ, Çolakoğlu AS. Potential health benefits of rose hip products. Proceedings of the First International Rose Hip Conference, Acta Hort. 2005; 253-257. Doi: 10.17660/ActaHortic.2005.690.39.
[39] Dogan A, Kazankaya A. Fruit properties of rose hip species grown in Lake Van Basin (Eastern Anatolia Region). Asian Journal of Plant Sciences. 2006;5(1):120-122. DOI: 10.3923/ajps.2006.120.122.
[40] Yerlikaya H, Toker A. Obesity and trace elements. Dialogue in Endocrinology. 2012;9 (2):64-70.
[41] Kaya C, Higgs D. Improvements in the physiological and nutritional developments of tomato cultivars grown at high zinc by foliar application of phosphorus and iron. Journal of Plant Nutrition. 2002;25(9):1881-1894.
[42] Dastan T, Sarac. H. Determination of the nutritional element concentrations of Evelik plant (Rumex crispus L.). Cumhuriyet Science Journal. 2018;39(4):1020-1024. DOI: 10.17776/csj.455688.
[43] Turan M, Kordali S, Zengin H, Dursun A, Sezen Y. Macro and micro mineral content of some wild edible leaves consumed in eastern Anatolia. Acta

Agriculture. Scandinavica, Sec. B- Plant Soil Science. 2003;53(3):129-137.

[44] [Ezeagu IE, Akinsoyinu AO, and Tarawali G. Nutritional factors in some fodder legume treess and shrubs. Nigerian Journal Animal Science. 2013; 15:191-198.

[45] Kaya I, Incekara N, Nemli Y. Ingreddients of same weeds consumed as food Aegean Region. Van Yüzüncü Yıl University Faculty of Agriculture Journal of Agricultural Sciences. 2007;14(1):1-6.

[46] Holland ID, Unwin DH, Buss A. Fruit and nuts the composition of foods the royal society of chemistry and ministry of agriculture. Fisheries and Food. 1992;2 (5):21-29.

[47] Toncer O, Karaman S, Kamci G, Erdem E. Yield and essential oil composition of lippia citriodora hbk leaves and flowers in semi-arid conditions. Journal of Essential Oil Bearing Plants. 2022;25(1):9-19.

[48] Stashenko EE, Martínez JR, Ruíz CA, Arias G, Durán C, Salgar W. et al. Lippia origanoides chemotype differentiation based on essential oil GC-MS and principal component analysis. Journal of Separation Science. 2010;33(1):93-103.

[49] Keefover-Ring K. The chemical biogeography of a widespread aromatic plant species shows both spatial and temporal variation. Ecology and Evolution. 2022;12(9):14-19.

Volume 14, Issue 2, Page 92-102, 2025 https://doi.org/10.46810/tdfd.1441189 Research Article

BİNGÖL UNIVERSITY

Türk Doğa ve Fen Dergisi
Turkish Journal of Nature and Science
www.dergipark.gov.tr/tdfd

Engineering Geology and Bearing Capacity Calculation of Soil in Karacadağ Region

Mehmet Hayrullah AKYILDIZ[1*], Mahmut EKİNCİ[1]

[1] University of Dicle, Department of Civil Engineering, Diyarbakır, Türkiye
Mehmet Hayrullah Akyıldız ORCID No: 0000-0001-7239-3518
Mahmut Ekinci ORCID No: 0009-0001-5670-5590

**Corresponding author: hayrullah.akyildiz@dicle.edu.tr*

(Received: 22.02.2025, Accepted: 17.04.2025, Online Publication: 27.06.2025)

Keywords
Karacadağ, Rock soil, Engineering geology, Ultimate bearing capacity, Plaxis

Abstract: Geotechnical investigations are highly essential for optimal planning of quality, time, and cost management in engineering structures. Geotechnical analysis is used to determine the physical and chemical properties of soils by performing laboratory and field tests. This study examines the geotechnical engineering of the Karacadag region in the Southeast Anatolia region of Turkey by analyzing soil data from the study area in Diyarbakır city, Sur County, Yukarıkılıctası district and block no 7018, parcel 1. The aim is to obtain general information about the soil in this area and to produce faster and more practical solutions in terms of quality and economic aspects in construc-tion projects. Drilling was performed in the field using UD and SPT tubes, and various laboratory tests such as sieve analysis and Atterberg limits were conducted on the samples taken. Using the parameters obtained from these tests, the bearing capacity of the basalt-rock soil related to the Karacadag Volcanism was calculated using the Turkish Building Earthquake Regulation (TBDY) and Plaxis 2D geotechnical modeling program. The bearing capacity calculation was performed using different methods, and the results were compared and evaluated in terms of safety and the effect of the parameters considered in the calculation.

Karacadağ Bölgesi Zemininin Mühendislik Jeolojisi ve Taşıma Gücü Hesabı

Anahtar Kelimeler
Karacadağ, Kaya zemini, Mühendislik jeolojisi Nihai taşıma kapasitesi, Plaksis

Öz: Mühendislik yapılarında kalite, zaman ve maliyet yönetiminin optimum şekilde planlanması için jeoteknik araştırmalar son derece önemlidir. Geoteknik analiz, laboratuvar ve arazi testleri yapılarak zeminlerin fiziksel ve kimyasal özelliklerinin belirlenmesi amacıyla kullanılmaktadır. Bu çalışma, Türkiye'nin Güneydoğu Anadolu bölgesindeki Karacadağ bölgesinin geoteknik mühendisliğini, Diyarbakır ili, Sur ilçesi, Yukarıkılıçtası semti ve 7018 ada, 1 parseldeki çalışma alanından elde edilen toprak verilerini analiz ederek incelemektedir. bu alandaki toprakların işlenmesi ve inşaat projelerinde kalite ve ekonomik açıdan daha hızlı ve pratik çözümler üretmektir. UD ve SPT tüpleri kullanılarak sahada sondaj yapılmış, alınan numuneler üzerinde elek analizi, Atterberg limitleri gibi çeşitli laboratuvar testleri yapılmıştır. Bu testlerden elde edilen parametreler kullanılarak Karacadağ Volkanizmasına ilişkin bazalt-kaya zeminin taşıma kapasitesi Türkiye Bina Deprem Yönetmeliği (TBDY) ve Plaxis 2D jeoteknik modelleme programı kullanılarak hesaplanmıştır. Taşıma kapasitesi hesaplaması farklı yöntemler kullanılarak yapılmış olup, sonuçlar güvenlik ve hesaplamada dikkate alınan parametrelerin etkisi açısından karşılaştırılarak değerlendirilmiştir.

1. INTRODUCTION

The construction industry, which is rapidly evolving today, emphasizes creating more durable and environmentally friendly structures from an engineering perspective. In this process, understanding the physical and mechanical properties of the soil—the load-bearing foundation of any structure—is crucial. Geotechnical investigations are vital for determining these properties, as they reveal the engineering geology and mechanical characteristics of the soil using various analytical methods. These analyses yield critical parameters such as the soil's bearing capacity, which significantly influences

the durability and stability of structures (Chen et al., 2023a; Amin Soltanianfard et al., 2023).

Bearing capacity is a fundamental parameter in structural design, determining the soil's ability to support loads without failure. Various theoretical models and empirical methods, such as Terzaghi (1943), Meyerhof (1951), Hansen (1970), and Vesic (1973), are applied to calculate the bearing capacity from field and laboratory test data (Zhao et al., 2023). Recent advancements, such as semi-analytical methods incorporating three-dimensional strength factors, provide enhanced accuracy for complex geological settings (Chen et al., 2023a). Additionally, modern machine learning techniques have emerged as efficient tools for predicting end-bearing capacity, offering alternatives to traditional methods (Chen et al., 2023b).

Research conducted on the Dicle University campus and its surroundings focused on the Karacadağ Basalt formations, examining the lithological sequence and dominant lithology types in the area. Soil samples underwent sieve analysis and Atterberg limit tests to classify them according to the Unified Soil Classification System. High-plasticity clays (CH) with significant swelling properties were identified, which can affect volume stability (Xu et al., 2023). Experimental studies on basalt samples from the Diyarbakır region characterized their mechanical properties, such as uniaxial compressive strength and Young's modulus, revealing correlations essential for predicting the behavior of basalt as a construction material (Zhao et al., 2023).

Geotechnical investigations extend to addressing challenges such as soil swelling, which can lead to material loss and structural instability. For instance, swelling soils in the Diyarbakır region have been studied, revealing significant issues due to clay mineral expansion (Xu et al., 2023). Advanced field and laboratory techniques, including pressuremeter and seismic tests, have refined bearing capacity estimates, enabling safer structural designs (Chen et al., 2023a).

The seismicity of the Diyarbakır region has been highlighted, emphasizing the influence of fault lines and historical earthquake data on soil properties. The fault lines passing through the Diyarbakır province and plate tectonics have been specified. Studies have also examined the geotechnical characteristics of pumice soils in the Nevşehir region, noting similarities to sandy soils and applying Standard Penetration Tests (SPT) to evaluate bearing capacity (Xu et al., 2023). Additionally, swelling and shrinkage issues caused by high-plasticity clays were discussed, highlighting challenges in maintaining volume stability.

In conclusion, advancements in geotechnical engineering, including modern computational techniques and experimental studies, continue to refine our understanding of soil mechanics. These developments not only ensure safer and more sustainable structural designs but also expand the applications of geotechnical principles to diverse geological contexts.

1.1. Investigation Area

Diyarbakır is situated on the eastern edge of a vast basalt plateau that stretches between Karacadağ, an extinct volcano located 100 meters above the Diyarbakır Valley, and the Dicle River. The city is renowned for its ancient walls, mosques, churches, temples, caravanserais, baths, fountains, houses, and palaces. With a history dating back over 5,000 years, Diyarbakır began to expand beyond its historical walls in the 1950s. One of the reasons basalt stone is prevalent in the construction of many buildings in the city is due to its location on an extinct volcanic terrain (Karakaya et al., 2022; Çetin & Acar, 2023).

The Eastern Anatolian Fault, which connects to the North Anatolian Fault and runs through the regions of Hatay, Kahramanmaraş, Malatya, and Bingöl, is the primary fault system responsible for land movements in Diyarbakır (Çetin & Acar, 2023; Kaya et al., 2021). The city lies approximately 90 km away from the East Anatolian Fault, within a second-degree earthquake zone, and is also about 60 km from the Bitlis Zagros Fault. This places Diyarbakır in a geologically active area, where the interaction between the East Anatolian Fault and the Arabian Plate significantly influences seismic activity (Aksu & Yılmaz, 2021). The North Anatolian Fault - Eurasian Plate form a boundary, is shown in Figure 1.

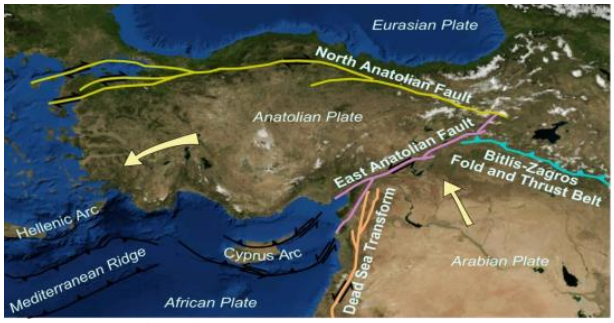

Figure 1. Anatolion Plate

Geological maps obtained through geological research allow us to learn about the age of rocks and soil, as well as the rocks found in the depths of the underground. Geological maps made at different scales reveal important regional characteristics, various geological time periods' paleogeography, and geodynamic events (MTA).

The Karacadag region is an area with significant potential for soil engineering. The geological and topographical features of the region should be taken into consideration when engineers design and implement construction projects.

Karacadag is a region shaped under the influence of volcanic activity. The rock structure is generally composed of volcanic origin materials such as basalt, andesite and tuff. These volcanic rocks have mountainous areas shaped by erosion and other natural effects over time.

The study area is located in Diyarbakir City, Sur County, Yukarıkılıctası District, block no. 7018, parcel 1. Neighboring cities; Elazig, Mus, Mardin, Adiyaman,

Malatya, Bingol, Batman, Sanliurfa. Counties; It has counties: Cermik, Cungus, Egil, Hani, Kocakoy, Lice, Silvan, Bismil, Cinar, Dicle, Ergani, Hazro, Kulp. It is located in the north of Mesopotamia. Surrounded by the cities of Elazig, Mus, Mardin, Adıyaman, Malatya, Bingol, Batman and Sanliurfa, Diyarbakir has all the characteristics of the region (Figure 2).

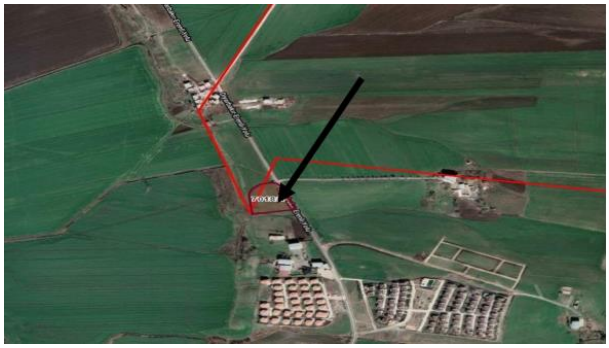

Figure 2. Site location map of investigation area

2. MATERIAL AND METHOD

2.1. Turkey Building Earthquake Regulation (TBDY) Bearing Capacity in Basic Design

The Turkish Building Earthquake Regulation (TBDY) is a technical regulation prepared to ensure that buildings in Turkey are constructed in an earthquake-resistant manner and thus reduce the risk of earthquakes. This regulation contains guidelines that ensure that the bearing capacity calculations of buildings are made according to certain criteria. The bearing capacity of the structure is calculated based on the results of the analysis. The bearing capacity calculation is made to determine the bearing capacity of the structure, and how it can behave under specified loads without exceeding the damage limit.

In the design of shallow and deep foundations, the design bearing capacity of the foundation soil will be evaluated according to the following equation in the design against failure:.

$$Et\ Rt \quad (1)$$

Where Et: Design effects related to loading conditions including static and seismic and Rt: Representing the design strength against deformation mechanism.
The vertical bearing capacity of the foundation base will meet the design axial force and bending moment. Design strength; in the design strength calculation, the characteristic strength is divided by the strength factor is taken as at least 1.4 in the calculation according to Table 1.

$$Rt = Rk/yRy \quad (2)$$

where Rt: Design strength related to loading conditions including static and seismic Rk: Characteristic strength and ɣRv: Strength factor.

Table 1. Strength Factor for Shallow Foundations

Strength Type	Strength factor Symbol	Strength factor Value
Foundation Bearing Capacity	ɣRv	1.4

Bearing Capacity of Shallow Foundations;

when loading conditions including static and seismic effects are taken into account, the following equation will be considered as:

$$q_o \leq q_t \quad (3)$$

q_o: Vertical load, shear and moment effects that cause foundation base pressure at the foundation level.
q_t: found by dividing the characteristic strength by the strength factor:

$$q_t = q_k / \gamma_{RV} \quad (4)$$

Foundation bearing capacity characteristic strength will be found from the following equation.

$$q_k = c.N_c.s_c.d_c.i_c.g_c.b_c + q.N_q.s_q.d_q.i_q.g_q.b_q + 0.5\gamma.B'.N\gamma.s\gamma.d\gamma.i\gamma.g\gamma.b\gamma \quad (5)$$

$$N_q = e^{\pi tan\varphi'} \tan^2(45+ \varphi'/2);\ N_c = (N_q - 1)\cot \varphi';\ N\gamma = 2(N_q - 1)\tan \varphi' \quad (6)$$

Where;

Nq, Nc, Nɣ : Bearing capacity factors
sc, sq, sɣ : Shape factors
dc, dq, dɣ : Depth factors
ic, iq, iɣ : inclination factor
gc, gq, gɣ : Ground Factors (Base on slop
bc, bq, bɣ : base factors (tilted base)

2.2. Plaxis Soil Modelling

Plaxis is a geotechnical engineering simulation software that can perform deformation analysis of soil and rock. The program can model finite element analysis, limit equilibrium, dynamics, transient groundwater flow and thermal applications with its different version. With Plaxis, soil structures can be designed, construction-excavation, topography, borehole and piezometer, and field applications can be visualized and optimized using geotechnical data. The necessary parameters are taken into account when modeling, and consolidation and safety analysis calculations are performed (Figure 3).

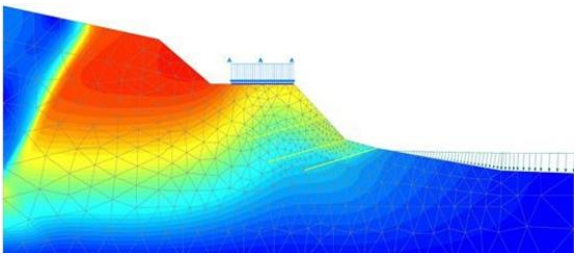

Figure 3. Example of Plaxis Modeling

2.3. Available Soil Data

2.3.1. Boring datas

A soil investigation was conducted by drilling 14 boreholes, each 20 meters deep and 280 meters in total. Standard Penetration Test (SPT) was conducted at 1.5 meter intervals to determine the consistency of the soil layers (Table 2).

Table 2. Coordinate and Depth Data in Boring

Boring No	Depth(m)	Grade(m)	Coordinate X	Coordinate Y
SK1	20	611	37.968542°	40.262508°
SK2	20	611	37.968734°	40.262395°
SK3	20	612	37.968891°	40.262289°
SK4	20	614	37.969075°	40.262207°
SK5	20	616	37.969249°	40.262115°
SK6	20	614	37.969192°	40.261835°
SK7	20	612	37.969023°	40.261899°
SK8	20	611	37.968835°	40.261972°
SK9	20	610	37.968656°	40.262020°
SK10	20	608	37.968479°	40.262058°
SK11	20	606	37.968454°	40.261755°
SK12	20	608	37.968634°	40.261716°
SK13	20	610	37.968835°	40.261694°
SK14	20	611	37.969016°	40.261660°

The dominant lithological units observed in the current site are a dark brown to red clay unit in the upper layers and as the depth increases, a sandy unit belonging to the Selmo Formation is observed.

2.3.2. Standard Penetration Tests (SPT)

SPT (Standard Penetration Test) is a geotechnical engineering test used to determine the strength and bearing capacity of soil. This test is performed to evaluate the resistance and compressibility of the soil. The SPT test is particularly used for estimating the bearing capacity of soil and for the design of building foundations.

On the current site, Standard Penetration Test (SPT) was conducted every 60 meters to determine the consistency or density of fine- and coarse-grained soils. The SPT test is conducted by driving a standard 2-inch diameter and 1 3/8-inch inside diameter sampler into the soil, by a 63.5 kg hammer falling freely from 76 cm height, for a total of 45 cm, in three equal 15 cm increments. The number of blows required to advance the sampler 15 cm is recorded as N-value. The first 15 cm of penetration is considered as the seating level and the last two 15 cm of penetration is combined and recorded as soil penetration strength (N-value).

The following table, which shows the empirical relationship between SPT-N and qu (one-axis pressure result in soils), has been used to classify the consistency class of cohesive soils.

According to Terzaghi and Peck (1948), the consistency of fine-grained soils was determined as very stiff and hard from Table 3.

Table 3. Standard Penetration Test (SPT) Boring Data

Boring No	SPT Depth(m)	15 cm	30 cm	45 cm	$SPTN_{30}$	Consistency	Lithology
SK1	1.50-1.95	10	7	8	15	Very stiff	
	3.00-3.45	11	8	9	17	Very stiff	
	4.50-4.95	12	12	13	25	Very stiff	
	6.00-6.45	13	13	14	27	Very stiff	
	7.50-7.95	14	15	15	30	Very stiff	
	9.00-9.45	14	15	16	31	Hard	
	10.50-10.95	16	17	18	35	Hard	
	12.00-12.45	17	18	20	38	Hard	
	13.50-13.95	20	21	21	42	Hard	
	15.00-15.45	20	21	22	43	Hard	
	16.50-16.95	21	22	22	44	Hard	
	18.00-18.45	22	23	22	45	Hard	
	19.50-19.95	22	24	24	48	Hard	
SK2	1.50-1.95	9	10	11	21	Very stiff	Dark brown reddish clay/gravelly sand
	3.00-3.45	7	8	15	23	Very stiff	
	4.50-4.95	10	12	12	24	Very stiff	
	6.00-6.45	11	13	15	28	Very stiff	
	7.50-7.95	8	14	16	30	Very stiff	
	9.00-9.45	9	16	17	33	Hard	
	10.50-10.95	10	15	19	34	Hard	
	12.00-12.45	9	15	22	37	Hard	
	13.50-13.95	11	18	21	39	Hard	
	15.00-15.45	12	20	20	40	Hard	
	16.50-16.95	12	21	22	43	Hard	
	18.00-18.45	15	23	24	47	Hard	
	19.50-19.95	15	25	24	49	Hard	

SK3	1.50-1.95	7	8	10	18	Very stiff	Dark brown reddish clay/gravelly sand
	3.00-3.45	8	9	10	19	Very stiff	
	4.50-4.95	9	11	12	23	Very stiff	
	6.00-6.45	11	13	14	27	Very stiff	
	7.50-7.95	13	15	19	34	Hard	
	9.00-9.45	15	17	19	36	Hard	
	10.50-10.95	16	18	20	38	Hard	
	12.00-12.45	17	19	20	39	Hard	
	13.50-13.95	20	21	21	42	Hard	
	15.00-15.45	20	21	22	43	Hard	
	16.50-16.95	21	22	23	45	Hard	
	18.00-18.45	22	23	24	47	Hard	
	19.50-19.95	23	24	24	48	Hard	
SK4	1.50-1.95	7	8	15	23	Very stiff	Dark brown reddish clay/gravelly sand
	3.00-3.45	10	12	12	24	Very stiff	
	4.50-4.95	12	12	13	25	Very stiff	
	6.00-6.45	13	14	14	28	Very stiff	
	7.50-7.95	14	15	16	31	Hard	
	9.00-9.45	15	16	17	33	Hard	
	10.50-10.95	16	18	18	36	Hard	
	12.00-12.45	18	18	19	37	Hard	
	13.50-13.95	20	21	21	42	Hard	
	15.00-15.45	20	21	22	43	Hard	
	16.50-16.95	21	22	22	44	Hard	
	18.00-18.45	22	23	22	45	Hard	
	19.50-19.95	22	24	24	48	Hard	
SK5	1.50-1.95	7	8	9	17	Very stiff	Dark brown reddish clay/gravelly sand
	3.00-3.45	8	10	12	22	Very stiff	
	4.50-4.95	9	12	14	26	Very stiff	
	6.00-6.45	9	12	15	27	Very stiff	
	7.50-7.95	11	13	15	28	Very stiff	
	9.00-9.45	12	15	15	30	Very stiff	
	10.50-10.95	14	16	17	33	Hard	
	12.00-12.45	17	18	19	37	Hard	
	13.50-13.95	19	20	21	41	Hard	
	15.00-15.45	18	20	22	42	Hard	
	16.50-16.95	20	22	23	45	Hard	
	18.00-18.45	20	23	25	48	Hard	
	19.50-19.95	22	25	25	50	Hard	
SK6	1.50-1.95	9	10	11	21	Very stiff	Dark brown reddish clay/gravelly sand
	3.00-3.45	7	8	15	23	Very stiff	
	4.50-4.95	10	12	12	24	Very stiff	
	6.00-6.45	10	12	13	25	Very stiff	
	7.50-7.95	13	15	15	30	Very stiff	
	9.00-9.45	14	16	18	34	Hard	
	10.50-10.95	15	19	17	36	Hard	
	12.00-12.45	148	17	18	35	Hard	
	13.50-13.95	15	20	20	40	Hard	
	15.00-15.45	19	19	20	39	Hard	
	16.50-16.95	20	21	20	41	Hard	
	18.00-18.45	23	19	25	44	Hard	
	19.50-19.95	24	23	25	48	Hard	
SK7	1.50-1.95	10	12	14	26	Very stiff	Dark brown reddish clay/gravelly sand
	3.00-3.45	12	13	14	27	Very stiff	
	4.50-4.95	13	15	14	29	Very stiff	

	6.00-6.45	15	14	16	30	Very stiff	
	7.50-7.95	17	18	18	36	Hard	
	9.00-9.45	19	20	21	41	Hard	
	10.50-10.95	20	22	26	48	Hard	
	12.00-12.45	15	17	18	35	Hard	
	13.50-13.95	16	17	23	40	Hard	
	15.00-15.45	17	20	22	42	Hard	
	16.50-16.95	20	20	21	41	Hard	
	18.00-18.45	20	21	22	43	Hard	
	19.50-19.95	21	22	23	45	Hard	
SK8	1.50-1.95	10	12	13	25	Very stiff	Dark brown reddish clay/gravelly sand
	3.00-3.45	13	15	15	30	Very stiff	
	4.50-4.95	14	16	18	34	Hard	
	6.00-6.45	15	19	17	36	Hard	
	7.50-7.95	18	17	18	35	Hard	
	9.00-9.45	15	20	20	40	Hard	
	10.50-10.95	19	19	20	39	Hard	
	12.00-12.45	20	21	20	41	Hard	
	13.50-13.95	23	19	25	44	Hard	
	15.00-15.45	20	20	26	46	Hard	
	16.50-16.95	19	21	25	46	Hard	
	18.00-18.45	18	22	26	48	Hard	
	19.50-19.95	20	25	24	49	Hard	
SK9	1.50-1.95	8	9	10	19	Very stiff	Dark brown reddish clay/gravelly sand
	3.00-3.45	10	11	12	23	Very stiff	
	4.50-4.95	12	12	12	24	Very stiff	
	6.00-6.45	11	13	12	25	Very stiff	
	7.50-7.95	10	12	13	25	Very stiff	
	9.00-9.45	12	13	15	28	Very stiff	
	10.50-10.95	13	15	16	31	Hard	
	12.00-12.45	15	16	17	33	Hard	
	13.50-13.95	18	19	20	39	Hard	
	15.00-15.45	20	21	23	44	Hard	
	16.50-16.95	20	23	23	46	Hard	
	18.00-18.45	22	24	24	48	Hard	
	19.50-19.95	23	24	26	50	Hard	
SK10	1.50-1.95	9	10	11	21	Very stiff	Dark brown reddish clay/gravelly sand
	3.00-3.45	7	8	15	23	Very stiff	
	4.50-4.95	10	12	12	24	Very stiff	
	6.00-6.45	10	12	13	25	Very stiff	
	7.50-7.95	12	13	13	26	Very stiff	
	9.00-9.45	11	13	15	28	Very stiff	
	10.50-10.95	12	14	16	30	Very stiff	
	12.00-12.45	13	15	16	31	Hard	
	13.50-13.95	15	16	16	32	Hard	
	15.00-15.45	18	19	20	39	Hard	
	16.50-16.95	21	22	22	44	Hard	
	18.00-18.45	23	24	25	49	Hard	
	19.50-19.95	24	25	25	50	Hard	
SK11	1.50-1.95	9	10	11	21	Very stiff	Dark brown reddish clay/gravelly sand
	3.00-3.45	7	8	15	23	Very stiff	
	4.50-4.95	10	12	12	24	Very stiff	
	6.00-6.45	12	12	13	25	Very stiff	
	7.50-7.95	12	12	13	25	Very stiff	
	9.00-9.45	11	11	12	23	Very stiff	
	10.50-10.95	14	15	15	30	Very stiff	
	12.00-12.45	18	18	20	38	Hard	

	13.50-13.95	20	22	23	45	Hard	
	15.00-15.45	22	23	24	47	Hard	
	16.50-16.95	23	24	24	48	Hard	
	18.00-18.45	22	24	25	49	Hard	
	19.50-19.95	20	25	25	50	Hard	
SK12	1.50-1.95	8	9	10	19	Very stiff	Dark brown reddish clay/gravelly sand
	3.00-3.45	10	11	12	23	Very stiff	
	4.50-4.95	10	12	12	24	Very stiff	
	6.00-6.45	12	14	12	26	Very stiff	
	7.50-7.95	11	13	15	28	Very stiff	
	9.00-9.45	12	15	15	30	Very stiff	
	10.50-10.95	14	15	17	32	Hard	
	12.00-12.45	15	16	17	33	Hard	
	13.50-13.95	18	19	20	39	Hard	
	15.00-15.45	18	19	22	41	Hard	
	16.50-16.95	20	20	21	41	Hard	
	18.00-18.45	20	21	22	43	Hard	
	19.50-19.95	21	22	23	45	Hard	
SK13	1.50-1.95	11	13	14	27	Very stiff	Dark brown reddish clay/gravelly sand
	3.00-3.45	13	15	18	33	Hard	
	4.50-4.95	16	17	18	35	Hard	
	6.00-6.45	18	18	19	37	Hard	
	7.50-7.95	19	20	20	40	Hard	
	9.00-9.45	20	21	21	42	Hard	
	10.50-10.95	17	20	23	43	Hard	
	12.00-12.45	19	21	24	45	Hard	
	13.50-13.95	21	22	25	47	Hard	
	15.00-15.45	22	23	27	50	Hard	
	16.50-16.95	22	23	23	46	Hard	
	18.00-18.45	22	24	24	48	Hard	
	19.50-19.95	23	25	25	50	Hard	
SK14	1.50-1.95	12	13	14	27	Very stiff	Dark brown reddish clay/gravelly sand
	3.00-3.45	13	14	14	28	Very stiff	
	4.50-4.95	14	15	15	30	Very stiff	
	6.00-6.45	15	16	17	33	Hard	
	7.50-7.95	16	16	18	34	Hard	
	9.00-9.45	18	20	20	40	Hard	
	10.50-10.95	21	22	23	45	Hard	
	12.00-12.45	20	21	23	44	Hard	
	13.50-13.95	22	23	24	47	Hard	
	15.00-15.45	22	23	23	46	Hard	
	16.50-16.95	20	21	24	45	Hard	
	18.00-18.45	22	23	24	47	Hard	
	19.50-19.95	24	25	25	50	Hard	

2.3.3. Mechanical properties of soil

Dark brown reddish clay and gravel units have been observed in the area under investigation. Natural density, water content, consistency limits (Liquid Limit, Plastic Limit, Plasticity Index), soil class, etc. of the soil were determined by performing grain size distribution (Sieve Analysis) on soil samples taken from boreholes both disturbed (SPT) and undisturbed (UD), triaxial compression test, consolidation and direct shear test (Table 4).

Table 4. Laboratory Test Results

					Triaxial Compression Test(UU)		Consolidation		Sieve Analysis		Atterberg Limits			
Boring No	Sample No	Depth (m)		Natural density	C (kgf/cm²)	φ (o)	Percentage of Swelling	Swelling Pressure (kgf/cm)	No:4 Retained (%)	No:200 Passing (%)	LL (%)	PL (%)	PI (%)	Soil Class
SK1	UD	1.00	23.25	1.78	0.56	6			4.17	61.96	55.6	22.1	33.5	CH
SK1	SPT	4.50	14.23						32.18	30.14	40.1	20.2	19.9	SC
SK2	UD	2.00	20.54	1.78	0.52	6			0	75.57	59.2	23.2	36	CH
SK2	SPT	6.00	11.5						17.56	28.87	34.6	18.5	16.1	SC
SK3	UD	1.50	22.29	1.74	0.60	5	2.20	0.198	2.23	73.03	57	19.4	37.6	CH
SK3	SPT	3.00	16.34						19.09	45.16	41.2	18.2	23	SC
SK4	UD	2.00	23.76	1.79	0.55	5			4.1	55.16	54.6	20.5	34.1	CH
SK4	SPT	4.50	12.21						16.2	35.02	36.5	21.2	15.3	SC
SK5	UD	1.50	28.74	1.77	0.57	6			4.17	73.42	53.6	20.3	33.3	CH
SK5	SPT	4.50	14.17						17.41	33.6	42.6	21.5	21.1	SC
SK6	UD	2.00	16.43	1.76	0.56	7			2.26	70.54	59.9	25.5	34.4	CH
SK6	SPT	4.50	6.53						10.14	24.71	39.6	23.2	16.4	SC
SK7	UD	1.50	18.35	1.72	0.54	5			0	70.7	60.2	27.5	32.7	CH
SK7	SPT	6.00	13.98						13.52	28.88	45.5	24.3	21.2	SC
SK8	UD	1.00	21.23	1.80	0.54	5			1.43	53.06	57.5	24.6	32.9	CH
SK8	SPT	4.50	14.28						19.82	36.73	48.3	26	22.3	SC
SK9	UD	1.00	20.96	1.79	0.53	6			6.62	69.98	58.8	24.1	34.7	CH
SK9	SPT	6.00	12.2						17.77	45.17	29.6	25.3	14.3	SC
SK10	UD	2.00	27.56	1.80	0.58	6			2.03	60.75	59.6	27.5	32.1	CH
SK10	SPT	3.00	16.43						20.21	44.05	33.5	20.5	13	SC
SK11	UD	1.00	23.54	1.72	0.56	5	2.47	0.245	1.45	62.26	56.6	23.4	33.2	CH
SK11	SPT	4.50	14.22						16.63	36.98	37.4	18.5	18.9	SC
SK12	UD	1.00	20.76	1.75	0.60	5			1.37	61.41	59.2	19.9	39.3	CH
SK12	SPT	6.00	14.06						10.35	26.02	40.3	22	18.3	SC
SK13	UD	1.00	22.02	1.77	0.57	5			1.22	58.23	54.2	21.6	32.6	CH
SK13	SPT	4.50	13.34						12.76	27.54	38.8	19.5	19.3	SC
SK14	UD	1.00	27.92	1.69	0.54	7			1.06	70.15	53.3	19.6	33.7	CH
SK14	SPT	4.50	11.45						14.98	33.01	39.6	20.2	19.4	SC

The average value for the undrained shear strength and the internal friction angle was taken from the samples taken from the boreholes as a result of laboratory and field tests;

$$Cu = 55 \text{ kPa } \varphi = 5\ 0 \quad (7)$$

2.3.4. Bearing Capacity Analysis

Turkey Building Earthquake Regulation;

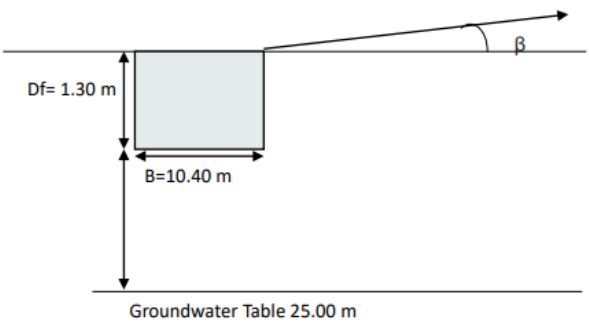

Cohesion Cu = 55 kPa Angle of Internal Friction φ = 5 0
Width of Foundation B = 10.40 m
Length of Foundation L = 12.90 m
Depth of Foundation Df = 1.30 m
Ground Water Table Dw = 25 m
Angle of soil with horizontal β = 0
Angle of base with horizontal η = 0
Natural unit Weight ɣN = 16 kPa
Saturated unit weight ɣsat = 20 kPa
Df= 1.30 mβ B=10.40 m
Groundwater Table 25.00 m
Unit Weight of water ɣw = 9.81 kPa Strength Factor ɣRv = 1.4
Effective unit weight ɣl = 16 kPa
Bearing capacity factors; (Meyerhof) inclination factor; (Meyerhof)
Nq = tan2
(45+φ/2) = 1.57 İc = [1- (β/90)]2 = 1.00
Nc = (Nq – 1)cotφ = 6.54 İq = İc = 1.00
Nɣ = 2(Nq – 1)tanφ = 0.45 İɣ = [1- (β/φ)]2 = 1.00
Shape factors ;(De Beer,1970) Ground Factors (Base on slope);(Vesic)
Sc = 1+[(B/L)*(Nq/Nc)] = 1.19 gc = β/147 = 1.00 (φ = 0 icin)
Sq = 1+[(B/L)*tanφ] = 1.07 gc = [1- (β/147)] =1.00 (for φ 0)
Sɣ = 1-[(B/L)*0.4] = 0.68 gɣ = gq = [1- (tan β)2] = 1.00

Depth Factor;(Hansen)
dc = 1+[0.4*(D/B)]= 1.05 (for D/B 1)
dc = 1+[0.4*atan(D/B)] = 1.05 (for D/B 1)
dq = 1+[2*(tanφ)]*[(1-sinφ)2]*[(D/B)] = 1.02 (for D/B 1)
dq = 1+[2*(tanφ)]*[(1-sinφ)2]*[atan(D/B)] = 1.17 (for D/B 1) dɣ = 1.00
base factors (tilted base);(Vesic)
bc = η/147 = 1.00 (φ = 0 icin) bc = 1-(η/147) = 1.00 (for φ 0)
bɣ = bq = [1-(η*tanφ)/57)]2 = 1.00
Surcharge load (ql) for Dw B+Df; ql = (Df* ɣn) = 20.8 kPa
qk = (c.Nc.sc.dc.ic.gc.bc) + (ql.Nq.sq.dq.iq.gq.bq)+ (0.5ɣ.B.l.Nɣ.sɣ.dɣ.iɣ.gɣ.bɣ)
qk = (55*6.54*1.19*1.05*1.00*1.00*1.00) + (20.8*1.57*1.07*1.02*1.00*1.00*1.00) + (0.5*16*10.40*0.45*0.68*1.00*1.00*1.00)
qk = 511.54 kPa
qt = qk / ɣRv = 511.54/1.4 = 365.39 kPa

According to the Turkish Building Earthquake Regulation (TBDY), the design strength of the foundation bearing capacity was found to be 365.39 kPa.

The soil was modeled by transferring the values of parameters such as cohesion cu, internal friction angle φ, natural unit weight ɣ natural, saturated unit weight ɣ saturated to Plaxis 2D program from the samples in the existing field and the data obtained from the laboratory and field conditions. Thus, the final bearing capacity analysis of the existing land has been made (Figure 4-7).

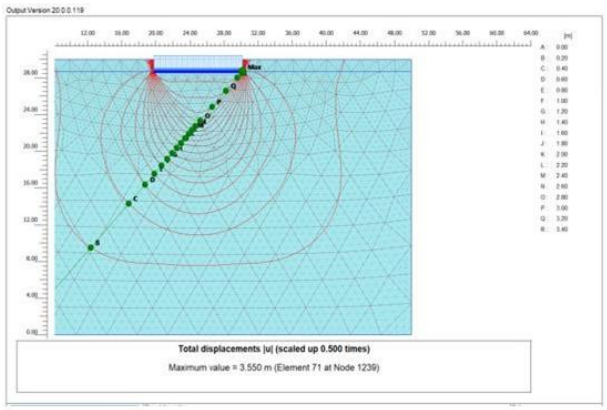

Figure 4. Plaxis 2D Soil Modelling and Displacements

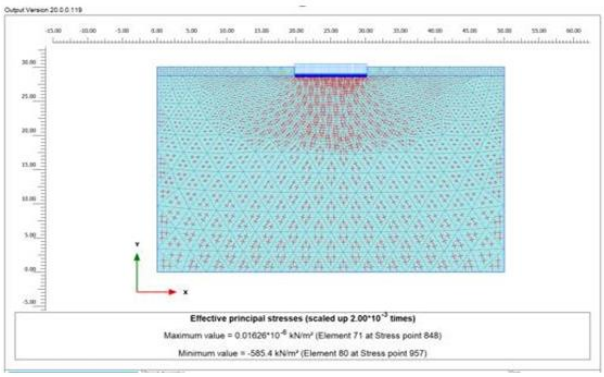

Figure 5. Plaxis 2D Effective Principal Stresses

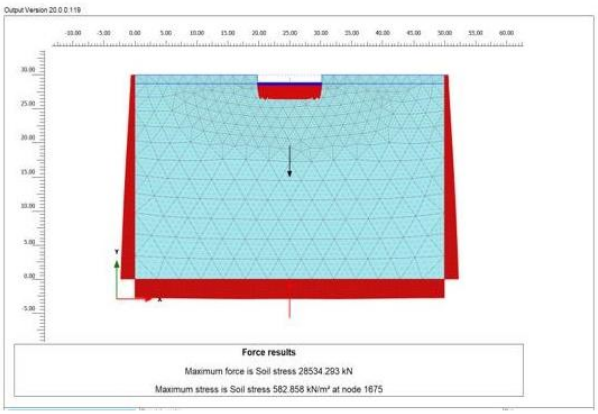

Figure 6. Plaxis 2D Soil Stress Values

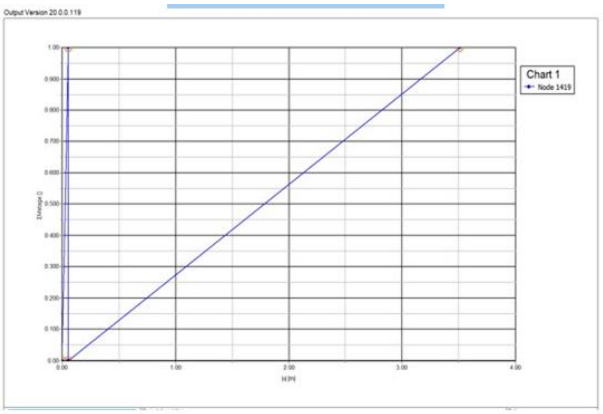

Figure 7. Total Displacement Curve at Soil

With the Plaxis 2D modeling program, the design strength of the foundation bearing capacity was found to be 457.2 kPa.

3. RESULTS

Within the scope of this study, field and laboratory tests were conducted in Diyarbakır City, Sur County, Yukarıkılıctası District, block no. 7018, parcel 1, and a soil investigation report was created. Additionally, previous studies on the engineering geology of the soil in the Karacadag region examined the basaltic lava flows outcropping the soil and the high plasticity clay with swelling properties (CH) by considering the soil class (Karakaya et al., 2022; Çetin & Acar, 2023). According to the soil investigation data report, it was observed that the soil cover on the basalt unit in the investigation area is composed of high plasticity clays in some places. The dominant lithology in the region was found to be dark brownish-red clay/gravelly sand, and the consistency of fine-grained soils was very stiff and hard.

It was noted that the high plasticity clay soil experiences swelling and shrinkage due to seasonal changes. These volumetric changes in the soil can lead to instability, causing differential settlements that may result in structural issues and financial challenges. To mitigate these effects, the use of geosynthetic clay liners (GCLs) with high tensile strength is recommended. These liners provide durability against cracking caused by freezing and thawing. Additionally, GCLs serve as effective hydraulic barriers, making them a low-cost solution for

improving soil strength and preventing changes in soil water content (Aksu & Yılmaz, 2021; Kaya et al., 2021).

During the calculation of bearing capacity, the stress value necessary to prevent sliding displacement of the foundation soil was determined. The undrained shear strength and internal friction angle, which affect the ultimate bearing capacity in the study area, were measured. Using these parameters and the calculation method outlined in the Turkish Building Earthquake Regulation, the design bearing capacity was calculated. Furthermore, the soil was modeled in the Plaxis 2D software using the parameters obtained from field and laboratory tests. The program helped determine the stress value for the ultimate bearing capacity. The values of the soil's bearing capacity design strength in the study area, as determined by both the Turkish Building Earthquake Regulation and Plaxis 2D, are shown in Table 5.

Table 5. Ultimate Bearing Capacity Design Strength

	TBDY	PLAXIS 2D
Ultimate Bearing Capacity Design Strength	365.39	457.20

When the bearing capacity design strength obtained from the Turkish Building Earthquake Regulation is taken as a reference, a 25.13% difference is observed between the design strength obtained through the Plaxis 2D program.

One reason for this significant percentage difference is that the design strength is determined by dividing the characteristic strength value found in TBDY with the strength factor. The bearing capacity found in Plaxis 2D is determined to be 326.57 kPa by performing this calculation with 457.20/1.4= 326.57 kPa.
457.20-365.39=91.81

$$25.13=(91.81x100)/(365.39)$$

The reason for this significant percentage difference is that the design strength is determined by dividing the characteristic strength value found in the Turkish Building Earthquake Regulation by the strength factor. When this calculation is performed for the bearing capacity found in Plaxis 2D, it is determined to be 326.57 kPa, thus, a lower percentage difference is considered.

4. DISCUSSION AND CONCLUSION

Based on the comprehensive analyses and evaluations conducted in this study, the final bearing strength value was determined, leading to the conclusion that calculations based on the Turkish Building Earthquake Regulation (TBDY) should be prioritized to ensure optimum design strength and structural safety. The TBDY norms specify how structures should respond under earthquake and other dynamic loads, aiming to achieve the highest safety standards. Thus, performing bearing capacity calculations in line with TBDY standards is crucial for maintaining the strength and durability of buildings (Çetin & Acar, 2023; Kaya et al., 2021).

In this study, the most appropriate approach was found to be evaluating the design bearing capacity at 365.39 kPa, which represents the critical bearing strength value. It is essential that any structure to be constructed in the study area is designed according to this value to ensure both stability and compliance with engineering standards. The results emphasize the importance of aligning structural design with TBDY guidelines, as these not only enhance the safety of the structure but also ensure that the design meets established engineering practices (Aksu & Yılmaz, 2021; Karakaya et al., 2022). Therefore, it is strongly recommended that bearing capacity calculations be based on TBDY standards, as they form the fundamental framework for safe and reliable structural design.

REFERENCES

[1] Aksu, B., & Yılmaz, H. (2021). Seismological assessment of the East Anatolian Fault. *Earthquake Engineering Review*.

[2] Amin Soltanianfard, M., et al. (2023). Experimental investigation of rock-like specimens' interface using 3D printing. *International Journal of Geomechanics*.

[3] Bowles, J. E. (1996). *Foundation Analysis and Design*. McGraw-Hill.

[4] Chen, H., & Zhang, L. (2023b). Machine learning-based prediction of end-bearing capacity of rock-socketed shafts. *Rock Mechanics and Rock Engineering*.

[5] Chen, H., Zhu, H., & Zhang, L. (2023a). Semi-analytical solution for ultimate bearing capacity of smooth and rough circular foundations on rock. *International Journal for Numerical and Analytical Methods in Geomechanics*.

[6] Çetin, K., & Acar, S. (2023). Seismic risk and fault systems in the Eastern Anatolian region. *Journal of Geological Research*.

[7] Hansen, J. B. (1970). "A Revised and Extended Formula for Bearing Capacity." *Danish Geotechnical Institute Bulletin*, 28, 5-11.

[8] Karakaya, S., et al. (2022). Geotechnical characteristics of volcanic terrains in the Diyarbakır region. *Geological Journal*.

[9] Kaya, E., et al. (2021). Faulting patterns and seismic hazards in the eastern Anatolian region. *Tectonic Studies Journal*.

[10] Meyerhof, G. G. (1951). "The Ultimate Bearing Capacity of Foundations." *Geotechnique*, 2(4), 301-332.

[11] Parry, R. H. G. (1977). *Soil Plasticity and Strength*. Thomas Telford.

[12] Terzaghi, K. (1943). *Theoretical Soil Mechanics*. John Wiley & Sons.

[13] Vesic, A. S. (1973). "Analysis of Ultimate Loads of Shallow Foundations." *Journal of the Soil Mechanics and Foundations Division*, 99(1), 45-73.

[14] Xu, Q., et al. (2023). Failure analysis of excavation in sand cobble stratum under cutting disturbance. *Engineering Failure Analysis*.

[15] Zhao, Y., et al. (2023). Mechanical behavior of sandstone during post-peak cyclic loading under hydromechanical coupling. *International Journal of Mining Science and Technology*.

Volume 14, Issue 2, Page 103-110, 2025 https://doi.org/10.46810/tdfd.1609064 Research Article

BİNGÖL UNIVERSITY

Türk Doğa ve Fen Dergisi
Turkish Journal of Nature and Science
www.dergipark.gov.tr/tdfd

In vitro Anti-amoebic and Cytotoxic Activity of *Rosa gallica* and *Picea orientalis* Leaf Aqueous Extracts

Erdoğan MALATYALI[1*], Ömer ERDOĞAN[2]

[1] Aydin Adnan Menderes University, Faculty of Medicine, Department of Parasitology, Aydin, Türkiye
[2] Gaziantep Islam Science and Technology University, Faculty of Medicine, Department of Biochemistry, Gaziantep, Türkiye
Erdoğan MALATYALI ORCID No: 0000-0002-3943-467X
Ömer ERDOĞAN ORCID No: 0000-0002-8327-7077

**Corresponding author: erdogan.malatyali@adu.edu.tr*

(Received: 28.12.2024, Accepted: 24.04.2025, Online Publication: 27.06.2025)

Keywords
Acanthamoeba spp., *Rosa gallica*, *Picea orientalis*, Extract, Cytotoxicity

Abstract: *Acanthamoeba* spp. are free-living amoebae that can cause keratitis and granulomatous encephalitis in humans. This study aimed to evaluate the anti-amoebic and cytotoxic effects of aqueous leaf extracts of *Rosa gallica* and *Picea orientalis* on *Acanthamoeba* spp. and two cell lines. An environmental isolate of *Acanthamoeba* spp. was cultured on non-nutrient agar with *Escherichia coli*, and viability was tested with the trypan blue method and microscopic observation of morphologies after exposure to extracts. Cytotoxicity was tested on SH-SY5Y (human neuroblastoma) and HaCaT (human keratinocyte) cell lines via the MTT assay. No viable trophozoites were observed after six hours of incubation with 30 mg/mL of *P. orientalis* extract, whereas 20.7% of trophozoite viability was found in *R. gallica* extract with the same concentration after 24 hours. Both extracts demonstrated limited efficacy against the encysted stage, with cysts remaining viable after 24 hours, over 70% viability. In addition, dose-dependent cytotoxicity was observed for both extracts on SH-SY5Y and HaCaT cells. This study provides the first in vitro evidence of the anti-amoebic activity of *R. gallica* and *P. orientalis* aqueous leaf extracts. However, their limited effect on cysts and cytotoxicity highlights the need for further in vivo studies to explore therapeutic potential.

Rosa gallica ve *Picea orientalis* Yaprağı Su Özütlerinin In vitro Anti-amebik ve Sitotoksik Aktiviteleri

Anahtar Kelimeler
Acanthamoeba spp., *Rosa gallica,* *Picea orientalis*, Özüt, Sitotoksisite

Öz: *Acanthamoeba* spp., potansiyel patojenik serbest yaşayan amipler arasında yer almakta olup, insanlarda keratit ve granulomatöz ensefalite neden olabilmektedir. Bu çalışmada, *Rosa gallica* ve *Picea orientalis*'in yaprak özütlerinin *Acanthamoeba* spp.'ye karşı anti-amebik ve iki faklı hücre hattında sitotoksik aktivitelerinin araştırılması amaçlanmıştır. Çevresel örnekten izole edilen bir *Acanthamoeba* spp. izolatı, *Escherichia coli* ile kaplanmış, besleyici değeri olmayan agar kültüründe çoğaltılmıştır. Farklı konsantrasyonlardaki özütler ile inkübe edilen parazitin canlılığı, trypan mavisi yöntemiyle ve morfolojik değişiklikler gözlemlenerek takip edilmiştir. Ayrıca, özütlerin sitotoksik aktiviteleri, SH-SY5Y (insan nöroblastoma) ve HaCaT (insan keratinosit) hücre hatlarında MTT yöntemiyle test edilmiştir. Altı saatlik 30 mg/mL *P. orientalis* özütü inkübasyonu sonrasında canlı trofozoite rastlanmazken, aynı konsantrasyonda *R. gallica* özütü ile 24 saatlik inkübasyon sonrası trofozoitlerin ortalama %20,7'sinin canlı kaldığı gözlemlenmiştir. Trofozoit formunun aksine, her iki özütün *Acanthamoeba* spp.'nin kist formuna karşı sınırlı etki gösterdiği ve 24 saatlik inkübasyon sonrasında kistlerin %70'inden fazlasının canlı kaldığı belirlenmiştir. Ayrıca, her iki özütün SH-SY5Y ve HaCaT hücrelerinde doza bağlı değişen sitotoksik etki gösterdiği saptanmıştır. Bu in vitro çalışmanın sonucunda, *R. gallica* ve *P. orientalis* yaprağı su özütlerinin anti-amebik aktivitesine dair ilk veriler elde edilmiştir. Bu özütlerin terapötik potansiyelinin daha kapsamlı olarak değerlendirilmesi için ileri in vivo çalışmalara ihtiyaç bulunmaktadır.

1. INTRODUCTION

Acanthamoeba species are the most prevalent free-living amoebae found in both natural and human-made environments. They have been isolated from a wide range of sources, including soil, freshwater, seawater, air, humidifiers, air conditioning systems, swimming pools, contact lens solutions, surgical instruments, and medical devices such as dialysis units [1]. *Acanthamoeba* spp. has a two-stage life cycle, consisting of an active trophozoite stage and a dormant cyst stage. The trophozoite is the metabolically active, feeding, and replicating form of the parasite. The cyst stage is highly resistant and formed in response to unfavourable environmental conditions. Therefore, the parasite can survive and spread in harsh environments. From an ecological perspective, *Acanthamoeba* spp. play crucial roles in maintaining microbial balance by feeding on bacteria, which serve as their primary source of nutrition. This grazing activity gradually reduces bacterial populations, enhances nutrient cycling, and promotes soil mineralization, eventually contributing to improved plant growth [2]. *Acanthamoeba* spp. was first identified in the 1930s as a contaminant in yeast cultures. However, their clinical significance was not recognized until the 1960s and 1970s, when they were isolated from patients with granulomatous amoebic encephalitis (GAE) and *Acanthamoeba* keratitis (AK) [3]. In humans, transmission typically occurs through the inhalation of free-living amoebae via nasal passages or through skin lesions. The parasite can reach the central nervous system in two ways: via haematogenous dissemination from a primary site of infection in the lungs or skin, or direct access through olfactory neuroepithelium in the nasal cavity. *Acanthamoeba* spp. are described as opportunistic parasites capable of causing severe infections in both immunocompetent and immunocompromised individuals [4]. However, it tends to progress more rapidly and invasively in immunocompromised patients. The parasite can also cause a sight-threatening corneal infection and can result in vision impairment if left untreated. Contact lens use is the primary risk factor for AK, accounting for approximately 90% of reported cases [5]. The prevalence of AK is increasing in many countries, particularly in hospital samples, making it an emerging public health concern [6].

There is currently no standardized protocol for the diagnosis of AK. It can be isolated in cultures and detected during histopathological examination. Additionally, molecular methods such as polymerase chain reaction (PCR) offer the opportunity to detect *Acanthamoeba* DNA in suspected samples. The combined use of culture and PCR assays may help to reduce the number of misdiagnosed AK cases. In addition, the quality of the sample is crucial for diagnostic sensitivity [7]. The culture method is widely used in most laboratories due to its simplicity and its ability to support further analysis of isolates. For instance, corneal scrapings can be inoculated onto 2.5% non-nutrient agar (NNA) overlaid with a lawn of *Escherichia coli* to promote *Acanthamoeba* growth. However, the sensitivity of culture methods is generally lower compared to in vivo confocal microscopy and PCR [8]. The treatment of AK typically involves the topical application of a combination therapy using a biguanide (e.g., polyhexamethylene biguanide or chlorhexidine) and a diamidine (e.g., hexamidine or propamidine). In some cases, these agents may also be used as monotherapy [9]. However, prolonged daily use of these treatments can result in significant side effects, including corneal degeneration, glaucoma, iris atrophy, corneal ulceration, formation of cataracts, hyperaemia, and photophobia [10]. In addition to these commonly used therapeutic agents, certain antifungal drugs, such as neomycin, itraconazole, and voriconazole, have also demonstrated efficacy in the management or treatment of AK [11]. Early treatment of AK with effective drug combinations is crucial to minimize long-term ocular complications.

The Rosaceae family are rich in natural compounds with diverse biological properties and activities. The well-known species are *Rosa damascena*, *Rosa alba*, *Rosa centifolia*, and *Rosa gallica*. The biological activities of the essential oils, hydrolates, and aqueous extracts of these plants have been extensively studied in the literature [12]. Water-soluble components of *R. gallica* have demonstrated significant biological properties, showing promising results in antimicrobial, antioxidant, and bifidogenic activities [13]. Furthermore, *R. gallica* hydrolate samples were found to contain high levels of gallic and ellagic acids. The antimicrobial activity of *R. gallica* extracts has been reported against foodborne pathogenic bacteria and *Candida* species, supporting their potential as natural antimicrobials in food and pharmaceutical applications [14]. Additionally, *R. gallica* extracts were effective in controlling cariogenic bacteria in the oral microenvironment [15]. Species of the Pinaceae family naturally produce a wide range of terpenoids, which are particularly involved in the defence mechanisms of the plant. These compounds exhibit bioactive effects against various microbial and multicellular pathogens, including insects and herbivores [16]. Extracts from stem wood and bark of certain Pinaceae species have shown antimicrobial activity against a variety of human pathogens [17]. Major active components were 13-epimanool, α-cedrol, abietic acid, dehydroabietic acid, astringin, and α-terpineol. The amount of these compounds varied between root or leaf extracts of the plant. Their antimicrobial activity and chemical composition have offered good potential for applications in pharmaceuticals and food preservation [18].

Many plant-derived products have been tested on *Acanthamoeba* spp. [19]. However, to the best of our knowledge, there was no study in the literature dealing with the anti-amoebic activity of *R. gallica* and *P. orientalis*. Plant-based compounds and extracts may offer promising potential for the development of novel therapeutic agents for the treatment of *Acanthamoeba* spp. infection in humans. The present study aimed to evaluate the anti-amoebic and cytotoxic activities of aqueous leaf extracts of *R. gallica* and *P. orientalis* on *Acanthamoeba* spp. and two different human cell lines.

2. MATERIAL AND METHOD

2.1. Isolate and Cultivation

Acanthamoeba spp. AduA1 isolate was used in the experiments. It was originally isolated from an environmental water sample and cultured on non-nutrient agar (NNA) medium. The isolate was defined as *Acanthamoeba* spp. by partial amplification of the 18S rRNA coding gene followed by BLAST analysis in GenBank (Acc. No. PQ651434). The culture medium was prepared as follows: a Ringer tablet (Merck) was dissolved in distilled water according to the manufacturer's instructions and autoclaved at 121°C for 15 minutes. Bacteriological agar was then added at a final concentration of 2.5%, re-autoclaved, cooled, and poured into Petri dishes to solidify. Finally, the dishes were covered with a lawn of *Escherichia coli* (ATCC 25922). The isolate was cultivated at 30ºC in a standard bacteriological incubator.

2.2. Preparation of Plant Extracts

Leaves of gallic rose (*Rosa gallica*) and Caucasian spruce (*Picea orientalis*) were collected in Gaziantep, Turkey (36°58'43.1"N and 37°18'04.6"E). A mixture of 200 mL ultrapure water and 100 g of leaf was prepared in 1000 mL Erlenmeyer. The mixture was boiled under continuous stirring using a magnetic stirrer for 2 hours. After cooling to room temperature, it was filtered using a funnel. The resulting filtrate was lyophilized, and the precipitated extract was stored at -20 °C until use [20].

2.3. Determination of Anti-amoebic Activities

Acanthamoeba spp. trophozoites were harvested from NNA medium two days after inoculation. The medium was overlaid with 10 mL of sterile phosphate-buffered saline (PBS), and trophozoites were scraped from the surface using cell scrapers (Corning®). The resulting suspension was centrifuged at 3000 × g for 5 minutes, and the final concentration was adjusted to 1 × 10^4 cells/mL using sterile PBS. *Acanthamoeba* spp. cysts were collected from two-week-old NNA cultures and prepared using the same method as for the trophozoite forms.

The viability of *Acanthamoeba* spp. trophozoites and cysts were observed for 24 hours (after one, 3, 6, 12, and 24 hours of incubation). The final concentrations of plant extracts were adjusted to 1, 5, 15, and 30 mg/mL. After each time interval, 25 µL of the sample was mixed with an equal volume of trypan blue (Biochrome, 0.5%) and immediately examined under a light microscope at 40× magnification. The viable cells (unstained) and non-viable cells (stained or morphologically degenerated) were counted [21]. The percentage of cell viability was calculated using the following formula: 100 X viable cells/ (viable + non-viable cells). Three samples were taken for each observation time, and the mean percentage of cell viabilities was calculated. The experiments were performed at room temperature.

2.4. Cell Cultures

Human keratinocytes (HaCaT) and human neuroblastoma (SH-SY5Y) cells were cultured in DMEM medium supplemented with 10% foetal bovine serum, 1% penicillin-streptomycin and HEPES. Cells were maintained in 75 cm2 culture flasks, with the medium renewed every two days. When cell confluence reached approximately 90%, the cells were passaged and subsequently used in cytotoxicity experiments [22].

2.5. Determination of Cytotoxic Activities

SH-SY5Y and HaCaT cell lines were seeded in 96-well plates at a density of $5x10^3$ cells per well. The cells were incubated for 24 hours in a CO_2 incubator for adherence to the bottom of the wells. Following incubation, the cells were treated with the extracts at concentrations of 1, 10, 100 and 1000 µg/mL for 24 hours. The logarithmic doses are typically used for to created dose–response curves in cytotoxicity studies. In the present study, a wide dose range of the extracts (1–1000 µg/mL) were tested on human cell lines. Subsequently, 10 µL of MTT dye (5 mg/mL) was added to each well. After 4 hours of incubation, the medium was removed, and the resulting formazan crystals were dissolved in 100 µL of DMSO. Absorbance was measured at 570 nm using a plate reader. The percentage cell viability was calculated using the following formula: (OD test sample/OD control) X 100 [23].

2.6. Statistical Analysis

Statistical analyses were performed using GraphPad Prism version 9.3. The measurements were repeated three times, and results were presented as mean ± standard deviation (SD). Differences between groups were determined using the one-way ANOVA test. Statistical significance levels were set as follows: $p < 0.05$; $p < 0.01$; $p < 0.001$; $p < 0.0001$.

3. RESULTS

3.1. Anti-Amoebic Activity of Plant Extracts

The anti-amoebic effects of the extracts were evaluated separately on the trophozoite and cyst forms of *Acanthamoeba* spp. Overall, the cyst forms were more resistant to the extracts compared to the trophozoite forms. After six hours of inoculation with 30 mg/mL of *P. orientalis* extract, all trophozoites were non-viable (Figure 1). In contrast, viable trophozoites were still observed after 24 hours of exposure to *R. gallica* extract (Figure 2). Cyst forms remained over 72% viable after 24 hours of treatment with both of the plant extracts (Figure 3). The time and dose-dependent activities of the extracts were presented in Figure 4 for *R. gallica* and Figure 5 for *P. orientalis*. The viability of trophozoites decreased significantly at concentrations of 5 mg/mL, 10 mg/mL, and 15 mg/mL ($p < 0.05$, $p < 0.0001$, and $p < 0.0001$, respectively) after 24 hours of treatment with *R. gallica*, however, no statistically significant decrease was observed in cyst viability over the same period ($p > 0.05$).

In contrast, the viability of trophozoites treated with *P. orientalis* for 24 hours decreased significantly at concentrations of 10 mg/mL and 15 mg/mL ($p < 0.0001$). Additionally, a statistically significant decrease in cyst viability was observed only at 30 mg/mL ($p < 0.05$) after 24-hour treatment with *P. orientalis*.

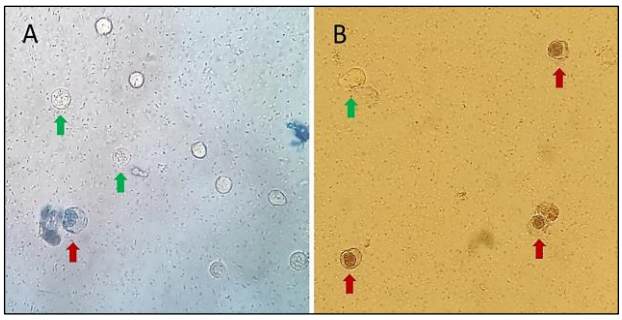

Figure 1. Effect of *R. galllica* aqueous extract on *Acanthamoeba* spp. trophozoites. Images display viable (green arrows) and non-viable (red arrows) trophozoites of *Acanthamoeba* spp. following treatment with 30 mg/mL of the extract: (A) after one hour of incubation and (B) after 24 hours of incubation.

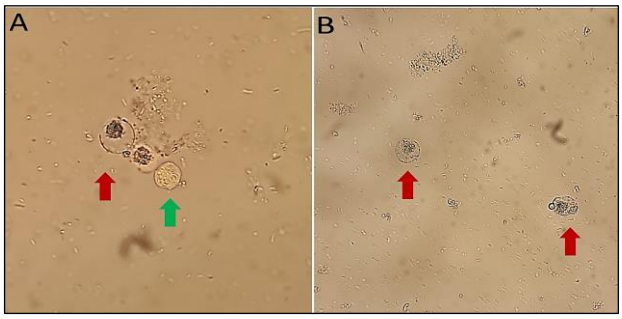

Figure 2. Effect of *P. orientalis* aqueous extract on *Acanthamoeba* spp. trophozoites. Images display viable (green arrows) and non-viable (red arrows) trophozoites of *Acanthamoeba* spp. following treatment with 30 mg/mL of the extract: (A) after 3 hours of incubation and (B) after 6 hours of incubation.

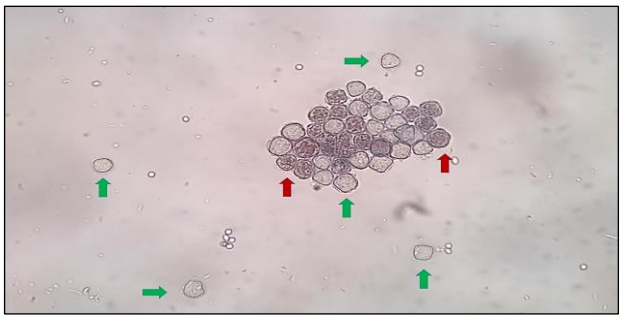

Figure 3. Viability of *Acanthamoeba* spp. cysts following treatment with 30 mg/mL of *P. orientalis* aqueous extract after 3 hours, viable cysts (green arrows) and non-viable cysts (red arrows).

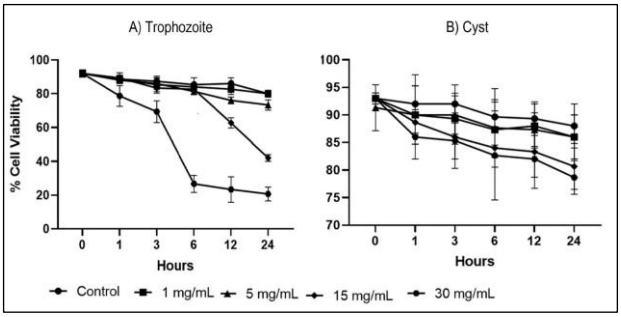

Figure 4. Graph showing the anti-amoebic activity of *R. gallica* aqueous extract on *Acanthamoeba* spp.: (A) trophozoite form and (B) cyst form.

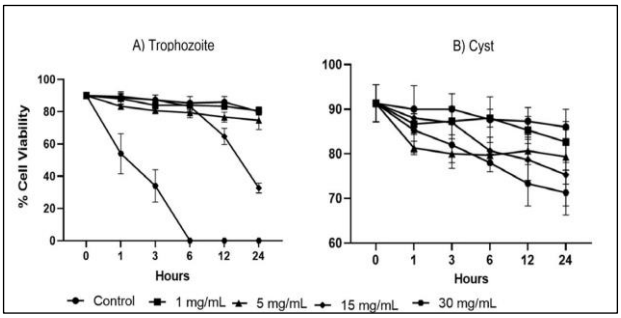

Figure 5. Graph showing the anti-amoebic activity of *P. orientalis* aqueous extract *Acanthamoeba* spp.: (A) trophozoite form and (B) cyst form.

3.2. Cytotoxic Effect of Plant Extracts

The cytotoxic effects of two aqueous extracts at concentrations of 1, 10, 100 and 1000 µg/mL on SH-SY5Y cells were evaluated by the MTT method. After 24 h of incubation, it was found that the cytotoxic effects of both aqueous extracts increased dose-dependently in both cell lines. The % cell viability rates of SH-SY5Y and HaCaT cells treated with 1000 µg/mL of *R. gallica* extract were found to be 31.27±1.62 and 25.04±0.04, respectively ($p<0.0001$) (Figure 6A and 6B). The % cell viability rates of SH-SY5Y and HaCaT cells treated with 1000 µg/mL *P. orientalis* were calculated as 33.18±8.84 and 34.30±7.61, respectively ($p<0.0001$) (Figure 6C and 6D).

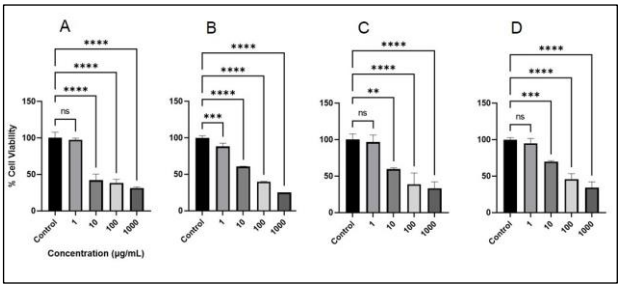

Figure 6. Graph showing the cytotoxic activities of plant extracts: (A) *R. galllica* on SH-SY5Y cells, (B) *R. galllica* on HaCaT cells, (C) *P. orientalis* on SH-SY5Y cells, and (D) *P. orientalis* on HaCaT cells. Statistical significance levels: *, $p<0.05$; **, $p<0.01$; ***, $p<0.001$; ****, $p<0.0001$.

4. DISCUSSION AND CONCLUSION

Acanthamoeba spp. are a common group of free-living amoeba in the environment and water sources. These free-living amoebas can act as opportunistic parasites, causing sight-threatening keratitis and life-threatening encephalitis in humans. Accurate and early diagnosis is crucial for identifying the causative agent and differentiating it from other pathogens. Effective treatment is essential to prevent long-term clinical complications. In recent years, resistance of *Acanthamoeba* spp. to conventional therapies and chlorine has been reported, highlighting the need for alternative therapeutic options, including plant-derived compounds and chemical agents [24, 25].

In the present study, we tested the anti-amoebic activity of *R. gallica* and *P. orientalis* leaf aqueous extracts against both the trophozoite and cyst forms of *Acanthamoeba* spp. The extracts showed a time- and dose-dependent effect on the parasite. To the best of our knowledge, reviewing the literature, no previous studies have investigated the amoebicidal activity of these two extracts. The extract of *P. orientalis* exhibited rapid and effective amoebicidal activity, with complete trophozoite mortality observed after six hours of exposure at a concentration of 30 mg/mL. However, *R. gallica* extract did not achieve total trophozoite mortality even after 24 hours. In addition, morphological changes caused by the two extracts differed, with *P. orientalis* extract causing more disruptions. The cyst forms were highly resistant to both extracts, with over 70% remaining viable even after 24 hours of incubation. The resistance of *Acanthamoeba* spp. cysts were probably related to the double-walled structure and reduced metabolic activity, making them less susceptible to many therapeutic agents [26]. It was reported that the colour and contrast of stains vary according to the developmental stages of free-living amoebas including *Acanthamoeba* spp. and *Naegleria* spp. [27]. Since cysts at different stages of maturation may differ in dye uptake, distinguishing immature and non-viable cysts can be challenging. To minimize this variability, two-week-old NNA cultures were used in the present study to ensure a more consistent level of cyst maturation, and morphological changes were also documented.

The differences in the anti-amoebic activities of the two extracts are likely due to variations in their bioactive components. Studies have reported that rose extracts exhibit diverse biological effects, including antimicrobial and antioxidant properties [28]. The composition of rose plant extracts includes high amounts of polyphenols, anthocyanins, and flavonoids [29]. Another study identified phenethyl alcohol, β-citronellol, and geraniol as the major chemical components in rose water samples, with a total of 22 different constituents detected [30]. The chemical composition of rose plant leaf has been extensively studied, revealing the presence of flavonoids, hydroxycinnamic acids, phenols, tannins, terpenes, aldehydes, alcohols, minerals, fatty acids, and vitamin C. These components contribute to various biological functions, such as diuretic properties and applications as natural dyes [31]. Rose aromatherapy is a widely recognized traditional approach, used to treat dysmenorrhea, stress, depression, and anxiety. In addition to its therapeutic effects, the antimicrobial properties of rose extracts against various microorganisms have been documented. The growth of several bacteria was significantly inhibited by rose extract [32]. Different parts of the rose plant exhibit distinct chemical compositions and biological activities. Rose hip extracts, for example, have shown potential antimicrobial properties, with *R. rugosa* fruit extract exhibiting the highest antimicrobial activity against *Staphylococcus* spp. [33]. A study demonstrated antimicrobial and antioxidant activities of methanol extract of *R. gallica var. aegyptiaca* against a range of microorganisms [14]. The antimicrobial activity of extract varied depending on the extraction method including hexane, methanol, hydromethanol 80%, chloroform, and water. The hydromethanol method showed the highest antimicrobial activity. Essential oils derived from *R. damascena* exhibited promising fungicidal and antibacterial activity [34]. The diverse chemical compositions and biological activities of different rose plant parts and their extracts have been highlighted in the literature, contributing to applications for a wide range of therapeutic and antimicrobial purposes. A comprehensive study from Turkey investigated the chemical components and antimicrobial activity of *P. orientalis*. They reported limonene, β-pinene, and α-pinene as the major components. In addition, monoterpene hydrocarbons were abundant in essential oils in resin. A total of 22 microorganism species were tested with the agar well diffusion method and the highest antibacterial activity was noted against *S. typhimurium* and *S. aureus*. In addition, antifungal activity was highest for *C. albicans* [35]. In contrast, another species of *Picea* (*P. abies*) did not show any promising antimicrobial activity on both *E. coli* and *S. aureus* [36]. A study reported that the major components of *P. abies* wood and bark extracts were di-hydroxyverrucosane and larixol. The extracts also had antimicrobial activities against a variety of human pathogen, foodborne, and agricultural microorganisms [37].

A variety of plant-derived materials has been tested for their anti-amoebic activity against *Acanthamoeba* spp., with some studies reporting promising results. For example, a study evaluating 200 plant extracts from South Asia identified three with significant amoebicidal activity [38]. Because of its geographical location, plant biodiversity in Turkey is very high. Previous studies in Turkey have identified several plant extracts with different levels of anti-amoebic activity against *Acanthamoeba* spp., including extracts from *Allium species, Ceratophyllum spp.,* and *Pastinaca* spp. [39-41]. Consistent with our findings, most studies also observed that the cyst forms of *Acanthamoeba* spp. were more resistant to plant extracts than the trophozoites.

Cell cytotoxicity refers to the ability of a substance to cause damage to cells, leading to cell dysfunction or death. It is an important parameter in toxicology, pharmacology, and cancer research [42-44]. Plant extracts

can be used as supportive agents in cancer treatment to minimize the side effects of chemotherapy due to their cytotoxic phytoconstituents [45]. The extract of *R. gallica* has been reported to contain cytotoxic components such as glycyrrhetinic acid, hyperoside, caffeic acid, quercetin and ferulic acid [46]. At the highest concentration (1000 µg/mL) of *R. gallica* extract, the viabilities of SH-SY5Y and HaCaT cells were 31.3% and 25%, respectively. In addition, at the same concentration of *P. orientalis*, the cell viabilities were 33.2% and 34.3%, respectively. It was reported that the cytotoxic activity of rose extracts was directly dependent on the extraction method, the concentration, and the target cell. For example, the sensitivity of normal cells from animals and humans, as well as cancer cell lines were different after being treated with aqueous extracts of Iranian rose [47]. The cytotoxic activity of the aqueous extract differed between human HeLa tumour cells and human lymphocytes. Lower concentrations of the extract were effective against cancer cells, while higher concentrations were required to affect healthy human cells. Another study investigated the effects of both aqueous and ethanolic extracts of *Rosa damascena* on human gastric cancer cells [48]. Although all concentrations significantly reduced cell viability, the ethanolic extract exhibited a stronger inhibitory effect than the aqueous extract, probably due to differences in chemical composition. The IC_{50} values of the ethanolic and aqueous extracts were 2.517 µg/mL and 3.887 µg/mL, respectively. Hydrosols from Bulgarian rose flowers, extracted by water–steam distillation using a semi-industrial process, exhibited low cytotoxic and genotoxic effects in cell-based assays, suggesting their potential for safe human use [49]. The cytotoxic activity of aqueous extracts from spruce bark (*P. abies*), via classical water bath extraction, was tested on tumour and non-tumour cell lines. These extracts were not cytotoxic on the human keratinocyte cell line and stimulated the proliferation of the cells [50]. Essential oils from another *Picea* species demonstrated strong anti-tumour activity against MCF-7 breast cancer cells [51]. Additionally, a hot water extract of black spruce (*P. mariana*) showed promising antioxidant and anti-inflammatory properties [52].

Although our study was designed as an in vitro study, it provides the first data on the anti-amoebic effects of *R. gallica* and *P. orientalis*. The extracts show varying potential as anti-amoebic agents, particularly against trophozoites. However, their efficacy against cyst forms requires further investigation to test their therapeutic efficiencies. Future research on in vivo effects, toxicity assessments, and the development of standardized formulations for clinical applications will be valuable.

Acknowledgement

The present study has not received any funding.

REFERENCES

[1] Chan LL, Mak JW, Low YT, Koh TT, Ithoi I, Mohamed SM. Isolation and characterization of *Acanthamoeba* spp. from air-conditioners in Kuala Lumpur, Malaysia. Acta Trop. 2011;117:23-30.

[2] Bonkowski M. Protozoa and plant growth: the microbial loop in soil revisited. New Phytologist. 2004;162(3):617–631.

[3] Raghavan A, Rammohan R. *Acanthamoeba* keratitis - A review. Indian J Ophthalmol. 2024;72:473-82.

[4] Sharma G, Kalra SK, Tejan N, Ghoshal U. Nanoparticles based therapeutic efficacy against *Acanthamoeba*: Updates and future prospect. Exp Parasitol. 2020;218:108008.

[5] Carnt N, Robaei D, Minassian DC, Dart JKG. *Acanthamoeba* keratitis in 194 patients: risk factors for bad outcomes and severe inflammatory complications. Br J Ophthalmol. 2018;102:1431-5.

[6] Bullé DJ, Benittez LB, Rott MB. Occurrence of *Acanthamoeba* in hospitals: a literature review. RECI. 2020;10(2):174-80.

[7] Yera H, Ok V, Lee Koy Kuet F, Dahane N, Ariey F, Hasseine L, et al. PCR and culture for diagnosis of *Acanthamoeba* keratitis. Br J Ophthalmol. 2021;105:1302-6.

[8] Goh JWY, Harrison R, Hau S, Alexander CL, Tole DM, Avadhanam VS. Comparison of in vivo confocal microscopy, PCR and culture of corneal scrapes in the diagnosis of *Acanthamoeba* Keratitis. Cornea. 2018;37:480-5.

[9] Papa V, Rama P, Radford C, Minassian DC, Dart JKG. *Acanthamoeba* keratitis therapy: time to cure and visual outcome analysis for different antiamoebic therapies in 227 cases. Br J Ophthalmol. 2020;104:575-81.

[10] Rayamajhee B, Williams NLR, Siboni N, Rodgers K, Willcox M, Henriquez FL, et al. Identification and quantification of *Acanthamoeba* spp. within seawater at four coastal lagoons on the east coast of Australia. Sci Total Environ. 2023;901:165862.

[11] Buchele MLC, Nunes BF, Filippin-Monteiro FB, Caumo KS. Diagnosis and treatment of *Acanthamoeba* Keratitis: A scoping review demonstrating unfavorable outcomes. Cont Lens Anterior Eye. 2023;46:101844.

[12] Mileva M, Ilieva Y, Jovtchev G, Gateva S, Zaharieva MM, Georgieva A, et al. Rose flowers-a delicate perfume or a natural healer? Biomolecules. 2021;11.

[13] Babich O, Zhikhreva A, Kulikova Y. Phytochemical composition of Rosa Gallica and prospects of its use. IJCBS 2024;25(19):1078-1084.

[14] Abdelbaky AS, Mohamed A, Alharthi SS. Antioxidant and antimicrobial evaluation and chemical investigation of *Rosa gallica* var. aegyptiaca leaf extracts. Molecules. 2021;26.

[15] Vargas-Segura AI, Silva-Belmares SY, Segura-Ceniceros EP, Ascacio-Valdés JA, Méndez-González L, Ilyina A. Screening and characterization of medicinal plants extracts with bactericidal activity against Streptococcus mutans. Nat Prod Res. 2020;34(18):2672-2676.

[16] Alicandri E, Paolacci AR, Osadolor S, Sorgona A, Badiani M, Ciaffi M. On the evolution and functional diversity of terpene synthases in the Pinus species: A review. J Mol Evol. 2020;88:253-83.
[17] Salem MZ, Elansary HO, Elkelish AA, Zeidler A, Ali HM, El-Hefny M, et al. In vitro bioactivity and antimicrobial activity of Picea abies and Larix decidua wood and bark extracts. Bio Resources. 2016;11(4):9421-9437.
[18] Tanase C, Boz I, Oroian S, Coşarcă S, Toma F, Mare A, et al. Antibacterial activity of spruce bark (Picea abies l.) extract against E. coli. Acta Biol Maris. 2018;1(1):5-9.
[19] Niyyati M, Dodangeh S, Lorenzo-Morales J. A Review of the current research trends in the application of medicinal plants as a source for novel therapeutic agents against *Acanthamoeba* infections. Iran J Pharm Res. 2016;15:893-900.
[20] Erdoğan Ö, Paşa S, Demirbolat GM, Birtekocak F, Abbak M, Çevik Ö. Synthesis, characterization, and anticarcinogenic potent of green-synthesized zinc oxide nanoparticles via Citrus aurantium aqueous peel extract. Inorg Nano-Met Chem. 2025;55(1),67-75.
[21] Strober W. Trypan Blue Exclusion Test of Cell Viability. Curr Protoc Immunol. 2015;111:A3 B 1-A3 B.
[22] Wang F. Culture of animal cells: a manual of basic technique. In Vitro Cell Dev Biol Anim. 2006;42(5):169-169.
[23] Supino R. MTT Assays. In vitro toxicity testing protocols; O'Hare S and Atterwill CK, Eds.; Humana Press: Totowa, NJ, 1995;137-149.
[24] Campolo A, Pifer R, Walters R, Thomas M, Miller E, Harris V, et al. *Acanthamoeba* spp. aggregate and encyst on contact lens material increasing resistance to disinfection. Front Microbiol. 2022;13:1089092.
[25] Gabriel AA, Panaligan DC. Heat and chlorine resistance of a soil *Acanthamoeba* sp. cysts in water. J Appl Microbiol. 2020;129:453-64.
[26] Coulon C, Collignon A, McDonnell G, Thomas V. Resistance of *Acanthamoeba* cysts to disinfection treatments used in health care settings. J Clin Microbiol. 2010;48:2689-97.
[27] Ithoi I, Ahmad AF, Mak JW, Nissapatorn V, Lau YL, Mahmud R. Morphological characteristics of developmental stages of *Acanthamoeba* and Naegleria species before and after staining by various techniques. Southeast Asian J Trop Med Public Health. 2011;42:1327-38.
[28] Masek A, Latos M, Chrzescijanska E, Zaborski M. Antioxidant properties of rose extract (*Rosa villosa* L.) measured using electrochemical and UV/Vis spectrophotometric methods. Int J Electrochem Sci. 2017;12(11): 10994–11005.
[29] Lee MH, Nam TG, Lee I, Shin EJ, Han AR, Lee P, et al. Skin anti-inflammatory activity of rose petal extract (Rosa gallica) through reduction of MAPK signalling pathway. Food Sci Nutr. 2018;6:2560-7.
[30] Moein M, Zarshenas MM, Delnavaz S. Chemical composition analysis of rose water samples from Iran. Pharm Biol. 2014;52:1358-61.
[31] Wang H. Beneficial medicinal effects and material applications of rose. Heliyon. 2024;10:e23530.
[32] Cendrowski A, Krasniewska K, Przybyl JL, Zielinska A, Kalisz S. Antibacterial and antioxidant activity of extracts from rose fruits (Rosa rugosa). Molecules. 2020;25.
[33] Milala J, Piekarska-Radzik L, Sojka M, Klewicki R, Matysiak B, Klewicka E. *Rosa* spp. extracts as a factor that limits the growth of *Staphylococcus* spp. bacteria, a food contaminant. Molecules. 2021;26.
[34] Ren G, Xue P, Sun X, Zhao G. Determination of the volatile and polyphenol constituents and the antimicrobial, antioxidant, and tyrosinase inhibitory activities of the bioactive compounds from the by-product of Rosa rugosa Thunb. var. plena Regal tea. BMC Complement Altern Med. 2018;18:307.
[35] Öz M. Chemical composition and antimicrobial properties of essential oils obtained from the resin of *Picea orientalis*. J Essent Oil-Bear Plants. 2022;25(2),326–37.
[36] Hofmann T, Albert L, Németh L, Vršanská M, Schlosserová N, Voběrková S, et al. Antioxidant and antibacterial properties of Norway Spruce (*Picea abies* H. Karst.) and Eastern Hemlock (*Tsuga canadensis* (L.) Carrière) Cone Extracts. Forests. 2021;12,1189.
[37] Salem MZM, Elansary HO, Elkelish AA, Zeidler A, Ali HM, Mervat E H, et al. In vitro bioactivity and antimicrobial activity of *Picea abies* and *Larix decidua* wood and bark extracts. Bio Res. 2016;11(4):9421-37.
[38] Chu DM, Miles H, Toney D, Ngyuen C, Marciano-Cabral F. Amebicidal activity of plant extracts from Southeast Asia on *Acanthamoeba* spp. Parasitol Res. 1998;84:746-52.
[39] Tas B, Koloren Z, Koloren O. In vitro, amoebicidal activities of submerged plant Ceratophyllum demersum L. extract against *Acanthamoeba* castellanii trophozoites. Aquatic Res. 2024;7(4),178-88.
[40] Degerli S, Berk S, Malatyali E, Tepe B. Screening of the in vitro amoebicidal activities of Pastinaca armenea (Fisch. & C.A.Mey.) and Inula oculus-christi (L.) on *Acanthamoeba* castellanii cysts and trophozoites. Parasitol Res. 2012;110:565-70.
[41] Polat ZA, Vural A, Ozan F, Tepe B, Ozcelik S, Cetin A. In vitro evaluation of the amoebicidal activity of garlic (Allium sativum) extract on *Acanthamoeba* castellanii and its cytotoxic potential on corneal cells. J Ocul Pharmacol Ther. 2008;24:8-14.
[42] Ayna A, Tunc A, Ozbolat SN, Bengu AS, Aykutoğlu G, Canlı D, et al. Anticancer, and antioxidant activities of royal jelly on HT-29 colon cancer cells and melissopalynological analysis. Turk J Bot. 2021;45(8):809-819.
[43] Ayna A, Ozbolat SN, Darendelioglu E. Quercetin, chrysin, caffeic acid and ferulic acid ameliorate cyclophosphamide-induced toxicities in SH-SY5Y cells. Mol Biol Rep. 2020;47:8535-43.
[44] Ozbolat SN, Ayna A. Chrysin suppresses HT-29 cell death induced by diclofenac through apoptosis and oxidative damage. Nutr Cancer. 2021;73:1419-28.

[45] Choudhari AS, Mandave PC, Deshpande M, Ranjekar P, Prakash O. Corrigendum: Phytochemicals in cancer treatment: from preclinical studies to clinical practice. Front Pharmacol. 2020;11:175.
[46] Puladze M, Mulkijanyan K, Gogitidze N, Sulakvelidze M, Novikova Z, Mushkiashvili N, et al. Phytochemical and pharmacological study of Rosa gallica L. Georgian cultivar essential oil production waste. GSC Biol Pharm Sci. 2022;19:213-22.
[47] Kashami DA, Rasooli I, Rezaee MB, Owlia P. Antioxidative properties and toxicity of white rose extract. Iran. J Med Aromat Plants. 2011;5:415-425.
[48] Meimandi K, Yaghoobi MM. Effects of aqueous and ethanolic extract of *Rosa damascena* Mill L. against human gastric cancer cells. J Mol Cell Res. 2015;28(2):299-309.
[49] Gerasimova T, Gateva S, Jovtchev G, Angelova T, Topashka-Ancheva M, Dobreva A, et al. Rosa damascena Mill. essential oil: analysis of in vitro and in vivo genotoxic and cytotoxic potentials by employing three cytogenetic endpoints. Molecules. 2024;30.
[50] Coșarcă SL, Moacă EA, Tanase C, Muntean DL, Pavel IZ, et al. Spruce and beech bark aqueous extracts: Source of polyphenols, tannins and antioxidants correlated to in vitro antitumor potential on two different cell lines. Wood Sci Technol. 2019;53:313-330.
[51] Namshir J, Shatar A, Khandaa O, Tserennadmid R, Shiretorova VG, Nguyen MC. Antimicrobial, antioxidant and cytotoxic activity on human breast cancer cells of essential oil from *Pinus sylvestris*. var mongolica needle. Mong J Chem. 2020;21(47):19-26.
[52] Diouf PN, Stevanovic T, Cloutier A. Study on chemical composition, antioxidant and anti-inflammatory activities of hot water extract from *Picea mariana* bark and its proanthocyanidin-rich fractions. Food Chem. 2009;113(4):897-902.

Volume 14, Issue 2, Page 111-123, 2025 https://doi.org/10.46810/tdfd.1613491 Research Article

BİNGÖL UNIVERSITY

Türk Doğa ve Fen Dergisi
Turkish Journal of Nature and Science
www.dergipark.gov.tr/tdfd

Identification and Diagnosis of Asynchronous Motor Imbalance Faults Using Surrogate Models

Özgür AYDIN[1*], Erhan AKIN[2]

[1] Bingöl University, Informatics Department, Bingöl, Türkiye
[2] Fırat University, Engineering Faculty, Elazığ, Türkiye
Özgür AYDIN ORCID No: 0000-0001-8130-277X
Erhan AKIN ORCID No: 0000-0001-6476-9255

**Corresponding author: iamozguraydin@gmail.com*

(Received: 15.01.2025, Accepted: 28.04.2025, Online Publication: 27.06.2025)

Keywords
Asynchronous motor fault diagnosis, Surrogate model, Imbalance fault, Vibration analysis, Multi-Model classification

Abstract: Asynchronous motors have a wide range of industrial applications due to their robust structure, low maintenance costs, and high reliability. However, these motors can be exposed to electrical and mechanical faults caused by environmental and operational conditions. Among the types of faults are problems such as bearing failures, stator winding faults, and rotor bar breakages, with mechanical imbalance faults standing out as a critical issue that adversely affects motor performance. This study aims to compare the performance of surrogate models (RBF and KRG) and deep learning models (RNN, GRU, LSTM), which represent a novel approach for diagnosing imbalance faults in asynchronous motors. For this purpose, experimentally collected current (Ia, Ib, Ic) and vibration (X, Y, Z) signals were analyzed in the frequency domain, and the features obtained via FFT were used in classification processes for three classes (Healthy, DA_1, DA_2). According to the results, the RBF model exhibited the best performance with an accuracy of 97.78% and a precision of 97.64%, while the KRG model showed remarkable success with an accuracy of 93.89% and a precision of 93.71%. In contrast, the deep learning models with the highest accuracy, RNN and LSTM, demonstrated lower performance with an accuracy of 87.22% and a precision of 87.23%. Compared to the RNN model, which is the most accurate deep learning model, the RBF model achieved an improvement of 12.11% in accuracy and 11.93% in precision, proving to be a superior tool in diagnosing imbalance faults. Notably, it achieved 100% accuracy in the DA_2 class and distinguished itself from other classes with its distinct features. These findings show that surrogate models offer an effective solution in asynchronous motor fault diagnosis by providing high accuracy and precision rates along with limited data requirements and low computational cost.

Asenkron Motor Dengesizlik Arızalarının Vekil Modellerle Tanımlanması ve Teşhisi

Anahtar Kelimeler
Asenkron motor arıza teşhisi, Vekil model, Dengesizlik arızası, Titreşim analizi, Çoklu model sınıflandırma

Öz: Asenkron motorlar, sağlam yapıları, düşük bakım maliyetleri ve yüksek güvenilirlikleri ile endüstride geniş bir kullanım alanına sahiptir. Ancak, bu motorlar çevresel ve operasyonel koşullardan kaynaklanan elektriksel ve mekanik arızalara maruz kalabilmektedir. Arıza türleri arasında rulman problemleri, stator sargı hataları ve rotor çubuğu kırılmaları gibi sorunlar yer almakta, özellikle mekanik dengesizlik arızaları motor performansını olumsuz etkileyen kritik bir sorun olarak öne çıkmaktadır. Bu çalışma, asenkron motorlarda dengesizlik arızalarının teşhis edilmesine yönelik yeni bir yaklaşım olan vekil modeller (RBF ve KRG) ile derin öğrenme modellerinin (RNN, GRU, LSTM) performansını karşılaştırmayı amaçlamaktadır. Bu amaçla, deneysel olarak toplanan akım (Ia, Ib, Ic) ve titreşim (X, Y, Z) sinyalleri, frekans alanında analiz edilmiş ve FFT ile elde edilen özellikler, üç sınıf (Sağlıklı, DA_1, DA_2) için sınıflandırma süreçlerinde kullanılmıştır. Sonuçlara göre, RBF modeli, %97.78 doğruluk ve %97.64 keskinlik oranı ile en iyi performansı sergilemiş, KRG modeli ise %93.89 doğruluk ve %93.71 keskinlik oranı ile dikkate değer bir başarı göstermiştir. Buna karşılık, derin öğrenme modellerinden en yüksek doğruluk oranına sahip olan RNN ve LSTM

%87.22 doğruluk ve %87.23 keskinlik oranı ile daha düşük bir performans göstermiştir. RBF modeli, en yüksek doğruluklu derin öğrenme modeli olan RNN'e göre doğruluk oranında %12.11, keskinlik oranında ise %11.93'lük bir artış sağlamış, bu da dengesizlik arızalarının teşhisinde üstün bir araç olduğunu kanıtlamıştır. Özellikle DA_2 sınıfında %100 doğruluk oranına ulaşarak, belirgin özellikleri sayesinde diğer sınıflardan ayrışmıştır. Bu bulgular, vekil modellerin sınırlı veri gereksinimi ve düşük hesaplama maliyetiyle birlikte yüksek doğruluk ve keskinlik oranları sunarak, asenkron motor arıza teşhisinde etkili bir çözüm sunduğunu göstermektedir.

1. INTRODUCTION

Induction motors (IMs) are electric motors widely used in many sectors such as petroleum, automotive, and similar industries. The fact that they constitute 80% of alternating current motors in industry reveals how critically important these motors are [1, 2, 3]. Thanks to their robust structure, low maintenance requirements, and high reliability, induction motors are preferred over other types of motors. Therefore, ensuring the smooth operation of induction motors is of vital importance for the continuity of industrial processes. This is because failures in these motors can lead to serious problems such as production line stoppages, environmental damage, loss of life, and operational disruptions [4, 5, 6]. In order to prevent such negative outcomes, it is crucial to detect motor faults at an early stage. In this way, unplanned downtimes can be prevented and costly losses can be avoided [7-9].

Asynchronous motors are exposed to electrical and mechanical faults due to environmental conditions [10, 11]. Electrical faults involve the rotor and stator, while mechanical faults include bearing problems, eccentricity, and misalignment issues. 41% of motor faults originate from bearings, 36% from stators, 9% from rotors, and the remaining 14% from other causes [12].

Although rotor damages constitute a small portion of motor faults, they can lead to serious secondary problems. Rotor faults cause an increase in vibration, paving the way for bearing damage, air gap eccentricity, and winding problems. Therefore, early detection of rotor faults is critically important to prevent other faults in the motor [13, 14]. For this reason, various diagnostic techniques have been developed to detect faults [15-17].

Modern diagnostic methods for IM faults are generally based on mathematical modeling. However, these approaches are limited because full access to the system model is restricted [18]. Therefore, data-driven methods have gained popularity recently. These methods, which do not require analytical models, offer a significant advantage by eliminating the need to model complex industrial processes [19-20].

Motor faults are detected using variables such as vibration, temperature, current, and acoustics through signal processing methods. These methods include time, frequency, and time-frequency domain approaches [21-26]. The increasing amount of data has made artificial intelligence methods that provide automatic diagnosis more important. Techniques such as Artificial Neural Networks (ANN), Support Vector Machines (SVM), and k-Nearest Neighbor (k-NN), along with feature-extracted data, perform fault detection with high accuracy [17, 24, 27, 28]. While asynchronous motor fault diagnosis faces challenges such as limited datasets and varying operating conditions, deep learning offers an effective solution to overcome these problems. In particular, pre-trained models perform well with limited data, reducing overfitting and balancing data inconsistencies under different conditions. Next-generation learning approaches enable the development of more general and adaptable models in this field, while also shortening training times and accelerating the process [29, 30].

Traditional fault diagnosis methods have long provided a reliable foundation for detecting and analyzing faults in asynchronous motors. However, in the era of Industry 4.0, where digitalization is accelerating, these methods are gradually being replaced by more innovative and flexible approaches. In this context, surrogate models emerge as an important part of this transformation [31, 32]. Also known as meta-models or response surfaces, surrogate models represent the behavior of complex physical systems using simplified mathematical or artificial intelligence-based methods and are highly advantageous in scenarios with limited data and restricted computational resources [33]. This method aims to mimic the behavior of physical systems or complex simulation models as accurately as possible. The structure of surrogate model types is shown in Figure 1. Surrogate models are generally divided into two main categories: analytical surrogate models and learned surrogate models [34].

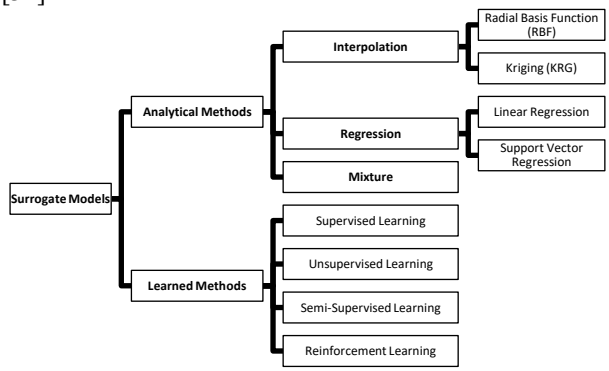

Figure 1. Surrogate Modeling Methods

Analytical models simplify complex functions using mathematical methods and typically utilize interpolation and regression techniques. While interpolation provides highly accurate predictions between data points, regression methods model the relationship between inputs and outputs to minimize the error rate. Additionally, hybrid approaches are also used. Learned models, on the other hand, operate in a data-driven manner and benefit

from large datasets. These models employ machine learning techniques such as supervised, unsupervised, and reinforcement learning, and achieve high accuracy by incorporating physical knowledge [32]. Especially for the simulation and analysis of various fault conditions in asynchronous motors, surrogate models offer a powerful tool, reducing training time and enabling the development of systems that can easily adapt to different operating conditions.

For example, Lu et al. (2019) developed a Kriging (KRG)-based surrogate model using FEM-based analysis and super-harmonic components to determine the location and depth of breathing cracks in rotating rotors. The method, optimized with particle swarm optimization (PSO), achieved over 95% accuracy with limited data and was also effective on noisy data. The study made a significant contribution to crack diagnosis by providing high accuracy at low cost [35].

Chevalier-Jabet et al. (2024) developed an ANN-based surrogate model to detect fuel rod defects in pressurized water reactors. The model, trained on 2,000 scenarios simulated with a physical model, predicted defects with a 2.6% error rate. RNN, GRU, and LSTM autoencoder models used for anomaly detection achieved 100% accuracy, with LSTM showing superior performance especially in long data sequences. This approach contributed to real-time applications by reducing computational costs through the fast and accurate detection of fuel defects [36].

Han et al. (2013) developed a method combining a KRG surrogate model and a DE algorithm to determine bearing parameters and imbalances in rotor-bearing systems. By using a surrogate model instead of FEM, computational costs were reduced, and an error below 1% was achieved in stiffness coefficients using the differential evolution (DE) algorithm. The method provided reliable parameter identification by delivering faster and more accurate results compared to PSO and GA [37].

Yang et al. (2024) developed a surrogate model based on Radial Basis Functions (RBF), optimized with PSO, to optimize the vibration performance of tracked vehicles. The PSO–RBF model predicted vertical vibration acceleration with a 0.67% error using suspension parameters and reduced the simulation time from 670 seconds to 107 seconds. This method offers a fast and accurate solution in parameter optimization [38]. An overview of these studies is presented in Table 1.

Table 1. An Overview of Surrogate Model Studies

Study	Method Used	Input	Output – Predicted Parameters	Output – Additional Performance Indicators
Lu ve ark. (2019) [35]	KRG PSO, FEM	Sensor data Finite Element Method (FEM)	Crack parameters (location and depth) Diagnosis accuracy (95%)	High accuracy with limited data (95%), high performance even with noisy data
Chevalier-Jabet ve ark. (2024) [36]	RNN, GRU LSTM Autoencoder	Simulation and sensor data, 2000 scenario data	Activity in the coolant (2.6% error) Detection of defective fuel rods	2.6% error with ANN, 100% accuracy with LSTM, real-time detection
Han ve ark. (2013) [37]	KRG DE, FEM	Sensor data	Stiffness coefficients (1% error) Damping coefficients	%1 error
Yang ve ark. (2024) [38]	RBF PSO	Vehicle suspension parameters, vibration acceleration sensor data	RMS value of vibration acceleration (0.67% error) Optimization of suspension parameters	0.67% error rate

When the studies presented in Table 1 are examined, it is observed that KRG and RBF models are generally used for surrogate modeling. The main feature of these models is their ability to predict function values at new locations to be tested. KRG was developed based on the studies of mining engineer D.G. Krige in 1951 and holds a significant place in the field of surrogate model-based optimization. This method uses the Gaussian process to model the observed data points, enabling the prediction of complex systems and aiming to minimize the error rate [39]. The Radial Basis Function (RBF) was developed by Hardy in 1971 and later improved by Dyn and colleagues [40]. This method models the function values based on the positions of the input data and is widely used in Sequential Global Optimization (SGO) algorithms and engineering applications [41]. The RBF model is particularly successful in capturing the details of nonlinear and complex functions. KRG, on the other hand, is a powerful tool for representing both local and global trends and is comparable to RBF in terms of accuracy [42]. In addition, Cheng and colleagues (2024) conducted a comprehensive review of data-driven surrogate model techniques developed to reduce the computational burden encountered in the design optimization process of electric motors. In the study, the performance, advantages, and limitations of statistical models (RSM, Kriging), machine learning models (SVM, RF, ANNs), and deep learning models (CNN, GAN, DNN) were evaluated. It was particularly emphasized that Kriging models can make performance predictions with high accuracy, while DL-based models stand out in handling high-dimensional design variables. This review reveals that data-based surrogate models have become not only complements to traditional analysis methods but also essential components that accelerate the design process [43].

These innovative methods have introduced a new dimension to engineering applications by increasing

accuracy while reducing computational costs. The approaches examined in the literature review will be used in the next section to develop real-time fault diagnosis methods for asynchronous motors.

This study emerged from the need to provide more accurate, faster, and cost-effective solutions against the limitations of existing methods used in the diagnosis of imbalance faults occurring in asynchronous motors. Considering the importance of real-time diagnosis in industrial fields, there is an increasing demand for approaches that can operate with limited data while offering high accuracy. In this context, the main motivation of the study is to investigate the applicability of surrogate modeling methods in diagnosing motor faults and to compare these methods with deep learning models. Furthermore, identifying models that can perform effectively even in cases where class separation is challenging will contribute to the development of decision support systems applicable in the field.

2. METHODOLOGY

2.1. Data Collection

Electrical (current signals) and mechanical (vibration velocities) performance data of the motor under different speeds and rotor fault levels were collected using the experimental setup shown in Figure 2.

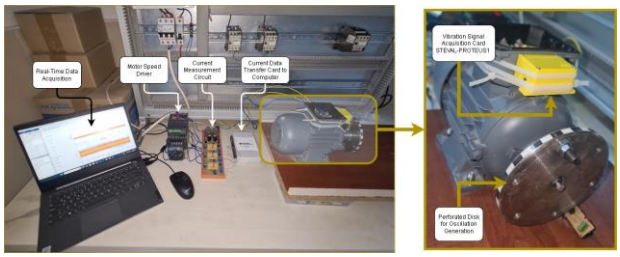

Figure 2. Experimental Setup

The dataset was obtained using a 0.37 kW asynchronous motor with the parameters specified in Table 2. The motor was examined by recording current and vibration signals for 60 seconds at different operating frequencies. Electrical fault was modeled by creating an imbalance with a disk attached to the rotor.

In the first stage, the motor was operated without any imbalance, and a dataset representing the "healthy" condition was collected. Subsequently, a screw was placed in one of the holes on the disk, and to increase vibration amplitude, a second screw was added to another hole. Using this method, a three-class dataset (Healthy, DA_1, DA_2) was created.

Table 2. Asynchronous Motor Parameters

Parametre	Değer
Power	0.37 Kw
Full Load Current	1.2 A
Supply Frequency	50 Hz
Number of Poles	4
Full Load Speed	**1390 Rpm**
Supply Voltage	**380 V**

The dataset consists of phase currents Ia, Ib, and Ic obtained from the asynchronous motor, along with vibration signals from the X, Y, and Z axes collected via a vibration sensor. To enable the motor to operate at different speeds and to acquire various current and vibration signals, a Delta VFD007EL21A, EL-0.75kW/220V AC Motor Driver was used. The vibration signals were collected using the STEVAL-PROTEUS1 data processing card. Both current and vibration signals were recorded at a sampling frequency of 10 kHz. This dataset serves as a fundamental resource for analyzing and classifying different operating conditions of the motor, representing a significant cornerstone for analyses focused on asynchronous motor fault diagnosis.

2.1. Feature Extraction

The dataset includes electrical and mechanical signals for two different fault classes and one healthy class. It was created under three different load conditions, each lasting 60 seconds. The sampling frequency for vibration signals was set to 10,000 Hz, while the sampling frequency for electrical signals was 55,611 Hz. Differences in the number of samples between current and vibration signals must be synchronized to ensure accurate and reliable classification. In the literature, methods such as Windowing, Fourier Transform (FFT), Wavelet Transform, and Resampling are commonly used to align these two time series. In this study, as shown in Figure 3, the raw data (both current and vibration signals) were first subjected to data segmentation. Then, they were transformed into the frequency domain using Fourier Transform (FFT), followed by band power analysis to extract meaningful and compact features.

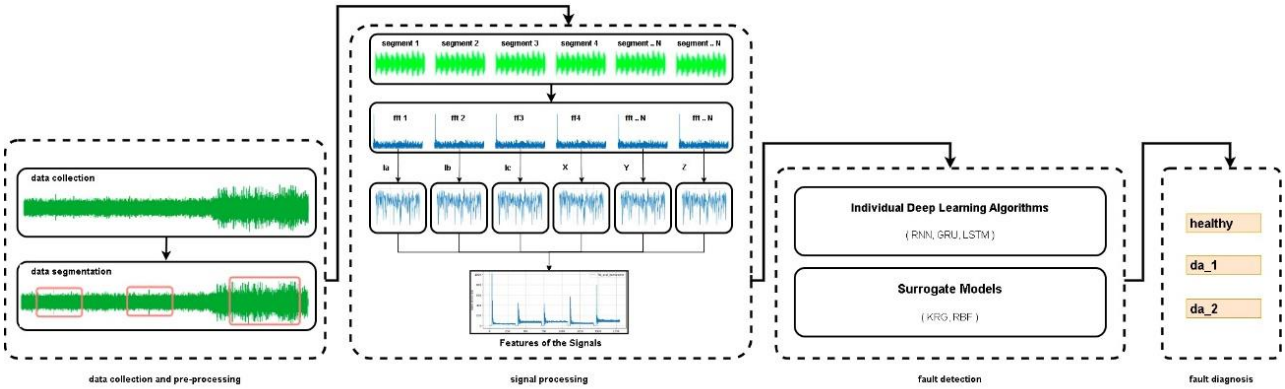

Figure 3. Signal processing, feature extraction, and classification stages

Figure 4 illustrates the signals obtained after the FFT process for current and vibration data corresponding to each output class. The visuals only display the transformations of the Ia current and vibration signals in the X direction. Additionally, all current and vibration signals have been subjected to the same processing.

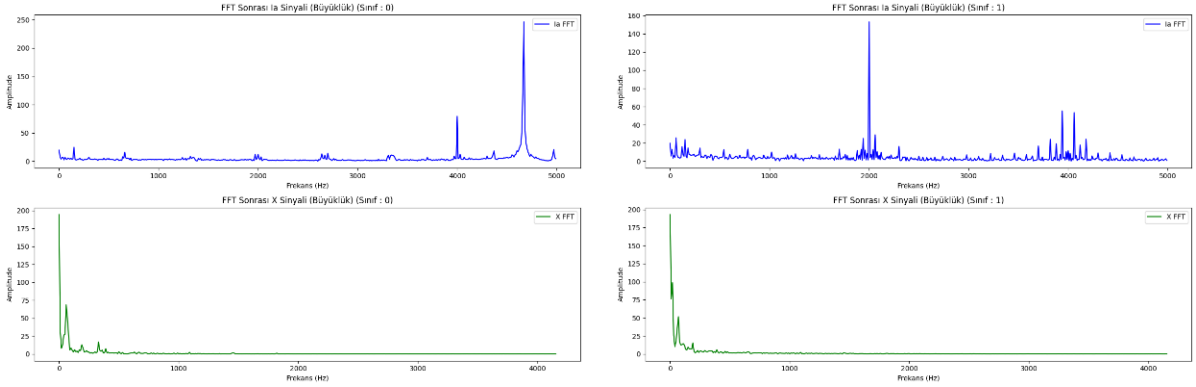

(a) (b)

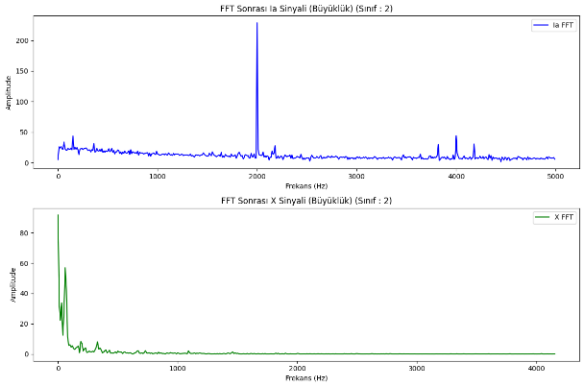

(c)

Figure 4. FFT transformation of Ia and X signals for all classes **a)** Healthy **b)** Imbalance Fault 1 (DA_1) **c)** Imbalance Fault 2 (DA_2)

The time series data were divided into predefined segment sizes, and FFT was applied to each segment. This segmentation ensured uniform processing of the data and enabled the analysis of frequency components over specific time intervals. The power spectral density (PSD) obtained through FFT was divided into specific frequency bands, summarizing the energy only within the relevant bands. This approach facilitated the extraction of meaningful features by reducing high-dimensional and noisy data. For instance, fault-specific characteristic frequencies stood out with high energy levels in the relevant bands. Figure 5 presents the band power transformations of current and vibration data for each class label.

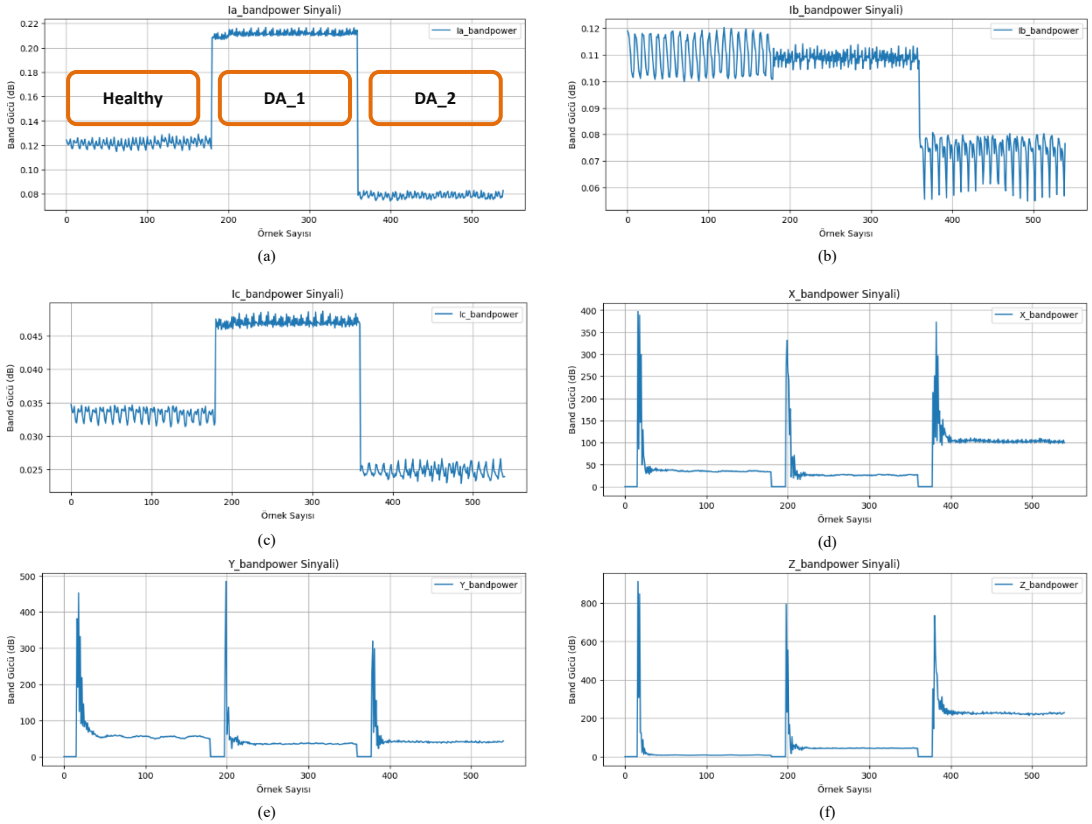

Figure 5. Combined band power transformations for all output classes **a)** Ia Signal **b)** Ib Signal **c)** Ic Signal **d)** X Signal **e)** Y Signal **f)** Z Signal

The dataset includes band power information of the current signals Ia, Ib, Ic and vibration signals X, Y, Z, as well as data related to the fault class labels. This dataset will later be used for the development of individual deep learning and surrogate model studies.

2.3. Classification Algorithms

2.3.1. Individual deep learning models: RNN, GRU ve LSTM

RNNs are models designed to learn dependencies in sequential data and are widely used in areas such as time series analysis and signal processing. However, issues such as vanishing gradients may arise when learning long-term dependencies [44, 45]. GRU, developed to overcome this problem, controls the flow of information through gates to provide more efficient learning and stands out with its low computational cost [46, 47]. GRU is a variant of RNN developed by Chung et al. (2014) and contains gate mechanisms similar to LSTM but requires fewer parameters, making it more advantageous in terms of training time. GRU is particularly preferred in time series data due to its ability to provide high accuracy with low computational cost [48]. LSTM successfully learns long-term dependencies through its forget and output gates, although it requires a higher computational cost [49, 50]. LSTM, developed by Hochreiter and Schmidhuber (1997), is widely used in time series analysis due to its ability to learn long-term dependencies [51].

The success of LSTM- and GRU-based methods in fault diagnosis of motors has been strongly emphasized in recent studies. Lale and Yüksek (2024) compared GRU- and LSTM-based models for diagnosing short-circuit and demagnetization faults occurring in permanent magnet synchronous motors (PMSM) and showed that the GRU model achieved 98.72% accuracy, while the LSTM model achieved 98.23% accuracy. In this study, systems modeled under different fault levels and multiple operating conditions were fed with time series-based input data, and the classification performance was found to be high. This indicates that RNN-based deep learning methods such as GRU and LSTM stand out as prominent alternatives in fault classification [52]. In this study, these three models were preferred for motor fault detection due to their ability to learn long-term dependencies.

2.3.2. Surrogate learning models: RBF ve KRG

In this study, the Python-based Surrogate Modeling Toolbox (SMT) library was used to develop surrogate models, which are widely employed in the analysis of complex problems with high computational cost [53]. SMT provides a powerful and flexible framework for easily applying various surrogate modeling methods and conducting detailed analyses. Within the scope of the study, particularly the RBF and KRG methods were tested and their model performances were compared.

3. EXPERIMANTAL STUDIES

The experimental studies were conducted using a high-computing-capacity infrastructure to effectively handle data processing, model training, and performance evaluation processes. This infrastructure included a computer with 64 GB RAM and an NVIDIA RTX A5000 GPU with 45 GB VRAM capacity. MATLAB was

employed for data collection, while Python programming language was utilized for implementing deep learning and surrogate models. Python libraries, in particular, were used to accelerate and enhance the development of deep learning algorithms. This setup significantly improved efficiency and computational speed during model development.

For solving the classification problem, input data consisted of current signals (Ia, Ib, Ic) and vibration signals (X, Y, Z). Correspondingly, the output classes were categorized into three groups: "healthy" and imbalance faults (DA_1, DA_2). At the initial stage of classification, RNN, GRU, and LSTM models were individually evaluated. During model training, 90% of the dataset was allocated for training, while the remaining 10% was used for validation and testing. To ensure reproducibility and comparability of results, the random_state parameter was fixed at 42 across all models. The Adam algorithm, a commonly used optimization method, was chosen for training, and the learning process was limited to 50 epochs. The architecture and hyperparameters used for RNN, GRU, and LSTM models were structured consistently to ensure uniformity. Figure 6 provides detailed information about the architecture and hyperparameters of the RNN model, which were applied similarly to GRU and LSTM models. This methodology facilitated the investigation of classification performance and ensured the comparability of results.

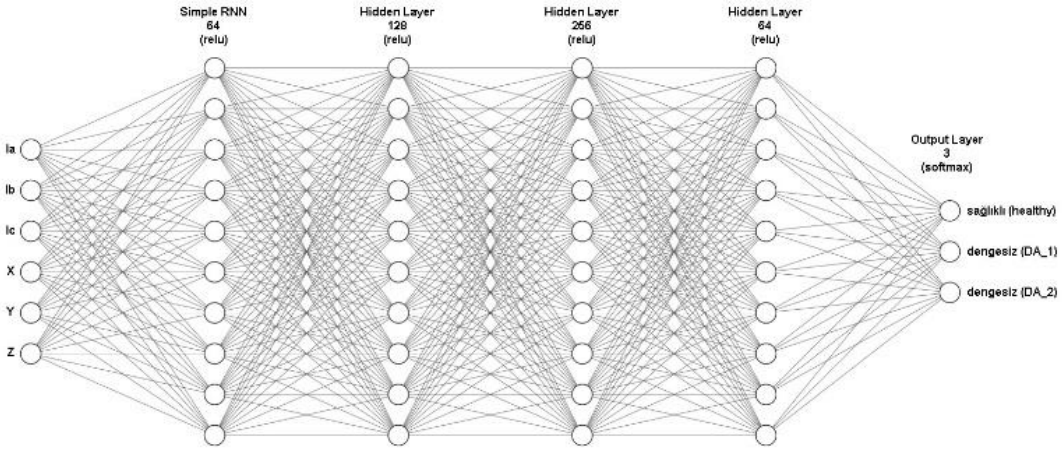

Figure 6. RNN Deep Learning Model Architecture and Hyperparameters

In the second phase of the experimental studies, RBF and KRG models were trained using the Python SMT library with appropriate parameters for each method, optimized to accurately represent the input-output relationships in the dataset. During model training, SMT's optimization tools were utilized to automatically determine each model's hyperparameters (e.g., correlation functions and kernel parameters). The trained models were evaluated on the test dataset, and their accuracy performances were analyzed in detail.

In this study, the "One-vs-Rest (OvR)" approach was preferred to solve the multi-class classification problem. This strategy creates a separate binary classifier for each class: each model considers one class as "positive" and all other classes as "negative." A total of three different models were trained for the three classes (Healthy, DA_1, DA_2). When a new data sample is received, each model generates a probability output for that sample, and the class with the highest probability is predicted. This structure is illustrated in the schematic diagram below. The classification strategy related to this process is shown in Figure 7.

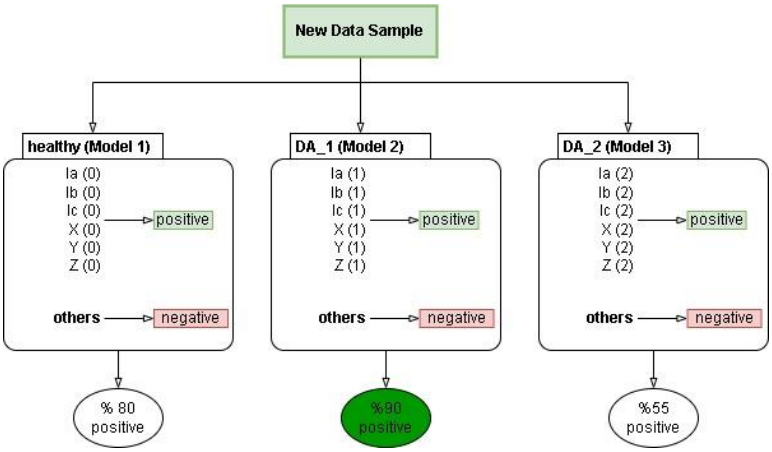

Figure 7. Modeling Classes with the One-vs-Rest Strategy

According to the strategy, each class is treated as the "positive" class, while the remaining classes are considered "negative." Since there are three classes in the study, three separate binary classifiers (models) will be created. Each model treats only one class as positive and the other two classes as negative. The implementation of the One-vs-Rest strategy is as follows:

Model 1: Healthy (Positive) vs. Others (DA_1, DA_2) : This model considers Healthy as positive based on the Ia, Ib, Ic, X, Y, Z inputs, and all remaining inputs as negative.

Model 2: DA_1 (Positive) vs. Others (Healthy, DA_2) : This model considers DA_1 as positive based on the Ia, Ib, Ic, X, Y, Z inputs, and all remaining inputs as negative.

Model 3: DA_2 (Positive) vs. Others (Healthy, DA_1): This model considers DA_2 as positive based on the Ia, Ib, Ic, X, Y, Z inputs, and all remaining inputs as negative.

When a new data sample arrives, each model predicts the class membership of the sample. The class with the highest probability among the predictions determines the predicted class of the sample. For instance:

Model 1 predicts the sample belongs to the Healthy class with an 80% probability.

Model 2 predicts the sample belongs to the DA_1 class with a 90% probability.

Model 3 predicts the sample belongs to the DA_2 class with a 55% probability.

The class with the highest probability is predicted by Model 2, indicating that the sample belongs to the DA_1 class.

4. FINDINGS

Each of the three distinct individual deep learning models aimed to approach the classification problem in the dataset from different perspectives, ensuring accurate and reliable predictions of the motor's health status. The performance results of the models are presented in Table 3.

Table 3. Performance Results of Individual Deep Learning Models

Model	Accuracy	Precision	Recall	F1-score
RNN	0.8722	0.8723	0.8722	0.8722
GRU	0.8611	0.8656	0.8611	0.8603
LSTM	0.8722	0.8727	0.8722	0.8721

According to the results presented in Table 3, the performance of three different deep learning models (RNN, LSTM, and GRU) in addressing the motor health classification problem was evaluated. Both the RNN and LSTM models achieved almost identical results in terms of Accuracy, Precision, Recall, and F1-Score metrics, with each demonstrating a successful performance at an accuracy rate of 87.22%. This indicates that both models effectively captured the time-series dynamics of the dataset. On the other hand, the GRU model performed slightly lower, with an accuracy rate of 86.11%, compared to RNN and LSTM. The GRU model's lower values across other metrics suggest that it was not as well-suited to the characteristics of the dataset or did not contribute as robustly to solving the classification problem as the other two models. Overall, RNN and LSTM models appear to provide more consistent and reliable results for this type of classification problem compared to the GRU model. Table 4 presents the accuracy and loss graphs, confusion matrices, and t-SNE visualizations for the models.

Table 4. Accuracy and Loss Graphs

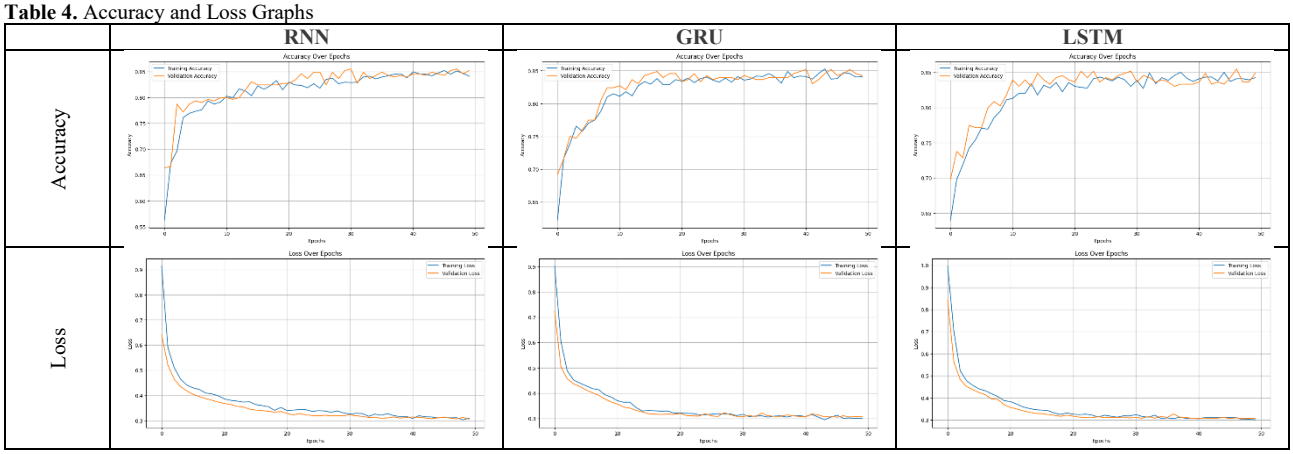

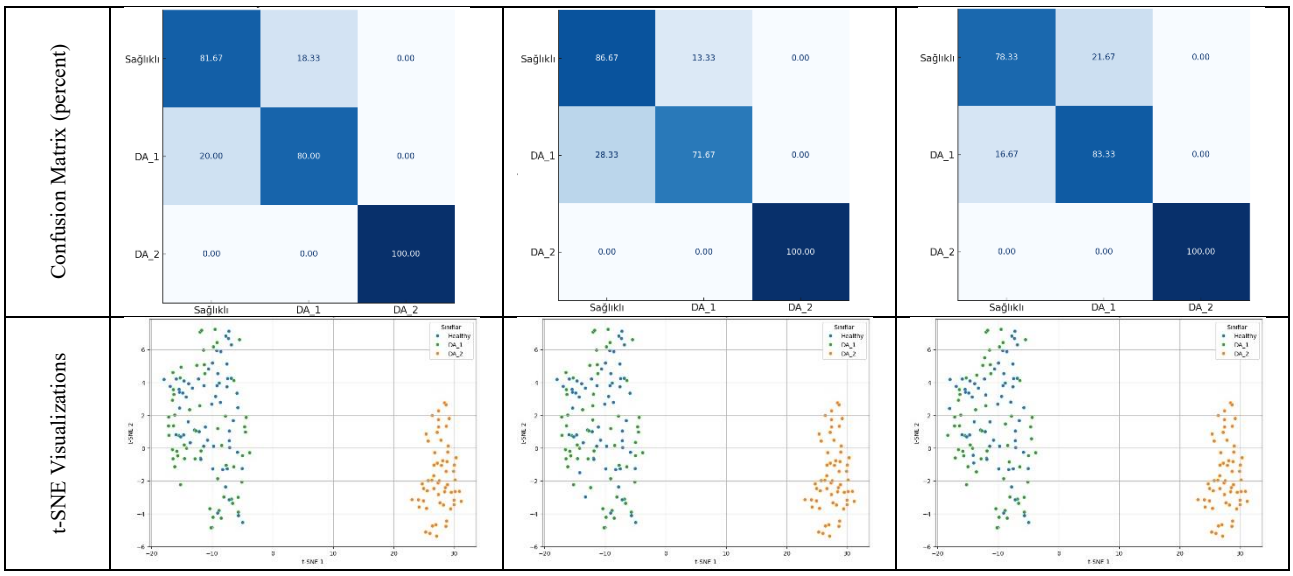

According to the confusion matrices, it is observed that all models particularly struggled to distinguish between the Healthy and DA_1 classes. The RNN model achieved an accuracy of 81.67% in the Healthy class, with 18.33% misclassification, and an accuracy of 80% in the DA_1 class, with 20% misclassification. Similarly, the LSTM model classified the Healthy group with 78.33% accuracy and 21.67% misclassification, while achieving 83.33% accuracy and 16.67% misclassification for the DA_1 class. The GRU model, on the other hand, demonstrated better performance for the Healthy class with 86.67% accuracy and 13.33% misclassification, but its accuracy decreased for the DA_1 class, achieving 71.67% accuracy and 28.33% misclassification. This indicates that the Healthy and DA_1 classes have similar characteristics, making their separation more challenging. In contrast, all models achieved error-free results for the DA_2 class, suggesting that this class has more distinct features compared to the others.

Additionally, the t-SNE visualization results presented in Table 4 show that the DA_2 class is clearly separated from other classes across all models. However, no clear distinction was observed between the Healthy and DA_1 classes, as their samples are positioned in close proximity to each other. When comparing the RNN, GRU, and LSTM models, it is noted that although all models exhibited similar distributions, the GRU and LSTM models displayed more overlap between the Healthy and DA_1 class clusters. This further highlights the difficulty in separating the Healthy and DA_1 classes, which impacts model performance. Notably, the clear distinction of the DA_2 class from other classes confirms that it possesses more distinct features.

In the second phase, the results of the surrogate model approach were examined. Accordingly, Table 5 lists the performance results of the surrogate models created using the RBF and KRG methods.

Table 5. Surrogate Model Performance Results

Model	Accuracy	Precision	Recall	F1-score
RBF	0.9778	0.9764	0.9776	0.9768
KRG	0.9389	0.9371	0.9352	0.9360

According to the data in Table 5, the RBF and KRG models demonstrate impressive results, with performance exceeding 93%, establishing themselves as highly effective surrogate learning methods. The RBF model, in particular, stands out as a highly reliable and successful prediction tool due to its high metric values. Although the KRG model shows slightly lower results compared to the RBF model, it is similarly successful, and both models can be considered to provide consistent and accurate results. Table 6 presents the OvR accuracy and loss graphs, the confusion matrix, and the t-SNE visualizations for the surrogate models.

Table 6. Accuracy/Loss Graphs, Confusion Matrix, and t-SNE Visualizations for Surrogate Models

	RBF Model	KRG Model
Accuracy/Loss Graphs	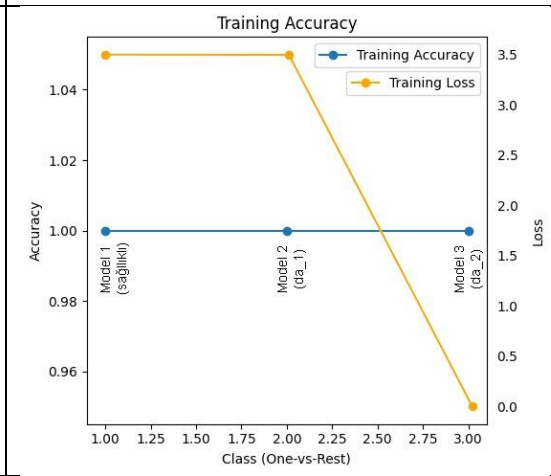	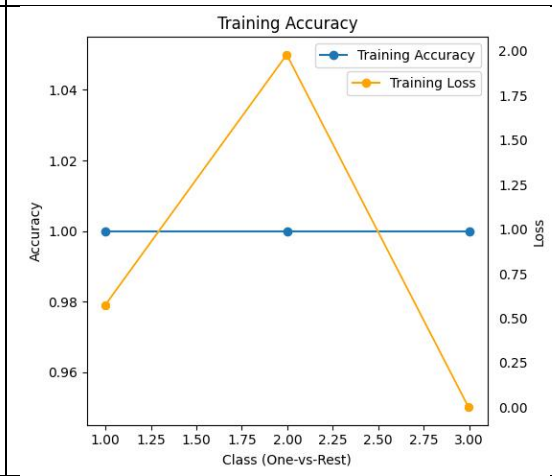
Confusion Matrix	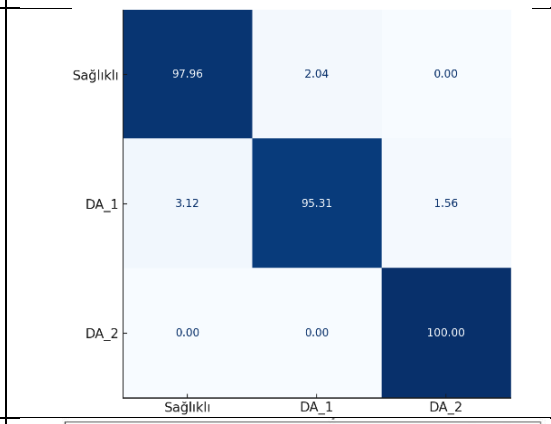	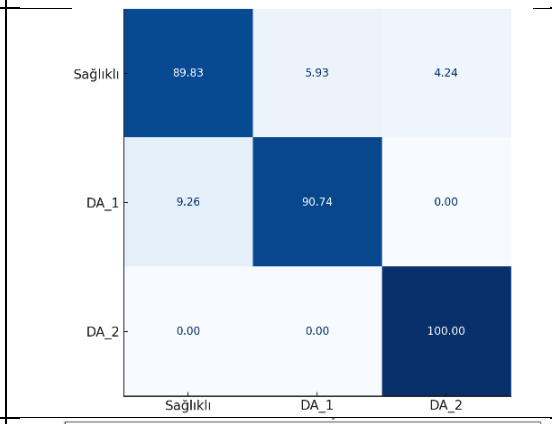
t-SNE Visualizations	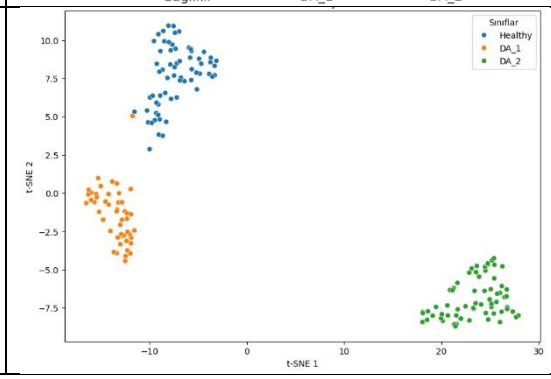	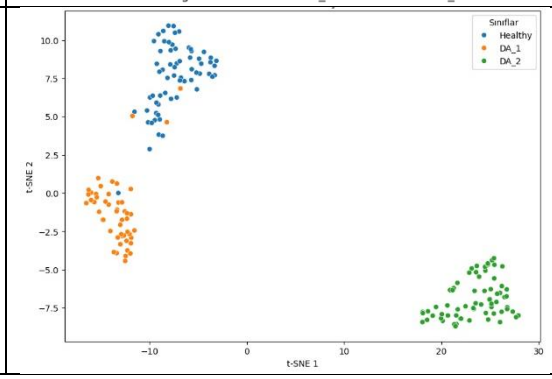

When Table 6 is examined, the accuracy and loss values for the RBF and KRG models are visualized by class. In both models, the accuracy values on a class basis are quite high, indicating the success of the classification models. The loss values are relatively low (0.01%-0.035%), which reflects that the models were well-trained during the optimization process.

Looking at the confusion matrices, the RBF model exhibits a notably high performance in the Healthy class, achieving an accuracy rate of 97.96%. Misclassifications in this class constitute 2.04%, which are shifted to the DA_1 class. For the DA_1 class, an accuracy rate of 95.31% was achieved, with misclassifications of 3.12% into the Healthy class and 1.56% into the DA_2 class. In the DA_2 class, a perfect accuracy rate of 100% was achieved, with no misclassifications. Overall, the RBF model demonstrates high performance across all classes, although slightly more misclassifications are observed in the DA_1 class compared to other classes.

For the KRG model, the accuracy in the Healthy class drops to 89.83%, with misclassifications of 5.93% into the DA_1 class and 4.24% into the DA_2 class. The DA_1 class achieved 90.74% accuracy, with misclassifications of 9.26% into the Healthy class. Similar to the RBF model, the DA_2 class achieved a perfect accuracy rate of 100%, with no misclassifications. The KRG model, however, exhibits lower accuracy rates in the Healthy and DA_1 classes compared to the RBF model, while both models perform perfectly in the DA_2 class.

Additionally, the table includes a visualization of class separability using t-SNE, showing that the DA_2 and Healthy classes are distinctly observed as separate groups. Figure 8 presents a collective overview of the

performance results for individual deep learning and surrogate models.

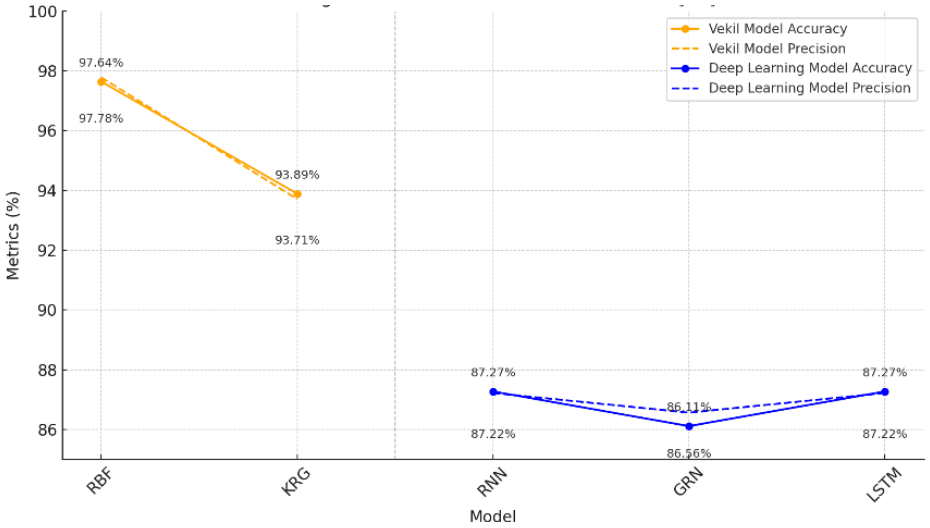

Figure 8. Performance results for all models

In Figure 8, a significant distinction is observed between surrogate models and individual deep learning models. When evaluated based on metrics such as Accuracy and Precision, the results clearly reveal the strengths and weaknesses of the models. Surrogate models (RBF and KRG) generally provide higher accuracy and precision values compared to other methods.In particular, the RBF model demonstrated the highest performance among all examined models, with an accuracy of 97.78% and a precision of 97.64%. The KRG model followed closely, achieving an accuracy of 93.71% and a precision of 93.89%. These findings support the capability of surrogate models to deliver high classification performance and accuracy on large datasets. Moreover, the advantages of surrogate models, such as fast computation capacity and low resource requirements, highlight their effectiveness as a dynamic alternative for use in evolving datasets.

5. RESULTS

This study revealed that, as a result of performance analysis of different classification models for the diagnosis of imbalance faults in asynchronous motors, surrogate learning models (RBF and KRG) achieved superior success compared to deep learning models (RNN, GRU, LSTM). The RBF model exhibited the highest performance with an accuracy of 97.78% and a precision of 97.64%, showing an increase of 12.11% in accuracy and 11.93% in precision compared to deep learning models. Similarly, the KRG model achieved notable success with an accuracy of 93.89% and a precision of 93.71%, increasing the accuracy by 6.67% and the precision by 7.44%.

In particular, the RBF model reached 100% accuracy in the DA_2 class, enabling a clear separation of this class from the others. This proves the RBF model's success in reducing ambiguity between classes. In contrast, deep learning models made less distinct separations between the Healthy and DA_1 classes, and the highest-performing models, RNN and LSTM, showed lower performance with 87.22% accuracy and 87.23% precision. The GRU model, with an accuracy rate of 86.11%, produced weaker results compared to the other models.

This study provides a comprehensive evaluation not only in terms of classification performance but also regarding practical parameters such as computational cost, data requirement, and model generalizability. The ability of surrogate models to provide high accuracy even in cases of class ambiguity increases their potential for use in industrial environments. However, the sensitivity of deep learning models to data volume and their tendency for weak separation among complex classes make it necessary to support these models with hybrid structures. In future studies, it is planned to test the proposed methods on different motor types (e.g., squirrel cage motors, synchronous motors) and adapt them to the diagnosis of different fault types (e.g., bearing fault, misalignment, eccentricity). Furthermore, real-time tests will be conducted under field conditions to evaluate the operational agility and reliability levels of these models. It is also aimed to further improve classification performance and reduce training time by testing hybrid models (e.g., GRU + RBF).

REFERENCES

[1] Yeh, C. C., Sizov, G. Y., Sayed-Ahmed, A., Demerdash, N. A., Povinelli, R. J., Yaz, E. E., & Ionel, D. M. (2008). A reconfigurable motor for experimental emulation of stator winding interturn and broken bar faults in polyphase induction machines. IEEE tra.

[2] Peroutka, Z., Glasberger, T., & Janda, M. (2009, September). Main problems and proposed solutions to induction machine drive control of multisystem locomotive. In 2009 IEEE Energy Conversion Congress and Exposition (pp. 430-437). IEEE..

[3] Hughes, A., & Drury, B. (2019). Electric motors and drives: fundamentals, types and applications. Newnes..
[4] Rangel-Magdaleno, J., Ramirez-Cortes, J., & Peregrina-Barreto, H. (2013, May). Broken bars detection on induction motor using MCSA and mathematical morphology: An experimental study. In 2013 IEEE International Instrumentation and Measurement Technology Co.
[5] Sen, P. C. (2021). Principles of Electric Machines and Power Electronics, International Adaptation. John Wiley & Sons..
[6] Liu, Y., & Bazzi, A. M. (2017). A review and comparison of fault detection and diagnosis methods for squirrel-cage induction motors: State of the art. ISA transactions, 70, 400-409..
[7] Chen, C., & Mo, C. (2004). A method for intelligent fault diagnosis of rotating machinery. Digital Signal Processing, 14(3), 203-217..
[8] Talhaoui, H., Menacer, A., Kessal, A., & Tarek, A. (2018). Experimental diagnosis of broken rotor bars fault in induction machine based on Hilbert and discrete wavelet transforms. The International Journal of Advanced Manufacturing Technology, 95(1), 1399.
[9] Boldea, I. (2020). Induction Machines Handbook: Transients, Control Principles, Design and Testing. CRC press..
[10] Jigyasu, R., Sharma, A., Mathew, L., & Chatterji, S. (2018, June). A review of condition monitoring and fault diagnosis methods for induction motor. In 2018 Second International Conference on Intelligent Computing and Control Systems (ICICCS) (pp. 1713-17.
[11] Nandi, S., Bharadwaj, R., Toliyat, H. A., & Parlos, A. G. (1999, October). Study of three phase induction motors with incipient rotor cage faults under different supply conditions. In Conference Record of the 1999 IEEE Industry Applications Conference. Th.
[12] Nandi, S., Toliyat, H. A., & Li, X. (2005). Condition monitoring and fault diagnosis of electrical motors—A review. IEEE transactions on energy conversion, 20(4), 719-729..
[13] Aydın, Ö., & Akın, E. (2024). Kırık Rotor Çubuğu Arızalarının Belirlenmesinde Derin Öğrenme Yaklaşımları ve Motor Akım İmza Analizi. Türk Doğa ve Fen Dergisi, 13(3), 1-7..
[14] Hassan, O. E., Amer, M., Abdelsalam, A. K., & Williams, B. W. (2018). Induction motor broken rotor bar fault detection techniques based on fault signature analysis–a review. IET Electric Power Applications, 12(7), 895-907..
[15] Dias, C. G., & Pereira, F. H. (2018). Broken rotor bars detection in induction motors running at very low slip using a Hall effect sensor. IEEE Sensors Journal, 18(11), 4602-4613..
[16] Dişli, F., Gedikpınar, M., & Sengur, A. (2023). Deep transfer learning-based broken rotor fault diagnosis for Induction Motors. Turkish Journal of Science and Technology, 18(1), 275-290..
[17] Aydin, I., & Akin, E. (2024, July). Multi-sensory Fault Diagnosis of Broken Rotor Bars Using Transfer Learning. In International Conference on Intelligent and Fuzzy Systems (pp. 349-356). Cham: Springer Nature Switzerland..
[18] Gao, Z., Cecati, C., & Ding, S. X. (2015). A survey of fault diagnosis and fault-tolerant techniques—Part I: Fault diagnosis with model-based and signal-based approaches. IEEE transactions on industrial electronics, 62(6), 3757-3767..
[19] Tariq, M. F., Khan, A. Q., Abid, M., & Mustafa, G. (2018). Data-driven robust fault detection and isolation of three-phase induction motor. IEEE Transactions on Industrial Electronics, 66(6), 4707-4715..
[20] Liu, T., Luo, H., Kaynak, O., & Yin, S. (2019). A novel control-performance-oriented data-driven fault classification approach. IEEE Systems Journal, 14(2), 1830-1839..
[21] Doğan, Z. (2012). Ayrıklaştırma yöntemleri ve yapay sinir ağı kullanarak asenkron motorlarda arıza teşhisi (Doctoral dissertation, Marmara Universitesi (Turkey))..
[22] Gundewar, S. K., & Kane, P. V. (2021). Condition monitoring and fault diagnosis of induction motor. Journal of Vibration Engineering & Technologies, 9, 643-674..
[23] Guo, C., Al-Shudeifat, M. A., Yan, J., Bergman, L. A., McFarland, D. M., & Butcher, E. A. (2013). Application of empirical mode decomposition to a Jeffcott rotor with a breathing crack. Journal of Sound and Vibration, 332(16), 3881-3892..
[24] Dişli, F., Gedikpınar, M., & Sengur, A. (2023). Kırık Rotor Çubuğu Sayısının Ampirik Mod Ayrışımı ve Makine Öğrenmesi Yaklaşımları İle Belirlenmesi. Fırat Üniversitesi Mühendislik Bilimleri Dergisi, 35(2), 783-795..
[25] Rangel-Magdaleno, J., Peregrina-Barreto, H., Ramirez-Cortes, J., Morales-Caporal, R., & Cruz-Vega, I. (2016). Vibration analysis of partially damaged rotor bar in induction motor under different load condition using DWT. Shock and Vibration, 2016(1), 3530.
[26] Henao, H., Capolino, G. A., Fernandez-Cabanas, M., Filippetti, F., Bruzzese, C., Strangas, E., ... & Hedayati-Kia, S. (2014). Trends in fault diagnosis for electrical machines: A review of diagnostic techniques. IEEE industrial electronics magazine, 8(2),.
[27] Rapur, J. S., & Tiwari, R. (2017). Experimental time-domain vibration-based fault diagnosis of centrifugal pumps using support vector machine. ASCE-ASME Journal of Risk and Uncertainty in Engineering Systems, Part B: Mechanical Engineering, 3(4), 044501..
[28] Yang, H., Mathew, J., & Ma, L. (2005). Fault diagnosis of rolling element bearings using basis pursuit. Mechanical Systems and Signal Processing, 19(2), 341-356..
[29] Jigyasu, R., Shrivastava, V., Singh, S., & Bhadoria, V. (2022, April). Transfer learning based bearing and rotor fault diagnosis of induction motor. In 2022 2nd International Conference on Advance Computing and Innovative Technologies in Engineering (ICAC.

[30] Li, X., Zhang, W., Ding, Q., & Li, X. (2019). Diagnosing rotating machines with weakly supervised data using deep transfer learning. IEEE transactions on industrial informatics, 16(3), 1688-1697..
[31] Bhosekar, A., & Ierapetritou, M. (2018). Advances in surrogate based modeling, feasibility analysis, and optimization: A review. Computers & Chemical Engineering, 108, 250-267..
[32] Jiang, P., Zhou, Q., Shao, X., Jiang, P., Zhou, Q., & Shao, X. (2020). Surrogate-model-based design and optimization (pp. 135-236). Springer Singapore..
[33] Zhou, Q., Wang, Y., Choi, S. K., Jiang, P., Shao, X., & Hu, J. (2017). A sequential multi-fidelity metamodeling approach for data regression. Knowledge-Based Systems, 134, 199-212..
[34] Mohammadi, S., Bui, V. H., Su, W., & Wang, B. (2024). Surrogate Modeling for Solving OPF: A Review. Sustainability, 16(22), 9851..
[35] Lu, Z., Lv, Y., & Ouyang, H. (2019). A super-harmonic feature based updating method for crack identification in rotors using a kriging surrogate model. Applied Sciences, 9(12), 2428..
[36] Chevalier-Jabet, K., Verma, L., & Kremer, F. (2024). Using a surrogate model for the detection of defective PWR fuel rods. Annals of Nuclear Energy, 209, 110779..
[37] Han, F., Guo, X., & Gao, H. (2013). Bearing parameter identification of rotor-bearing system based on Kriging surrogate model and evolutionary algorithm. Journal of Sound and Vibration, 332(11), 2659-2671..
[38] Yang, H., Bai, X., & Wang, C. (2024). Research on surrogate models and optimization of equipment dynamics for complex systems. AIP Advances, 14(3)..
[39] Krige, D. G. (1951). A statistical approach to some basic mine valuation problems on the Witwatersrand. Journal of the Southern African Institute of Mining and Metallurgy, 52(6), 119-139..
[40] Hardy, R. L. (1971). Multiquadric equations of topography and other irregular surfaces. Journal of geophysical research, 76(8), 1905-1915..
[41] Dyn, N., Levin, D., & Rippa, S. (1986). Numerical procedures for surface fitting of scattered data by radial functions. SIAM Journal on Scientific and Statistical Computing, 7(2), 639-659..
[42] Myers, R. H., Montgomery, D. C., & Anderson-Cook, C. M. (2016). Response surface methodology: process and product optimization using designed experiments. John Wiley & Sons..
[43] CHENG, Mengyu, et al. A review of data-driven surrogate models for design optimization of electric motors. IEEE Transactions on Transportation Electrification, 2024..
[44] Poudel, S. (2023, August 28). Recurrent neural network (RNN) architecture explained. Medium. URL : https://medium.com/@poudelsushmita878/recurrent-neural-network-rnn-architecture-explained-1d69560541ef , Last Access Date : 10.12.2024.
[45] Akbari Asanjan, A., Yang, T., Hsu, K., Sorooshian, S., Lin, J., & Peng, Q. (2018). Short-term precipitation forecast based on the PERSIANN system and LSTM recurrent neural networks. Journal of Geophysical Research: Atmospheres, 123(22), 12-543..
[46] Dey, P., Hossain, E., Hossain, M. I., Chowdhury, M. A., Alam, M. S., Hossain, M. S., & Andersson, K. (2021). Comparative analysis of recurrent neural networks in stock price prediction for different frequency domains. Algorithms, 14(8), 251..
[47] Anishnama. (2023, May 4). Understanding gated recurrent unit (GRU) in deep learning. Medium. URL : https://medium.com/@anishnama20/understanding-gated-recurrent-unit-gru-in-deep-learning-2e54923f3e2 , Last Access Date : 10.12.2024.
[48] CHUNG, Junyoung, et al. Empirical evaluation of gated recurrent neural networks on sequence modeling. arXiv preprint arXiv:1412.3555, 2014..
[49] Rojas, C. A. (2024, April 8). What is LSTM (Long Short Term Memory)? Medium. URL : https://blog.ai-evergreen.club/what-is-lstm-long-short-term-memory-221099a981f7 , Last Access Date : 10.12.2024.
[50] Elmaz, F., Eyckerman, R., Casteels, W., Latré, S., & Hellinckx, P. (2021). CNN-LSTM architecture for predictive indoor temperature modeling. Building and Environment, 206, 108327.
[51] HOCHREITER, Sepp; SCHMIDHUBER, Jürgen. Long short-term memory. Neural computation, 1997, 9.8: 1735-1780..
[52] LALE, Timur; YÜKSEK, Gökhan. Identification and Classification of Turn ShortCircuit and Demagnetization Failures in PMSM Using LSTM and GRU Methods. Bulletin of the Polish Academy of Sciences Technical Sciences, 2024, e15158-e15158.
[53] SMT: Surrogate Modeling Toolbox, https://smt.readthedocs.io/en/latest/ , Last Access Date : 26.12.2024.

Volume 14, Issue 2, Page 124-133, 2025 https://doi.org/10.46810/tdfd.1628295 Research Article

BİNGÖL UNIVERSITY

Türk Doğa ve Fen Dergisi
Turkish Journal of Nature and Science
www.dergipark.gov.tr/tdfd

Comparative Review of Graphical User Interface Based Data Visualization Tools

Faruk AKSOY [1*], Mehmet ÖZDEM [2], Resul DAŞ [3]

[1] Dicle University, Ergani Vocational School, Department of Computer Technologies, Diyarbakır, Türkiye
[2] Türk Telekom, Ankara, Türkiye
[3]Fırat University, Technology Faculty, Department of Software Engineering, Elazığ, Türkiye
Faruk AKSOY ORCID No: 0000-0002-1076-5248
Mehmet Özdem ORCID No: 0000-0002-2901-2342
Resul DAŞ ORCID No: 0000-0002-6113-4649

**Corresponding author: faruk.aksoy@dicle.edu.tr*

(Received: 28.01.2025, Accepted: 28.04.2025, Online Publication: 27.06.2025)

Keywords
Data visualization, Data visualization tools, Big data, Data analytic, Interactive visualization software

Abstract: Due to the dizzying development of technology, the concept of big data has given way to huge data. With digital transformation and the Internet of Things, organizing the increasing amount of data and deriving meaningful results has become much more valuable and difficult. Along with this difficulty, visualization tools play an effective role in producing meaningful results faster and more accurately. In this article, a comprehensive literature review has been conducted on data visualization tools with graphical user interfaces that have wide application areas in different disciplines, and 15 widely known data visualization tools are presented comparatively. The important findings obtained as a result of this research and the trends that will be needed in new visualization tools are presented in the conclusion section. The use of complex methods by integrating artificial intelligence to produce meaningful results from data has great potential in the field of data visualization. This study aims to make significant contributions to the studies to be conducted in the field of data visualization.

Grafik Kullanıcı Arayüz Tabanlı Görselleştirme Araçlarının Karşılaştırmalı İncelenmesi

Anahtar Kelimeler
Veri görselleştirme, Veri görselleştirme araçları, Büyük veri, Veri analitiği, Etkileşimli görselleştirme yazılımı

Öz: Teknolojinin başdöndürücü şekildeki gelişimine bağlı olarak büyük veri kavramı yerini huge veriye bıraktı. Dijital dönüşüm ve Nesnelerin interneti ile birlikte artan veri miktarının organize edilip anlamlı sonuçlar çıkarılması çok daha kıymetli ve zor bir hale gelmiştir. Bu zorlukla birlikte, anlamlı sonuçların daha hızlı ve doğru üretilmesi için görselleştirme araçları etkili bir rol oynamaktadır. Bu makale çalışmasında, farklı disiplinlerde, geniş uygulama alanlarına sahip olan grafik kullanıcı arayüzüne sahip veri görselleştirme araçları hakkında kapsamlı bir literatür araştırması yapılmış, yaygın olarak bilinen 15 adet veri görselleştirme aracı, karşılaştırmalı olarak sunulmuştur. Bu araştırma sonucunda elde edilen önemli bulgular ve yeni görselleştirme araçlarında ihtiyaç duyulacak yönelimler sonuç bölümünde sunulmuştur. Verilerden anlamlı sonuçlar üretmek için yapay zekâ ile kompleks yöntemlerin entegre edilerek kullanılması, veri görselleştirme alanında büyük bir potansiyel barındırmaktadır. Bu çalışma ile verilerin görselleştirilmesi alanında yapılacak çalışmalara, önemli katkılar sunulması hedeflenmektedir.

1. INTRODUCTION

With the development of information and communication technologies, the amount of data in the digital environment is increasing significantly. Data is obtained from many digital [1] applications such as web-based platforms, social media applications, smart solutions developed within the scope of the Internet of Things (IoT) [2] and data received from multiple wireless sensors [3–5]. These structures, called big data, are stored in critical data centers [6] [7]. The continuation of modern life continues with the production and consumption of this data [8]. For this reason, it is of great importance that the data is obtained in a healthy way, evaluated and interpreted correctly. In this dense and continuous data flow, the best way to correctly understand the

relationships between the data and present them to users so that they can correctly evaluate the types as in Figure 1 is to visualize the data. In addition, the field of data visualization is also developing with the advancements in the fields of database, graphics and visualization [9] .

The main purpose of data visualization is to represent information more intuitively and effectively using different graphics [10,11]. Effectively represented data facilitates decision-making stages and in this way, analysts can make more accurate decisions with visual support. In the 2019 Future of Partnership report, FSN Publishing Limited [12], states that 81% of CFOs (Chief Financial Officer) are looking for future technology that will help data visualization to make improvements in business partnerships [12]. On the other hand, visualization of big data becomes difficult due to its large volume [13].

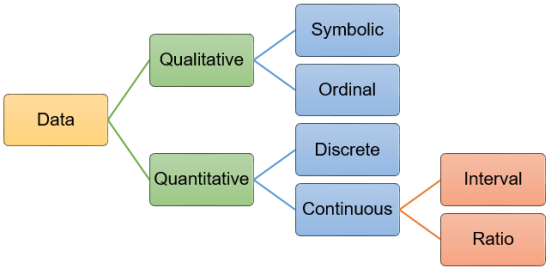

Figure 1. Data Types for Visualization

Data visualization focuses on dealing with unstructured high-dimensional data such as textual, numerical, financial and multimedia data, both before and today in the era of generative artificial intelligence. Data visualization tools try to visualize the endless flow of information collected by intelligent systems in order to increase the value of data with the meaningful insights they provide in the IoT field. Appropriate mechanisms are implemented to ensure that the visualized information is accurate and reliable and to detect these anomalies [14]. For this purpose, there are studies where a large number of visualization libraries are used and examined [15]. As a result of the extensive literature review, it has been determined that the studies on GUI-based data visualization tools are very narrow in scope. For this reason, a comprehensive review is needed. This study aims to close an important gap in the literature regarding GUI-based data visualization tools.

The biggest challenge when working with big data is not only to process the volume of data, but also to analyze different types of data effectively. Big data refers to the collection of large, complex, unstructured and continuous data collected from multiple and often disparate data sources [16]. While the main idea behind IoT is that every object gets an IP address and is connected to other things, Big Data focuses on managing the enormous amounts of data generated from IoT usage [14]. While these processes are carried out, we encounter features such as volume, variety and speed [17] [18]. In order to deal with this data efficiently and effectively, the focus is on capturing, storing, processing and visualizing the data with highly scalable, distributed architectural infrastructures. This study consists of 4 main sections. In Section 2, visualization tools developed and used within the scope of data visualization tools are presented. Studies using data visualization tools are examined in Section 3. The application areas and study results of these studies are summarized and presented in table 2. In section 4, the tools examined within the scope of the article are evaluated in terms of needs and trends obtained from the studies. In addition, suggestions are made for future studies.

2. DATA VISUALIZATION TOOLS

Visualization technologies are applied strongly on data for different purposes. For this purpose, visualizations can be made with both programming languages and certain tools without using any language. Visualization processes are also applied in different areas such as smart cities and big data management. It is seen in the literature that they are applied in very different disciplines in terms of application areas. For example, studies have been conducted in which the author's collaboration relationships are presented with a two-dimensional image according to the minimum spanning tree algorithm to visualize the collaboration of an author with his/her collaborators [19]. When these studies are performed on citations, implicit relationships between authors can also be discovered. In addition, there are studies in various fields such as education [20], Data Analytics [21,22], Internet of Things (IoT) [23], Urban Planning [24], Health [25], Biotechnology [26], Geography [27], Cyber Security [28] and Smart Cities [29] in web-based searches [30], visualization of analysis types [31], data research [32] and visual analysis and discovery of data [33].

Visualization tools enable users to transform each element in the data into interactive visuals. Using these tools, users who do not have coding skills can spend more time on design decisions instead of the implementation process [34] . The visualization tools examined in this study are GUI-based tools that do not require programming language knowledge. Tools where coding and programming language libraries are actively used by the user are ignored in this study.

2.1. GUI Based Tools

This section introduces data visualization tools with graphical user interfaces. These tools are also effectively used as business intelligence tools under the field of data science. They are designed to meet the needs of users without programming knowledge, such as data analysis, filtering, visualization, and reporting. The classification of visualization tools in this group is presented in the table 1.

Table 1. GUI-based data visualization tools with outstanding features

Ref	Tool	Release Year	Data Sources	Platforms	Data Import Features	Customization and Advanced Features	Support	Advantages	Disadvantages
[35]	Tableau	2003	csv, xls, json, pdf	Desktop, Mobile, Web	Fast Data Upload, Multiple Data Sources	Advanced Visualization Options	Cloud and Local	Powerful visualization tools, wide data source and AI support	Expensive, time-consuming to learn, complex reporting
[36]	Power BI	2014	csv, xls, json, pdf	Desktop, Mobile, Web	Fast Data Upload, Multiple Data Sources	Advanced Analysis and Reporting	Cloud and Local	Affordable, strong data analysis and reporting features, AI support	Limited features in web version, performance issues
[37]	Looker Studio	2016	csv, xls, json, xml, sql	Web	Multiple Data Sources, Data Source Integration	Customizable Reports	Cloud-Based	Integration with Google ecosystem, free basic version, AI support	Cloud-dependent, limited visualization options
[38]	Amazon Quicksight	2016	csv, xls, json, tsv	Web, Mobile	Multiple Data Sources, Data Source Integration	Fast Visualization	Fully Cloud-Based	Integration with AWS, quick setup, AI support	Limited data sources, steep learning curve
[39]	Oracle Analytics	2019	csv, xls, json, xml	Web, Mobile	Multiple Data Sources, SQL Integration	Advanced Analysis, Database Support	Cloud-Based	Powerful data analysis tools with AI, integration with Oracle	High cost, complex usage
[40]	Sisense	2010	csv, xls, sql	Web, Mobile	Multiple Data Sources, Database Integration	Advanced Data Modeling	Cloud-Based	High scalability, powerful data modeling and AI support	Complex setup, steep learning curve
[41]	Biovia Pipeline Pilot	2018	csv, xls	Desktop	Limited Data Source Integration	Customizable Reports	Local Storage	Scientific data integration, customization possibilities	Desktop-only, limited mobile access
[42]	Domo	2010	csv, json, xml, xls	Web	Fast Data Upload, Multiple Data Sources	Advanced Visualization Options	Fully Cloud-Based	Easy to use, strong integration features	Expensive, limited free version
[43]	Infogram	2012	csv, json, xls	Web, Mobile	Fast Data Upload, Limited Data Sources	Simple Visualization	Cloud-Based	Fast and simple visualization, templates	Limited customization, poor data management
[44]	Carto	2012	csv, GeoJSON, GeoPackage, kml, kmz, tab	Web	Geospatial Data Integration	Map Visualization Options	Fully Cloud-Based	Powerful map visualization, geospatial data support	Only for geospatial data, complex to use
[45]	RAW Graphs	2013	tsv, csv, dsv, json	Web	Fast Data Upload	Simple Visualization	Local Storage	Fast and free, simple visualizations	Limited visualization, inadequate data processing
[46]	Visualize Free	2016	csv, txt, xls	Web	Fast Data Upload	Simple Visualization	Local Storage	Free, fast to use	Limited visualization, poor data management
[47]	Dundas BI	2001	csv, xml, json, SQL, Oracle	Web, Mobile, Embedded	Multiple Data Sources, SQL Integration	Advanced Visualization and Reporting	Cloud-Based	Advanced features, multi-platform support	High cost, steep learning curve
[48]	Qlik Sense	2014	csv, xls, json, sql, odbc	Desktop, Mobile	Fast Data Upload, Multiple Data Sources	Dynamic Reporting and Analysis	Cloud-Based	Multi-source data integration, strong analytical capabilities with AI	High cost, steep learning curve
[49]	Kibana	2013	csv, json, log, Elasticsearch	Web, Desktop	Multiple Data Sources, Elasticsearch Integration	Rich Visualization and Search Features	Cloud-Based	Deep integration with Elasticsearch, powerful visualization and search features, AI support	User interface may be complex

2.1.1. Tableau

Tableau is a widely used desktop software for business intelligence and data analysis [50]. It was selected as one of the market leaders for the 12th time in the Gartner Magic Quadrant for Analytics and Business Intelligence Platforms in 2024 [51]. It can work on local and server data files. It supports data file formats such as txt, json, pdf, csv, Microsoft Access, Microsoft Excel. Apart from these, it also offers an interface that can receive data from

various servers (Salesforce, Oracle, Microsoft, Amazon, Google, etc.) online. It also has the ability to run the desired functions by determining the x and y axes over the fields that can be determined as dimension and measure. It also has the ability to work with maps. For example, in a study conducted to view online shopping preferences and users' shopping activities within the scope of web content mining, [52] was used. In addition, eBay, an auction company, sells products to millions of active users every month and as a result, produces a huge amount of data. eBay uses the Tableau tool to make all this data understandable and visualize big data. Tableau has the ability to transform large and complex data sets into intuitive images. Apart from this, eBay employees can also visualize their customers' search behavior with this tool to track customer feedback and conduct sentiment analysis.

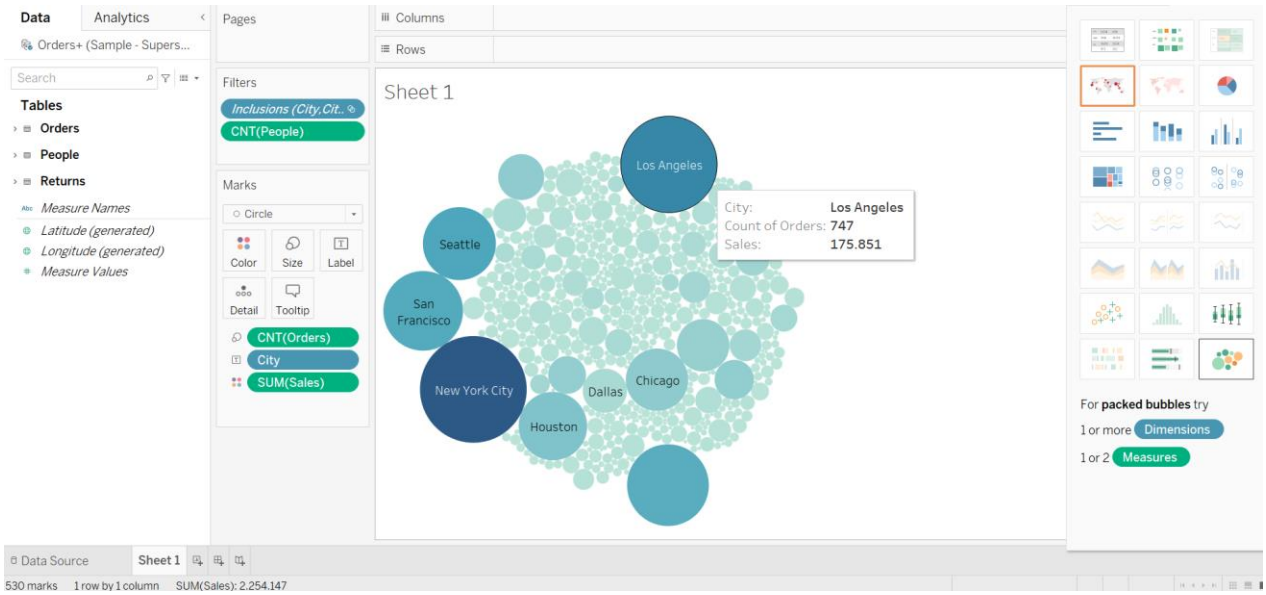

Figure 2. Packed bubbles chart with Tableau tool

2.1.2. PowerBI

It was added to Microsoft Excel in 2011 under the name "Power Pivot". It emerged as a standalone application under the name "Power BI" in 2014. With its easy-to-use interface and drag-and-drop feature, it can transform complex data into meaningful reports. Its success in visualizing the data in these reports has also been an important factor in the preference of the application. In the analytics and business intelligence platform report prepared by Gartner for 2024, Microsoft Power BI , Tableau and Qlik [51] were selected as market leaders.

2.1.3. Looker studio

It is a free application, previously known as Google Data Studio. It allows customization and reporting of data. It is offered within the Google Analytics 360 product suite, which was introduced on March 15, 2016. It is a free online tool for transforming data into dashboards. Looker Studio Pro offers advanced entity management, team collaboration capabilities, and access to technical support for businesses [37] .

2.1.4. Amazon quicksight

It enables data understanding by asking natural language questions, exploring through interactive dashboards, and automatically searching for machine learning-powered patterns and outliers [38]. Amazon QuickSight is built on "SPICE", a **S**uper-fast, **P**arallel, **I**n-memory **C**alculation **E**ngine. Built entirely for the cloud, SPICE uses a combination of columnar storage and in-memory technologies to run interactive queries on large datasets and get fast answers. It enables organizations to scale their business analytics capabilities to hundreds of thousands of users and delivers fast, responsive query performance using a robust in-memory engine (SPICE) [38].

2.1.5. Oracle analytics

Oracle Analytics Cloud and Oracle Analytics Desktop are business-oriented products that load and query data sources, create visualizations to analyze data, create and work with workbooks, and import and export workbooks [39] . Oracle Analytics Cloud was designed from the ground up to be a globally available cloud service. Oracle's suite of analytics applications, Fusion Analytics, is advancing the way organizations deploy analytics.

2.1.6. Sisense

Sisense offers a wide range of BI tools, including data modeling, data visualization, and AI analytics. Founded in 2004 in Tel Aviv, Sisense launched its first product in 2010. In 2019, Sisense acquired Periscope, a fully SaaS company. Sisense Fusion, an AI-driven analytics platform designed to make data analytics simple, scalable, and actionable, was introduced in 2021. It was named a Visionary in the 2022 Gartner® Magic Quadrant™ for Analytics and Business Intelligence Platforms and a niche player in the 2024 version of the same report [51]. The platform is designed to be easily scalable and includes security features such as attack surface monitoring and

disaster recovery. GitLab is used by over 2,000 global companies including Nasdaq, Rolls Royce, Seismic, ZoomInfo and Philips Healthcare [53].

2.1.7. Biovia pipeline pilot

Pipeline Pilot, a desktop software program sold by Dassault Systèmes for processing and analyzing data, initially used in the natural sciences, has expanded its core ETL and analytics capabilities over time. Pipeline Pilot supports end-to-end automated workflow creation and execution. It can connect to internal and external data sources. It can access and analyze all types of scientific data. It can connect to external data sources of types Sql/NoSql/Mql, tabular data, structured data (json, xml, etc.), office documents (ppt, xls, etc.), pdf, Streaming (Kafka), 3DExperience Platform, REST/SOAP/HTML/S3 via an extensive API library. It also includes ready-to-use connections to various 3rd party databases [41].

2.1.8. Domo

Domo's data visualization software has an intuitive dashboard. It also automates reporting, allowing you to present an automatically updated report. Domo also works on mobile platforms. It is a cloud-based platform that offers business intelligence tools tailored to a variety of industries, including financial services, healthcare, manufacturing, and education, and roles such as CEOs, sales, BI specialists, and IT professionals. Most of the work on Domo can be done without using SQL [42].

2.1.9. Infogram

Infogram is a web-based application for creating graphs and charts related to data. Registered users can upload their own data files (.xls, .csv, .xlsx) to the website and also export data to GoogleDrive, Dropbox, OneDrive or JSON stream. Personalized chart suggestions are also provided with AI support. The problem with Infogram is that the project is created with a public URL, so there is no data privacy. If users want to protect the privacy of their data, the only way is to become a paid member [43]. A membership is also required to download the visualizations prepared with the online editor.

2.1.10. Carto

Founded in Madrid in 2012 by Javier de la Torre and Sergio Álvarez, CARTO has become the world's leading location intelligence platform, enabling hundreds of thousands of users to unlock the power of spatial analysis. It's a cloud-based tool that can visualize without coding. Data scientists, developers, and analysts use CARTO to optimize business processes and predict future outcomes with the power of spatial data science. It's a cloud computing platform that provides GIS, web mapping, and spatial data science tools for businesses in real estate, financial services, telecommunications, government, and more. CARTO is a location intelligence platform that enables organizations to use spatial data and analytics for more efficient delivery routes, better behavioral marketing, strategic store layouts, and more [54] [44].

2.1.11. RAW graphs

RAW Graphs is an open web-based tool that can be used directly without registration. It supports data formats such as tsv, dsv, csv, json or xls files, even online data from a public API or public cloud platform. It provides users with 21 types of graph models for data visualizations and also supports creating custom vector-based visualizations natively on top of the D3.js library by M. Bostock. They can also export the created graph as a vector (svg) or raster (png) image, or embed their graphs in web pages using the codes automatically generated in raw graphs [55] [45].

2.1.12. Visualize free

Visualize Free is a free and lightweight web-based application that requires registration before use. Users can upload data files (xls, xlsx, csv or txt) with a 5 MB file limit. Users can easily visualize their data with multiple charts by dragging and dropping data to shape the size of the chart. Free visual analysis is provided so that users can compile detailed analysis of the uploaded data. Charts created from data uploaded to Visualize Free can be downloaded and shared in pdf, xls or ppt format [46].

2.1.13. Dundas dashboard

Dundas BI is a data visualization platform that includes integrated dashboards, reporting tools, data analytics, and browser-based business intelligence. It allows end users to create interactive, customizable dashboards and reports, run ad hoc queries, analyze and drill down into their data and performance metrics. The Dundas BI platform allows users to connect and integrate with any data source in real time on any device. Dundas BI is part of insightsoftware [47]. With its touch-based interface and responsive design, it allows users to create and view dashboards and reports on any device from desktop to mobile. The software is designed to be embedded. It provides full customization and integration support through a programmable open API platform offering .NET, REST, and JavaScript APIs. Dundas BI can be installed anywhere and supports a SaaS/Multi-tenant architecture that allows all clients to be on a single server [17].

2.1.14. Qlik sense

Qlik [48] is a visualization software developed by Qlik, which allows users to analyze large amounts of data by visualizing them, and provides interactive reporting, data analysis, visualization, and self-service analysis capabilities, allowing users to work more interactively with data [56]. It can pull data from different data sources (databases, Excel files, cloud storage, etc.) and combine and analyze this data [57]. It uses a special engine called Associative Engine. This engine ties all the data together, allowing users to easily connect and navigate between data. It can work in both local (on-premise) and cloud (Qlik Sense Cloud) environments. It is ranked in the

Leaders category in the 2024 Gartner Magic Quadrant for Analytics and Business Intelligence Platforms [51].

2.1.15. Kibana

Kibana is an open-source data visualization platform that integrates with Elasticsearch [49]. It helps users visualize, analyze, and create reports on Elasticsearch data [58]. Kibana is often used in conjunction with Elasticsearch and Logstash (ELK Stack), as seen in figure 3, where the trio simplifies the data collection, indexing, and visualization processes.

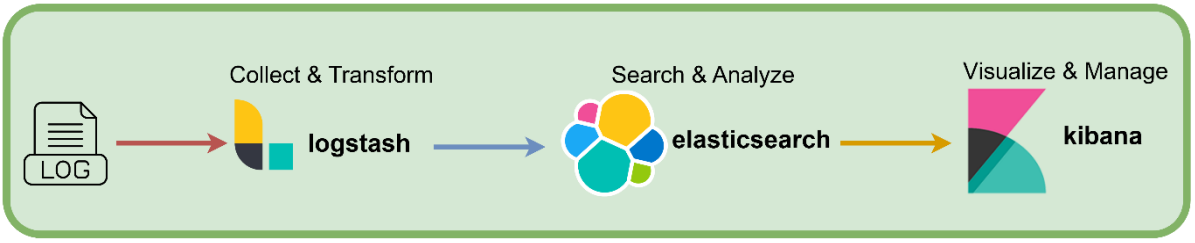

Figure 3. ELK Stack

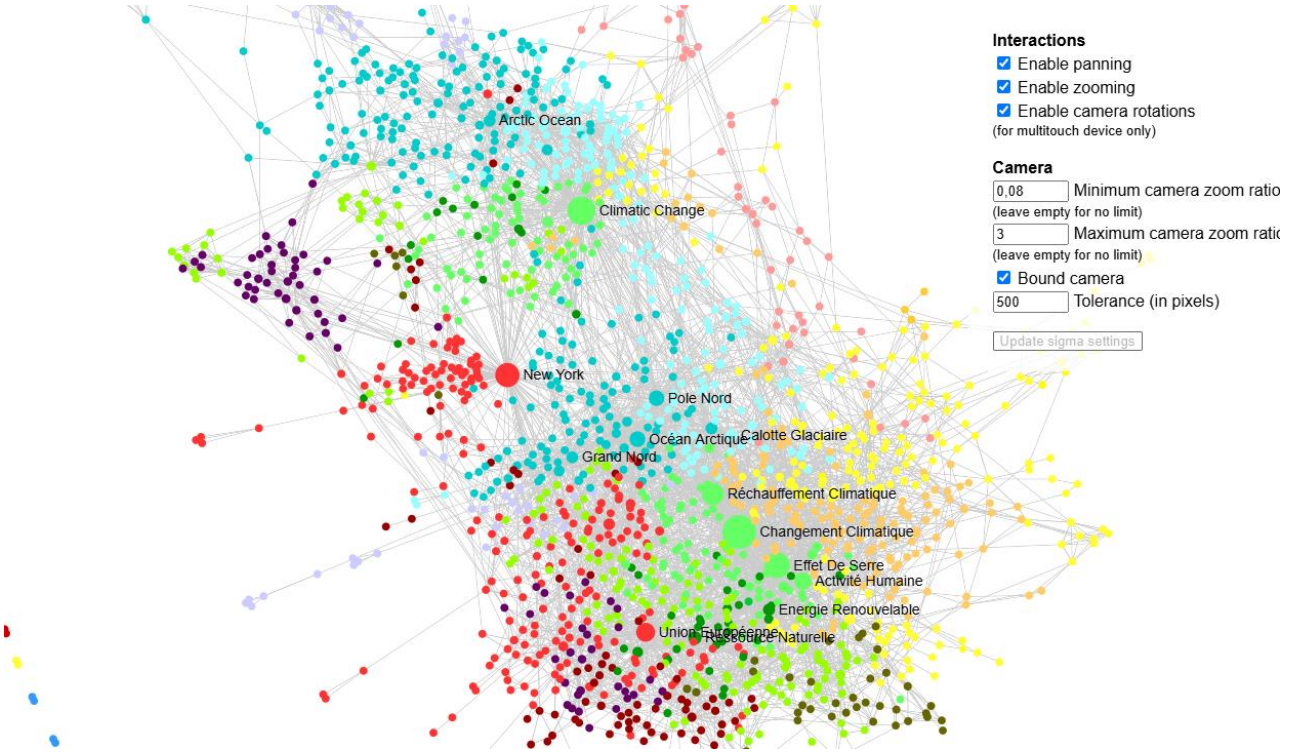

Figure 4. A graph visualization application with Sigma.js

3. GUI-BASED APPLICATIONS EXAMPLES

In this section, studies on the use of data visualization tools with visual user interfaces in the literature are examined and summarized in a table. These studies were obtained by filtering the literature through application-oriented articles.

The application areas of these studies and the diversity and richness of the fields are shown in the table. In addition, the results of these current studies are listed and presented in the table. When the application areas are examined, it is seen that the application examples are concentrated in the fields of Software and Data Analytics, Education and Technology, Environmental Technologies and Internet of Things (IoT), Urban Planning and Data Analytics, Health and Social Sciences, Artificial Intelligence and Data Analytics, Biotechnology and Health, Health and Data Visualization, Geography, Smart Cities and Transportation, Environment and Health, Academic Research and Data Analytics, Industrial Production and Digital Management Systems, Cyber Security and Smart Cities. These studies, which date back to recent years, show that data visualization tools with visual interfaces will be used in studies in many different disciplines in the future. In this context, the methodologies of the relevant studies were examined and the techniques and algorithms used by data visualization tools were evaluated. The analyses conducted reveal how interactive visualization features improve user experience and accelerate decision-making processes. In addition, the effectiveness of data visualization tools used in different disciplines was compared and it was determined in which areas they were more widely preferred. It was seen that the majority of the studies focused especially on big data analytics, machine learning-supported visualizations and real-time data monitoring systems. Based on these findings, it is also seen that there is a great potential in the

field of graph-based visualization of data. Especially in network (graph)-based data visualizations, libraries such as Sigma.js offer powerful and interactive solutions. Sigma.js is widely used in fields such as social network analysis, biological networks, and internet traffic monitoring, and can dynamically visualize large-scale network data. It also provides a flexible structure to make data visualization processes more meaningful with customizable node and edge styles, as seen in Figure 4. With these features, Sigma.js supports decision-making mechanisms by making data analysis processes more intuitive.

Commonly used tools such as Tableau and Power BI have achieved successful results in analytical data engines and education-focused decision support systems. Looker Studio and RAW Graphs have been used in environmental data analysis and health research to reveal the effects of factors such as air pollution on human health. Amazon Quicksight and Carto have provided effective visualization solutions in areas such as urban planning and transportation in the context of smart cities and urban data analytics. In the field of health and biotechnology, the use of tools such as Domo, Oracle Analytics and Biovia Pipeline Pilot is notable. In particular, studies using Oracle Analytics have shown that neuropsychiatric symptoms increase the social costs of dementia, while Domo has emerged as a reliable decision support system for healthcare professionals in Saudi Arabia. In the fields of industrial production and cybersecurity, Qlik Sense has been used to increase the effectiveness of digital management systems, while Kibana has been applied to develop ontological models for analyzing cyber threats in smart cities.

Table 1. Applications of GUI-based visualization tools in literature

Ref.	Date	Tool	Application Field	Conclusion
[59]	2011	Tableau	Development of a custom analytical data engine that integrates with the Tableau data visualization system, focusing on efficient data processing	The developed Tableau Data Engine is shown to provide efficient data processing with real-life visualization scenarios in desktop and server environments.
[20]	2024	Power BI	Development and implementation of a Power BI based interactive data visualization platform	Improving educational decision-making processes
[23]	2024	Looker Studio	Air quality, IoT	Creation of AQuality32 for open source air quality monitoring
[24]	2024	Amazon Quicksight	Urban visual analytics	A roadmap for the effective development and improvement of urban visual analytics systems
[60]	2024	Oracle Analytics	Determining the social costs of dementia and neuropsychiatric symptoms (NPS)	The NPS has been shown to triple the societal costs of dementia, resulting in long-term care services and benefits for more people.
[21,22]	2024,2018	Sisense	Recommendation systems, Developments in visual exploratory data analysis (EDA)	Automatic recommendation systems have achieved significant success for visualization panels, Traditional data exploration tools have evolved in recent years to analyze large data sets.
[26]	2016	Biovia Pipeline Pilot	HIV infection, eye diseases, immunology	In dry eye disease patients with HIV infection, EGF and IP-10 levels were found to be high and GRO levels were found to be low.
[25]	2024	Domo	Health data analytics, visual analytics, decision support systems and health information technologies	DOMO BI visual analytics tool has been found to be the most secure and robust tool for healthcare professionals in Saudi Arabia
[61]	2023	Infogram	Web-based data visualizations, COVID-19 tracking tools, and visual analytics	Dashboards and tracking tools presenting data related to the COVID-19 pandemic face challenges in providing accurate and reliable information to the public due to the lack of data sources and design differences.
[27]	2017	Carto	Visualization of heterogeneous spatiotemporal data (vehicle routes, points of interest, etc.) obtained from embedded sensors in cities	A web-based smart urban visualization system called SURV that provides interactive maps and 3D visualizations using HTML, CSS, Mapbox.js, CARTO.js, and Python
[62]	2024	RAW Graphs	Analyzing the relationship between air pollution and abdominal aortic aneurysm (AAA) using data visualization techniques	Vehicle emissions have a strong temporal relationship with AAA mortality, and air pollution has a similar relationship to cigarette smoking on AAA mortality.
[63]	2018	Visualize Free	Visualization and visual analysis of scientific data	It provides a comprehensive overview of existing data visualization tools, techniques, and systems and proposes new solutions to open problems encountered in academic data visualization.
[29]	2023	Dundas BI	Developing an end-to-end solution based on IoT for smart factories to facilitate data-driven decisions in industrial production.	Successful development of a middleware application that collects data via OPC-UA protocol and integrates with BI toolsy
[64]	2025	Qlik Sense	Increasing the effectiveness of the Digital Shopfloor Management (SFM) system by identifying a suitable platform for managing digital daily meetings.	It demonstrates that a hybrid Digital SFM solution, where Microsoft SharePoint is used as the main platform and Qlik Sense is integrated for data visualization and consolidation, offers a balanced and effective approach.
[28]	2025	Kibana	Development of ontological models to analyze and represent cyber threats in smart city infrastructures (SCI)	This study proposes a framework called Scope that extends UCO and CASE ontologies, enabling better identification, sharing, and analysis of SCI-specific threats, digital evidence, and cybercrimes.

4. CONCLUSION

With the development of IoT, as the number of smart devices increases and IoT networks continue to flow data from various sources, the field of visualization will also develop in a way that is open to innovation and change. This review presents important findings in terms of innovative approaches in the field of data visualization and their effects on user experience. Most of the tools examined accelerate data visualization processes and present complex data sets in an understandable way thanks to their user-friendly graphical interfaces. Especially features such as interactive, 3D visualization and dynamic time series analysis make it easier for users to explore data. Tools such as Tableau, Power BI and Qlik Sense are particularly notable for their drag-and-drop functionality and data integration capabilities. Their ability to work with many different formats regardless of data sources and to produce fast visualizations are among their prominent features. However, some tools still have a high learning curve and technical hurdles. Especially in projects that require big data processing and in-depth modeling and analysis, existing tools often encounter performance issues. In addition, the future of visualization tools will be shaped by their integration with artificial intelligence (AI) and machine learning (ML), in particular. In addition to adding more powerful AI-powered features for data modeling and predictive analysis, the use of generative AI will allow users to visualize not only current data but also future trends, allowing them to make meaningful interpretations. In addition, cloud-based platforms and mobile compatibility are becoming increasingly important. Web-based and mobile visualization tools will increase user flexibility by making it faster and easier to access and share data. Another potential possibility is that the ability of tools to seamlessly connect more data sources will enable more efficient use in big data analytics and real-time data visualizations. The limited flexibility of graphical interfaces is also a limitation for more advanced users. Most tools struggle to offer advanced functionality such as customizable analysis features, advanced data processing techniques, customizable reporting, or dynamic data processing. Furthermore, the lack of data visualization typologies leads to an inability to effectively present data contextually. Performance improvements require optimizing timing and processing capacity when working with large datasets.

In this study, data visualization tools with graphical user interfaces comprehensively examine and the user interaction, effectiveness and limitations of existing tools in data analysis were evaluated. Future developments will enable more sophisticated and contextual analyses in data analysis, supported by AI. The effectiveness of these tools will increase depending on how users interact not only with existing data but also with the broader data ecosystem.

REFERENCES

[1] Mathur V, Saini Y, Giri V, Choudhary V, Bharadwaj U, Kumar V. Weather Station Using Raspberry Pi. 2021 Sixth International Conference on Image Information Processing (ICIIP), Shimla, India: IEEE; 2021, p. 279–83. https://doi.org/10.1109/ICIIP53038.2021.9702687.

[2] Sarker IH. Smart City Data Science: Towards Data-Driven Smart Cities with Open Research Issues. Internet of Things 2022;19:100528. https://doi.org/10.1016/j.iot.2022.100528.

[3] Supekar VS, Ahmadina A. Sensor Data Visualization on Google Maps using AWS, and IoT Discovery Board. 2020 7th International Conference on Internet of Things: Systems, Management and Security (IOTSMS), 2020, p. 1–6. https://doi.org/10.1109/IOTSMS52051.2020.9340202.

[4] Sarker IH. Data Science and Analytics: An Overview from Data-Driven Smart Computing, Decision-Making and Applications Perspective. SN Computer Science 2021;2:377. https://doi.org/10.1007/s42979-021-00765-8.

[5] Sarker IH. Deep Learning: A Comprehensive Overview on Techniques, Taxonomy, Applications and Research Directions. SN Computer Science 2021;2:420. https://doi.org/10.1007/s42979-021-00815-1.

[6] Gündüz MZ, Daş R. Internet of things (IoT): Evolution, components and applications fields. Pamukkale University Journal of Engineering Sciences 2018;24:327–35. https://doi.org/10.5505/pajes.2017.89106.

[7] Potdar V, Chandan A, Batool S, Patel N. Big Energy Data Management for Smart Grids—Issues, Challenges and Recent Developments. In: Mahmood Z, editor. Smart Cities: Development and Governance Frameworks, Cham: Springer International Publishing; 2018, p. 177–205. https://doi.org/10.1007/978-3-319-76669-0_8.

[8] Nayak J, Vakula K, Dinesh P, Naik B, Mohapatra S, Swarnkar T, et al. Intelligent Computing in IoT-Enabled Smart Cities: A Systematic Review. In: Sharma R, Mishra M, Nayak J, Naik B, Pelusi D, editors. Green Technology for Smart City and Society, Singapore: Springer; 2021, p. 1–21. https://doi.org/10.1007/978-981-15-8218-9_1.

[9] Qin X, Luo Y, Tang N, Li G. Making Data Visualization More Efficient and Effective: A Survey. The VLDB Journal 2020;29:93–117. https://doi.org/10.1007/s00778-019-00588-3.

[10] Simoff S, Böhlen MH, Mazeika A. Visual Data Mining: Theory, Techniques and Tools for Visual Analytics. Springer Science & Business Media; 2008.

[11] Demirol D, Das R, Hanbay D. A Key Review on Security and Privacy of Big Data: Issues, Challenges, and Future Research Directions. Signal, Image and Video Processing 2022:1–9. https://doi.org/10.1007/s11760-022-02341-w.

[12] FSN. The Future of Business Partnering Global Survey 2019. FSN Publishing: Board International; 2019.
[13] Demirol D, Das R, Hanbay D. Büyük Veri Üzerine Perspektif Bir Bakış. 2019 International Artificial Intelligence and Data Processing Symposium (IDAP), IEEE; 2019, p. 1–9.
[14] Il-Agure Z, Dempere J. Review of Data Visualization Techniques in IoT Data. 2022 8th International Conference on Information Technology Trends (ITT), 2022, p. 167–71. https://doi.org/10.1109/ITT56123.2022.9863948.
[15] Aksoy F, Özdem M, Daş R. A perspective view on data visualization libraries used in data analytics. European Journal of Technique (EJT) 2025;15.
[16] Gorodov EY, Gubarev VV. Analytical Review of Data Visualization Methods in Application to Big Data. Journal of Electrical and Computer Engineering 2013;2013:1–7. https://doi.org/10.1155/2013/969458.
[17] Agrawal R, Kadadi A, Dai X, Andres F. Challenges and Opportunities with Big Data Visualization. Proceedings of the 7th International Conference on Management of computational and collective intElligence in Digital EcoSystems, Caraguatatuba Brazil: ACM; 2015, p. 169–73. https://doi.org/10.1145/2857218.2857256.
[18] Chawla G, Bamal S, Khatana R. Big Data Analytics for Data Visualization: Review of Techniques. International Journal of Computer Applications 2018;182:37–40. https://doi.org/10.5120/ijca2018917977.
[19] Liu J, Tang T, Wang W, Xu B, Kong X, Xia F. A Survey of Scholarly Data Visualization. IEEE Access 2018;6:19205–21. https://doi.org/10.1109/ACCESS.2018.2815030.
[20] Belghith M, Ben Ammar H, Elloumi A, Hachicha W. A new rolling forecasting framework using Microsoft Power BI for data visualization: A case study in a pharmaceutical industry. Annales Pharmaceutiques Françaises 2024;82:493–506. https://doi.org/10.1016/j.pharma.2023.10.013.
[21] Soni P, de Runz C, Bouali F, Venturini G. A survey on automatic dashboard recommendation systems. Visual Informatics 2024;8:67–79. https://doi.org/10.1016/j.visinf.2024.01.002.
[22] Ghosh A, Nashaat M, Miller J, Quader S, Marston C. A comprehensive review of tools for exploratory analysis of tabular industrial datasets. Visual Informatics 2018;2:235–53. https://doi.org/10.1016/j.visinf.2018.12.004.
[23] Pineda-Tobón DM, Espinosa-Bedoya A, Branch-Bedoya JW. Aquality32: A low-cost, open-source air quality monitoring device leveraging the ESP32 and google platform. HardwareX 2024;20:e00607. https://doi.org/10.1016/j.ohx.2024.e00607.
[24] Ferreira L, Moreira G, Hosseini M, Lage M, Ferreira N, Miranda F. Assessing the landscape of toolkits, frameworks, and authoring tools for urban visual analytics systems. Computers & Graphics 2024;123:104013. https://doi.org/10.1016/j.cag.2024.104013.
[25] Al-Rami Al-Ghamdi BAM. Analyzing the impact of data visualization applications for diagnosing the health conditions through hesitant fuzzy-based hybrid medical expert system. Ain Shams Engineering Journal 2024;15:102705. https://doi.org/10.1016/j.asej.2024.102705.
[26] Agrawal R, Balne PK, Veerappan A, Au VB, Lee B, Loo E, et al. A distinct cytokines profile in tear film of dry eye disease (DED) patients with HIV infection. Cytokine 2016;88:77–84. https://doi.org/10.1016/j.cyto.2016.08.026.
[27] Huacón CF, Pelegrin L. SURV: A system for massive urban data visualization. 2017 IEEE MIT Undergraduate Research Technology Conference (URTC), 2017, p. 1–4. https://doi.org/10.1109/URTC.2017.8284174.
[28] Tok YC, Zheng DY, Chattopadhyay S. A Smart City Infrastructure ontology for threats, cybercrime, and digital forensic investigation. Forensic Science International: Digital Investigation 2025;52:301883. https://doi.org/10.1016/j.fsidi.2025.301883.
[29] Avşar V, Tamer Ö. System-Independent Server-Side Infrastructure for IoT Applications. The European Journal of Research and Development 2023;3:381–9. https://doi.org/10.56038/ejrnd.v3i4.412.
[30] Dörk M, Carpendale S, Collins C, Williamson C. VisGets: Coordinated Visualizations for Web-based Information Exploration and Discovery. IEEE Transactions on Visualization and Computer Graphics 2008;14:1205–12. https://doi.org/10.1109/TVCG.2008.175.
[31] Beck F, Koch S, Weiskopf D. Visual Analysis and Dissemination of Scientific Literature Collections with Survis. IEEE Transactions on Visualization and Computer Graphics 2016;22:180–9. https://doi.org/10.1109/TVCG.2015.2467757.
[32] Yalçın MA, Elmqvist N, Bederson BB. Keshif: Rapid and Expressive Tabular Data Exploration for Novices. IEEE Transactions on Visualization and Computer Graphics 2018;24:2339–52. https://doi.org/10.1109/TVCG.2017.2723393.
[33] Luo Y, Qin X, Tang N, Li G. DeepEye: Towards Automatic Data Visualization. 2018 IEEE 34th International Conference on Data Engineering (ICDE), 2018, p. 101–12. https://doi.org/10.1109/ICDE.2018.00019.
[34] Vázquez-Ingelmo A, García-Peñalvo FJ, Therón R. Metaviz – a Graphical Meta-Model Instantiator for Generating Information Dashboards and Visualizations. Journal of King Saud University - Computer and Information Sciences 2022:S1319157822003445. https://doi.org/10.1016/j.jksuci.2022.09.015.
[35] https://www.tableau.com/node/62770. Tableau: Business Intelligence and Analytics Software. Tableau 2024.
[36] https://info.microsoft.com/ww-landing-2022-gartner-mq-report-on-bi-and-analytics-platforms.html?LCID=EN-US. 2022 Gartner® Magic Quadrant™ I Microsoft Power BI n.d.
[37] Looker Studio. https://lookerstudio.google.com/overview 2024.

[38] Amazon QuickSight - İş Zekası Hizmeti - Amazon Web Services. https://aws.amazon.com/tr/quicksight/. Amazon Web Services, Inc 2024.
[39] Oracle Analytics Desktop. https://docs.oracle.com/en/middleware/bi/analytics-desktop/index.html. Oracle Help Center 2024.
[40] Sisense. Sisense n.d.
[41] Biovia - Dassault Systèmes®. Pipeline Pilot 2024. https://www.3ds.com/products-services/biovia/products/data-science/pipeline-pilot/.
[42] Domo. Domo Data Visualiation. Drive data exploration with visualizations. 2024. https://www.domo.com/business-intelligence/visualization
[43] Infogram. Create Infographics, Reports and Maps. Infogram 2024. https://infogram.com/en/.
[44] Carto. Location Intelligence & GIS for Cloud Natives 2024. https://carto.com/.
[45] RAWGraphs 2024. https://www.rawgraphs.io/.
[46] Visualize Free. Data Visualization Software Free Visual Analytics Application 2024. https://www.visualizefree.com/.
[47] Insight Software. Dundas BI. Insightsoftware 2024. https://insightsoftware.com/dundas/.
[48] Qlik. https://help.qlik.com/en-US/cloud-services/Subsystems/Hub/Content/Sense_Hub/Sheets/visualization-filters.htm. QlikCom 2023.
[49] Elastic. Kibana: Explore, Visualize, Discover Data 2024. https://www.elastic.co/kibana.
[50] Tableau Named a Leader in the 2024 Gartner® Magic Quadrant™ for Analytics and BI Platforms 2024. https://www.tableau.com/blog/tableau-leader-gartner-magic-quadrant-analytics-business.
[51] Gartner. 2024 Magic Quadrant for Analytics and Business Intelligence Platforms. Gartner; 2024.
[52] Razali NFC, Mohamad M, Salleh KA, Sani MHAR, Alfat L. Online Shopping Preferences Visualization System Using Web Content Mining. 2021 2nd International Conference on Artificial Intelligence and Data Sciences (AiDAS), 2021, p. 1–6. https://doi.org/10.1109/AiDAS53897.2021.9574386.
[53] Sisense. Infuse Analytics Everywhere 2024. https://www.sisense.com/.
[54] Lavanya A, Darsha P, Akhil P, Lloret J, Yogeshwar N. A Real-Time Human Mobility Visualization of Covid-19 Spread from East Asian Countries. 2021 Eighth International Conference on Social Network Analysis, Management and Security (SNAMS), Gandia, Spain: IEEE; 2021, p. 1–8. https://doi.org/10.1109/SNAMS53716.2021.9732103.
[55] Mauri M, Elli T, Caviglia G, Uboldi G, Azzi M. RAWGraphs: A Visualisation Platform to Create Open Outputs. Proceedings of the 12th Biannual Conference on Italian SIGCHI Chapter, New York, NY, USA: Association for Computing Machinery; 2017, p. 1–5. https://doi.org/10.1145/3125571.3125585.
[56] Morishita M, Fukuda H, Muraoka K, Nakamura T, Hayashi M, Yoshioka I, et al. Evaluating GPT-4V's performance in the Japanese national dental examination: A challenge explored. Journal of Dental Sciences 2024;19:1595–600. https://doi.org/10.1016/j.jds.2023.12.007.
[57] Dominic N, Elwirehardja GN, Pardamean B. Data Mining for the Global Multiplex Weekly Average Income Analysis. Procedia Computer Science 2023;219:52–9. https://doi.org/10.1016/j.procs.2023.01.263.
[58] Shah N, Willick D, Mago V. A framework for social media data analytics using Elasticsearch and Kibana. Wireless Netw 2022;28:1179–87. https://doi.org/10.1007/s11276-018-01896-2.
[59] Wesley R, Eldridge M, Terlecki PT. An Analytic Data Engine for Visualization in Tableau. Proceedings of the 2011 ACM SIGMOD International Conference on Management of data, New York, NY, USA: Association for Computing Machinery; 2011, p. 1185–94. https://doi.org/10.1145/1989323.1989449.
[60] Zumeta-Olaskoaga L, Ibarrondo O, del Pozo R, Zapiain A, Larrañaga I, Mar J. The Excess Direct Social Costs of Dementia-Related Neuropsychiatric Symptoms: A Regionwide Cohort Study Beyond Silos. Value in Health 2024. https://doi.org/10.1016/j.jval.2024.10.3855.
[61] Web-Based COVID-19 Dashboards and Trackers in the United States: Survey Study. JMIR Human Factors 2023;10. https://doi.org/10.2196/43819.
[62] Musto L, Saratzis A, Hansell A, Bown M. Potential Associations Between Abdominal Aortic Aneurysm, Smoking, and Air Pollution: A Data Visualisation Journey. EJVES Vascular Forum 2024;61:S4–5. https://doi.org/10.1016/j.ejvsvf.2024.01.010.
[63] Liu J, Tang T, Wang W, Xu B, Kong X, Xia F. A Survey of Scholarly Data Visualization. IEEE Access 2018;6:19205–21. https://doi.org/10.1109/ACCESS.2018.2815030.
[64] Torres D, Cerejo A, Pimentel C, Matias J. Digital SFM: Definition of a platform for the digital daily meetings. Procedia Computer Science 2025;253:3059–68. https://doi.org/10.1016/j.procs.2025.02.030.

Volume 14, Issue 2, Page 134-143, 2025 https://doi.org/10.46810/tdfd.1644789 Research Article

BİNGÖL UNIVERSITY

Türk Doğa ve Fen Dergisi
Turkish Journal of Nature and Science
www.dergipark.gov.tr/tdfd

Design and Implementation of a GPS-Based UAV Tracking Antenna System Using LabVIEW

Mohamad RACHIDI[1*], Hüsamettim OSMANOĞLU[2], Gökhan ATALI[3], Onur DEMİREL[3]

[1] Sakarya University of Applied Sciences, Department of Electrical and Electronics Engineering, Sakarya, Türkiye
[2] Istinye University, Faculty of Engineering and Natural Sciences, Computer Engineering Department, İstanbul, Türkiye
[3] Sakarya University of Applied Sciences, Department of Mechatronics Engineering, Sakarya, Türkiye
Mohamad RACHIDI ORCID No: 0009-0005-3994-6447
Hüsamettim OSMANOĞLU ORCID No: 0000-0002-1027-2945
Gökhan ATALI ORCID No: 0000-0003-1215-9249
Onur DEMİREL ORCID No: 0000-0002-4221-3739

**Corresponding author: 23500405039@subu.edu.tr*

(Received: 23.02.2025, Accepted: 28.04.2025, Online Publication: 27.06.2025)

Keywords
UAV-Antenna tracker, LabVIEW, Ground control station, Mission planner

Abstract: In disaster monitoring missions, unmanned aerial vehicles (UAVs) must cover large areas to assess the impact of a disaster. Critical to the success of such missions is the continuous transmission of Air Data and Attitude Heading Reference System (ADAHRS) data, along with stable RSSI and video feed transmission to the Ground Control Station (GCS). However, the vast coverage area poses a challenge, as omnidirectional antennas are limited by the UAV's operational range. To overcome this limitation, a high-gain directional antenna is required, which needs to be constantly aimed at the UAV to maintain a stable connection. This study presents an antenna tracker, designed and implemented using an ATmega328P microcontroller, two servo motors, and a GPS receiver, providing two degrees of freedom. The tracker allows 180-degree rotation on the azimuth axis (yaw) and 90-degree rotation on the elevation axis (pitch). The system interface was developed using LabVIEW. Experimental results demonstrate that the proposed antenna tracker significantly extends the UAV's operational range while maintaining a stable connection with minimal RSSI fluctuations compared to systems without an antenna tracker. The continuous availability of ADAHRS data, stable RSSI, and video feed ensures the success of critical mission operations.

LabVIEW Kullanarak GPS Tabanlı İHA Takip Anten Sisteminin Tasarımı ve Uygulaması

Anahtar Kelimeler
İHA-Anten izleyici, LabVIEW, Yer kontrol istasyonu, Görev planlayıcı

Öz: Afet izleme görevlerinde, insansız hava araçları (İHA'lar) bir afetin etkisini değerlendirmek için geniş alanları kapsamalıdır. Bu tür görevlerin başarısı için kritik olan, Hava Verileri ve Tutum Yön Referans Sistemi (ADAHRS) verilerinin sürekli olarak iletilmesinin yanı sıra Yer Kontrol İstasyonuna (GCS) istikrarlı RSSI ve video besleme iletimi sağlanmasıdır. Bununla birlikte, çok yönlü antenler İHA'nın operasyonel menzili ile sınırlı olduğundan, geniş kapsama alanı bir zorluk teşkil etmektedir. Bu sınırlamanın üstesinden gelmek için, istikrarlı bir bağlantıyı sürdürmek için sürekli olarak İHA'ya yönlendirilmesi gereken yüksek kazançlı bir yönlü anten gereklidir. Bu çalışmada, ATmega328P mikrodenetleyici, iki servo motor ve bir GPS alıcısı kullanılarak tasarlanan ve uygulanan, iki serbestlik derecesi sağlayan bir anten izleyici sunulmaktadır. İzleyici, azimut ekseninde (yaw) 180 derecelik dönüşe ve yükseklik ekseninde (pitch) 90 derecelik dönüşe izin verir. Sistem arayüzü LabVIEW kullanılarak geliştirilmiştir. Deneysel sonuçlar, önerilen anten izleyicinin İHA'nın operasyonel menzilini önemli ölçüde genişlettiğini ve anten izleyicisi olmayan sistemlere kıyasla minimum RSSI dalgalanmaları ile istikrarlı bir bağlantı sağladığını göstermektedir. ADAHRS verilerinin sürekli kullanılabilirliği, kararlı RSSI ve video beslemesi, kritik görev operasyonlarının başarısını garanti eder.

1. INTRODUCTION

Unmanned Aerial Systems (UAS) consist of various components, including Unmanned Aerial Vehicles (UAVs) and Ground Control Stations (GCS) [1]. The GCS is crucial for overseeing UAV missions and ensuring their safe and efficient operation. It plays a key role in displaying real-time air data and Attitude Heading Reference System (ADAHRS) data, which enables operators to monitor UAV flight autonomously. Moreover, the GCS facilitates the transmission of live First Person View (FPV) video feeds from the UAV to the ground, providing operators with crucial visual information for decision-making and mission planning [2].

A critical component of UAS is the telemetry module, operating at 915 MHz for continuous data transmission to facilitate UAV monitoring. Operators utilize the GCS to plan navigation missions by setting waypoints and monitoring real-time UAV flight data. In the case where video transmission is required, a separate communication system is typically used, employing a high frequency 5.8 GHz band. The antennas, which is connected to a tracker, efficiently transmit the video to the ground using Rapid Fire modules [3]. Signal transmission requires two types of antennas: omnidirectional and directional.

Omnidirectional antennas emit radiation uniformly in all directions, resulting in a directivity of 1 dB or 0 dB [4]. In contrast, directional antennas concentrate the electromagnet wave radiation within a specific angle, reducing the signal beam-width while increasing the directivity beyond 1 dB [5]. Telemetry transmission efficiency is ensured by using a Team BlackSheep (TBS) module. Because stationary antenna systems maintain a constant position and are configured to radiate or receive signals in a predefined direction, their performance can be significantly affected by environmental factors when communicating with mobile objects [16]. These limitations make fixed antennas unsuitable for applications where signal quality, reliability, and consistent connectivity are critical, even if they are cost-effective.

In contrast, an antenna tracker is essential for maintaining a high-gain directional antenna's alignment with its target, as illustrated in Figure 1. In this context, the mobile target is a UAV. Directional antennas focus their electromagnetic radiation within a specific angle and area to achieve higher signal strength and range. However, UAVs typically employ omnidirectional antennas that radiate signals uniformly in all directions, leading to a potential mismatch in coverage [6]. An antenna tracker overcomes this challenge by dynamically adjusting the directional antenna's position to ensure the UAV remains within its radiation zone, thereby maintaining uninterrupted communication.

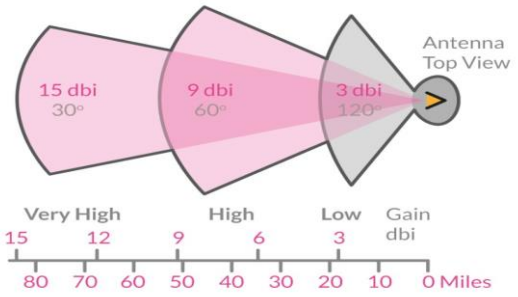

Figure 1. The Impact of Gain on Antenna Range [3]

The mechanical design of the antenna tracker must adhere to specific criteria, ensuring two degrees of freedom. The azimuth angle (yaw) must be capable of rotating 180 degrees, while the elevation angle (pitch) should achieve a 90-degree range of motion perpendicular to the planar geometry. Servo or DC motors are required to maneuver the frame along the azimuth and elevation axes [6]. To ensure high torque and smooth rotation, the design incorporates suitable gearing mechanisms. The major contributions of this work are highlighted as the following

1. A detailed mathematical model of the GPS-based antenna tracking system was developed and presented, outlining the theoretical framework and equations governing its operation.
2. The practical implementation of this tracking system was achieved using LabVIEW, which provided an intuitive interface for monitoring and control, coupled with the precise motor control of the custom PCB board.
3. To test the control system performance, Mission Planner software was employed. This software was primarily used to simulate UAV flights and provide essential GPS data, ensuring the tracking system could accurately follow the UAV's movements. The combination of LabVIEW for user interface and control logic, ATmega328P for hardware control, and Mission Planner for simulation testing resulted in a highly effective and efficient antenna tracking system.

The rest of this paper is organized as follows. Section 2 reviews tracked antenna. Section 3 gives in details about the methodology implemented. The design and the used algorithm is detailed in Section 4. Section 5 presents the simulation study of the GPS tracked antenna in the real field. Finally, Section 6 presents the conclusions and future remarks.

2. STATE-OF-THE-ART

The UAV antenna tracking problem arises when a ground control station (GCS) must maintain communication with single or multiple UAVs whose exact locations are dynamically uncertain. This uncertainty complicates antenna alignment and tracking, often leading to signal degradation or loss [19–25]. Previous research has primarily focused on fundamental design principles (e.g., MUltiple SIgnal Classification (MUSIC) algorithm for SDR-based localization [24]) and system-level

integration [19, 22]. Many studies aim to optimize tracking accuracy through improved antenna alignment mechanisms [19, 21], while others explore control strategies such as PID-based stabilization [8, 23] or adaptive beamforming via deep learning [18].

However, a critical gap remains: few studies address the end-to-end workflow—spanning design, manufacturing, testing, and real-world deployment—for UAV tracking systems. Most existing work relies on simulation-driven approaches (e.g., MATLAB/Simulink [7, 9, 23, 24]) but lacks empirical validation under real-world disturbances. For example, Smith and Doe uses MATLAB-based optimization for antenna tracker systems but under idealized conditions without real-world disturbances [7]. Chen and Liu simulates UAV antenna tracking using theoretical models without extensive hardware validation [9]. Moreover, Codău et al. [24] propose an SDR-based localization system but test it only in controlled environments.

This fragmentation between theory and practice is further exacerbated by the neglect of environmental adaptability (e.g., wind, multipath interference) and real-time dynamic response in UAV missions [6, 19, 22]. While simulations provide valuable insights, their limited empirical grounding [7, 24] restricts applicability in field deployments.

To bridge these gaps, this paper presents a holistic two-degree-of-freedom (DoF) antenna tracker that integrates:
1. Design and manufacturing a hardware-software co-design approach.
2. Mathematical Modeling by leveraging LabVIEW for dynamic simulation.
3. Real-World Testing to validation under variable operational conditions, e.g., wind, signal occlusion.

Unlike prior works, this system prioritizes practical viability, enhancing UAV operational reliability and adaptability in critical applications (e.g., remote sensing, disaster response). By unifying theoretical rigor with empirical validation, this research offers a scalable framework for future UAV tracking systems, addressing both performance gaps and deployment challenges.

3. METHODOLOGY

To realize the flowchart depicted in Figure 2, a series of sequential steps must be meticulously followed:
The initial step involves the detailed design of a custom printed circuit board (PCB) using Altium Designer for the electronic control system, integrating an ATmega328P microcontroller, a GPS module, and various other essential electronic components. Utilizing the Arduino IDE, the LIFA BASE firmware is uploaded to ensure seamless communication with the LabVIEW interface.

The ensuing stage requires the careful creation of a detailed 3D model utilizing Catia Software [17]. Prior to commencing the actual design process, it is imperative to define the design requirements with utmost precision. In this critical phase, existing open-source designs [11] are carefully sourced and subsequently tailored to harmonize seamlessly with the specific design and its unique requirements.

Subsequently, a python script is developed to extract essential data from the MAVLink stream [14], including latitude, longitude, and altitude. This data is formatted to be compatible with LabVIEW, enabling easy access for subsequent mathematical calculations. The following step involves modeling the entire system in LabVIEW (using the student version) to accurately calculate angles and transmit data to the servo motors, ensuring precise control.

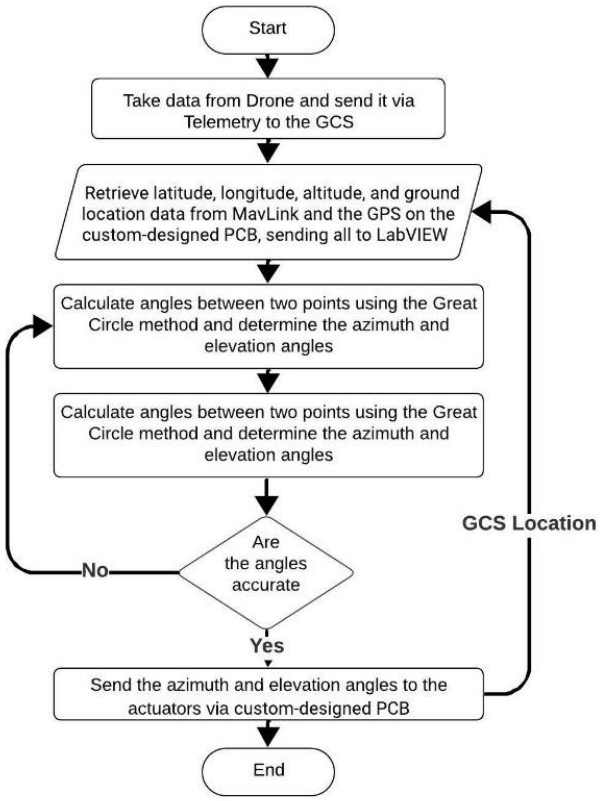

Figure 2. The flowchart of the proposed antenna tracking conceptual in this study

Table 1. Axis Rotation and Torque Magnitude

Axis	Gear Ratio	Rotation Speed (RPM)	Pinion	Gear	Torque Out (kg.cm)
Azimuth (Yaw)	3	20.67	10	30	45
Elevation (Pitch)	3	20.67	10	30	45

In this study, the proposed method was rigorously tested in a simulated environment, with real-world testing pending. Initial results were obtained by simulating the electronic board and using a small servo for demonstration purposes. Work on integrating the larger servo into the design is currently ongoing. The insightful findings presented in this paper are based on thorough experiments conducted using the initial simulation results.

4. ANTENNA TRACKER DESIGN AND IMPLEMENTATION

The antenna tracker system's custom-designed board was completely developed in our lab to meet the specific needs of the mission. Using the ATmega328P microcontroller, servo motors, and a GPS receiver, the board was engineered to provide precise control over the antenna's movement, ensuring continuous alignment with the UAV. This hands-on design process allowed us to tailor the system's functionality and performance to the unique requirements of the disaster monitoring mission, ensuring reliability and stability in real-world conditions. In the following sections, we detailed this design.

4.1 The Electronic Control System of Antenna Tracker

The antenna tracker was powered by a custom-built DIY Electronic Control System, as illustrated in Figure 3. This system integrates key components to manage power, communication, and actuation, ensuring seamless operation of the antenna tracker. The specifications of the system are as follows:

1. A Microcontroller (Atmega328P) with the following features:
- 20 MHz CPU for efficient real-time processing.
- Memory: 32KB Flash, 2KB SRAM, and 1KB EEPROM for program storage, data handling, and persistent memory needs.
- Adequate GPIO and PWM pins for peripheral control and expandability.

2. A GPS Module (NEO GPS) with the following characteristics:
- Operating voltage: 3-5V, compatible with most microcontroller systems.
- Positional accuracy: 2.5m, suitable for precise antenna orientation.
- Capable of tracking up to 16 satellites, ensuring robust GPS signal acquisition.
- Integrated 25x25mm antenna and 25x35mm module for compactness.
- Baud rate: 9600, enabling stable communication with the microcontroller.

3. Signal Amplifier (LM7805): It consists of voltage regulation from 7-35V to a stable 5V output as well as features thermal and short-circuit protection for reliability in diverse operating conditions.

4. USB-to-Serial Converter (CH340): It facilitates seamless communication between the microcontroller and a computer. Additionally, it has a wide operating system (OS) compatibility, ensuring ease of use across various development platforms.

Figure 3. The designed GPS control system with its main component

The microcontroller, Atmega328P, serves as the central control unit of the system, ensuring seamless coordination among the various components. It communicates with the NEO GPS module via a UART (Universal Asynchronous Receiver-Transmitter) interface, receiving precise real-time positioning data critical for tracking. This communication ensures the antenna aligns accurately with the target, such as a UAV, based on GPS coordinates.

The LM7805 voltage regulator plays a vital role in the system's power management. By stepping down input voltages in the range of 7–35V to a stable 5V output, it provides a reliable power supply to the Atmega328P and connected peripherals. Additionally, its built-in thermal and short-circuit protection mechanisms enhance the system's safety and reliability, especially under varying operating conditions. To facilitate connectivity and programmability, the CH340 USB-to-serial converter bridges the Atmega328P with a computer. This connection enables firmware updates, real-time data logging, and debugging during development. Its wide compatibility with multiple operating systems makes it versatile for use in diverse development environments. Finally, the system employs two Pulse Width Modulation (PWM) pins of the Atmega328P to control servo motors, which are responsible for orienting the antenna dynamically. The reserved PWM pins provide scalability, allowing for future integration of stepper motor drivers or additional actuators, thereby enhancing the system's precision and functionality.

These components form the core infrastructure for the antenna tracker, ensuring robust communication, precise actuation, and reliable power management. This modular design not only facilitates current functionality but also accommodates potential upgrades for more advanced tracking requirements.

4.2 Data Acquisition and Processing using LabVIEW

The system utilizes the pymavlink library [15] to fetch real-time positional data—latitude, longitude, and altitude—from the MAVLink stream [14]. MAVLink is a lightweight communication protocol designed for UAV communication, enabling robust telemetry data exchange. Figure 4a shows part of the python setup code, which provides a flexible interface for both real-world and simulated environments:

```python
from pymavlink import mavutil
connection_string = 'tcp:127.0.0.1:5762'
mav = mavutil.mavlink_connection(connection_string)
mav.mav.request_data_stream_send(
    mav.target_system, mav.target_component,
    mavutil.mavlink.MAV_DATA_STREAM_ALL, 1, 1)
latest_data = [None, None, None]
def get_latest_data():
    global latest_data
    return latest_data
while True:
    msg = mav.recv_msg()
    if msg is not None:
        if msg.get_type() == 'GPS_RAW_INT':
            latitude = msg.lat / 1.0e7
            longitude = msg.lon / 1.0e7
            altitude = (msg.alt / 1000.0) - 200
            latest_data = [latitude, longitude, altitude]
    print(get_latest_data())
```

(a) Python script

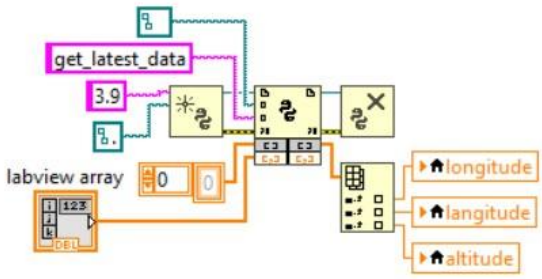

(b) The block diagram that calls python function.

Figure 4. The interface between the python position code with the LabVIEW

- Real UAVs: The telemetry stream is accessed via the serial 0 interface, ensuring reliable data acquisition directly from the drone's onboard systems.
- Simulations: For testing and validation, the library connects via a network TCP interface to interact with simulated drone telemetry streams.

The positional data is retrieved as floating-point values and stored in an array. This structured format ensures seamless integration with LabVIEW, a graphical programming environment. LabVIEW can parse this array for further processing, as depicted in Figure 4b by calling the python function. This integration allows the antenna tracker to dynamically adjust its position based on the UAV's real-time location.

4.3 The Antenna Tracker Actuator

The servo motor serves as the actuator for the antenna tracker, providing precise mechanical movement to align the antenna with the UAV. The actuation system supports two critical axes of movement:

- Azimuth Axis (Yaw): Enables horizontal rotation through a full 180-degree range.
- Elevation Axis (Pitch): Provides vertical rotation with a range of 90 degrees.

To achieve these movements, the servo motor employs a gear transmission system, enhancing torque output for handling the mechanical load of the antenna tracker. This ensures smooth and reliable operation, even under challenging environmental conditions.

4.4 The Mechanical Design of Antenna Tracker

The mechanical design of the antenna tracker was tailored to align with the specific requirements of UAV missions, focusing on portability, ease of operation, and precision. The Ground Control Station (GCS) plays a pivotal role in UAV operations by providing real-time data and live video feeds that ensure safe operation and facilitate mission planning. To support this functionality, the antenna tracker was designed for high portability, allowing for easy disassembly and transportation to accommodate dynamic mission requirements.

The antenna tracker's mechanical system, designed and modeled using Catia CAD (Figure 5), incorporates a two-degree of freedom structure for precise tracking capabilities. These degrees of freedom correspond to the following movements:

1. Azimuth Axis:
   - Enables horizontal rotation of the antenna over a 180-degree range.
   - Ensures the system can align with the UAV's changing positions in real-time.

2. Elevation Axis:
   - Facilitates vertical rotation with a 90-degree range.
   - Allows the tracker to maintain line-of-sight communication even as the UAV gains or loses altitude.
   - Each axis is powered by a high-torque servo motor (Figures 6a and 6b), providing precise positioning through a gear transmission system. The gear transmission ensures:
   - Smooth and constant rotation without stuttering.
   - Increased torque output, enabling the tracker to handle heavier antenna payloads or resist environmental forces such as wind.

Figure 5. 3D design of antenna tracker

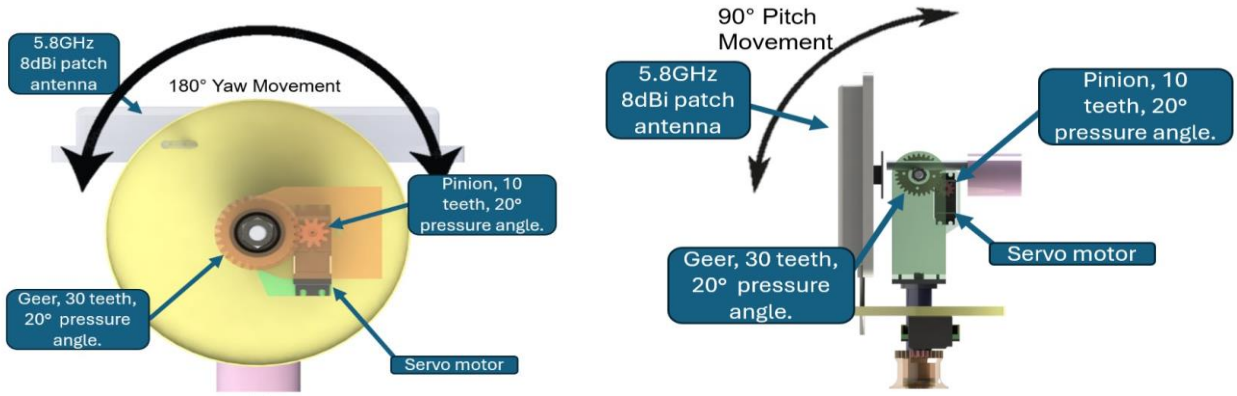

(a) The azimuth axis (yaw) (b) The elevation axis (pitch).

Figure 6. Movement of every axis: (a) azimuth axis (yaw); (b) elevation axis (pitch)

Figure 6 illustrates the motion of the antenna tracker's two axes—azimuth and elevation—driven by high-torque servo motors. To achieve smooth movement and sufficient torque output, a gear transmission system with carefully calculated gear ratios was implemented for each axis. The gear ratio ensures that the servo motors can deliver both the required angular precision and torque to handle the antenna's weight under various operating conditions.

The mechanical and rotational characteristics of the system were analyzed using the following equations:

$$GearRatio \cong \frac{n_{in}}{n_{out}} \quad (1)$$

$$AngularSpeed \cong \omega_{in} GearRatio \quad (2)$$

$$TorqueOut \cong \frac{\tau_{in}}{GearRatio} \quad (3)$$

where n_{in} is rotation speed input; n_{out} is rotation speed output; ω_{in} is angular speed input and τ_{in} is torque input. Using these equations, the rotation and torque requirements for each axis of the antenna tracker were calculated to ensure optimal operation. Table 1 and 2 summarize the derived values, which guided the selection of a suitable servo motor for the design.

Table 2. Rotation and torque requirements for the antenna tracker axes

Axis	Required Rotation	Angular Speed	Torque Output
	(Degrees)	Speed (rad/s)	(Nm)
Azimuth	180	1.08	0.75
Elevation	90	0.54	0.40

4.5 Telemetry Configuration

The proper configuration of the radio and telemetry systems is crucial for establishing seamless communication between the GCS, antenna tracker, and UAV. This setup ensures that the antenna tracker can effectively maintain alignment with the UAV during its operations, as illustrated in Figure 7. To achieve secure and reliable telemetry communication, an encrypted 915 MHz telemetry system was employed [12]. This system not only provides robust resistance to interference, but also it ensures the integrity and confidentiality of data transmission.

The telemetry system operates consists of the ground telemetry computer and antenna tracker. The ground telemetry computer transmits positional and command data through a serial port to the antenna tracker. The antenna tracker, equipped with the custom-designed control board, utilizes a separate serial port to communicate with its onboard systems, including motor controllers, and to relay commands for real-time adjustments. This dual-serial configuration ensures that telemetry data is processed efficiently and enables precise control of the antenna tracker, even under dynamic conditions.

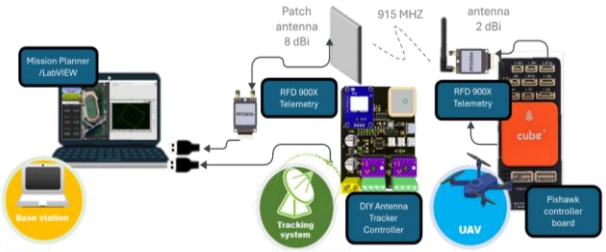

Figure 7. Telemetry configuration

4.6 Antenna

To guarantee proper data transmission between the UAV and the ground station, a directional antenna was selected for its performance characteristics and suitability for the application [7]. The antenna operates within the frequency range of 902–928 MHz, offering optimal compatibility with the 915 MHz telemetry system. Its technical specifications are summarized as follows:

- Gain: 8 dBi, providing significant signal amplification for extended communication range.
- Horizontal Beam Width: 75 degrees, ensuring broad coverage for azimuth tracking.
- Vertical Beam Width: 65 degrees, facilitating reliable elevation adjustments.
- Impedance: 50 Ohm, optimizing power transfer and minimizing signal reflection.
- VSWR (Voltage Standing Wave Ratio): Less than 1.5:1, ensuring minimal signal loss and high transmission efficiency.

The antenna's directional radiation pattern, shown in Figure 8, highlights its focused coverage, essential for maintaining a stable connection with the UAV even over extended distances.

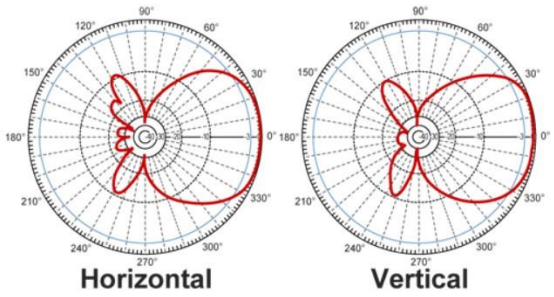

Figure 8. Radiation pattern for 8 dBi patch antenna [7]

4.7 Tracking Algorithm

To understand the operation of an antenna tracker, it is essential to delve into the principles of spherical trigonometry [8] and geolocation. The process consists of two phases: first, identifying the UAV's position, and second, steering the antenna using spherical trigonometry to ensure accurate alignment [19]. Spherical trigonometry provides the mathematical foundation for calculating positions, distances, and angles on the Earth's curved surface. These principles are indispensable for accurate navigation and location-based tracking, forming the core of the antenna tracker's algorithm.

4.7.1 Locating UAV

Given the geolocation data of both the flying platform (UAV) and the antenna tracker (GCS) in terms of latitude (φ) and longitude (ϕ), the necessary angles for orienting the tracker to the UAV location can be derived as shown in Algorithm 1. This process hinges on spherical trigonometric calculations to ensure precise alignment to dynamically locate UAVs [9]. The final output is finding the yaw angle, which serves as the azimuth reference relative to north.

Algorithm 1: Finding the Azimuth Angle to dynamically locate UAVs

- **Input:** The longitude and the latitude of the GCS and UAV.
- **Output:** Azimuth angle

Step 1: Longitude Difference Calculation [20]

$$\triangle\varphi = \varphi_2 - \varphi_1 \tag{4}$$

where φ_1 and φ_2 are the longitude of the GCS and UAV, respectively.

Step 2: Intermediate Components for Azimuth Calculation [20]

$$y = sin(\triangle\varphi) * cos\phi_2 \tag{5}$$

$$x = (cos\phi_1 * sin\phi_2) - (sin\phi_1 * cos\phi_2 * cos(\triangle\varphi)) \tag{6}$$

where ϕ_1 is the latitude of the GCS and ϕ_2 is the latitude of the UAV.

Step 3: Azimuth Angle Computation

$$\psi = tan^{-1}(y/x) \tag{7}$$

where ψ is the Azimuth angle, representing the UAV's horizontal position relative to the north pole.

4.7.2 Steering system

Accurate geolocation data for both the UAV and the GCS, including latitude (φ), longitude (ϕ), and altitude (h), is essential for precise UAV tracking. The steering system serves as the core component of the UAV tracking system, tasked with rotating the antenna in both elevation and azimuth angles, and calculated using Algorithm 1. Latitude (φ) measures the angle north or south of the equator, while longitude (ϕ) varies with latitude due to Earth's curvature, as lines of longitude converge at the poles. To ensure accuracy across Earth's spherical surface, the Spherical Law of Cosines is applied to calculate the great-circle distance, a reliable method for determining the shortest path between two points on a sphere [13]. The process is outlined in equations (8) and (9).

$$\triangle\varphi = \varphi_2 - \varphi_1 \tag{8}$$
$$\triangle\phi = \phi_2 - \phi_1 \tag{9}$$

where φ_1 and φ_2 are the latitudes of the GCS and UAV, respectively, and ϕ_1, ϕ_2 are their respective longitudes. The distance d between the UAV and the GCS is calculated using

$$d = cos^{-1}(sin\phi_1 * sin\phi_2 + cos\phi_1 * cos\phi_2 * cos\triangle\varphi * R) \tag{10}$$

where R is the Earth's radius, typically taken as 6371 km [6]. This equation accounts for the spherical nature of the Earth, ensuring accuracy over large distances. The vertical elevation difference, $\triangle h$, is given by (11)

$$\triangle h = h_2 - h_1 \tag{11}$$

where h_1 and h_2 are the altitudes of the GCS and UAV, respectively. Using d and $\triangle h$, the elevation angle θ, which represents the angular inclination from the GCS to the UAV, is calculated as:

$$\theta = \tan^{-1}(\triangle h/d) \tag{12}$$

In this context, θ is the rotation angle of the antenna tracker relative to the horizon and ensures vertical alignment based on altitude differences, with h_1 being the altitude of the GCS and h_2 being the altitude of the UAV. The distance d remains positive, and θ varies between $-90^o$and $+90^o$.

5. EXPERIMENTS AND RESULTS

This section presents the experimental setup, results, and observations regarding the implementation and testing of the antenna tracker system. The experiments were designed to validate the functionality of the tracking algorithm, servo motor control, and the integration of real-time data with LabVIEW.

5.1 The Software

The development and testing of the antenna tracker relied on several key software tools to ensure seamless integration and operation. LabVIEW was used for the mathematical calculations, real-time data visualization, and controlling the servo motors via PWM signals. Its graphical programming environment facilitated the design and simulation of the control system, while its serial communication capabilities ensured smooth data transfer between the antenna tracker and external devices. Mission Planner, an open-source software, was employed for simulating UAV movements, planning missions, and visualizing the UAV's path in real-time, which helped test the antenna tracker's ability to accurately follow the UAV's position. Python, using the pymavlink library, enabled communication with the UAV's telemetry system through the MAVLink protocol, retrieving real-time positional data such as latitude, longitude, and altitude for processing by LabVIEW. This integration allowed for a comprehensive system that could track the UAV's movements with precision, linking theoretical calculations to practical hardware control. These software platforms provided a robust framework for the antenna tracking system, ensuring accurate operation through real-time monitoring, and precise motor control. They facilitated the development, testing, and validation of the antenna tracker, showcasing the successful integration of hardware and software in a dynamic tracking environment.

5.2 The Mathematical Modulations in LabVIEW

One of the primary goals of this experiment was to implement the mathematical calculations necessary for determining the azimuth and elevation angles, as well as the distance between the UAV and the ground station, within the LabVIEW environment. The calculations were employed to generate a graphical representation of the motor rotation angles responsible for azimuth and elevation. These values were dynamically updated to track the live movement of the UAV in real time, as illustrated in Figure 9, which shows the LabVIEW block diagram. LabVIEW was also used to simulate PWM signals corresponding to the calculated angles, which were then transmitted through the serial port (COM*). The servo motors, in turn, interpreted these signals to adjust their positions, providing a direct link between theoretical computations and physical outcomes. This workflow demonstrates the seamless integration of LabVIEW's graphical programming capabilities with the real-world actuation of servo motors.

5.3 GPS Location Visualization

The GPS location data, acquired from the UAV and ground station, was plotted graphically in LabVIEW. Figure 10 depicts the GPS location graph, showcasing the tracking of live UAV positions relative to the ground station. This visualization confirmed the accurate acquisition and processing of GPS data.

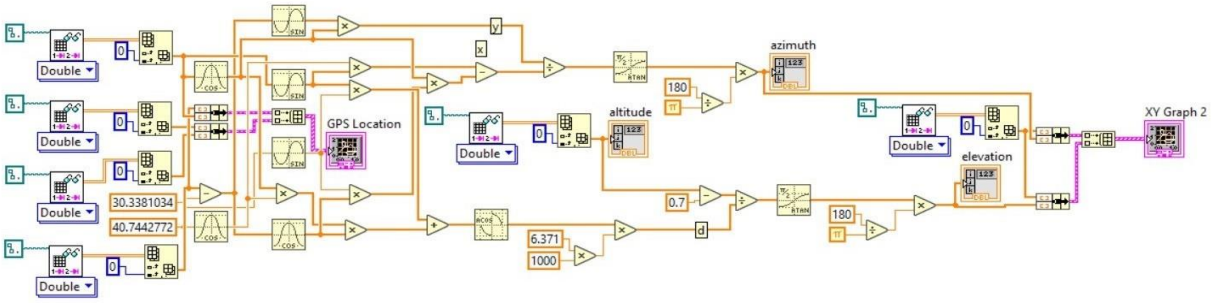

Figure 9. The LabVIEW Block diagram of mathematical calculations

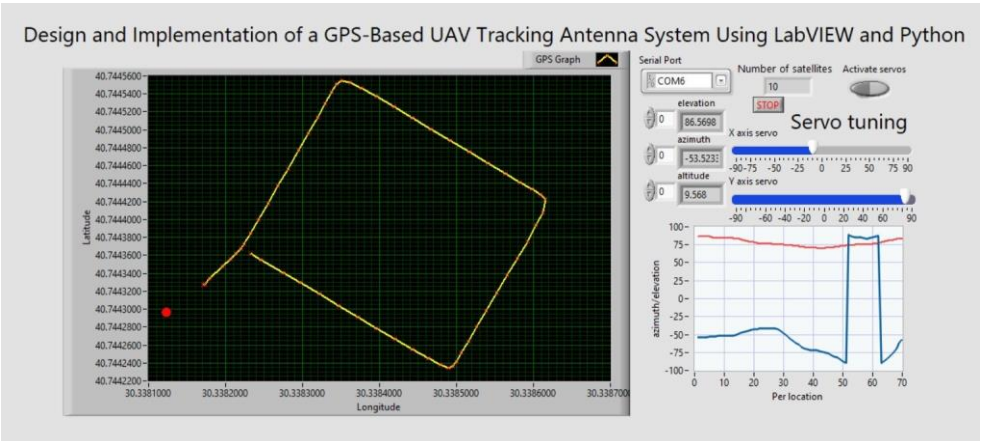

Figure 10. The LabVIEW front panel

5.4 Mission Simulation and Monitoring

The Mission Planner software autonomously executed a simulation mission, as demonstrated in Figure 11. The map-based visualization highlighted the UAV's path, confirming the successful integration of telemetry data with the Mission Planner. This step was critical for ensuring the UAV's trajectory was correctly tracked and communicated to the antenna tracker.

Figure 11. Simulation Mission planner at Skaraya University Stadium

5.5 LabVIEW Front Panel

The LabVIEW front panel provided a centralized control interface, displaying all relevant data, including GPS coordinates, calculated angles, and servo motor outputs. As shown in Figure 10, this interface facilitated the real-time observation of system performance, linking live data acquisition to actuator control.

5.6 Gimbal Verification and Testing

To validate the system's overall functionality, a gimbal setup was used to test the accuracy of servo motor control. Figure 12 illustrates the gimbal used during this test. The system demonstrated accurate tracking of the UAV's position and orientation in a virtual environment, confirming the reliability of the implemented tracking algorithm and servo settings.

Figure 12. The Gimbal

5.7 Environmental Robustness

Further testing was conducted to evaluate the antenna tracker's performance under various environmental conditions. The system was subjected to:

- Rain: Ensuring waterproofing and consistent data transmission.
- Wind: Testing the stability of the antenna tracker's mechanical structure.
- Temperature Fluctuations: Verifying the system's reliability under extreme hot and cold conditions.

The tracker maintained stable operation across these scenarios, demonstrating its suitability for diverse mission environments.

5.8 Comparative Benchmarking Against Existing Tracking Methods

To validate the efficacy of the proposed antenna tracker, a quantitative comparison was performed against two state-of-the-art approaches, e.g. PID-Based Tracking [23] and Lyapunov-based control system [6], shown in Table 3. Compared to İşcan et al. [6], the proposed system's 3:1 gear ratio yields 18% higher torque at a comparable rotation speed (20.67 vs. 15 RPM), enabling better resistance to environmental disturbances (Sec. 5.7) without requiring complex Lyapunov stability proofs. While [23] achieves higher torque (50 kg·cm), its 25 RPM operation may introduce oscillations in turbulent conditions, as evidenced by their need for aggressive PID tuning.

Table 3. Comparative Comparison

Metric	Proposed System	İşcan et al. [6]	Jayadi et al. [23]
Controller Type	PID-controlled	Lyapunov-based control	PID-controlled
Gear Ratio	3:1	4:1	2.5:1
Torque Output	45 kg·cm	38 kg·cm	50 kg·cm
Rotation Speed	20.67 RPM	15 RPM (stabilized)	25 RPM (high-speed)

6. DISCUSSION AND CONCLUSION

This work presents a holistic design, implementation, and validation of a two-degree-of-freedom (DOF) antenna tracking system for UAV applications, addressing critical gaps in prior research by integrating real-time data processing, adaptive control, and environmental robustness. In this study, we demonstrated a fully integrated antenna tracking system capable of real-time acquisition of a drone's positional data and seamless processing through LabVIEW's graphical programming environment. This work advances UAV antenna tracking by proving that real-time data fusion (GPS, inertial measurements) with adaptive control (PID tuning via LabVIEW) can significantly enhance tracking accuracy and mission efficiency.

While this study focused on drone tracking, the underlying principles of real-time data processing and seamless integration with physical systems can be extended to other domains, including autonomous vehicles and robotics, where accurate and reliable tracking is crucial.

ACKNOWLEDGEMENT

The authors are grateful to the faculty and educators at the Institute of Graduate Education at Sakarya University of Applied Sciences for their invaluable support and guidance throughout this research. Their expertise and encouragement have been instrumental in the successful completion of this project.

Ethics Committee Approval

There is no need for an Ethics Committee Certificate for our study.

REFERENCES

[1] Laghari AA, Jumani AK, Laghari RA, Nawaz H. Unmanned aerial vehicles: A review. Cognitive Robotics. 2023;3:8-22.

[2] Mohsan SAH, Khan MA, Noor F, Ullah I, Alsharif MH. Towards the unmanned aerial vehicles (UAVs): A comprehensive review. Drones. 2022;6(6):147.

[3] Xiamen Four-Faith Communication Technology. What does DBI mean? Detailed Introduction of DBI in Wireless Routers — Four-Faith;. Accessed: Dec. 22, 2024. https://www.fourfaith.com/industry-news/what-does-dbi-mean.html.

[4] Bevelacqua PJ. Antenna arrays: Performance limits and geometry optimization. Arizona state university; 2008.

[5] Saunders SR, Aragon-Zavala AA. Antennas and propagation for wireless communication systems. John Wiley & Sons; 2024.´

[6] İşcan M, Taş AI, Vural B, Ozden AB, Yılmaz C. Antenna tracker design with a discrete lyapunov stability based controller for mini unmanned aerial vehicles. International Journal of Multidisciplinary Studies and Innovative Technologies. 2022;6(1):77-85.

[7] Smith J, Doe J. Optimization of Antenna Tracker Systems for UAV Communication. IEEE Transactions on Antennas and Propagation. 2017;56(7):234556.

[8] Brown M, Green L. Real-time Adaptive Antenna Tracking for UAVs in Challenging Environments. In: Proceedings of the International Conference on UAV Technology. Springer; 2019. p. 123-30.

[9] Chen W, Liu Z. Design and Simulation of Antenna Tracker for UAV Applications. Aerospace Science and Technology. 2015; 45:17-28.

[10] Davis A, Thomas P. Modeling and Simulation of Antenna Tracker Systems. New York: Wiley-IEEE Press; 2018.

[11] GrabCAD, Inc . FPV Antenna Tracker OPEN-SOURCE CAD FILES;. Accessed: Dec. 06, 2024. https://grabcad.com/library/fpv-antenna-tracker-1.

[12] Changoluisa I, Barzallo J, Pantoja J, Cayo S, Navarro-Mendez DV, Cruz PJ. A Portable UAV Tracking System for Communications and Video Transmission. In: 2019 IEEE 4th Colombian Conference on Automatic Control (CCAC); 2019. p. 1-6.

[13] Stojcsics D, Molnar A. AirGuardian–UAV hardware and software system for small size UAVs. International Journal of Advanced Robotic Systems; 2012. 9(5):174.

[14] Allouch, A., Cheikhrouhou, O., Koubâa, A., Khalgui, M., & Abbes, T. (2019). MAVSec: Securing the MAVLink Protocol for Ardupilot/PX4 Unmanned Aerial Systems. In 2019 15th International Wireless Communications & Mobile Computing Conference (IWCMC) (pp. 621-628). IEEE. doi:10.1109/IWCMC.2019.8766580

[15] Using Pymavlink Libraries (mavgen); Accessed: Dec. 06, 2024. https://mavlink.io/en/mavgen_python/

[16] Zhu L, Ma W, Xiao Z and Zhang R. Performance Analysis and Optimization for Movable Antenna Aided Wideband Communications. IEEE Transactions on Wireless Communications. 2024; 23(12): pp. 18653-18668.

[17] 3D CAD Software: Shape the World We Live In; Accessed: Dec. 06, 2024. https://www.3ds.com/products/catia

[18] Zhang, J., Zhou, F., Li, W. et al. Beam prediction and tracking mechanism with enhanced LSTM for mmWave aerial base station. Wireless Netw 30, 7513–7525 (2024). https://doi.org/10.1007/s11276-024-03673-w

[19] Kelechi AH, Alsharif MH, Oluwole DA, Achimugu P, Ubadike O, Nebhen J, Aaron-Anthony A, Uthansakul P. The Recent Advancement in Unmanned Aerial Vehicle Tracking Antenna: A Review. Sensors (Basel). 2021 Aug 23;21(16):5662. doi: 10.3390/s21165662. PMID: 34451102; PMCID: PMC8402316.

[20] Nugroho G, Dectaviansyah D. Design, manufacture and performance analysis of an automatic antenna tracker for an unmanned aerial vehicle (UAV). Journal of Mechatronics, Electrical Power, and Vehicular Technology, 2018, 9.1: 32-40.

[21] Yousaf, J, Zia, H, Alhalabi, M, Yaghi, M, Basmaji, T, Shehhi, EA, Ghazal, M. Drone and controller detection and localization: Trends and challenges. Applied Sciences; 2022. 12(24), 12612.

[22] Kandregula, V. R., Zaharis, Z. D., Ahmed, Q. Z., Khan, F. A., Loh, T. H., Schreiber, J., Serres, A. J. R., & Lazaridis, P. I. (2024). A Review of Unmanned Aerial Vehicle Based Antenna and Propagation Measurements. Sensors, 24(22), 7395. https://doi.org/10.3390/s24227395.

[23] Jayadi A, Adhinata FD, Sembiring JP, Adhi CG, Selsily WH, Amiruddin A. Design And Implementation Of A PID Control System On A UAV Tracker Antenna. In 2023 International Conference on Advanced Mechatronics, Intelligent Manufacture and Industrial Automation (ICAMIMIA) 2023 Nov 14 (pp. 769-773).

[24] Codău, C., Buta, R.-C., Păstrăv, A., Dolea, P., Palade, T., & Puschita, E. (2024). Experimental Evaluation of an SDR-Based UAV Localization System. Sensors, 24(9), 2789. https://doi.org/10.3390/s24092789

Volume 14, Issue 2, Page 144-149, 2025 https://doi.org/10.46810/tdfd.1605923 Research Article

BİNGÖL UNIVERSITY

Türk Doğa ve Fen Dergisi
Turkish Journal of Nature and Science
www.dergipark.gov.tr/tdfd

Rupture Degree of Some Wheel Related Graphs

Betül ATAY[1*]

[1]Ağrı İbrahim Çeçen University, Faculty of Education, Dept. of Computer Education and Instructional Technology, Ağrı, Türkiye
Betül ATAY ORCID No: 0000-0003-1964-3287

**Corresponding author: batay@agri.edu.tr*

(Received: 23.12.2024, Accepted: 29.04.2025, Online Publication: 27.06.2025)

Keywords
Network vulnerability, Rupture degree, Wheel related graphs

Abstract: It is desirable that computer or communication networks continue to operate without interruption in the case of an attack or partial disruption. If a network modeled by a graph, then there are various graph theoretical parameters used to express the stability and vulnerability of communication networks. One of them is the concept of rupture degree. In this paper, we determine exact values for the rupture degree of wheel related graphs.

Tekerlekle İlgili Bazı Çizgelerin Kopukluk Derecesi

Anahtar Kelimeler
Ağ hassasiyeti, Kopukluk derecesi, Tekerlekle ilgili çizgeler

Öz: Bilgisayar ya da iletişim ağlarının bir saldırı ya da kısmi bozulma durumunda kesintiye uğramadan çalışmaya devam etmesi arzu edilen bir durumdur. Bir ağ bir çizge ile modellenirse, ağın kararlılığını ve hassasiyetini ifade etmek için kullanılan çeşitli teorik çizge parametreleri mevcuttur. Bunlardan biri de kopukluk derecesi kavramıdır. Bu makalede tekerlekle ilgili çizgelerin kopukluk derecesi için kesin değerleri belirledik.

1. INTRODUCTION

In this paper, we consider simple, finite, undirected graphs. Let G be a graph with a vertex set $V(G)$ and an edge set $E(G)$. The number of vertices and the number of edges of the graph G are denoted by $|V(G)|, |E(G)|$ respectively [1]. We denote the number of components of a graph G by $\omega(G)$ and the order of the largest component of G by $m(G)$. We use $\lfloor x \rfloor$ for the largest integer not larger than x and $\lceil x \rceil$ for the smallest integer not smaller than x. Two vertices are said to cover each other in a graph G if they are incident in G. A vertex cover in G is a set of vertices that covers all edges of G. The minimum cardinality of a vertex cover in a graph G is called the vertex covering number of G and is denoted by $\alpha(G)$. An independent set of vertices of a graph G is a set of vertices of G whose elements are pairwise nonadjacent. The independence number $\beta(G)$ of G is the maximum cardinality among all independent sets of vertices of G [2, 3]. If G is a graph of order n, then $\alpha(G) + \beta(G) = n$. The *connectivity* of G, denoted by $\mathrm{K}(G)$, is the minimal size of a vertex set S such that $G - S$ is disconnected or has only one vertex [4]. Terminology and notation not defined in this paper can be found in [4]. We denote the minimum vertex degree of a graph G by $\delta(G)$. A set $S \subseteq V(G)$ is a vertex cut of G, if either $G - S$ is disconnected or $G - S$ has only one vertex. The graph $W_n = K_1 + C_n$ is called a *wheel graph*. In wheel graph, the vertex c of degree n is called the *central vertex* while the vertices on the cycle C_n are called *rim vertices*.

A communication network is composed of processors and communication links. Network designers attach importance the reliability and stability of a network. If the network begins losing communication then there is a loss in its effectiveness. This event is called as the vulnerability of communication networks. In a communication network, vulnerability measures the resistance of the network after a breakdown of some of its processors or communication links [5]. If we think of a graph as modeling a network, then we have some graph parameters to measure the vulnerability. In a communication network, the vulnerability measures are essential to guide the designers in choosing an appropriate topology. They have an impact on solving difficult optimization problems for networks and they can also be investigated in different metric spaces by looking at the algebraic relationship with the topologies of the graph structures we consider [6, 7, 8].

The vulnerability of communication networks measures the resistance of a network to a disruption in operation

after the failure of certain processors and communication links. Network designers require greater degree of stability and reliability or less vulnerability in communication networks. Many graph theoretical parameters have been used to describe the stability and reliability of communication networks. These parameters deal with some or all of the following three questions:

(1) What is the number of elements that are not functioning?
(2) What is the number of remaining connected subnetworks?
(3) What is the size of a largest remaining group within which mutual communication can still occur?

The *tenacity* of an incomplete connected graph G is defined as

$$T(G) = \left\{\frac{|S| + m(G-S)}{w(G-S)} : S \subset V(G) \text{ and } \omega(G-S) > 1\right\}$$

and the tenacity of K_n is defined as n. It is natural to consider the additive dual of tenacity. We call this parameter *the rupture degree* of graphs. Formally, the rupture degree of an incomplete connected graph G is defined by

$$r(G) = max\{\omega(G-S) - |S| - m(G-S) : S \subset V(G), \omega(G-S) \geq 2\}$$

and the rupture degree of K_n is defined as $1-n$ [9, 10].

When we compare the tenacity number and rupture degree parameters, which deal with all three questions above, Zhang et al. shows that there exist graphs G_1 and G_2 such that $T(G_1) = T(G_2)$ and $r(G_1) \neq r(G_2)$. That is, the rupture degree and tenacity differ in showing the vulnerability of networks [9]. Consequently the rupture degree is a better parameter to measure the vulnerability of some networks. Zhang et al. obtained several results on the rupture degree of a graph. Li, F and Li, X [10] showed the relationship between tenacity and rupture degree as $r(G) \leq \alpha(G)\big(1 - T(G)\big)$.

Kırlangıç et al. calculated the rupture degree of complete $k-ary\ tree$, graph operations and gear graphs [11, 12]. Aytaç et al. calculated the rupture degree of thorn graphs and E_p^t consisting of t legs such that each leg is a path graph of order p and they gave the formulas for the rupture degree of the corona operation of some special graphs and they calculated the rupture degree for composite graphs [13, 14, 15]. Agnes et al. determined the exact values of the rupture degree of the wheel graph and also that of cartesian product of graphs [16].

Zhang et al. presented some results about rupture degree of join graphs and Nordhaus−Gaddum type results. They also gave some results on bounds for rupture degree and following theorems.

Theorem 1.1. [9] The rupture degree of the comet $C_{t,r}$ is

$$r(C_{t,r}) = \begin{cases} r-1, & if\ t\ is\ even \\ r-2, & if\ t\ is\ odd. \end{cases}$$

Theorem 1.2. [9] The rupture degree of the path P_n $(n \geq 3)$ is

$$r(P_n) = \begin{cases} -1, & if\ n\ is\ even \\ 0, & if\ n\ is\ odd. \end{cases}$$

Theorem 1.3. [9] The rupture degree of the cycle C_n is

$$r(C_n) = \begin{cases} -1, & if\ n\ is\ even \\ -2, & if\ n\ is\ odd. \end{cases}$$

Theorem 1.4. [9] The rupture degree of the star $K_{1,n-1}(n \geq 3)$ is $n-3$.

Theorem 1.5. [9] Let G be a non−complete connected graph of order n. Then

(a) $r(G) \leq n - 2\delta - 1$,
(b) $3 - n \leq r(G) \leq n - 3$,
(c) $2\beta(G) - n - 1 \leq r(G) \leq \frac{(\beta(G)^2 - \mathrm{K}(G))(\beta(G)-1)-n}{\beta(G)}$.

Theorem 1.6. [16] The rupture degree of the wheel W_n $(n \geq 5)$ is

$$r(W_n) = \begin{cases} -3, & if\ n\ is\ even \\ -2, & if\ n\ is\ odd. \end{cases}$$

In this paper, we obtain rupture degree of some wheel related graphs such as the helm graph H_n, the closed helm CH_n, the flower graph Fl_n, the sunflower graph SF_n and the web graph $W(t,n)$.

2. RUPTURE DEGREE OF SOME WHEEL RELATED GRAPHS

In this section, firstly the graphs mentioned in the paper are introduced with their figures, and then the rupture degree of these graphs are calculated.

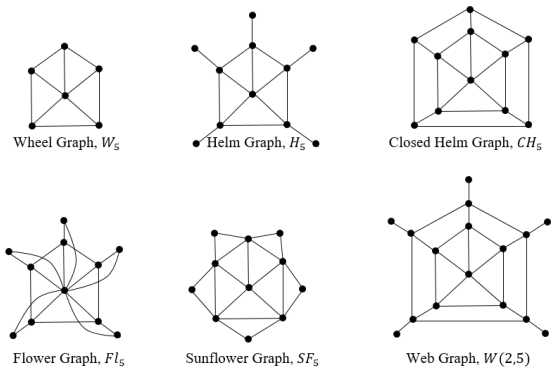

Figure 1. Some wheel related graphs

Definition 2.1. [17] The *helm* H_n is a graph obtained from a wheel W_n with central vertex c, by attaching a pendant edge to each rim vertex of W_n.

Theorem 2.1. Let H_n be a Helm graph of order $2n+1$. Then

$$r(H_n) = \begin{cases} \dfrac{n-6}{2}, & if\ n\ is\ even \\ \dfrac{n-7}{2}, & if\ n\ is\ odd \end{cases}$$

Proof. **Case 1.** n is even.

Let S be an arbitrary vertex cut of H_n and $|S| = k$. If $k \leq \frac{n}{2} + 1$, then $\omega(H_n - S) \leq n = 2(k-1)$. Therefore we have $m(H_n - S) \geq \left\lceil \frac{2n+1-k}{2(k-1)} \right\rceil$. Hence

$$\begin{aligned}\omega(H_n - S) - |S| - m(H_n - S) &\leq 2k - 2 - k - \left\lceil \frac{2n+1-k}{2(k-1)} \right\rceil \\ &\leq k - \left\lceil \frac{2n+1-k}{2(k-1)} \right\rceil - 2 \\ &\leq \frac{n}{2} + 1 - \left\lceil \frac{2n+1-k}{2(k-1)} \right\rceil - 2 \\ &\leq \frac{n}{2} - 3.\end{aligned}$$

If $|S| = k > \frac{n}{2} + 1$, then $\omega(H_n - S) < n$ and $m(H_n - S) \geq 2$. Hence

$$\begin{aligned}\omega(H_n - S) - |S| - m(H_n - S) &\leq n - \frac{n}{2} - 1 - 2 \\ &= \frac{n}{2} - 3.\end{aligned}$$

$= \frac{n}{2} - 3.$

From the choice of S, we obtain $r(H_n) \leq \frac{n}{2} - 3$. It is easy to see that there is a vertex cut S^* of H_n such that $|S^*| = \frac{n+2}{2}$, $\omega(H_n - S^*) = n$ and $m(H_n - S^*) = 2$. From the definition of rupture degree , we have

$$\begin{aligned}r(H_n) &\geq \omega(H_n - S^*) - |S^*| - m(H_n - S^*) \\ &\geq n - \frac{n+2}{2} - 2 \\ &= \frac{n-6}{2}.\end{aligned}$$

This implies that $r(H_n) = \frac{n-6}{2}$.

Case 2. n is odd.

Let S be an arbitrary vertex cut of H_n and $|S| = k$. If $k \leq \frac{n+3}{2}$, then $\omega(H_n - S) \leq n = 2k - 3$. Therefore we have $m(H_n - S) \geq \left\lceil \frac{2n+1-k}{2k-6} \right\rceil$. Hence

$$\begin{aligned}\omega(H_n - S) - |S| - m(H_n - S) &\leq 2k - 3 - k - \left\lceil \frac{2n+1-k}{2k-6} \right\rceil \\ &\leq k - 3 - \left\lceil \frac{2n+1-k}{2k-6} \right\rceil \\ &\leq \frac{n+3}{2} - 3 - \left\lceil \frac{2n+1-k}{2k-6} \right\rceil \\ &\leq \frac{n+3}{2} - 5 = \frac{n-7}{2}.\end{aligned}$$

If $|S| = k > \frac{n+3}{2}$, then $\omega(H_n - S) < n$ and $m(H_n - S) \geq 2$. Hence

$$\begin{aligned}\omega(H_n - S) - |S| - m(H_n - S) &\leq n - \frac{n+3}{2} - 2 \\ &= \frac{n-7}{2}.\end{aligned}$$

From the choice of S, we obtain $r(H_n) \leq \frac{n-7}{2}$. It is easy to see that there is a vertex cut S^* of H_n such that $|S^*| = \frac{n+3}{2}$, $\omega(H_n - S^*) = n$ and $m(H_n - S^*) = 2$. From the definition of rupture degree , we have

$$\begin{aligned}r(H_n) &\geq \omega(H_n - S^*) - |S^*| - m(H_n - S^*) \\ &\geq n - \frac{n+3}{2} - 2 \\ &= \frac{n-7}{2}.\end{aligned}$$

This implies that $r(H_n) = \frac{n-7}{2}$.

Definition 2.2. [17] The *closed helm* CH_n is the graph with central vertex c, obtained from a helm by joining each pendant vertex to form a cycle.

Theorem 2.2. Let CH_n be a closed Helm graph of order $2n + 1$. Then

$$r(CH_n) = \begin{cases} -2 & , if\ n\ is\ even \\ -4 & , if\ n\ is\ odd \end{cases}$$

Proof. **Case 1.** n is even.

Let S be an arbitrary vertex cut of CH_n and $|S| = k$. If $k \leq n + 1$, then $\omega(CH_n - S) \leq n = k - 1$. Therefore we have $m(CH_n - S) \geq \left\lceil \frac{2n+1-k}{k-1} \right\rceil$. Hence

$$\begin{aligned}\omega(CH_n - S) - |S| - m(CH_n - S) &\leq k - 1 - k - \left\lceil \frac{2n+1-k}{k-1} \right\rceil \\ &\leq \left\lceil \frac{2n}{k-1} - 1 \right\rceil - 1 \\ &\leq -2.\end{aligned}$$

If $|S| = k > n + 1$, then $\omega(CH_n - S) < n$ and $m(CH_n - S) \geq 1$. Hence

$$\begin{aligned}\omega(CH_n - S) - |S| - m(CH_n - S) &\leq n - n - 1 - 1 \\ &= -2\end{aligned}$$

$= -2.$

From the choice of S, we obtain $r(CH_n) \leq -2$. It is easy to see that there is a vertex cut S^* of CH_n such that $|S^*| = n + 1$, $\omega(CH_n - S^*) = n$ and $m(CH_n - S^*) = 1$. From the definition of rupture degree , we have

$$\begin{aligned}r(CH_n) &\geq \omega(CH_n - S^*) - |S^*| - m(CH_n - S^*) \\ &\geq n - n - 1 - 1 \\ &= -2.\end{aligned}$$

This implies that $r(CH_n) = -2$.

Case 2. n is odd.

Let S be an arbitrary vertex cut of CH_n and $|S| = k$. If $k \leq n + 2$, then $\omega(CH_n - S) \leq n - 1 = k - 3$. Therefore we have $m(CH_n - S) \geq \left\lceil \frac{2n+1-k}{k-3} \right\rceil$. Hence

$$\begin{aligned}\omega(CH_n - S) - |S| - m(CH_n - S) &\leq k - 3 - k - \left\lceil \frac{2n+1-k}{k-3} \right\rceil \\ &\leq -4\end{aligned}$$

If $|S| = k > n + 2$, then $\omega(CH_n - S) < n - 1$ and $m(CH_n - S) \geq 1$. Hence

$$\begin{aligned}\omega(CH_n - S) - |S| - m(CH_n - S) &\leq n - 1 - n - 2 - 1 \\ &= -4.\end{aligned}$$

From the choice of S, we obtain $r(CH_n) \leq -4$. It is easy to see that there is a vertex cut S^* of CH_n such that $|S^*| = n+1$, $\omega(CH_n - S^*) = n-1$ and $m(CH_n - S^*) = 2$. From the definition of rupture degree , we have

$$\begin{aligned} r(CH_n) &\geq \omega(CH_n - S^*) - |S^*| - m(CH_n - S^*) \\ &\geq n - 1 - n - 1 - 2 \\ &= -4. \end{aligned}$$

This implies that $r(CH_n) = -4$.

Definition 2.3. [17]The *flower graph* Fl_n is the graph obtained from a helm H_n by joining each pendant vertex to the central vertex c of the helm.

Theorem 2.3. Let Fl_n be a Flower graph of order $2n+1$. Then

$$r(Fl_n) = \begin{cases} \dfrac{n-6}{2} & ,if\ n\ is\ even \\ \dfrac{n-7}{2} & ,if\ n\ is\ odd \end{cases}$$

Proof. **Case 1.** n is even

Let S be an arbitrary vertex cut of Fl_n and $|S| = k$. If $k \leq \frac{n}{2} + 1$, then $\omega(Fl_n - S) \leq 2k - 2$ and $m(Fl_n) - S \geq 2$. Hence, $r(Fl_n) \leq \max_k \{2k - 2 - k - 2\} = \max_k\{k - 4\}$. The function $f(k) = k - 4$ is an increasing function and takes its maximum value at $k = \frac{n}{2} + 1$. Then

$$r(Fl_n) \leq \frac{n}{2} + 1 - 4 = \frac{n}{2} - 3$$

From the choice of S, we obtain $r(Fl_n) \leq \frac{n}{2} - 3$. On the other hand there is a vertex cut $S^*$of Fl_n such that $|S^*| = \frac{n+2}{2}$, $\omega(Fl_n - S^*) = n$ and $m(Fl_n - S^*) = 2$. From the definition of rupture degree, we have

$$\begin{aligned} r(Fl_n) &\geq \omega(Fl_n - S^*) - |S^*| - m(Fl_n - S^*) \\ &\geq n - \frac{n+2}{2} - 2 \\ &= \frac{n-6}{2} \end{aligned}$$

This implies that $r(Fl_n) = \frac{n-6}{2}$.

Case 2. n is odd

Let S be an arbitrary vertex cut of Fl_n and $|S| = k$. If $k \leq \frac{n+3}{2}$, then $\omega(Fl_n - S) \leq 2k - 3$ and $m(Fl_n) - S \geq 2$. Hence, $r(Fl_n) \leq \max_k \{2k - 3 - k - 2\} = \max_k\{k - 5\}$. The function $f(k) = k - 5$ is an increasing function and takes its maximum value at $k = \frac{n+3}{2}$. Then

$$r(Fl_n) \leq \frac{n+3}{2} - 5 = \frac{n-7}{2}$$

From the choice of S, we obtain $r(Fl_n) \leq \frac{n-7}{2}$. On the other hand there is a vertex cut $S^*$of Fl_n such that $|S^*| = \frac{n+3}{2}$, $\omega(Fl_n - S^*) = n$ and $m(Fl_n - S^*) = 2$. From the definition of rupture degree, we have

$$\begin{aligned} r(Fl_n) &\geq \omega(Fl_n - S^*) - |S^*| - m(Fl_n - S^*) \\ &\geq n - \frac{n+3}{2} - 2 \\ &= \frac{n-7}{2} \end{aligned}$$

This implies that $r(Fl_n) = \frac{n-7}{2}$.

Definition 2.4. [17]The *sunflower graph* SF_n is a graph obtained from a wheel with central vertex c, $n-cycle$ $v_0, v_1, \dots, v_{n-1}$ and additional n vertices $w_0, w_1, \dots, w_{n-1}$ where w_i is joined by edges to v_i, v_{i+1} for $i = 0, 1, \dots, n-1$ where $i+1$ is taken modulo n.

Theorem 2.4. Let SF_n be a sunflower graph of order $2n+1$. Then $r(SF_n) = 0$.

Proof. Let S be an arbitrary vertex cut of SF_n and $|S| = k$. If $k \leq n$, then $\omega(Fl_n - S) \leq n + 1 = k + 1$. Thefore $m(SF_n) - S \geq \left\lceil \frac{2n+1-(t+1)}{t+1} \right\rceil$. Hence,

$$\begin{aligned} \omega(SF_n - S) - |S| - m(SF_n - S) &\leq k + 1 - k - \left\lceil \frac{2n-k}{k+1} \right\rceil \\ &\leq 0 \end{aligned}$$

If $|S| = k > n$, then $\omega(SF_n - S) < n + 1$ and $m(CH_n - S) \geq 1$. Hence

$$\begin{aligned} \omega(SF_n - S) - |S| - m(SF_n - S) &\leq n + 1 - n - 1 \\ &\leq 0 \end{aligned}$$

≤ 0.

From the choice of S, we obtain $r(SF_n) \leq 0$. On the other hand there is a vertex cut $S^*$of SF_n such that $|S^*| = n$, $\omega(SF_n - S^*) = n + 1$ and $m(SF_n - S^*) = 1$. From the definition of rupture degree, we have

$$\begin{aligned} r(SF_n) &\geq \omega(SF_n - S^*) - |S^*| - m(SF_n - S^*) \\ &\geq n + 1 - n - 1 \\ &\geq 0 \end{aligned}$$

This implies that $r(SF_n) = 0$.

Definition 2.5. [17] A *web graph* is the graph obtained by joining a pendant edge to each vertex on the outer cycle of the closed helm. $W(t, n)$ is the generalized web with t cycles each of order n.

Theorem 2.5. Let $W(t, n)$ be a web graph of order $nt + n + 1$. Then

$$r(W(t,n)) = \begin{cases} \dfrac{n-6}{2} & ,if\ n\ is\ even \\ \dfrac{n-t-6}{2} & ,if\ n\ is\ odd\ and\ t\ is\ odd \\ \dfrac{n-t-5}{2} & 'if\ n\ is\ odd\ and\ t\ is\ even \end{cases}$$

Proof. **Case 1.** n is even

Let S be an arbitrary vertex cut of $W(t,n)$ and $|S| = k$. If $k \leq \frac{nt}{2} + 1$, then $\omega(W(t,n) - S) \leq \frac{n}{2} + k - 1$.

Therefore we have $m(W(t,n) - S) \geq \left\lceil \frac{nt+n+1-k}{\frac{nt+n}{2}} \right\rceil$.

Hence

$$\begin{aligned}\omega(W(t,n) - S) - |S| - m(W(t,n) - S) &\leq \frac{n}{2} + k - 1 - k - \left\lceil \frac{nt+n+1-k}{\frac{nt+n}{2}} \right\rceil \\ &\leq \frac{n}{2} - 1 - 2\left\lceil 1 + \frac{1-k}{nt+n} \right\rceil \\ &\leq \frac{n}{2} - 3.\end{aligned}$$

If $|S| = k > \frac{nt}{2} + 1$, then $\omega(W(t,n) - S) < \frac{n}{2}(t+1)$ and $m(W(t,n) - S) \geq \left\lceil \frac{nt+n+1-k}{\frac{nt+n}{2}} \right\rceil$. Hence

$$\begin{aligned}\omega(W(t,n) - S) - |S| - m(W(t,n) - S) &\leq \frac{nt}{2} + \frac{n}{2} - \frac{nt}{2} - 1 - 2\left\lceil \frac{nt+n+1-k}{nt+n} \right\rceil \\ &\leq \frac{n}{2} - 1 - 2\left\lceil 1 + \frac{1-k}{nt+n} \right\rceil \\ &\leq \frac{n}{2} - 3\end{aligned}$$

From the choice of S, we obtain $r(W(t,n) \leq \frac{n-6}{2}$. It is easy to see that there is a vertex cut S^* of $W(t,n)$ such that $|S^*| = \frac{nt+2}{2}$, $\omega(W(t,n) - S^*) = \frac{n}{2}(t+1)$ and $m(W(t,n) - S^*) = 2$. From the definition of rupture degree, we have

$$\begin{aligned}r(W(t,n)) &\geq \omega(W(t,n) - S^*) - |S^*| - m(W(t,n) - S^*) \\ &\geq \frac{nt}{2} + \frac{n}{2} - \frac{nt}{2} - 1 - 2 \\ &= \frac{n-6}{2}\end{aligned}$$

This implies that $r(W(t,n)) = \frac{n-6}{2}$.

Case 2. n is odd.

Subcase 2.1. t is odd

Let S be an arbitrary vertex cut of $W(t,n)$ and $|S| = k$. If $k \leq \frac{nt+3}{2}$, then $\omega(W(t,n) - S) \leq \frac{n-1}{2}(t+1) + 1 = k + 1 + \frac{n-t}{2}$. Therefore we have $m(W(t,n) - S) \geq \left\lceil \frac{nt+n+1-k}{\frac{(n-1)(t+1)}{2}+1} \right\rceil$. Hence

$$\begin{aligned}\omega(W(t,n) - S) - |S| - m(W(t,n) - S) &\leq \frac{n-t}{2} + 1 + k - k - \left\lceil \frac{nt+n+1-k}{\frac{nt+n}{2}} \right\rceil \\ &\leq \frac{n-t}{2} + 1 - 2\left\lceil \frac{nt+n+1-k}{nt+n-t+1} \right\rceil \\ &\leq \frac{n-t}{2} + 1 - 4 \\ &\leq \frac{n-t-6}{2}.\end{aligned}$$

If $|S| = k > \frac{nt+3}{2}$, then $\omega(W(t,n) - S) < \frac{nt}{2} - \frac{t}{2} + \frac{n}{2} + \frac{1}{2}$ and $m(W(t,n) - S) \geq 2$. Hence

$$\begin{aligned}\omega(W(t,n) - S) - |S| - m(W(t,n) - S) &\leq \frac{nt}{2} - \frac{t}{2} + \frac{n}{2} + \frac{1}{2} - \frac{nt}{2} - \frac{3}{2} - 2 \\ &\leq \frac{n-t}{2} - 3 \\ &\leq \frac{n-t-6}{2}.\end{aligned}$$

From the choice of S, we obtain $r(W(t,n) \leq \frac{n-t-6}{2}$. It is easy to see that there is a vertex cut S^* of $W(t,n)$ such that $|S^*| = \frac{nt+3}{2}$, $\omega(W(t,n) - S^*) = \frac{nt}{2} - \frac{t}{2} + \frac{n}{2} + \frac{1}{2}$ and $m(W(t,n) - S^*) = 2$. From the definition of rupture degree, we have

$$\begin{aligned}r(W(t,n)) &\geq \omega(W(t,n) - S^*) - |S^*| - m(W(t,n) - S^*) \\ &\geq \frac{nt}{2} - \frac{t}{2} + \frac{n}{2} + \frac{1}{2} - \frac{nt}{2} - \frac{3}{2} - 2 \\ &\geq \frac{n-t-6}{2}.\end{aligned}$$

This implies that $r(W(t,n)) = \frac{n-t-6}{2}$.

Subcase 2.2. t is even.

Let S be an arbitrary vertex cut of $W(t,n)$ and $|S| = k$. If $k \leq \frac{nt+2}{2}$, then $\omega(W(t,n) - S) \leq \frac{n-1}{2}(t+1) + 1 = \frac{nt}{2} - \frac{t}{2} + \frac{n}{2} + \frac{1}{2} = k - \frac{1}{2} + \frac{n-t}{2}$. Therefore we have $m(W(t,n) - S) \geq \left\lceil \frac{nt+n+1-k}{\frac{2k+n-t-1}{2}} \right\rceil$. Hence

$$\begin{aligned}\omega(W(t,n) - S) - |S| - m(W(t,n) - S) &\leq \frac{n-t}{2} - \frac{1}{2} + k - k - 2\left\lceil \frac{nt+n+1-k}{2k+n-t-1} \right\rceil \\ &\leq \frac{n-t-5}{2}.\end{aligned}$$

If $|S| = k > \frac{nt+2}{2}$, then $\omega(W(t,n) - S) < \frac{nt}{2} - \frac{t}{2} + \frac{n}{2} + \frac{1}{2}$ and $m(W(t,n) - S) \geq 2$. Hence

$$\begin{aligned}\omega(W(t,n) - S) - |S| - m(W(t,n) - S) &\leq \frac{nt}{2} - \frac{t}{2} + \frac{n}{2} + \frac{1}{2} - \frac{nt}{2} - 1 - 2 \\ &\leq \frac{n-t}{2} - \frac{5}{2} \\ &\leq \frac{n-t-5}{2}.\end{aligned}$$

From the choice of S, we obtain $r(W(t,n)) \leq \frac{n-t-5}{2}$. It is easy to see that there is a vertex cut S^* of $W(t,n)$ such that $|S^*| = \frac{nt+2}{2}$, $\omega(W(t,n) - S^*) = \frac{nt}{2} - \frac{t}{2} + \frac{n}{2} + \frac{1}{2}$ and $m(W(t,n) - S^*) = 2$. From the definition of rupture degree, we have

$$\begin{aligned}r(W(t,n)) &\geq \omega(W(t,n) - S^*) - |S^*| - m(W(t,n) - S^*) \\ &\geq \frac{nt}{2} - \frac{t}{2} + \frac{n}{2} + \frac{1}{2} - \frac{nt}{2} - 1 - 2 \\ &\geq \frac{n-t-5}{2}.\end{aligned}$$

This implies that $r(W(t,n)) = \frac{n-t-5}{2}$.

4. DISCUSSION AND CONCLUSION

When we make a comparison by looking at the results between the graphs with the same order examined in this study, we see that there is an inequality $r(CH_n) < r(SF_n) < r(Fl_n) = r(H_n)$. Therefore, we can say that the stability of the flower graph and the helm graph is more

powerful than the stability of the sunflower graph and the stability of the closed helm graph is the least powerful. In the web graph $W(t,n)$, we see that the rupture degree decreases as the value of t increases in the case of n is odd. This reduces the stability and robustness of the graph. The results obtained show the effect on the graphs considered in case of an external attack. Hence, designers for choosing the appropriate topology can use these results.

REFERENCES

[1] F. Harary. Graph Theory. Addison Wesley, 1972.
[2] G. Chartrand, L. Lesniak. Graphs and Digraphs. California: Wadsworth and Brooks. 1986.
[3] D. West. Introduction to Graph Theory. Prentice Hall, NJ. 2001.
[4] J. Bondy, U. Murty. Graph Theory with Applications, London: Macmillan, 1976.
[5] F. Li, Q. Ye, B. Sheng. Computing the Rupture Degree of Some Graphs. Wseas Transactions on Math. 11(1), pp. 23-33, 2012.
[6] K. Polat,A. Çağman. Polcag Spaces: I. group-like Structures. Thai Journal of Mathematics. 19(1), pp. 87-92, 2021.
[7] A. Şahin. Dichromatic polynomial for graph of a (2,n)-torus knot. Applied Mathematics and Nonlinear Sciences. 6(1), pp. 397-402, 2020.
[8] B. Şahin, A. Şahin. The Hosoya Polynomial of the Schreier Graphs of the Grigorchuk Group and the Basilica Group. Turkish Journal of Science. 5(3), pp. 262-267, 2020.
[9] Y. Li, S. Zhang, X. Li. Rupture Degree of Graphs. International Journal of Computer Mathematics. 82(7), pp. 793-803, July 2005.
[10] F. Li, X. Li. Computing the Rupture Degrees of Graphs. Proceedings of the 7th International Symposiumon Parallel Architectures, Algorithms and Networks(ISPAN'04), 2004,IEEE.
[11] A. Kırlangıç, G. B. Turan. On the Rupture Degree of a Graph. Neural Network World. 1(12), pp. 39-51, 2012.
[12] A. Kırlangıç.The Rupture Degree and Gear Graphs. Bulletin of the Malaysian Mathematical Sciences Society. 32(1), pp. 31-36, 2009.
[13] A. Aytaç, H. Aksu. Some Results for the Rupture Degree. International Journal of Foundations of Computer Science. 24(8), pp. 1329-1338, 2013.
[14] A. Aytaç, H. Aksu. The Rupture Degree of Some Graphs. Mathematica Balkanica. 24(12), pp. 85-101, 2010.
[15] A. Aytaç, Z. N. Odabaş. Computing the Rupture Degree in Composite Graphs. International Journal of Foundations of Computer Science. 21(3), pp. 311-319, 2010.
[16] V. Agnes, R. Geethanjaliyadav. Rupture Degree of Some Classes of Graphs. Palestine Journal of Mathematics. 12(2), pp. 34-43, 2023.
[17] B. Basavanagoud, S. Policepatil. Integrity of Wheel Related Graphs. Punjab University Journal of Mathematics. 53(5), pp. 329-336, 2021.

Volume 14, Issue 2, Page 150-161, 2025 https://doi.org/10.46810/tdfd.1607611 Research Article

BİNGÖL UNIVERSITY

Türk Doğa ve Fen Dergisi
Turkish Journal of Nature and Science
www.dergipark.gov.tr/tdfd

Numerical Analysis of Structural Behavior and Damage Mechanisms in Shear-Deficient Reinforced Concrete Columns Retrofitted with RC Jacketing

Fatih Avcil[1*], Hüseyin Bilgin[2], Enes Arkan[3], Ercan Işık[4]

[1]Bitlis Eren University, Department of Civil Engineering, Bitlis, Türkiye
[2]Epoka University, Department of Civil Engineering, Tirana, Albania
[3]Bitlis Eren University, Department of Civil Engineering, Bitlis, Türkiye
[4]Bitlis Eren University, Department of Architecture, Bitlis, Türkiye
Fatih Avcil ORCID No: 0000-0001-6550-550X
Hüseyin Bilgin ORCID No: 0000-0002-5261-3939
Enes Arkan ORCID No: 0000-0002-6588-7234
Ercan Işık ORCID No: 0000-0001-8057-065X

**Corresponding author: favcil@beu.edu.tr*

(Received: 26.12.2024, Accepted: 02.05.2025, Online Publication: 27.06.2025)

Keywords
Earthquake, Transverse reinforcement, Concrete, Column, Shear force, RC jacketing

Abstract: Designing reinforced concrete columns in accordance with earthquake-resistant design principles and ensuring their proper implementation during construction are among the fundamental factors that determine the seismic performance of reinforced concrete structures. In light of the widespread damage observed in the columns of reinforced concrete buildings during the February 6, 2023, Kahramanmaraş (Türkiye) earthquakes, this study aims to investigate the underlying causes of these failures. Initially, the structural damages are analyzed from earthquake engineering and structural mechanics perspectives. Subsequently, numerical analyses were carried out using a representative reinforced concrete building model to enable a more detailed evaluation. In this context, three different structural models were examined: one reference model and two variations, including different strengthening scenarios. The reference model incorporated C8/10 grade concrete, S220 reinforcement, and transverse reinforcement spacing of 300 mm. For structural elements exceeding their shear force capacity, reinforced concrete jacketing was proposed as the strengthening method. Accordingly, shear-deficient columns were identified, and the jacketing technique was applied incrementally, first to a single column and then to all columns within the structure. When comparing the limit and demand shear forces across the three models, it was observed that strengthening significantly increased the shear strength of the structural elements and offered an effective solution for enhancing seismic performance.

Betonarme Sargılama ile Güçlendirilmiş Kesme Kapasitesi Yetersiz Betonarme Kolonlarda Yapısal Davranış ve Hasar Mekanizmalarının Sayısal Analizi

Anahtar Kelimeler
Deprem, Enine donatı, Beton, Kolon, Kesme kuvveti, Sargılama

Öz: Depreme dayanıklı tasarım ilkelerine uygun olarak betonarme kolonların projelendirilmesi ve bu tasarımın inşaat aşamasında eksiksiz şekilde uygulanması, betonarme yapıların sismik performansını belirleyen temel unsurlar arasındadır. 6 Şubat 2023 tarihinde meydana gelen Kahramanmaraş (Türkiye) depremleri sonrasında betonarme binaların kolonlarında gözlemlenen yaygın hasarlar doğrultusunda, bu çalışma söz konusu hasarların temel nedenlerini araştırmayı amaçlamaktadır. Öncelikle, meydana gelen yapısal hasarlar deprem mühendisliği ve yapısal mekanik bakış açılarıyla analiz edilmiştir. Ardından, daha ayrıntılı bir değerlendirme için örnek bir betonarme bina modeli üzerinde sayısal analizler gerçekleştirilmiştir. Bu kapsamda, biri referans model olmak üzere üç farklı yapısal model incelenmiştir; diğer iki model ise çeşitli güçlendirme senaryolarını içermektedir. Referans modelde C8/10 dayanım sınıfında beton, S220 donatı ve 300 mm enine donatı aralığı kullanılmıştır. Kesme kuvveti kapasitesini aşan elemanlar için güçlendirme yöntemi olarak betonarme sargılama önerilmiştir. Bu doğrultuda, kesme dayanımı yetersiz olan kolonlar belirlenmiş ve sargılama işlemi kademeli olarak uygulanmıştır, ilk aşamada tek bir kolona, ikinci aşamada ise yapının tüm kolonlarına müdahale edilmiştir. Üç farklı modelin limit ve hedef kesme kuvvetleri karşılaştırıldığında, güçlendirme yapısal elemanların kesme dayanımını anlamlı ölçüde artırdığı ve sismik performansın iyileştirilmesinde etkili bir yöntem sunduğu görülmüştür.

1. INTRODUCTION

The impact of earthquakes on existing structures and the preventive measures implemented before such events are crucial in mitigating potential loss of life and property. Among natural disasters, earthquakes are responsible for the most severe destruction; however, their effects can be significantly reduced through proactive measures taken before the event. Both pre- and post-earthquake strategies are essential for the construction of safer buildings and the development of seismic design codes, which are instrumental in minimizing the impact on existing structures in high seismic-risk areas [1-3]. Furthermore, such studies provide valuable insights for urban planners and decision-makers, enabling the assessment and enhancement of earthquake resilience in existing infrastructure and guiding the implementation of necessary precautions. Also, some papers developed and applied rapid visual or mobile-based methods to assess seismic vulnerability of buildings in various international contexts [4-6]. Additionally, some authors offered comparative or code-based analyses to refine the structural evaluation of RC buildings under seismic conditions [7-9] and contributed to regional seismic risk analysis by integrating empirical damage data with predictive and AI-based assessment tools [10-12]. These efforts also support the formulation of intervention plans to be executed both before and after a disaster [13-14].

The seismic resilience of reinforced concrete (RC) structures is a pressing concern, particularly in regions prone to earthquakes. Given that a significant portion of the built environment consists of these structures, enhancing their capacity to withstand seismic events is critical. Various methodologies have been developed to improve the seismic performance of existing RC buildings, particularly those that do not meet contemporary seismic design standards. This discussion synthesizes recent research findings on retrofitting techniques aimed at bolstering the seismic resilience of these structures. For reinforced concrete buildings exhibiting inadequate seismic performance, several methods can be employed to enhance their seismic capacity to meet the requirements set by earthquake design regulations [15-20]. Strengthening the load-bearing systems of existing reinforced concrete structures, using various techniques applied at the element or system level, is a commonly adopted approach. Particular emphasis is placed on vertical load-bearing elements, as their capacity significantly influences the overall structural performance during seismic events. In addition to increasing the number or size of these vertical elements, the seismic resilience of the structure can be further enhanced through the application of various strengthening methods. Several major earthquakes in Türkiye have provided critical case studies for understanding structural vulnerability and damage patterns. The 1999 Kocaeli, 2003 Bingöl, 2011 Van, and 2020 Elazığ-Sivrice earthquakes revealed common deficiencies in reinforced concrete buildings, such as inadequate detailing, poor construction practices, and insufficient seismic design [21-25].

Over the past two decades in Türkiye, particularly following the devastating Kahramanmaraş earthquakes on February 6, 2023, one of the primary causes of large-scale damage in reinforced concrete (RC) structures has been the failure of vertical load-bearing elements. Structural damage to RC columns, occurring at various levels, is primarily attributed to low-strength concrete and inadequate transverse reinforcement. Studies assessing the damage in RC structures after several earthquakes in Türkiye have highlighted that these two fundamental issues have led to varying degrees of damage in columns, significantly compromising the seismic performance of the structures. As a result, some buildings have experienced partial or total collapse [26-37].

Theoretical and experimental studies in the literature have extensively explored the damage to reinforced concrete (RC) columns and the seismic performance of these load-bearing elements. These studies include evaluations and recommendations on the main causes of damage, increasing the load-bearing capacities of the columns to reduce seismic effects, and improving the regulatory conditions for these elements. Shear force, in particular, is an important factor in determining the durability of structural elements. Proper design of columns and enhancing their resistance to shear forces is critical for the safety of structures. Studies in the literature have provided significant insights into the effects of shear force on columns and have guided design parameters. Paulay and Priestley [38] thoroughly examined the effect of shear forces in reinforced concrete columns and how these forces reflect on the plasticization zones of the column. This study is an important reference for understanding the relationship between shear forces and column durability. Fardis [39] emphasized the need to consider shear forces in the seismic design of columns and the measures to be taken against them. The study presents different design strategies to enhance the durability of reinforced concrete columns. Priestley [40] addressed the relationship between shear forces and plastic deformations in columns and provided important conclusions regarding how shear forces affect the seismic performance of columns. Therefore, it is essential to carefully assess the effects of shear forces on columns during both static and dynamic analyses and incorporate appropriate safety measures into the design process.

Numerous academic studies have explored various strengthening methods for reinforced concrete (RC) columns, comparing the results either experimentally or theoretically [41-48]. One of the primary strategies for enhancing the seismic capacity of existing RC buildings is through the strengthening of vertical load-bearing elements. These elements, such as columns and walls, play a crucial role in the overall structural integrity during seismic events. Methods such as RC jacketing, which involves encasing existing columns with additional concrete and reinforcement, have been shown to improve the ductility and strength of these elements significantly [49-50]. This technique not only increases the load-bearing capacity but also enhances the energy dissipation characteristics of the structure, thereby reducing the

likelihood of catastrophic failure during an earthquake [51].

In the eleven provinces affected by the February 6, 2023, Kahramanmaraş earthquake, varying levels of damage and destruction occurred in reinforced concrete structures that constitute a large part of the urban building stock. The structural damages that occurred after this and similar earthquakes reveal the necessity of increasing the earthquake resistance of existing structures. One of the precautions to be taken is to strengthen existing structures on an element or system basis. In this study, structural damages occurring in reinforced concrete columns were first evaluated in light of the February 6, 2023, Kahramanmaraş earthquakes. The main reasons for structural damage in RC columns in such earthquakes are insufficient transverse reinforcement and low-strength concrete. Within this study, a 6-story symmetrical reinforced concrete building model was created, taking into account low-strength concrete and insufficient transverse reinforcement spacing, and structural analyses were carried out. This study distinguishes itself by employing a staged concrete jacketing approach to realistically simulate the retrofitting process and assess the evolution of seismic performance. In contrast to many earlier investigations, this research conducts a comparative analysis of single-column, partial, and full retrofitting strategies within a numerically modeled six-story reinforced concrete building. Columns exhibiting insufficient shear strength were identified, and strengthening was applied initially to a single column, followed by all columns in the structure through concrete wrapping, thereby strengthening them. The limit and demand shear forces were compared for these three different structural models. Additionally, performance ratios for these columns were also compared. The study primarily demonstrates the feasibility of using concrete wrapping in columns with insufficient shear strength.

The flow chart of this study is given in Figure 1.

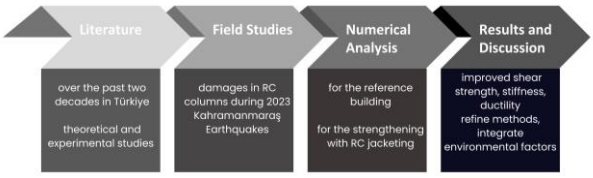

Figure 1. The flow chart of this study

2. MATERIAL AND METHOD

2.1. Damages in Columns Due to the Kahramanmaraş Earthquakes

Türkiye, a country highly vulnerable to seismic risks, faced a major disaster as a result of the Kahramanmaraş earthquakes that occurred on February 6, 2023. These two powerful earthquakes, with epicenters in the Pazarcık and Elbistan districts of Kahramanmaraş province, caused widespread destruction and significant loss of life across 11 provinces. The earthquakes, with magnitudes of Mw=7.7 and Mw=7.6, struck on the same day within the same region, and aftershocks further worsened the severity of the damage, complicating rescue efforts. The most severe damage occurred in the provinces of Hatay, Kahramanmaraş, and Adıyaman, while Malatya, Elazığ, Adana, Gaziantep, Osmaniye, Şanlıurfa, Kilis, and Diyarbakır were also significantly affected. In the aftermath of the earthquakes, thousands of buildings were damaged or collapsed to varying degrees. The region's infrastructure, including transportation, communication, and other essential services, also suffered extensive damage. More than 50,000 lives were lost, and thousands were injured. Tens of thousands of buildings experienced various levels of damage, with many completely collapsing. It was found that most of these buildings were aged structures that had not received adequate engineering attention, with many suffering extensive damage due to poor seismic performance. Weak construction practices, particularly the inadequacy of column and beam systems, were identified as key factors contributing to the widespread destruction. Examples of completely collapsed reinforced concrete buildings are shown in Figure 2.

Figure 2. Examples of reinforced concrete buildings that have collapsed completely (Photos taken by authors)

In some reinforced concrete structures, partial collapses have occurred due to structural irregularities and/or deficiencies. Examples of such damage are illustrated in Figure 3.

Figure 3. Examples of partial collapses due to various irregularities and deficiencies (Photos taken by authors).

Field observations have shown that the use of insufficient transverse reinforcement in columns is one of the main causes of damage. In order to reduce the brittle nature of concrete, the excessive spacing of transverse reinforcement that surrounds the core concrete has resulted in a decrease in the strength and ductility capacity of the concrete. The use of transverse reinforcement well beyond the spacing limits defined in earthquake-resistant design principles has caused an increase in the buckling lengths of longitudinal reinforcements, leading to buckling damage in the longitudinal reinforcement even under smaller critical load values. Poor workmanship, insufficient anchorage, the application of transverse reinforcement to longitudinal reinforcements with 90º hooks instead of 135º hooks, and inadequate concrete cover thickness have resulted in many of the expected functions of transverse reinforcement not being achieved. Insufficient transverse reinforcement and low-strength concrete have directly negatively affected the shear

strength capacities of columns, causing damage at varying levels. Particularly, columns on the ground floor have caused the structural system to collapse through a failure mechanism in the columns on the lower floors, due to shear force-induced out-of-plane displacement. Moreover, the lack of transverse reinforcement tightening in the lower and upper confinement zones of the columns has led to the formation of plastic hinges in these areas. Additionally, various utility elements passing through the columns reduce the concrete cross-section, which can lead to a decrease in the load-bearing capacity of the element. Apart from all these factors, the degradation of core concrete, improper mix ratios, inadequate compaction, excessive loading, and chemical and other influences can also contribute to the damage. Furthermore, insufficient transverse reinforcement used to reduce the brittle nature of the core concrete may also lead to this issue. Another cause of damage observed in the field was the use of either only plain reinforcement or both plain and ribbed reinforcement together. The formation of short columns, whose shear capacity is lower than their bending capacity, is another reason for the damage. In buildings constructed in close proximity to one another, the hammering effect generates additional shear forces in the load-bearing elements of adjacent structures, making it easier to exceed the limit of shear forces. Examples of damage resulting from these combined factors are shown in Figure 4.

Numerical analyses were carried out for a medium-height regular reinforced concrete structure in order to reveal the effects of the causes of damage at different levels in the columns as a result of field observations on the structural analyses**.** A reference structural model was created by taking into account the main causes of damages frequently encountered in columns as a result of field investigations in damaged reinforced concrete structures, which are the dominant urban building stock in the earthquake region, such as low strength concrete (C8/10), insufficient transverse reinforcement spacing (ϕ8/300) and the use of plain reinforcement (S220).

Figure 4. Examples of damage in columns caused by various factors (Photos taken by authors)

In order to represent these structures, a 6-story building without any irregularities was modeled. Afterwards, the rate at which the capacity of the structure changed was determined by using reinforced concrete wrapping. Pushover analysis was preferred in the structural models considered. This type of analysis is widely used to calculate how structures will behave under earthquake effects. Pushover analysis is a nonlinear static analysis method used to understand how structures will behave under dynamic loads such as earthquakes. In addition, it requires fewer calculations than nonlinear time history analyses, which makes it preferred in engineering applications. The reason for choosing this approach, which is particularly preferred as a numerical analysis method, is that it can represent the earthquake behavior of the structures in question as close to reality as possible and contribute to the understanding of existing damages. The structures analyzed in the study are limited to mid-rise reinforced concrete buildings with a certain type of load-bearing system. Therefore, the analysis method is valid for this group of structures and may not give the same accurate results in different systems, such as steel structures or mixed systems.

3. RESULTS

3.1. Numerical Analysis

In this section, a reinforced concrete building model has been developed to illustrate the effects of confinement-based strengthening methods on the shear force of columns. The model incorporates low-strength concrete

and reinforcement conditions as the materials used. Specifically, C8/10 concrete and S220 plain reinforced concrete bars were selected. For the transverse reinforcement in the columns, ϕ8/300 mm spacing was applied throughout the entire column length. All other structural characteristics in this model have been considered fixed, establishing this model as the reference building for evaluation. The numerical model was analyzed using a pushover analysis performed in the Seismostruct software [52].

In the modelling of all structural samples, force-based plastic hinge frame elements (in-frmFBPH) were employed for both columns and beams. These elements simulate the distribution of inelastic behavior along a defined length by applying force-based plasticity, thereby confining nonlinearity to a finite region. To accurately capture the stress–strain distribution, a total of 100 fibers were assigned to the cross-sections, which is considered sufficient for this modelling approach. The plastic hinge length (L_p/L) was set to 16.67%, based on relevant structural analysis and design guidelines. This ratio indicates the portion of the column or beam length where plastic deformations are expected to concentrate under seismic loading, allowing the structure to dissipate energy effectively while maintaining its stability. The selected value aligns with widely accepted engineering practice for estimating plastic hinge lengths in components exhibiting inelastic behaviour. Uniform load distributions were taken into account in all structural analyses.

Pushover analysis is a method used to determine the seismic behavior of structures, especially under horizontal loads. This approach is integral in evaluating the seismic performance of buildings, providing critical insights into the safety and functionality of a structure. The results of static pushover analysis are essential for identifying areas where excessive deformation or material strength limits may be exceeded, signaling the need for design modifications. Furthermore, these analyses are valuable for optimizing designs and reducing costs throughout the design process. At the same time, these types of analyses are also used to determine the potential performance of existing structures in the event of an earthquake. As a structural analysis technique, push-over analysis is used to explore the non-linear behavior of buildings, especially in the context of earthquake engineering and seismic evaluation. It offers a more comprehensive understanding of a structure's response to dynamic loads, such as those induced by earthquakes, by accounting for non-linear deformations beyond the elastic limit [53-60]. The flow chart for this type of analysis is shown in Figure 5.

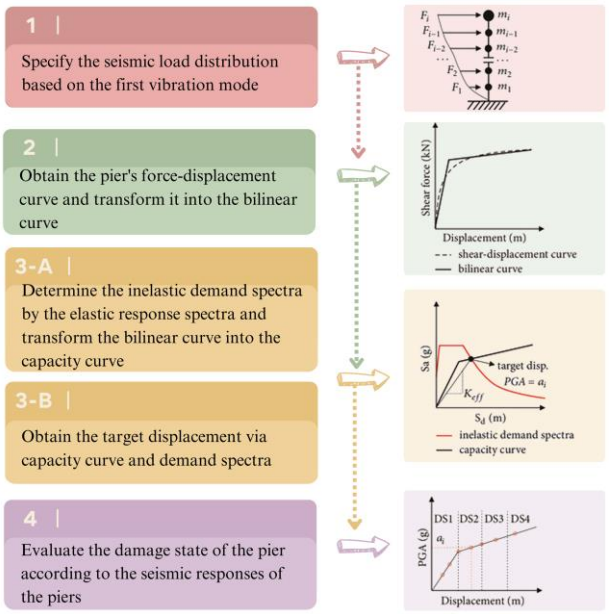

Figure 5. Flowchart of pushover analysis modified from Guo et al. [61]

The reinforced concrete building model used in the pushover analysis is symmetrical and comprises four equal spans of 4.50 m in both the X and Y directions. The numerical model represents a six-story structure, with each floor having a height of 3 m, resulting in a total structural height of 18 m. The floor plan and the designation of the columns for the numerical analyses are provided in Figure 6.

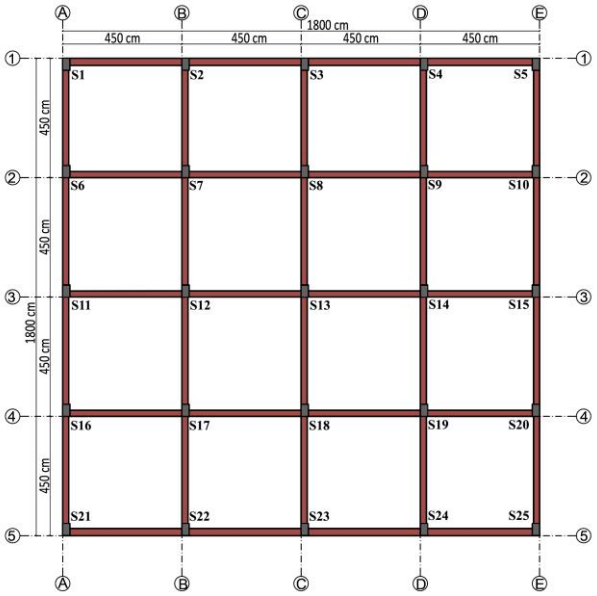

Figure 6. Floor plan and column names of the sample building.

The 2D and 3D models created in the software program, the applied loads, and the depiction of some columns are shown in Figure 7.

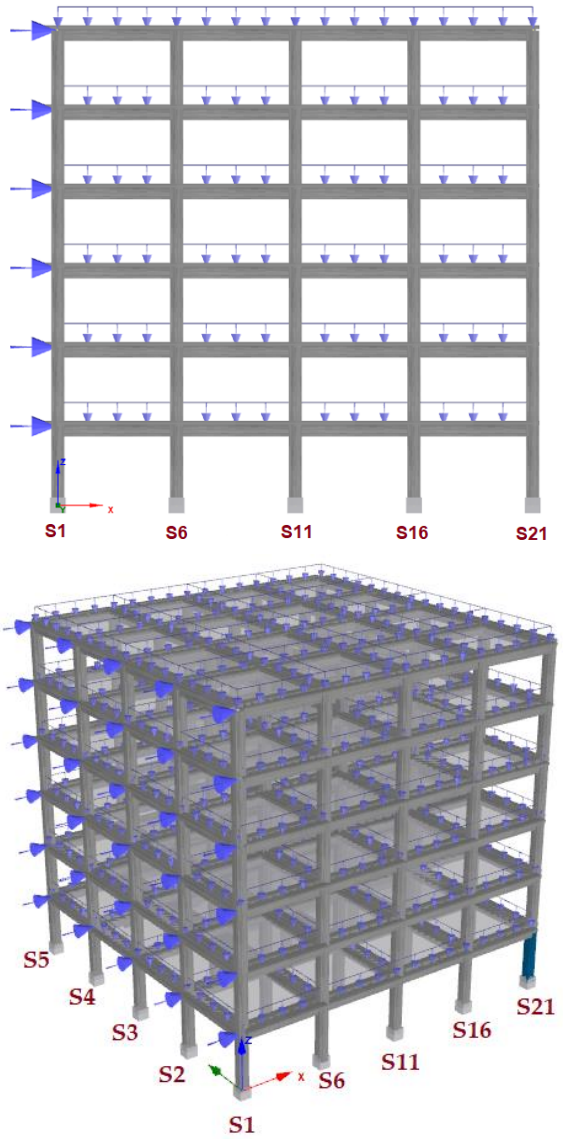

Figure 7. 2D and 3D structural models and representation of some columns

The structural parameters and dimensions of the structural elements considered in the reference RC building model are shown in Table 1.

Table 1. The RC building parameters considered in the study

Parameters		Values	Parameters	Values
Concrete Class		C8/10	Column Stirrup	Φ8/300
Reinforcement Class		S220	Beam Stirrup	Φ8/200
Beam dimensions (mm)		250x600	Concrete Cover (mm)	25
Slab height (mm)		120	Material model for Concrete Material model for Steel	Non-linear (Mander et al) Menegotto/ Pinto
Story height (m)		3		
Columns (mm)		400*500	Type of constraint	Rigid diaphragm
Longitudinal bars (columns)	Corners	4Φ20	Local Soil Class	ZA
	Top bottom side	4Φ16	Damping ratio	5%
	Left right side	4Φ16	Importance class	II

When selecting the reinforced concrete structures for the structural analyses, the more widely used Eurocode 8 [62] was taken into consideration. The selected reinforced concrete building was considered for residential purposes and was selected as building importance class II (Ordinary buildings; not belonging to the other categories). The characteristics of the local soil class considered in the study are given in Table 2.

Table 2. Local soil class and its characteristics (Eurocode-8)

Soil class	Description of Stratigraphic Profile	V_{s30} (m/s)	N_{SPT} (blows/30cm)	C_u (kPa)
A	Rock or other rock-like geological formation, including at most 5 m of weaker material at the surface	>800	---	---

This study focuses on determining whether the shear forces are exceeded in reinforced concrete columns and applying the confinement method for strengthening in columns where shear forces are exceeded. For all columns where the confinement method was applied, a confinement thickness of 100 mm, which is the minimum confinement thickness specified in the Turkish Building Earthquake Code (TBEC-2018), was considered. The column cross-sections before and after confinement are shown in Figure 8.

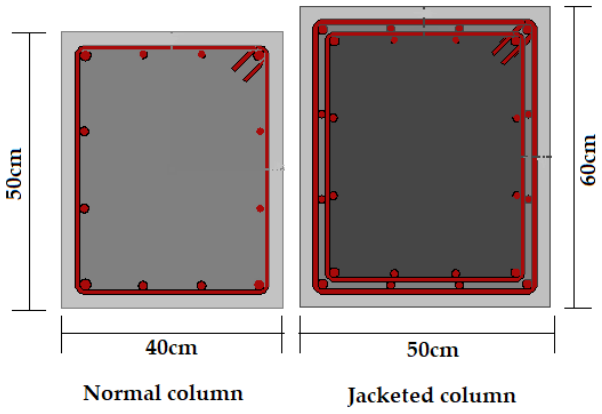

Figure 8. Column cross-sections before and after jacketing

The material and dimensional properties of the cross-sections before and after jacketing are shown in Table 3; examples of the application are provided in Figure 9.

Table 3. The material and dimensions of the cross-sections before and after jacketing

Section Material (s)		Section Dimensions	
External Longitudinal reinforcement	S420	External height	60 cm
Internal Longitudinal/transverse reinforcement	S220	Internal height	50 cm
External transverse reinforcement	S420	External width	50 cm
Concrete Jacket	C25/30	Internal width	40 cm
Concrete core	C8/10	Cover thickness	2.5 cm

Figure 9. Example of the structural member strengthening with the jacketing method (Photos taken by authors)

For the element strengthening using the jacketing method, structural analyses were first performed on the reference building model. Following this, the jacketing method was applied to columns where the shear force capacity was exceeded. Initially, the jacketing method was applied to a single column that exceeded its shear force capacity, referred to as Model I, which represented a minimal intervention scenario, serving as a baseline for evaluating the incremental impact of jacketing. In Model II, the jacketing method was applied to all columns of the structure. The 2D and 3D building drawings for Model I are presented in Figure 10.

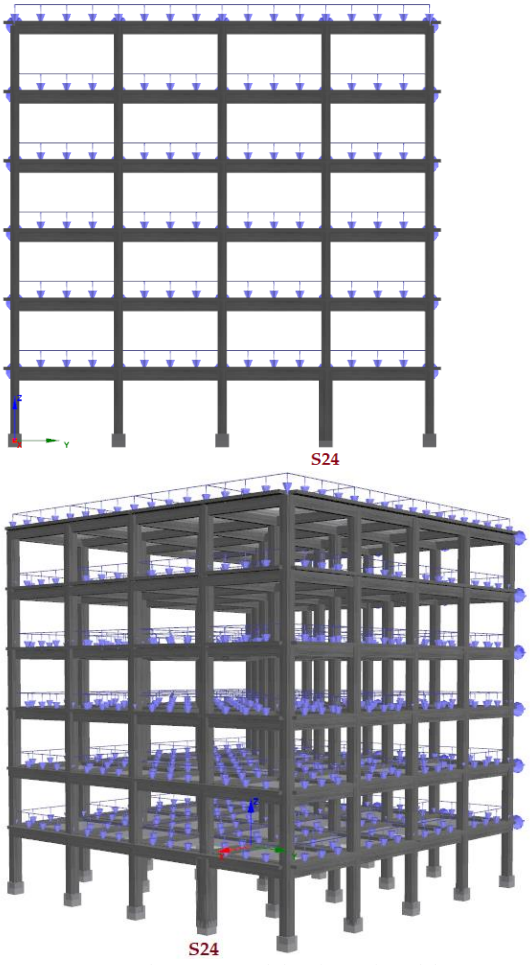

Figure 10. 2D and 3D structural drawings of Model I

The 2D and 3D structural drawings of Model II, created similarly, are shown in Figure 11.

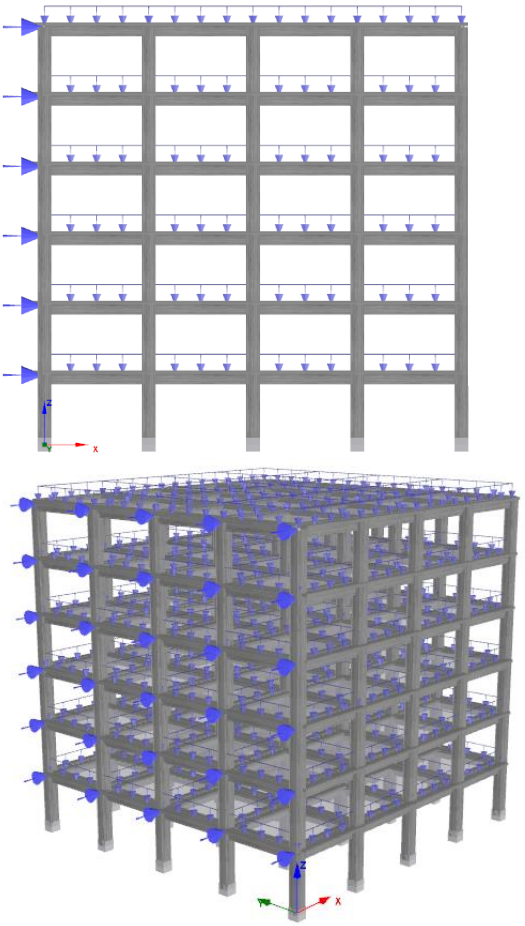

Figure 11. 2D and 3D structural drawings of Model II

The main objective of performance-based earthquake engineering is to determine the performance of structures under different limit states. For all the models considered in the study, the period, base shear force, as well as elastic and effective stiffness values, have been obtained. Additionally, the target displacements specified in Eurocode-8, which is widely used worldwide, including damage limitation (DL), significant damage (SD), and near collapse (NC), have been separately obtained. All these values are shown on the pushover curve in Figure 12.

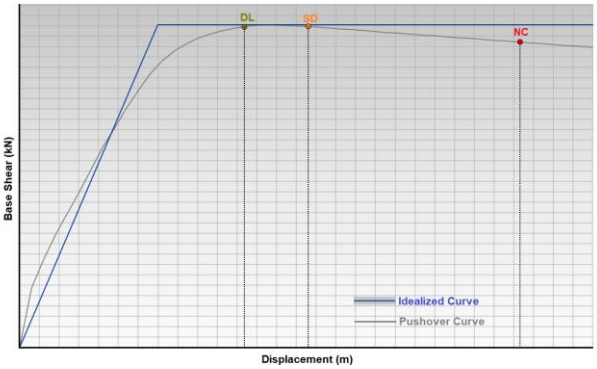

Figure 12. Typical pushover and idealized capacity curves

Table 4 shows comprehensive explanations for the limit state values considered in this study.

Table 4. Limit states in Eurocode-8

Limit State	Description	Return Period (Year)	Probability of Exceedance (in 50 Years)
Damage limitation (DL)	Only lightly damaged; damage to non-structural components is economically repairable	225	0.20
Significant damage (SD)	Significantly damaged; some residual strength and stiffness; non-structural components damaged; uneconomic to repair	475	0.10
Near-collapse (NC)	Heavily damaged; very low residual strength and stiffness; large permanent drift, but still standing	2475	0.02

All the result values for all models considered in the study are presented in Table 5.

Table 5. Results obtained for structural models

Model	Period (s)	Base Shear (kN)	K-elas (kN/m)	K-eff (kN/m)	Target Displacement (m)		
					DL	SD	NC
Reference	0.61	3910.89	141810.23	87579.85	0.0392	0.0503	0.0873
Model I	0.60	4266.82	143842.78	83955.93	0.0417	0.0535	0.0928
Model II	0.45	10296.89	202400.94	111922.93	0.0357	0.0458	0.0794

The results demonstrate that the jacketing method has increased the rigidity of the structure, leading to a reduction in the period value. In turn, the target displacements for earthquake safety have also been reduced in the more rigid structures. The deformation states obtained for the shear force capacities of the structural models considered in the study are shown in Figure 13.

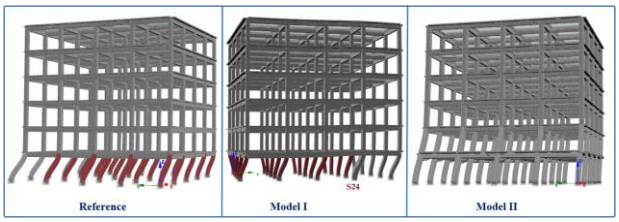

Figure 13. Deformations obtained for shear force capacities.

The structural analyses conducted for the reference model revealed that shear forces were exceeded in a total of 20 columns on the ground floor. In Model I, only the S24 column on the ground floor was strengthened using the jacketing method. In Model II, where element strengthening was applied to all columns in the structure, additional analyses were carried out. A comparison of the demand, limit, and performance ratio (PR) values for the columns on the ground floor across all models is presented in Table 6.

Table 6. Comparison of performance ratios for shear forces in structural models

	Reference			Model I			Model II		
	Demand	Limit	PR	Demand	Limit	PR	Demand	Limit	PR
S1	111.56	73.65	1.51	105.93	70.19	1.51	280.89	465.67	0.60
S2	108.65	71.31	1.52	107.44	71.92	1.49	290.60	464.59	0.63
S3	107.04	71.34	1.50	110.11	73.25	1.50	291.00	463.84	0.63
S4	109.16	71.22	1.53	113.83	73.33	1.55	289.72	464.10	0.62
S5	No exceed			No exceed			No exceed		
S6	97.53	77.57	1.26	90.32	70.85	1.27	330.23	514.05	0.64
S7	92.78	75.06	1.24	92.23	72.56	1.27	351.63	535.94	0.66
S8	90.83	73.86	1.23	96.50	76.33	1.26	335.71	523.95	0.64
S9	95.03	73.75	1.29	104.58	79.89	1.31	335.49	523.30	0.64
S10	No exceed			No exceed			No exceed		
S11	88.72	72.37	1.23	77.82	69.88	1.11	333.55	523.98	0.64
S12	83.97	68.20	1.23	82.12	68.20	1.20	339.03	531.11	0.64
S13	83.33	68.20	1.22	88.62	70.67	1.25	338.28	532.49	0.64
S14	84.31	68.20	1.24	98.96	76.15	1.30	337.88	531.13	0.64
S15	No exceed			No exceed			No exceed		
S16	83.23	68.20	1.22	72.82	67.47	1.08	340.72	532.69	0.64
S17	78.30	66.53	1.18	78.45	67.47	1.16	346.33	541.18	0.64
S18	76.24	66.53	1.15	91.84	74.30	1.24	347.63	543.54	0.64
S19	78.35	66.53	1.18	107.02	79.50	1.35	346.60	541.42	0.64
S20	No exceed			No exceed			No exceed		
S21	72.55	65.02	1.12	66.51	64.94	1.02	347.81	558.38	0.62
S22	66.92	64.62	1.04	71.95	64.67	1.11	346.09	559,45	0,62
S23	66.89	64.62	1.04	92.97	75.79	1.23	344.95	559,86	0,62
S24	66.98	64.62	1.04	No exceed			345.78	559.32	0.62
S25	No exceed			No exceed			No exceed		

With the applied jacketing method, the shear force capacity was not exceeded in all columns. In Model I, where the jacketing method was applied to a single column, the shear force was still exceeded in the other columns. However, no exceedance occurred in Model II, where jacketing was applied to all columns. This clearly demonstrates the applicability of the jacketing method in increasing the shear force capacity. It should be noted that this condition can only be achieved if the rules provided in TBEC-2018 regarding this method are followed. The ratios of columns where the shear force is exceeded for all structural models are given in Table 7.

Table 7. Number of columns where the shear force has been exceeded

Model	Total number of columns on the 1st floor	Total number of columns	Exceeded the number of columns	%
Reference	25	150	20	13.33
Model I	25	150	19	12.66
Model II	25	150	0	0

In column strengthening using jacketing methods, increasing the shear and compressive strength to enhance the ductility of the columns can help address the weaknesses associated with lap splices. However, these

methods cannot increase the bending capacity of the columns (TBEC-2018).

4. DISCUSSION AND CONCLUSION

Improving the performance of the load-bearing system under earthquake effects is of critical importance in terms of ensuring the safety of existing structures. In this context, strengthening reinforced concrete columns is a common engineering practice, especially in terms of increasing ductility, strength, and energy absorption capacity. Jacketing, which is one of these strengthening methods, aims to increase the load-bearing capacity by externally jacketing the column section with various materials.

This study investigated the seismic vulnerability of shear-deficient reinforced concrete columns and the effectiveness of concrete jacketing as a strengthening method, using lessons learned from the 2023 Kahramanmaraş earthquakes and numerical analyses of representative structural models. Observations from the earthquake highlighted that low-strength concrete and inadequate transverse reinforcement are primary contributors to structural damage. Numerical analysis confirmed that these deficiencies lead to a significant reduction in the seismic capacity of columns, necessitating effective retrofitting strategies.

Through the implementation of concrete jacketing, this study demonstrated a marked improvement in the shear force capacity and overall seismic performance of reinforced concrete columns. Incremental jacketing application, starting with single-column strengthening and extending to all columns, resulted in enhanced rigidity, reduced structural period, and lower target displacements. The findings highlight the ability of the jacketing technique to mitigate brittle failure mechanisms and increase column ductility when applied in accordance with code provisions.

This study underscores the importance of addressing shear deficiencies in seismic retrofitting practices. By effectively applying techniques like concrete jacketing, engineers can improve the resilience of aging infrastructure in seismically active regions. The results also contribute to the growing body of knowledge on seismic strengthening methods, providing practical insights for enhancing the safety and durability of existing structures.

In the context of this study, the observed reduction in structural period was considered a favorable outcome, as it signifies enhanced stiffness and improved seismic performance, particularly for mid-rise, regular reinforced concrete buildings. The target displacement in the pushover curve represents the anticipated maximum displacement under seismic loading, and its reduction generally signifies improved performance. This is accompanied by an increase in horizontal force-resisting capacity, as demonstrated in Model II, where the strengthened columns exhibited higher base shear values and reduced displacements. The results of this study are primarily relevant to mid-rise, regular reinforced concrete buildings with shear-deficient columns.

In conclusion, the enhancement of seismic resilience in existing RC structures is a multifaceted challenge that requires a combination of innovative techniques and technologies. From traditional methods like RC jacketing to modern solutions involving advanced materials and digital technologies, a wide array of options exists for improving the seismic performance of these buildings. As the frequency and intensity of seismic events continue to rise globally, the urgency for effective retrofitting strategies becomes increasingly apparent. Future research should focus on refining these techniques, exploring new materials, and developing comprehensive frameworks that integrate economic, environmental, and social considerations into the retrofitting process.

Before applying jacketing to reinforced concrete columns, technical and structural factors such as the current damage status, material compatibility, reinforcement and geometry information, their effect on the general behavior of the structure, and application conditions should be taken into consideration. Achieving the purpose of reinforcement depends on the sensitivity with which it is implemented. Otherwise, it will not be possible to provide the functions expected from the reinforcement.

Acknowledgement

The results presented in this scientific paper have been partially obtained through the research activities within the project 2023-1-HR01-KA220-HED-000165929 “Intelligent Methods for Structures, Elements and Materials” [https://im4stem.eu/en/home/ (accessed on 25 July 2024)], co-funded by the European Union under the program Erasmus+ KA220-HED-Cooperation partnerships in higher education.

REFERENCES

[1] Harirchian E, Lahmer T, Buddhiraju S, Mohammad K, Mosavi A. Earthquake safety assessment of buildings through rapid visual screening. Buildings, 2020;10(3), 51.

[2] Blagojević N, Brzev S, Petrović M, Borozan J, Bulajić B, Marinković M, et al. Residential building stock in Serbia: classification and vulnerability for seismic risk studies. Bulletin of earthquake engineering, 2023;21(9), 4315-4383.

[3] Büyüksaraç A, Isik E, Harirchian E. A case study for the determination of seismic risk priorities in Van (Eastern Turkey). Earthquake and structures, 2021;20(4), 445-455.

[4] Işık M, Işık E, Haricihian E. Application of IOS/Android rapid evaluation of post-earthquake damages in masonry buildings. Gazi Mühendislik Bilimleri Dergisi, 2021;7(1), 36-50.

[5] Kassem MM, Beddu S, Ooi JH, Tan CG, Mohamad El-Maissi A, Mohamed Nazri F. Assessment of seismic building vulnerability using rapid visual screening method through web-based application for Malaysia. Buildings, 2021;11(10), 485.

[6] Khemis A, Athmani A, Ademović N. Rapid application of the RISK-UE LM2 method for the seismic vulnerability analysis of the Algerian masonry buildings. International Journal of Architectural Heritage, 2024;18(5), 788-808.
[7] Jain SK, Mitra K, Kumar M, Shah M. A proposed rapid visual screening procedure for seismic evaluation of RC-frame buildings in India. Earthquake Spectra, 2010;26(3), 709-729.
[8] Bilgin H, Hadzima-Nyarko M, Işık E, Ozmen HB, Harirchian E. A comparative study on the seismic provisions of different codes for RC buildings. Structural Engineering and Mechanics, An Int'l Journal, 2022;83(2), 195-206.
[9] Aynur S, Atalay HM. Comparative analysis of existing reinforced concrete buildings damaged at different levels during past earthquakes using rapid assessment methods. Struct. Eng. Mech. 2023;85, 793–808.
[10] Başgöze A, Güncü A. Determining the regional disaster risk analysis of buildings in Erzincan. Građevinar 2023;75.03.257-272.
[11] Nemutlu ÖF, Sarı A, Balun B. 06 Şubat 2023 Kahramanmaraş Depremlerinde (Mw 7.7-Mw 7.6) Meydana Gelen Gerçek Can Kayıpları Ve Yapısal Hasar Değerlerinin Tahmin Edilen Değerler İle Karşılaştırılması. Afyon Kocatepe Üniversitesi Fen Ve Mühendislik Bilimleri Dergisi, 2023;23(5), 1222-1234.
[12] Bektaş N, Kegyes-Brassai O. Enhancing seismic assessment and risk management of buildings: A neural network-based rapid visual screening method development. Engineering Structures, 2024;304, 117606.
[13] Işık E, Hadzima-Nyarko M, Radu D, Bulajić B. Study on effectiveness of regional risk prioritisation in reinforced concrete structures after earthquakes. Applied Sciences, 2024;14(16), 6992.
[14] Apostolaki S, Riga E, Pitilakis D. Rapid damage assessment effectiveness for the 2023 Kahramanmaraş Türkiye earthquake sequence. International Journal of Disaster Risk Reduction, 2024;111, 104691.
[15] Sezgin SK, Sakcalı GB, Özen S, Yıldırım E, Avcı E, Bayhan B, Çağlar N. Reconnaissance report on damage caused by the February 6, 2023, Kahramanmaraş Earthquakes in reinforced-concrete structures. Journal of Building Engineering, 2024;89, 109200.
[16] Akar F, Işık E, Avcil F, Büyüksaraç A, Arkan E, İzol R. Geotechnical and structural damages caused by the 2023 Kahramanmaraş Earthquakes in Gölbaşı (Adıyaman). Applied Sciences, 2024;14(5), 2165.
[17] Işık E, Avcil F, Hadzima-Nyarko M, İzol R, Büyüksaraç A, Arkan E, et al. Seismic performance and failure mechanisms of reinforced concrete structures subject to the earthquakes in Türkiye. Sustainability, 2024;16(15), 6473.
[18] Demir A, Celebi E, Ozturk H, Ozcan Z, Ozocak A, Bol E, et al. Destructive impact of successive high magnitude earthquakes occurred in Türkiye's Kahramanmaraş on February 6, 2023. Bulletin of Earthquake Engineering, 2024;1-27.
[19] İnce O. Structural damage assessment of reinforced concrete buildings in Adıyaman after Kahramanmaraş (Türkiye) Earthquakes on 6 February 2023. Engineering Failure Analysis, 2024;156, 107799.
[20] Avğın S, Köse MM, Özbek A. Damage assessment of structural and geotechnical damages in Kahramanmaraş during the February 6, 2023 earthquakes. Engineering Science and Technology, an International Journal, 2024;57, 101811.
[21] Saatcioglu, M., Mitchell, D., Tinawi, R., Gardner, N. J., Gillies, A. G., Ghobarah, A., ... & Lau, D. The August 17, 1999, Kocaeli (Turkey) earthquake damage to structures. Canadian Journal of Civil Engineering, 2001; 28(4), 715-737.
[22] Doğangün, A. Performance of reinforced concrete buildings during the May 1, 2003 Bingöl Earthquake in Turkey. Engineering Structures, 2004; 26(6), 841-856.
[23] Taskin, B., Sezen, A., Tugsal, U. M., & Erken, A. The aftermath of 2011 Van earthquakes: evaluation of strong motion, geotechnical and structural issues. Bulletin of Earthquake Engineering, 2013; 11, 285-312.
[24] Isik, E., Aydin, M. C., & Buyuksarac, A. (2020). 24 January 2020 Sivrice (Elazığ) earthquake damages and determination of earthquake parameters in the region. Earthquakes and Structures, 19(2), 145-156.
[25] Nemutlu, O. F., Balun, B., & Sari, A. Damage assessment of buildings after 24 January 2020 Elazığ-Sivrice earthquake. Earthquakes and Structures, 2021; 20(3), 325-335.
[26] Binici B, Yakut A, Kadas K, Demirel O, Akpinar U, Canbolat A, et al. Performance of RC buildings after Kahramanmaraş earthquakes: lessons toward performance-based design. Earthquake Engineering and Engineering Vibration, 2023; 22(4), 883-894.
[27] Mertol HC, Tunç G, Akış T, Kantekin Y, Aydın İC. Investigation of RC buildings after 6 February 2023, Kahramanmaraş, Türkiye earthquakes. Buildings, 2023;13(7), 1789.
[28] Karasin IB. Comparative analysis of the 2023 Pazarcık and Elbistan Earthquakes in Diyarbakır. Buildings, 2023;13(10), 2474.
[29] Işık E, Avcil F, İzol R, Büyüksaraç A, Bilgin H, Harirchian E, Arkan, E. Field Reconnaissance and Earthquake Vulnerability of the RC Buildings in Adıyaman during 2023 Türkiye Earthquakes. Applied Sciences, 2024;14(7), 2860.
[30] Ozturk M, Arslan MH, Korkmaz HH. Effect on RC buildings of 6 February 2023 Turkey earthquake doublets and new doctrines for seismic design. Engineering Failure Analysis, 2023;153, 107521.
[31] Altunişik, A. C., Arslan, M. E., Kahya, V., Aslan, B., Sezdirmez, T., Dok, G., ... & Nas, M. (2023). Field observations and damage evaluation in reinforced concrete buildings after the February 6th, 2023, Kahramanmaraş–Türkiye Earthquakes. Journal of Earthquake and Tsunami, 17(06), 2350024.
[32] Yuzbasi J. Post-Earthquake Damage Assessment: Field Observations and Recent Developments with Recommendations from the Kahramanmaraş

Earthquakes in Türkiye on February 6th, 2023 (Pazarcık M7. 8 and Elbistan M7. 6). Journal of Earthquake Engineering, 2024;1-26.
[33] Altunişik AC, Arslan ME, Kahya V, Aslan B, Sezdirmez T, Dok G., et al. Field Observations and Damage Evaluation in Reinforced Concrete Buildings After the February 6th, 2023, Kahramanmaraş–Türkiye Earthquakes. Journal of Earthquake & Tsunami, 2023;17(6).
[34] Jaiswal K, Hancilar U, Askan A, Erberik MA., Cakti E, Rao A, et al. A synopsis of rapid characterization and field-based performance assessment of RC structures from the M7. 8 Kahramanmaras earthquake sequence. In AGU Fall Meeting Abstracts 2023; U44A-02.
[35] Tunç G, Mertol HC, Akış T. Lessons learned from four recent Turkish earthquakes: Sivrice-Elazığ, Aegean Sea, and Dual Kahramanmaraş. Natural Hazards, 2024;1-33.
[36] Balun, B. Developing a regression model for predicting the seismic input energy of rc buildings using 6 February 2023 Kahramanmaraş Earthquake. Türk Doğa ve Fen Dergisi, 2024; 13(1), 142-151.
[37] Kahya, V., Genç, A. F., Sunca, F., Roudane, B., Altunişik, A. C., Yilmaz, S., ... & Akgül, T. Evaluation of earthquake-related damages on masonry structures due to the 6 February 2023 Kahramanmaraş-Türkiye earthquakes: A case study for Hatay Governorship Building. Engineering Failure Analysis, 2024; 156, 107855.
[38] Paulay T, Priestley MJN. Seismic Design of Reinforced Concrete and Masonry Buildings. John Wiley & Sons: New York,1992.
[39] Fardis MN. Seismic design, assessment and retrofitting of concrete buildings: based on EN-Eurocode 8 Berlin: Springer. 2009;8
[40] Priestley MJN. Displacement-based seismic assessment of reinforced concrete buildings. Journal of earthquake engineering, 1997;1(01), 157-192.
[41] Ozcan O, Binici B, Ozcebe G. Seismic strengthening of rectangular reinforced concrete columns using fiber reinforced polymers. Engineering Structures, 2021;32(4), 964-973.
[42] Khalifa ES, Al-Tersawy SH. Experimental and analytical behavior of strengthened reinforced concrete columns with steel angles and strips. International Journal of Advanced Structural Engineering (IJASE), 2024;6, 1-14.
[43] Raza S, Khan MK, Menegon SJ, Tsang HH, Wilson JL. Strengthening and repair of reinforced concrete columns by jacketing: State-of-the-art review. Sustainability, 2019;11(11), 3208.
[44] Gholampour A, Hassanli R, Mills JE, Vincent T, Kunieda M. Experimental investigation of the performance of concrete columns strengthened with fiber reinforced concrete jacket. Construction and Building Materials, 2019;194, 51-61.
[45] Murugan K, Sengupta AK. Seismic performance of strengthened reinforced concrete columns. Structures, 2020;27,487-505.
[46] Koteš P, Vavruš M, Jošt J, Prokop J. Strengthening of concrete column by using the wrapper layer of fibre reinforced concrete. Materials, 2020;13(23), 5432.
[47] Sayed MA, Rashwan MM, Helmy ME. Experimental behavior of cracked reinforced concrete columns strengthened with reinforced concrete jacketing. Materials, 2020;13(12), 2832.
[48] Naji A J, Al-Jelawy HM, Saadoon SA, Ejel AT. Rehabilitation and strengthening techniques for reinforced concrete columns. In Journal of Physics: Conference Series 2021;1895,1,012049.
[49] Putra RR, Ono Y, Syah N, Cantika AA. Seismic performance evaluation of existing building in earthquake prone area based on seismic index and seismic demand method. Civil Engineering and Architecture, 2021;9(4), 1237-1245.
[50] Maleknia M. Seismic reliability analysis for strengthening of reinforced-concrete hospital building with base isolation frames. Journal of Civil Engineering Researchers, 2022;4(3), 40.
[51] Yin J, Tang D, Chen T, Yang Y, Ju L, Wan Y, et al. Seismic risk assessment and rehabilitation method of existing rcc structures using micro concrete. Civil Engineering Journal, 2023;9(12), 3008-3018.
[52] Seismosoft. SeismoStruct 2023—A Computer Program for Static and Dynamic Nonlinear Analysis of Framed Structures. 2023. Available online: http://www.seismosoft.com (accessed on 5 January 2024).
[53] Antoniou S, Pinho R. SeismoStruct–Seismic Analysis Program by Seismosoft. In Technical User Manuel; SeismoStruct: Pavia, Italy, 2003.
[54] Bilgin H, Plaku B. (2024). Influence of Confined Concrete Models on the Seismic Response of RC Frames. Structural Durability & Health Monitoring, 2024;18(3),1-26.
[55] Krawinkler H, Seneviratna GDPK. Pros and cons of a pushover analysis of seismic performance evaluation. Engineering structures, 1998;20 (4),452–464.
[56] Shendkar MR, Kontoni DPN, Işık E, Mandal S, Maiti PR, Harirchian E. Influence of Masonry Infill on Seismic Design Factors of Reinforced-Concrete Buildings. Shock and Vibration, 2022;(1), 5521162.
[57] Chopra AK, Goel RK. A modal pushover analysis procedure for estimating seismic demands for buildings. Earthquake engineering & structural dynamics, 2002;31(3), 561-582.
[58] Elnashai AS. Advanced inelastic static (pushover) analysis for earthquake applications. Structural engineering and mechanics, 2001;12(1), 51-69.
[59] Pinho, R. (2007). Using pushover analysis for assessment of buildings and bridges. In Advanced earthquake engineering analysis. Vienna, 2007;91-120
[60] Papanikolaou VK, Elnashai AS, Pareja JF. (2006). Evaluation of conventional and adaptive pushover analysis II: Comparative results. Journal of earthquake engineering, 2006;10(01), 127-151.
[61] Guo W, Hu Y, Liu H, Bu D. Seismic Performance Evaluation of Typical Piers of China's High-Speed Railway Bridge Line Using Pushover Analysis. Mathematical Problems in Engineering, 2019(1), 9514769.

[62] EN 1998-3; Eurocode-8: Design of Structures for Earthquake Resistance-Part 3: Assessment and Retrofitting of Buildings. European Committee for Standardization: Bruxelles, Belgium, 2005.

Volume 14, Issue 2, Page 162-178, 2025 https://doi.org/10.46810/tdfd.1640839 Research Article

BİNGÖL UNIVERSITY

Türk Doğa ve Fen Dergisi
Turkish Journal of Nature and Science
www.dergipark.gov.tr/tdfd

Soft Intersection Bi-quasi Ideals of Semigroup

Aslıhan SEZGİN[1*], Beyza ONUR[2]

[1]Amasya University, Faculty of Education, Department of Mathematics and Science Education, Amasya, Türkiye
[2]Amasya University, Graduate School of Natural and Applied Science, Department of Mathematics, Amasya, Türkiye
Aslıhan SEZGİN ORCID No: 0000-0002-1519-7294
Beyza ONUR ORCID No: 0009-0004-3376-7678

**Corresponding author: aslihan.sezgin@amasya.edu.tr*

(Received: 16.02.2025, Accepted: 02.05.2025, Online Publication: 27.06.2025)

Keywords
Soft set, Semigroups, Bi-quasi ideals, Soft intersection bi-quasi ideals, Simple* semigroups,

Abstract: Mathematicians find it valuable to extend the concept of ideals within algebraic structures. The bi-quasi (ƁQ) ideal was introduced as a broader version of quasi-ideal, bi-ideal, and left (right) ideals in semigroups. This paper applies this concept to soft set theory and semigroups, introducing the "Soft intersection (S-int) ƁQ ideal." The goal is to explore the relationships between S-int ƁQ ideals and other types of S-int ideals in semigroups. It is shown that every S-int bi-ideal, S-int ideal, S-int quasi-ideal, and S-int interior ideal of an idempotent soft set are S-int ƁQ ideals. Counterexamples demonstrate that the reverse is not always true unless the semigroup is simple* or regular. For soft simple* semigroups, the S-int ƁQ ideal coincides with the S-int bi-ideal, S-int left (right) ideal, and S-int quasi-ideal. The main theorem shows that if a subsemigroup of a semigroup is a ƁQ ideal, its soft characteristic function is an S-int ƁQ ideal, and vice versa. This connects semigroup theory with soft set theory. The paper also discusses how this concept integrates into classical semigroup structures, providing characterizations and analysis using soft set operations, soft image, and soft inverse image, supported by examples.

Yarıgrupların Esnek Kesişimsel Bi-quasi İdealleri

Anahtar Kelimeler
Esnek kümeler, Yarıgruplar, Bi-quasi ideals, Esnek kesişimsel bi-quasi ideals, Basit* yarıgrup

Öz: Matematikçiler, cebirsel yapılardaki ideal kavramını genişletmeyi değerli bulmaktadır. Bi-quasi (ƁQ) ideal, yarıgruplarda quasi-ideal, bi-ideal ve sol (sağ) idealin daha geniş bir versiyonu olarak tanıtılmıştır. Bu makale, bu kavramı esnek küme teorisi ve yarıgruplara uygulayarak "Esnek kesişimsel (EK) ƁQ ideali" tanıtmaktadır. Amaç, EK ƁQ idealleri ile diğer EK ideal türleri arasındaki ilişkileri incelemektir. Bir idempotent esnek küme için her EK-bi-ideal, EK-ideal, EK-quasi-ideal ve EK-iç idealin aynı zamanda bir EK*ƁQ ideal olduğu gösterilmiştir. Ancak, tersinin her zaman geçerli olmadığı, yalnızca yarıgrubun basit* veya regüler olduğunda sağlandığı aksine örneklerle gösterilmiştir. Esnek basit* yarıgruplarda, EK-ƁQ idealin EK-bi-ideal, EK-sol (sağ) ideal ve EK-wuazi-ideal ile çakıştığı kanıtlanmıştır.Ana teorem, bir yarıgrubun alt yarıgrubu bir ƁQ ideal ise, onun esnek karakteristik fonksiyonunun bir EK-ƁQ ideal olduğunu ve bunun tersinin de geçerli olduğunu göstermektedir. Bu sonuç, yarıgrup teorisi ile esnek küme teorisi arasındaki bağlantıyı kurmaktadır. Ayrıca, bu kavramın klasik yarıgrup yapılarıyla nasıl bütünleştiği tartışılmakta ve esnek küme işlemleri, esnek görüntü ve esnek ters görüntü kullanılarak çeşitli karakterizasyonlar ve analizler yapılmıştır. Bulgular örneklerle desteklenmiştir.

1. INTRODUCTION

Semigroups are crucial in various areas of mathematics as they provide the abstract algebraic foundation for "memoryless" systems, which reset after every iteration. Initially studied in the early 1900s, semigroups serve as key models for linear time-invariant systems in applied mathematics. Their connection to finite automata makes the study of finite semigroups particularly important in theoretical computer science. The concept of ideals is vital for understanding the structure and applications of mathematical systems, and thus, many mathematicians have focused on extending the theory of ideals in algebraic structures. By utilizing the concept and

properties of generalized ideals, mathematicians have made significant contributions by characterizing algebraic of algebraic structures. Dedekind introduced ideals in the context of algebraic number theory and Noether expanded this concept to include associative rings.

In 1952, Good and Hughes [1] introduced the concept of bi-ideals for semigroups. Steinfeld [2] was the first to present the idea of quasi-ideals for semigroups, later extending it to rings. Quasi-ideals generalize right and left ideals, while bi-ideals are a further generalization of quasi-ideals. The concept of interior ideals was initially introduced by Lajos [3] and later explored by Szasz [4,5]. Interior ideals represent a generalization of the traditional ideal concept. Rao [6-9] developed several novel types of semigroup ideals that generalize existing ones, such as bi-interior ideals, bi-quasi ideals, quasi-ideal, interior ideals, weak-interior ideals, and bi-quasi-interior ideals. Baupradist et al. [10] proposed the concept of essential ideals in semigroups. As a more generalized form of various types of ideals, the notion of "almost" ideals was introduced, with a thorough examination of their characteristics and the relationships between them. The idea of almost ideals for semigroups was first introduced in [11], and a subsequent paper [12] expanded the concept to include almost bi-ideals. The concept of almost quasi-ideals was first presented in [13], and the study of almost interior ideals and weakly almost interior ideals followed in [14]. The authors proposed various types of soft intersection (S-int) almost ideals of semigroups in [15–18]. Additionally, in [13, 15–20], several fuzzy almost ideal types for semigroups were explored.

In 1999, Molodtsov [21] introduced "Soft Set Theory" to address problems involving uncertainty and to develop effective solutions for them. Since its inception, significant research has been conducted on various aspects of soft sets, particularly in relation to soft set operations. Maji et al. [22] provided definitions for soft sets and introduced several operations on them. Pei and Mia [23], along with Ali et al. [24], expanded on the operations of soft sets. For a more comprehensive overview of the growing body of research on soft set operations, we refer to [25-37].

The concept and operations of soft sets were further refined by Çağman and Enginoğlu [38]. Building on this work, Çağman et al. [39] introduced the concept of S-int groups, which spurred the investigation of various soft algebraic systems. In the context of semigroup theory, Sezer et al. [40,41] applied soft sets to define and explore soft intersection (S-int) semigroups, as well as left, right, and two-sided ideals, interior ideals, quasi-ideals, and generalized bi-ideals of semigroups, thoroughly analyzing their key properties. Sezgin and Orbay [42] further studied the soft intersection (S-int) substructures of semigroups, classifying various types, including semisimple semigroups, duo semigroups, and different categories of zero and simple semigroups, along with the semi-lattices of left and right simple semigroups, left and right groups, and groups. S-int almost ideals were introduced and examined as a generalization of various types of S-int ideals in [43-54]. Additionally, the soft versions of different algebraic structures were explored in [55-67].

As a result of the reviews conducted in the literature, some important studies on bi-quasi ideals are identified. The first of these is the study by Rao [69] on the bi-quasi ideals of Γ-semigroups and the fuzzy bi-quasi ideals of these semigroups. Rao [70,71] provided an extensive study on the bi-quasi ideals of semirings. Additionally, the bi-quasi ideals of Γ-semirings were examined by Rao, Venkateswarlu and Rafi [72]. Similarly, Rao [8] made significant contributions to the study of bi-quasi ideals of semigroups. In this paper, we extend the concept to soft set theory and semigroups by introducing "Soft intersection (S-int) bi-quasi (Ƀ) ideals of semigroups." We explore the relationships between S-int Ƀ ideals and other types of S-int ideals within a semigroup. Under certain necessary conditions, it is demonstrated that an S-int ideal (bi-ideal, quasi-ideal, or interior ideal) is indeed an S-int Ƀ ideal of a semigroup. Counterexamples are provided to show that the reverse of these statements does not always hold. It is also proven that for the converse to be true, the semigroup must be a soft simple* (see Definition 2.19) or regular semigroup. Our key theorem reveals that if a nonempty subset of a semigroup is a Ƀ ideal, its soft characteristic function is an S-int Ƀ ideal, and vice versa. This result facilitates the integration of semigroup theory with soft set theory. We illustrate how this concept connects to established algebraic structures in classical semigroup theory by utilizing this theorem. Moreover, we offer conceptual characterizations and analyses of the new idea in the context of soft set operations, soft image, and soft inverse image, supporting our findings with detailed and insightful examples.

The paper is organized into four sections. Section 1 presents an introduction to the subject, whereas Section 2 delves into the basic concepts of semigroups and soft set ideals, detailing their essential definitions and significance. In Section 3, we define S-int Ƀ ideals, examine their properties, and discuss their relationships with other forms of S-int ideals, supported by practical examples. Finally, Section 4 offers a summary of our findings and suggests potential avenues for future research.

2. MATERIAL AND METHOD

In this study, S is used to represent a semigroup. A nonempty subset $\mathcal{K}$ of S is called a subsemigroup of S if $\mathcal{K}\mathcal{K} \subseteq \mathcal{K}$, is called a bi-ideal of S if $\mathcal{K}\mathcal{K} \subseteq \mathcal{K}$ and $\mathcal{K}S\mathcal{K} \subseteq \mathcal{K}$, is called an interior ideal of S if $S\mathcal{K}S \subseteq \mathcal{K}$, and is called a quasi-ideal of S if $\mathcal{K}S \cap S\mathcal{K} \subseteq \mathcal{K}$.

A subsemigroup $\mathcal{K}$ of S is called a left (L-) Ƀ ideal of S if $S\mathcal{K} \cap \mathcal{K}S\mathcal{K} \subseteq \mathcal{K}$, is called a right (R-) Ƀ ideal of S if $\mathcal{K}S \cap \mathcal{K}S\mathcal{K} \subseteq \mathcal{K}$, and is called a Ƀ ideal of S if it is both L-Ƀ ideal of S and R-Ƀ ideal [8].

Definition 2.1. [21] Let E be the parameter set, U be the universal set, $P(U)$ be the power set of U, and $\mathcal{D} \subseteq E$. The soft set (SS) $\mathcal{g}_{\mathcal{D}}$ over U is a function such that $\mathcal{g}_{\mathcal{D}}: E \to P(U)$, where for all $\mathcal{v} \notin \mathcal{D}$, $\mathcal{g}_{\mathcal{D}}(\mathcal{v}) = \emptyset$. That is,

$$\mathfrak{g}_{\mathfrak{D}} = \{(\mathfrak{v}, \mathfrak{g}_{\mathfrak{D}}(\mathfrak{v})) : \mathfrak{v} \in E, \mathfrak{g}_{\mathfrak{D}}(\mathfrak{v}) \in P(U)\}$$

The set of all SSs over U is designated by $S_E(U)$ throughout this paper.

Definition 2.2. [38] Let $\mathfrak{g}_{\mathfrak{D}} \in S_E(U)$. If $\mathfrak{g}_{\mathfrak{D}}(t) = \emptyset$ for all $t \in E$, then $\mathfrak{g}_{\mathfrak{D}}$ is called a null SS and indicated by $\emptyset_E$.

Definition 2.3. [38] Let $\mathfrak{g}_{\mathcal{M}}, \mathfrak{g}_{\mathfrak{N}} \in S_E(U)$. If $\mathfrak{g}_{\mathcal{M}}(\mathfrak{w}) \subseteq \mathfrak{g}_{\mathfrak{N}}(\mathfrak{w})$, for all $\mathfrak{w} \in E$, then $\mathfrak{g}_{\mathcal{M}}$ is a soft subset of $\mathfrak{g}_{\mathfrak{N}}$ and indicated by $\mathfrak{g}_{\mathcal{M}} \tilde{\subseteq} \mathfrak{g}_{\mathfrak{N}}$. If $\mathfrak{g}_{\mathcal{M}}(\varsigma) = \mathfrak{g}_{\mathfrak{N}}(\varsigma)$, for all $\varsigma \in E$, then $\mathfrak{g}_{\mathcal{M}}$ is called soft equal to $\mathfrak{g}_{\mathfrak{N}}$ and denoted by $\mathfrak{g}_{\mathcal{M}} = \mathfrak{g}_{\mathfrak{N}}$.

Definition 2.4. [38] Let $\mathfrak{a}_{\mathcal{M}}, \mathfrak{a}_{\mathfrak{U}} \in S_E(U)$. The union (intersection) of $\mathfrak{a}_{\mathcal{M}}$ and $\mathfrak{a}_{\mathfrak{U}}$ is the SS $\mathfrak{a}_{\mathcal{M}} \tilde{\cup} \mathfrak{a}_{\mathfrak{U}}$ ($\mathfrak{a}_{\mathcal{M}} \tilde{\cap} \mathfrak{a}_{\mathfrak{U}}$), where $(\mathfrak{a}_{\mathcal{M}} \tilde{\cup} \mathfrak{a}_{\mathfrak{U}})(\upsilon) = \mathfrak{a}_{\mathcal{M}}(\upsilon) \cup \mathfrak{a}_{\mathfrak{U}}(\upsilon)$ $\left((\mathfrak{a}_{\mathcal{M}} \tilde{\cap} \mathfrak{a}_{\mathfrak{U}})(\upsilon) = \mathfrak{a}_{\mathcal{M}}(\upsilon) \cap \mathfrak{a}_{\mathfrak{U}}(\upsilon)\right)$, for all $\upsilon \in E$, respectively.

Definition 2.5. [39] Let $\mathfrak{f}_{\mathfrak{K}}, \mathfrak{f}_{\mathfrak{H}} \in S_E(U)$, and ϕ be a function from $\mathfrak{K}$ to $\mathfrak{H}$. Then, the soft image of $\mathfrak{f}_{\mathfrak{K}}$ under ϕ, and the soft pre-image (or soft inverse image) of $\mathfrak{f}_{\mathfrak{H}}$ under ϕ are the SSs $\phi(\mathfrak{f}_{\mathfrak{K}})$ and $\phi^{-1}(\mathfrak{f}_{\mathfrak{H}})$ such that

$$\left(\phi(\mathfrak{f}_{\mathfrak{K}})\right)(\mathfrak{r}) = \begin{cases} \bigcup \{\mathfrak{f}_{\mathfrak{K}}(t) | t \in \mathfrak{K} \text{ and } \phi(t) = \mathfrak{r}\}, & \text{if } \phi^{-1}(\mathfrak{r}) \neq \emptyset \\ \emptyset, & \text{otherwise} \end{cases}$$

for all $\mathfrak{r} \in \mathfrak{H}$ and $\left(\phi^{-1}(\mathfrak{f}_{\mathfrak{H}})\right)(t) = \mathfrak{f}_{\mathfrak{H}}(\phi(t))$ for all $t \in \mathcal{H}$.

Definition 2.6. [39] Let $\mathfrak{f}_{\mathfrak{K}} \in S_E(U)$ and $\alpha \subseteq U$. Then, upper α-inclusion of $\mathfrak{f}_{\mathfrak{K}}$, denoted by $\mathcal{U}(\mathfrak{f}_{\mathfrak{K}}; \alpha)$, is defined as $\mathcal{U}(\mathfrak{f}_{\mathfrak{K}}; \alpha) = \{x \in \mathfrak{K} \mid \mathfrak{f}_{\mathfrak{K}}(x) \supseteq \alpha\}$.

Definition 2.7. [40] Let $\mathfrak{y}_S, g_S \in S_S(U)$. S-int product $\mathfrak{y}_S \circ g_S$ is defined by

$$(\mathfrak{y}_S \circ g_S)(\mathfrak{v}) = \begin{cases} \bigcup_{\mathfrak{v}=yz} \{\mathfrak{y}_S(y) \cap g_S(z)\}, & \text{if } \exists y, z \in S \text{ such that } \mathfrak{v} = yz \\ \emptyset, & \text{otherwise} \end{cases}$$

Theorem 2.8. [40] Let $\mathfrak{h}_S, \mathfrak{p}_S, \mathfrak{n}_S \in S_S(U)$. Then,

i. $(\mathfrak{h}_S \circ \mathfrak{p}_S) \circ \mathfrak{n}_S = \mathfrak{h}_S \circ (\mathfrak{p}_S \circ \mathfrak{n}_S)$
ii. $\mathfrak{h}_S \circ \mathfrak{p}_S \neq \mathfrak{p}_S \circ \mathfrak{h}_S$
iii. $\mathfrak{h}_S \circ (\mathfrak{p}_S \tilde{\cup} \mathfrak{n}_S) = (\mathfrak{h}_S \circ \mathfrak{p}_S) \tilde{\cup} (\mathfrak{h}_S \circ \mathfrak{n}_S)$
$(\mathfrak{h}_S \tilde{\cup} \mathfrak{p}_S) \circ \mathfrak{n}_S = (\mathfrak{h}_S \circ \mathfrak{n}_S) \tilde{\cup} (\mathfrak{p}_S \circ \mathfrak{n}_S)$
iv. $\mathfrak{h}_S \circ (\mathfrak{p}_S \tilde{\cap} \mathfrak{n}_S) = (\mathfrak{h}_S \circ \mathfrak{p}_S) \tilde{\cap} (\mathfrak{h}_S \circ \mathfrak{n}_S)$
$(\mathfrak{h}_S \tilde{\cap} \mathfrak{p}_S) \circ \mathfrak{n}_S = (\mathfrak{h}_S \circ \mathfrak{n}_S) \tilde{\cap} (\mathfrak{p}_S \circ \mathfrak{n}_S)$
v. If $\mathfrak{h}_S \tilde{\subseteq} \mathfrak{p}_S$, then $\mathfrak{h}_S \circ \mathfrak{n}_S \tilde{\subseteq} \mathfrak{p}_S \circ \mathfrak{n}_S$ and $\mathfrak{n}_S \circ \mathfrak{h}_S \tilde{\subseteq} \mathfrak{n}_S \circ \mathfrak{p}_S$
vi. If $\mathfrak{j}_S, \mathfrak{u}_S \in S_S(U)$ such that $\mathfrak{j}_S \tilde{\subseteq} \mathfrak{h}_S$ and $\mathfrak{u}_S \tilde{\subseteq} \mathfrak{p}_S$, then $\mathfrak{j}_S \circ \mathfrak{u}_S \tilde{\subseteq} \mathfrak{h}_S \circ \mathfrak{p}_S$.

Definition 2.9. [40] Let $\emptyset \neq \mathcal{T} \subseteq S$. The soft characteristic function (SCF) of $\mathcal{T}$, denoted by $S_{\mathcal{T}}$, is defined as

$$S_{\mathcal{T}}(v) = \begin{cases} U, & \text{if } v \in \mathcal{T} \\ \emptyset, & \text{if } v \in S \backslash \mathcal{T} \end{cases}$$

Theorem 2.10. [40, 49] Let $\mathfrak{F}, \mathfrak{T} \subseteq S$. Then,

i. $\mathfrak{F} \subseteq \mathfrak{T}$ if and only if (iff) $S_{\mathfrak{F}} \tilde{\subseteq} S_{\mathfrak{T}}$
ii. $S_{\mathfrak{F}} \tilde{\cap} S_{\mathfrak{T}} = S_{\mathfrak{F} \cap \mathfrak{T}}$ and $S_{\mathfrak{F}} \tilde{\cup} S_{\mathfrak{H}} = S_{\mathfrak{F} \cup \mathfrak{T}}$
iii. $S_{\mathfrak{F}} \circ S_{\mathfrak{T}} = S_{\mathfrak{F}\mathfrak{T}}$

Definition 2.11. [40] An SS $\mathfrak{h}_S$ over U is called an S-int subsemigroup of S if $\mathfrak{h}_S(\varsigma \mathfrak{v}) \supseteq \mathfrak{h}_S(\varsigma) \cap \mathfrak{h}_S(\mathfrak{v})$ for all $\varsigma, \mathfrak{v} \in S$.

Note that in [40], the definition of "S-int subsemigroup of S" is given as "S-int semigroup of S"; however in this paper, without loss of generality, we prefer to use "S-int subsemigroup of S".

Definition 2.12. [40] An SS $\mathfrak{h}_S$ over U is called an S-int L-(R-) ideal of S if $\mathfrak{h}_S(\mathfrak{z}\mathfrak{v}) \supseteq \mathfrak{h}_S(\mathfrak{v})$ $(\mathfrak{h}_S(\mathfrak{z}\mathfrak{v}) \supseteq \mathfrak{h}_S(\mathfrak{z}))$ for all $\mathfrak{z}, y \in S$, and is called an S-int two-sided ideal (S-int ideal) of S if it is both S-int L-ideal of S over U and S-int R-ideal of S over U. An S-int subsemigroup $\mathfrak{h}_S$ is called an S-int bi-ideal of S if $\mathfrak{h}_S(ry\mathfrak{v}) \supseteq \mathfrak{h}_S(r) \cap \mathfrak{h}_S(\mathfrak{v})$ for all $r, y, \mathfrak{v} \in S$. An SS $\mathfrak{h}_S$ over U is called an S-int interior ideal of S if $\mathfrak{h}_S(ry\mathfrak{v}) \supseteq \mathfrak{h}_S(y)$ for all $r, y, \mathfrak{v} \in S$.

It is easy to see that if $\mathfrak{h}_S(\mathfrak{v}) = U$ for all $\mathfrak{v} \in S$, then $\mathfrak{h}_S$ is an S-int subsemigroup (L-ideal, R-ideal, ideal, bi-ideal, interior ideal). We denote such a kind of S-int subsemigroup (L-ideal, R-ideal, ideal, bi-ideal, interior ideal) by $\tilde{\mathfrak{S}}$. It is obvious that $\tilde{\mathfrak{S}} = S_S$, that is, $\tilde{\mathfrak{S}}(\mathfrak{v}) = U$ for all $\mathfrak{v} \in S$ [40].

Definition 2.13. [41] An SS $\mathfrak{h}_S$ over U is called an S-int quasi-ideal of S over U if $\left(\tilde{\mathfrak{S}} \circ \mathfrak{h}_S\right) \tilde{\cap} \left(\mathfrak{h}_S \circ \tilde{\mathfrak{S}}\right) \tilde{\subseteq} \mathfrak{h}_S$.

Theorem 2.14. [40] Let $\mathfrak{h}_S \in S_S(U)$. Then,

i. $\tilde{\mathfrak{S}} \circ \tilde{\mathfrak{S}} \tilde{\subseteq} \tilde{\mathfrak{S}}$
ii. $\tilde{\mathfrak{S}} \circ \mathfrak{h}_S \tilde{\subseteq} \tilde{\mathfrak{S}}$ and $\mathfrak{h}_S \circ \tilde{\mathfrak{S}} \tilde{\subseteq} \tilde{\mathfrak{S}}$
iii. $\mathfrak{h}_S \tilde{\cup} \tilde{\mathfrak{S}} = \tilde{\mathfrak{S}}$ and $\mathfrak{h}_S \tilde{\cap} \tilde{\mathfrak{S}} = \mathfrak{h}_S$

Theorem 2.15. [40, 41] Let $\mathfrak{D}$ be a nonempty subset of a semigroup S. Then, $\mathfrak{D}$ is a subsemigroup (L-ideal, R-ideal, two-sided ideal, bi-ideal, interior ideal, quasi-ideal) of S iff $S_{\mathfrak{D}}$ is an S-int subsemigroup (L-ideal, R-ideal, two-sided ideal, bi-ideal, interior ideal, quasi-ideal).

Theorem 2.16. [40, 41] Let $\mathfrak{h}_S \in S_S(U)$. Then,

i. $\mathfrak{h}_S$ is an S-int subsemigroup $\Leftrightarrow (\mathfrak{h}_S \circ \mathfrak{h}_S) \tilde{\subseteq} \mathfrak{h}_S$,
ii. $\mathfrak{h}_S$ is an S-int L-(R-) ideal $\Leftrightarrow \left(\tilde{\mathfrak{S}} \circ \mathfrak{h}_S\right) \tilde{\subseteq} \mathfrak{h}_S$ and $\left(\mathfrak{h}_S \circ \tilde{\mathfrak{S}}\right) \tilde{\subseteq} \mathfrak{h}_S$,

iii. $\mathfrak{h}_S$ is an S-int bi-ideal $\Leftrightarrow (\mathfrak{h}_S \circ \mathfrak{h}_S) \tilde{\subseteq} \mathfrak{h}_S$ and $\left(\mathfrak{h}_S \circ \tilde{\mathfrak{S}} \circ \mathfrak{h}_S\right) \tilde{\subseteq} \mathfrak{h}_S$,

iv. $\mathfrak{h}_S$ is an S-int interior ideal $\Leftrightarrow \left(\tilde{\mathfrak{S}} \circ \mathfrak{h}_S \circ \tilde{\mathfrak{S}}\right) \tilde{\subseteq} \mathfrak{h}_S$.

Theorem 2.17. [40, 41] The following assertions hold:

i. Every S-int L-(R-/two-sided) ideal is an S-int subsemigroup (S-int bi-ideal/S-int quasi-ideal),
ii. Every S-int ideal is an S-int bi-ideal.

Proposition 2.18. [40] Let $\mathfrak{h}_S \in S_S(U)$, α be a subset of U, $Im(\mathfrak{h}_S)$ be the image of $\mathfrak{h}_S$ such that $\alpha \in Im(\mathfrak{h}_S)$. If $\mathfrak{h}_S$ is an S-int subsemigroup of S, then $\mathcal{U}(\mathfrak{h}_S; \alpha)$ is a subsemigroup of S.

Definition 2.19. [68] Let $\mathfrak{h}_S \in S_S(U)$. Then, S is called a soft left simple* semigroup (with respect to $\mathfrak{h}_S$) if $\tilde{\mathfrak{S}} = \tilde{\mathfrak{S}} \circ \mathfrak{h}_S$, is called a soft right simple* semigroup (with respect to $\mathfrak{h}_S$) if $\tilde{\mathfrak{S}} = \mathfrak{h}_S \circ \tilde{\mathfrak{S}}$, is called a soft simple* semigroup (with respect to $\mathfrak{h}_S$) if $\tilde{\mathfrak{S}} = \tilde{\mathfrak{S}} \circ \mathfrak{h}_S = \mathfrak{h}_S \circ \tilde{\mathfrak{S}}$. If S is a soft (left/right) simple* semigroup with respect to all soft sets over U, then it is called a soft (left/right) simple* semigroup .

For the sake of brevity, soft (left/right) simple* semigroup is abbreviated by soft (L-/ R-) simple*.

Corollary 2.20. [40] For a semigroup S, the following conditions are equivalent:

i. S is regular.
ii. $\mathfrak{h}_S \circ \mathfrak{p}_S = \mathfrak{h}_S \tilde{\cap} \mathfrak{p}_S$ for every S-int ideals $\mathfrak{h}_S$ and $\mathfrak{p}_S$ of S over U.

3. RESULTS

Definition 3.1. A soft set η_S over U is called a soft intersection left (right) (L-(R-) bi-quasi ideal of S over U if

$$\left(\tilde{\mathfrak{S}} \circ \eta_S\right) \tilde{\cap} \left(\eta_S \circ \tilde{\mathfrak{S}} \circ \eta_S\right) \tilde{\subseteq} \eta_S$$

$$\left(\left(\eta_S \circ \tilde{\mathfrak{S}}\right) \tilde{\cap} \left(\eta_S \circ \tilde{\mathfrak{S}} \circ \eta_S\right) \tilde{\subseteq} \eta_S\right)$$

A soft set over U is called a soft intersection bi-quasi ideal of S if it is both a soft intersection left bi-quasi ideal and a soft intersection right bi-quasi ideal of S over U. For the sake of brevity, soft intersection bi-quasi ideal of S over U is abbreviated by S-int ƁQ ideal.

Example 3.2. Consider the semigroup $S = \{\mathfrak{f}, h, \mathfrak{r}\}$ defined by the following table:

Table 1. Cayley table of '♦' binary operation.

♦	$\mathfrak{f}$	h	$\mathfrak{r}$
$\mathfrak{f}$	$\mathfrak{f}$	$\mathfrak{r}$	$\mathfrak{r}$
h	$\mathfrak{r}$	h	$\mathfrak{r}$
$\mathfrak{r}$	$\mathfrak{r}$	$\mathfrak{r}$	$\mathfrak{r}$

Let η_S and $\mathfrak{K}_S$ be SSs over $U = D_3 = \{< x, y >: x^3 = y^2 = e,\ xy = yx^2\} = \{e, x, x^2, y, yx, yx^2\}$ as follows:

$$\eta_S = \{(\mathfrak{f}, \{e, x, x^2\}), (h, \{e, x\}), (\mathfrak{r}, \{e, x, x^2, y\})\}$$

$$\mathfrak{K}_S = \{(\mathfrak{f}, \{e, x, y\}), (h, \{e, x\}), (\mathfrak{r}, \{e, x^2, y, yx^2\})\}$$

It can be readily proven that η_S is an S-int ƁQ ideal of S. Here, we find it appropriate to give a few concrete examples of elements for ease of illustration in order to be more understandable. In fact,

$$\left[\left(\tilde{\mathfrak{S}} \circ \eta_S\right) \tilde{\cap} \left(f_S \circ \tilde{\mathfrak{S}} \circ \eta_S\right)\right](\mathfrak{f}) = \eta_S(\mathfrak{f}) \subseteq \eta_S(\mathfrak{f})$$

$$\left[\left(\tilde{\mathfrak{S}} \circ \eta_S\right) \tilde{\cap} \left(\eta_S \circ \tilde{\mathfrak{S}} \circ \eta_S\right)\right](h) = \eta_S(h) \subseteq \eta_S(h)$$

$$\left[\left(\tilde{\mathfrak{S}} \circ \eta_S\right) \tilde{\cap} \left(\eta_S \circ \tilde{\mathfrak{S}} \circ \eta_S\right)\right](\mathfrak{r}) = \eta_S(h) \cup \eta_S(\mathfrak{r}) \cup \eta_S(\mathfrak{f}) \subseteq \eta_S(\mathfrak{r})$$

It can be easily shown that the SS η_S satisfies the S-int L-ƁQ ideal condition for all other element combinations of the set S. Similarly,

$$\left[\left(\eta_S \circ \tilde{\mathfrak{S}}\right) \tilde{\cap} \left(\eta_S \circ \tilde{\mathfrak{S}} \circ \eta_S\right)\right](\mathfrak{f}) \subseteq \eta_S(\mathfrak{f})$$

$$\left[\left(\eta_S \circ \tilde{\mathfrak{S}}\right) \tilde{\cap} \left(\eta_S \circ \tilde{\mathfrak{S}} \circ \eta_S\right)\right](h) \subseteq \eta_S(h)$$

$$\left[\left(\eta_S \circ \tilde{\mathfrak{S}}\right) \tilde{\cap} \left(\eta_S \circ \tilde{\mathfrak{S}} \circ \eta_S\right)\right](\mathfrak{r}) \subseteq \eta_S(\mathfrak{r})$$

It can be easily shown that the SS η_S satisfies the S-int R-ƁQ ideal condition for all other element combinations of the set S, thus η_S is an S-int ƁQ ideal. However, since

$$\left[\left(\tilde{\mathfrak{S}} \circ \mathfrak{K}_S\right) \tilde{\cap} \left(\mathfrak{K}_S \circ \tilde{\mathfrak{S}} \circ \mathfrak{K}_S\right)\right](\mathfrak{r}) = [\mathfrak{K}_S(h) \cup \mathfrak{K}_S(\mathfrak{r}) \cup \mathfrak{K}_S(\mathfrak{f})] \not\subseteq \mathfrak{K}_S(\mathfrak{r})$$

$\mathfrak{K}_S$ is not an S-int ƁQ ideal.

Corollary 3.3. $\tilde{\mathfrak{S}}$ and $\emptyset_S$ are S-int ƁQ ideals.

Theorem 3.4. Let $\mathfrak{H}$ be a subsemigroup of S. Then, $\mathfrak{H}$ is a ƁQ ideal of S iff $S_{\mathfrak{H}}$, the SCF of $\mathfrak{H}$, is an S-int ƁQ ideal.
Proof: Let $\mathfrak{H}$ be a ƁQ ideal of S. Then, $S\mathfrak{H} \cap \mathfrak{H}S\mathfrak{H} \tilde{\subseteq} \mathfrak{H}$ and $\mathfrak{H}S \cap \mathfrak{H}S\mathfrak{H} \tilde{\subseteq} \mathfrak{H}$. By Theorem 2.10,

$$\left(\tilde{\mathfrak{S}} \circ S_{\mathfrak{H}}\right) \tilde{\cap} \left(S_{\mathfrak{H}} \circ \tilde{\mathfrak{S}} \circ S_{\mathfrak{H}}\right) = (S_S \circ S_{\mathfrak{H}}) \tilde{\cap} \left(S_{\mathfrak{H}} \circ S_S \circ S_{\mathfrak{H}}\right) = S_{S\mathfrak{H}} \tilde{\cap} S_{\mathfrak{H}S\mathfrak{H}} = S_{S\mathfrak{H} \cap \mathfrak{H}S\mathfrak{H}} \tilde{\subseteq} S_{\mathfrak{H}}$$

and

$$\left(S_{Hϳ} \circ \widetilde{S}\right) \widetilde{\cap} \left(S_{Hϳ} \circ \widetilde{S} \circ S_{Hϳ}\right) = \left(S_{Hϳ} \circ S_S\right) \widetilde{\cap} \left(S_{Hϳ} \circ S_S \circ S_{Hϳ}\right)$$
$$= S_{HϳS} \widetilde{\cap} S_{HϳSHϳ} = S_{HϳS \cap HϳSHϳ} \widetilde{\subseteq} S_{Hϳ}$$

Hence, $S_{Hϳ}$ is an S-int ƁQ ideal.

Conversely, let $S_{Hϳ}$ be an S-int ƁQ ideal and $Hϳ$ be a subsemigroup of S. Then,

$$\left(\widetilde{S} \circ S_{Hϳ}\right) \widetilde{\cap} \left(S_{Hϳ} \circ \widetilde{S} \circ S_{Hϳ}\right) \widetilde{\subseteq} S_{Hϳ}$$

and

$$\left(S_{Hϳ} \circ \widetilde{S}\right) \widetilde{\cap} \left(S_{Hϳ} \circ \widetilde{S} \circ S_{Hϳ}\right) \widetilde{\subseteq} S_{Hϳ}.$$

Let $ɾ \in SHϳ \cap HϳSHϳ$. Then,

$$S_{Hϳ}(ɾ) \supseteq \left(\widetilde{S} \circ S_{Hϳ}\right)(ɾ) \cap \left(S_{Hϳ} \circ \widetilde{S} \circ S_{Hϳ}\right)(ɾ)$$
$$\supseteq S_{SHϳ}(ɾ) \cap S_{HϳSHϳ}(ɾ) \supseteq S_{SHϳ \cap HϳSHϳ}(ɾ)$$
$$= U$$

Thus, $S_{Hϳ}(ɾ) = U$ and so $ɾ \in Hϳ$, implying that $SHϳ \cap HϳSHϳ \subseteq Hϳ$. Hence, $Hϳ$ is an L-ƁQ ideal of S. Similarly, let $ƶ \in HϳS \cap HϳSHϳ$. Then,

$$S_{Hϳ}(ƶ) \supseteq \left(S_{Hϳ} \circ \widetilde{S}\right)(ƶ) \cap \left(S_{Hϳ} \circ \widetilde{S} \circ S_{Hϳ}\right)(ƶ) \supseteq S_{HϳS}(ƶ) \cap S_{HϳSHϳ}(ƶ) \supseteq S_{HϳS \cap HϳSHϳ}(ƶ) = U$$

Thus, $S_{Hϳ}(ƶ) = U$, and so $ƶ \in Hϳ$, implying that $HϳS \cap HϳSHϳ \subseteq Hϳ$. Hence, $Hϳ$ is an R-ƁQ ideal of S. Therefore, $Hϳ$ is a ƁQ ideal of S.

Example 3.5. We consider the semigroup in Example 3.2. One can show that $B = \{ƒ, ɾ\}$ is a ƁQ ideal of S. By the definition of SCF, $S_B = \{(ƒ, U), (h, \emptyset), (ɾ, U)\}$. One can easily show that S_B is an S-int ƁQ ideal. Conversely, by choosing the S-int ƁQ ideal as $\eta_S = \{(ƒ, \emptyset), (h, U), (ɾ, U)\}$, which is the SCF of $K = \{h, ɾ\}$, one can show that K is a ƁQ ideal of S.

Now, we continue with the relationships between S-int ƁQ ideals and other types of S-int ideals of S.

Proposition 3.6. Every S-int bi-ideal is an S-int R-ƁQ ideal.

Proof: Let $ɱ_S$ be an S-int bi-ideal of S. Then, $ɱ_S \circ \widetilde{S} \circ ɱ_S \widetilde{\subseteq} ɱ_S$. Thus,

$$\left(ɱ_S \circ \widetilde{S}\right) \widetilde{\cap} \left(ɱ_S \circ \widetilde{S} \circ ɱ_S\right) \widetilde{\subseteq} ɱ_S \circ \widetilde{S} \circ ɱ_S \widetilde{\subseteq} ɱ_S$$

Hence, $ɱ_S$ is an S-int R-ƁQ ideal of S.

We show with a counterexample that the converse of Proposition 3.6 is not true:

Example 3.7. Consider the semigroup $S = \{ə, y, ɾ, ƨ\}$ defined by the following table:

Table 1. Cayley table of '⸗' binary operation.

⸗	ə	y	ɾ	ƨ
ə	ə	ə	ə	ə
y	ə	ə	ə	ə
ɾ	ə	ə	ə	Y
ƨ	ə	ə	y	ɾ

Let $ɱ_S$ be an SS over $U = N$ as follows:

$$ɱ_S = \{(ə, \{1,2,3,4\}), (y, \{1,2,3\}), (ɾ, \{4\}), (ƨ, \{1,2\})\}$$

Here, $ɱ_S$ is an S-int R-ƁQ ideal. In fact,

$$\left[\left(ɱ_S \circ \widetilde{S}\right) \widetilde{\cap} \left(ɱ_S \circ \widetilde{S} \circ ɱ_S\right)\right](ə)$$
$$= ɱ_S(ə) \cup ɱ_S(y) \cup ɱ_S(ɾ) \cup ɱ_S(ƨ)$$
$$\subseteq ɱ_S(ə)$$

$$\left[\left(ɱ_S \circ \widetilde{S}\right) \widetilde{\cap} \left(ɱ_S \circ \widetilde{S} \circ ɱ_S\right)\right](y) = ɱ_S(ƨ) \subseteq ɱ_S(y)$$

$$\left[\left(ɱ_S \circ \widetilde{S}\right) \widetilde{\cap} \left(ɱ_S \circ \widetilde{S} \circ ɱ_S\right)\right](ɾ) = \emptyset \subseteq ɱ_S(ɾ)$$

$$\left[\left(ɱ_S \circ \widetilde{S}\right) \widetilde{\cap} \left(ɱ_S \circ \widetilde{S} \circ ɱ_S\right)\right](ƨ) = \emptyset \subseteq ɱ_S(ƨ)$$

Thus, $ɱ_S$ is an S-int R-ƁQ ideal of S. However, since $(ɱ_S \circ ɱ_S)(ɾ) = ɱ_S(ƨ) \cap ɱ_S(ƨ) \not\subseteq ɱ_S(ɾ)$, $ɱ_S$ is not an S-int bi-ideal.

Proposition 3.8 shows that the converse of Proposition 3.6 holds for soft L-simple* semigroups.

Proposition 3.8. Let $ɱ_S \in S_S(U)$ and S be a soft L-simple* semigroup. Then, the following conditions are equivalent:

(1) $ɱ_S$ is an S-int bi-ideal.
(2) $ɱ_S$ is an S-int R-ƁQ ideal.

Proof: (1) implies (2) is obvious by Proposition 3.6. Assume that $ɱ_S$ is an S-int R-ƁQ ideal. By assumption, $\widetilde{S} = \widetilde{S} \circ ɱ_S$. Thus,

$$ɱ_S \circ ɱ_S = (ɱ_S \circ ɱ_S) \widetilde{\cap} (ɱ_S \circ ɱ_S) \widetilde{\subseteq} \left(ɱ_S \circ \widetilde{S}\right) \widetilde{\cap} \left(ɱ_S \circ \widetilde{S}\right)$$
$$= \left(ɱ_S \circ \widetilde{S}\right) \widetilde{\cap} \left(ɱ_S \circ \widetilde{S} \circ ɱ_S\right) \widetilde{\subseteq} ɱ_S$$

Hence, $ɱ_S$ is an S-int subsemigroup. Moreover,

$$ɱ_S \circ \widetilde{S} \circ ɱ_S = \left(ɱ_S \circ \widetilde{S} \circ ɱ_S\right) \widetilde{\cap} \left(ɱ_S \circ \widetilde{S} \circ ɱ_S\right)$$
$$= (ɱ_S \circ \widetilde{S}) \widetilde{\cap} \left(ɱ_S \circ \widetilde{S} \circ ɱ_S\right) \widetilde{\subseteq} ɱ_S$$

Thus, $ɱ_S$ is an S-int bi-ideal.

Proposition 3.9. Every S-int bi-ideal is an S-int L-ƁQ ideal.

Proof: Let $ɱ_S$ be an S-int bi-ideal of S. Then, $ɱ_S \circ \widetilde{S} \circ ɱ_S \widetilde{\subseteq} ɱ_S$. Thus,

$$\left(\widetilde{\mathfrak{S}} \circ \mathfrak{H}_S\right) \widetilde{\cap} \left(\mathfrak{H}_S \circ \widetilde{\mathfrak{S}} \circ \mathfrak{H}_S\right) \widetilde{\subseteq} \mathfrak{H}_S \circ \widetilde{\mathfrak{S}} \circ \mathfrak{H}_S \widetilde{\subseteq} \mathfrak{H}_S$$

Hence, $\mathfrak{H}_S$ is an S-int L-BQ ideal of S.

We show with a counterexample that the converse of Proposition 3.9 is not true:

Example 3.10. Consider the SS $\mathfrak{H}_S$ in Example 3.7. The SS $\mathfrak{H}_S$ is an S-int L-BQ ideal. Since,

$$\left[\left(\widetilde{\mathfrak{S}} \circ \mathfrak{H}_S\right) \widetilde{\cap} \left(\mathfrak{H}_S \circ \widetilde{\mathfrak{S}} \circ \mathfrak{H}_S\right)\right](a) = \mathfrak{H}_S(a) \cup \mathfrak{H}_S(b) \cup \mathfrak{H}_S(r) \cup \mathfrak{H}_S(s) \subseteq \mathfrak{H}_S(a)$$

$$\left[\left(\widetilde{\mathfrak{S}} \circ \mathfrak{H}_S\right) \widetilde{\cap} \left(\mathfrak{H}_S \circ \widetilde{\mathfrak{S}} \circ \mathfrak{H}_S\right)\right](b) = \mathfrak{H}_S(s) \subseteq \mathfrak{H}_S(b)$$

$$\left[\left(\widetilde{\mathfrak{S}} \circ \mathfrak{H}_S\right) \widetilde{\cap} \left(\mathfrak{H}_S \circ \widetilde{\mathfrak{S}} \circ \mathfrak{H}_S\right)\right](r) = \emptyset \subseteq \mathfrak{H}_S(r)$$

$$\left[\left(\widetilde{\mathfrak{S}} \circ \mathfrak{H}_S\right) \widetilde{\cap} \left(\mathfrak{H}_S \circ \widetilde{\mathfrak{S}} \circ \mathfrak{H}_S\right)\right](s) = \emptyset \subseteq \mathfrak{H}_S(s)$$

Hence, $\mathfrak{H}_S$ is an S-int L-BQ ideal. However, since

$$(\mathfrak{H}_S \circ \mathfrak{H}_S)(r) = \mathfrak{H}_S(s) \cap \mathfrak{H}_S(s) \not\subseteq \mathfrak{H}_S(r)$$

$\mathfrak{H}_S$ is not an S-int bi-ideal.

Proposition 3.11 shows that the converse of Proposition 3.9 holds for soft R-simple* semigroups.

Proposition 3.11. Let $\mathfrak{H}_S \in S_S(U)$ and S be a soft R-simple* semigroup. Then, the following conditions are equivalent:

(1) $\mathfrak{H}_S$ is an S-int bi-ideal.
(2) $\mathfrak{H}_S$ is an S-int L-BQ ideal.

Proof: (1) implies (2) is obvious by Theorem 3.9. Assume that $\mathfrak{H}_S$ is an S-int L-BQ ideal. By assumption, $\widetilde{\mathfrak{S}} = \mathfrak{H}_S \circ \widetilde{\mathfrak{S}}$. Thus,

$$\mathfrak{H}_S \circ \mathfrak{H}_S = (\mathfrak{H}_S \circ \mathfrak{H}_S) \widetilde{\cap} (\mathfrak{H}_S \circ \mathfrak{H}_S) \widetilde{\subseteq} \left(\mathfrak{H}_S \circ \widetilde{\mathfrak{S}}\right) \widetilde{\cap} \left(\mathfrak{H}_S \circ \widetilde{\mathfrak{S}}\right) = \left(\mathfrak{H}_S \circ \widetilde{\mathfrak{S}}\right) \widetilde{\cap} \left(\mathfrak{H}_S \circ \widetilde{\mathfrak{S}} \circ \mathfrak{H}_S\right) \widetilde{\subseteq} \mathfrak{H}_S$$

Hence, $\mathfrak{H}_S$ is an S-int subsemigroup. Moreover,

$$\mathfrak{H}_S \circ \widetilde{\mathfrak{S}} \circ \mathfrak{H}_S = \left(\mathfrak{H}_S \circ \widetilde{\mathfrak{S}} \circ \mathfrak{H}_S\right) \widetilde{\cap} \left(\mathfrak{H}_S \circ \widetilde{\mathfrak{S}} \circ \mathfrak{H}_S\right) = (\widetilde{\mathfrak{S}} \circ \mathfrak{H}_S) \widetilde{\cap} \left(\mathfrak{H}_S \circ \widetilde{\mathfrak{S}} \circ \mathfrak{H}_S\right) \widetilde{\subseteq} \mathfrak{H}_S$$

Thus, $\mathfrak{H}_S$ is an S-int bi-ideal.

Theorem 3.12. Every S-int bi-ideal is an S-int BQ ideal.

Proof: It is followed by Proposition 3.6 and Proposition 3.9.

Theorem 3.13 shows that the converse of Theorem 3.12 holds for soft simple* semigroup.

Theorem 3.13. Let $\mathfrak{H}_S \in S_S(U)$ and S be a soft simple* semigroup. Then, the following conditions are equivalent:

(1) $\mathfrak{H}_S$ is an S-int bi-ideal.
(2) $\mathfrak{H}_S$ is an S-int BQ ideal.

Proof: (1) implies (2) is obvious by Theorem 3.12. Assume that $\mathfrak{H}_S$ is an S-int BQ ideal. Then, by Definition 2.19, S is both a soft L-simple* and a soft R-simple* semigroup. The rest of the proof follows from Proposition 3.8 and Proposition 3.11.

Proposition 3.14. Every S-int R-ideal is an S-int R-BQ ideal.

Proof: Let η_S be an S-int R-ideal of S. Then, $\eta_S \circ \widetilde{\mathfrak{S}} \widetilde{\subseteq} \eta_S$. Thus, $\left(\eta_S \circ \widetilde{\mathfrak{S}}\right) \widetilde{\cap} \left(\eta_S \circ \widetilde{\mathfrak{S}} \circ \eta_S\right) \widetilde{\subseteq} \eta_S \circ \widetilde{\mathfrak{S}} \widetilde{\subseteq} \eta_S$. Hence, η_S is an S-int R-BQ ideal of S.

Additionally, since η_S is an S-int R-ideal, by Theorem 2.17, it is an S-int bi-ideal. Therefore, by Proposition 3.6, η_S is an S-int R-BQ ideal.

We show with a counterexample that the converse of Proposition 3.14 is not true:

Example 3.15. Consider the semigroup $S = \{x, z\}$ defined by the following table:

Table 3: Cayley table of '☼' binary operation.

☼	x	z
x	x	z
z	x	z

Let η_S be an SS over $U = \mathbb{Z}$ as follows:

$$\eta_S = \{(x, \{1,3\}), (z, \{1,2\})\}$$

Here, η_S is an S-int R-BQ ideal. In fact,

$$\left[\left(\eta_S \circ \widetilde{\mathfrak{S}}\right) \widetilde{\cap} \left(\eta_S \circ \widetilde{\mathfrak{S}} \circ \eta_S\right)\right](x) = (\eta_S \circ \widetilde{\mathfrak{S}})(x) \cap \left(\eta_S \circ \widetilde{\mathfrak{S}} \circ \eta_S\right)(x) = \eta_S(x) \subseteq \eta_S(x)$$

$$\left[\left(\eta_S \circ \widetilde{\mathfrak{S}}\right) \widetilde{\cap} \left(\eta_S \circ \widetilde{\mathfrak{S}} \circ \eta_S\right)\right](z) = \left(\eta_S \circ \widetilde{\mathfrak{S}}\right)(z) \cap \left(\eta_S \circ \widetilde{\mathfrak{S}} \circ \eta_S\right)(z) = \eta_S(z) \subseteq \eta_S(z)$$

Thus, η_S is an S-int R-BQ ideal of S. However, since

$$\left(\eta_S \circ \widetilde{\mathfrak{S}}\right)(x) = \left[\eta_S(x) \cap \widetilde{\mathfrak{S}}(x)\right] \cup \left[\eta_S(z) \cap \widetilde{\mathfrak{S}}(x)\right] = \eta_S(x) \cup \eta_S(z) \not\subseteq \eta_S(x)$$

$$\left(\eta_S \circ \widetilde{\mathbb{S}}\right)(z) = \left[\eta_S(y) \cap \widetilde{\mathbb{S}}(z)\right] \cup \left[\eta_S(z) \cap \widetilde{\mathbb{S}}(z)\right] = \eta_S(y) \cup \eta_S(z) \not\subseteq \eta_S(z)$$

η_S is not an S-int R-ideal.

Proposition 3.16 shows that the converse of Proposition 3.14 holds for soft L-simple* semigroups.

Proposition 3.16. Let $\eta_S \in S_S(U)$ and S be a soft L-simple* semigroup. Then, the following conditions are equivalent:

(1) η_S is an S-int R-ideal.
(2) η_S is an S-int R-BQ ideal.

Proof: (1) implies (2) is obvious by Proposition 3.14. Assume that η_S is an S-int R-BQ ideal. By assumption, $\widetilde{\mathbb{S}} = \widetilde{\mathbb{S}} \circ \eta_S$. Thus,

$$\left(\eta_S \circ \widetilde{\mathbb{S}}\right) = \left(\eta_S \circ \widetilde{\mathbb{S}}\right) \widetilde{\cap} \left(\eta_S \circ \widetilde{\mathbb{S}}\right) = (\eta_S \circ \widetilde{\mathbb{S}}) \widetilde{\cap} \left(\eta_S \circ \widetilde{\mathbb{S}} \circ \eta_S\right) \cong \eta_S$$

Hence, η_S is an S-int R-ideal.

Proposition 3.17. Every S-int R-ideal is an S-int L-BQ ideal.

Proof: Let η_S be an S-int R-ideal of S. Then, $\eta_S \circ \widetilde{\mathbb{S}} \cong \eta_S$ and $\eta_S \circ \eta_S \cong \eta_S$. Thus,

$$\left(\widetilde{\mathbb{S}} \circ \eta_S\right) \widetilde{\cap} \left(\eta_S \circ \widetilde{\mathbb{S}} \circ \eta_S\right) \cong \eta_S \circ \widetilde{\mathbb{S}} \circ \eta_S \cong \eta_S \circ \eta_S \cong \eta_S$$

Hence, η_S is an S-int L-BQ ideal of S.

Additionally, since η_S is an S-int R-ideal, by Theorem 2.17, it is an S-int bi-ideal. Therefore, by Proposition 3.9, η_S is an S-int L-BQ ideal.

We show with a counterexample that the converse of Proposition 3.17 is not true:

Example 3.18. Consider the SS η_S in Example 3.15. The SS η_S is an S-int L-BQ ideal. Since,

$$\left[\left(\widetilde{\mathbb{S}} \circ \eta_S\right) \widetilde{\cap} \left(\eta_S \circ \widetilde{\mathbb{S}} \circ \eta_S\right)\right](y) = \left(\widetilde{\mathbb{S}} \circ \eta_S\right)(y) \cap \left(\eta_S \circ \widetilde{\mathbb{S}} \circ \eta_S\right)(y) = \eta_S(y) \subseteq \eta_S(y)$$

$$\left[\left(\widetilde{\mathbb{S}} \circ \eta_S\right) \widetilde{\cap} \left(\eta_S \circ \widetilde{\mathbb{S}} \circ \eta_S\right)\right](z) = \left(\widetilde{\mathbb{S}} \circ \eta_S\right)(z) \cap \left(\eta_S \circ \widetilde{\mathbb{S}} \circ \eta_S\right)(z) = \eta_S(z) \subseteq \eta_S(z)$$

Hence, η_S is an S-int L-BQ ideal. However, since

$$\left(\eta_S \circ \widetilde{\mathbb{S}}\right)(y) = \left[\eta_S(y) \cap \widetilde{\mathbb{S}}(y)\right] \cup \left[\eta_S(z) \cap \widetilde{\mathbb{S}}(y)\right] = \eta_S(y) \cup \eta_S(z) \not\subseteq \eta_S(y)$$

$$\left(\eta_S \circ \widetilde{\mathbb{S}}\right)(z) = \left[\eta_S(y) \cap \widetilde{\mathbb{S}}(z)\right] \cup \left[\eta_S(z) \cap \widetilde{\mathbb{S}}(z)\right] = \eta_S(y) \cup \eta_S(z) \not\subseteq \eta_S(z)$$

η_S is not an S-int R-ideal.

Proposition 3.19 shows that the converse of Proposition 3.17 holds for soft simple* semigroups.

Proposition 3.19. Let $\eta_S \in S_S(U)$ and S be a soft simple* semigroup. Then, the following conditions are equivalent:

(1) η_S is an S-int R-ideal.
(2) η_S is an S-int L-BQ ideal.

Proof: (1) implies (2) is obvious by Theorem 3.17. Assume that η_S is an S-int L-BQ ideal. By assumption, $\widetilde{\mathbb{S}} = \eta_S \circ \widetilde{\mathbb{S}} = \widetilde{\mathbb{S}} \circ \eta_S$. Thus,

$$\left(\eta_S \circ \widetilde{\mathbb{S}}\right) = \left(\eta_S \circ \widetilde{\mathbb{S}}\right) \widetilde{\cap} \left(\eta_S \circ \widetilde{\mathbb{S}}\right) = (\widetilde{\mathbb{S}} \circ \eta_S) \widetilde{\cap} \left(\eta_S \circ \widetilde{\mathbb{S}} \circ \eta_S\right) \cong \eta_S$$

η_S is an S-int R-ideal.

Theorem 3.20. Every S-int R-ideal is an S-int BQ ideal.

Proof: It is followed by Proposition 3.14 and Proposition 3.17.

Here note that the converse of Theorem 3.20 is not true follows from Example 3.15 and Example 3.18. Theorem 3.21 shows that the converse of Theorem 3.20 holds for soft simple* semigroup.

Theorem 3.21. Let $f_S \in S_S(U)$ and S be a soft simple* semigroup. Then, the following conditions are equivalent:

(1) η_S is an S-int R-ideal.
(2) η_S is an S-int BQ ideal.

Proof: (1) implies (2) is obvious by Theorem 3.20. (2) implies (1) is obvious by Proposition 3.16 and Proposition 3.19.

Proposition 3.22. Every S-int L-ideal is an S-int R-BQ ideal.

Proof: Let f_S be an S-int L-ideal of S. Then, $\widetilde{\mathbb{S}} \circ f_S \cong f_S$ and $f_S \circ f_S \cong f_S$. Thus,

$$\left(f_S \circ \widetilde{\mathbb{S}}\right) \widetilde{\cap} \left(f_S \circ \widetilde{\mathbb{S}} \circ f_S\right) \cong f_S \circ \widetilde{\mathbb{S}} \circ f_S \cong f_S \circ f_S \cong f_S$$

Hence, f_S is an S-int R-BQ ideal of S.

Additionally, since f_S is an S-int L-ideal, by Theorem 2.17, it is an S-int bi-ideal. Therefore, by Proposition 3.6, f_S is an S-int R-BQ ideal.

We show with a counterexample that the converse of Proposition 3.22 is not true:

Example 3.23. Consider the semigroup $S = \{\varrho, \mathfrak{Q}\}$ defined by the following table:

Table 4: Cayley table of '֍' binary operation.

֍	ϱ	$\mathfrak{Q}$
ϱ	ϱ	ϱ
$\mathfrak{Q}$	$\mathfrak{Q}$	$\mathfrak{Q}$

Let $\mathfrak{q}_S$ be an SS over $U = \mathbb{Z}$ as follows:

$$\mathfrak{q}_S = \{(\varrho, \{3,6\}), (\mathfrak{Q}, \{3,9\})\}$$

Here, $\mathfrak{q}_S$ is an S-int R-BQ ideal. In fact,

$$\begin{aligned}\left[\left(\mathfrak{q}_S \circ \widetilde{\mathfrak{S}}\right) \widetilde{\cap} \left(\mathfrak{q}_S \circ \widetilde{\mathfrak{S}} \circ \mathfrak{q}_S\right)\right](\varrho) &= (\mathfrak{q}_S \circ \widetilde{\mathfrak{S}})(\varrho) \cap \left(\mathfrak{q}_S \circ \widetilde{\mathfrak{S}} \circ \mathfrak{q}_S\right)(\varrho) \\ &= \mathfrak{q}_S(\varrho) \subseteq \mathfrak{q}_S(\varrho)\end{aligned}$$

$$\begin{aligned}\left[\left(\mathfrak{q}_S \circ \widetilde{\mathfrak{S}}\right) \widetilde{\cap} \left(\mathfrak{q}_S \circ \widetilde{\mathfrak{S}} \circ \mathfrak{q}_S\right)\right](\mathfrak{Q}) &= (\mathfrak{q}_S \circ \widetilde{\mathfrak{S}})(\mathfrak{Q}) \cap \left(\mathfrak{q}_S \circ \widetilde{\mathfrak{S}} \circ \mathfrak{q}_S\right)(\mathfrak{Q}) \\ &= \mathfrak{q}_S(\mathfrak{Q}) \subseteq \mathfrak{q}_S(\mathfrak{Q})\end{aligned}$$

Thus, $\mathfrak{q}_S$ is an S-int R-BQ ideal of S. However, since

$$\begin{aligned}\left(\widetilde{\mathfrak{S}} \circ \mathfrak{q}_S\right)(\varrho) &= \left[\widetilde{\mathfrak{S}}(\varrho) \cap \mathfrak{q}_S(\varrho)\right] \cup \left[\widetilde{\mathfrak{S}}(\varrho) \cap \mathfrak{q}_S(\mathfrak{Q})\right] \\ &= \mathfrak{q}_S(\varrho) \cup \mathfrak{q}_S(\mathfrak{Q}) \not\subseteq \mathfrak{q}_S(\varrho)\end{aligned}$$

$$\begin{aligned}\left(\widetilde{\mathfrak{S}} \circ \mathfrak{q}_S\right)(\mathfrak{Q}) &= \left[\widetilde{\mathfrak{S}}(\mathfrak{Q}) \cap \mathfrak{q}_S(\varrho)\right] \cup \left[\widetilde{\mathfrak{S}}(\mathfrak{Q}) \cap \mathfrak{q}_S(\mathfrak{Q})\right] \\ &= \mathfrak{q}_S(\varrho) \cup \mathfrak{q}_S(\mathfrak{Q}) \not\subseteq \mathfrak{q}_S(\mathfrak{Q})\end{aligned}$$

$\mathfrak{q}_S$ is not an S-int L-ideal.

Proposition 3.24 shows that the converse of Proposition 3.22 holds for soft simple* semigroups.

Proposition 3.24. Let $\mathfrak{q}_S \in S_S(U)$ and S be a soft simple* semigroup. Then, the following conditions are equivalent:

(1) $\mathfrak{q}_S$ is an S-int L-ideal.
(2) $\mathfrak{q}_S$ is an S-int R-BQ ideal.

Proof: (1) implies (2) is obvious by Proposition 3.22. Assume that $\mathfrak{q}_S$ is an S-int R-BQ ideal. By assumption, $\widetilde{\mathfrak{S}} = \mathfrak{q}_S \circ \widetilde{\mathfrak{S}} = \widetilde{\mathfrak{S}} \circ \mathfrak{q}_S$. Thus,

$$\begin{aligned}\widetilde{\mathfrak{S}} \circ \mathfrak{q}_S &= \left(\widetilde{\mathfrak{S}} \circ \mathfrak{q}_S\right) \widetilde{\cap} \left(\widetilde{\mathfrak{S}} \circ \mathfrak{q}_S\right) \\ &= (\mathfrak{q}_S \circ \widetilde{\mathfrak{S}}) \widetilde{\cap} \left(\mathfrak{q}_S \circ \widetilde{\mathfrak{S}} \circ \mathfrak{q}_S\right) \cong \mathfrak{q}_S\end{aligned}$$

$\mathfrak{q}_S$ is an S-int L-ideal.

Proposition 3.25. Every S-int L-ideal is an S-int L-BQ ideal.

Proof: Let $\mathfrak{q}_S$ be an S-int L ideal of S. Then, $\widetilde{\mathfrak{S}} \circ \mathfrak{q}_S \cong \mathfrak{q}_S$. Thus, $\left(\widetilde{\mathfrak{S}} \circ \mathfrak{q}_S\right) \widetilde{\cap} \left(\mathfrak{q}_S \circ \widetilde{\mathfrak{S}} \circ \mathfrak{q}_S\right) \cong \widetilde{\mathfrak{S}} \circ \mathfrak{q}_S \cong \mathfrak{q}_S$. Hence, $\mathfrak{q}_S$ is an S-int L-BQ ideal of S.

Additionally, since $\mathfrak{q}_S$ is an S-int L-ideal, by Theorem 2.17, it is an S-int bi-ideal. Therefore, by Proposition 3.9, $\mathfrak{q}_S$ is an S-int L-BQ ideal.

We show with a counterexample that the converse of Proposition 3.25 is not true:

Example 3.26. Consider the SS $\mathfrak{q}_S$ in Example 3.23. The SS $\mathfrak{q}_S$ is an S-int L-BQ ideal. Since,

$$\begin{aligned}\left[\left(\widetilde{\mathfrak{S}} \circ \mathfrak{q}_S\right) \widetilde{\cap} \left(\mathfrak{q}_S \circ \widetilde{\mathfrak{S}} \circ \mathfrak{q}_S\right)\right](\varrho) &= \left(\widetilde{\mathfrak{S}} \circ \mathfrak{q}_S\right)(\varrho) \cap \left(\mathfrak{q}_S \circ \widetilde{\mathfrak{S}} \circ \mathfrak{q}_S\right)(\varrho) \\ &= \mathfrak{q}_S(\varrho) \subseteq \mathfrak{q}_S(\varrho)\end{aligned}$$

$$\begin{aligned}\left[\left(\widetilde{\mathfrak{S}} \circ \mathfrak{q}_S\right) \widetilde{\cap} \left(\mathfrak{q}_S \circ \widetilde{\mathfrak{S}} \circ \mathfrak{q}_S\right)\right](\mathfrak{Q}) &= (\widetilde{\mathfrak{S}} \circ \mathfrak{q}_S)(\mathfrak{Q}) \cap \left(\mathfrak{q}_S \circ \widetilde{\mathfrak{S}} \circ \mathfrak{q}_S\right)(\mathfrak{Q}) \\ &= \mathfrak{q}_S(\mathfrak{Q}) \subseteq \mathfrak{q}_S(\mathfrak{Q})\end{aligned}$$

Hence, $\mathfrak{q}_S$ is an S-int L-BQ ideal. However, since

$$\begin{aligned}\left(\widetilde{\mathfrak{S}} \circ \mathfrak{q}_S\right)(\varrho) &= \left[\widetilde{\mathfrak{S}}(\varrho) \cap \mathfrak{q}_S(\varrho)\right] \cup \left[\widetilde{\mathfrak{S}}(\varrho) \cap \mathfrak{q}_S(\mathfrak{Q})\right] \\ &= \mathfrak{q}_S(\varrho) \cup \mathfrak{q}_S(\mathfrak{Q}) \not\subseteq \mathfrak{q}_S(\varrho)\end{aligned}$$

$$\begin{aligned}\left(\widetilde{\mathfrak{S}} \circ \mathfrak{q}_S\right)(\mathfrak{Q}) &= \left[\widetilde{\mathfrak{S}}(\mathfrak{Q}) \cap \mathfrak{q}_S(\varrho)\right] \cup \left[\widetilde{\mathfrak{S}}(\mathfrak{Q}) \cap \mathfrak{q}_S(\mathfrak{Q})\right] \\ &= \mathfrak{q}_S(\varrho) \cup \mathfrak{q}_S(\mathfrak{Q}) \not\subseteq \mathfrak{q}_S(\mathfrak{Q})\end{aligned}$$

$\mathfrak{q}_S$ is not an S-int L-ideal.

Proposition 3.27 shows that the converse of Proposition 3.25 holds for soft R-simple* semigroups.

Proposition 3.27. Let $\mathfrak{q}_S \in S_S(U)$ and S be a soft R-simple* semigroup. Then, the following conditions are equivalent:

(1) $\mathfrak{q}_S$ is an S-int L-ideal.
(2) $\mathfrak{q}_S$ is an S-int L-BQ ideal.

Proof: (1) implies (2) is obvious by Theorem 3.25. Assume that $\mathfrak{q}_S$ is an S-int L-BQ ideal. By assumption, $\widetilde{\mathfrak{S}} = \mathfrak{q}_S \circ \widetilde{\mathfrak{S}}$. Thus,

$$\begin{aligned}\widetilde{\mathfrak{S}} \circ \mathfrak{q}_S &= \left(\widetilde{\mathfrak{S}} \circ \mathfrak{q}_S\right) \widetilde{\cap} \left(\widetilde{\mathfrak{S}} \circ \mathfrak{q}_S\right) \\ &= (\widetilde{\mathfrak{S}} \circ \mathfrak{q}_S) \widetilde{\cap} \left(\mathfrak{q}_S \circ \widetilde{\mathfrak{S}} \circ \mathfrak{q}_S\right) \cong \mathfrak{q}_S\end{aligned}$$

$\mathfrak{q}_S$ is an S-int L-ideal.

Theorem 3.28. Every S-int L-ideal is an S-int BQ ideal.
Proof: It is followed by Proposition 3.22 and Proposition 3.25.

Here note that the converse of Theorem 3.28 is not true follows from Example 3.23 and Example 3.26.

Theorem 3.29 shows that the converse of Theorem 3.28 holds for soft simple* semigroup.

Theorem 3.29. Let $\mathfrak{q}_S \in S_S(U)$ and S be a soft simple* semigroup. Then, the following conditions are equivalent:

(1) $\mathfrak{q}_S$ is an S-int L-ideal.
(2) $\mathfrak{q}_S$ is an S-int ƁQ ideal.

Proof: (1) implies (2) is obvious by Theorem 3.28. (2) implies (1) is obvious by Proposition 3.24 and Proposition 3.27.

Theorem 3.30. Every S-int ideal is an S-int ƁQ ideal.

Proof: It is followed by Theorem 3.20 and Theorem 3.28. Theorem 3.31 shows that the converse of Theorem 3.30 holds for soft simple* semigroup.

Theorem 3.31. Let $\mathfrak{q}_S \in S_S(U)$ and S be a soft simple* semigroup. Then, the following conditions are equivalent:

(1) $\mathfrak{q}_S$ is an S-int ideal.
(2) $\mathfrak{q}_S$ is an S-int ƁQ ideal.

1.

Proof: (1) implies (2) is obvious by Theorem 3.30. (2) implies (1) is obvious by Proposition 3.21 and Proposition 3.28.

Proposition 3.32. Every S-int quasi-ideal is an S-int R-ƁQ ideal.

Proof: Let f_S be an S-int quasi-ideal of S. Then, $(\mathfrak{ƀ}_S \circ \widetilde{\mathfrak{S}}) \widetilde{\cap} (\widetilde{\mathfrak{S}} \circ \mathfrak{ƀ}_S) \cong \mathfrak{ƀ}_S$.

Thus,

$$\left(\mathfrak{ƀ}_S \circ \widetilde{\mathfrak{S}}\right) \widetilde{\cap} \left(\mathfrak{ƀ}_S \circ \widetilde{\mathfrak{S}} \circ \mathfrak{ƀ}_S\right) \cong \left(\mathfrak{ƀ}_S \circ \widetilde{\mathfrak{S}}\right) \widetilde{\cap} \left(\widetilde{\mathfrak{S}} \circ \widetilde{\mathfrak{S}} \circ \mathfrak{ƀ}_S\right) \cong (\mathfrak{ƀ}_S \circ \widetilde{\mathfrak{S}}) \widetilde{\cap} (\widetilde{\mathfrak{S}} \circ \mathfrak{ƀ}_S) \cong \mathfrak{ƀ}_S$$

Hence, $\mathfrak{ƀ}_S$ is an S-int R-ƁQ ideal of S.

We show with a counterexample that the converse of Proposition 3.32 is not true:

Example 3.33. Consider the SS $\mathfrak{ƀ}_S$ in Example 3.7. The SS $\mathfrak{ƀ}_S$ is an S-int R-ƁQ ideal. Since,

$$\left[\left(\mathfrak{ƀ}_S \circ \widetilde{\mathfrak{S}}\right) \widetilde{\cap} \left(\widetilde{\mathfrak{S}} \circ \mathfrak{ƀ}_S\right)\right](y) = \mathfrak{ƀ}_S(\mathfrak{r}) \cup \mathfrak{ƀ}_S(\mathfrak{s}) \not\subseteq \mathfrak{ƀ}_S(y)$$

Hence, $\mathfrak{ƀ}_S$ is not an S-int quasi ideal.

Proposition 3.34 shows that the converse of Proposition 3.32 holds for soft R-simple* semigroups.

Proposition 3.34. Let $\mathfrak{ƀ}_S \in S_S(U)$ and S be a soft R-simple* semigroup. Then, the following conditions are equivalent:

(1) $\mathfrak{ƀ}_S$ is an S-int quasi-ideal.
(2) $\mathfrak{ƀ}_S$ is an S-int R-ƁQ ideal.

Proof: (1) implies (2) is obvious by Theorem 3.32. Assume that $\mathfrak{ƀ}_S$ is an S-int R-ƁQ ideal. By assumption, $\widetilde{\mathfrak{S}} = \mathfrak{ƀ}_S \circ \widetilde{\mathfrak{S}}$. Thus,

$$\left(\mathfrak{ƀ}_S \circ \widetilde{\mathfrak{S}}\right) \widetilde{\cap} \left(\widetilde{\mathfrak{S}} \circ \mathfrak{ƀ}_S\right) = \left(\mathfrak{ƀ}_S \circ \widetilde{\mathfrak{S}}\right) \widetilde{\cap} \left(\mathfrak{ƀ}_S \circ \widetilde{\mathfrak{S}} \circ \mathfrak{ƀ}_S\right) \cong \mathfrak{ƀ}_S$$

$\mathfrak{ƀ}_S$ is an S-int quasi-ideal.

Proposition 3.35. Every S-int quasi-ideal is an S-int L-ƁQ ideal.

Proof: Let $\mathfrak{g}_S$ be an S-int quasi-ideal of S. Then, $(\mathfrak{g}_S \circ \widetilde{\mathfrak{S}}) \widetilde{\cap} (\widetilde{\mathfrak{S}} \circ \mathfrak{g}_S) \cong \mathfrak{g}_S$. Thus,

$$\left(\widetilde{\mathfrak{S}} \circ \mathfrak{g}_S\right) \widetilde{\cap} \left(\mathfrak{g}_S \circ \widetilde{\mathfrak{S}} \circ \mathfrak{g}_S\right) \cong \left(\widetilde{\mathfrak{S}} \circ \mathfrak{g}_S\right) \widetilde{\cap} \left(\mathfrak{g}_S \circ \widetilde{\mathfrak{S}} \circ \widetilde{\mathfrak{S}}\right) \cong (\widetilde{\mathfrak{S}} \circ \mathfrak{g}_S) \widetilde{\cap} (\mathfrak{g}_S \circ \widetilde{\mathfrak{S}}) \cong \mathfrak{g}_S$$

Hence, $\mathfrak{g}_S$ is an S-int L-ƁQ ideal of S.

We show with a counterexample that the converse of Proposition 3.35 is not true:

Example 3.36. Consider the SS $\mathfrak{ƀ}_S$ in Example 3.7. The SS $\mathfrak{ƀ}_S$ is an S-int L-ƁQ ideal. Since,

$$\left[\left(\mathfrak{ƀ}_S \circ \widetilde{\mathfrak{S}}\right) \widetilde{\cap} \left(\widetilde{\mathfrak{S}} \circ \mathfrak{ƀ}_S\right)\right](y) = \mathfrak{ƀ}_S(\mathfrak{r}) \cup \mathfrak{ƀ}_S(\mathfrak{s}) \not\subseteq \mathfrak{ƀ}_S(y)$$

$\mathfrak{ƀ}_S$ is not an S-int quasi-ideal.

Proposition 3.37 shows that the converse of Proposition 3.35 holds for soft simple* semigroups.

Proposition 3.37. Let $\mathfrak{g}_S \in S_S(U)$ and S be a soft simple* semigroup. Then, the following conditions are equivalent:

(1) $\mathfrak{g}_S$ is an S-int quasi-ideal.
(2) $\mathfrak{g}_S$ is an S-int L-ƁQ ideal.

Proof: (1) implies (2) is obvious by Theorem 3.35. Assume that $\mathfrak{g}_S$ is an S-int L-ƁQ ideal. By assumption, $\widetilde{\mathfrak{S}} = \mathfrak{g}_S \circ \widetilde{\mathfrak{S}} = \widetilde{\mathfrak{S}} \circ \mathfrak{g}_S$. Thus,

$$\left(\mathfrak{g}_S \circ \widetilde{\mathfrak{S}}\right) \widetilde{\cap} \left(\widetilde{\mathfrak{S}} \circ \mathfrak{g}_S\right) = \left(\widetilde{\mathfrak{S}} \circ \mathfrak{g}_S\right) \widetilde{\cap} \left(\mathfrak{g}_S \circ \widetilde{\mathfrak{S}} \circ \mathfrak{g}_S\right) \cong \mathfrak{g}_S$$

$\mathfrak{g}_S$ is an S-int quasi-ideal.

Theorem 3.38. Every S-int quasi-ideal is an S-int ƁQ ideal.

Proof: It is followed by Theorem 3.32 and Theorem 3.35. Here note that the converse of Theorem 3.38 is not true follows from Example 3.33 and Example 3.36.

Theorem 3.39 shows that the converse of Theorem 3.38 holds for soft simple* semigroup.

Theorem 3.39. Let $\mathfrak{g}_S \in S_S(U)$ and S be a soft simple* semigroup. Then, the following conditions are equivalent:

(1) $\mathcal{g}_S$ is an S-int quasi-ideal.
(2) $\mathcal{g}_S$ is an S-int ƁQ ideal.

Proof: (1) implies (2) is obvious by Theorem 3.38. (2) implies (1) is obvious by Proposition 3.34 and Proposition 3.37.

Proposition 3.40. Let ϑ_S be an idempotent SS over U. If ϑ_S is an S-int interior ideal, then ϑ_S is an S-int L-ƁQ ideal.
Proof: Let ϑ_S be an idempotent S-int interior ideal of S. Then, $\vartheta_S \circ \vartheta_S = \vartheta_S$ and $\widetilde{S} \circ \vartheta_S \circ \widetilde{S} \cong \vartheta_S$. Thus,

$$(\widetilde{S} \circ \vartheta_S) \cap (\vartheta_S \circ \widetilde{S} \circ \vartheta_S) \cong \widetilde{S} \circ \vartheta_S$$
$$= \widetilde{S} \circ \vartheta_S \circ \vartheta_S \cong \widetilde{S} \circ \vartheta_S \circ \widetilde{S} \cong \vartheta_S$$

Hence, ϑ_S is an S-int L-ƁQ ideal of S.

Proposition 3.41. Let ϑ_S be an idempotent SS over U. If ϑ_S is an S-int interior ideal, then ϑ_S is an S-int R-ƁQ ideal.

Proof: Let ϑ_S be an idempotent S-int interior ideal of S. Then, $\vartheta_S \circ \vartheta_S = \vartheta_S$ and $\widetilde{S} \circ \vartheta_S \circ \widetilde{S} \cong \vartheta_S$. Thus,

$$(\vartheta_S \circ \widetilde{S}) \cap (\vartheta_S \circ \widetilde{S} \circ \vartheta_S) \cong \vartheta_S \circ \widetilde{S}$$
$$= \vartheta_S \circ \vartheta_S \circ \widetilde{S} \cong \widetilde{S} \circ \vartheta_S \circ \widetilde{S} \cong \vartheta_S$$

Hence, ϑ_S is an S-int R-ƁQ ideal of S.

Theorem 3.42. Let ϑ_S be an idempotent SS over U. If ϑ_S is an S-int interior ideal, then ϑ_S is an S-int ƁQ ideal.

Proof: It is followed by Theorem 3.40 and Theorem 3.41.

Proposition 3.43. Let $\vartheta_S \in S_S(U)$ and S be a soft simple* semigroup. Then, the following conditions are equivalent:

(1) ϑ_S is an S-int interior ideal.
(2) ϑ_S is an S-int L-ƁQ ideal.

Proof: First assume that (1) holds. Where ϑ_S is an S-int interior ideal of S. Then, $\widetilde{S} \circ \vartheta_S \circ \widetilde{S} \cong \vartheta_S$. By assumption, $\widetilde{S} = \vartheta_S \circ \widetilde{S} = \widetilde{S} \circ \vartheta_S$. Thus,

$$(\widetilde{S} \circ \vartheta_S) \cap (\vartheta_S \circ \widetilde{S} \circ \vartheta_S) \cong \vartheta_S \circ \widetilde{S} \circ \vartheta_S$$
$$= \widetilde{S} \circ \vartheta_S \circ \vartheta_S \cong \widetilde{S} \circ \vartheta_S \circ \widetilde{S} \cong \vartheta_S$$

ϑ_S is an S-int L-ƁQ ideal.

Conversely, assume that (2) holds. Where ϑ_S is an S-int L-ƁQ ideal of S. Then, $(\widetilde{S} \circ \vartheta_S) \cap (\vartheta_S \circ \widetilde{S} \circ \vartheta_S) \cong \vartheta_S$. In order to show that ϑ_S S-int interior ideal, we need to show that $\widetilde{S} \circ \vartheta_S \circ \widetilde{S} \cong \vartheta_S$. By assumption, $\widetilde{S} = \vartheta_S \circ \widetilde{S} = \widetilde{S} \circ \vartheta_S$. Thus,

$$\widetilde{S} \circ \vartheta_S \circ \widetilde{S} = \left(\widetilde{S} \circ \vartheta_S \circ \widetilde{S}\right) \cap \left(\widetilde{S} \circ \vartheta_S \circ \widetilde{S}\right)$$
$$= \left(\vartheta_S \circ \widetilde{S} \circ \widetilde{S}\right) \cap \left(\vartheta_S \circ \widetilde{S} \circ \widetilde{S}\right) \cong \left(\vartheta_S \circ \widetilde{S}\right) \cap \left(\vartheta_S \circ \widetilde{S}\right)$$
$$= \left(\vartheta_S \circ \widetilde{S}\right) \cap \left(\vartheta_S \circ \widetilde{S} \circ \vartheta_S\right) \cong \vartheta_S$$

Hence, ϑ_S is an S-int interior ideal.

Proposition 3.44. Let $\vartheta_S \in S_S(U)$ and S be a soft simple* semigroup. Then, the following conditions are equivalent:

(1) ϑ_S is an S-int interior ideal.
(2) ϑ_S is an S-int R-ƁQ ideal.

Proof: First assume that (1) holds.Where ϑ_S is an S-int interior ideal of S. Then, $\widetilde{S} \circ \vartheta_S \circ \widetilde{S} \cong \vartheta_S$. By assumption, $\widetilde{S} = \vartheta_S \circ \widetilde{S} = \widetilde{S} \circ \vartheta_S$. Thus,

$$(\vartheta_S \circ \widetilde{S}) \cap (\vartheta_S \circ \widetilde{S} \circ \vartheta_S) \cong \vartheta_S \circ \widetilde{S} \circ \vartheta_S$$
$$= \widetilde{S} \circ \vartheta_S \circ \vartheta_S \cong \widetilde{S} \circ \vartheta_S \circ \widetilde{S} \cong \vartheta_S$$

Therefore, ϑ_S is an S-int R-ƁQ ideal.

Conversely, assume that (2) holds, where ϑ_S is an S-int R-ƁQ ideal of S. Then, $(\vartheta_S \circ \widetilde{S}) \cap (\vartheta_S \circ \widetilde{S} \circ \vartheta_S) \cong \vartheta_S$. In order to show that ϑ_S S-int interior ideal, we need to show that $\widetilde{S} \circ \vartheta_S \circ \widetilde{S} \cong \vartheta_S$. By assumption, $\widetilde{S} = \vartheta_S \circ \widetilde{S} = \widetilde{S} \circ \vartheta_S$. Thus,

$$\widetilde{S} \circ \vartheta_S \circ \widetilde{S} = \left(\widetilde{S} \circ \vartheta_S \circ \widetilde{S}\right) \cap \left(\widetilde{S} \circ \vartheta_S \circ \widetilde{S}\right)$$
$$= \left(\vartheta_S \circ \widetilde{S} \circ \widetilde{S}\right) \cap \left(\vartheta_S \circ \widetilde{S} \circ \widetilde{S}\right) \cong \left(\vartheta_S \circ \widetilde{S}\right) \cap \left(\vartheta_S \circ \widetilde{S}\right)$$
$$= \left(\vartheta_S \circ \widetilde{S}\right) \cap \left(\vartheta_S \circ \widetilde{S} \circ \vartheta_S\right) \cong \vartheta_S$$

Therefore, ϑ_S is an S-int interior ideal.

Theorem 3.45. Let $\vartheta_S \in S_S(U)$ and S be a soft simple* semigroup. Then, the following conditions are equivalent:

(1) ϑ_S is an S-int interior ideal.
(2) ϑ_S is an S-int ƁQ ideal.

Proof: It is followed by Theorem 3.43 and Theorem 3.44.

Proposition 3.46. Let $\mathfrak{p}_S$ and $\mathfrak{t}_S$ be S-int L-(R-) ƁQ ideals. Then, $\mathfrak{p}_S \cap \mathfrak{t}_S$ is an S-int L-(R-) ƁQ ideal.

Proof: The proof is presented only for S-int L-ƁQ ideal, as the proof for S-int R-ƁQ ideal can be shown similarly. Let $\mathfrak{p}_S$ and $\mathfrak{t}_S$ be S-int L-ƁQ ideals of S. Then,

$$\left(\widetilde{S} \circ \mathfrak{p}_S\right) \cap \left(\mathfrak{p}_S \circ \widetilde{S} \circ \mathfrak{p}_S\right) \cong \mathfrak{p}_S$$

$$\left(\widetilde{S} \circ \mathfrak{t}_S\right) \cap \left(\mathfrak{t}_S \circ \widetilde{S} \circ \mathfrak{t}_S\right) \cong \mathfrak{t}_S$$

Thus,

$$\left[\widetilde{S} \circ (\mathfrak{p}_S \cap \mathfrak{t}_S)\right] \cap \left[(\mathfrak{p}_S \cap \mathfrak{t}_S) \circ \widetilde{S} \circ (\mathfrak{p}_S \cap \mathfrak{t}_S)\right] \cong$$
$$\left(\widetilde{S} \circ \mathfrak{p}_S\right) \cap \left(\mathfrak{p}_S \circ \widetilde{S} \circ \mathfrak{p}_S\right) \cong \mathfrak{p}_S$$

$$\left[\widetilde{S} \circ (\mathfrak{p}_S \cap \mathfrak{t}_S)\right] \cap \left[(\mathfrak{p}_S \cap \mathfrak{t}_S) \circ \widetilde{S} \circ (\mathfrak{p}_S \cap \mathfrak{t}_S)\right] \cong$$
$$\left(\widetilde{S} \circ \mathfrak{t}_S\right) \cap \left(\mathfrak{t}_S \circ \widetilde{S} \circ \mathfrak{t}_S\right) \cong \mathfrak{t}_S$$

Hence,

$$\left[\widetilde{S}\circ(p_S\,\widetilde{\cap}\,t_S)\right]\widetilde{\cap}\left[(p_S\,\widetilde{\cap}\,t_S)\circ\widetilde{S}\circ(p_S\,\widetilde{\cap}\,t_S)\right]\cong p_S\,\widetilde{\cap}\,t_S$$

Thus, $p_S\,\widetilde{\cap}\,t_S$ is an S-int L-BQ ideals.

Theorem 3.47. Let p_S and t_S be S-int BQ ideals. Then, $p_S\,\widetilde{\cap}\,t_S$ is an S-int BQ ideals.

Corollary 3.48. The finite intersection of S-int BQ ideals is an S-int BQ ideal.

Proposition 3.49. Let q_S and t_S be S-int L-(R-) ideals. Then, $q_S\,\widetilde{\cap}\,t_S$ is an S-int L-(R-) BQ ideal.

Proof: The proof is presented only for S-int L-BQ ideal, as the proof for S-int R-BQ ideal can be shown similarly. Let q_S and t_S be S-int L-ideals of S. Then, $\widetilde{S}\circ q_S\cong g_S$ and $\widetilde{S}\circ t_S\cong t_S$. Thus,

$$\left[\widetilde{S}\circ(q_S\,\widetilde{\cap}\,t_S)\right]\widetilde{\cap}\left[(q_S\,\widetilde{\cap}\,t_S)\circ\widetilde{S}\circ(q_S\,\widetilde{\cap}\,t_S)\right]\cong$$
$$(\widetilde{S}\circ q_S)\,\widetilde{\cap}\,(q_S\circ\widetilde{S}\circ q_S)\cong\widetilde{S}\circ q_S\cong q_S$$

$$\left[\widetilde{S}\circ(q_S\,\widetilde{\cap}\,t_S)\right]\widetilde{\cap}\left[(q_S\,\widetilde{\cap}\,t_S)\circ\widetilde{S}\circ(q_S\,\widetilde{\cap}\,t_S)\right]\cong$$
$$(\widetilde{S}\circ t_S)\,\widetilde{\cap}\,(t_S\circ\widetilde{S}\circ t_S)\cong\widetilde{S}\circ t_S\cong t_S$$

Hence,

$$\left[\widetilde{S}\circ(q_S\,\widetilde{\cap}\,t_S)\right]\widetilde{\cap}\left[(q_S\,\widetilde{\cap}\,t_S)\circ\widetilde{S}\circ(q_S\,\widetilde{\cap}\,t_S)\right]\cong q_S\,\widetilde{\cap}\,t_S$$

Thus, $q_S\,\widetilde{\cap}\,t_S$ is an S-int L-BQ ideals.

Theorem 3.50. Let q_S and t_S be S-int ideals. Then, $q_S\,\widetilde{\cap}\,t_S$ is an S-int BQ ideals.

Theorem 3.51. Let q_S be an S-int R-ideal and t_S be an S-int L-ideal. Then, $q_S\,\widetilde{\cap}\,t_S$ is an S-int BQ ideal.

Proof: Let q_S be an S-int R-ideal and f_S be an S-int L-ideal. Then, $q_S\circ\widetilde{S}\cong q_S$, $\widetilde{S}\circ t_S\cong t_S$, and $q_S\circ q_S\cong q_S, t_S\circ t_S\cong t_S$.Thus,

$$\left[\widetilde{S}\circ(q_S\,\widetilde{\cap}\,t_S)\right]\widetilde{\cap}\left[(q_S\,\widetilde{\cap}\,t_S)\circ\widetilde{S}\circ(q_S\,\widetilde{\cap}\,t_S)\right]\cong$$
$$\left(\widetilde{S}\circ t_S\right)\widetilde{\cap}\left(q_S\circ\widetilde{S}\circ q_S\right)\cong t_S\,\widetilde{\cap}\,(q_S\circ q_S)\cong t_S\,\widetilde{\cap}\,q_S$$

Hence, $q_S\,\widetilde{\cap}\,t_S$ is an S-int L-BQ ideal. Similarly, since

$$\left[(q_S\,\widetilde{\cap}\,t_S)\circ\widetilde{S}\right]\widetilde{\cap}\left[(q_S\,\widetilde{\cap}\,t_S)\circ\widetilde{S}\circ(q_S\,\widetilde{\cap}\,t_S)\right]\cong$$
$$(q_S\circ\widetilde{S})\,\widetilde{\cap}\,\,(t_S\circ\widetilde{S}\circ t_S)\cong q_S\,\widetilde{\cap}\,(t_S\circ t_S)\cong q_S\,\widetilde{\cap}\,t_S$$

$q_S\,\widetilde{\cap}\,t_S$ is an S-int R-BQ ideal. Therefore, $q_S\,\widetilde{\cap}\,t_S$ is an S-int BQ ideal.

Theorem 3.52. Let ϑ_S be an S-int L-BQ ideal and t_S be an S-int L-ideal. Then, $\vartheta_S\,\widetilde{\cap}\,t_S$ is an S-int BQ ideal.

Proof: Let ϑ_S be an S-int L-BQ ideal and t_S be an S-int L-ideal. Then, $(\widetilde{S}\circ\vartheta_S)\,\widetilde{\cap}\left(\vartheta_S\circ\widetilde{S}\circ\vartheta_S\right)\cong\vartheta_S$ and $\widetilde{S}\circ t_S\cong t_S$. Thus,

$$\left[\widetilde{S}\circ(\vartheta_S\,\widetilde{\cap}\,t_S)\right]\widetilde{\cap}\left[(\vartheta_S\,\widetilde{\cap}\,t_S)\circ\widetilde{S}\circ(\vartheta_S\,\widetilde{\cap}\,t_S)\right]\cong$$
$$(\widetilde{S}\circ\vartheta_S)\,\widetilde{\cap}\left(\vartheta_S\circ\widetilde{S}\circ\vartheta_S\right)\cong\vartheta_S$$

$$\left[\widetilde{S}\circ(\vartheta_S\,\widetilde{\cap}\,t_S)\right]\widetilde{\cap}\left[(\vartheta_S\,\widetilde{\cap}\,t_S)\circ\widetilde{S}\circ(\vartheta_S\,\widetilde{\cap}\,t_S)\right]\cong$$
$$(\widetilde{S}\circ t_S)\,\widetilde{\cap}\left(t_S\circ\widetilde{S}\circ t_S\right)\cong\widetilde{S}\circ t_S\cong t_S$$

Hence,

$$\left[\widetilde{S}\circ(\vartheta_S\,\widetilde{\cap}\,t_S)\right]\widetilde{\cap}\left[(\vartheta_S\,\widetilde{\cap}\,t_S)\circ\widetilde{S}\circ(\vartheta_S\,\widetilde{\cap}\,t_S)\right]\cong\vartheta_S\,\widetilde{\cap}\,t_S$$

Thus, $\vartheta_S\,\widetilde{\cap}\,t_S$ is an S-int L-BQ ideal.

Theorem 3.53. Let t_S be an S-int L-ideal and p_S be an SS over U. Then, $t_S\circ p_S$ is an S-int L-BQ ideal.

Proof: Let t_S be an S-int L-ideal. Then, $\widetilde{S}\circ t_S\cong t_S$. Thus,

$$\left[\widetilde{S}\circ(t_S\circ p_S)\right]\widetilde{\cap}\left[(t_S\circ p_S)\circ\widetilde{S}\circ(t_S\circ p_S)\right]\cong\widetilde{S}\circ(t_S\circ p_S)$$
$$=\left(\widetilde{S}\circ t_S\right)\circ p_S\cong t_S\circ p_S$$

Hence, $t_S\circ p_S$ is an S-int L-BQ ideal.

Theorem 3.54. Let t_S be an S-int R-ideal and p_S be an SS over U. Then, $p_S\circ t_S$ is an S-int R-BQ ideal.

Proof: Let t_S be an S-int R-ideal. Then, $t_S\circ\widetilde{S}\cong t_S$. Thus,

$$\left[(p_S\circ t_S)\circ\widetilde{S}\right]\widetilde{\cap}\left[(p_S\circ t_S)\circ\widetilde{S}\circ(p_S\circ t_S)\right]\cong(p_S\circ t_S)\circ\widetilde{S}$$
$$=p_S\circ(t_S\circ\widetilde{S})\cong p_S\circ t_S$$

Hence, $p_S\circ t_S$ is an S-int R-BQ ideal.

Theorem 3.55. Let h_S be a nonempty SS over U. Then, every soft subset of h_S containing $\left(\widetilde{S}\circ h_S\right)\,\widetilde{\cup}\left(h_S\circ\widetilde{S}\right)$ is an S-int BQ ideal.

Proof: Let p_S be a soft subset of h_S containing $\left(\widetilde{S}\circ h_S\right)\,\widetilde{\cup}\left(h_S\circ\widetilde{S}\right)$. Since,

$$\widetilde{S}\circ p_S\cong\widetilde{S}\circ h_S\cong\left(\widetilde{S}\circ h_S\right)\,\widetilde{\cup}\left(h_S\circ\widetilde{S}\right)\cong p_S$$

$\left(\widetilde{S}\circ p_S\right)\cong p_S$ is obtained. Hence, p_S is an S-int L-ideal.

$$p_S\circ\widetilde{S}\cong h_S\circ\widetilde{S}\cong(\widetilde{S}\circ h_S)\,\widetilde{\cup}\left(h_S\circ\widetilde{S}\right)\cong p_S$$

Thus, $p_S\circ\widetilde{S}\cong p_S$. Hence, p_S is an S-int R-ideal. Therefore, p_S is an S-int BQ ideal. Thus, by Theorem 3.30, p_S is an S-int BQ ideal. Hence, every soft subset of h_S containing $\left(\widetilde{S}\circ h_S\right)\,\widetilde{\cup}\left(h_S\circ\widetilde{S}\right)$ is an S-int BQ ideal.

Theorem 3.56. Let ϑ_S be a nonempty SS over U. Then, every soft subset of ϑ_S containing $\widetilde{\mathfrak{S}} \circ \vartheta_S$ is an S-int L-BQ ideal.

Proof: Let $\mathfrak{h}_S$ be a soft subset of ϑ_S containing $\widetilde{\mathfrak{S}} \circ \vartheta_S$. Since, $\widetilde{\mathfrak{S}} \circ \mathfrak{h}_S \cong \widetilde{\mathfrak{S}} \circ \vartheta_S \cong \mathfrak{h}_S$. Thus, $\widetilde{\mathfrak{S}} \circ \mathfrak{h}_S \cong \mathfrak{h}_S$. Hence, $\mathfrak{h}_S$ is an S-int L-ideal. Thus, by Theorem 3.25, $\mathfrak{h}_S$ is an S-int BQ ideal. Hence, every soft subset of ϑ_S containing $\widetilde{\mathfrak{S}} \circ \vartheta_S$ is an S-int L-BQ ideal.

Theorem 3.57. Let ϑ_S be a nonempty SS over U. Then, every soft subset of ϑ_S containing $(\widetilde{\mathfrak{S}} \circ \vartheta_S) \widetilde{\cap} (\vartheta_S \circ \widetilde{\mathfrak{S}} \circ \vartheta_S)$ is an S-int L-BQ ideal.

Proof: Let $\mathfrak{h}_S$ be a soft subset of ϑ_S containing $(\widetilde{\mathfrak{S}} \circ \vartheta_S) \widetilde{\cap} (\vartheta_S \circ \widetilde{\mathfrak{S}} \circ \vartheta_S)$. Then,

$$\widetilde{\mathfrak{S}} \circ \mathfrak{h}_S \cong \widetilde{\mathfrak{S}} \circ \vartheta_S \text{ and } \mathfrak{h}_S \circ \widetilde{\mathfrak{S}} \circ \mathfrak{h}_S \cong \vartheta_S \circ \widetilde{\mathfrak{S}} \circ \vartheta_S$$

Since,

$$\left(\widetilde{\mathfrak{S}} \circ \mathfrak{h}_S\right) \widetilde{\cap} \left(\mathfrak{h}_S \circ \widetilde{\mathfrak{S}} \circ \mathfrak{h}_S\right) \cong \left(\widetilde{\mathfrak{S}} \circ \vartheta_S\right) \widetilde{\cap} (\vartheta_S \circ \widetilde{\mathfrak{S}} \circ \vartheta_S) \cong \mathfrak{h}_S$$

Hence, $\mathfrak{h}_S$ is an S-int L-ideal.

Proposition 3.58. Let ρ_S be an S-int subsemigroup over U, σ be a subset of U, $Im(\rho_S)$ be the image of ρ_S such that $\sigma \in Im(\rho_S)$. If ρ_S is an S-int L $-$(R-) BQ ideal of S, then $\mathcal{U}(\rho_S; \sigma)$ is a L-(R-) BQ ideal of S.

Proof: The proof is presented only for S-int L-BQ ideal, as the proof for S-int R-BQ ideal can be shown similarly. Since, $\rho_S(\mathfrak{x}) = \sigma$ for some $\mathfrak{x} \in S$, $\emptyset \neq \mathcal{U}(\rho_S; \sigma) \subseteq S$. Let $\kappa \in \left(S.\mathcal{U}(\rho_S; \sigma)\right) \cap \left(\mathcal{U}(\rho_S; \sigma).S.\mathcal{U}(\rho_S; \sigma)\right)$. Then, there exist $\mathfrak{x}, y, z \in \mathcal{U}(\rho_S; \sigma)$ and r, $\mathfrak{s} \in S$ such that $\kappa = \mathfrak{s}\mathfrak{x} = yrz$. Thus, $\rho_S(x) \supseteq \sigma$, $f_S(y) \supseteq \sigma$ and $\rho_S(z) \supseteq \sigma$. Since ρ_S is an S-int L-BQ ideal,

$$\left(\widetilde{\mathfrak{S}} \circ \rho_S\right)(\kappa) = \bigcup_{\kappa = \mathfrak{m}n} \left\{\widetilde{\mathfrak{S}}(\mathfrak{m}) \cap \rho_S(n)\right\} \supseteq \widetilde{\mathfrak{S}}(\mathfrak{s}) \cap \rho_S(\mathfrak{x}) = U \cap \rho_S(\mathfrak{x}) = \rho_S(\mathfrak{x}) \supseteq \sigma$$

$$\begin{aligned}\left(\rho_S \circ \widetilde{\mathfrak{S}} \circ \rho_S\right)(\kappa) &= \bigcup_{\kappa = \mathfrak{m}n} \left\{\rho_S(\mathfrak{m}) \cap \left(\widetilde{\mathfrak{S}} \circ \rho_S\right)(n)\right\} \\ &\supseteq \rho_S(\mathfrak{x}) \cap \left(\widetilde{\mathfrak{S}} \circ \rho_S\right)(yz) \\ &= \rho_S(\mathfrak{x}) \cap \bigcup_{yz = pq} \left\{\widetilde{\mathfrak{S}}(p) \cap \rho_S(q)\right\} \\ &\supseteq \rho_S(\mathfrak{x}) \cap \rho_S(y) \cap \rho_S(z) \\ &\supseteq \sigma \cap \sigma \cap \sigma = \sigma\end{aligned}$$

Thus, $(\widetilde{\mathfrak{S}} \circ \rho_S)(\kappa) \cap (\rho_S \circ \widetilde{\mathfrak{S}} \circ \rho_S)(\kappa)) \supseteq \sigma$. Since ρ_S is an S-int L-BQ ideal,

$$\rho_S(\kappa) \supseteq (\widetilde{\mathfrak{S}} \circ \rho_S)(\kappa) \cap (\rho_S \circ \widetilde{\mathfrak{S}} \circ \rho_S)(\kappa) \supseteq \sigma$$

Thus, $\kappa \in \mathcal{U}(\rho_S; \sigma)$. Therefore,

$$[S.\mathcal{U}(\rho_S; \sigma)] \cap [\mathcal{U}(\rho_S; \sigma).S.\mathcal{U}(\rho_S; \sigma)]$$

Hence, $\mathcal{U}(\rho_S; \sigma)$ is a BQ ideal of S.

Theorem 3.59. Let ρ_S be an S-int subsemigroup over U, σ be a subset of U, $Im(\rho_S)$ be the image of ρ_S such that $\sigma \in Im(\rho_S)$. If ρ_S is an S-int BQ ideal of S, then $\mathcal{U}(\rho_S; \sigma)$ is a BQ ideal ideal of S.

We illustrate Theorem 3.59 with Example 3.60.

Example 3.60. Consider the SS η_S in Example 3.2. By considering the image set of η_S, that is,

$$Im(\eta_S) = \{\{e, x, x^2, y\}, \{e, x, x^2\}, \{e, x\}\}$$

we obtain the following:

$$\mathcal{U}(\eta_S; \sigma) = \begin{cases} \{\mathfrak{f}, h, \mathfrak{r}\}, & \sigma = \{e, x\} \\ \{\mathfrak{f}, \mathfrak{r}\}, & \sigma = \{e, x, x^2\} \\ \{\mathfrak{r}\}, & \sigma = \{e, x, x^2, y\} \end{cases}$$

Here, $\{f, h, \mathfrak{r}\}, \{f, \mathfrak{r}\}$ and $\{\mathfrak{r}\}$ are all BQ ideals of S. In fact, since

$$\{\mathfrak{r}\}.\{\mathfrak{r}\} \subseteq \{\mathfrak{r}\}, \{\mathfrak{f}, \mathfrak{r}\}.\{\mathfrak{f}, \mathfrak{r}\} \subseteq \{\mathfrak{f}, \mathfrak{r}\}, \{\mathfrak{f}, h, \mathfrak{r}\}.\{\mathfrak{f}, h, \mathfrak{r}\} \subseteq \{\mathfrak{f}, h, \mathfrak{r}\}$$

each $\mathcal{U}(\eta_S; \sigma)$ is a subsemigroup of S. Similarly, since

$$\begin{gathered}(S.\{\mathfrak{r}\}) \cap (\{\mathfrak{r}\}.S.\{\mathfrak{r}\}) \subseteq \{\mathfrak{r}\} \cap \{\mathfrak{r}\} \subseteq \{\mathfrak{r}\} \\ (S.\{\mathfrak{f}, \mathfrak{r}\}) \cap (\{\mathfrak{f}, \mathfrak{r}\}.S.\{\mathfrak{f}, \mathfrak{r}\}) \subseteq \{\mathfrak{f}, \mathfrak{r}\} \cap \{\mathfrak{f}, \mathfrak{r}\} \subseteq \{\mathfrak{f}, \mathfrak{r}\} \\ (S.\{\mathfrak{f}, h, \mathfrak{r}\}) \cap (\{\mathfrak{f}, h, \mathfrak{r}\}.S.\{\mathfrak{f}, h, \mathfrak{r}\}) \subseteq \{\mathfrak{f}, h, \mathfrak{r}\} \cap \{\mathfrak{f}, h, \mathfrak{r}\} \subseteq \{\mathfrak{f}, h, \mathfrak{r}\}\end{gathered}$$

each $\mathcal{U}(\eta_S; \sigma)$ is an L-BQ ideal of S. Similarly, since

$$(\{\mathfrak{r}\}.S) \cap (\{\mathfrak{r}\}.S.\{\mathfrak{r}\}) \subseteq \{\mathfrak{r}\} \cap \{\mathfrak{r}\} \subseteq \{\mathfrak{r}\}$$

$$(\{\mathfrak{f}, \mathfrak{r}\}.S) \cap (\{\mathfrak{f}, \mathfrak{r}\}.S.\{\mathfrak{f}, \mathfrak{r}\}) \subseteq \{\mathfrak{f}, \mathfrak{r}\} \cap \{\mathfrak{f}, \mathfrak{r}\} \subseteq \{\mathfrak{f}, \mathfrak{r}\}$$

$$(\{\mathfrak{f}, h, \mathfrak{r}\}.S) \cap (\{\mathfrak{f}, h, \mathfrak{r}\}.S.\{\mathfrak{f}, h, \mathfrak{r}\}) \subseteq \{\mathfrak{f}, h, \mathfrak{r}\} \cap \{\mathfrak{f}, h, \mathfrak{r}\} \subseteq \{\mathfrak{f}, h, \mathfrak{r}\}$$

each $\mathcal{U}(\eta_S; \sigma)$ is an R-BQ ideal of S, and thus each of $\mathcal{U}(\eta_S; \sigma)$ is a BQ ideal of S.

Now, consider the SS $\mathfrak{K}_S$ in Example 3.2. By taking into account

$$Im(\mathfrak{K}_S) = \{\{e, x^2, y, yx^2\}, \{e, x, y\}, \{e, x\}\}$$

we obtain the following:

$$\mathcal{U}(\mathfrak{K}_S; \sigma) = \begin{cases} \{\mathfrak{f}, h\}, & \sigma = \{e, x\} \\ \{\mathfrak{f}\}, & \sigma = \{e, x, y\} \\ \{\mathfrak{r}\}, & \sigma = \{\mathrm{e}, x^2, y, yx^2\} \end{cases}$$

Here, $\{\mathfrak{f}, h\}$ is not a BQ ideal of S. In fact, since

$$(S.\{\mathfrak{f}, h\}) \cap (\{\mathfrak{f}, h\}.S.\{\mathfrak{f}, h\}) \subseteq \{\mathfrak{f}, h, \mathfrak{r}\} \cap \{\mathfrak{f}, h, \mathfrak{r}\} \not\subseteq \{\mathfrak{f}, h\}$$

one of the $\mathcal{U}(\aleph_S;\sigma)$ is not an L-ƁQ ideal of S, hence it is not a ƁQ ideal of S, It is seen that each of $\mathcal{U}(\aleph_S;\sigma)$ is not a ƁQ ideal of S. On the other hand, in Example 3.2 it was shown that $\aleph_S$ is not an S-int ƁQ ideal of S.

Proposition 3.61. For a semigroup S, the following conditions are equivalent:

(1) S is regular.
(2) $\eta_S = (\widetilde{\mathbb{S}} \circ \eta_S) \widetilde{\cap} \left(\eta_S \circ \widetilde{\mathbb{S}} \circ \eta_S\right)$ for every S-int L-ƁQ ideal.

Proof: First assume that (1) holds. Let S be a regular semigroup, η_S be an S-int L-ƁQ ideal and $\mathfrak{x} \in S$. Then, $(\widetilde{\mathbb{S}} \circ \eta_S) \widetilde{\cap} \left(\eta_S \circ \widetilde{\mathbb{S}} \circ \eta_S\right) \cong \eta_S$ and there exist an element $y \in S$ such that $\mathfrak{x} = \mathfrak{x}y\mathfrak{x}$. Since

$$\left(\widetilde{\mathbb{S}} \circ \eta_S\right)(\mathfrak{x}) = \bigcup_{\mathfrak{x}=kn} \left\{\widetilde{\mathbb{S}}(k) \cap \eta_S(n)\right\} \supseteq \widetilde{\mathbb{S}}(\mathfrak{x}y) \cap \eta_S(\mathfrak{x}) = U \cap \eta_S(\mathfrak{x}) = \eta_S(\mathfrak{x})$$

$$\begin{aligned}\left(\eta_S \circ \widetilde{\mathbb{S}} \circ \eta_S\right)(\mathfrak{x}) &= \bigcup_{\mathfrak{x}=kn} \left\{\eta_S(k) \cap (\widetilde{\mathbb{S}} \circ \eta_S)(n)\right\} \\ &\supseteq \eta_S(\mathfrak{x}) \cap \left(\widetilde{\mathbb{S}} \circ \eta_S\right)(y\mathfrak{x}) \\ &= \eta_S(\mathfrak{x}) \\ &\cap \bigcup_{y\mathfrak{x}=rs} \left\{\widetilde{\mathbb{S}}(r) \cap \eta_S(s)\right\} \\ &\supseteq \eta_S(\mathfrak{x}) \cap \widetilde{\mathbb{S}}(y) \cap \eta_S(\mathfrak{x}) \\ &= \eta_S(\mathfrak{x}) \cap U \cap \eta_S(\mathfrak{x}) = \eta_S(\mathfrak{x})\end{aligned}$$

Thus,

$$\left(\widetilde{\mathbb{S}} \circ \eta_S\right)(\mathfrak{x}) \cap \left(\eta_S \circ \widetilde{\mathbb{S}} \circ \eta_S\right)(\mathfrak{x}) \supseteq \eta_S(\mathfrak{x}) \cap \eta_S(\mathfrak{x}) \supseteq \eta_S(\mathfrak{x})$$

implying that $\eta_S \cong \left(\widetilde{\mathbb{S}} \circ \eta_S\right) \widetilde{\cap} \left(\eta_S \circ \widetilde{\mathbb{S}} \circ \eta_S\right)$. Therefore, $\eta_S = (\widetilde{\mathbb{S}} \circ \eta_S) \widetilde{\cap} \left(\eta_S \circ \widetilde{\mathbb{S}} \circ \eta_S\right)$.

Conversely, let $\mathfrak{n}_S = (\widetilde{\mathbb{S}} \circ \eta_S) \widetilde{\cap} \left(\eta_S \circ \widetilde{\mathbb{S}} \circ \eta_S\right)$, where f_S is an S-int L-ƁQ ideal. In order to show that S is regular, we need to show that $\mathcal{P} = S\mathcal{P} \cap \mathcal{P}S\mathcal{P}$ for every L-ƁQ ideal of S. It is obvious that $S\mathcal{P} \cap \mathcal{P}S\mathcal{P} \subseteq \mathcal{P}$. Thus, it is enough to show that $\mathcal{P} \subseteq S\mathcal{P} \cap \mathcal{P}S\mathcal{P}$. Let $d \in \mathcal{P}$ and $\mathcal{P}$ be any L-ƁQ ideal of S. Thus, $S_{\mathcal{P}}$ is an S-int L-ƁQ ideal ideal. Hence,

$$\begin{aligned}S_{\mathcal{P}}(d) &= \left(\widetilde{\mathbb{S}} \circ S_{\mathcal{P}}\right)(d) \cap \left(S_{\mathcal{P}} \circ \widetilde{\mathbb{S}} \circ S_{\mathcal{P}}\right)(d) \\ &= (S_S \circ S_{\mathcal{P}})(d) \cap (S_{\mathcal{P}} \circ S_S \circ S_{\mathcal{P}})(d) \\ &= S_{S\mathcal{P} \cap \mathcal{P}S\mathcal{P}}(d) = U\end{aligned}$$

implying that $d \in S\mathcal{P} \cap \mathcal{P}S\mathcal{P}$. Hence, $\mathcal{P} = S\mathcal{P} \cap \mathcal{P}S\mathcal{P}$ so S is a regular semigroup.

Proposition 3.62. For a semigroup S, the following conditions are equivalent:

(1) S is regular.
(2) $\mathfrak{b}_S = (\mathfrak{b}_S \circ \widetilde{\mathbb{S}}) \widetilde{\cap} \left(\mathfrak{b}_S \circ \widetilde{\mathbb{S}} \circ \mathfrak{b}_S\right)$ for every S-int R-ƁQ ideal.

Proof: First assume that (1) holds. Let S be a regular semigroup, $\mathfrak{b}_S$ be an S-int R-ƁQ ideal and $\mathfrak{x} \in S$. Then, $(\mathfrak{b}_S \circ \widetilde{\mathbb{S}}) \widetilde{\cap} \left(\mathfrak{b}_S \circ \widetilde{\mathbb{S}} \circ \mathfrak{b}_S\right) \cong \mathfrak{b}_S$ and there exist an element $t \in S$ such that $\mathfrak{x} = \mathfrak{x}t\mathfrak{x}$. Since,

$$\begin{aligned}\left(\mathfrak{b}_S \circ \widetilde{\mathbb{S}}\right)(\mathfrak{x}) &= \bigcup_{\mathfrak{x}=kn} \left\{\mathfrak{b}_S(k) \cap \widetilde{\mathbb{S}}(n)\right\} \supseteq \mathfrak{b}_S(\mathfrak{x}) \cap \widetilde{\mathbb{S}}(t\mathfrak{x}) \\ &= \mathfrak{b}_S(\mathfrak{x}) \cap U = \mathfrak{b}_S(\mathfrak{x})\end{aligned}$$

$$\begin{aligned}\left(\mathfrak{b}_S \circ \widetilde{\mathbb{S}} \circ \mathfrak{b}_S\right)(\mathfrak{x}) &= \cup_{\mathfrak{x}=kn} \left\{\mathfrak{b}_S(k) \cap (\widetilde{\mathbb{S}} \circ \mathfrak{b}_S)(n)\right\} \supseteq \\ &\mathfrak{b}_S(\mathfrak{x}) \cap \left(\widetilde{\mathbb{S}} \circ \mathfrak{b}_S\right)(t\mathfrak{x}) = \mathfrak{b}_S(\mathfrak{x}) \cap \cup_{t\mathfrak{x}=qs} \left\{\widetilde{\mathbb{S}}(q) \cap \right. \\ &\left. \mathfrak{b}_S(s)\right\} \supseteq \mathfrak{b}_S(\mathfrak{x}) \cap \widetilde{\mathbb{S}}(y) \cap \mathfrak{b}_S(\mathfrak{x}) = \mathfrak{b}_S(\mathfrak{x}) \cap U \cap \\ &\mathfrak{b}_S(\mathfrak{x}) = \mathfrak{b}_S(\mathfrak{x}).\end{aligned}$$

Thus,

$$\left(\mathfrak{b}_S \circ \widetilde{\mathbb{S}}\right)(\mathfrak{x}) \cap \left(\mathfrak{b}_S \circ \widetilde{\mathbb{S}} \circ \mathfrak{b}_S\right)(\mathfrak{x}) \supseteq \mathfrak{b}_S(\mathfrak{x}) \cap \mathfrak{b}_S(\mathfrak{x}) \supseteq \mathfrak{b}_S(\mathfrak{x})$$

implying that $\mathfrak{b}_S \cong \left(\mathfrak{b}_S \circ \widetilde{\mathbb{S}}\right) \widetilde{\cap} \left(\mathfrak{b}_S \circ \widetilde{\mathbb{S}} \circ \mathfrak{b}_S\right)$. Therefore, $\mathfrak{b}_S = \left(\mathfrak{b}_S \circ \widetilde{\mathbb{S}}\right) \widetilde{\cap} \left(\mathfrak{b}_S \circ \widetilde{\mathbb{S}} \circ \mathfrak{b}_S\right)$.

Conversely, let $\mathfrak{b}_S = \left(\mathfrak{b}_S \circ \widetilde{\mathbb{S}}\right) \widetilde{\cap} \left(\mathfrak{b}_S \circ \widetilde{\mathbb{S}} \circ \mathfrak{b}_S\right)$ where $\mathfrak{b}_S$ is an S-int R-ƁQ ideal. In order to show that S is regular, we need to show that $\mathfrak{M} = \mathfrak{M}S \cap \mathfrak{M}S\mathfrak{M}$ for every R-ƁQ ideal of S. It is obvious that $\mathfrak{M}S \cap \mathfrak{M}S\mathfrak{M} \subseteq \mathfrak{M}$. Thus, it is enough to show that $\mathfrak{M} \subseteq \mathfrak{M}S \cap \mathfrak{M}S\mathfrak{M}$. Let $\mathfrak{v} \in \mathfrak{M}$ and $\mathfrak{M}$ be any R-ƁQ ideal of S. Thus, $S_{\mathfrak{M}}$ is an S-int R-ƁQ ideal ideal. Hence,

$$\begin{aligned}S_{\mathfrak{M}}(\mathfrak{v}) &= \left(S_{\mathfrak{M}} \circ \widetilde{\mathbb{S}}\right)(\mathfrak{v}) \cap \left(S_{\mathfrak{M}} \circ \widetilde{\mathbb{S}} \circ S_{\mathfrak{M}}\right)(\mathfrak{v}) \\ &= \left(S_{\mathfrak{M}} \circ S_S\right)(\mathfrak{v}) \cap \left(S_{\mathfrak{M}} \circ S_S \circ S_{\mathfrak{M}}\right)(\mathfrak{v}) \\ &= S_{\mathfrak{M}S \cap \mathfrak{M}S\mathfrak{M}}(\mathfrak{v}) = U\end{aligned}$$

implying that $\mathfrak{v} \in \mathfrak{M}S \cap \mathfrak{M}S\mathfrak{M}$. Hence, $\mathfrak{M} = \mathfrak{M}S \cap \mathfrak{M}S\mathfrak{M}$ so S is a regular semigroup.

Theorem 3.63. For a semigroup S, the following conditions are equivalent:

(1) S is regular.
(2) $\mathfrak{n}_S = \left(\widetilde{\mathbb{S}} \circ \mathfrak{n}_S\right) \widetilde{\cap} \left(\mathfrak{n}_S \circ \widetilde{\mathbb{S}} \circ \mathfrak{n}_S\right) = \left(\mathfrak{n}_S \circ \widetilde{\mathbb{S}}\right) \widetilde{\cap} \left(\mathfrak{n}_S \circ \widetilde{\mathbb{S}} \circ \mathfrak{n}_S\right)$ for every S-int ƁQ ideal.

Proof: It is followed by Proposition 3.61 and Proposition 3.62.

Proposition 3.64. Let S be a regular semigroup. Then every S-int L-ƁQ ideal of a semigroup S is an S-int quasi ideal of semigroup.

Proof: Let f_S be an S-int L-BQ ideal of S. Then, $\left(\tilde{S} \circ \mathfrak{q}_S\right) \tilde{\cap} \left(\mathfrak{q}_S \circ \tilde{S} \circ \mathfrak{q}_S\right) \tilde{\subseteq} \mathfrak{q}_S$. We know that $\mathfrak{q}_S \circ \tilde{S}$ and $\tilde{S} \circ \mathfrak{q}_S$ are S-int R-and S-int L-ideals of the semigroup S respectively. By Corollary 2.20, we have $\left(\mathfrak{q}_S \circ \tilde{S}\right) \tilde{\cap} \left(\tilde{S} \circ \mathfrak{q}_S\right) = \mathfrak{q}_S \circ \tilde{S} \circ \tilde{S} \circ \mathfrak{q}_S$. Thus,

$$(\mathfrak{q}_S \circ \tilde{S}) \tilde{\cap} (\tilde{S} \circ \mathfrak{q}_S) \tilde{\subseteq} \tilde{S} \circ \mathfrak{q}_S \text{ and } \left(\mathfrak{q}_S \circ \tilde{S}\right) \tilde{\cap} \left(\tilde{S} \circ \mathfrak{q}_S\right) = \mathfrak{q}_S \circ \tilde{S} \circ \tilde{S} \circ \mathfrak{q}_S \tilde{\subseteq} \mathfrak{q}_S \circ \tilde{S} \circ \mathfrak{q}_S$$

Hence,

$$\left(\mathfrak{q}_S \circ \tilde{S}\right) \tilde{\cap} \left(\tilde{S} \circ \mathfrak{q}_S\right) \tilde{\subseteq} \left(\tilde{S} \circ \mathfrak{q}_S\right) \tilde{\cap} (\mathfrak{q}_S \circ \tilde{S} \circ \mathfrak{q}_S) \tilde{\subseteq} \mathfrak{q}_S$$

Therefore, $\mathfrak{q}_S$ is an S-int quasi ideal.

Proposition 3.65. Let S be a regular semigroup. Then every S-int R-BQ ideal of a semigroup S is an S-int quasi ideal of semigroup.

Proof: Let $\mathfrak{q}_S$ be an S-int R-BQ ideal of S. Then, $\left(\mathfrak{q}_S \circ \tilde{S}\right) \tilde{\cap} \left(\mathfrak{q}_S \circ \tilde{S} \circ \mathfrak{q}_S\right) \tilde{\subseteq} \mathfrak{q}_S$. We know that $\mathfrak{q}_S \circ \tilde{S}$ and $\tilde{S} \circ \mathfrak{q}_S$ are S-int R-and S-int L-ideals of the semigroup S respectively. By Corollary 2.20, we have

$$\left(\mathfrak{q}_S \circ \tilde{S}\right) \tilde{\cap} \left(\tilde{S} \circ \mathfrak{q}_S\right) = \mathfrak{q}_S \circ \tilde{S} \circ \tilde{S} \circ \mathfrak{q}_S$$

Thus,

$$\left(\mathfrak{q}_S \circ \tilde{S}\right) \tilde{\cap} \left(\tilde{S} \circ \mathfrak{q}_S\right) \tilde{\subseteq} \mathfrak{q}_S \circ \tilde{S}$$

$$\left(\mathfrak{q}_S \circ \tilde{S}\right) \tilde{\cap} \left(\tilde{S} \circ \mathfrak{q}_S\right) = \mathfrak{q}_S \circ \tilde{S} \circ \tilde{S} \circ \mathfrak{q}_S \tilde{\subseteq} \mathfrak{q}_S \circ \tilde{S} \circ \mathfrak{q}_S.$$

Hence,

$$\left(\mathfrak{q}_S \circ \tilde{S}\right) \tilde{\cap} \left(\tilde{S} \circ \mathfrak{q}_S\right) \tilde{\subseteq} \left(\mathfrak{q}_S \circ \tilde{S}\right) \tilde{\cap} (\mathfrak{q}_S \circ \tilde{S} \circ \mathfrak{q}_S) \tilde{\subseteq} \mathfrak{q}_S$$

Therefore, $\mathfrak{q}_S$ is an S-int quasi ideal.

Theorem 3.66. Let S be a regular semigroup. Then every S-int BQ ideal of a semigroup S is an S-int quasi ideal of semigroup.

Proof: It is followed by Proposition 3.64 and Proposition 3.65.

4. DISCUSSION AND CONCLUSION

Rao [8] expanded the notions of quasi-ideal, bi-ideal, L-(R-) ideal, and ideal in semigroups by defining BQ ideals and examining their characteristics. In this study, we have applied the concept of "S-int BQ ideals of semigroups" to both SS theory and semigroup theory. It has been shown that every S-int bi-ideal, S-int ideal, S-int quasi-ideal, and S-int interior ideal of an idempotent SS is an S-int BQ ideal. Counterexamples show that the converse is not always true, and for the converse to hold, the semigroup must be simple* or regular. It has also been demonstrated that in a soft simple* semigroup, the S-int BQ ideal coincides with the S-int bi-ideal, S-int L-(R-) ideal, S-int quasi-ideal, and S-int interior ideal. To link SS theory and classical semigroup theory, it is shown that if a subsemigroup is an S-int BQ ideal, its upper α-inclusion set is also a BQ ideal. Furthermore, if a subsemigroup is a BQ ideal, its SCF is an S-int BQ ideal, and the reverse is also true. The finite soft intersections of S-int BQ ideals are shown to be S-int BQ ideals, as are the soft intersections of S-int ideals. Additionally, the relationship between regular semigroups and S-int BQ ideals is explored. In future studies, the characterization of S-int BQ ideals of semigroups can be conducted with respect to various types of semigroups, such as L-(R-) simple semigroups, L-(R-) zero semigroups, and intra-regular semigroups.

The relation between several S-int ideals and their generalized ideals is depicted in the following figure, where $\mathcal{A} \rightarrow \mathcal{B}$ denotes that $\mathcal{A}$ is $\mathcal{B}$ but $\mathcal{B}$ may not always be $\mathcal{A}$.

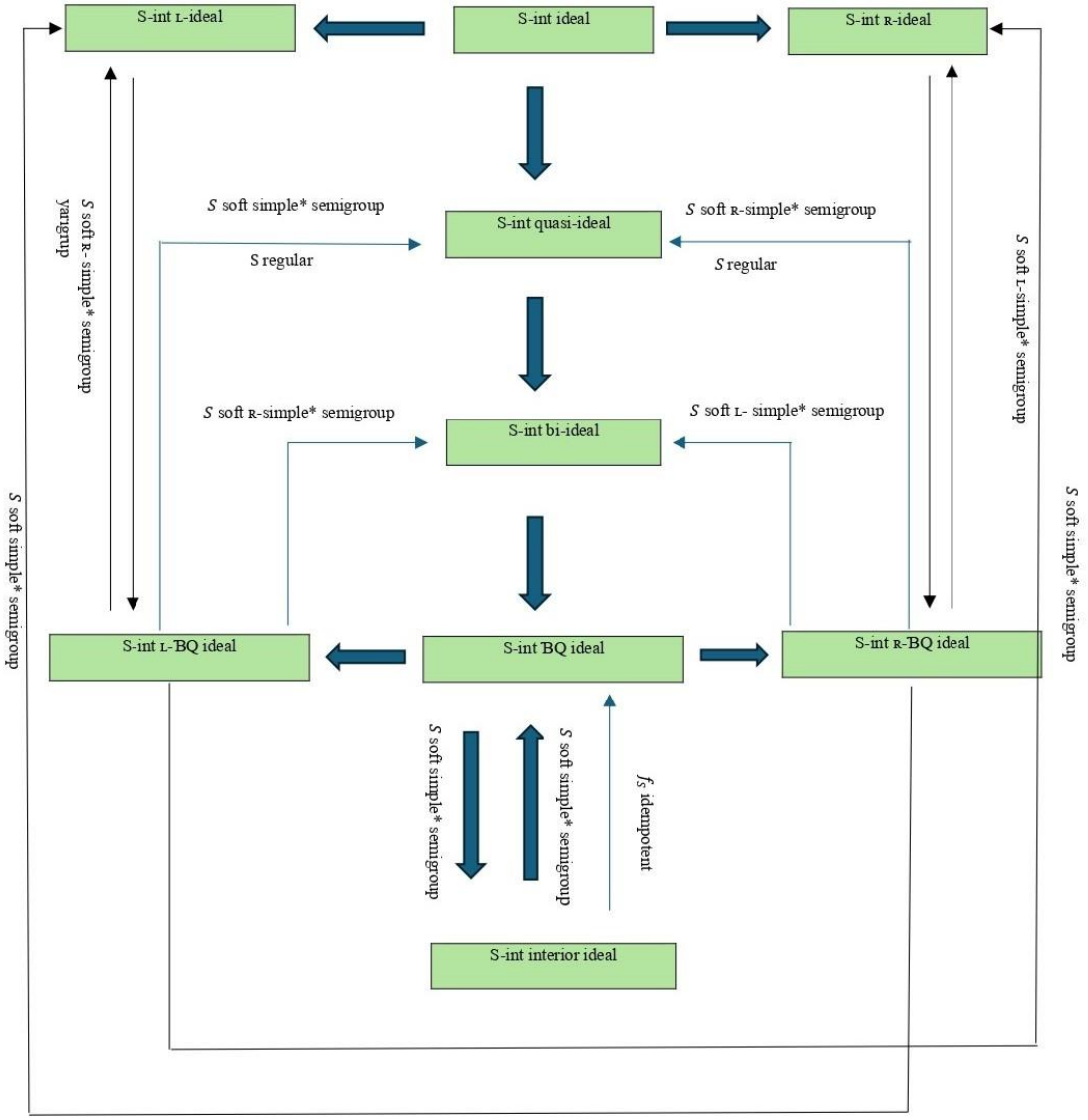

Figure 1. Diagram illustrating the relationships between some S-int ideals

Acknowledgement

This paper is derived from the second author's master's thesis supervised by the first author at Amasya University, Türkiye**.**

REFERENCES

[1] Good RA, Hughes DR. Associated groups for a semigroup. Bull Amer Math Soc. 1952;58(6):624-625.

[2] Steinfeld O. Uher die quasi ideals. Von halbgruppend Publ Math Debrecen. 1956;4:262-275.

[3] Lajos S. (m;k;n)-ideals in semigroups. Notes on Semigroups II, Karl Marx Univ. Econ., Dept. Math. Budapest. 1976;(1):12-19.

[4] Szasz G. Interior ideals in semigroups. Notes on semigroups IV, Karl Marx Univ. Econ., Dept. Math. Budapest. 1977;(5):1-7.

[5] Szasz G. Remark on interior ideals of semigroups. Studia Scient. Math. Hung. 1981;(16):61-63.

[6] Rao MMK. Bi-interior ideals of semigroups. Discuss Math Gen Algebra Appl. 2018;38(1) 69-78.

[7] Rao MK. A study of a generalization of bi-ideal, quasi-ideal and interior ideal of semigroup. Mathematica Moravica. 2018;22(2):103-115.

[8] Rao MK. Left bi-quasi ideals of semigroups. Southeast Asian Bull Math. 2020;44:369-376.

[9] Rao MMK. Quasi-interior ideals and weak-interior ideals. Asia Pac Journal Mat. 2020;7:7-21.

[10] Baupradist S, Chemat B, Palanivel K, Chinram R. Essential ideals and essential fuzzy ideals in semigroups. J Discrete Math Sci Cryptogr. 2021;24(1): 223-233.

[11] Grošek O, Satko L. A new notion in the theory of semigroup. Semigroup Forum. 1980;20(1):233-240.

[12] Bogdanovic S. Semigroups in which some bi-ideal is a group. Univ u Novom Sadu Zb Rad Prirod Mat Fak Ser Mat. 1981;11:261-266.

[13] Wattanatripop K, Chinram R, Changphas T. Quasi-A-ideals and fuzzy A-ideals in semigroups. J Discrete Math Sci Cryptogr. 2018;21(5):1131-1138.

[14] Kaopusek N, Kaewnoi T, Chinram R. On almost interior ideals and weakly almost interior ideals of

semigroups. J Discrete Math Sci Cryptogr. 2020;23(3):773-778.
[15] Iampan A, Chinram R, Petchkaew P. A note on almost subsemigroups of semigroups. Int J Math Comput Sci. 2021;16:1623-1629.
[16] Chinram R, Nakkhasen W. Almost bi-quasi-interior ideals and fuzzy almost bi-quasi-interior ideals of semigroups. J Math Comput Sci. 2022;26:128-136.
[17] Gaketem T. Almost bi-interior ideal in semigroups and their fuzzifications. Eur J Pure Appl Math. 2022;15(1):281-289.
[18] Gaketem T, Chinram R. Almost bi-quasi ideals and their fuzzifications in semigroups. Ann Univ Craiova Math Comput Sci Ser. 2023;50(2):342-352.
[19] Wattanatripop K, Chinram R, Changphas T. Fuzzy almost bi-ideals in semigroups. Int J Math Comput Sci. 2018;13(1):51-58.
[20] Krailoet W, Simuen A, Chinram R, Petchkaew P. A note on fuzzy almost interior ideals in semigroups. Int J Math Comput Sci. 2021;16(2):803-808.
[21] Molodtsov D. Soft set theory-first results. Comput Math Appl. 1999;37(1):19-31.
[22] Maji PK, Biswas R, Roy AR. Soft set theory. Comput Math Appl. 2003;45(1):555-562.
[23] Pei D, Miao D. From soft sets to information systems. In: Proceedings of Granular Computing. IEEE 2005;2 617–621.
[24] Ali MI, Feng F, Liu X, Min WK, Shabir M. On some new operations in soft set theory. Comput Math Appl. 2009;57(9):1547–1553.
[25] Sezgin A, Dagtoros K. Complementary soft binary piecewise symmetric difference operation: A novel soft set operation. Scientific Journal of Mehmet Akif Ersoy University. 2023;6(2):1457-1467.
[26] Sezgin A, Sarıalioğlu M. A new soft set operation: complementary soft binary piecewise theta (**θ**) operation. Journal of Kadirli Faculty of Applied Sciences. 2024;4(2):325-357.
[27] Ali MI, Shabir M, Naz M. Algebraic structures of soft sets associated with new operations. Comput Math Appl. 2011;61(9):2647-2654.
[28] Sezgin A, Çağman N, Atagün AO, Aybek FN. A. Complemental binary operations of sets and their application to group theory. Matrix Science Mathematic, 2023;7(2):114-121.
[29] Stojanović NS. A new operation on soft sets: extended symmetric difference of soft sets. Military Technical Courier. 2021;69(4):779-791.
[30] Sezgin A, Yavuz E. Soft binary piecewise plus operation: A new type of operation for soft sets. Uncertainty Discourse and Applications. 2024;1(1):79-100.
[31] Sezgin A, Çalışıcı H. A comprehensive study on soft binary piecewise difference operation. Eskişeh Tek Univ Bilim Teknol Derg Teor Bilim. 2024;12:32-54.
[32] Sezgin A, Atagün AO, Çağman N. A complete study on and-product of soft sets. Sigma J Eng Nat Sci. 2025;43(1):1-14.
[33] Sezgin A, Aybek FN, Güngör NB. A new soft set operation: complementary soft binary piecewise union operation. Acta Informatica Malaysia. 2023;7(1):38-53.
[34] Sezgin A, Sarıalioğlu M. Complementary extended gamma operation: A new soft set operation. Natural and Applied Sciences Journal. 2024;7(1):15–44.
[35] Sezgin A, Yavuz E. A new soft set operation: complementary soft binary piecewise lambda operation. Sinop University Journal of Natural Sciences. 2023;8(5):101-133.
[36] Sezgin A, Yavuz E. A new soft set operation: soft binary piecewise symmetric difference operation. Necmettin Erbakan University Journal of Science and Engineering. 2023;5(2):189-208.
[37] Sezgin A, Çağman N. A new soft set operation: complementary soft binary piecewise difference operation. Osmaniye Korkut Ata Üniv Fen Biliml Derg. 2024;7(1):58-94.
[38] Çağman N, Enginoğlu S. Soft set theory and uni-int decision making. Eur J Oper Res. 2010;207(2):848-855.
[39] Çağman N, Çıtak F, Aktaş H. Soft int-group and its applications to group theory. Neural Comput Appl. 2012;21:151-158.
[40] Sezer AS, Çağman N, Atagün AO, Ali MI, Türkmen E. Soft intersection semigroups, ideals and bi-ideals; a new application on semigroup theory I. Filomat. 2015;29(5):917-946.
[41] Sezer AS, Çağman N, Atagün AO. Soft intersection interior ideals, quasi-ideals and generalized bi-ideals: a new approach to semigroup theory II. J Mult-Valued Log Soft Comput. 2014;23 (1–2) 161-207.
[42] Sezgin A, Orbay M. Analysis of semigroups with soft intersection ideals. Acta Univ Sapientiae Math. 2022;14(1):166-210.
[43] Sezgin A, İlgin A. Soft intersection almost ideals of semigroups. J Innovative Eng Nat Sci. 2024;4(2):466-481.
[44] Sezgin A, İlgin A. Soft intersection almost bi-interior ideals of semigroups. J Nat Appl Sci Pak. 2024;6(1):1619-1638.
[45] Sezgin A, İlgin A. Soft intersection almost bi-quasi ideals of semigroups. Soft Computing Fusion with Applications. 2024;1(1):27-42.
[46] Sezgin A, İlgin A. Soft intersection almost weak-interior ideals of semigroups. Journal of Natural Sciences and Mathematics of UT. 2024;9(17-18):372-385.
[47] Sezgin A, Onur B. Soft intersection almost bi-ideals of semigroups. Syst Anal. 2024;2(1):95-105.
[48] Sezgin A, Kocakaya FZ, İlgin A. Soft intersection almost quasi-interior ideals of semigroups. Eskişeh Tek Univ Bilim Teknol Derg Teor Bilim. 2024;12(2):81-99.
[49] Sezgin A, İlgin A. Soft intersection almost subsemigroups of semigroups. Int J Math Phys. 2024;15(1):13-20.
[50] Sezgin A, Baş ZH, İlgin A. Soft intersection almost bi quasi-interior ideals of semigroups. J Fuzzy Ext Appl. 2025;6(1),43-58.
[51] Sezgin A, Onur B, İlgin A. Soft intersection almost tri-ideals of semigroups. SciNexuses. 2024;1:126-138.

[52] Sezgin A, Ilgin A, Atagun AO. Soft intersection almost tri-bi-ideals of semigroups. Sci Technol Asia. 2024;29(4):1-13.
[53] Sezgin A, Kocakaya FZ. Soft intersection almost quasi-ideals of semigroups. Songklanakarin J Sci Technol. 2025;47(2): in press.
[54] Sezgin A, Baş ZH. Soft-int almost interior ideals for semigroups. Information Information Sci Appl. 2024;4:25-36.
[55] Atagün AO, Kamacı H, Taştekin İ, Sezgin A. P-properties in near-rings. J. Math. Fundam. Sci. 2019;51(2):333-350.
[56] Jana C, Pal M, Karaaslan F, Sezgin A. (α, β)-Soft intersectional rings and ideals with their applications. New Math Nat Comput. 2019;15(02):333-350.
[57] Atagün AO, Sezgin A. More on prime, maximal and principal soft ideals of soft rings. New Math Nat Comput. 2022;18(1):195-207.
[58] Atagün AO, Sezgin A. Int-soft substructures of groups and semirings with applications. Applied Mathematics & Information Sciences (AMIS). 2017;11(1):105-113.
[59] Manikantan T, Ramasany P, Sezgin A. Soft quasi-ideals of soft near-rings. Sigma J. Eng. Nat. Sci. 2023;41(3):565-574.
[60] Atagün AO, Sezgin A. A new view to near-ring theory: Soft near-rings. South East Asian J. of Math. & Math. Sci. 2013;14(3):1-14.
[61] Atagün AO, Sezgin A. Soft subnear-rings, soft ideals and soft N-subgroups of near-rings. Math Sci Letters. 2018;7:37-42.
[62] Sezgin A. A new view on AG-groupoid theory via soft sets for uncertainty modeling. Filomat. 2018;32(8):2995-3030.
[63] Sezer AS, Atagün AO, Çağman N. A new view to N-group theory: soft N-groups. Fasc Math. 2013;51:123-140.
[64] Sezer AS, Atagün AO, Çağman N. N-group SI-action and its applications to N-group theory. Fasc Math. 2014;52:139-153.
[65] Gulistan M, Feng F, Khan M, Sezgin A. Characterizations of right weakly regular semigroups in terms of generalized cubic soft sets, Mathematics. 2018;6:293.
[66] Khan A, Izhar M, Sezgin A. Characterizations of Abel Grassmann's groupoids by the properties of double-framed soft ideals. Int J Anal Appl. 2017:15(1):62-74.
[67] Atagün AO, Sezer AS. Soft sets, soft semimodules and soft substructures of semimodules. Math Sci Lett. 2015;4(3):235-242.
[68] Sezgin A, İlgin A. Soft Intersection bi-interior ideals of semigroups. J Innov Sci Eng. 2025; 9(1): in press.
[69] Rao MMK. Bi-quasi ideals and fuzzy bi-quasi ideals of semigroups. Bull. Int. Math. Virtual Inst. 2017;7(2):231-242.
[70] Rao MMK. Left bi-quasi ideals of semirings. Bull. Int. Math. Virtual Inst. 2018;8(1):45-53.
[71] Rao MMK. Fuzzy left and right bi-quasi ideals of semiring. Bull. Int. Math. Virtual Inst. 2018;8(3):449-460.
[72] Rao MMK, Venkateswarlu B, Rafi N. Left bi-quasi ideals of Γ-semirings. Asia Pac J Math. 2017;4(2):144-153.

Volume 14, Issue 2, Page 179-187, 2025 https://doi.org/10.46810/tdfd.1622670 Research Article

BİNGÖL UNIVERSITY

Türk Doğa ve Fen Dergisi
Turkish Journal of Nature and Science
www.dergipark.gov.tr/tdfd

Artificial Intelligence and Classification Algorithms In Heart Disease Data: Modern Approaches And Performance Comparison

Berat ELİAÇIK[1*], Ali Hakan IŞIK[1]

[1] Mehmet Akif Ersoy University, Engineering-Architecture Faculty, Computer Engineering Department, Burdur, Türkiye
Berat ELİAÇIK ORCID No: 0009-0008-7897-9200
Ali Hakan IŞIK ORCID No: 0000-0003-3561-9375

**Corresponding author: eliacikberat@gmail.com*

(Received: 20.01.2025, Accepted: 07.05.2025, Online Publication: 27.06.2025)

Keywords
Heart disease, Artificial intelligence, Performance comparison

Abstract: This study presents a data mining application aimed at investigating the prediction performance of classification algorithms on heart disease datasets. In this research, the likelihood of individuals having heart disease based on specific features was evaluated using various classification algorithms. The study utilised several classification algorithms, including regression, k- nearest neighbours (KNN), Naive Bayes, random forest, decision trees and support vector machines (SVM). All algorithms were implemented using the Python programming language and the Jupyter Notebook environment, and their classification performances were compared. The evaluation of success was based on metrics such as accuracy, sensitivity, specificity, and F1 score. According to the results, KNN, support vector machines and random forest algorithms achieved the highest performance with an accuracy rate of 86.79%, outperforming the other algorithms. This study highlights the potential of classification algorithms in the early diagnosis of heart disease, emphasising the significance of artificial intelligence and data mining applications in the healthcare field.

Kalp Hastalığı Verilerinde Yapay Zekâ ve Sınıflandırma Algoritmaları: Modern Yaklaşımlar ve Performans Karşılaştırması

Anahtar Kelimeler
Kalp hastalıkları, Yapay zekâ, Performans karşılaştırması

Öz: Bu çalışmada, sınıflandırma algoritmalarının kalp hastalıkları verilerindeki tahmin performansını incelemek amacıyla bir veri madenciliği uygulaması gerçekleştirilmiştir. Araştırma kapsamında, belirli özelliklere sahip bireylerin kalp hastalığı taşıma olasılığı, farklı sınıflandırma algoritmaları kullanılarak değerlendirilmiştir. Çalışmada regresyon, k-en yakın komşu (KNN), Naive Bayes, rastgele orman, karar ağaçları ve destek vektör makineleri (SVM) algoritmaları kullanılmıştır. Tüm algoritmalar Python programlama dili ve Jupyter Notebook ortamında uygulanmış ve sınıflandırma performansları karşılaştırılmıştır. Başarı değerlendirmesi doğruluk oranı, duyarlılık, özgüllük ve F1 skoru gibi ölçütler üzerinden yapılmıştır. Elde edilen sonuçlara göre, KNN, destek vektör makineleri ve rastgele orman algoritmaları %86,79 doğruluk oranıyla diğer algoritmalara kıyasla en yüksek başarıyı göstermiştir. Bu çalışma, kalp hastalıklarının erken teşhisinde sınıflandırma algoritmalarının potansiyelini ortaya koyarak, sağlık alanında yapay zekâ ve veri madenciliği uygulamalarının önemini vurgulamaktadır.

1. INTRODUCTION

Rapid developments in data storage technologies and the increasing impact of digitalisation have led to the rapid growth of large datasets. These developments have led to an increase in the number and capacity of databases, thus enabling data management to become more comprehensive and efficient. Systematic collection and analysis of data, especially health data, plays an important role in critical areas such as early diagnosis of diseases as well as transforming it into meaningful information. However, raw data are not meaningful on their own; they must be processed and analysed using the right methods and algorithms. In this context, data mining has an

important place as the process of extracting meaningful patterns from large data sets [13]. Data mining has a great potential in the field of health and the use of correct classification algorithms can contribute to critical decisions such as early diagnosis.

Heart diseases are one of the most common health problems in the world, and data-based analyses are of great importance for early diagnosis and correct treatment methods. In this study, the performance of different classification algorithms on data for early diagnosis of heart diseases is analysed. Data mining stands out as a powerful tool for the diagnosis of heart diseases and the main purpose of this study is to investigate how various classification algorithms can give successful results in this field.

This study was carried out on heart disease data created by John Moore's University in Liverpool, England and updated on 6 June 2020. The dataset consists of 1190 samples consisting of 11 features, and analyses were performed on these data with various classification algorithms. The algorithms used in the study include regression, k-nearest neighbour (KNN), Naive Bayes, random forest, decision trees and support vector machines (SVM). All algorithms were implemented in Python programming language and Jupyter Notebook environment and their classification performances were compared. Metrics such as accuracy rate, sensitivity, specificity and F1 score were used as success measures.

The findings revealed that KNN, support vector machines and random forest algorithms showed the highest success with an accuracy rate of 86.79%. These results reveal the potential of classification algorithms in the early diagnosis of heart diseases and emphasise the importance of artificial intelligence and data mining applications in the field of healthcare. This study constitutes a valuable example in terms of the applications of data mining and artificial intelligence techniques in the field of health and contributes to the scientific literature in this field.

2. LITERATURE REVIEW

Early diagnosis of heart diseases is of critical importance in the field of healthcare. In recent years, the use of machine learning and data mining techniques in this field has increased and many studies have been carried out on the performance of various classification algorithms.
In a study by Mustafa Coşar (2021), the use of machine learning algorithms in the detection of heart diseases was discussed. In this study, Random Forest algorithm gave the most successful results with an accuracy rate of 88%. Logistic Regression and k-nearest neighbour (kNN) algorithms showed lower performance with 85% and 70% accuracy rates, respectively.

Gamze Kaba and Seda Bağdatlı Kalkan (2022) compared machine learning classification algorithms for early diagnosis of cardiovascular diseases. In this study, Naive Bayes, Logistic Regression, Random Forest, k-nearest neighbour (kNN) and Support Vector Machines (SVM) algorithms were used. The results revealed the performance differences of different algorithms and contributed to the determination of the most successful algorithm.

These studies reveal the effectiveness of machine learning and data mining techniques and the performance of different algorithms in the early diagnosis of heart diseases. In our study, we aim to compare the performance of regression, k-nearest neighbour (KNN), Naive Bayes, Random Forest, decision trees and Support Vector Machines (SVM) algorithms on heart disease data, taking into account the findings in this literature.

3. FEATURES REQUIRED FOR COMPARISON OF CLASSIFICATION ALGORITHMS

Machine learning and artificial intelligence applications play a major role in data analysis and classification processes. This process consists of a series of steps such as data collection, data preparation, selection of appropriate algorithms and evaluation of model performance. In this section, the main steps used to evaluate the effectiveness of classification algorithms will be discussed.

3.1. Data Collection and Preparation

Data collection is the first stage of machine learning projects and this stage has a direct impact on the accuracy of the model. This process can be performed in one of two main ways: open data sources and closed data collection methods.

Open Data Sources: Open data collection is a method that is usually carried out with the permission of users. Users are subjected to a certain transparency and consent process when providing data to platforms. Such data can be collected from social media posts, publicly available data sets or open access surveys. These data sources offer great potential for analysis.

Closed Data Sources: Closed data collection focuses more on user interactions and behaviour. This process collects data by tracking users' online activities on digital platforms. For example, websites, mobile applications or e-commerce platforms use this data to deliver personalised content by tracking user behaviour.

3.2. Machine Learning Stages and Data Preparation

In the machine learning process, the correct processing of data is a critical factor that determines the success of the model. These stages are of great importance to ensure the accuracy of the data, increase the generalisation ability of the model and make sense of the results. These processes usually consist of the following steps:

3.2.1. Data selection and cleaning

Data selection aims to improve the accuracy and reliability of available data sources. Data cleaning ensures the elimination of missing or erroneous data that may adversely affect the accuracy of the model. In machine learning applications, eliminating erroneous data entries accelerates the learning process of the model and prevents unnecessary complexities.

3.2.2. Data integration

Data integration is the process of combining data from different sources. This stage ensures that information from multiple data sources is presented in a consistent and harmonised manner. In modern machine learning algorithms, data integration enables the model to produce more accurate and comprehensive results.

3.2.3. Data transformation and feature selection

In machine learning algorithms, it is important that the data is in a certain format. Data transformation is the process of making raw data processable and analysable. Feature selection ensures that only the variables that are meaningful for the model are selected. This process accelerates the learning process of the algorithm and enables the model to work more efficiently.

3.2.4. Model selection and training process

The correct selection of machine learning algorithms is critical to the success of the project. This stage includes the process of selecting the most appropriate algorithm from different algorithms such as classification or regression and training it on the data. In this study, classification of heart disease data was performed using algorithms such as decision trees, KNN, Naive Bayes and random forest.

3.2.5. Evaluation of model performance

The success of the model is measured by various evaluation metrics. These metrics include accuracy rate, sensitivity, specificity and F1 score. These metrics evaluate how well the model fits real-world data and its ability to make accurate predictions. In this study, the performance of the algorithms used in was evaluated with a comparative analysis and it was observed that KNN, SVM and random forest algorithms stand out with high accuracy rates.

3.2.6. Visualisation and presentation of results

Presenting the results obtained with visual tools is an important step to understand and share the success of the model. The results are presented in the form of user-friendly reports, graphs or tables using visualisation techniques. This stage enables the data obtained to be shared in a more understandable and effective way.

3.2.7. Translating results into practice

Translating results into practice demonstrates the capacity of machine learning models to solve real-world problems. This stage demonstrates how the results of the model contribute to real-world applications in the healthcare field, for example, early detection of heart disease.The results enable the creation of supportive tools for healthcare professionals.

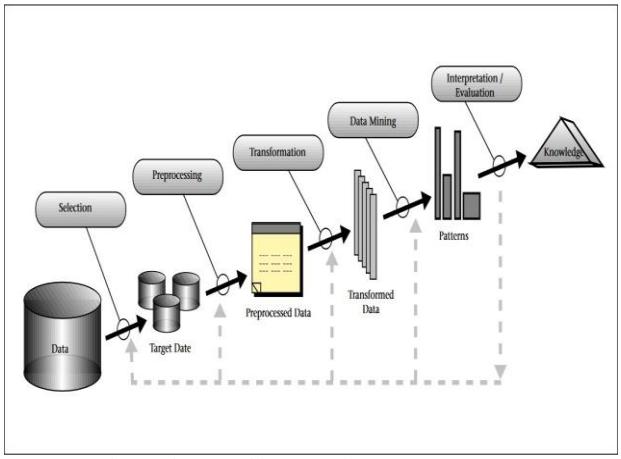

Figure 1. The Modern Machine Learning Process: From Raw Data to Actionable Insights

As illustrated in Figure 1 (The Modern Machine Learning Process: From Raw Data to Actionable Insights), the journey from raw data to valuable insights follows a structured and iterative process. This process begins with the careful selection of relevant data sources that align with the objectives of the study. Once selected, the data undergoes preprocessing steps such as cleaning, filtering, and standardization to ensure its quality and consistency. The next stage involves data transformation, where techniques like normalization, feature extraction, and dimensionality reduction are applied to prepare the data for analysis. At the core of the process lies the application of machine learning algorithms, whether supervised or unsupervised, which are used to uncover hidden patterns, make predictions, or classify data effectively. Finally, the outcomes are interpreted and evaluated to translate algorithmic results into actionable insights, assess model performance, and validate findings for practical use. This modern approach emphasizes not just extracting data, but actively learning from it using advanced machine learning methods to derive meaningful knowledge.

3.3. Machine Learning Models

Machine learning involves advanced analysis techniques used to discover meaningful patterns and relationships within large data sets. These techniques are supported by statistical models, machine learning algorithms, deep learning methods, and mathematical approaches such as decision trees, support vector machines, and neural networks. The models employed in this study enable accurate results by performing classification processes on the data, thus improving prediction capabilities and decision-making effectiveness.

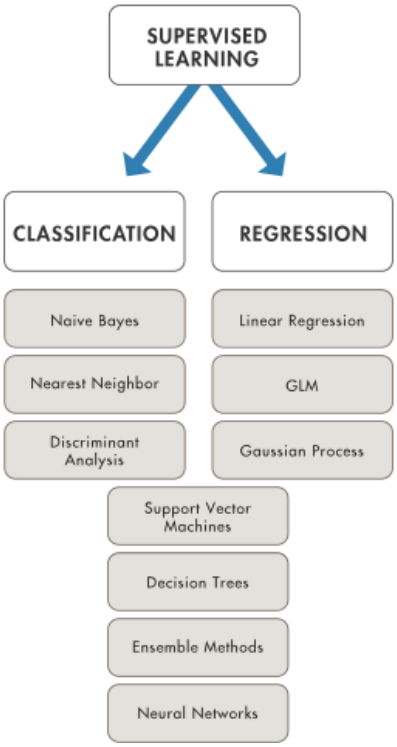

Figure 2. Supervised Learning Models

As shown in Figure 2 (Supervised Learning Models), supervised learning techniques are broadly divided into two main categories: classification and regression. Classification methods include algorithms such as Naive Bayes, Nearest Neighbor, Discriminant Analysis, Support Vector Machines, Decision Trees, Ensemble Methods, and Neural Networks, all of which are applied to categorical outcome predictions. On the other hand, regression methods, including Linear Regression, Generalized Linear Models (GLM), and Gaussian Processes, are designed to predict continuous outcomes.In the context of this study, the classification models outlined in Figure 2 were used to analyze heart disease data, aiming to distinguish between patients with and without heart disease. The selection of these models was based on their proven performance in medical data classification tasks, and their implementation has been thoroughly evaluated to ensure the robustness and accuracy of the results obtained.

3.3.1. Clustering

Clustering is one of the unsupervised learning methods and aims to group data with similar characteristics. This method is used to discover relationships in the data set and identify similarities between different data points. Clustering algorithms divide data points into natural clusters, allowing the features within each data group to be closer to each other. In analyses of health data such as heart disease, clustering methods are useful in identifying different groups of patients.

3.3.2. Association rules

Association rules are an approach to identifying relationships between variables in a data set. This method helps us to understand how a particular event can influence other events. Association rules can be classified into three main groups: multilevel association rules, multidimensional association rules and quantitative association rules. In machine learning and artificial intelligence applications, association rules are often used to discover possible relationships in health data. For example, it is possible to observe risk factors related to heart diseases together thanks to such analyses.

3.3.3. Classification

Classification is one of the supervised learning methods and is used to classify data into predefined classes. This method aims to predict which class each data point belongs to with various classifier algorithms. In this study, it is aimed to make accurate disease predictions by using various algorithms for the classification of heart disease data. Such classification problems offer an important application area for the analysis of health data.

3.4. Types of Classification Models

Classification can be performed using different algorithms and methods. These methods can be categorised according to the mathematical models and learning techniques used. Below are descriptions of the most common classification algorithms and how they are applied to health problems such as heart disease.

3.4.1. Regression

Regression is a method used to predict a continuous target variable and is often used in modelling linear relationships. Different types of regression, such as linear regression, multiple linear regression and non-linear regression, are used to better understand the relationship between data. In heart disease prediction, regression analysis can be used to predict possible disease development by performing risk analyses based on patients' health histories.

3.4.2. Naive Bayes

Naive Bayes is an algorithm for classification problems based on Bayes theorem. In particular, it gives effective results under the assumption of independence between data points. Naive Bayes classifier has the advantage of obtaining fast and accurate results,especially in large data sets. In the classification of medical data such as heart diseases, the Naive Bayes algorithm is widely used to estimate the probability of individuals carrying the disease.

3.4.3. K-nearest neighbours (knn)

K-Nearest Neighbours (KNN) is one of the lazy learning methods and does not create a trained model. Instead, it stores all the training data and performs classification by finding the nearest neighbours similar to the new incoming data. The KNN algorithm is widely used, especially to minimise classification errors. In heart disease data, the KNN algorithm can be effective as a

method of grouping people with similar characteristics to determine the risk status of individuals.

3.4.4. Decision tree

The decision tree is one of the most widely used algorithms for classification of data. This algorithm produces a set of rules that make decisions by sorting the data and is easy to visualise. Decision trees are particularly useful for making data more understandable and require low data preprocessing. In heart disease prediction, decision trees can be used to classify patients' possible disease states by considering different risk factors.

3.4.5. Random forest

Random forest is an algorithm that consists of a combination of many decision trees and combines the prediction of each tree to create a more powerful classifier. This algorithm is often used to improve accuracy and shows high performance on large data sets. In health data such as heart diseases, the random forest algorithm can improve the accuracy of disease predictions by evaluating various factors.

3.4.6. Support vector machine (svm)

Support Vector Machine (SVM) is a classification algorithm that gives effective results in high dimensional data sets and tries to separate data points in the best way. SVM is a preferred method to obtain accurate and generalisable results, especially in classification processes. In the classification of medical data such as heart diseases, the SVM algorithm has the ability to make accurate classifications according to the health status of patients.

3.5. Evaluation of Model Success

Various metrics are used to evaluate artificial intelligence and machine learning modelsuccess. Performance metrics such as accuracy, precision, sensitivity, F-score and AUC-ROC are basic tools for understanding the effectiveness and accuracy of the model.One of the most common methods used to evaluate model performance is the confusion matrix. The confusion matrix visually represents the performance of classification algorithms, allowing the model's predictions to be compared with the actual labels.

Table 1. Confusion Matrix

		Projected Status	
		Class = 1	Class = 0
Actual Situation	Class=1	TP (True Positive)	FN (False Negative)
	Class=0	FP (False Positive)	TN (True Negative)

3.5.1. Accuracy

Accuracy is a key performance metric that measures how often the model makes correct predictions. The accuracy of a model is calculated as the ratio of correct predictions to total predictions. Although high accuracy indicates the overall success level of the model, it can be misleading in unbalanced data sets. Accuracy is calculated by the following formula:

$$\text{Accuracy} = \frac{\text{TP} + \text{TN}}{\text{TP} + \text{TN} + \text{FP} + \text{FN}}$$

In our study, although the accuracy of the model is high in the classification processes performed on heart disease data, it is necessary to pay attention to some class imbalances.

3.5.2. Precision

Precision indicates how many of the model's predictions of the positive class are correct. The precision metric is particularly useful when false positive predictions should be low. In health data, it is desirable to have fewer false positives (e.g. patients predicted to be healthy). Precision is calculated as follows:

$$\text{Precision} = \frac{\text{TP}}{\text{TP} + \text{FP}}$$

In the study on heart disease prediction, we tried to keep the precision metric high in order to minimise the false positive rate.

3.5.3. Recall

Sensitivity measures the rate at which the true positive class is predicted. This metric is particularly critical in situations where false negatives (true positives that are incorrectly assigned to the negative class by the model) need to be minimised. In health data, minimising false negatives prevents patients from being missed. Sensitivity is calculated as follows:

$$\text{Recall} = \frac{\text{TP}}{\text{TP} + \text{FN}}$$

In our study, the sensitivity metric was prioritised especially for the detection of diseases, and it was aimed to identify the patients accurately.

3.5.4. F-Score

The F-score is used to evaluate the trade-off between precision and sensitivity. The F- score combines both metrics and presents the model performance as a single value. The F- score is maximised when the balance between precision and sensitivity is achieved. By taking both factors into account, this metric more accurately measures the overall success of the model. The F-score is calculated by the following formula:

$$\text{F Score} = \frac{2 \text{ x Precision x Sensitivity}}{\text{Precision} + \text{Sensitivity}}$$

In our study, a high F- score was targeted so that the model performs in a balanced way by reducing both false positives and false negatives.

4. APPLICATION

In this study, the data of individuals in Hungary, Switzerland, Cleveland, Ohio, USA and Long Beach, California were analysed. In this dataset, patients with chest pain complaints were analysed whether they had any of the heart diseases as a result of the examinations.Based on this data, a machine learning model was developed to predict whether an individual has heart disease or not. The success of the developed model was measured by the performance evaluation metrics used.

4.1. Dataset Used

The dataset used in this study has been compiled and merged to support research into the development of machine learning and artificial intelligence algorithms focused on Coronary Artery Disease (CAD). Last updated on 6 June 2020, the dataset includes 1190 examples with 13 key features, including age, sex, chest pain type (cp), resting blood pressure (trestbps), serum cholesterol (chol), fasting blood sugar (fbs), resting electrocardiographic results (restecg), maximum heart rate achieved (thalach), exercise-induced angina (exang), ST depression induced by exercise (oldpeak), slope of the peak exercise ST segment (slope), number of major vessels (ca), and thalassemia status (thal), along with the target variable indicating the presence of heart disease.

age	sex	cp	trestbps	chol	fbs	restecg	thalach	exang	oldpeak	slope	ca	thal	target
63	1	3	145	233	1	0	150	0	2.3	0	0	1	1
37	1	2	130	250	0	1	187	0	3.5	0	0	2	1
41	0	1	130	204	0	0	172	0	1.4	2	0	2	1
56	1	1	120	236	0	1	178	0	0.8	2	0	2	1
57	0	0	120	354	0	1	163	1	0.6	2	0	2	1
...	...	...	...	...	...	...	...	...	...	...	...	...	...

Figure 3. Sample Rows Illustrating the Heart Disease Dataset

To enhance understanding of the dataset, example rows are provided in Figure 3, offering a snapshot of the data's structure and values. Sharing these sample data points helps clarify the nature of the features and supports a better grasp of the inputs used in model development.

4.2. Python and Data Mining Libraries

The operations on the data were performed using the Python programming language. Python is a software language that was released in 1990 and is widely used today for data science, machine learning and artificial intelligence applications. Python's simple syntax and ease of learning have made this language popular in both academic and industrial fields. Python, which contains the necessary libraries for data mining and machine learning, is an ideal choice for high performance computing. Within the scope of the study, data classification was performed using Jupyter Notebook, which is included in the Anaconda Navigator platform developed for Python. Jupyter Notebook is a powerful tool that facilitates interactive data analysis and modelling processes.

4.3. Data Preprocessing Steps

The dataset contains 76 attributes (features) and only 11 attributes have been analysed in existing studies. These attributes reflect the most important features of heart disease. In the data preprocessing stage, only these 11 attributes were evaluated in order to increase the success of the model. The selection of attributes is a step towards improving the accuracy and generalisability of the model. The data were cleaned and appropriately transformed to avoid any missing information or anomalies.

The dataset used in the study was created by John Moore's University in Liverpool, England. The data provides a wide range of information on the health status of individuals in the region. During the comparison of data mining algorithms, model successes were evaluated using the data of individuals in this region.

4.4. Partitioning the Dataset into Training and Test Sets

In order to accurately evaluate the performance of machine learning models, the data is divided into training and test sets. The training data set is used for the learning process of the model, while the test data set is used to evaluate the overall performance of the model. The data is divided as 80% training set and 20% test set. This data splitting technique is important to predict how the model will perform on new and unseen data. Splitting the data into training and test sets increases the ability of the model to generalise without overfitting. In this way, the probability of heart disease was estimated as a result of the tests of the model on the patient. While the model learnt to classify with the data used in the training process, the accuracy and generalisation power of the model were measured with the test set.

4.5. Performance Results of Classification Algorithms

In this study, the performance of different machine learning algorithms on heart disease prediction is evaluated. The results obtained with the sensitivity, precision, accuracy and F-score metrics of the algorithms used are presented below.

Table 2. Performance Comparison of Various Classification Algorithms

Algorithm	Recall	Precision	Accuracy	F- score
Logistic Regression	%85,18	%85,18	%86,88	%85,18
KNN	%85,18	%88,46	%88,52	%86,79
SVM	%85,18	%88,46	%88,52	%86,79
Naive Bayes	%85,18	%85,18	%86,88	%85,18
Decision Tree	%77,78	%70	%75,40	%73,68
Random Forest	%85,18	%88,46	%88,52	%86,79

Table 2 presents a comparative analysis of several classification algorithms based on key performance metrics, namely recall, precision, accuracy, and F- score. Logistic Regression shows a stable performance, with an accuracy of 86.88% and an F-measure of 85.18%,

reflecting its reliable predictive capabilities. In contrast, the K Nearest Neighbour (KNN), Support Vector Machine (SVM), and Random Forest algorithms display higher efficacy, with accuracy values of 88.52% and corresponding F- score scores of 86.79%. These results suggest that these algorithms are more effective in terms of balancing precision and recall. On the other hand, the Decision Tree algorithm exhibits a lower performance across all metrics, particularly in certainty and F- score, which suggests its relative inefficiency compared to the other models evaluated. This discrepancy highlights the Decision Tree's tendency to overfit or underperform in certain data scenarios, making it less suitable for tasks requiring high accuracy and certainty.

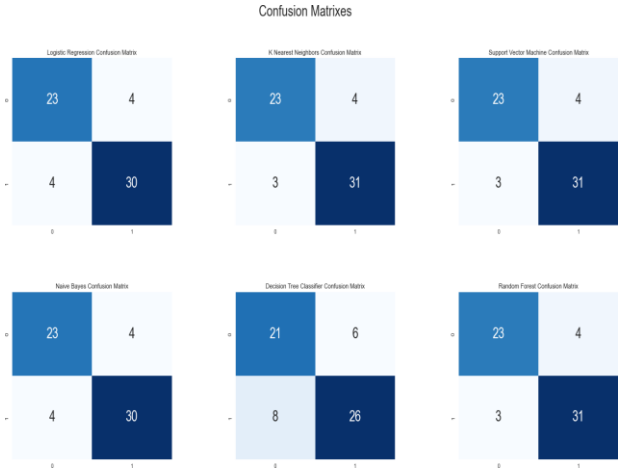

Figure 4. Confusion matrix images of Logistic Regression, KNN, SVM, Naive Bayes, Decision Tree and Random Forest algorithms.

The figure showing the effect of gender on the risk of heart disease can be interpreted as follows:

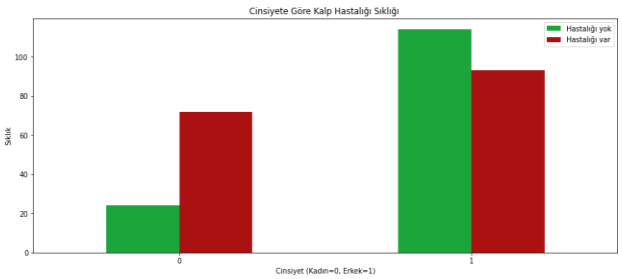

Figure 5. Frequency of Heart Disease by Gender

The graph shows the differences between female (0) and male (1) individuals with heart disease. The prevalence of heart disease is higher in men than in women. This finding reveals that men are in the higher risk group for heart disease. The frequency of heart disease according to age groups is shown in the graph below:

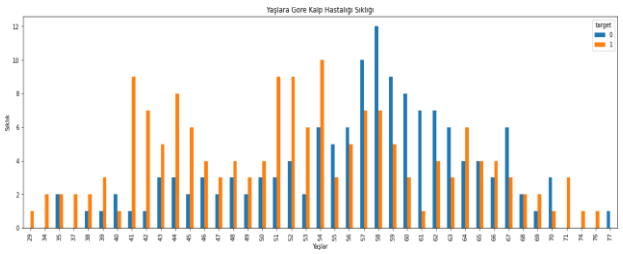

Figure 6. Frequency of Heart Disease by Age

When the age groups were analysed, it was observed that the risk of heart disease increased significantly in the 50-60 age range. This indicates that middle-aged individuals should be more careful about heart health. The relationship between the slope of the ST segment after exercise and the frequency of heart disease is shown in the graph below:

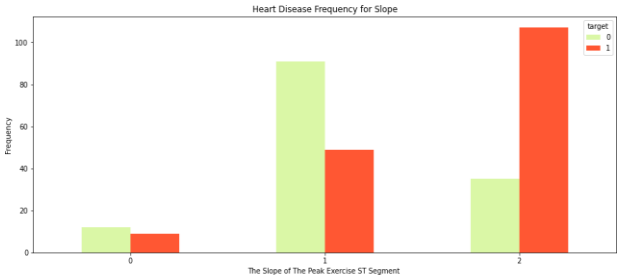

Figure 7. Exercise ST Segment Slope and Frequency of Heart Disease

This graph shows the distribution of individuals with heart disease at various levels of the slope (0, 1, 2). Individuals with a positive slope (2) were found to have a much higher risk of heart disease than the other groups. This supports that cardiac function after exercise may be an important predictor.

5. CONCLUSION AND EVALUATION

In this study, different machine learning classification algorithms were used to predict individuals who may have heart disease. In line with the results obtained, the accuracy, precision, sensitivity and F1-score measures of the algorithms are analysed in detail. In addition, the performance metric of each algorithm is supported by confusion matrix visualisations (Figure 3). According to the confusion matrix analyses, K-Nearest Neighbors (KNN), Support Vector Machine (SVM) and Random Forest algorithms showed the best performance in all measurement criteria. These three algorithms were the most successful algorithms with 88.52% accuracy, 88.46% precision and 86.79% F1-score. On the other hand, Logistic Regression and Naive Bayes algorithms achieved satisfactory results in terms of accuracy and precision with 86.88% and 85.18% respectively. On the other hand, the Decision Tree algorithm showed the lowest performance with an accuracy of 75.40%. Confusion matrix visualisations (Figure 3) present the classification success of the algorithms in more detail. For example, KNN, SVM and Random Forest algorithms managed to keep the false positive and false negative classification rates at a minimum level, while the Decision Tree algorithm was found to have higher rates. Logistic Regression and Naive Bayes algorithms provide satisfactory results in correct classification, but have some error margin in false positive and negative classifications.

It is an important finding of this study that sensitivity and precision criteria should be considered together. In particular, the sensitivity criteria of KNN, SVM and Random Forest algorithms were calculated as 85.18%. The high performance of these algorithms can be attributed to the balanced representation of the classes in the data set and the generalisation capabilities of the algorithms. On the other hand, the sensitivity of the

Decision Tree algorithm was significantly lower than the other algorithms with 77.78%.

In addition, in line with the studies in the literature, it should be emphasised that the performance of an algorithm may vary depending on the data set used (Alan & Karabatak, 2020). In this context, it has been observed that factors such as the size of the data set, class distribution and data preprocessing steps directly affect the performance of algorithms in data mining processes.In conclusion, in this study, KNN, SVM and Random Forest algorithms showed the highest success in heart disease prediction. However, algorithm selection in data mining studies should take into account the characteristics of the data set, the performance measures used and the requirements specific to the application area. The findings of this study provide an important guide for the selection of the right algorithm in medical diagnosis systems and other classification problems.

REFERENCES

[1] Alan A, Karabatak M. Evaluation of Factors Affecting Performance in Data Set - Classification Relationship. Fırat University Müh. Bil. Journal. 2020.

[2] Aydın S, Özkul AE. Data mining and an application in Anadolu University open education system. Journal of Education and Training Research. 2015.

[3] Berry MJ, Linoff GS. Data Mining Techniques: For Marketing, Sales, and Customer Relationship Management. Wiley. 2004.

[4] Ergün K. Data Mining. Abdullah Baykal; [cited 2015 Dec 10]. Available from: http://abdullahbaykal.com.tr/verimaden.pdf.

[5] Fayyad U, Piatetsky-Shapiro G, Smyth AP. From Data Mining to Knowledge Discovery in Databases. American Association for Artificial Intelligence. 2008.

[6] Gürbüz F, Özbakır L, Yapıcı H. A Data Mining Application on Parts Removal Reports of an Airline Business in Turkey. Journal of Gazi University Faculty of Engineering and Architecture. 2013.

[7] Hungarian Institute of Cardiology. Heart Disease. Budapest; 2017.

[8] JavaPoint. Data Mining Techniques. [Internet]. 2011 [cited 2021 Mar 10]. Available from: https://www.javatpoint.com/data-mining-techniques.

[9] Kalıkov A. Data Mining and an E-Commerce Application. PegemA; 2006.

[10] Kaya M, Özel SA. Comparison of Open Source Data Mining Software. Academic Informatics. 2017.

[11] Özekes S. Data Mining Models and Application Areas. Istanbul Commerce University Journal. 2003.

[12] Park BH, Kargupta H. Distributed Data Mining: Algorithms, Systems, and Applications. CiteSeerx. 2002.

[13] Ramageri MB. Data Mining Techniques and Applications. Indian Journal of Computer Science and Engineering. 2010.

[14] Chollet F. Xception: Deep Learning with Depthwise Separable Convolutions. arXiv preprint arXiv:1610.02357. 2017.

[15] Sandler M, Howard A, Zhu M, Zhmoginov A, Chen LC. Mobilenetv2: Inverted residuals and linear bottlenecks. In: Proceedings of the IEEE Conference on Computer Vision and Pattern Recognition; 2018. p. 4510-20.

[16] Tan M, Le QV. EfficientNet: Rethinking Model Scaling for Convolutional Neural Networks. In: International Conference on Machine Learning; 2019. p. 6105-14.

[17] So-In C, Mongkonchai N, Aimtongkham P, Wijitsopon K, Rujirakul K. An evaluation of data mining classification models for network intrusion detection. In: Fourth International Conference on Digital Information and Communication Technology and its Applications (DICTAP); 2014.

[18] Şengür D, Tekin A. Prediction of Graduation Grades of Students with Data Mining Methods. Journal of Information Technologies. 2014.

[19] Rajak R. Deep Learning for Marble Defect Classification. Medium. 2022 Mar 20 [cited 2022 Mar 20]. Available from: https://rishirajak.medium.com/deep-learning-for-marble-defect-classification-f7928d077056.

[20] Selver MA, Akay O. Feature Extraction for Quantitative Classification of Marbles. ResearchGate. 2007.

[21] T.C. Ministry of Health. Turkish Society of Cardiology. [Internet]. 2015 [cited 2015 Oct 5]. Available from: https://tkd.org.tr/TKDData/Uploads/files/Turkiye-kalp-ve-damar-hastaliklari-onleme-ve-kontrol-programi.pdf.

[22] He K, Zhang X, Ren S, Sun J. Identity mappings in deep residual networks. In: European Conference on Computer Vision; 2016. p. 630-45.

[23] Srivastava N, Hinton G, Krizhevsky A, Sutskever I, Salakhutdinov R. Dropout: A Simple Way to Prevent Neural Networks from Overfitting. The Journal of Machine Learning Research. 2014;15(1):1929-58.

[24] Iandola FN, Han S, Moskewicz MW, Ashraf K, Dally WJ, Keutzer K. SqueezeNet: AlexNet-level Accuracy with 50x Fewer Parameters and <0.5MB Model Size. arXiv preprint arXiv:1602.07360. 2016.

[25] Howard AG, Zhu M, Chen B, Kalenichenko D, Wang W, Weyand T, et al. Mobilenets: Efficient Convolutional Neural Networks for Mobile Vision Applications. arXiv preprint arXiv:1704.04861. 2017.

[26] Szegedy C, Vanhoucke V, Ioffe S, Shlens J, Wojna Z. Rethinking the Inception Architecture for Computer Vision. In: Proceedings of the IEEE Conference on Computer Vision and Pattern Recognition; 2016. p. 2818-26.

[27] He K, Zhang X, Ren S, Sun J. Spatial Pyramid Pooling in Deep Convolutional Networks for Visual Recognition. In: European Conference on Computer Vision; 2015. p. 346-61.

[28] Talend. Data Mining Techniques: The Complete List. [Internet]. 2020 [cited 2020 Jul 10]. Available

from: https://www.talend.com/resources/data-mining-techniques/.
[29] Taylor D. Data Mining Tutorial: What is | Process | Techniques & Examples. guru99. [Internet]. 2021 [cited 2021 Jan 8]. Available from: https://www.guru99.com/data-mining-tutorial.html#11.
[30] Tekerek A. Data Mining Processes and Open Source Data Mining Tools. Academic Informatics. 2011.
[31] Visa S, Ramsay B, Ralescu A, Knaap Ev. Confusion Matrix-based Feature Selection. Omnipress - Madison, WISCONSIN. 2011.
[32] Waikato. Weka 3: Machine Learning Software in Java. [Internet]. 2017 [cited 2017 Mar 25]. Available from: https://www.cs.waikato.ac.nz/ml/weka/.

Volume 14, Issue 2, Page 188-194, 2025 https://doi.org/10.46810/tdfd.1626235 Research Article

BİNGÖL UNIVERSITY

Türk Doğa ve Fen Dergisi
Turkish Journal of Nature and Science
www.dergipark.gov.tr/tdfd

Use of L-Lactate Dehydrogenase Immobilized on Carboxylated Multiwalled Carbon Nanotubes/Polyaniline/Pencil Graphite Electrode as a Lactate Biosensor

Ali TOPRAK[1], Nazlı Ece VARAN[2], Gökmen SIĞIRCIK[2], Deniz YILDIRIM[3], Tunç TÜKEN[2], S. Seyhan TÜKEL[2], Dilek ALAGÖZ[4*]

[1] Nevsehir Hacı Bektaş Veli University, Acıgöl Vocational School of Technical Sciences, Laboratory Technology Department, Nevşehir, Türkiye
[2] Cukurova University, Faculty of Arts and Sciences, Chemistry Department, Adana, Türkiye
[3] Cukurova University, Faculty of Ceyhan Engineering, Chemical Engineering Department Adana, Türkiye
[4] Cukurova University, İmamoğlu Vocational School, Laboratory Technology Department, Adana, Türkiye
Ali TOPRAK ORCID No: 0000-0002-6520-3226
Nazlı Ece VARAN ORCID No: 0000-0003-1570-9509
Gökmen SIĞIRCIK ORCID No: 0000-0002-5457-8372
Deniz YILDIRIM ORCID No: 0000-0002-5041-8160
Tunç TÜKEN ORCID No: 0000-0002-0559-2848
S. Seyhan TÜKEL ORCID No: 0000-0003-2503-2781
Dilek ALAGÖZ ORCID No: 0000-0001-6761-6385

**Corresponding author: dalagoz@cu.edu.tr*

(Received: 24.01.2025, Accepted: 07.05.2025, Online Publication: 27.06.2025)

Keywords
Biosensor, Lactate dehydrogenase, Pencil graphite electrode, Carbon nanotubes

Abstract: In this study, L-Lactate dehydrogenase (L-LDH) was covalently immobilized on carboxylated multiwalled carbon nanotubes (cMWCNT)/polyaniline (PANI)/pencil graphite electrode (PGE). LDH/cMWCNT/PANI/PGE was used as a lactate biosensor. Electrochemical polymerization of PANI was carried out using a three-electrode cell technique via cyclic voltammetry (CV). The characterization of LDH/cMWCNT/PANI/PGE electrode was achieved using electrochemical and scanning electron microscopy (SEM) techniques. The effect of pH and lactate concentration (with and without NAD^+) on biosensor was assessed. The optimal pH was determined as 7.0. The current densities tend to increase with increasing of lactate concentration in NAD^+ containing solution during the forward potential scan. These current values were obtained as 0.026 and 0.038 mA cm^{-2} for 0.166 and 1.331 mM lactate solution with NAD^+ as a cofactor, respectively at +0.2 V. As a result, LDH/cMWCNT/PANI/PGE biosensor showed good bio-electrocatalytic activity.

Karboksillenmiş Çok Duvarlı Karbon Nanotüpler/Polianilin/Kalem Grafit Elektrot Üzerine İmmobilize Edilen L-Laktat Dehidrojenazın Laktat Biyosensörü Olarak Kullanımı

Anahtar Kelimeler
Biyosensör, Laktat dehidrojenaz, Kalem grafit elektrot, Karbon nanotüpler

Öz: Bu çalışmada, L-Laktat dehidrojenaz (L-LDH), karboksillenmiş çok duvarlı karbon nanotüpler (cMWCNT)/polianilin (PANI)/kalem grafit elektrot (PGE) üzerinde kovalent olarak immobilize edilmiştir. LDH/cMWCNT/PANI/ laktat biyosensörü olarak kullanılmıştır. PANI'nin elektrokimyasal polimerizasyonu, dönüşümlü voltametri (CV) ile üç elektrot tekniği kullanılarak gerçekleştirildi. LDH/cMWCNT/PANI/PGE elektrotunun karakterizasyonu, elektrokimyasal ve taramalı elektron mikroskobu (SEM) teknikleriyle gerçekleştirilmiştir. pH ve laktat derişiminin (NAD^+ ile ve olmadan) biyosensör üzerine etkileri araştırılmıştır. Optimum pH 7,0 olarak belirlendi. Akım yoğunlukları, ileri potansiyel taraması boyunca NAD^+ içeren çözeltideki laktat derişiminin artmasıyla birlikte artma eğilimindedir. +0,2 V' ta akım değerleri, kofaktör olarak NAD^+ ile 0,166 ve 1,331 mM laktat çözeltisi için sırasıyla 0,026 ve 0,038 mA cm^{-2} olarak belirlenmiştir. Sonuç olarak, LDH/cMWCNT/PANI/PGE biyosensörü iyi bir biyo-elektrokatalitik aktivite göstermiştir.

1. INTRODUCTION

Lactate is an important metabolite, being formed in all tissues, such as the skeletal brain, muscle, red blood cells, and kidneys under anaerobic conditions [1]. The determination of lactate level is also a crucial indicator for clinical diagnostics, fermentation, food analysis and sports medicine [2,3]. Blood lactate concentration is one of the important parameters in predicting some diseases such as multiple organ failure. Lactate balance is related to acid–base homeostasis, which its accumulation leads to lactic acidosis. Lactic acidosis causes some discomfort such as muscle cramps, body weakness and diarrhea [4,5].

To date, various non-enzymatic methods have been used for the determination of lactate, such as colorimetric method [6], spectrophotometric and titrimetric techniques [7], liquid chromatography [8,9], voltammetric [10], and proton nuclear resonance methods [11]. L-lactate dehydrogenase (L-LDH) is a usually used enzyme in the design of L-lactate biosensors for the determination of lactate because of their simple sensor design and comparatively effective enzymatic detection. This enzyme works in the presence of an oxidized/reduced form of nicotinamide adenine dinucleotide (NADH or NAD) that is electrochemically detected using an appropriate detector [12]. L-LDH has a high catalytic activity in the conversion of lactate to pyruvate and NAD^+ to its reduced form NADH (Fig. 1).

There is a need for a requirement that acts as a shuttle for its electrons and electrode installation. For this, NAD/NADH is used as a mediator because NADH can provide high sensitivity to measure the amount of lactate. LDH immobilization on the electrode surface is also necessary to increase the performances of the electrochemical detectors, mainly their sensitivity and performance. Therefore, there is an increasing momentum for the immobilization of L-LDH as well as selection of electrode materials to obtain robust lactate biosensor. Different electrodes have been used to determine the lactate, such as gold electrodes, platinum electrodes, and carbon-based electrodes [13,14]. Carbon-based electrodes are preferred because of their wide usage range, low cost, and inertness [15]. Additionally, carbon electrodes have more advanced electrochemical properties than noble metals. They cause the oxidation/reduction of both of organic and biological molecules in aqueous and non-aqueous reaction mediums. Some materials can easily crack and fall from the surface of the electrode, and this situation leads to the loss of enzymes.

Pencil graphite electrodes have attracted much attention because their preparation and surface modification are easier than other carbon-based electrodes. They are preferred for immobilizing of L-LDH or binding nanoparticles to form reliable modified biosensors when conducting polymers like polyaniline are used [16]. Among the advantages of coating the electrode surface with PANI film are the controllable oxidative polymerization properties, such as superior environmental stability, anti-interference properties, thickness, and permeability. Investigation of excellent biosensor designs using PANI together with various different nanomaterials (carbon nanotubes (CNT), graphene (GR), platinum nanoparticles (PtNPs), gold nanoparticles (AuNPs), etc.) has popularized the use of these materials to obtain wide-ranging biosensors [17-19].

Recently, the use of CNTs has appeared as a versatile tool to provide important supports for the stabilization of enzymes [20-22]. Nanoparticles strongly affect the mechanical properties of the materials such as stiffness and elasticity. Furthermore, they offer biocompatible environment for enzyme immobilization. CNTs have attracted enormous interest because of their unique structural, small size, large surface area, and mechanical and electronic properties [23-25]. Modified electrodes with CNTs have most frequently been used for electro-analytical purposes to improve many biosensors [26-28]. Multi-walled carbon nanotubes are regarded as electrical conductors with highly effective properties as electrodes for enzyme biosensors [29].

This study describes the development of an L-LDH biosensor modified with PANI and cMWCNT on PGE. The surface morphology of LDH/cMWCNT/PANI/PGE electrode was achieved via SEM techniques. The optimal pH value was found as 7.0. The influence of lactate concentration (in the absence and presence of NAD^+) was also studied on biosensor properties. The current values increased in NAD^+ containing environment with increasing of lactate concentration during the potential scan (from -0.2 to 0.6 V).

2. MATERIAL AND METHOD

2.1. Materials

L-lactate dehydrogenase (from porcine), sodium L-lactate (98%), and NAD^+ (nicotinamide adenine dinucleotide disodium hydrate), and carboxylic acid-functionalized multi-walled carbon nanotubes (MCNT-COOH) were purchased from Merck. All other chemicals were used without further purification. Pencil lead (2B) was purchased from the local market.

2.2. Activation of Carboxylated Multiwalled Carbon Nanotubes

MWCNT-COOH was activated according to our previous publication [30]. Briefly, 1.0 mL of MES buffer (50 mM pH 6.1) and 4.0 mL of 5% N-hydroxysuccinimide (NHS) solution were treated with 1.0 g of MWCNT and stirred for 10 min at 25 °C. Subsequently, 1.2 mL of 1% fresh N-(3-Dimethylaminopropyl)-N′-ethyl carbodiimide (EDC) solution was added. The mixture was stirred for 2 hours at 25 °C. Then, the supports obtained were filtered under vacuum and washed with distilled water. Finally, the activated supports were kept at 5 °C overnight.

2.3. Preparation of L-Lactate dehydrogenase/Carboxylated Multiwalled Carbon Nanotubes/Polyaniline/Pencil Graphite Electrode

The biosensor preparation process is schematically presented in Fig. 2. In this study, PANI was electrochemically synthesized on PGE in 0.1 M HCl solution containing 0.1 M aniline with electrochemical analyzer. A conventional three-electrode setup was used, employing PGE as the working electrode and a platinum sheet (2 cm^2) as the counter electrode where an Ag/AgCl (3 M KCl) was the reference. All the potentials were reported with respect to the reference electrode. CV method was utilized for the electrochemical polymerization of aniline. Applied potential range was between -1.0 and +1.0 V with 100 mV s^{-1} scan rate. After that, activated cMWCNT was adsorbed on the working electrode by the dripping and drying method. In the last step, 5 mL of L-LDH solution (1.0 mg mL^{-1}) was dripped on the electrode surface. L-LDH was immobilized and dried at 4 °C for 6 h.

2.4. Electrochemical Measurements

An electrochemical analyzer (CHI660C) was used to perform all electrochemical measurements. A lactate biosensor was fabricated by connecting of LDH/cMWCNT/PANI/PGE as the working electrode. In addition, platinum sheet (2 cm^2) and Ag/AgCl (3 M KCl) was utilized to be counter, and reference electrodes, respectively. Cyclic voltammograms of the LDH/cMWCNT/PANI/PGE electrode was recorded in buffer solution with and without NAD^+ containing lactate (0.166 – 1.331 mM) from -0.2 and +0.6 V with 50 mVs^{-1} scan rate.

2.5. Surface Morphology of the Materials

Surface morphology of the different electrodes was examined by field emission scanning electron microscopy (FE-SEM, Zeiss, Supra 55).

3. RESULTS AND DISCUSSION

In this study, pencil leads (pencil graphite electrode) were preferred for the modified LDH biosensor because of their good electrical conductivity, low cost, and easy availability. When compared to many other electrodes, the regeneration of the surface has an important effect for subsequent analysis since it may easily cause a change in the electrochemical reaction of the molecule, and in the surface properties of electrode. The regeneration of the electrode surface may change the selectivity and sensitivity of the lactate measurements. In the literature, Purushothama et al. developed a simple electrochemical sensor for investigation of chlorpromazine using pencil leads and they reported good electrocatalytic activity [31]. Batra et al. designed LDH/GrONPs/PGE based on immobilization of LDH on graphene oxide nanoparticles-PGE and characterized the surface of the electrode by SEM [32].

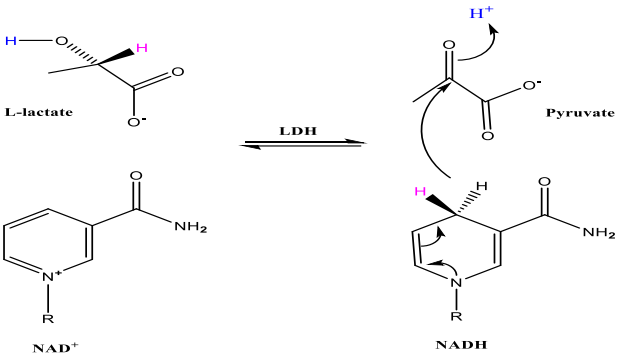

Figure 1. Schematic representation of L-LDH catalytic activity.

Fig. 2. shows the schematic demonstration of construction of enzyme working electrode based on the covalent immobilization of L-LDH on cMWCNT/PANI/PGE. One of the most significant aspects in the development of the LDH biosensor is the immobilization of LDH on the surface of the PGE. First, the PGE surface was successfully coated with PANI film using the electropolymerization method before L-LDH was immobilized, as shown in Fig. 3.

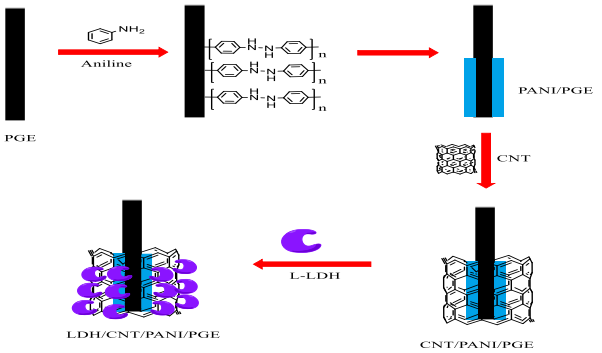

Figure 2. Schematic representation of steps and chemical reaction involved in the preparation of LDH/cMWCNT/PANI/PGE.

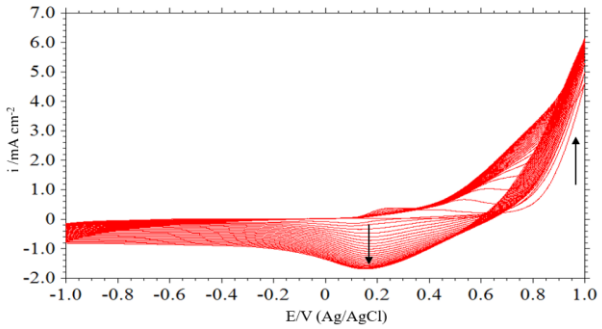

Figure 3. Electropolymerization of PANI on PGE with 100 mV s^{-1} scan rate.

The film thickness can be controlled for PANI-coated PGE using CV. PANI is used here as a good electron transfer provider because of its good reduction and oxidation properties between the reaction site and the PGE surface and biomolecules. cMWCNT is generally used as electron tunneling center to increase the electrocatalytic behavior of PANI. Thus, synergistic enhancement between PANI and cMWCNT can improve the biosensor property by facilitating the electron transfer rate. As a result, PANI offers an efficient material for

novel electrochemical L-LDH biosensors with cMWCNT.

Recently, a lot of enzyme biosensors based on nanoparticles or nanotubes have been developed to increase the performance of enzyme-based biosensors [33-35]. Zhang et.al reported that direct electrochemical oxidation of NADH at classic electrodes had large overpotential (>1 V), and performance (stability, sensitivity etc.) of electrochemical determination of NADH have been inadequate in the samples [36]. Therefore, carbon nanotubes (CNTs)-based electrodes are used to significantly decrease overpotential for electrochemical oxidation of NADH [37-39]. CNTs have been offered in development of sensors design thanks to electrical properties, chemical stability, and high surface-to-volume ratio [40-43]. In the literature, Luo et.al reported that effect of PANI/CNT for HRP biosensor and enhanced stability and eight times more sensitivity [44]. Granot et al. reported that charge transport property of CNT/PANI hybride system as 3.5 times higher than without CNT biosensor system for glucose measurements [45]. The surface morphology of different electrodes was investigated by SEM. Figs. 4a and b shows SEM images of bare PGE. SEM image of PANI/PGE shows that PGE covered with PANI layer as given in Figs. 4c and d. The binding of cMWCNT onto PANI/PGE was depicted in Figs. 4e and f. SEM image for LDH/cMWNT/PANI/PGE in Figs. 4g and h shows different morphology from cMWCNT/PANI/PGE. The obtained image indicates that LDH successfully immobilized to the surface of the cMWCNT/PANI/PGE. The step by step modification of PGE can be seen clearly from these presented SEM images.

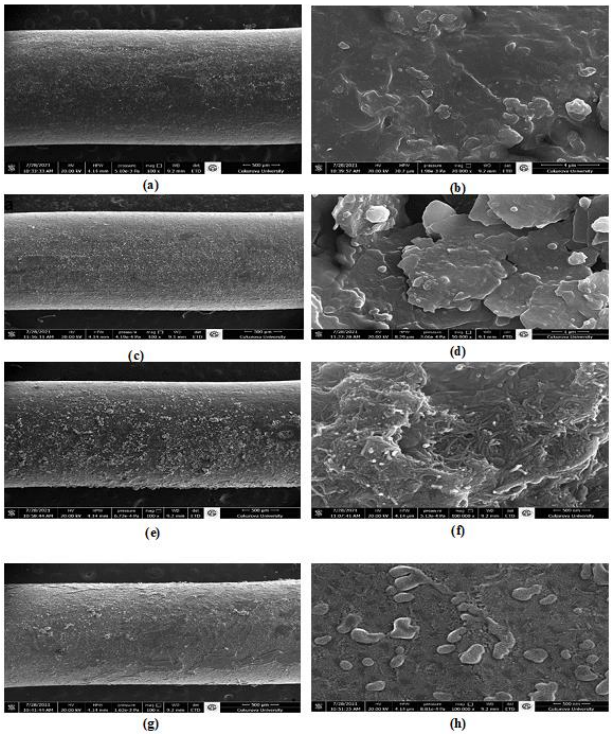

Figure 4. SEM images of materials: PGE a (100x) and b (20000x), PANI/PGE c (100x) and d (50000x), cMWCNT/PANI/PGE e (100x) and f (100000x), LDH/cMWCNT/PANI/PGE g (100x) and h (100000x).

L-LDH enzyme activity depends on the working pH. LDH activity of the biosensor at different pH values is not the same; the structural differences of the enzyme at different conditions are associated with changes in the surface regions of the LDH molecule. A plot of relative activity on the LDH/cMWNT/PANI/PGE with different pH values (5.0-9.0) in buffer solution was determined spectrometrically, as shown in Fig. 5. Different pH buffer solutions showed a strong impact on activity of biosensing layers. The relative activity increases with increasing pH from 4.0 to 7.0. The relative activity reaches a maximum value at pH 7.0. The activity decreases with an increase in pH above 7.0. This situation is raleted to NAD^+ which is unstable in alkali medium. Thus, pH 7.0 is the optimal pH for the lactate biosensor. This range of values was reported as optimal pH range for this enzyme, which is between 6.0 and 8.0 [38,46]. Istrate et al. reported that an increase in LDH activity was obtained in pH range 2.0-7.5 and maximum value was 7.5 for GA-LDH/AuNPs-ERGO-PAH/SPE [38]. Rahman et al. prepared pTTCA/MWNT/LDH/NAD^+ as a modified electrode for lactate determination and characterized the surface modification of the designed electrode by SEM. In their study, LDH and NAD^+ were covalently immobilized on the surface, and determined as 7.0 effect of pH on the current responses [39].

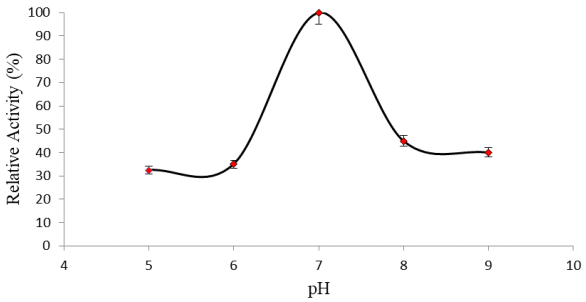

Figure 5. The effect of pH value on LDH/cMWCNT/PANI/PGE.

NAD^+/NADH coenzymes behave to be mediators to shuttle electrons between electrode and enzyme. Nevertheless, the difficulty in incorporating the coenzymes into the biosensor, as well as its regeneration (high oxidation potential) frequently poses problems. Therefore, L-LDH has attracted more attention for the production of amperometric lactate sensors [47].

The obtained CV results for the LDH/cMWCNT/PANI/PGE electrode were given in Figs. 6a and b in buffer solutions without and with NAD^+ containing lactate solution (0.166 – 1.331 mM), respectively. The applied potential range was from -0.2 to +0.6 V with 50 mV s^{-1} scan rate. As seen from Fig. 6a, current densities from -0.2 to +0.6 V potential scan decreased generally with increasing of lactate concentration. In this forward potential scan, current values were found as 0.034, 0.027, 0.030 and 0.024 mA cm^{-2} at +0.2 V for lactate solutions from 0.166 to 1.331 mM without NAD^+, respectively. On the other hand, these current densities were determined as 0.026, 0.031, 0.037 and 0.038 mA cm^{-2} at +0.2 V for from 0.166 to 1.331 mM lactate solutions with NAD^+, respectively. Thus, current values have a tendency to increase in NAD^+ containing

solution with increasing of lactate concentration at the forward potential scan. These results show that NAD^+ as a cofactor has an important effect on the increase of the current densities after 0.332 mM lactate solution.

In the literature, Tian et al., [43] was produced a biosensor with the immobilization of lactate oxidase and horseradish peroxidase on flower-like $NiCo_2O_4$ microspheres coupled with single-walled carbon nanotubes (SWCNTs). It was found that synergistic effect between SWCNTs and $NiCo_2O_4$ increase the conductivity and the active surface area of the material. Chronoamperometry method was used for the electrode at different lactate concentrations. The results showed that current response increases with increasing of the lactate concentration.

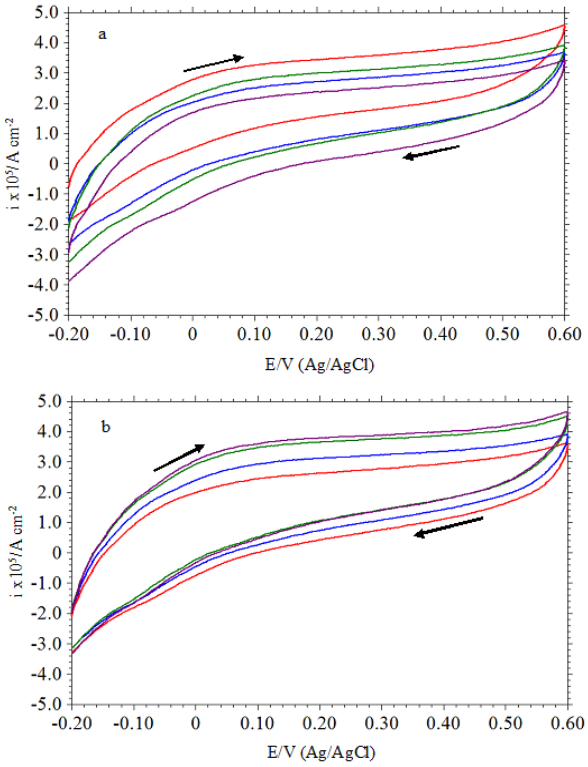

Figure 6. CV results of biosensor without (a) and with (b) NAD^+; 0.166: —, 0.332: —, 0.998: —, 1.331 mM: — containing lactate solution.

4. CONCLUSIONS

LDH/cMWCNT/PANI/PGE electrode showed a good electrocatalytic property to the oxidation of lactate when the cMWCNT was used for the design of the biosensor. The formation of cMWCNT/PANI composite improves the electrical and mechanical properties of the conductive polymer material. Furthermore, NAD^+ is not need to measure low lactate concentrations. However, NAD^+ as a mediator is required at high lactate concentrations. The current densities increased with the increasing of lactate concentration in NAD^+ containing solution during the forward potential scan. These current densities at +0.2 V were found as 0.026 and 0.038 mA cm^{-2} for 0.166 and 1.331 mM lactate solution with NAD^+, respectively. Consequently, LDH/cMWCNT/PANI/PGE biosensor exhibited good bio-electrocatalytic activity.

Acknowledgements

The authors would like to thank Cukurova University Scientific Research Project Unit for supporting the study (Project Number: FBA-2020-13283).

REFERENCES

[1] Kemp G. Lactate accumulation, proton buffering, and pH change in is chemically exercising muscle. Am J Physiol Regul Integr Comp Physiol. 2005;289(3):895-901.

[2] Bravo I, Revenga-Parra, M, Pariente, F, Lorenzo, E. Reagent-Less and Robust Biosensor for Direct Determination of Lactate in Food Samples. 2017;Sensors:17(1), 144.

[3] Kucherenko IS, Topolnikova YV, Soldatkin OO. Advances in the biosensors for lactate and pyruvate detection for medical applications: A review. Trac-Trends Anal. Chem.2019;110: 160-172.

[4] Bakker J, Gris P, Coffernils M, Kahn RJ, Vincent JL.Serial blood lactate levels can predict the development of multiple organ failure following septic shock. Am. J. Surg.1996;171: 221-226.

[5] Artiss JD, Karcher RE, Cavanagh, KT, Collins SL, Peterson VJ, Varma, S, et al. A liquid-stable reagent for lactic acid levels. Am. J. Clin. Pathol.2000;114:139-143.

[6] Kuşbaz A, Göcek İ, Baysal G, Kök FN, Trabzon L, Kizil H, K et al. Lactate detection by colorimetric measurement in real human sweat by microfluidic based biosensor on flexible substrate. J. Text. Inst. 2019;110(12):1725-1732.

[7] Basavaiah K, Nagegowda P, Somashekar BC, Ramakrishna V. Spectrophotometric and titrimetric determination of ciprofloxacin based on reaction with cerium (IV) sulphate. Sci. Asia. 2006;32:403-409.

[8] Yang L, Overdorf G, Kissinger P. Determination of Lactate with liquid chromatography/electrochemistry coupled with a lactate oxidase imer. Curr. Sep. 1997; 16:15-18.

[9] Suzuki M, Akaguma H. Chemical cross-talk in flow-type integrated enzyme sensors. Sens. Actuat. B. 2000;64:136–141.

[10] Schmitt RE, Molitor HR, Wu T. Voltammetric method for the determination of lactic acid using a carbon paste electrode modified with cobalt phthalocyanine. Int. J. Electrochem. Sci. 2012;7:10835-10841.

[11] Nishijima T, Nishina M, Fujiwara K. Measurement of lactate levels in serum and bile using proton nuclear magnetic resonance in patients with hepatobiliary diseases: Its utility in detection of malignancies. Jpn. J. Clin. Oncol. 1997;27:13-17.

[12] Rathee K, Dhull V, Dhull R, Singh S. Biosensors based on electrochemical lactate detection: A comprehensive review. Biochem. Biophys. Rep. 2016;5:35-54.

[13] Salimi A, Noorbakhsh A, Mamkhezri H. Ghavam R. Electrocatalytic Reduction of H2O2 and Oxygen on the Surface of Thionin Incorporated onto MWCNTs Modified Glassy Carbon Electrode: Application to

Glucose Detection. Electroanalysis. 2007;19:1100-1108.
[14] He XR, Yu JH, Ge SG, Zhang XM, Lin Q, Zhu H, at al. Amperometric l-lactate biosensor based on sol–gel film and multi-walled carbon nanotubes/platinum nanoparticles enhancement. Chin. J. Anal. Chem. 2010;38:57-61.
[15] McCreery RL. Advanced Carbon Electrode Materials for Molecular Electrochemistry. Chem. Rev. 2008;108:2646-2687.
[16] Simon E, Halliwell CM, Toh CS, Cass AEG, Bartlett PN. Oxidation of NADH produced by a lactate dehydrogenase immobilised on poly(aniline)–poly(anion) composite films. J. Electroanal. Chem. 2002;538-539:253-259.
[17] Syedmoradi L, Daneshpour M, Alvandipour M, Gomez FA, Hajghassem H, Omidfar K. Point of care testing: The impact of nanotechnology. Biosens Bioelectron. 2017;87:373-387.
[18] Lai J, Yi Y, Zhu P, Shen J, Wu K, Zhang L. et al. Polyaniline-based glucose biosensor: A review. J Electroanal Chem. 2016; 782:138-153.
[19] Yazdanparast S, Benvidi A, Banaei M, Nikukar H, Tezerjani MD, Azimzadeh M. Dual-aptamer based electrochemical sandwich biosensor for MCF-7 human breast cancer cells using silver nanoparticle labels and a poly(glutamic acid)/MWNT nanocomposite. Mikrochim Acta 2018;185:405.
[20] Hadian NS, Faridnouri Hassan, Zare EN. Glucose biosensing based on glucose oxidase immobilization on carboxymethyl chitosan/polyaniline/multi-walled carbon nanotubes nanocomposite. Diamond and Related Materials. 2024;148:111423.
[21] Özdemir I, Tülek A, Karaaslan B, Yildirim D. Evaluation of multi-walled carbon nanotubes bearing aldehyde groups of different lengths for the immobilization of Geobacillus kaustophilus l-asparaginase. Molecular Catalysis. 2024;555:113903.
[22] Varan N, Alagöz D, Toprak A, Korkmaz H, Yildirim D. Immobilization of pullulanase from Bacillus licheniformis on magnetic multi-walled carbon nanotubes for maltooligosaccharide production. Chemical Papers. 2024;7878:9529–9542.
[23] Musameh M, Wang J, Merkoci A, Lin Y. Low-potential stable NADH detection at carbon-nanotube-modified glassy carbon electrodes. Electrochem Commun. 2002;4(10): 743-746.
[24] Goran JM, Lyon JL, Stevenson KJ. Amperometric detection of L-lactate using nitrogen-doped carbon nanotubes modified with lactate oxidase. Anal Chem. 2011;83(21):8123-8129.
[25] Agui L, Eguilaz M, Pena-Farfal C, Yanez-Sedeno P, Pingarron JM. Lactate dehydrogenase biosensor based on an hybrid carbon nanotube-conducting polymer modified electrode. Electroanalysis. 2009; 21(3-5):386-391.
[26] Jaryal VB, Kumar S, Singh D, Gupta N. Thiourea-Modified Multiwalled Carbon Nanotubes as Electrochemical Biosensor for Ultra-Precise Detection of Dopamine. ChemNanoMat. 2024;10(6): e202300637.
[27] Silva W, Guedes EAB, Faustino LC, Goulart MOF, Gerôncio ETS. Tailored Electrochemical Biosensor with poly-diallydimethylammonium chloride-functionalised multiwalled carbon nanotubes/gold nanoparticles/manganese dioxide, and Haemoglobin for Sensitive Hydrogen Peroxide Detection. Talanta. 2024:276;126290.
[28] Yulianti ES, Rahman S, Rizkinia M, Zakiyuddin A. Low-cost electrochemical biosensor based on a multi-walled carbon nanotube-doped molecularly imprinted polymer for uric acid detection. Arabian Journal of Chemistry. 2024;17(4):105692.
[29] Salimi A, Noorbakhsh A, Mamkhezri H, Ghavami R. Electrocatalytic reduction of H_2O_2 and oxygenon the surface of thionin incorporated onto MWCNTs modified glassy carbon electrode: application to glucose detection. Electroanalysis. 2007; 19(10):1100-1108.
[30] Alagoz D, Toprak A, Yildirim D, Tükel SS, Fernandez-Lafuente R. Modified silicates and carbon nanotubes for immobilization of lipase from Rhizomucor miehei: Effect of support and immobilization technique on the catalytic performance of the immobilized biocatalysts. Enzyme Microb. Technol. 2021;144:109739.
[31] Purushothama HT, Arthoba Nayaka Y, Vinay MM, Manjunatha P, Yathisha RO, Basavarajappa KV. Pencil graphite electrode as an electrochemical sensor for the voltammetric determination of chlorpromazine. Journal of Science: Advanced Materials and Devices. 2018;3:161-166.
[32] Batra B, Narwal V, Pundir CS. An amperometric lactate biosensor based on lactate dehydrogenase immobilized onto graphene oxide nanoparticles-modified pencil graphite electrode. Eng. Life Sci. 2016;16:786-794.
[33] Tamborelli A, Mujica ML, Amaranto M, Barra JL, Rivas G, Godino A, Dalmasso P. L-Lactate Electrochemical Biosensor Based on an Integrated Supramolecular Architecture of Multiwalled Carbon Nanotubes Functionalized with Avidin and a Recombinant Biotinylated Lactate Oxidase. Biosensors (Basel). 2024;14:196.
[34] Xia Z, Zuo W, Li H, Qiu L, Mu R,Wang Q, et al. Wearable cellulose textile matrix self-powered biosensor sensing lactate in human sweat. J Appl Electrochem. 2024;54:1137–1152.
[35] Darshna, Nandi I, Srivastava P, Chandra P. Clinically Deployable Electro-Immunosensing Device Comprising Bioactive Glass-MWCNT for Alkaline Phosphatase Detection in Human Serum Samples. ACS Appl Bio Mater. 2025;20;8(1):741-753.
[36] Zhang M, Gorski W. Electrochemical sensing based on redox mediation at carbon nanotubes. Anal. Chem. 2002;77:3960-3965.
[37] Musameh M, Wang, J, Merkoci A, Lin Y. Low-potential stable NADH detection at carbon-nanotube-modified glassy carbon electrodes. Electrochem. Commun. 2002;4:743-746.
[38] Istrate OM. Rotariu L, Bala C. Amperometric L-Lactate Biosensor Based upon a Gold Nanoparticles/Reduced Graphene

Oxide/Polyallylamine Hydrochloride Modified Screen-Printed Graphite Electrode. Chemosensors. 2021; 9:74.
[39] Rahman MM, Shiddiky MJA, Rahman MA, Shim YB. Lactate biosensor based on lactate dehydrogenase/nictotinamide adenine dinucleotide (oxidized form) immobilized on a conducting polymer/multiwall carbon nanotube composite film. Analytical Biochemistry. 2009;384:159-165.
[40] Wang J, Musameh M. Carbon nanotube/Teflon composite electrochemical sensors and biosensors. Anal. Chem. 2003;75:2075-2079.
[41] Chen J, Bao J, Cai C, Lu T. Electrocatalytic oxidation of NADH at an ordered carbon nanotubes modified glassy carbon electrode, Anal. Chim. Acta. 2004;516:29-34.
[42] Banks CE, Moore RR, Davies TJ, Compton RG. Investigation of modified basal plane pyrolytic graphite electrodes: definitive evidence for the electrocatalytic properties of the ends of carbon nanotubes. Chem. Commun. 2004;16:1804-1805.
[43] Tian L, Cai L, Ding Z, Zhou Y, Zhang Y, Liu Q, et al. Sweat lactate biosensor based on lactate oxidase immobilized with flower-like $NiCo_2O_4$ and carbon nanotubes, Microchemical Journal. 2024;200:11041.
[44] Luo X, Killard AJ, Morrin A, Smyth MR. Enhancement of a conducting polymer-based biosensor using carbon nanotube-doped polyaniline. Anal Chim Acta. 2006;575:39-44.
[45] Granot E, Basnar B, Cheglakov Z, Katz E, Willner I. Enhanced bioelectrocatalysis using single-walled carbon nanotubes (SWCNTs)/polyaniline hybrid systems in thin-film and microrod structures associated with electrodes. Electroanalysis. 2006;18:26-34.
[46] Tsai YC, Chen SY, Liaw HW. Immobilization of lactate dehydrogenase within multiwalled carbon nanotube-chitosan nanocomposite for application to lactate biosensors. Sens. Actuators B Chem. 2007;125(2):474-481.
[47] Rassaei L, Olthuis W, Tsujimura S, Sudhölter EJ, Berg AVD. Lactate biosensors: current status and outlook. Anal Bioanal Chem. 2014;406(1);123-37.

Volume 14, Issue 2, Page 195-203, 2025 https://doi.org/10.46810/tdfd.1633814 Research Article

BİNGÖL UNIVERSITY

Türk Doğa ve Fen Dergisi
Turkish Journal of Nature and Science

www.dergipark.gov.tr/tdfd

Inverse Kinematic Analysis of a 5 DOF Gantry Type Welding Robot

Nülifer GÜNDOĞAN[1*], Cengiz DOĞAN[2]

[1] Adıyaman Üniversitesi, Besni Ali Erdemoğlu MYO Vocational School, Electronics and Automation Department, Adıyaman, Türkiye
[2] Harran University, Engineering Faculty, Mechanical Engineering Department, Şanlıurfa, Türkiye
Nülifer GÜNDOĞAN ORCID No: 0000-0002-9464-0855
Cengiz DOĞAN ORCID No: 0000-0002-1468-8462

**Nülifer GÜNDOĞAN: ngundogan@adiyaman.edu.tr*

(Received: 05.02.2025, Accepted: 08.05.2025, Online Publication: 27.06.2025)

Keywords
Homogeneous transformation matrix, Kinematic diagram, Inverse kinematic, Denavit-Hartenberg (D-H) convention

Abstract: In this study, a gantry type welding robot having three prismatic and two rotational joints was used. By creating the kinematic diagram of this robot in Cartesian space its inverse kinematic equations were obtained. Denavit-Hartenberg rules defining the movement of one-link relative to another, were applied in drawing the kinematic diagram. The D-H method provides great easiness in forward and inverse kinematics calculations. With this method, the D-H parameters table to be used in kinematic calculations was created and inverse kinematic equations were obtained. Using inverse kinematic equations, the known position and orientation of the robot's end effector and the parameters of the position and orientation of each link were obtained. All these kinematic calculations were performed with a user interface software (GUI) prepared in Microsoft Visual Studio C# program. In this software, Mach3 program was also used as an assistant to control the motors with the position and orientation information obtained for each motor. In this way, a smooth welding application in the desired position and orientation is aimed.

5 DOF Gantry Tip Bir Kaynak Robotunun Ters Kinematik Hesaplamaları

Anahtar Kelimeler
Homojen dönüşüm matrisi, Kinematik diyagram, Ters kinematik, Denavit-Hartenberg (D-H) yöntemi

Öz: Bu çalışmada, üç adet prizmatik ve iki adet döner ekleme sahip gantry tipi bir kaynak robotu kullanılmıştır. Bu robotun Kartezyen uzayında kinematik diyagramı oluşturularak ters kinematik denklemleri elde edilmiştir. Kinematik diyagramın çizilmesinde bir uzvun diğerine göre hareketini tanımlayan Denavit Hartenberg kuralları uygulanmıştır. D-H yöntemi, ileri ve ters kinematik hesaplamalarında oldukça kolaylık sağlamaktadır. Bu yöntem ile kinematik hesaplamalarda kullanılacak olan D-H parametreleri tablosu oluşturulmuş ve ters kinematik denklemler elde edilmiştir. Ters kinematik denklemler kullanılarak robotun uç efektörünün bilinen konum ve yönelimi ile her bir uzvun konum ve yönelimine ait parametreler elde edilmiştir. Tüm bu kinematik hesaplamalar Microsoft Visual Studio C# programında hazırlanan bir kullanıcı arayüz yazılımı (GUI) ile gerçekleştirildi. Bu yazılımda ayrıca her bir motora ait elde edilen konum ve yönelim bilgileri ile motorların kontrolünü yapabilmek için yardımcı olarak Mach3 programı kullanılmıştır. Bu sayede istenilen konum ve yönelimde düzgün bir kaynak uygulaması hedeflenmiştir.

1. INTRODUCTION

A robot is a multifunctional manipulator that can be created and programmed to perform a set of desired movements. According to ISO Standard 8373:1994, industrial robots should also have three or more joints. Robots are used in the manufacturing, transportation, etc. of many products in the industry, provide many advantages in the processes in which they are used. These can be listed as speed, positioning accuracy, repeatability in operations, durability, safety, etc. Robots should be easily programmable in order to perform the operations given in production. Therefore, kinematic and dynamic

equations of the manipulator movements must be obtained [1-4].

The subfield of mechanics known as kinematics studies a mechanism's displacement, acceleration, and speed independent of the forces and moments forcing it to move [3].

The analytical study of manipulator movements is known as "robot kinematics". Kinematic modelling is very important for the analysis of the movements of the robot. In kinematic modelling, two space systems called three-dimensional Cartesian and four-dimensional Quaternion space are used [5]. Since the transformation data used in Cartesian Space is done using matrices or vectors, this model is called “point transformation”. In Quaternion Space, linear vectors and quaternions are used to create the kinematic model, so this model is called “linear transformation method”. Although Quaternion space provides ease of use in theoretical application with the use of complex numbers and is a method that provides faster results in computer environment, it is not preferred as much as Cartesian space in practice [6].

In Cartesian space geometry, five methods are generally used for kinematic modelling of the robot. These are the Homogeneous transformation method, Exponential method, SRK (Zero Reference Position) method, Pieper-Roth method, and TPS (Fully and Parametrically Continuous) method [6].

In the Cartesian coordinate, the transformation of robot arms relative to each other system is defined in two ways as rotation and translation. These transformations can be performed using the following methods: The definition of the Euler angle, calculation of the Gibbs vector, application of the Cayley-Klein parameters, Pauli spin matrices, orthonormal matrices, axis-angle, and Hamilton quaternions. In these expressions, homogeneous transformations based on 4x4 real matrices, called orthonormal matrices, are most widely used. In 1955, Denavit and Hartenberg found that the general transformation of the axes of two joints with respect to each other depends on four parameters. These parameters, called Denavit-Hartenberg (D-H) parameters, have been standardized to generate the kinematics of the robot [7]. Robot kinematics is analyzed in two parts as forward and inverse kinematics. Forward kinematics examines the relationships between the positions, velocities and accelerations of the robot links in space and the transformation matrices showing the relationship between the links are obtained. Inverse kinematics is the inverse of forward kinematics, where the link parameters are calculated based on the position and orientation values of the end-effector. Forward kinematics solutions are simple and straightforward. Therefore, we can say that the forward kinematic equation solutions of all manipulators can be obtained. On the other hand, inverse kinematic solutions of manipulators are a more difficult problem and solutions may not always be obtained. Inverse kinematics solutions for manipulators are primarily needed for calculating the torques of actuator joints and trajectory planning. The relationship between forward and inverse kinematics is shown in Figure 1 [8].

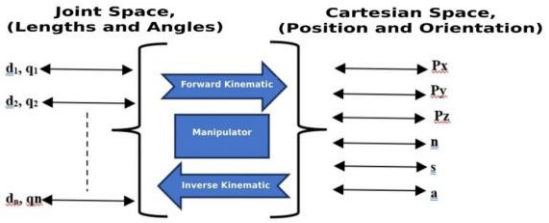

Figure 1. Schematic representation of the relationship between inverse kinematics and forward kinematics

There are many studies in the literature on forward and inverse kinematics:

Karakoyun et al. [1], in their study used the Bees Algorithm to determine the PID parameters for position control of a robot arm. In this study, mathematical modelling of the robot arm was performed with dynamic and kinematic calculations. Based on the simulations and calculations obtained, it was observed that the algorithms used to determine these parameters produced accurate results, and the robot's limb successfully reached the targeted reference point.

Altawile et al. [2], in their study realized a new methodology for the multitasking of a 2-wrist, 4-degree-of-freedom robotic arm to be used in agricultural applications. In this study, they used the Denavit-Hardenberg (D-H) method together with Lagrangian mechanics for kinetic and kinematic calculations of the robot.

Two different spaces, Cartesian and Quaternion, are used for kinematic modelling of robots. Some of the kinematic equation methods used in these models are suitable for forward kinematics, while others are useful for inverse kinematic solutions. When describing the same kinematic relation, the matrices obtained from the methods in Cartesian space contain more elements than the vector obtained in Quaternion space. Therefore, in a computer environment, the kinematic method described in Quaternion space works faster than the kinematic methods described in Cartesian space.

Kütük et al. [5], had used the Matlab programme to conduct forward and inverse kinematic analysis of a 6-axis DENSO robot with using a fully analytical solution. The Robotic Toolbox in Matlab® was included in studies of GUI (user interface) software, and simulation examples were obtained with this modelling. The outcomes were found to be identical when compared to analytical solutions.

Tonbul et al. [9], conducted inverse kinematic computations and trajectory planning of a five-axis Edubot robot with using the Matlab 5.02 program in their studies. They also observed changes in the robot's arms' joint angles, angular speeds, and angular accelerations

with time, and then applied the findings to the Edubot robot.

Kebria et al. [10], have simulated the mathematical kinematics and dynamics of a UR5 (universal robot) robot with 6 degrees of freedom by creating a position control system with a set of Matlab and Simmechanics models. Forward and inverse kinematics calculations were performed using DH parameters. The models are publicly available and can be easily used in Matlab environment.

Kaya et al. [11], created a D-H table according to the transformations of the lengths and axes of the robot arm produced from PLA material by additive manufacturing method in their study. According to this table, transformation matrices were found and forward and inverse kinematic calculations were obtained. In the study, image processing techniques and U2 -Net artificial intelligence technique were used to detect objects and calculate their center of gravity.

Duran et al. [12], used the PID method to control the trajectory of a PUMA type robot arm with three degrees of freedom in their study. The joint parameters required for trajectory control using Cartesian coordinates were calculated using the inverse kinematics method. In this study, the system results obtained with three trajectory function inputs in the form of cycloid, harmonic and polynomial were compared in terms of proximity to the targeted trajectory.

Dikmenli [23], the kinematic analysis of robot was performed using analytical calculations in the study.

Filiposka et al. [24], developed a complete kinematic model for a 6-degree-of-freedom gantry-type CNC machine in their study. Using the Denavit-Hartenberg method, forward kinematic analysis was performed. The Jacobian matrix was utilized to examine singular configurations, and the reachable workspace was visualized in the Matlab environment. The presented parametric solutions were offered as a reference for both analysis of existing systems and the design of new machines.

In this study, the kinematic analysis of this robot was performed using analytical calculations. The kinematic diagram, frames and parameters of robot links were determined according to D-H rules and representation. Inverse kinematic equations were obtained with using D-H representation. All of these kinematic calculations were performed using a graphical user GUI developed in Microsoft Visual Studio C#. The welding operations have been applied correctly in the desired position and orientation.

2. MATERIAL AND METHOD

5 Degrees of Freedom (DOF) gantry-type welding robot was used, as shown in Figure 2. The robot has 3 prismatic and 2 rotary joints called as PPPRR notation. The robot's X, Y, and Z axes are supported by 1300 mm-long and 200 mm × 90 mm I-beam steel components.

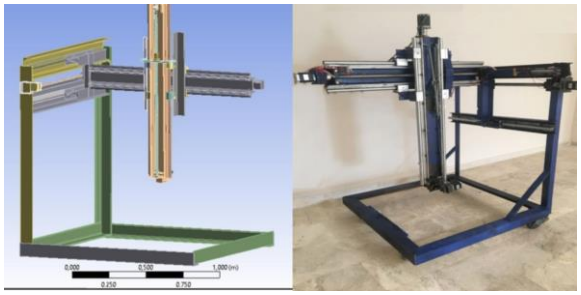

Figure 2. The welding robot's body

2.1. Robot Kinematic Modelling

The kinematic diagram of the robot was created in the Cartesian space. A schematic layout of the prismatic and rotational joints used in the robot was made to guide the robot end function from the base frame to the tool frame. One of the most common methods for constructing the kinematic diagram is D-H rules. Using the kinematic diagram, transformation matrices are obtained that give the transformation information of the joints with respect to each other (Figure 3).

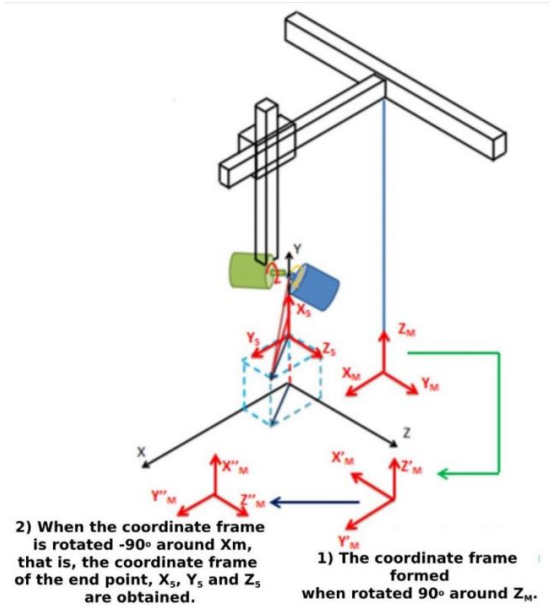

Figure 3. Rotational transformation based on axes

In 1955, Denavit and Hartenberg developed a standard for drawing kinematic diagrams of robotic applications with a set of rules.

While creating the kinematic diagram, the degree of freedom parameters was determined by considering the joint type as joint revolute and joint prismatic. The parameters for rotary joints were denoted by "θ" (angle) and for prismatic joints were denoted by "d" (distance). In the kinematic diagram the join offsets are indicated by "d", the link lengths are indicated by "a" and the numbering of the links is done according to the joint number.

According to Denavit-Hartenberg rules, the joint axes are defined as following:

- The Z-axis is always aligned with the axis of the joint. If the joint is rotational, the Z-axis serves as the axis of rotation; for a prismatic joint, the Z-axis represents the axis along which the joint moves,

- The X-axis must be orthogonal to both the previous and current Z-axes and must intersect them,

- The Y-axis is determined using the right-hand rule, based on the assigned X and Z axes.

According to Denavit-Hartenberg rules, axes X_i, Y_i, Z_i all of joints of the robot were determined and a kinematic diagram was created as shown in Figure 4.

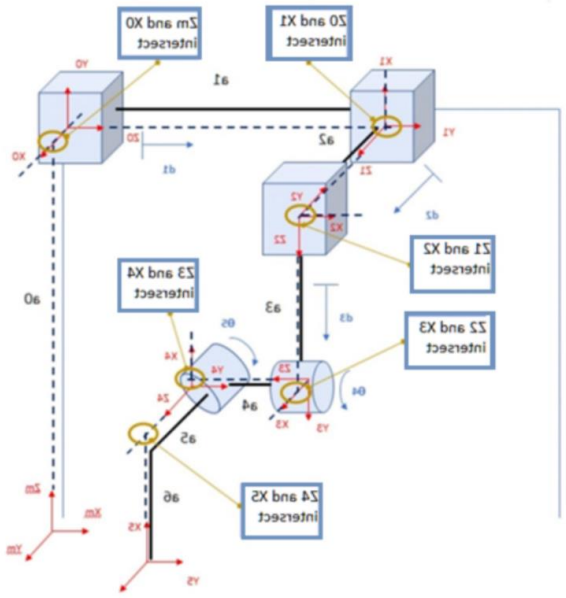

Figure 4. Determination of all axes and kinematic diagram according to D-H rules

The D-H convention is commonly used convention for obtaining frames in robotic applications. According to Denavit-Hartenberg convention, the link parameters are defined as following [16- 20]:

For i= 1...n;

α_{i-1} =(link twist) the angle between Z_{i-1} and Z_i measured about X_{i-1};

r_{i-1} =(link length) the distance between Z_{i-1} and Z_i measured along X_{i-1};

d_i =(joint offset) the distance between X_{i-1} and X_i measured along Zi;

θ_i =(joint angle) the angle between X_{i-1} and X_i measured along Z_i;

According to these D-H definitions, the parameters are obtained in Table1.

Table 1. Robot D-H parameters

I	θ_i	$\alpha i\text{-}1$	r_i	d_{i-1}
1	90	90	0	a_0
2	90	90	0	d1+a1
3	90	-90	0	d2+a2
4	-90	90	0	d3+a3
5	-90+θ4	-90	0	a4
6	θ_5	0	$-a_6$	a_5

where a_0= 1m, a_1= 0.7m, a_2=0.7m, a_3 =0.7m, a_4= 0.1m, a_5= 0.1m and a_6 = 0.3m.

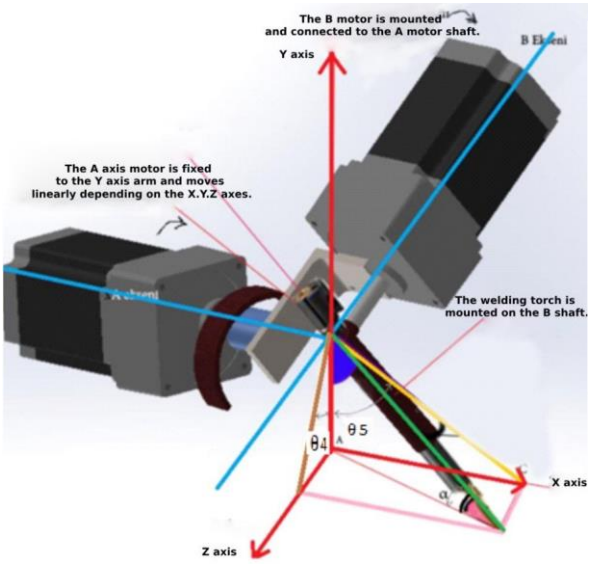

Figure 5. Perspective view of the robot's end-effector torch unit

In D-H convention, each homogeneous transformation matrices H_i is defined as multiplying four basic transformation matrices [21-26].

$$H= R_{z,\theta}\, Trans_{z,d} Trans_{x,a} R_{x,\alpha} \quad (1)$$

$$H_i^{i-1} = \begin{bmatrix} c_i & -s_i & 0 & 0 \\ s_i & c_i & 0 & 0 \\ 0 & 0 & 1 & 0 \\ 0 & 0 & 0 & 1 \end{bmatrix} \begin{bmatrix} 1 & 0 & 0 & 0 \\ 0 & 1 & 0 & 0 \\ 0 & 0 & 1 & d_{i-1} \\ 0 & 0 & 0 & 1 \end{bmatrix} \begin{bmatrix} 1 & 0 & 0 & r_i \\ 0 & 1 & 0 & 0 \\ 0 & 0 & 1 & 0 \\ 0 & 0 & 0 & 1 \end{bmatrix} \begin{bmatrix} 1 & 0 & 0 & 0 \\ 0 & c_j & -s_j & 0 \\ 0 & s_j & c_j & 0 \\ 0 & 0 & 0 & 1 \end{bmatrix} \quad (2)$$

The homogeneous transformation matrix for each joint is obtained as following (Equation 3.). Where c_i and s_i are shorthand for $cos\theta_i$ and $sin\theta_i$ and c_j and s_j are shorthand for $cos\alpha_i$ and $sin\alpha_i$ respectively.

$$H_i^{i-1} = \begin{bmatrix} cos\theta_i & -sin\theta_i cos\alpha_i & sin\theta_i sin\alpha_i & r_i cos\theta_i \\ sin\theta_i & cos\theta_i cos\alpha_i & -cos\theta_i sin\alpha_i & r_i sin\theta_i \\ 0 & sin\alpha_i & cos\alpha_i & d_{i-1} \\ 0 & 0 & 0 & 1 \end{bmatrix} \quad (3)$$

Equation 3. is homogeneous transformation matrix following by Equation 4. :

$$H_i^{i-1} = \begin{bmatrix} c_i & -s_i c_j & s_i s_j & r_i c_i \\ s_i & c_i c_j & -c_i s_j & r_i s_i \\ 0 & s_j & c_j & d_{i-1} \\ 0 & 0 & 0 & 1 \end{bmatrix} \quad (4)$$

The DH variables in Table 1 are substituted in Equation 4. to obtain the matrices in Equation 4.- Equation 8. :

$$H_0^M = \begin{bmatrix} 0 & 0 & 1 & 0 \\ 1 & 0 & 0 & 0 \\ 0 & 1 & 0 & a_0 \\ 0 & 0 & 0 & 1 \end{bmatrix} \quad (5)$$

$$H_1^0 = \begin{bmatrix} 0 & 0 & 1 & 0 \\ 1 & 0 & 0 & 0 \\ 0 & 1 & 0 & d_1 + a_1 \\ 0 & 0 & 0 & 1 \end{bmatrix} \quad (6)$$

$$H_2^1 = \begin{bmatrix} 0 & 0 & -1 & 0 \\ 1 & 0 & 0 & 0 \\ 0 & -1 & 0 & d_2 + a_2 \\ 0 & 0 & 0 & 1 \end{bmatrix} \quad (7)$$

$$H_3^2 = \begin{bmatrix} 0 & 0 & -1 & 0 \\ -1 & 0 & 0 & 0 \\ 0 & 1 & 0 & d_3 + a_3 \\ 0 & 0 & 0 & 1 \end{bmatrix} \quad (8)$$

$$H_4^3 = \begin{bmatrix} s_4 & 0 & c_4 & 0 \\ c_4 & 0 & s_4 & 0 \\ 0 & -1 & 0 & a_4 \\ 0 & 0 & 0 & 1 \end{bmatrix} \quad (9)$$

$$H_5^4 = \begin{bmatrix} c_5 & -s_5 & 0 & a_5 c_5 \\ s_5 & c_5 & 0 & a_5 s_5 \\ 0 & 0 & 1 & -a_6 \\ 0 & 0 & 0 & 1 \end{bmatrix} \quad (10)$$

The general homogeneous matrix used in forward kinematic calculations is determined. The general homogeneous matrix is obtained by multiplying the homogeneous matrices derived from the robot's base machine frame (denoted by "*M*") to the end-effector frame (5th frame) as shown in Equation 11. .

$$H_5^M = H_0^M H_1^0 H_2^1 H_3^2 H_4^3 H_5^4 = H_0^M H_2^1 H_3^2 H_4^3 H_5^4 \quad (11)$$

$$H_5^4 = \begin{bmatrix} s_5 & c_5 & 0 & a_1 - a_4 + d_1 + a_5 s_5 \\ s_4 c_5 & -s_4 s_5 & c_4 & a_2 - a_6 c_4 + d_2 + a_5 s_4 c_5 \\ -c_4 c_5 & c_4 s_5 & -s_4 & a_0 - a_3 - a_5 c_4 c_5 - d_3 + a_6 s_4 \\ 0 & 0 & 0 & 1 \end{bmatrix} \quad (12)$$

2.2. Inverse Kinematic

Inverse kinematic is the transformation process of position and orientation of robot end-effector tip from Cartesian space to joint space [2]. Also, determining joint parameters based on the end function's orientation (translation and rotational) data is known as inverse kinematics. Inverse kinematics solution is a commonly used and crucial technique for welding robot applications, handling robot applications, computing actuator joint torques, online control, trajectory planning, etc.

While forward kinematics is used to calculate the configuration of the robot's kinematic chain at the targeted location; inverse kinematics is used to obtain the parameters of the joints that generate these link movements. Inverse kinematics is used to derive the mathematical expression that computes the angular values for each link when the desired position and orientation are given.

$H_5^M = \begin{bmatrix} r_{11} & r_{12} & r_{13} & p_x \\ r_{21} & r_{22} & r_{23} & p_y \\ r_{31} & r_{32} & r_{33} & p_z \\ 0 & 0 & 0 & 1 \end{bmatrix}$ is the general homogeneous matrix

The machine link (*Mth*) inverse transformation matrix is premultiplied by each side of Equation 11. by using one of the matrix multiplication rules to find the identity matrix. It is given in Equation 13.;

$$(H_0^M)^{-1} * H_0^M = I \quad (13)$$

$$H_0^M * H_1^0 * H_2^1 * H_3^2 * H_4^3 * H_5^4 = H_5^M \quad (14)$$

Both sides of the Equation 14. is multiplied by $(H_0^M)^{-1}$ and this expression turns into the following:

$$(H_0^M)^{-1} H_0^M H_1^0 H_2^1 H_3^2 H_4^3 H_5^4 = H_5^M (H_0^M)^{-1} \quad (15)$$

$$(H_0^M)^{-1} * H_5^M = \begin{bmatrix} r_{21} & r_{22} & r_{23} & P_y \\ r_{31} & r_{32} & r_{33} & P_z - a_0 \\ r_{11} & r_{12} & r_{13} & P_x \\ 0 & 0 & 0 & 1 \end{bmatrix} \quad (16)$$

$$(H_0^M)^{-1} * H_5^M = \begin{bmatrix} s_4 c_5 & -s_4 s_5 & c_4 & a_2 - a_6 c_4 + d_2 + a_5 s_4 c_5 \\ -c_4 c_5 & c_4 s_5 & -s_4 & -a_3 - a_5 c_4 c_5 - d_3 + a_6 s_4 \\ s_5 & c_5 & 0 & a_1 - a_4 + d_1 + a_5 s_5 \\ 0 & 0 & 0 & 1 \end{bmatrix} \quad (17)$$

The following equations are obtained from the known r_{ij} and P_x, P_y ve P_z robot end-effect coordinate values in Equation 16. And Equation 17. The two matrices calculated in these equations are equal to each other. The following equations are obtained by equating each (*i*, *j*) element of the matrices in these equations (Equation 16. and Equation 17.);

$$r_{11} = sin\theta_5 \quad (18)$$

$$r_{12} = cos\theta_5 \quad (19)$$

$$r_{13} = 0 \quad (20)$$

$$r_{21} = sin\theta_4 cos\theta_5 \quad (21)$$

$$r_{22} = -sin\theta_4 sin\theta_5 \quad (22)$$

$$r_{23} = cos\theta_4 \quad (23)$$

$$r_{31} = -cos\theta_4 cos\theta_5 \quad (24)$$

$$r_{32} = cos\theta_4 sin\theta_5 \quad (25)$$

$$r_{33} = -sin\theta_4 \quad (26)$$

$$P_x = a_1 - a_4 + d_1 + a_5 \sin\theta_5 \quad (27)$$

$$P_y = a_2 - a_6 \cos\theta_4 + d_2 + a_5 \sin\theta_4 \cos\theta_5 \quad (28)$$

$$P_z - a_0 = -a_3 - a_5 * \cos\theta_4 \cos\theta_5 - d_3 + a_6 \sin\theta_4 \quad (29)$$

By dividing Equation 16. and Equation 17. , θ_5 angle is found as following;

$$tan\,\theta_5 = \frac{sin\,\theta_5}{cos\,\theta_5} = \frac{r_{11}}{r_{12}} \quad (30)$$

$$\theta_5 = Atan2\,(\frac{sin\,\theta_5}{cos\,\theta_5}) \quad (31)$$

By dividing Equation 21. and Equation 24., θ_4 angle is found as following;

$$tan\,\theta_4 = \frac{-sin\,\theta_4}{cos\,\theta_4} \quad (32)$$

$$\theta_4 = Atan2\,(\frac{sin\,\theta_4}{cos\,\theta_4}) \quad (33)$$

Using the known P_x , a_1, a_4, a_5 and θ_5 parameters the "d_1" parameter is calculated from Equation 27. as following;

$$d_1 = P_x - a_1 + a_4 - a_5\,sin\,\theta_5 \quad (34)$$

Using the known P_y, a_2, a_5, a_6 , $\theta_4$and θ_5 parameters the "d_2" parameter is calculated from Equation 28. as following;

$$d_2 = P_y - a_2 + a_6\,cos\,\theta_4 - a_5\,cos\,\theta_5\,sin\,\theta_4 \quad (35)$$

Using the known P_z , $a_0, a_3, a_4, a_5, a_6, \theta_5$ and θ_4 parameters the "d_3" parameter is calculated from Equation 29. as following;

$$d_3 = -a_3 - a_5\,cos\,\theta_4\,cos\,\theta_5 + a_6\,sin\,\theta_4 - P_z + a_0 \quad (36)$$

The inverse kinematic equations for the 5-axis robot used in this study were provided above. Consequently, the inverse kinematic equations for the robot, whose end effector coordinates P_x, P_y ve P_z are known, were derived for the angle values $\theta_4$and θ_5 of the A and B rotational axes, as well as for the feed amounts d_1, $d_2$and d_3.

All these equations were carried out in a C# editor, and a user control GUI was developed. The developed GUI enabled the command of movement of the motors connected to the control unit at the desired rotational angles of θ_4 and θ_5 , as well as at the desired feed distances of d_1, $d_2$and d_3 (Figure 6). The Mach3 program is added to GUI that is prepared in the Microsoft C# editor, as reference program. The obtained joint position parameters can be prepared in the form of a G-code text file using the GUI, as shown in Equation 37. .

$$N00\ G01\ X\ \ Y\ \ Z\ \ A\ (A)\ B\ (B)\ F\ 40 \quad (37)$$

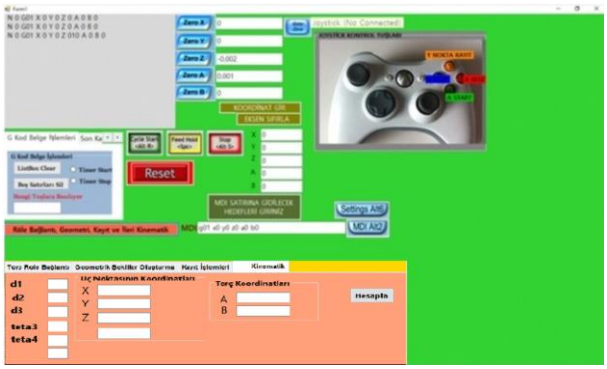

Figure 6. (GUI) User interface program

In the developed GUI, a trajectory text file was created to perform welding in the shape of the letter 'A'. For this welding application, the input data selected as the optimal welding parameters were a speed of 40 units/min, a 10 mm free wire length, and a 30° welding torch angle. These values were entered via the keyboard in the interface software, and the robot was instructed to perform the welding application (Figure 7).

Figure 7. Welding application for the letter "A"

Additionally, a G-code text file was created with the GUI for the word 'HARRAN' (Figure 8).

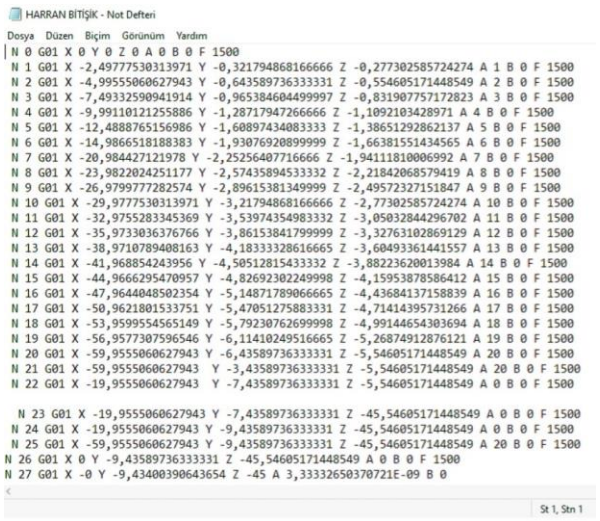

HARRAN BİTİŞİK - Not Defteri

Dosya Düzen Biçim Görünüm Yardım

```
N 0 G01 X 0 Y 0 Z 0 A 0 B 0 F 1500
N 1 G01 X -2,49777530313971 Y -0,3217948681666666 Z -0,277302585724274 A 1 B 0 F 1500
N 2 G01 X -4,99555060627943 Y -0,6435897363333331 Z -0,554605171448549 A 2 B 0 F 1500
N 3 G01 X -7,49332590941914 Y -0,9653846044999997 Z -0,831907757172823 A 3 B 0 F 1500
N 4 G01 X -9,99110121255886 Y -1,28717947266666 Z -1,1092103428971 A 4 B 0 F 1500
N 5 G01 X -12,4888765156986 Y -1,60897434083333 Z -1,38651292862137 A 5 B 0 F 1500
N 6 G01 X -14,9866518188383 Y -1,93076920899999 Z -1,66381551434565 A 6 B 0 F 1500
N 7 G01 X -20,984427121978 Y -2,25256407716666 Z -1,94111810006992 A 7 B 0 F 1500
N 8 G01 X -23,9822024251177 Y -2,57435894533332 Z -2,21842068579419 A 8 B 0 F 1500
N 9 G01 X -26,9799777282574 Y -2,89615381349999 Z -2,49572327151847 A 9 B 0 F 1500
N 10 G01 X -29,9777530313971 Y -3,21794868166666 Z -2,77302585724274 A 10 B 0 F 1500
N 11 G01 X -32,9755283345369 Y -3,53974354983332 Z -3,05032844296702 A 11 B 0 F 1500
N 12 G01 X -35,9733036376766 Y -3,86153841799999 Z -3,32763102869129 A 12 B 0 F 1500
N 13 G01 X -38,9710789408163 Y -4,18333328616665 Z -3,60493361441557 A 13 B 0 F 1500
N 14 G01 X -41,968854243956 Y -4,50512815433332 Z -3,88223620013984 A 14 B 0 F 1500
N 15 G01 X -44,9666295470957 Y -4,82692302249998 Z -4,15953878586412 A 15 B 0 F 1500
N 16 G01 X -47,9644048502354 Y -5,14871789066665 Z -4,43684137158839 A 16 B 0 F 1500
N 17 G01 X -50,9621801533751 Y -5,47051275883331 Z -4,71414395731266 A 17 B 0 F 1500
N 18 G01 X -53,9599554565149 Y -5,79230762699998 Z -4,99144654303694 A 18 B 0 F 1500
N 19 G01 X -56,9577307596546 Y -6,11410249516665 Z -5,26874912876121 A 19 B 0 F 1500
N 20 G01 X -59,9555060627943 Y -6,43589736333331 Z -5,54605171448549 A 20 B 0 F 1500
N 21 G01 X -59,9555060627943  Y -3,43589736333331 Z -5,54605171448549 A 20 B 0 F 1500
N 22 G01 X -19,9555060627943  Y -7,43589736333331 Z -5,54605171448549 A 0 B 0 F 1500

 N 23 G01 X -19,9555060627943 Y -7,43589736333331 Z -45,54605171448549 A 0 B 0 F 1500
N 24 G01 X -19,9555060627943 Y -9,43589736333331 Z -45,54605171448549 A 0 B 0 F 1500
N 25 G01 X -59,9555060627943 Y -9,43589736333331 Z -45,54605171448549 A 20 B 0 F 1500
N 26 G01 X 0 Y -9,43589736333331 Z -45,54605171448549 A 0 B 0 F 1500
N 27 G01 X -0 Y -9,43400390643654 Z -45 A 3,333326503707 21E-09 B 0
```

St 1, Stn 1

Figure 8. G code text document created with the interface program prepared in C# editor for the word "HARRAN"

3. RESULTS AND DISCUSSION

For this study, the proposed D-H convention was applied to draw the kinematic diagram. The D-H convention facilitates the calculation of forward and inverse kinematic calculations. The values of Table 1 given in Section 2.1 were obtained with this convention. Using the transformation matrices obtained with the help of the data in this table, the amounts of feed and rotation of each link required for inverse kinematic calculations were calculated both in the GUI and in Excel. In this way, the accuracy of the calculations with the use of these two programs was also proved. With these calculations, the amount of feeds (d_1, d_2 and d_3) and rotations (θ_4 and θ_5) required to be given to each motor that provides movement to the robot links at the coordinates where the end effector is desired to be found. According to the study, the solution results for 5 randomly selected test data are given in Table2.

Table 2. Solutions to the inverse kinematic problem

Solution 1:

$$H^{M}_{5} = \begin{vmatrix} 0.77 & 0.64 & 0.00 & 600.00 \\ 0.41 & -0.49 & 0.77 & 600.00 \\ 0.49 & -0.59 & -0.64 & 150.00 \\ 0.00 & 0.00 & 0.00 & 1.00 \end{vmatrix}$$

Inverse Kinematics Input Values (End Effector Position)		**Inverse Kinematics Output Values**	
X	600 mm	d_1	638 mm
Y	600 mm	d_2	82.3566 mm
Z	150 mm	d_3	743.24 mm
		θ_4	40º
		θ_5	50 º

Solution 2:

$$H^{M}_{5} = \begin{vmatrix} 0.50 & 0.87 & 0.00 & 300.00 \\ 0.75 & -0.43 & 0.50 & 300.00 \\ 0.43 & -0.25 & -0.87 & 100.00 \\ 0.00 & 0.00 & 0.00 & 1.00 \end{vmatrix}$$

Inverse Kinematics Input Values (End Effector Position)		**Inverse Kinematics Output Values**	
X	300 mm	d_1	325.00 mm
Y	300 mm	d_2	-187.50 mm
Z	100 mm	d_3	785.05 mm
		θ_4	60º
		θ_5	30 º

Solution 3:

$$H^{M}_{5} = \begin{vmatrix} 0.71 & 0.71 & 0.00 & 400.00 \\ 0.66 & -0.66 & 0.34 & 230.00 \\ 0.24 & -0.24 & -0.94 & 80.00 \\ 0.00 & 0.00 & 0.00 & 1.00 \end{vmatrix}$$

Inverse Kinematics Input Values (End Effector Position)		**Inverse Kinematics Output Values**	
X	400 mm	d_1	435.36 mm
Y	230 mm	d_2	-253.88 mm
Z	80 mm	d_3	810.92 mm
		θ_4	20º
		θ_5	45 º

Solution 4:

$$H^{M}_{5} = \begin{vmatrix} 0.71 & 0.71 & 0.00 & 400.00 \\ 0.66 & -0.66 & 0.34 & 230.00 \\ 0.24 & -0.24 & -0.94 & 80.00 \\ 0.00 & 0.00 & 0.00 & 1.00 \end{vmatrix}$$

Inverse Kinematics Input Values (End Effector Position)		**Inverse Kinematics Output Values**	
X	280 mm	d_1	435mm
Y	110 mm	d_2	-264.381mm
Z	105 mm	d_3	809.021mm
		θ_4	30º
		θ_5	45 º

Solution 5:

$$H^{M}_{5} = \begin{vmatrix} 0.77 & 0.64 & 0.00 & 400.00 \\ 0.63 & -0.75 & 0.17 & 90.00 \\ 0.11 & -0.13 & -0.98 & 80.00 \\ 0.00 & 0.00 & 0.00 & 1.00 \end{vmatrix}$$

Inverse Kinematics Input Values (End Effector Position)		**Inverse Kinematics Output Values**	
X	400 mm	d_1	435mm
Y	90 mm	d_2	-404.381mm
Z	80 mm	d_3	809.021mm
		θ_4	10º
		θ_5	40 º

In this study, kinematic calculations can be used with GUI to enable the robot to perform fully automatic welding with desired trajectory. The welding applications were successfully realized and the continuity of surface

welding was ensured. The developed Gantry welding robot provides a superior welding performance and it is seen that the GUI program is a user-friendly software.

4. DISCUSSION AND CONCLUSION

In this study, a gantry type 5-DoF welding robot with three prismatic and two rotary joints is used. According to the reviews in the literature, the majority of industrial robots have 6 DOF degrees of freedom and have complex link structures. Therefore, analytical simplification of inverse kinematic solutions is difficult. Considering these limitations, an optimized welding robot has been designed especially for practical applications with high linear motion capability. For the motion analysis of this robot, a kinematic diagram in Cartesian space is constructed and inverse kinematic equations are obtained. D-H rules were applied to draw the kinematic diagram. The D-H method provides great convenience in forward and inverse kinematics calculations. The D-H parameters table to be used in kinematic calculations was created and inverse kinematic equations were obtained. Using the inverse kinematic equations, the known position and orientation of the end effector of the robot and the parameters of the position and orientation of each link were obtained. The analytical expressions obtained from the kinematic model calculation using the D-H convention were visually tested and checked with a user interface (GUI) in Microsoft C#. In this interface, user intervention is kept to a minimum and the superior capabilities of system automation are utilized by integrating Mach3 software. The use of G-code outputs used in CNC in Mach3 software provides an important convenience to the welding operator. In this way, welding applications were successfully realized and the continuity of surface welding was ensured.

The results obtained show that solvable systems are suitable for repeatable welding applications at industrial level. An effective position and orientation is provided in welding applications. Furthermore, the system can be quickly adapted to new positions with the use of GUI. The efficiency of this physical, kinematic model and the effectiveness of the software have been regularly verified. The flexible configuration of the system also supports various applications such as inspection, packaging and control. The 5-DoF robot is an important option for small-scale industries looking for automation solutions, both in terms of cost and usability. The system can be further developed to adapt complex applications such as image processing, AI-assisted healing or welding on non-linear surfaces. The design and manufacturing of the welding robot used in this study were carried out in the workshop of Harran University.

REFERENCES

[1] Karakoyun, E., Çakan, A., & Kalyoncu, M. İki serbestlik dereceli bir robot kolun konum kontrolü için PID kontrol parametrelerinin arı algoritması (AA) kullanılarak belirlenmesi. Balıkesir Üniversitesi Fen Bilimleri Enstitüsü Dergisi. 2022;24(1): 111-124.

[2] Altawil, B., & Can, F. C. Design and Analysis of a Four DoF Robotic Arm with Two Grippers Used in Agricultural Operations. International Journal of Applied Mathematics Electronics and Computers. 2023; 11(2): 79-87.

[3] Sağlamer, E. Çoğul Robotlarda Hareket Koordinasyonunun Kuaternionlar ile Kinematik Olarak Modellenmesi ve Çözümü [Yüksek lisans Tezi]. İstanbul: İstanbul Teknik Üniversitesi Fen Bilimleri Enstitüsü; 2008.

[4] Koç, S., & Şani, İ. Yapısal ve Kuvvet Analizi ile Doğrusal Tahrikli 3 Eksenli Endüstriyel Robotun Avantajlarının Belirlenmesi. Avrupa Teknik Dergisi. 2023; (EJT), 13(2): 174-183. https://doi.org/10.36222/ejt.1230193

[5] Kütük, M. E., Daş, M. T., & Dülger, L. C. Forward and Inverse Kinematics Analysis of Denso Robot. In Proceedings of The International Symposium of Mechanism and Machine Science, 2017. Baku Azerbaijan: pp. 71-78.

[6] Küçük, S., & Bingül, Z. Robot Sistemlerinde Kinematik Yöntemlerin Karşılaştırılması. Politeknik Dergisi. 2004; 7(2): 107-117.

[7] Kucuk, S., ve Bingul, Z. Robot kinematics: Forward and Inverse Kinematics. INTECH Open Access Publisher. 2006; pp. 117-148).

[8] Türker, K. S. Endüstride Kaynak Robotları (Proseslerin İncelenmesi ve Geliştirilmesi) [Yüksek lisans Tezi]. İstanbul: Gedik Üniversitesi Fen Bilimleri Enstitüsü; 2015.

[9] Tonbul, T., & Sarıtaş, M. Beş Eksenli Bir Edubot Robot Kolunda Ters Kinematik Hesaplamalar ve Yörünge Planlamasi. Gazi Üniversitesi Mühendislik Mimarlık Fakültesi Dergisi. 2013; 18(1).

[10] Kebria, P. M., Al-Wais, S., Abdi, H., & Nahavandi. Kinematic and dynamic modelling of UR5 manipulator. In 2016 IEEE İnternational Conference on Systems, Man, and Cybernetics (SMC), 2016. Budapest, Hungary: pp. 004229-004234.

[11] Kaya, Z., Aksoy, B., & Özsoy, K. Eklemeli İmalat Yöntemiyle Üretilen Altı Eksenli Robot Kol ile Görüntü İşleme ve Yapay Zeka Tabanlı Ürünlerin Tasniflemesi. Journal of Materials and Mechatronics. 2023; A, 4(1): 193-210.

[12] Duran, M. A., & Ankaralı, A. Üç serbestlik dereceli Puma tipi bir manipülatörün PID kontrolü. Selcuk University Journal of Engineering Sciences. 2010; 9(1): 79-98. https://sujes.selcuk.edu.tr/sujes/article/view/125/604

[13] Eberly, D. Euler Angle Formulas, Geometric Tools. Redmond WA 98052. USA:2020. https://www.geometrictools.com/Documentation/EulerAngles.pdf

[14] De Luca . A. Robotics 1-Position and orientation of rigid bodies. Sapienza University. Rome: 2020. https://homes.cs.washington.edu/~todorov/courses/cseP590/05_Kinematics.pdf

[15] Bingül, Z. ve Küçük, S. Robot Tekniği. Birsen Yayınevi, İstanbul: 2005.

[16] Abut, T., Soygüder, S., ve Alli, H. Bir Yılansı Robotun Dinamik Analizi ve Kontrolü. 16. Ulusal Makina Teorisi Sempozyumu, Atatürk Üniversitesi,

2013. Erzurum. http://dx.doi.org/10.13140/RG.2.1.1316.8080

[17] Garip, Z. Seri Robot Manipülatöründe Ters Kinematik Problemi Çözmek İçin Kaotik Tabanlı Çiçek Tozlaşma Algoritmasının Uygulanması. Journal of the Institute of Science and Technology. 2022; 12(1): 80-90.

[18] Dereli, S., & Köker, R. 7-DOF Seri Robotun ters kinematik çözümünde eğitme amaçlı kullanılan çok katmanlı yapay sinir ağının tasarlanması ve sonuçların analizi. Gaziosmanpaşa Bilimsel Araştırma Dergisi. 2017; 6(1): 60-71.

[19] Hocaoğlu, G. S., Çavli, N., & Benli, E. Altı Serbestlik Dereceli Robot Manipülatörün Ters Kinematik Analizi Için Gko Ve Çdde Algoritmalarının Karşılaştırmalı Analizi. Dokuz Eylül Üniversitesi Mühendislik Fakültesi Fen ve Mühendislik Dergisi. 2024; 26(78): 449-457.

[20] Ertugrul, S., Kaya, O., Turkmen, D., Eraslan, H., Taglioglu, G. B., & Gulec, M. O. Humanoid robot arm design, simulation, kinesthetic learning, impedance control and suggestions. Journal of the Faculty of Engıneerıng And Archıtecture of Gazı Unıversıty. 2022.

[21] Duymazlar, O. 6 serbestlik dereceli seri robot kolunun ters kinematik analizi için hızlı algoritma geliştirilmesi ve uygulaması Yüksek lisans Tezi]. İzmir: İzmir Üniversitesi Fen Bilimleri Enstitüsü; 2020.

[22] Noreils, F. R. Inverse kinematics for a Humanoid Robot: a mix between closed form and geometric solutions. 2017; 1-31.

[23] Dikmenli, S. Ofset ve küresel bilekli 6 serbestlik dereceli robotların ileri ve ters kinematik çözümü. Avrasya Bilim Mühendislik ve Teknoloji Dergisi. 2022; 3 (1): 14-28.

[24] Filiposka, M., Djuric, A. M., & ElMaraghy, W. Kinematic analysis of a 6 dof gantry machine. 2015; SAE Technical Paper.

Volume 14, Issue 2, Page 204-212, 2025 https://doi.org/10.46810/tdfd.1614991 Research Article

BİNGÖL UNIVERSITY

Türk Doğa ve Fen Dergisi
Turkish Journal of Nature and Science
www.dergipark.gov.tr/tdfd

Investigation of Radiation Interaction Parameters of Anti-Human Immunodeficiency Virus Drugs in Wide Energy Region

Uğur AKBABA[1*], Kübra KAMACI[2], Erdem ŞAKAR[3]

[1] Kafkas University, Dede Korkut Education Faculty, Science Education Department, Kars, Türkiye
[2] Atatürk University, Science Institute, Physics Department, Erzurum, Türkiye
[3]Atatürk University, Science Faculty, Physics Department, Erzurum, Türkiye
Uğur AKBABA ORCID No: 0000-0002-7043-0749
Kübra KAMACI ORCID No: 0000-0003-1936-3816
Erdem ŞAKAR ORCID No: 0000-0002-1359-4464

**Uğur AKBABA: ugurakbaba82@gmail.com*

(Received: 07.01.2025, Accepted: 24.05.2025, Online Publication: 27.06.2025)

Keywords
Anti-HIV drugs, Radiation attenuation, Radiation-matter interaction, Cancer treatment, Phy-X/PSD software

Abstract: Human Immunodeficiency Virus (HIV) positive patients are exposed to radiation therapy for the treatment of various types of cancer. During these treatments, it is inevitable that radiation will interact with the antiviral drugs used. Determining the radiation attenuation parameters of drugs used in HIV treatment is, therefore, considered essential. In this context, the radiation attenuation capabilities of the HIV drugs were analyzed based on the parameters mass attenuation coefficient (MAC), atomic cross section (ACS), electronic cross section (ECS), effective atomic number (Z_{eff}), exposure build-up factor (EBF) and energy absorption build-up factor (EABF). The values were investigated in the 0.015-15 MeV range using the Phy-X/PSD software. The build-up factors were also analyzed using the geometric progression (G-P) method up to a penetration depth of 40 mean free path (MFP). Based on the results, Efavirenz and Indinavir were found to have the highest and lowest radiation attenuation capacities, respectively. It is believed that these findings can be used to make medical processes more beneficial.

Anti-İnsan İmmün Yetmezlik Virüsü İlaçlarının Geniş Enerji Bölgesindeki Radyasyon Etkileşim Parametrelerinin İncelenmesi

Anahtar Kelimeler
Anti-HIV ilaçlar, Radyasyon zayıflaması, Radyasyon-madde etkileşimi, Kanser tedavisi, Phy-X/PSD yazılımı

Öz: İnsan İmmün Yetmezlik Virüsü (HIV) taşıyan hastalar, çeşitli kanser türlerinin tedavisi için radyasyon tedavisine maruz kalmaktadır. Bu tedaviler sırasında radyasyonun kullanılan antiviral ilaçlarla etkileşime girmesi kaçınılmazdır. Bu nedenle HIV tedavisinde kullanılan ilaçların radyasyon zayıflatma parametrelerinin belirlenmesi elzem kabul edilmektedir. Bu bağlamda, HIV ilaçlarının radyasyon zayıflatma yetenekleri kütle zayıflatma katsayısı (MAC), atomik zayıflatma tesir kesit (ACS), elektronik zayıflatma tesir kesit (ECS), etkin atom numarası (Z_{eff}), maruz kalma birikim faktörü (EBF) ve enerji soğurma birikim faktörü (EABF) parametreleri temel alınarak analiz edilmiştir. Değerler Phy-X/PSD yazılımı kullanılarak 0.015-15 MeV aralığında incelenmiştir. Ayrıca birikim faktörleri 40 ortalama serbest yol (MFP) penetrasyon derinliğine kadar geometrik ilerleme (G-P) yöntemi kullanılarak analiz edilmiştir. Sonuçlara göre, Efavirenz ve Indinavir ilaçlarının sırasıyla en yüksek ve en düşük radyasyon azaltma kapasitelerine sahip oldukları bulunmuştur. Bu bulguların tıbbi süreçleri daha faydalı hale getirmek için kullanılabileceğine inanılmaktadır.

1. INTRODUCTION

Ionizing radiation is a widely used therapeutic instrument in the field of medicine. Radiation, especially in low doses, has become indispensable for modern medical practices. Low-dose ionizing radiation is used in the treatment of different cancers, infections, inflammations, autoimmune and neurodegenerative diseases, traumatic brain injuries, and damaged parts of the brain after cerebral palsy. In addition, radiation in imaging systems

used in the diagnosis phase before treatment is quite common [1-3]. Life expectancy in HIV-positive patients has increased significantly with effective antiretroviral treatments. As life expectancy increases, the incidence of cancer in HIV-positive individuals has also increased. As it is known, the incidence of various types of cancer increases with the weakening of the immune system in HIV-positive patients. In other words, individuals with HIV infection and AIDS have a high risk of cancer. The most common cancer types in these patients include cervix cancer, anal and oropharyngeal cancers, liver cancer associated with hepatitis B infection, Lung cancer, Kaposi's sarcoma, and non-Hodgkin lymphomas [4, 5]. In this context, HIV-positive patients are likely to be exposed to ionizing radiation during cancer treatments, especially due to chemotherapy applications. There is a high probability that antiretroviral drug treatments and cancer treatments will be used together in the treatment processes of these patients. Detecting the interactions of drugs used in HIV treatment with ionizing radiation may be useful in terms of treatment processes.

Many studies aim to determine the radiation attenuation parameters of drugs that treat different diseases. These studies are particularly focused on cancer drugs. Lomustine, Cisplatin, Carmustine, and Chlorambucil are drugs in the alkylating agent class most commonly used in chemotherapy. The radiation attenuation parameters of these drugs have been calculated theoretically in the range of 1 KeV-100 GeV. The parameters examined are MAC, linear attenuation coefficient (LAC), half-value layer (HVL), mean free path (MFP), and Z_{eff}. As a result of the investigations, it was determined that the changes in these values differ depending on the energy range of the radiation. The highest MAC, LAC, and Z_{eff} parameter values were reached in the low-energy region. Cisplatin, the drug with the highest physical density and molecular weight, was determined to have the best radiation attenuation feature [6]. Again, in a study examining the radiation attenuation parameters of cancer drugs, the Z_{eff} and electron density (N_{el}) of Anastrozole, Epirubicin, Gemcitabine, Ifosfamide, Methotrexate, and Paclitaxel were calculated theoretically in the energy region of 1 keV to 100 GeV. Energy absorption buildup factors (EABF) and exposure buildup factors (EBF) for these chemotherapy drugs were also examined by applying the Geometric Progression (GP) fitting method. It has been observed that Z_{eff} and N_{el} values depend on photon energies. It has been determined that buildup factors depend on photon energy, the chemical composition of the drug, and MFP. For the drug Ifosfamide, which has a high radiation attenuation capacity, the highest deposition factors were calculated at 15 MeV and the lowest buildup factors at 0.015, 0.15, and 15 MeV energy values [7].

Radiation attenuation parameters of some molecules used in chemotherapy drugs were examined. The investigations were carried out using the XCOM program in the energy range of 1 keV to 100 GeV, using the parameters of Z_{eff}, effective electron density (N_{eff}), and mass attenuation coefficient (μ/ρ). Z_{eff} and N_{eff}'s values were calculated for the drugs Cisplatin, Carboplatin, Oxaliplatin, Ifosfamide, Gemcitabine, Fluorouracil, Pemetrexed, Etoposide, Vincristine, Tamoxifen, and Paclitaxel. Sharp changes in these values have been detected in molecules with high atomic numbers. Especially Cisplatin, Carboplatin, and Oxaliplatin molecules containing the Platinum (Pt) element have the highest Z_{eff} value and showed the best radiation attenuation performance [8].

Antibiotics were also examined in terms of their radiation interaction properties. The study considered the stability, effectiveness, and structural integrity of the relevant drugs under the influence of radiation. The parameters examined are basic parameters such as attenuation coefficients LAC, MAC, N_{eff}, EBF, and EABF, as well as photon transmission factors (TF). This modeling study was conducted using MCNPX Monte Carlo simulation. Theoretical calculations were made using the Phy-X/PSD software. The data shows that the properties of antibiotics exposed to radiation change significantly. It has been observed that serious molecular changes occur, especially in antibiotics that accumulate high radiation in terms of MeV/g. Ceftriaxone/Cefotaxime is the drug with the highest accumulation. These data may be considered in terms of the effectiveness and safety of the drug in intense radiation environments [9].

Similar studies have been conducted on radioprotective materials used in radiation therapy. Natural products such as Apigenin, Bergenin, Caffeine, Chlorogenic acid, Coniferyl aldehyde, Curcumin, Delphinidin, and Quinic acid, which have low toxicity, are the most commonly used radio protectants. The radiation interaction mechanisms of these radioprotectors with gamma and neutron radiation were investigated. The research was conducted on MAC, Z_{eff}, equivalent atomic number (Z_{eq}), N_{eff}, EBF, and EABF parameters. According to the data obtained, Z_{eff} values were determined to be higher in low-energy regions. These results indicate that radio shields are suitable for shielding low-energy gamma radiation. Quinic acid showed the best radioprotective properties for thermal and fast neutrons among the radio protectants examined [10].

As seen in the literature review above, many studies have shown the radiation attenuation properties of drugs and molecules used to make drugs. However, studies on HIV drugs are scarce. In a study, the drugs Combivir, Kivexa, Trizivir, Truvada, Tenofovir, Lopinavir, and Nelfinavir used in the treatment of HIV were examined. Examination: 0.015–15 MeV via MAC, ACS, ECS, Z_{eff} and N_{eff} parameters, Phy-X/PSD software program made with. In addition, EBF and EABF values were determined with the G-P method up to a penetration depth of 40 MFP. The data shows that Combivir has a high content of heavy elements and has the best radiation attenuation ability [11]. In this study presented in this context, other drugs used by HIV-positive patients have been examined in terms of their radiation attenuation abilities. Examined drugs are Tipranavir, Efavirenz, Nevirapine, Atazanavir, Darunavir, Fosamprenavir, Indinavir and Ritonavir. The review was conducted on the parameters MAC, ACS, ECS, Z_{eff}, N_{eff}, EBF, and EABF. EBF and EABF parameters were analyzed up to 40 MFP penetration

depth. The motivation of the presented study is to provide more comprehensive data on the radiation attenuation parameters of antiviral drugs used by HIV-positive patients. Studying how drugs interact with radiation can provide valuable data for medical applications. This information can be used to adjust the dosage of drugs and radiation to be administered during the treatment process. This insight can be considered an additional motivation for this study.

2. MATERIAL AND METHOD

In this study, the radiation attenuation parameters of seven drugs (Tipranavir, Efavirenz, Atazanavir, Darunavir, Fosamprenavir, Indinavir, and Ritonavir) used by HIV-positive patients are presented comparatively. The chemical formulas, compositions, and elemental weight percentages of the investigated drugs are given in Table 1.

Table 1. Chemical formulas and compositions of the investigated drugs in weight fraction.

Drug	Chemical Formula	Molecular Weight (g/mol)	C	H	N	O	S	Cl	F	P
Tipranavir	$C_{31}H_{33}F_3N_2O_5S$	602.669	0,6178	0,0552	0,0465	0,1327	0,0532	-----	0,0946	-----
Efavirenz	$C_{14}H_9ClF_3NO_2$	315.676	0,5327	0,0287	0,0444	0,1014	-----	0,1123	0,1806	-----
Atazanavir	$C_{38}H_{52}N_6O_7$	704.869	0,6475	0,0744	0,1192	0,1589	-----	-----	-----	-----
Darunavir	$C_{27}H_{37}N_3O_7S$	547.667	0,5921	0,0681	0,0767	0,2045	0,0586	-----	-----	-----
Fosamprenavir	$C_{25}H_{36}N_3O_9PS$	585.609	0,5127	0,0620	0,0718	0,2459	0,0548	-----	-----	0,0529
Indinavir	$C_{36}H_{47}N_5O_4$	613.803	0,7045	0,0772	0,1141	0,1043		-----	-----	-----
Ritonavir	$C_{37}H_{48}N_6O_5S_2$	720.948	0,6164	0,0671	0,1166	0,1110	0,0890	-----	-----	-----

The MAC value is the most commonly used parameter to evaluate radiation-matter interaction. The well-known Beer-Lambert law states that the relationship between un-attenuated (I_0) and attenuated (I) photon intensities as following formula:

$$I=I_0\, e^{(-\mu t)} \qquad (1)$$

where, μ is the linear attenuation coefficient. In experimental studies, the MAC value can be obtained by dividing the LAC value by the density value of the material. In theoretical studies, the energy-dependent MAC value is obtained by using the elemental content of the material. Many studies in the literature state how these calculations are made [12, 13, 14, 15, 16]. EBF and EABF parameters were calculated using the G-P fitting method. The coefficients (a, b, c, d, and Xk) used in this method were taken from the ANSI database [17, 18]. Theoretical calculations were made in the 0.015-15 MeV range using the Phy-X/PSD software [19]. This software is designed to analyze the interactions of X and gamma rays with matter. It is widely used in fields such as radiation physics, radiotherapy, and radiation protection. The software can perform high-accuracy calculations thanks to detailed physical models and a comprehensive database. It facilitates operations such as shielding design and calculation of interaction cross-sections thanks to its user-friendly interface. It stands out as a reliable tool in scientific research and industrial applications.

3. RESULTS AND DISCUSSION

The MAC is the most fundamental parameter in photon-matter interactions. This parameter presents the interaction cross-section of the incident photons with the target material [13]. This value expresses all interaction processes, including scattering, according to the structure of the absorbing material and the incoming photon energy [14]. The change in MAC values of the drugs examined is presented in Figure 1.

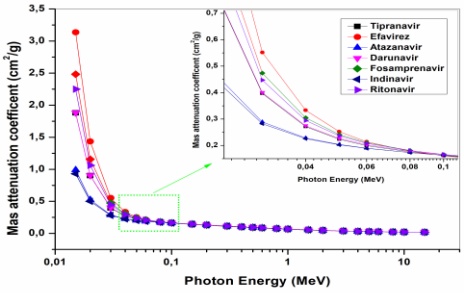

Figure 1. The investigated drugs' MAC values differ from the incoming photon energy.

By looking at the MAC values of the drugs, they can be listed from highest to lowest as Efavirez, Fosamprenavir, Ritonavir, Darunavir =Tipranavir, Atazanavir, Indinavir. It is known that materials with a high abundance of elements with high atomic numbers have a better absorption capacity for excitation photons. Among the analyzed drugs, Efavirenz, which has the composition $C_{14}H_9ClF_3NO_2$, contains 0.5327% Cl element in its structure. Cl element has a higher atomic number and density than other elements such as C, H, and O. The high Cl ratio and density of the drug are the main reasons for the higher MAC value of this drug. The dominant photon-matter interaction mechanism in the low energy range (E<0.2 MeV) is the photoelectric interaction [11]. As is known, this interaction is effective at low energies and occurs when a bound electron completely absorbs the incoming photon. In this interaction, at any given energy value, the entire energy of the incident photon is transferred to an electron of the target material [13]. The dependence of the photoelectric absorption cross-section

on the incident energy and atomic number of the target material is $1/E^{3-5}$ and Z^{4-5}, respectively [6]. Therefore, the target materials exhibit excellent shielding characteristics at such a low energy level. After the energy value of 0.05 MeV, the MAC values of the drugs show a sharp decrease, and the values begin to stabilize. The mechanisms by which photons of medium (0.2 <E< 1 MeV) and high (E>1 MeV, especially E>3 MeV) energy interact with matter are Compton scattering and pair production, respectively [20]. Medium-energy photons interact with matter via Compton scattering. In Compton scattering, electrons in the target material absorb some of the incident photon's energy, and the photon is scattered. At the same time, the interacting electron is scattered in another direction. Again, the scattered photon may undergo multiple scattering in matter. Pair production is the primary photon-matter interaction mechanism when the incident photon's energy is more significant than 1.022 MeV. Here, when the incident photon approaches the atom, it is converted into an electron-positron pair due to the interaction. This phenomenon can be described as the conversion of energy into matter.

The variation of ACS, which represents the interaction cross sections per unit atom, is shown in Figure 2. The ACS value is another radiation attenuation parameter and expresses the probability of interaction of primary photons with atoms in the material. As the likelihood of interaction increases, the ability to attenuate radiation also increases. This interaction is again directly proportional to the presence of heavy nuclei atoms in the target material. The main reason for the difference in ACS values is the different mole percentages of the elements in the target materials. Incident photon energy and atomic content of the target are the factors that directly affect the ACS value. The higher the mole percentage of the heavy element in the material, the higher the ACS value. Thus, the indicator of radiation attenuation ability is a high ACS value. Examining the ACS values in Figure 2 shows that their changes are similar to the MAC values. Again, it is seen that ACS values are high at low energy levels. However, unlike the course of MAC values, the uniformity in values with increasing photon energy started from 0.06 MeV, not 0.04 MeV. When the ACS values of the investigated drugs are examined, the ranking is from the highest value to the lowest value; they are Efavirenz, Fosamprenavir, Ritonavir, Tipranavir, Darunavir, Atazanavir, Indinavir. At 0.015 MeV energy, the highest ACS value is $5.47x10^{-23}$ (cm^2/atom) for the drug Efavirenz, while the lowest ACS value is $1.03x10^{-23}$ (cm^2/atom) for the drug Indinavir. While the ACS value for all drugs is $1.7x10^{-23}$ (cm^2/atom) at 0.06 MeV energy, where convergence begins, this value is determined as $0.033x10^{-23}$ (cm^2/atom) at 15 MeV energy.

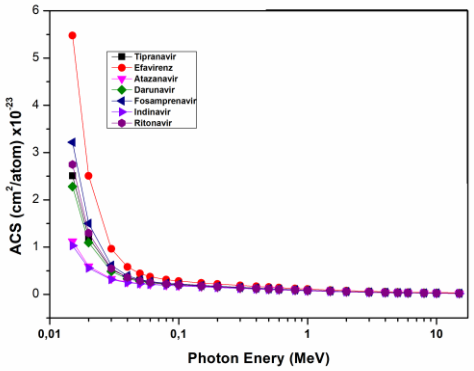

Figure 2. The changes in ACS values of drugs according to incoming photon energy.

Another parameter of drugs that is examined is the ECS parameter. This parameter is critical. It allows the calculation of the adequate atomic numbers of the target materials when evaluated with ACS. The variations in the investigated drugs' ECS values versus the incoming photon energy. The ECS values change according to the incident photon energy, as depicted in Figure 3. The ordering of ECS values is similar to the ordering of MAC and ACS values, as expected. The order is Efavirez, Fosomprenavir, Ritonavir=Tipranavir, Darunavir, Atazanavir and Indinavir. These values show that the drugs examined may have the ability to attenuate incoming radiation at low energies. While there is a difference in the range of 0.015-0.06 MeV, as the energy of the incoming radiation increases, the ECS values of all drugs decrease and become equal at 0.06 MeV. The differentiation at low energies and the decrease in differentiation with increasing energy can be seen more clearly in the inset in Figure 3. The highest ECS value at 0.015 MeV is $5x10^{-24}$ (cm^2/electron) for the drug Efavirenz, while the lowest ECS value is $1.86x10^{-24}$ (cm^2/electron) for the drug Indinavir. At 0.06 MeV energy, where uniformity begins, the ECS value is $0.6x10^{-24}$ (cm^2/electron) for all drugs. The decrease in the ECS value with increasing photon energy is due to the increased possibility of high penetration of high-energy photons in drugs. The ECS value obtained for all drugs at 15 MeV energy is $0.05x10^{-24}$ (cm^2/electron). Contrary to ACS values, it is observed that the uniformity in ECS values begins at lower energies. This is because, as stated before, ACS values depend on the elements' mole percentages, atomic weights, incoming photon energy, and MAC value. In contrast, ECS values are affected by atomic numbers as well as these factors [21].

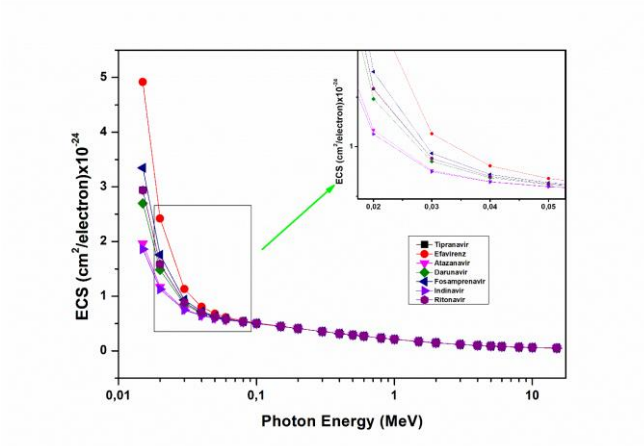

Figure 3. The variations in the investigated drugs' ECS values versus the incoming photon energy.

Z_{eff} value expresses the virtual atomic number of the target material and varies according to the incoming photon energy [22]. This value, shaped by the material's response to incoming photon energy, is an essential indicator of radiation attenuation ability. Z_{eff}, which reflects the complex atomic characteristics of a material containing more than one type of atom, can be used to evaluate the radiation interactions of alloys, compounds, composites, etc. The changes in the Z_{eff} values of the examined drugs in the 15 keV-15 MeV energy range are shown in Figure 4.

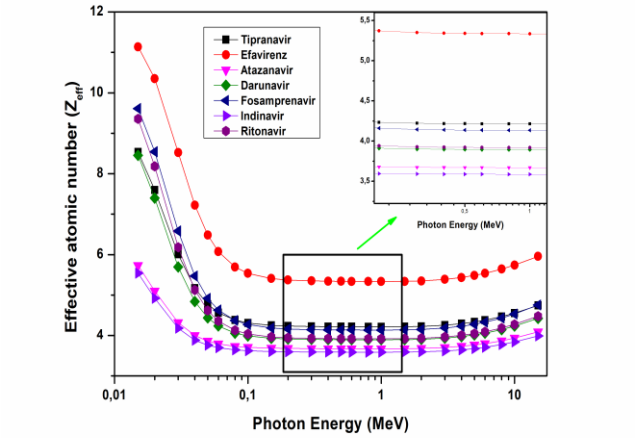

Figure 4. The variations in the investigated drugs' Z_{eff} values versus the incoming photon energy.

As seen in Figure 4, the Z_{eff} values of the drugs are listed from high to low as Efavirenz, Fosamprenavir, Ritonavir, Tipranavir, Darunavir, Atazanavir, and Indinavir. It is observed that Z_{eff} values decrease with increasing photon energy in low-energy regions (0.015-0.15 MeV). In the energy range of 0.2-1.5 MeV, it is observed that the Z_{eff} values of all drugs follow a stable course despite increasing energy. In the range of 1.5-15 MeV, it is observed that there is a slight increase in Z_{eff} values with increasing photon energy. This can be interpreted as drugs' slightly increased radiation attenuation ability in the high-energy region. In the high-energy areas, the incoming photon can turn into an electron-positron pair (pair production). In the range of 1.5-15 MeV, this may become dominant. This can cause attenuation of the incoming photon. The presence of the Cl atom, which has a relatively heavy nucleus, in the content of the Efavirenz drug, which has a high Z_{eff} value, draws attention. The Z_{eff} value of Efavirenz is 11.14 at 0.015 MeV and 5.96 at 15 MeV. The Z_{eff} values of the drug Indinavir, which has the second highest Z_{eff} value, at 0.015 and 15 MeV energies, are 9.61 and 4.74, respectively. The fact that Z_{eff} values of drugs follow a different course compared to MAC, ACS, and ECS values can be considered a reflection of the fact that this value depends more firmly on the energy of the incoming photons and the content and density of the target material. The decrease, stabilization, and slight increase in the Z_{eff} value with increasing energy can be attributed to the change in the dominance of partial photon interaction mechanisms relative to each other according to the incident photon energy. Z_{eff} values are high in the low-energy region where photoelectric interaction dominates. The high Z_{eff} values in low-energy areas can be attributed to the fact that the cross-section of the photoelectric effect is directly proportional to Z^{4-5}. In the medium energy region where Compton scattering is effective, Z_{eff} values of drugs are relatively low and uniform. The reason for observing relatively low and constant Z_{eff} values in the Compton region can be attributed to the fact that the Compton scattering process is proportional to Z. In the high-energy areas where the possibility of pair production is high, the Z_{eff} values of drugs increase slightly since the pair formation mechanism depends on the Z^2 value [20].

In a healthy radiation attenuation analysis in non-vacuum environments, scattering in the air must be considered. These effects can be understood by examining EBF and EABF values. These two values can be thought of as values that indicate the amount of secondary scattering produced by the radiation in the material and the medium. The higher these two values are, the greater the scattering in the material and environment. They also indicate the exposure of the target to the scattered radiation and the mechanisms used to transfer energy within the material. A high value of these means too much secondary radiation in the environment. This is undesirable for radiation protection and attenuation [23]. EBF can be defined as the energy accumulation that occurs during radiation propagation within the material, which includes scattering. This value varies depending on the depth of the material and the energy and type of the incoming photon. All factors contributing to the scattering of the incident photon are included in the EBF value [24].

The EABF value is a value that expresses the amount of radiation absorption by the environment and material through which it passes. The amount of radiation absorption may increase depending on the path it follows in the environment or material. Determining these values is essential in examining the material's ability to reduce radiation. In other words, EBF and EABF values are indicators of the ability of the material or medium to absorb and accumulate incoming radiation [25]. The geometric progression (G-P) method was used to calculate these values. This method incorporates the Monte Carlo simulation method with iterative, invariant accumulation properties. Previous studies have stated that

this method is suitable for calculating these two factors [26].

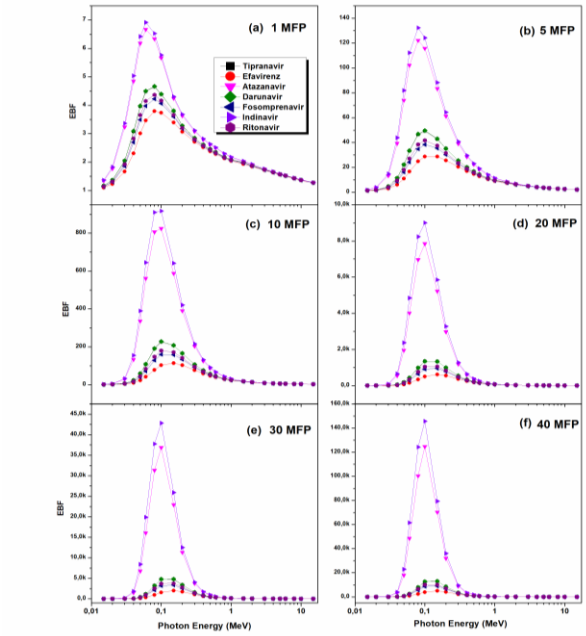

Figure 5. The variations in EBF with photon energy at 1, 5, 10, 20, 30, and 40 MFP for the investigated drugs.

Looking at the general trend in Figure 5, the order of EBF values of the drugs from highest to lowest is Indinavir, Atazanavir, Darunavir = Tipranavir, Ritonavir, Fosamprenavir, and Efavirenz. As expected, this order is the opposite of the MAC values. The uniformity of the EBF values in the low energy region at all depths is related to the high level of photoelectric effect in this region. The activation of Compton scattering explains the high EBF values in the intermediate energy regions. In the case of Compton scattering, the EBF values increase due to the amount of second scattering. In the high energy region, as the cross section for pair production is high, the scattering is reduced, and the EBF values decrease [27].

Efavirenz, which has the highest MAC value, shows the lowest EBF value here. It is an expected result that this drug, which has the highest radiation attenuation according to MAC values, will show the lowest EBF value at all depths due to its chemical content. The graphs are examined in detail; it is seen that the EBF values of the drugs increase in the range of 0.015 MeV-0.1 MeV as the photon energy increases at all depths. At a depth of 1 MFP, the value of Indinavir and Atazanavir drugs reach the highest value with 0.06 MeV, while other drugs reach their peak values with 0.08 MeV. At depths of 5 and 10 MFP, the EBF values of all drugs exhibit a peak at 0.08 MeV energy. At depths of 20, 30, and 40 MFP, the EBF values of all drugs are highest at 0.1 MeV energy. After this energy range, EBF values decrease as energy increases. With increasing penetration depth, the EBF behavior of the drugs becomes similar. This can be expressed in terms of the differences in the content of the drugs becoming insignificant as the depth of penetration increases. Since photoelectric absorption in the low-energy region and pair formation in the high-energy regions are dominant, the photon is completely absorbed in these interaction mechanisms. Consequently, the probability of secondary scattering is decreased, and the values of the scattering factor are low. Compton scattering is dominant in the interaction of the target sample with medium energy photons. Since photon energy cannot be removed entirely in this scattering, secondary multiple scattering is intense. Therefore, high scattering factors are expected [10, 20].

The changes in EBF values according to MFP and energy values were examined, and the following figure has been determined.

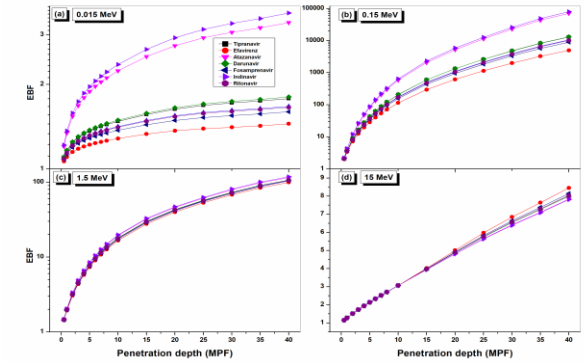

Figure 6. The EBF values for the investigated drugs up to 40 MFP at 0.015, 0.15, 1.5, and 15 MeV.

By examining Figure 6, it is seen that as the depth increases at 0.015 MeV, the EBF values of all drugs increase. Generally, the high to low order is Indinavir, Atazanavir, Darunavir, Tipranavir, Ritonavir, Fosamprenavir, and Efavirenz. The EBF values of all drugs increased with increasing depth at this energy level. After 15 MFP, the increasing values decreased compared to deeper depths. At 40 MFP, Indinavir and Efavirenz have EBF values of 3.58 and 1.44, respectively. The course of EBF values of drugs at 0.15 MeV energy value is similar to the course at 0.015 MeV energy value. However, the difference between them is gradually decreasing. Indinavir 79366 and Efavirenz 4963 show EBF values at 40 MFP at 0.15 MeV energy. Efavirenz has the highest MAC value and the lowest EBF at all depths, which is an expected result. However, the difference between the EBF values of Efavirenz and Indinavir, which showed the highest and lowest attenuation ability at 0.015 MeV, is remarkable. At 0.015 MeV, the percentage difference between the two values is 1.5 %, while at 0.15 MeV, the difference increases to 15 %. At energies below 0.5 MeV, the photoelectric interaction is more dominant. From 0.5 MeV to 1.022 MeV, Compton scattering comes into play, and the scattering rate increases with increasing energy in the photon energy ranges given.

The EBF values of Indinavir and Efavirenz at 0.015 and 0.15 MeV and 40 MFP depth show a difference of 22% and 3.44%, respectively. The difference between the EBF values for Efavirenz, which has a high ability to attenuate radiation at two energies, is more minor. This may mean that the radiation attenuation capacity of the target material, which contains heavy nuclei in its content, follows a more stable course in these two energy ranges. However, in the case of the drug Indinavir, which has the

lowest attenuation, it is seen that the attenuation capacity of the drug decreases more rapidly with increasing energy. At an energy level of 1.5 MeV, although there is an increase in the EBF values of the drugs with depth, the values are close to each other. The drug content is less effective at this energy level than at lower energies. The EBF value of Indinavir is 106, while Efavirenz's is 104 at 1.5 MeV energy and 40 MFP. The difference between the two values in percentage terms is 0.019, which is a minimal difference.

At 15 MeV, the drugs behave differently compared to other energies. The EBF values are the same for all drugs up to 15 MFP, and they differ slightly after this energy level. The order of EBF values in the relevant region, from highest to lowest, is Efavirenz, Fosamprenavir, Ritonavir ≈ Tipranavir ≈ Darunavir, and Indinavir ≈ Atazanavir. Notably, the drug Efavirenz, which has a high ability to attenuate radiation, exhibits the highest EBF value. Efavirenz is expected to have the lowest EBF value when evaluated based on MAC values. Indinavir, on the other hand, shows the lowest EBF values. This can be interpreted as a reduced ability of Efavirenz to attenuate radiation at high energies. Efavirenz has an EBF of 8.45 and Indinavir 7.81 at 40 MFP at 15 MeV. The difference is slight, 0.082%. Based on these results, it can be said that since the radiation-matter interaction mechanism is in the form of pair production rather than scattering, there may be unexpected changes in the radiation attenuation capabilities of the drugs at high energy levels. When the MAC values are analyzed, the decrease and sameness of MAC values with an increase in energy values are compatible with this unexpected situation. Suppose this unexpected situation is analyzed in terms of Z_{eff}. In that case, the slight increase in the Z_{eff} value after 1.5 MeV for all the drugs is related to the rise in the non-scattering interaction mechanisms.

The compositional dependence and the rate at which the EBF increases vary with the incident photon energy. At the energy of 0.015 MeV, the rate of increase of the accumulation factor is lowest, and the effect of the compositional dependence is small. As mentioned, the EBF values of the drugs are maximal at 0.15 MeV. Due to the Compton scattering regime, the importance of the drugs' compositional content is further reduced at this energy. At energies of 1.5 and 15 MeV, the rate of increase of the buildup factor decreases, and the chemical content becomes even less important. This is due to the weak dependence of the Compton scattering cross section on the Z_{eff} value at high energies. In the case of pair production, the cross-section is directly proportional to the square of Z_{eff} [27].

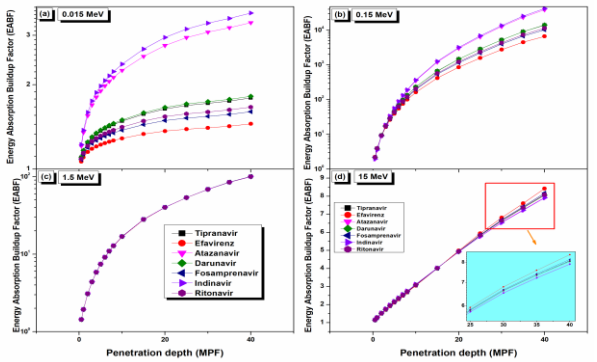

Figure 7. The EABF values for the investigated drugs up to 40 MFP at 0.015, 0.15, 1.5, and 15 MeV.

The results obtained for EABF values are given in Figure 7. These results show that the drugs with an energy value of 0.015 MeV are listed from high to low as Indinavir, Atazanavir, Darunavir, Tipranavir, Ritonavir, Fosamprenavir, and Efavirenz. This ranking is parallel to the EBF values. Although the differences between the behaviors exhibited by drugs for the 0.15 MeV energy value decrease, they are similar to the behaviors they exhibit at 0.015 MeV. However, a complete convergence was observed at 1.5 MeV. For the EABF values, the compositional dependence completely disappears at all depths at this energy value.

As energy increases, the absorption behavior of drugs changes significantly. This change becomes quite evident at 15 MeV, and with increasing depth, the EABF values of the drugs show themselves in a different order, unlike the values in the low-energy regions. At 15 MeV energy value, a slight difference in the values began after 20 MFP depth. The differentiation became more observable after 25 MFP, and the order of the values was from high to low: Efavirenz, Fosamprenavir, Ritonavir ≈ Darunavir ≈ Tipranavir, Atazanavir ≈ Indinavir. Notably, the Efavirenz drug, which has a high MAC value with increasing penetration depth at this energy value, also shows a high EBAF value. In terms of EABF values, other drugs exhibited the opposite behavior in the relevant region to their behavior in the low-energy areas. At 15 MeV, this behavior of the EBF values has the same reasons as that of the EBF values at this energy. At photon energies higher than 0.15 MeV, EABF values decrease due to decreased scattering interactions. At 0.015 MeV, Indinavir has an EABF value of 3.6, while Efavirenz has an EABF value of 1.45.

4. CONCLUSION

This study is an investigation of the radiation attenuation capabilities of several HIV drugs. In the specific case of HIV, this study aims to elucidate the drug-radiation interaction processes. Analyses were performed on the parameters MAC, ACS, ECS, ECS, Z_{eff}, EBF, and EABF. It was found that Efavirenz, the drug with the highest compositional content, had the highest radiation attenuation capacity. Indinavir had the lowest radiation attenuation capacity. It is seen that the radiation attenuation capabilities of the drugs are effective in low-energy regions. If MAC values are analyzed at 0.015 MeV

for the lowest and highest performing drugs, Indinavir and Efavirenz, 0.92 and 3.13 (cm^2/g) values are found, respectively. Z_{eff} values for the same drugs are 5.53 and 11.14, respectively, supporting the results obtained with MAC values. When reviewing the literature on the radiation attenuation capabilities of various HIV drugs, it becomes evident that drugs containing heavy elements with high atomic numbers exhibit greater radiation attenuation capabilities. In a study involving different HIV drugs, it was found that Combivir, with the chemical formula $C_{10}H_{16}N_5O_{13}P_3$, had the highest MAC value. Compared to other elements, the higher atomic number (15) of phosphorus (P) in Combivir contributes to this ability. Furthermore, Truvada, which was administered before HIV and contains sulfur (S) with an atomic number of 16, demonstrated the second highest attenuation capacity [11]. In a study of cancer drugs, Ciplatin, with the chemical formula $Pt(NH_3)_2Cl_2$, showed the highest radiation attenuation ability among the drugs examined [6]. The presence of platinum (Pt), with an atomic number of 78, in Ciplatin is noteworthy. A consistent finding from the reviewed studies indicates that the radiation attenuation ability of these drugs increases, particularly at low energy levels, while this ability decreases at higher energy levels. These findings align with the results of the present study. By identifying the mechanisms of drug interaction with radiation, the effectiveness of drug use can be enhanced. It is hoped that the data obtained in this study will assist in radiotherapy applications and dosimetry calculations for patients who must use HIV drugs.

Acknowledgement

1. Conflict of Interest: The authors declare that there is no conflict of interest or competing interest relevant to the content of this manuscript.

2. Data Availability Statement: All data in the article can be used and shared on all platforms deemed appropriate by the Turkish Journal of Nature and Science.

3. Financial Support: No financial support has been received from any organization or person to prepare this manuscript.

REFERENCES

[1] Au, N. P. B., Wu, T., Kumar, G., Jin, Y., Li, Y. Y. T., Chan, S. L., ... & Ma, C. H. E. (2024). Low-dose ionizing radiation promotes motor recovery and brain rewiring by resolving inflammatory responses after brain injury and stroke. *Brain, Behavior, and Immunity*, *115*, 43-63.

[2] Evans, E., & Stafford, J. (2018). Principles of cancer treatment by radiotherapy. *Surgery (Oxford)*, *36*(3), 111-116.

[3] Cuttler, J. M. (2020). Application of low doses of ionizing radiation in medical therapies. *Dose-response*, *18*(1), 1559325819895739.

[4] Chirenje, Z. M. (2005). HIV and cancer of the cervix. *Best practice & research Clinical obstetrics & gynaecology*, *19*(2), 269-276.

[5] Shiels, M. S., Pfeiffer, R. M., Gail, M. H., Hall, H. I., Li, J., Chaturvedi, A. K., ... & Engels, E. A. (2011). Cancer burden in the HIV-infected population in the United States. *Journal of the National Cancer Institute*, *103*(9), 753-762.

[6] Akman, F., & Kaçal, M. R. (2018). Investigation of radiation attenuation parameters of some drugs used in Chemotherapy in the Wide Energy Region. *Journal of Radiology and Oncology*, *2*, 047-052.

[7] Çağlar, İ., & Cengiz, G. B. (2021). Evaluation of radiation attenuation properties of some cancer drugs. *Adıyaman University Journal of Science*, *11*(2), 503-522.

[8] Tuğrul, T. (2020). Investigation of mass attenuation coefficients, effective atomic numbers, and effective electron density for some molecules: study on chemotherapy drugs. *Journal of Radiation Research and Applied Sciences*, *13*(1), 758-764.

[9] Almansoori, A., Almisned, G., Baykal, D. S., Kilic, C. S., & Tekin, H. O. (2024). Energy deposition responses, transmission factors, and radiation interaction properties of some antibiotics: A critical assessment for substantial molecular alterations as a function of radiation exposure. *Radiation Physics and Chemistry*, *216*, 111473.

[10] Hiremath, G. B., Ayachit, N. H., & Badiger, N. M. (2023). Investigation of shielding properties of gamma and neutrons in some natural radioprotective drugs. *Radiation Effects and Defects in Solids*, 1-14.

[11] Akbaba, U., Şakar, E., Sayyed, M. I., Alim, B., & Özpolat, Ö. F. (2022). Evaluation of photon interaction parameters of Anti-HIV drugs. *Radiation Physics and Chemistry*, *201*, 110441.

[12] Alım, B., Şakar, E., Baltakesmez, A., Han, İ., Sayyed, M. I., & Demir, L. (2020). Experimental investigation of radiation shielding performances of some important AISI-coded stainless steels: Part I. *Radiation Physics and Chemistry*, *166*, 108455.

[13] Ardiansyah, A., Heryanto, H., Armynah, B., Salah, H., Sulieman, A., Bradley, D. A., & Tahir, D. (2023). Physical, mechanical, optical, and gamma radiation shielding properties of the BaO-based glass system prepared by the melt-quench technique: A review. *Radiation Physics and Chemistry*, 111059.

[14] Erkoyuncu, İ., Demirkol, İ., Akman, F., Kaçal, M. R., Polat, H., & Dilsiz, K. (2025). A study on the mechanical and radiation shielding characteristics of concrete samples reinforced with brass alloy and boron carbide. *Applied Radiation and Isotopes*, *217*, 111641.

[15] Oğul, H., Akman, F., Özdoğan, H., Kaçal, M. R., Turşucu, A., Polat, H., & Erkoyuncu, İ. (2025). Evaluation of radiation shielding, secondary radiation, and radiation damage in boron carbide and chromium diboride reinforced polymer composites. *Materials Chemistry and Physics*, *339*, 130775.

[16] Akman, F., Turhan, M. F., Oğul, H., Turşucu, A., Erdoğan, T., Kaçal, M. R., & Polat, H. (2025). Production and evaluation of the polyester composites containing pyrite and niobium diboride

for radiation protection. *Radiation Physics and Chemistry*, *226*, 112326.

[17] Harima, Y. (1983). An approximation of gamma-ray buildup factors by modified geometrical progression. *Nuclear Science and Engineering*, *83*(2), 299-309.

[18] Trubey, D. K., Eisenhauer, C. M., Foderaro, A., Gopinath, D. V., Harima, Y., Hubbell, J. H., & Shure, K. (1991). Gamma-ray attenuation coefficients and buildup factors for engineering materials.

[19] Şakar, E., Özpolat, Ö. F., Alım, B., Sayyed, M. I., & Kurudirek, M. (2020). Phy-X/PSD: development of a user friendly online software for calculation of parameters relevant to radiation shielding and dosimetry. *Radiation Physics and Chemistry*, *166*, 108496.

[20] Hiremath, G. B., Muddapur, G. V., Srinivasa, H. T., Ayachit, N. H., & Badiger, N. M. (2024). Investigation of gamma and neutron interaction parameters of synthesized diketone derivatives as potential anti-cancer. Journal of Radioanalytical and Nuclear Chemistry, 1-10.

[21] Polatoğlu, A., & Şakar, E. (2024). A comprehensive research on γ-ray and particle radiation interaction parameters of Cerium doped heavy oxide inorganic scintillators. Progress in Nuclear Energy, 174, 105297.

[22] Ardiansyah, A., Heryanto, H., Armynah, B., Salah, H., Sulieman, A., Bradley, D. A., & Tahir, D. (2023). Physical, mechanical, optical, and gamma radiation shielding properties of the BaO-based glass system prepared by the melt-quench technique: a review. Radiation Physics and Chemistry, 210, 111059.

[23] Alalawi, A., Al Huwayz, M., Alrowaili, Z. A., & Al-Buriahi, M. S. (2023). Radiation attenuation of SiO2–MgO glass system for shielding applications. Journal of Radiation Research and Applied Sciences, 16(4), 100746.

[24] Karpuz, N. (2023). Radiation shielding properties of glass composition. Journal of Radiation Research and Applied Sciences, 16(4), 100689.

[25] Sayyed, M. I., Mhareb, M. H. A., Alajerami, Y. S. M., Mahmoud, K. A., Imheidat, M. A., Alshahri, F., ... & Al-Abdullah, T. (2021). Optical and radiation shielding features for a new series of borate glass samples. Optik, 239, 166790.

[26] Alım, B., Sakar, E., Han, ˙I., Sayyed, M., 2020b. Evaluation the gamma, charged particle and fast neutron shielding performances of some important AISI-coded stainless steels: Part II. Radiation Radiat. Phys. Chem 166, 108454. https://doi.org/10.1016/ j.radphyschem.2019.108454.

[27] Singh, J., Kaur, P., Kaur, P., Kumar, V., Singh, K., & Singh, T. (2023). Evaluation of radiation shielding parameters of SiO2-Na2O-K2O-P2O5-BaO glass system. *Materials Today: Proceedings*.

Volume 14, Issue 2, Page 213-219, 2025 https://doi.org/10.46810/tdfd.1633751 Research Article

BİNGÖL UNIVERSITY

Türk Doğa ve Fen Dergisi
Turkish Journal of Nature and Science
www.dergipark.gov.tr/tdfd

Poly(ε-Caprolactone)/Poly(Ethylene Glycol)Dithiol Electrospun Nanofibers As a Carrier for the Potent Phytomedicine Bromelain

Ozan YESILTEPE[1], Nefise YILMAZ[2], Ozge KOZGUS GULDU[1*],Ecem SAYGILI[3], Emin Ilker MEDINE[1], Dilek ODACI[2]

[1] Ege University, Institute of Nuclear Sciences, Department of Nuclear Application, Izmir, Türkiye
[2] Ege University, Faculty of Science, Department of Biochemistry, Izmir, Türkiye
[3] Izmir Democracy University, Faculty of Engineering, Department of Biomedical Engineering, Izmir, Türkiye
Ozan YESILTEPE : 0000-0003-1914-1201
Nefise YILMAZ : 0009-0008-3219-3907
Ozge KOZGUS GULDU : 0000-0001-7028-0720
Ecem SAYGILI : 0000-0002-8389-9079
Emin Ilker MEDINE : 0000-0003-0139-7110
Dilek ODACI : 0000-0002-7954-1381

Corresponding author: ozgekzgs@gmail.com

(Received: 05.02.2025, Accepted: 28.05.2025, Online Publication: 27.06.2025)

Keywords
Bromelain, Nanofiber, Poly(ε-caprolactone), Poly(ethylene glycol)dithiol

Abstract: Bromelain (Bro), known for its anticancer, immunomodulatory, and anti-inflammatory properties, is a mixture of cysteine proteinases widely utilized in cosmetics and burn debridement. Its effects on wound healing are linked to enhance tissue reconstitution. In this study, we introduced a blend of poly(ethylene glycol)dithiol (PEGdt) an poly(ε-caprolactone) (PCL) electrospun nanofibers (ENs) for the delivery of the potent phytomedicine Bro. Following the determination of the optimum concentration of PEGdt, we observed the enhancing effect of Bro addition on both the physical and chemical characteristics of ENs. An increased concentration of Bro was found to enhance the hydrophilicity of PCL/PEGdt surfaces, as indicated by contact angle analysis. The addition of Bro also created a favourable surface for potential applications on wound healing. Overall, the proven positive effect on cell viability and wettability of Bro-added PCL/PEGdt ENs reveal their potential to address problems of existing cosmetic solutions in wound dressings, such as insufficient ability to absorb excess wound exudate.

Güçlü Bir Bitkisel İlaç Olan Bromelainin Taşınması İçin Elektroeğirilmiş Poli(E-Kaprolakton)/Poli(Etilen Glikol)-Ditiol Nanolifleri

Anahtar Kelimeler
Bromelain, Nanolif, Poli(ε-kaprolakton), Ditiyol-poli(etilen glikol)

Öz: Bromelain (Bro), antikanser, immünomodülatör ve antiinflamatuar özellikleriyle bilinen ve kozmetik ile yanık debridmanı alanlarında yaygın olarak kullanılan sistein proteazlarının bir karışımıdır. Yara iyileşmesi üzerindeki etkileri, doku yenilenmesini desteklemesiyle ilişkilidir. Bu çalışmada, güçlü bir fitoterapötik ajan olan bromelainin kontrollü salımını sağlamak amacıyla, poli(ε-kaprolakton) (PCL) ve poli(etilen glikol) ditiyol (PEGdt) elektroeğrilmiş nanofiberlerden (ENs) oluşan bir karışım geliştirilmiştir. Optimum PEGdt konsantrasyonunun belirlenmesinin ardından, Bro eklenmesinin elektroeğirme ile üretilen ENlerin fiziksel ve kimyasal özellikleri üzerindeki olumlu etkileri gözlemlenmiştir. Temas açısı analizi ile gösterildiği üzere, artan Bro konsantrasyonu PCL/PEGdt'nin yüzeyinin hidrofilikliğini artırmıştır. Ayrıca yara iyileşmesi için potansiyel uygulamalara uygun bir yüzey oluşturmuştur. Genel olarak, Bro-eklenmiş PCL/PEGdt ENlerin hücre canlılığı üzerindeki pozitif etkileri ve ıslanabilirliği kanıtlanmıştır, mevcut yara örtülerinde sıkça karşılaşılan fazla yara eksüdasını emme yetersizliği gibi problemlere çözüm sunma potansiyeline sahip olduğu gösterilmiştir.

1. INTRODUCTION

Engineered polymeric biomaterials, meticulously designed to respond to environmental stimuli, have garnered considerable attention within the fields of biosensors [1], drug delivery [2] and tissue engineering [3]. Along with the transition from macro- to micro-scale in theragnostic approaches, significant advancements in material sciences have also covered the personalized medicine. This heightened interest attributed to their remarkable adaptability, which is contingent upon precise modulation of parameters such as temperature [4], pH [5], electrical/magnetic conductivity [6,7] in addition to their aptitudeıı for reacting to chemical [8] and biological [9] stimuli. Especially the combinations of drug delivery systems with tissue engineering approaches have paved the way for theragnostic applications in the form of wearable sensors. The non-invasive structures of these systems, which allow direct drug delivery into the bloodstream through the layers of the skin without undergoing first-pass metabolism in the liver, have been proven advanced treatment systems through both preclinical and clinical research.

Holding a significant promise in the field of cosmetics, electrospun nanofibers (ENs) are fibrous nanostructures that possess a notable feature of having a substantial surface area-to-volume ratio, enabling the efficient delivery of both hydrophilic and hydrophobic active molecules and drugs [10]. Moreover, the fibrous structures found in blends of polymers reveal remarkable characteristics, including a 3D- structural network, high porosity and permeability, which make them useful tools for tissue engineering applications. Hence, prior research endeavors sought to create structures by blending or layering polymers with significantly diverse characteristics, to harness the various attributes offered by different materials in nanofiber fabrication [11]. Being one of the most advantageous polymers, poly(ethylene glycol) (PEG) is a good example due to their permeable and biodegradable features, and their resistance to protein adsorption makes them suitable as plasticizer to blend or incorporate to other materials[12,13]. As such, the PEG incorporated graphene oxide structure has been proved to reduce protein adsorption by creating an interface for protein interaction through PEGylation [14]. Besides, PEG blended polylactide (PLA)[12] , poly(vinyl alcohol) (PVA) [13] or poly(ε-caprolactone) (PCL) [15] polymers have been reported to be changed their structural and physicochemical features such as printability, biocompatibility, and biodegradability, proving that the PEG can be use when a faster degradation is required. Notably, for targeted drug delivery, thiol functionalized PEG polymers are widely used due to their enhanced biocompatibility, and antifouling properties.

In this study, we introduced the utilization of poly(ethylene glycol)dithiol (PEGdt) and PCL blend for the delivery of the potent phytomedicine bromelain (Bro) [16]. Being a proteolytic enzyme extracted from pineapple stems [17], Bro has attracted significant attention due to its multiple physiological effects, including antioxidant [18], anti-inflammatory [19], and anticancer [20] properties. In addition to these versatile biological activities, Bro exhibits a well-documented positive effect on wound healing, making it a promising candidate for advanced wound care applications [21]. Remarkably, the integration of Bro into nanostructured materials *via* electrospinning has further enhanced its therapeutic potential by improving its bioavailability and facilitating controlled delivery. Recent studies have consistently demonstrated that Bro-loaded ENs not only promote tissue regeneration but also significantly accelerate the wound healing process [22,23,24]. Herein this study, along with the well-defined physical features, the proven biocompatibility of Bro-loaded PCL/PEGdt (PCL/PEGdt/Bro) ENs have been shown their potential to be used as wound healing materials in the field of cosmetics and tissue engineering applications.

2. MATERIAL AND METHOD

2.1 Materials

PCL (Mn: 80000), PEGdt (Mn:1000) and Bro were purchased from Sigma-Aldrich. Formic acid (FA) and acetone (Ac) were obtained from Merck. Human keratinocytes cell line (HaCaT) was supplied by CLS. Dulbecco's Modified Eagle Medium (DMEM) cell culture media and fetal bovine serum (FBS), L-glutamine and penicillin/streptomycin supplements were purchased from Gibco. 3-(4,5-Dimethylthiazol-2-yl)-2,5-diphenyltetrazolium bromide (MTT) used for cell viability/cytotoxicity testing was obtained from Sigma-Aldrich.

2.2 Instrumentation

NanoWeb Electrospin 103 (MaviTech, Turkey) was used to obtain PCL/PEGdt ENs. The morphological structure of the ENs were examined through scanning electron microscopy (SEM; Carl Zeiss 300 VP). The contact angles of PCL/PEGdt ENs were measured with the Attention Theta Goniometer device. The Fourier-Transform Infrared Spectroscopy (FTIR) spectra of PCL, PCL/PEGdt and PCL/PEGdt/Bro ENs were determined by PerkinElmer Spectrum 100 instrument between the wavelengths of 400–4000 cm^{-1}. Multimode microplate reader (Thermo Varioscan Flash) was used to measure MTT absorbance.

2.3 Preparation of PCL/PEGdt and PCL/PEGdt/Bro ENs

10% (w:v) PCL polymer was dissolved in FA:Ac (at the ratio of 3:7; v:v) solvents and stirred at 350 rpm, 24 °C overnight. Followed by, 2.5-12.5% (w:v) PEGdt was added to blend the optimized PCL solution. The prepared PCL/PEGdt solution was transferred to a 21 G syringe at 2 mL volume and placed to syringe pump (ATABA AC–DC Adapter AT-511). Electrospinning was performed using an applied voltage of 16 kV, a solution flow rate of 0.3 $mL.h^{-1}$, and maintaining 15-20 cm between the syringe tip and the collector plate. The electrospinning occurred at a temperature range of 21–24 °C and a humidity level of 63–70%. As for the preparation of PCL/PEGdt/Bro

ENs, bromelain was added in certain amounts of (0.25-5% (w:v)) to the PCL/PEGdt polymer blend.

2.4 Assessment of the cytotoxicity of PCL/PEGdt/Bro ENs on HaCaT cells

HaCaT cells were used to test the effect of PCL/PEGdt/Bro ENs on cell viability. For the cultivation of HaCaT cells, DMEM medium containing 10 % fetal bovine serum (FBS), 1 mM sodium pyruvate, and 2 mM glutamine were used. The cell viability test of PCL/PEGdt/Bro ENs was assessed *via* MTT assay. Briefly, HaCaT cells were suspended in DMEM cell culture media at $2x10^4$ cell/well, seeded in 96-well plates and incubated at 37 °C and 5% CO_2 for 24 h. Following, the medium was removed and UV-sterilized ENs (2x2 cm) were fitted to each well as test groups within the fresh culture media. Only PCL ENs extract added group was considered as the positive controls. After 24 h of incubation, MTT assay was performed and the cell viability (%) was calculated.

2.5 Statistical analysis

Statistical analyses were carried out by Student's t-test cells were used in cell viability studies.

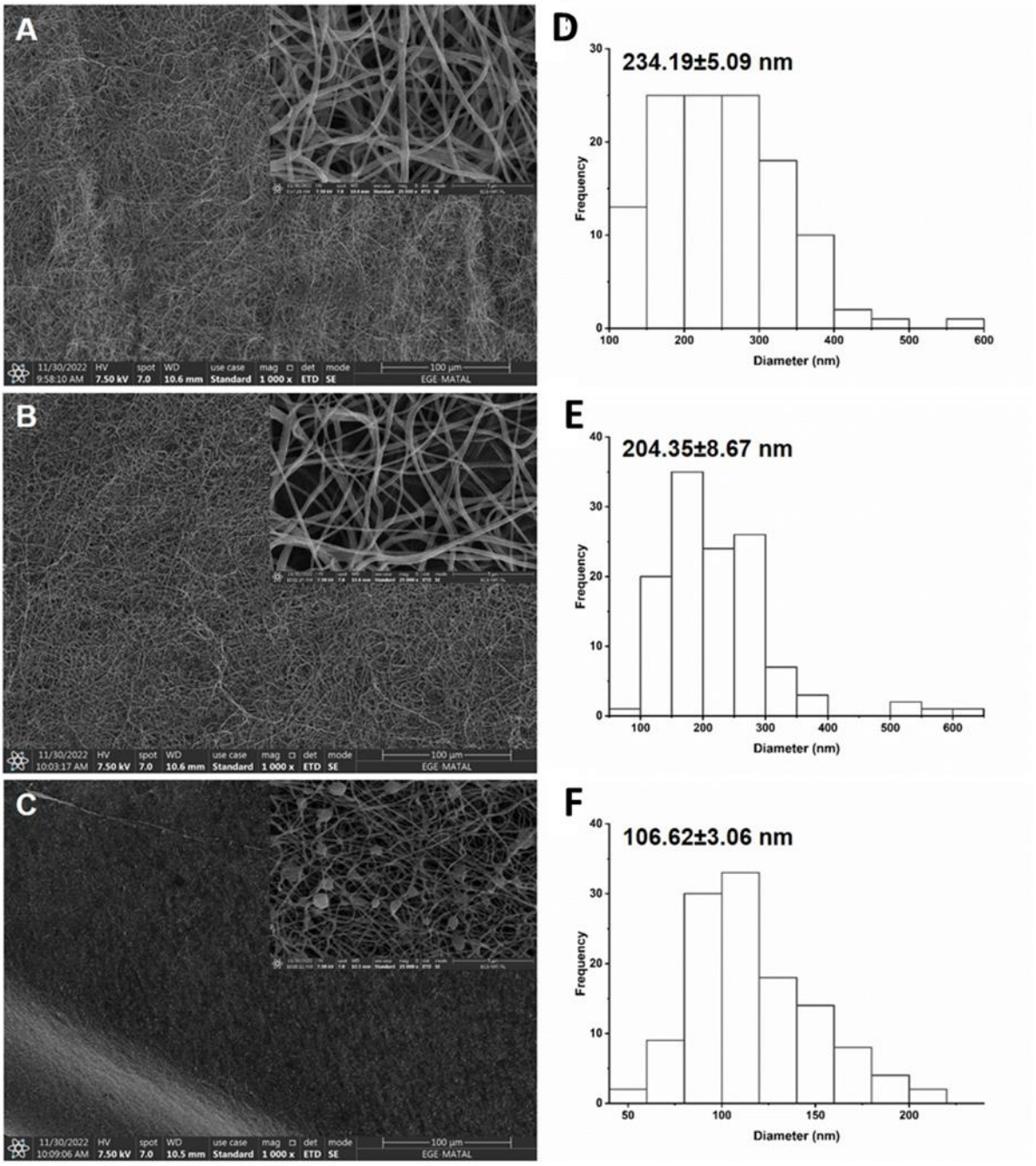

Figure 1. SEM micrographs of **A)** PCL (10%; w:v), **B)** PCL/PEGdt ([PCL]: 10%; w:v and [PEGdt]: 2.5%; w:v), **C)** PCL/PEGdt ENs ([PCL]: 10%; w:v and [PEGdt]: 5.0%; w:v) (Magnification 1000X, scale bar 100 µm and for inset figures, magnification 25000X, scale bar 5 µm). Histogram for ENs diameter distribution and average diameters of **D)** PCL (10%; w:v), **E)** PCL/PEGdt ([PCL]: 10%; w:v and [PEGdt]: 2.5%; w:v), **F)** PCL/PEGdt ENs ([PCL]: 10%; w:v and [PEGdt]: 5.0%; w:v).

Table 1. Selection parameters for the PCL/PEGdt blend ratio

PCL/PEGdt	Average diameter (nm)	Bead formation	Comment
PCL (10%; w:v)	234.19±5.09	No	uniform
PCL(10%; w:v)/PEGdt(2.5%; w:v)	204.35±8.67	No	uniform
PCL(10%; w:v)/PEGdt(5.0%; w:v)	106.62±3.06	Yes	non-uniform

3. RESULTS AND DISCUSSION

3.1 Characterization of PCL/PEGdt/Bro ENs

The impact of PEGdt on the ENs structure assessed through a comparison of SEM images, the diameters, and contact angles. Notably, due to its low molecular weight, PEG functions as a plasticizer between PCL chains, leading to a decrease in solution viscosity, and, consequently a reduced diameter [25]. Figure 1A-1C shows the SEM images of PCL and PCL/PEGdt ENs and Figure 1D-1F displays the histogram for the dimeter of the PCL/PEGdt ENs. As shown in SEM images (Figure 1A-1C), the presence of PCL and PCL/PEGdt ENs were observed. With the increase of PEGdt concentration, the formation of beads in PCL/PEGdt ENs was noticed. Therefore, the optimum PEGdt concentration was found to be 2.5%. As such, in contrast to the average diameter of fibers achieved with 10% (v:v) PCL, which is 234.19 ± 5.09 nm (Figure 1D), the diameters of PCL/PEGdt ENs with a 2.5% (v:v) PEGdt incorporated ENs were computed to be an average of 204.35 ± 8.67 nm (Figure 1E). Moreover, thinner fiber diameters (106.62 ± 3.06 nm) along with the bead formation have been observed with the increased PEGdt concentration (Figure 1C, F; Table 1).

Notably, although the addition of PEGdt did not affect the contact angles (CAs) of PCL ENs surfaces solely, the decrease on contact angles were observed along with the increasing amount of Bro. As such, the resulting homogeneous and bead-free PCL/PEGdt/Bro ENs surfaces demonstrated hydrophilic nature, as evidenced by contact angles both before and after the addition of Bro. Contact angles of PCL/PEGdt and PCL/PEGdt/Bro ENs were 123.24°±3.18°, 126.58°±2.77° ([Bro]: 0.25%; w:v), 124.01°±2.77° ([Bro]: 0.5%; w:v), 87.92°±28.85° ([Bro]: 1.25%, w:v), 83.84°±15.25° ([Bro]: 2.5%; w:v), and 66.57°±4.36° ([Bro]: 5.0%; w:v), respectively. Hydrophilicity of the ENs is crucial for wound healing applications, since the recent research have shown that hydrophilic polymers have the potential to address problems of existing wound dressings, such as insufficient ability to absorb excess wound exudations [26]. Moreover, literature findings prove that wounds tend to heal more rapidly in moist environments [27,28]. Hence, the hydrophilic characteristics and its capacity to sustain a moist environment of materials used for wound healing are pivotal as the material not only shields the wound area from potential secondary damage caused by bacteria and external mechanical stress but also promotes a prompt healing process. In addition to their benefits for wound healing, they can potentially serve as a scaffold in tissue engineering applications, providing a substrate for cell adhesion. The formation of PCL/PEGdt/Bro ENs also confirmed by FTIR analysis. In the PCL fibers' spectrum, the prominent peaks at 2900 cm^{-1} and 2869 cm^{-1} correspond to the asymmetric and symmetric stretching of the CH_2 group, respectively. The sharp peak at 1724 cm^{-1} corresponds to the stretching of the carbonyl group. In the spectrum of PEGdt, the peak at 2945 cm^{-1} is attributed to C–H stretching. Confirming the individual spectra of PCL and PCL/PEGdt, similar groups observed within the blended polymer mixture (Figure 2). Moreover, the C=O stretch of the aldehyde and amide group at 1645 in PCL/PEGdt/Bro ENs was attributed to the bromelain addition.

3.2 *in vitro* cytotoxicity test of PCL/PEGdt/Bro ENs

The cytotoxicity assays are practical methods for assessing the biological safety of materials according to standard guidelines. In this context, effects of five different concentrations (0.25, 0.5, 1.25, 2.5, 5.0 % (w:v)) of Bro-containing PCL/PEGdt/Bro ENs on cell viability were evaluated using *in vitro* cytotoxicity test (MTT). The cytotoxic effects of PEGdt and Bro were tested on the HaCaT cell line over a 24 h period. The results indicated that cell viability for ENs cells remained above 80%, showing no significant cytotoxic effect in any of the ENs formulations, whether with or without Bro. Additionally, the presence of Bro in PCL/PEGdt resulted in the highest and most significant proliferative effect, particularly at 0.25% (w:v) of Bro concentration, with cell viability reaching more than 100% and t-test was applied on the results (Figure 3). The observed high cell viability at a 0.25% (w:v) of Bro was thought to be related to the peptidase activity of bromelain [17], which becomes more pronounced at higher concentrations. As is well known, Bro is a proteolytic enzyme that breaks down proteins. At low concentrations, partial degradation of proteins in the cellular environment may lead to a favorable microenvironment that supports cell adhesion and proliferation. However, as the concentration of Bro increases, particularly at high levels such as 5.0 % (w:v) and above, its excessive peptidase activity may lead to the degradation of surface proteins, thereby limiting cell adhesion and reducing cell viability. It is worth noting that Bro is typically formulated at concentrations up to 3% (w/v) in cosmetic application [18], which suggests that concentrations exceeding this range may not be suitable for maintaining cellular compatibility. In our study, we interpret the relatively high cell viability observed at 0.25% (w:v) Bro concentration as a result of moderate enzymatic activity. In line with this, several studies in the literature have explored the use of ENs for wound healing purposes. A comparison of some key properties of these ENs is presented in Table 2.

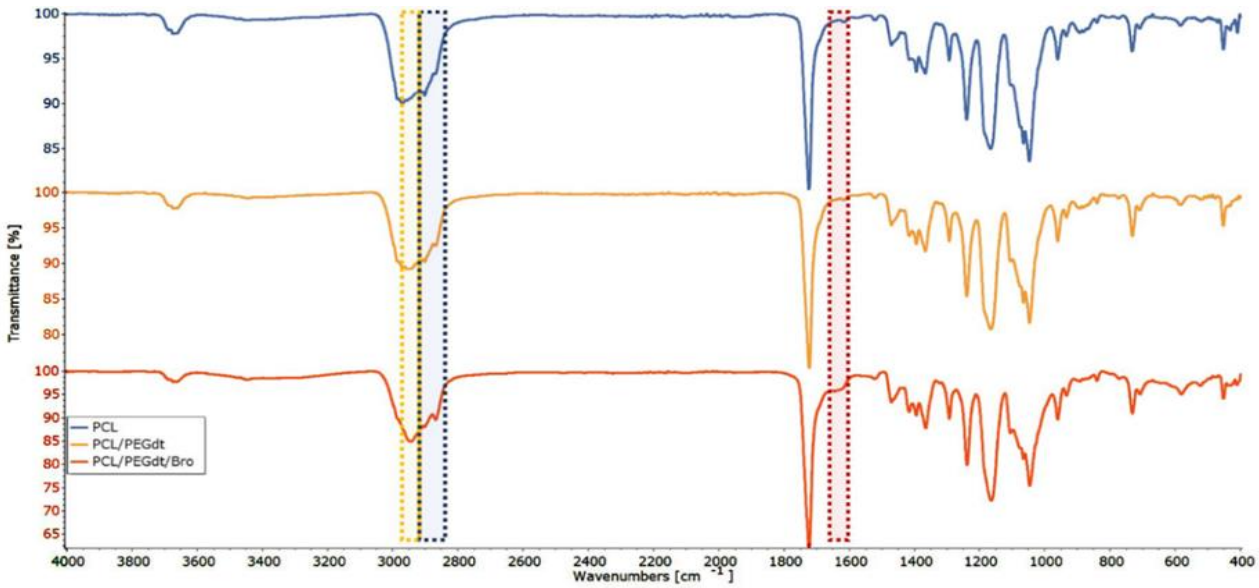

Figure 2. FTIR Spectra of PCL (blue line), PCL/PEGdt (yellow line; [PCL]: 10% (w:v) and [PEGdt]: 2.5% (w:v) and PCL/PEGdt/Bro (orange line; [PCL]: 10% (w:v), [PEGdt]: 2.5% (w:v), and [Bro]: 0.25% (w:v)). Each component's specific regions are highlighted with dotted boxes that match the colors of the lines.

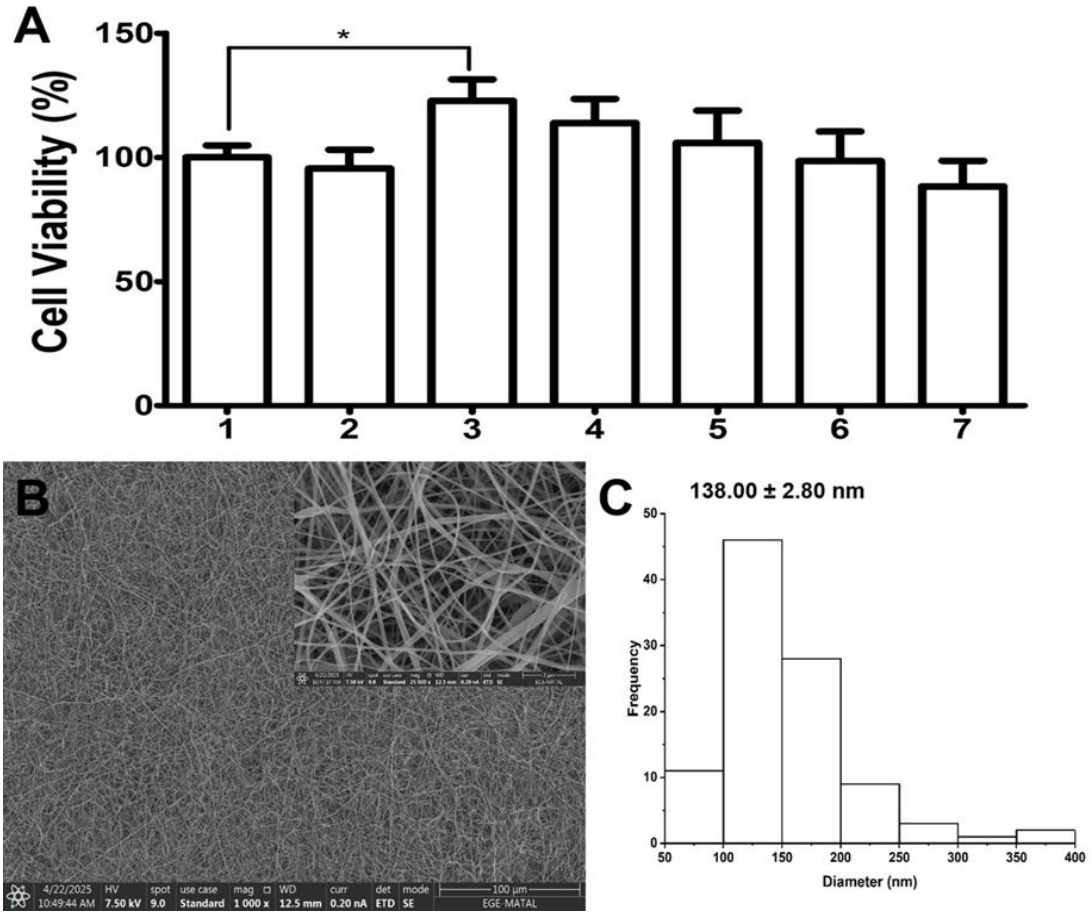

Figure 3. A) Effects of ENs on the cell viability of HaCaT cells after 24 h. **1)** PCL ENs, **2)** PCL/PEGdt ENs ([PCL]: 10%; w:v), [PEGdt]: 2.5%; w:v); **3)** PCL/PEGdt/Bro ([PCL]: 10%; w:v, [PEGdt]: 2.5%; w:v, [Bro]: 0.25%; w:v); **4)** PCL/PEGdt/Bro ([PCL]: 10%; w:v, [PEGdt]: 2.5%; w:v, [Bro]: 0.5%; w:v); **5)** PCL/PEGdt/Bro Bro ([PCL]: 10%; w:v, [PEGdt]: 2.5%; w:v, [Bro]: 1.25%; w:v); **6)** PCL/PEGdt/Bro Bro ([PCL]: 10%; w:v, [PEGdt]: 2.5%; w:v, [Bro]: 2.5%; w:v); **7)** PCL/PEGdt/Bro Bro ([PCL]: 10%; w:v, [PEGdt]: 2.5%; w:v, [Bro]: 5.0%; w:v) (Bars represent standard deviation, n=5, * ($P < 0.05$; t-test). **B)** SEM micrographs of PCL/PEGdt/Bro ([PCL]: 10%; w:v, [PEGdt]: 2.5%; w:v, [Bro]: 0.25%; w:v) (Magnification 1000X, scale bar 100 µm and for inset figures, magnification 25000X, scale bar 3 µm). **C)** Histogram for ENs diameter distribution and average diameters of PCL/PEGdt/Bro ([PCL]: 10%; w:v, [PEGdt]: 2.5%; w:v, [Bro]: 0.25%; w:v).

Table 2. Comparison of some properties of ENs prepared for wound healing in literature

EN material(s)	Bioactive ingredient	Diameter of ENs (nm)	Contact angle of ENs	Cell culture	Reference
Carboxymethyl cellulose/PVA	Colistin	-	78.44°	HFF-1	[29]
PCL/PLA	AgNP	397.23	133.4°	L929 and SK-MEL-30	[30]
PCL/Soy Protein	Tea tree oil	136	-	NIH3T3	[31]
PCL-Collagen/PVA	Collagen	191.8±113.9	35.8°	L929	[32]
PCL/ Chitosan	-	280 ± 89	60.9° ± 4.0°	Mesothelial cells	[33]
PCL/PEGdt	Bro	138.00±2.80	126.58°±2.77°	HaCaT	This study

4. CONCLUSION

In the present study, the functionality of both PCL/PEGdt and PCL/PEGdt/Bro ENs in terms of interpenetration of polymer networks as well as wettability and biocompatibility were assessed. The results revealed a successful utilization of a blend of PEGdt and PCL ENs for Bro incorporation, resulting in notable improvements in both physical characteristics and biological effects. These findings highlight the potential of Bro-loaded PCL/PEGdt ENs to overcome the limitations of existing wound dressings, particularly in their ability to absorb excess wound exudate and promote effective wound healing.

Acknowledgement

N. Yılmaz thanks to TUBITAK 2209-A-Research Project Support Programme for Undergraduate Students. Authors thank to Dr. Deniz Ertugrul Uygun for supporting SEM images of PCL/PEGdt/Bro ENs.

REFERENCES

[1] Lanzalaco S, Molina BG. Polymers and Plastics Modified Electrodes for Biosensors: A Review. Molecules 2020;25.

[2] Shahriar SMS, Mondal J, Hasan MN, Revuri V, Lee DY, Lee YK. Electrospinning nanofibers for therapeutics delivery. Nanomaterials 2019;9.

[3] Saygili E, Saglam-Metiner P, Cakmak B, Alarcin E, Beceren G, Tulum P, Kim YW, Gunes K, Eren-Ozcan GG, Akakin D, Sun JY, Yesil-Celiktas O. Bilayered laponite/alginate-poly(acrylamide) composite hydrogel for osteochondral injuries enhances macrophage polarization: An in vivo study. Biomaterials Advances 2022;134.

[4] Zarrintaj P, Jouyandeh M, Ganjali MR, Hadavand BS, Mozafari M, Sheiko SS, Vatankhah-Varnoosfaderani M, Gutiérrez TJ, Saeb MR. Thermo-sensitive polymers in medicine: A review. Eur Polym J 2019;117:402–23.

[5] Oh J, Kim B. Mucoadhesive and pH-responsive behavior of gelatin containing hydrogels for protein drug delivery applications. Korea Australia Rheology Journal 2020;32:41–6.

[6] Kaur G, Adhikari R, Cass P, Bown M, Gunatillake P. Electrically conductive polymers and composites for biomedical applications. RSC Adv 2015;5:37553–67.

[7] Na H, Kang YW, Park CS, Jung S, Kim HY, Sun JY. Hydrogel-based strong and fast actuators by electroosmotic turgor pressure. Science 2022;376:301–7.

[8] Fennell E, Huyghe JM. Chemically Responsive Hydrogel Deformation Mechanics: A Review. Molecules 2019;24.

[9] Onofrillo C, Duchi S, Francis S, O'Connell CD, Caballero Aguilar LM, Doyle S, Yue Z, Wallace GG, Choong PF, Di Bella C. FLASH: Fluorescently LAbelled Sensitive Hydrogel to monitor bioscaffolds degradation during neocartilage generation. Biomaterials 2021;264:120383.

[10] Ramakrishna S, Fujihara K, Teo WE, Yong T, Ma Z, Ramaseshan R. Electrospun nanofibers: solving global issues. Materials Today 2006;9:40–50.

[11] Tipduangta P, Belton P, Fábián L, Wang LY, Tang H, Eddleston M, Qi S. Electrospun Polymer Blend Nanofibers for Tunable Drug Delivery: The Role of Transformative Phase Separation on Controlling the Release Rate. Mol Pharm 2016;13:25–39.

[12] Kumar R, Alex Y, Nayak B, Mohanty S. Effect of poly (ethylene glycol) on 3D printed PLA/PEG blend: A study of physical, mechanical characterization and printability assessment. J Mech Behav Biomed Mater 2023;141:105813.

[13] Mohammed MI, El-Sayed F. PEG's impact as a plasticizer on the PVA polymer's structural, thermal, mechanical, optical, and dielectric characteristics. Opt Quantum Electron 2023;55:1–22.

[14] Tan X, Feng L, Zhang J, Yang K, Zhang S, Liu Z, Peng R. Functionalization of graphene oxide generates a unique interface for selective serum protein interactions. ACS Appl Mater Interfaces 2013;5:1370–7.

[15] Iglesias-Echevarria M, Durante L, Johnson R, Rafuse M, Ding Y, Bonani W, Maniglio D, Tan W. Coaxial PCL/PEG-thiol–ene microfiber with tunable physico-chemical properties for regenerative scaffolds. Biomater Sci 2019;7:3640–51.

[16] Pezzani R, Jiménez-Garcia M, Capó X, Sönmez Gürer E, Sharopov F, Rachel TYL, Ntieche Woutouoba D, Rescigno A, Peddio S, Zucca P, Tsouh Fokou PV, Martorell M, Gulsunoglu-Konuskan Z, Ydyrys A, Bekzat T, Gulmira T, Hano C, Sharifi-Rad J, Calina D. Anticancer properties of bromelain: State-of-the-art and recent trends. Front Oncol 2023;12.

[17] Varilla C, Marcone M, Paiva L, Baptista J. Bromelain, a group of pineapple proteolytic complex enzymes (Ananas comosus) and their possible therapeutic and clinical effects. a summary. Foods 2021;10.

[18] Marissa Z, Mita SR, Kusumawulan CK, Sriwidodo S. Antioxidant and Photoprotective Activity of

Bromelain Cream: An In Vitro and In Vivo Study. Cosmetics 2025;12:41.
[19] Kumar V, Mangla B, Javed S, Ahsan W, Kumar P, Garg V, Dureja H. Bromelain: a review of its mechanisms, pharmacological effects and potential applications. Food Funct 2023;14:8101–28.
[20] Pezzani R, Jiménez-Garcia M, Capó X, Sönmez Gürer E, Sharopov F, Rachel TYL, Ntieche Woutouoba D, Rescigno A, Peddio S, Zucca P, Tsouh Fokou PV, Martorell M, Gulsunoglu-Konuskan Z, Ydyrys A, Bekzat T, Gulmira T, Hano C, Sharifi-Rad J, Calina D. Anticancer properties of bromelain: State-of-the-art and recent trends. Front Oncol 2023;12.
[21] Saghafi Y, Baharifar H, Najmoddin N, Asefnejad A, Maleki H, Sajjadi-Jazi SM, Bonkdar A, Shams F, Khoshnevisan K. Bromelain- and Silver Nanoparticle-Loaded Polycaprolactone/Chitosan Nanofibrous Dressings for Skin Wound Healing. Gels 2023;9.
[22] Chen X, Wang X, Wang S, Zhang X, Yu J, Wang C. Mussel-inspired polydopamine-assisted bromelain immobilization onto electrospun fibrous membrane for potential application as wound dressing. Materials Science and Engineering C 2020;110.
[23] Shoba E, Lakra R, Syamala Kiran M, Korrapati PS. Fabrication of core–shell nanofibers for controlled delivery of bromelain and salvianolic acid B for skin regeneration in wound therapeutics. Biomedical Materials 2017;12:035005.
[24] Bayat S, Amiri N, Pishavar E, Kalalinia F, Movaffagh J, Hahsemi M. Bromelain-loaded chitosan nanofibers prepared by electrospinning method for burn wound healing in animal models. Life Sci 2019;229:57–66.
[25] Shadman-Manesh V, Gholipour-Kanani A, Najmoddin N, Rabbani S. Preclinical evaluation of the polycaprolactone-polyethylene glycol electrospun nanofibers containing egg-yolk oil for acceleration of full thickness burns healing. Scientific Reports 2023 13:1–12.
[26] Jin SG, Yousaf AM, Kim KS, Kim DW, Kim DS, Kim JK, Yong CS, Youn YS, Kim JO, Choi HG. Influence of hydrophilic polymers on functional properties and wound healing efficacy of hydrocolloid based wound dressings. Int J Pharm 2016;501:160–6.
[27] Junker JPE, Kamel RA, Caterson EJ, Eriksson E. Clinical Impact Upon Wound Healing and Inflammation in Moist, Wet, and Dry Environments. Adv Wound Care (New Rochelle) 2013;2:348–56.
[28] Winter GD. Formation of the scab and the rate of epithelization of superficial wounds in the skin of the young domestic pig. Nature 1962;193:293–4.
[29] Kazeminava F, Javanbakht S, Nouri M, Adibkia K, Ganbarov K, Yousefi M, et al. Electropun nanofibers based on carboxymethyl cellulose/polyvinyl alcohol as a potential antimicrobial wound dressing. Int J Biol Macromol. 2022;214:111-9.
[30] Güven Çimen C, Dündar MA, Demirel Kars M, Avcı A. Enhancement of PCL/PLA electrospun nanocomposite fibers comprising silver nanoparticles encapsulated with Thymus vulgaris L. molecules for antibacterial and anticancer activities. ACS Biomater Sci Eng. 2022;8(9):3779–90.
[31] Doustdar F, Ramezani S, Ghorbani M, Mortazavi Moghadam F. Optimization and characterization of a novel tea tree oil-integrated poly (ε-caprolactone)/soy protein isolate electrospun mat as a wound care system. Int J Pharm. 2022;627:122218.
[32] Anaya Mancipe JM, Pereira LCB, Borchio PGM, Dias ML, Thiré RMSM, et al. Novel polycaprolactone (PCL)-type I collagen core-shell electrospun nanofibers for wound healing applications. J Biomed Mater Res B Appl Biomater. 2022;110(8):1703–12.
[33] Kao HH, Kuo CY, Govindaraju DT, Chen KS, Chen JP, et al. Polycaprolactone/chitosan composite nanofiber membrane as a preferred scaffold for the culture of mesothelial cells and the repair of damaged mesothelium. Int J Mol Sci. 2022;23(17):9517.

Volume 14, Issue 2, Page 220-224, 2025 https://doi.org/10.46810/tdfd.1585498 Research Article

BİNGÖL UNIVERSITY

Türk Doğa ve Fen Dergisi
Turkish Journal of Nature and Science
www.dergipark.gov.tr/tdfd

Synthesis, Characterization and Investigation of Some Photophysical Properties of Novel Benzothiazole Based Pyridine Derivative

Hülya ELMALI GÜLBAŞ[1*]

[1]Usak University, Banaz Vocational School, Chemistry and Chemical Processing Technologies Department, Uşak, Türkiye
Hülya ELMALI GÜLBAŞ ORCID No: 0000-0002-6041-6054

**Corresponding author: hulya.elmali@usak.edu.tr*

(Received: 14.11.2024, Accepted: 31.05.2025, Online Publication: 27.06.2025)

Keywords
Benzothiazole, Picolinoyl chloride, Fluorescence, Organic synthesis

Abstract: Benzothiazole derivates have been play important role in chemical, biological and pharmacological reactions because of heterocyclic structure. In this study, fluorescent active novel benzothiazole substitute picolinoyl chloride derivate 6-((2-(benzothiazol-2 yl)phenyl)carbamoyl)picolinoyl chloride **(**BTPCP**)** successfully synthesized and characterized. BTPCP structure was identified by classic spectroscopic methods (FT-IR, ^{1}H-NMR and ^{13}C-NMR). BTPCP photophysical properties was investigated by using UV-Vis spectroscopy and Fluorescence spectroscopy. Benzothiazole substitute picolinoyl chloride derivate **(**BTPCP**)** has been shown fluorescence activity. The novel fluorescence active BTPCP is expected to find potential application studies in different biological, pharmacological and especially toxic heavy metal ion detection sensor as Hg^{2+}, Cu^{2+}, Cr^{3+}, Fe^{3+}…etc.

Yeni Benzotiyazol Bazlı Piridin Türevinin Sentezi, Karakterizasyonu ve Bazı Fotofiziksel Özelliklerinin Araştırılması

Anahtar Kelimeler
Benzotiyazol, Pikolinoil klorür, Floresans, Organik sentez

Öz: Benzotiyazol türevleri, heterosiklik yapıları nedeniyle kimyasal, biyolojik ve farmakolojik reaksiyonlarda önemli rol oynamaktadır. Bu çalışmada, floresans aktif yeni benzotiyazol substitue pikolinoil klorür türevi 6-((2-(benzotiyazol-2il)fenil)karbamoil)pikolinoil klorür (BTPCP) başarıyla sentezlenmiş ve karakterize edilmiştir. Sentezlenen BTPCP'nin molekül yapısı klasik spektroskopik yöntemler (FT-IR, ^{1}H-NMR ve ^{13}C-NMR) kullanılarak belirlenmiştir. BTPCP molekülünün fotofiziksel özellikleri Uv-Vıs spektroskopisi ve Fluoresans spektroskopisi kullanılarak incelenmiştir. Yapılan incelemeler sonucunda benzotiyazol substitue pikolinoyil klorür türevi BTPCP floresans aktivitesi gösterdiği belirlenmiştir. Yeni floresans aktif BTPCP'nin Hg^{2+}, Cu^{2+}, Cr^{3+}, Fe^{3+}… gibi ağır metal iyonlarının belirlenmesi kullanılabilecek sensör çalışmaları başta olmak üzere, farklı biyolojik ve farmakolojik çalışmalarda uygulama bulması beklenmektedir.

1. INTRODUCTION

Toxic heavy metals are harmful to environmental and human life and the most significant damage caused the environment occurred in soil and water. Nowadays, developing new methods for the detection of heavy metal ion pollution caused by industrial activities an important field of studies [1-6]. Heavy metal ions wastewater, which released uncontrollably into the environment from many different industrial areas such as leather, textile and paint, poses a danger to the environment and human life [7-9]. Detection and disposal of these metals constitute an important field of work. It has known that toxic heavy metals cause diseases in humans, especially the immune system, nervous system, digestive system, heart, kidney and neurological diseases [10-12]. Today, heavy metal analyzes of pollution are generally carried out using different analytical methods such as voltammetry, chromatography or spectroscopy. However, since all methods require expensive devices and involve complex, time-consuming procedures that can only be carried out by well-trained technical personnel, instrumental analysis methods used for the qualitative and quantitative detection of heavy metal ions, especially in water samples. However, studies continue to develop new methods with simple devices, cheap, fast and high

sensitivity [13-15]. Among the methods used to detect heavy metal ions, applications of fluorescent sensors are preferred over other common analytical methods due to their advantages such as high sensitivity, good selectivity, fast response and local observation [16]. The molecular structure modifications of chemosensors have been triggered the ability to selectively complex selective against the metal ions. [17-21].

Benzothiazole molecules have high quantum yields and large Stokes shifts due to their stable conjugated structures. Benzothiazole compounds constitute an interesting field of study for researchers who want to synthesize fluorescence sensors and chemosensors due to their excellent photophysical properties such as photostability [21-24].

The last decade, synthesis of new benzothiazole based fluorescence active compounds for detection of heavy metal ions have been an important research area. The synthesis and determination of photophysical properties benzothiazole based amide derivatives fluorescence sensor applications such as Hg^{2+}, Cu^{2+}, Cr^{3+}, CN^{-} have been in the literature [14, 25-26].

Benzothiazole based molecules are an important group of heterocyclic compounds that can exhibit various pharmacological activities such as anticancer, antibacterial, anti-inflammatory, analgesic and antidiabetic, as well as unique material properties due to their chemical and biological properties [27-29].

The aim of this study is to design, synthesize and characterize novel fluorescence active 6-((2-(benzothiazol-2-yl phenyl)carbamoyl)picolinoyl chloride **(**BTPCP**)** and BTPCP photophysical properties determined by using spectroscopic methods. (Uv-Vıs spectroscopy and Fluorescence spectroscopy). The novel fluorescence active BTPCP can be used in different fields as medicine, materials, toxic heavy metal ions detection sensors like Hg^{+2}, Cu^{+2}, Cr^{+3}, Fe^{+3}……etc.

2. MATERIAL AND METHOD

2.1. Reagents and Instruments

All chemical compounds and organic solvents were obtained from commercial sources (Merck, Sigma-Aldrich, and Alfa Aesar) without any purifications. For the column chromatography, silica gel 230–400 mesh was used and for thin layer chromatography (TLC) applications, pre-coated silica gel 60F254 aluminum sheets were used. The reaction was conducted in under inert (argon) atmosphere. FTIR spectra was performed on a Perkin Elmer Spectrum Two spectrophotometer equipped with ATR apparatus. The Bruker 400 MHz device was used for measuring the ^{1}H-NMR and ^{13}C-NMR spectra in chloroform solvent with the interior label of chemical shifts, tetramethyl silane. Fluorescence spectra were on the Agilent Cary Eclipse Spectrophotometer, while PerkinElmer Lambda 35 spectrophotometer was used to measure UV–Vis absorption spectra.

2.2. Synthesis of compound 6-((2-(benzothiazol-2-yl)phenyl)carbamoyl)picolinoyl chloride (BTPCP)

Na_2CO_3 (318 mg, 3 mmol) and 2-(2-aminophenyl)-benzothiazole (**1**) (226 mg, 1 mmol) were stirred for 1 h at room temperature in THF (25 ml) and then 2,6-pyridinedicarboxylic acid chloride (243,6 mg, 1,2 mmol) was added the mixture. The reaction mixture was refluxed for 8 h under Ar atmosphere. After the reaction mixture was cooled and poured into ice, the mixture was stirred for 1 h. The solid was filtered and the crude product was purified by column chromatography on silica gel. The synthesis of BTPCP is shown in Scheme 1.

White solid, Yield: 181,3 mg (45%). FT-IR (ATR, cm^{-1}) 3149 (NH), 1742 ($C=O_{acyl\ chloride}$) 1689 ($C=O_{amide}$), 752 (C-Cl). ^{1}H NMR (400 MHz, $CDCl_3$) δ: 13.64 (s, 1H, N*H*-Ar), 8.95 (dd, *J*=7 Hz, 1H, $H_{1.}$), 8.64- 8.55 (m, 2H, $H_{2,}$ H_3), 8.35 (d, *J*=8 Hz, 2H, $H_{8,}$ H_{11}), 8.26–8.10 (m, 2H, $H_{4,}$ H_7), 7.60–7.38 (m, 2H, $H_{5,}$ H_{10}), 7.14–7.19 (m, 2H, $H_{6,}$ $H_{9.}$);^{13}C NMR (100 MHz, $CDCl_3$) δ: 168.5 (1C, *Cl-C=O*), 165.3 (1C, *-NH-C=O*), 164.3 *(-S-C=N-*), 162.6 (*-N-C=C-*), 154.3 (*-C-C=N-*), 152.5 (*-N-C=*C-),138.1, 130.4, 129.1, 127.8, 124.1, 121.5, 120.7 (*Aromatic C*)

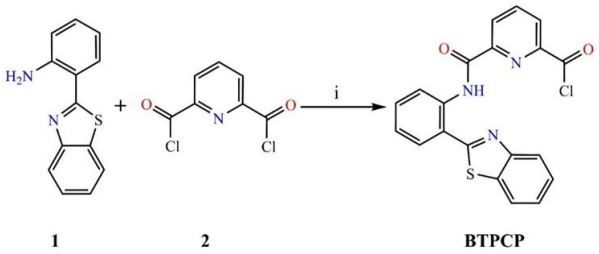

Scheme 1. The synthesis of BTPCP**;** ***i***: THF, Na_2CO_3, inert atmosphere, 8 h reflux.

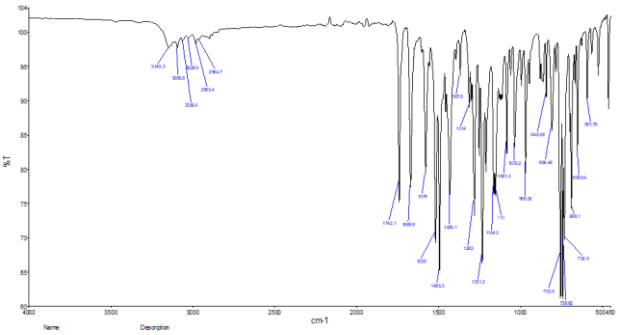

Figure 1. The FT-IR spectrum **o**f BTPCP

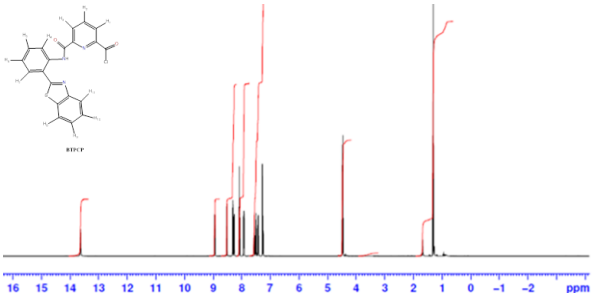

Figure 2. The ^{1}H-NMR spectrum of BTPCP

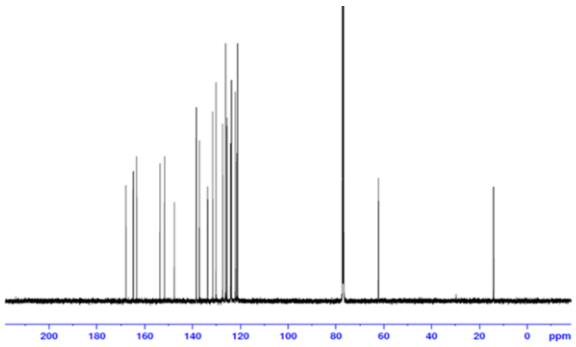

Figure 3. The ^{13}C-NMR spectrum of BTPCP

2.3.UV-Vis Spectroscopy

A novel benzothiazole substitute picolinoyl chloride derivate BTPCP was examined in UV-Vis spectrophotometer. In the UV-Vis spectrum, absorption bands were observed at wavelengths of 324 nm ($\lambda_{abs.}$) and 382 nm ($\lambda_{abs.}$), respectively, due to the influence of the chromophore C=C, C=N groups in the heterocycle and the C=O groups in the molecular structure. The Uv-Vis spectrum of BTPCP has been showed two absorbance bands: the π-π* transitions of the aromatic core are responsible for the absorbance band at 324 nm, while the n–π* electron transition, which results from the promotion of nonbonding electrons on the N atom of the pyridine and N ,S atoms of benzothiazole moiety to an anti-bonding orbital of BTPCP, is responsible for the bands at 382 nm. The UV-Vis spectrum of novel BTPCP shown in Figure 4.

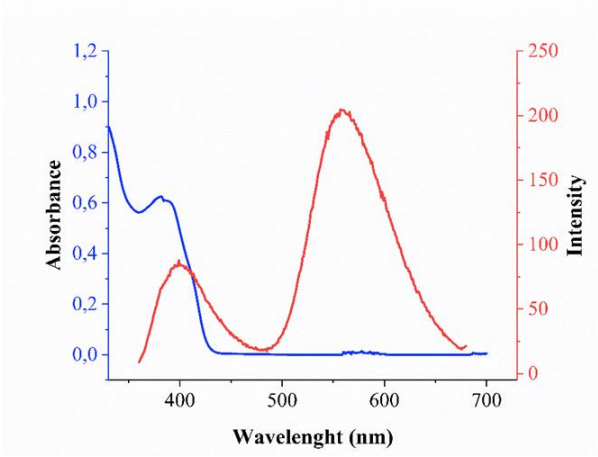

Figure 4. The UV-Vis spectrum of BTPCP

2.4. Fluorescence Spectroscopy

A novel benzothiazole substitute picolinoyl chloride derivate BTPCP's florescence properties was examined in two different solvents (Chloroform and H_2O) in Fluorescence Spectrophotometer. A novel benzothiazole derivate has been shown fluorescence properties in two solvents. Benzothiazoles have high quantum yields and large Stokes shifts due to their stable conjugated structure. The aromatic ring structure in the structure of benzothiazoles and the thiazole structure in the molecular skeleton provide the molecule with fluorescence properties. Excitation and emission wavelengths in the fluorescence spectrum of the BTPCP molecule were observed as 350 nm ($\lambda_{exc.}$) and 556 nm ($\lambda_{em.}$) in chloroform. The Fluorescence spectrum of novel BTPCP in chloroform is shown in Figure 5. Excitation and emission wavelengths in the fluorescence spectrum of the BTPCP molecule were observed as 350 nm ($\lambda_{exc.}$) and 564 nm ($\lambda_{em.}$) in H_2O. The Fluorescence spectrum of novel BTPCP in H_2O is shown in Figure 5.

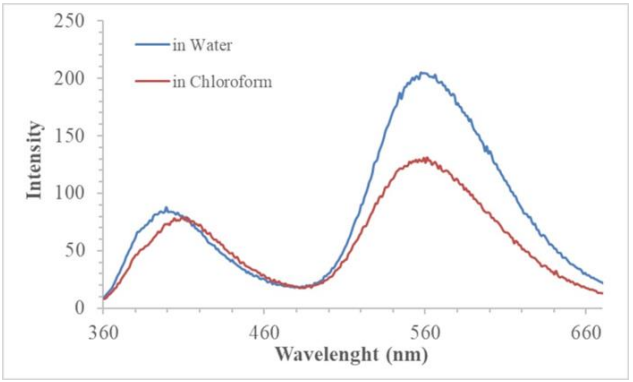

Figure 5. The Fluorescence spectrum of BTPCP in Chloroform and H_2O.

3. RESULTS

This study has two steps. In the first step of this study, novel benzothiazole substitute picolinoyl chloride derivate BTPCP's was synthesized by the condensation reaction of 2-(2-aminophenyl)-benzothiazole (1) with 2,6-Pyridinedicarboxylic acid chloride (2) (Scheme 1.). The chemical structure of compound BTPCP was characterized by spectroscopic methods (FT-IR, ^{1}H-NMR, ^{13}C-NMR) (Figure 1- Figure 3). The proposed structures are full agreement with the all spectroscopic data. In the FT-IR spectrum of BTPCP showed characteristic NH, C=N, C=O and C-Cl stretching bands at 3149, 1742, 1579, 1689 and 752 cm^{-1}, respectively [14]. (Figure 1.) In the ^{1}H-NMR spectrum, the low field singlet at 13.64 ppm was assigned to NH groups, doublet at 8.95 ppm ($H_{1.}$), multiplet at 8. 64-8.55 (H_2, H_3), 8.35 ppm doublet at (H_8, H_{11}), multiplet at 8.26–8.10 (m, 2H, H_4, H_7), 7.60–7.38 (m, 2H, H_5, H_{10}), 7.14–7.19 (m, 2H, H_6, H_9.) were assigned to the aromatic C-H. (Figure 2.) The carbonyl groups amide and acyl chloride peaks in the ^{13}C-NMR spectrum were confirmed at 168.5, 165.3 ppm respectively. The benzothiazole ring -*S*-*C*=*N*- aromatic carbon was confirmed at 164.3 ppm. The pyridine ring carbon atoms -*N*-*C*=*C*- peak at 162.6 ppm, -*C*-*C*=*N*- peak at 154.3 ppm, -*N*-*C*=C- peak at 152.5 ppm, the other aromatic carbons peaks between 164.3 and 120.7 ppm (Figure 3.).

The second step of this study, novel benzothiazole substitute picolinoyl chloride derivate BTPCP's the photophysical properties were determined by using UV-Vis spectrophotometer and Fluorescence spectrophotometer.

The absorption and fluorescence spectrums of BTPCP performed to its interaction in different solvents such as H_2O and chloroform. The UV-Vis spectrum of BTPCP is examined in chloroform, it has seen that it has two different absorbances at 324 and 382 nm wavelengths. (Figure 4.) Considering the UV spectra; when BTPCP was excited at 401 nm, emission of BTPCP was sighed at 556 nm with a large stokes' shift of 155 nm in the fluorescence spectrum in chloroform (Figure 5). And when BTPCP was excited at 350 nm, emission of BTPCP was monitored at 564 nm with a large stokes' shift of 158 nm in the fluorescence spectrum in H_2O (Figure 5).

Benzothiazole-based fluorescent sensor have emerged as powerful tools in chemosensor technology due to their photophysical properties and selective fluorescence quenching upon interaction with metal ions. The incorporation of electron-donating groups such as prydine heterocyle into an extended π-conjugated system enables benzothiazole heterocycles to function as efficient acceptors chromophores [25].

4. DISCUSSION AND CONCLUSION

Benzothiazole derivates have been play important role in chemical, biological and pharmacological reactions because of its heterocyclic structure that exhibit various important biological activities such as anti-inflammatory, antidiabetic, antibacterial, analgesic, anticancer, etc. Benzothiazole derivatives compounds are an important group of organic compounds with their properties that play an important role in chemical, biological and pharmacological reactions, as well as applications such as sensors and chemosensors for materials science. In this study, novel benzothiazole derivate potential chemosensor 6-((2-(benzothiazol-2-yl)phenyl)carbamoyl)picolinoyl chloride (BTPCP) has been successfully synthesized and characterized. The fluorescence properties of the synthesized molecule make into this molecule interesting in sensors studies. BTPCP is a compound that has the potential to be used in the detection of heavy metal pollution. It has been stated in the literature that compounds with similar molecular structures are sensitive and selective to Cu^{+2} ions, BTPCP a strong candidate for the detection of heavy metal ions. BTPCP is estimated that this new benzothiazole derivate will create a new perspective for research in many different fields such as material science, chemistry, biology, medicine, etc.

Acknowledgement

Assoc. Prof. Dr. Selahattin BOZKURT is gratefully acknowledged for helpful suggestions.

REFERENCES

[1] J.H. Wang, M. Li, D. Li, Chem. Sci. 4 (2013) 1793–1801.
[2] M.K. Amini, B. Khezri, A.R. Firooz, Sensor Actuat B-Chem. 131 (2008) 470–478.
[3] A.D. McFarland, R.P.V. Duyne, Nano Lett. 3 (2003) 1507–1511.
[4] H.S. Jung, M.S. Park, J.H. Han, J.H. Lee, C. Kang, J.H. Jung, J.S. Kim, Chem. Commun. 48 (2012) 5082–5084
[5] K.R. Dalton, M. J. Orr, A. J. Kwong, K. K. Deibler, H. H. Munshi, C. S. Bridges, T. J. Chen, X. Zhang, H. D. Lacorazza, K.A. Scheidt, ACS Medicinal Chemistry Letters 2023 14 (5), 606-613.
[6] J.P. Vacca, J.P. Maxwell, B. Williams, J.H. Come, S. Throner, World Intellectual Property Organization, WO2023064586 A1 2023-04-20 | Language: English, Database: Caplus ESPACENET
[7] J. Ling, J. Liu, World Intellectual Property Organization, WO2014183300 A1 2014-11-20 | Language: English, Database: CAplus ESPACENET
[8] Ge, H. Zhang, P. Wang, Chem. Soc. Rev. 40 (2011) 3483–3495; L.-J. Fan, Y. Zhang, C.B. Murphy, S.E. Angell, M.F.L. Parker, B.R. Flynn, W.E. Jones Jr., Coord. Chem. Rev. 253 (2009) 410–422.
[9] E. Hrishikesan, C. Saravanan, P. Kannan, Ind. Eng. Chem. Res. 50 (2011) 8225– 8229.
[10] J. Chan, S.C. Dodani, C.J. Chang, Nat. Chem. 4 (2012) 973–984.
[11] Q. Zou, H. Tian, Sensor Actuat. B-Chem. 149 (2010) 20–27.
[12] X. Zhang, Y. Shiraishi, T. Hirai, Tetrahedron Lett. 48 (2007) 5455–5459.
[13] A. Misra, M. Shahid, J. Phys. Chem. C 114 (2010) 16726–16739.
[14] H. E. Gülbaş, S. Bozkurt, E. Halay, J. Heterocycl. Chem. 2023, 60(7), 1223.
[15] O. A. Bozdemir, R. Guliyev, O. Buyukcakir, S. Selcuk, S. Kolamen,G. Gulseren, D. Nalbantoglu, H. Boyaci, E.U. Akkaya, *Journal of the American Chemical Society,* 132 (2010), 8029-8036.
[16] F.D. Natale, A. Lancia, A. Molino, M.D. Natale, D. Karatza, D. Musmarra, J. Hazard. Mater. 132 (2006), 220–225
[17] A. Renzoni, F. Zino, E. Franchi, Environ. Res. A 77 (1998) 68–72.
[18] J.M. Benoit, W.F. Fitzgerald, A.W.H. Damman, Environ. Res. A 78 (1998) 118–133.
[19] J. H. Wanga, Y. M. Liub, Z. M. Donga, J. B. Chaob, H. Wang, Y. Wanga, Journal of Hazardous Materials 382 (2020) 121056
[20] S. Das, H. K. Indurthi, P. Asati, P. Saha, D. K. Sharma, Dyes and Pigments 199 (2022) 110074.
[21] G. Dhaka, J. Singh, N. Kaur, Inorganica Chimica Acta 462 (2017), 152–157.
[22] R. Hussain, M. Ashraf, S. Khan, F. Rahim, W. Rehman, M. Taha, A. Sardar, Y. Khan, I. Khan, S.A.A. Shah, J. Mol. Struct. 1295 (2024) 136582.
[23] A. Sardar, O-ur-R. Abid, S. Daud, B.A. Shah, W. Shahid, M. Ashraf, M. Fatima, S. Ezzine, A.Shareef A.Wadood, H.A. Al-Ghulikah, S.A. Alissa, Arab. J. Chem. 15 (2022) 104300.
[24] A.K. Jain, S. Sharma, A. Vaidya, V. Ravichandran, R.K. Agrawal, Chem. Biol. Drug Des. 81 (2013) 557–576.
[25] Md. Mohasin, Z. Alam, S. Ahmad ,U. Salma , Q. Ullah , S. A. Khan, J.Mol.Struc.,1336 (2025), 142034.

[26] G.C. Santos, Y.G. Kappenberg, J.M. Rosa, A. Ketzer, M.A. Martins, G. Banacorsa, J. Photochem. Photobiol., A 444, (2023), 114900.
[27] T. Jabeen S. Aslam M. Yaseen, M.J. Saif, M. Ahmad, S.A. Al-Hussain M.E.A. Zaki, J. Saudi Chem. Soc. 27 (2023) 101679.
[28] Y. Khan, S. Khan, R. Hussain, A. Maalik, W. Rehman, M.W. Attwa, R. Masood, H. W. Darwish, H.A. Ghabbour, Pharmaceuticals, (Basel) 16 (2023) 1650.
[29] A. Khamitova, D. Berillo, A. Lozynskyi, Y. Konechnyi, D. Mural, V. Georgiyants, R. Lesyk, Mini. Rev. Med. Chem. 24 (2024).

Volume 14, Issue 2, Page 225-239, 2025 https://doi.org/10.46810/tdfd.1618491 Research Article

BİNGÖL UNIVERSITY

Türk Doğa ve Fen Dergisi
Turkish Journal of Nature and Science
www.dergipark.gov.tr/tdfd

Prediction of Turkish Constitutional Court Decisions in Terms of Admissibility and Violation of Rights With Artificial Intelligence

Emrah AYDEMİR[1*], Yusuf KAÇAR[2], Halil İbrahim CEBECİ[1], Görkem Kayacık[2]

[1] Sakarya University, Business Faculty, Management Information System Department, Sakarya, Türkiye
[2] Sakarya University, Law Faculty, Sakarya, Türkiye
Emrah AYDEMİR ORCID No: 0000-0002-8380-7891
Yusuf KAÇAR ORCID No: 0000-0002-0584-5702
Halil İbrahim CEBECİ ORCID No: 0000-0001-5058-7741
Görkem KAYACIK ORCID No: 0000-0001-7530-2722

**Corresponding author: emrahaydemir@sakarya.edu.tr*

(Received: 12.01.2025, Accepted: 04.06.2025, Online Publication: 27.06.2025)

Keywords
Constitutional court, Artificial intelligence, Individual application, Violation of rights, Admissibility

Abstract: The digitization of legal texts and advances in information processing theories and technologies have triggered several transformations in both the practice and teaching of law in recent years. Techniques developed in areas such as artificial intelligence, natural language processing, text mining, and machine learning have drawn the attention of legal practitioners and academics to this field. It is possible to remove obstacles to access to justice, improve legal security and certainty, and solve practical problems faced by legal practitioners by employing assistive tools to be created by using artificial intelligence technologies in the field of law. This study aims to develop an algorithm to predict the results of the Constitutional Court of the Republic of Turkiye on individual applications in terms of admissibility and whether there is a violation of rights by using machine learning and natural language processing techniques. In the study, the texts in the "Facts" title of the reference texts were used. A success rate of 91.56% was achieved for admissibility and 97.18% for whether there was a violation of rights. The study is unique in its field in that it performs a two-stage prediction task regarding admissibility and merit, provides a highly representative model since it includes all processable data, does not use a data augmentation method, and has a high success rate.

Yapay Zekâ ile Türk Anayasa Mahkemesi Kararlarının Kabul Edilebilirlik ve Hak İhlali Açısından Tahmini

Anahtar Kelimeler
Anayasa mahkemesi, Yapay zeka, Bireysel başvuru, Hak ihlali, Kabul edilebilirlik

Öz: Hukuk metinlerinin dijitalleştirilmesi ve bilgi işleme teorileri ve teknolojilerindeki ilerlemeler, son yıllarda hukukun hem uygulamasında hem de öğretiminde çeşitli dönüşümleri tetiklemiştir. Yapay zeka, doğal dil işleme, metin madenciliği ve makine öğrenmesi gibi alanlarda geliştirilen teknikler, hukuk uygulayıcılarının ve akademisyenlerin dikkatini bu alana çekmiştir. Hukuk alanında yapay zeka teknolojilerinin kullanılmasıyla oluşturulacak yardımcı araçların kullanılmasıyla adalete erişimin önündeki engellerin kaldırılması, hukuki güvenliğin ve kesinliğin artırılması ve hukuk uygulayıcılarının karşılaştığı pratik sorunların çözülmesi mümkündür. Bu çalışmada, makine öğrenmesi ve doğal dil işleme tekniklerini kullanarak Türkiye Cumhuriyeti Anayasa Mahkemesi'ne yapılan bireysel başvuruların usülen kabul edilebilirliğini ve hak ihlali olup olmadığını tahmin eden bir algoritma geliştirmeyi amaçlanmaktadır. Çalışmada, referans metinlerin "Olgular" başlığındaki metinler kullanılmıştır. Kabul edilebilirlik için %91,56, hak ihlali olup olmadığı için %97,18 başarı oranı elde edilmiştir. Çalışma, kabul edilebilirlik ve liyakat konusunda iki aşamalı bir tahmin görevi gerçekleştirmesi, tüm işlenebilir verileri içerdiğinden oldukça temsili bir model sunması, veri artırma yöntemi kullanmaması ve yüksek bir başarı oranına sahip olması bakımından kendi alanında benzersizdir.

1. INTRODUCTION

For centuries, legal experts have used doctrinal research methods to respond to the changing needs of society in the face of social, political, economic, and technological changes. This method includes describing laws, annotating legal regulations and judicial decisions, solving practical problems, and making systematic and theoretical inferences from all these studies. Doctrinal legal research is focused on providing a systematic interpretation of the norms prevailing in law, analyzing the relationships between the rules, explaining troubling issues, and predicting future developments [1-5]. However, in parallel with the pace of change in today's world, the law's ever-increasing and ever-changing scope of regulations, as well as the accumulation of precedent decisions that make it very difficult to be followed properly, make the work of legal practitioners very difficult. Developments, especially technological ones, which create this difficulty, also bring along opportunities to overcome these difficulties [6,7].

In contrast to doctrinal research methods, empirical or quantitative research techniques are rarely used in the field of law, especially when compared to the Anglo-American legal system. However, the ever-increasing caseload makes it impossible for legal researchers to read, analyze and systematize important international and national court decisions relevant to their field. Therefore, in these days of big data in law, it is argued that doctrinal and quantitative legal research can be combined to gain greater benefits from developing law, especially through case law [2, 8].

Although there are various quantitative research methods, studies using artificial intelligence are particularly in trend today. Since the day artificial intelligence came of age, artificial intelligence-based technologies have been used in various areas of life, from health to education, commerce to communication, and transportation to business management. In parallel with the development of artificial intelligence, in recent years, the digitization of legal texts and advances in information processing theory and technologies have triggered various transformations in both the practice and teaching of law. Techniques developed in areas such as artificial intelligence, natural language processing, text mining, and machine learning have attracted the attention of legal practitioners and academics. It is now seen that these techniques are actively used both in solving problems that arise during the practical application of law and in researching academic issues related to law and legal institutions [2][1].
It is important to note that it is impossible to automate all legal tasks regularly performed by legal practitioners, given the state of current Artificial Intelligence (AI) technologies. These tasks require very high intellectual skills and are well beyond the capacity of existing AI techniques. However, this does not mean that no legal work can be performed using artificial intelligence techniques. On the contrary, today's techniques allow a number of legal tasks to be completed by specially designed programs[2] [6, 9].

A wide range of legal tasks such as scanning and summarizing long and complex documents that law practitioners encounter in the conduct of litigation [10-13], classifying electronically stored documents in terms of their relevance to the dispute being litigated [3], determining the type of punishment to be applied by performing risk analysis in criminal cases [4] [14, 15], gathering and organizing information in court files [5], evaluating evidence and witness statements, identifying precedent decisions related to the subject matter of the case and pointing similarities[6], and making a decision on a legal dispute[7,8,9] [16], can be performed with very high success rates using artificial intelligence technologies.

At this point, it is worth mentioning machine learning, which is also very important for our work. Machine learning algorithms allow us to construct useful computer models of complex phenomena that can detect patterns in data and extract rules from them. It is also the case that

[1] The concept of judicial intelligence has been coined to describe the use of artificial intelligence in law. This concept describes a wide range of artificial intelligence applications to help solve legal problems, from predicting judgments to suggesting relevant legislation and identifying similar cases [31].

[2] The work of courts and judges is essentially information processing. The parties to a case submit some information to the court, the court process proceeds in a specific procedural manner, and in the end, the output is still information. Although this information processing process may seem quite complex, very few of the decisions rendered in the judicial process are related to complex disputes. In particular, most procedural disputes can be resolved with a simple assessment. A relatively large number of substantive disputes are repetitive disputes without any distinctive features, and their outcomes are predictable. Therefore, it is possible to use artificial intelligence at least as an auxiliary tool in the resolution of many legal disputes [15].

[3] In the US, this service offered by the "eDiscovery" application using artificial intelligence technology has achieved 76.7% success rate.

[4] In an application called COMPAS developed in the US, judges can use artificial intelligence technology, which enables risk analysis in criminal cases, to decide on the detention of the suspect or defendant or the type of punishment to be applied in case of conviction [14, 15].

[5] For example, in China, supporting artificial intelligence systems developed by Alibaba and iFLYTEK assist judges by using a technology-based speech recognition system called "Natural Language Processing" (NLP) and image processing technology. These systems are able to organize trial transcripts with a high degree of accuracy and extract important information from a wide range of evidence. With the help of these artificial intelligence-based systems, a saving of 30% to 50% of the time spent in trials has been achieved [16].

[6] For example, an application developed in China called "The 206 System" significantly assists judges in collecting, classifying, and verifying the accuracy of evidence; extracting important information from the evidence and eliminating irrelevant matters; and interpreting the evidence [16].

[7] In a pilot scheme launched in China in 2017 for the first time in history, AI-based robots preside over "smart courts" and rule on relatively small-scale disputes such as copyright issues and online shopping complaints [16].

[8] It has been stated that the outputs of artificial intelligence algorithms, which are trained by introducing a vast amount of existing judgments and legal rules, may be biased and therefore may lead to serious problems during their use in judicial processes. For more information on this issue, which is called the "black box" problem, see [14, 16].

[9] Upon the widespread use of AI-based technologies in judicial proceedings, the Council of Europe has specifically addressed the issue within the framework of Article 6 of the European Convention on Human Rights (the right to a fair trial) and established a set of ethical principles on what a reliable AI should look like, see https://op.europa.eu/en/publication-detail/-/publication/d3988569-0434-11ea-8c1f-01aa75ed71a1.

machine learning techniques can produce "intelligent" results by identifying proxies and patterns in data when performing complex and abstract tasks - albeit without being able to connect to the underlying conceptual content of the information. Therefore, some of the tasks performed manually by law practitioners can be performed semi-automatically by programs created using machine learning techniques, thereby achieving practical benefits [9, 17-20]. Moreover, researchers who have started to use machine learning techniques in the field of law use methods that minimize information loss and conduct more complex quantitative analyses with high-dimensional data than researchers who use traditional statistical methods such as regression analysis and work on lower-dimensional data by reducing the data to one or a few variables [2].

With the methods developed using machine learning algorithms, a data set containing legal issues that have been litigated and judged in the past can be created and the patterns in this data can be automatically detected and these patterns can then be used to predict future legal issues. One of these methods, closely related to our study, is supervised learning. In this method, the machine is expected to identify relationships between data that has been previously categorized by humans. Even if the constructed "predictive model" has only a few percentage points higher prediction success than a standard legal expert, it can be incorporated into legal advice services as an auxiliary tool [9, 21]. An inspiring and pioneering study was conducted in the United States. Throughout 2002, the US Supreme Court's decisions, which are considered by legal scholars to be very difficult to predict, were attempted to be predicted using two different methods. The first involved a statistical model that predicted outcomes based on six general case characteristics; the second involved a large group of legal experts, each making specific and independent predictions about one or more cases. In the end, the machine was significantly more successful than the legal experts. The experts correctly predicted 59.1% of court decisions, while the machine correctly predicted 75 [22]. On the other hand, the human mind has significant cognitive limitations[10] when it comes to processing and comprehending large amounts of data or paperwork. Even if one has access to all relevant information, in many cases, it is impossible to have a complete understanding of all aspects of the case or to process all data without the help of technology [17, 23]. While quantitative predictive models are not a solution to all of the potential cognitive limitations of the human mind, transparency in the development of predictive models can provide effective means of addressing some of these problems [6, 17].

Turning to the practical importance of quantitative predictive models and their development, it should first be noted that making informed and useful predictions of likely legal outcomes and liability is one of the fundamental qualities of being a lawyer. Lawyers are regularly expected to make predictions about quite different legal regulations [6, 9, 21, 24]. In the ordinary course of life, a client presents a lawyer with a legal problem consisting of complex facts and objectives. The lawyer, in the presence of legal and factual uncertainties, uses his or her judgment, experience, legal knowledge, education, and other cognitive abilities and intuitions to reasonably predict the likely outcome of the legal problem or who is legally responsible for it; then, based on these predictions and other factors, the lawyer draws a plan of action for the client with respect to the legal problem [6, 9][11].

The ability to assess overall legal outcomes and levels of liability risk in an environment of significant legal and factual uncertainty is one of the core functions of a good lawyer. However, increasingly, the assessment of these possible outcomes may be the subject of automated or semi-automated computer-based analysis. There is a significant amount of data available to enable this to be done, and machine learning techniques are rapidly acquiring the qualities to perform such a task. It is argued that the combination of human reasoning and machine learning algorithms will yield superior results compared to the use of the human mind alone in performing various legal prediction tasks [9, 17].

One of the various legal prediction tasks mentioned is the prediction of court judgments. Techniques in machine learning and natural language processing provide tools for automatically analyzing legal materials to build successful predictive models for predicting the outcomes of court decisions [25-27]. Using machine learning, it is possible to have a computer perform quantitative analyses based on the words, phrases, syntax, semantic and morphology used in court decisions and predict the court's decisions based on these analyses. If the results can be predicted accurately enough, it can then be determined which factors are influential in the formation of court decisions. In parallel with this situation, the study aims to provide a high-performance model that will provide support to users who want to make individual applications to the Constitutional Court and thus minimize possible loss of time and effort. However, it should be noted at this point that our aim in predicting court decisions is limited to the available data and the approaches we use. The aim of the present study is not to predict what the outcome would be if a victim who believes that his or her rights have been violated were to go to court - although of course this study and others like it aim to get closer to this broader goal [8]. On the other hand, as in all decision support models, the model presented in this study does not produce decisions, it only supports the decision maker. In this sense, it cannot be said that the results produced by the model have a legal binding.

[10] "Human reasoners have well-documented cognitive biases, such as the availability heuristic, optimism bias, anchoring, confirmation bias, illusion of validity, and the frequency illusion." [17]

[11] "Do I have a case? What is our likely exposure? How much is this going to cost? Are these documents relevant? What will happen if we leave this particular provision out of this contract? How can we best staff this particular legal matter? These are core questions asked by sophisticated clients such as general counsels as well as consumers at the retail level." [17]

Although there are different articles trying to predict constitutional court results with machine learning approaches, it is certain that it needs development at certain points. In his study, Sert [33] focused only on constitutional court decisions focused on "public morality and freedom of expression" and questioned their acceptability in terms of content. The author considered the "subject of the application" and "the evaluation" titles in the rapporteur draft text as the basic data set. These contents are partially formal in structure created by the rapporteur. Mumcuoğlu [7], while predicting decisions based on content, unlike Sert [33] model, used the "facts" heading containing the applicant's narrative, and the dataset was created with "data augmentation" methods. This study will present a machine learning model that works with balanced datasets that estimate decision acceptability in terms of form and content, taking into account the potential limitations in Sert [33] and Mumcuoğlu [7] studies, taking the "facts" heading in the rapporteur draft text as the basic data. The model will not work only focused on certain application types but will consider all individual constitutional court applications.

Before discussing the benefits of predicting court decisions using machine learning and natural language processing techniques, it is necessary to mention the function and importance of court decisions. First, it should be emphasized that court decisions play a critical role in resolving legal disputes, in legal education, and in future court decisions as a cyclical process. This is because some court decisions become precedents for the courts at the same level and lower levels. Prosecutors and judges follow and use these decisions to practice their profession in a way that is consistent with the legal system in which they practice. At the same time, lawyers analyze these decisions to predict the likelihood of winning in the cases their clients consult them on [28]. On the other hand, legal systems ensure legal certainty, which is a part of legal security, through court decisions. These decisions are of great importance both in terms of showing how abstract rules will be applied to concrete cases and in terms of demonstrating the legal consequences of individuals' behaviors in a more striking way [21].

Rapid developments in the social economy have complicated social relations and conflicts, which has significantly increased the workload on legal practitioners. On the other hand, the monopoly of the modern state over the judiciary has raised people's expectations of impartial and fair trials from the courts of modern states. Ensuring the balance between workload and fair trial has become an important problem of our time. Nowadays, legal data is a strategic resource and has significant economic value. Analyzing legal data using artificial intelligence can offer effective possibilities to alleviate the burden on legal practitioners and improve the quality and efficiency of adjudication [29, 30].

In this context, the benefits of predicting court decisions using artificial intelligence techniques are manifold and touch more than one point. First, we should start with the public benefits. For citizens who are not law practitioners but who wish to use judicial mechanisms and who have the poor legal knowledge, the use of AI for case analysis can ensure that the fair trial process is not affected by human factors and regional differences that have the potential to undermine it [31]. Automated decision prediction systems can play a role in delivering high-quality and cost-effective legal advice to people who do not work in the legal field and have difficulty understanding its terminology [32]. It can also be used to overcome the shortcomings of the legal aid institution, which is suffering from insufficient funds, imbalance of the supply structure, and low efficiency of the supply method. Thus, artificial intelligence can be used as a complementary tool that overcomes the limitations of the work experience of legal practitioners and provides relatively objective results [31].

Another important public benefit is legal security and certainty. Efforts to increase legal security and certainty for the orderly functioning of the social, political, economic, and cultural life of society constitute an integral part of human history. The publication of legal rules and court decisions are among these efforts. Leaving aside the question of whether it is important to predict judicial decisions from rule of law and procedural justice perspectives, analysis of legal texts using artificial intelligence techniques can enhance legal certainty [33]. Predicting court decisions is an important aspect of understanding the legal consequences of our behavior [21].

Just as important as legal security and certainty are the fundamental human rights to be tried within a reasonable time and to have access to the courts. Systems based on advanced decision prediction algorithms can be employed in courts as mechanisms to assist decision-making [34]. These systems can quickly identify cases and detect patterns that lead the decisions to turn out in a certain way. They can also be used to prioritize applications by identifying which applications are likely to involve violations of rights. This prioritization could increase the speed with which courts resolve applications where a violation of rights is more likely. This could encourage people who do not apply to the court due to long waiting times to do so when they believe their rights have been violated. This could contribute to promoting the right of access to a court [25, 33, 34].

In addition to the benefits above, AI-based applications, as auxiliary tools, can serve the public interest by saving time, reducing errors in practice, and increasing consistency [7]; help increase efficiency in judicial services [27] and promote legal equality and transparency [32]; facilitate the effective promotion of mediation activities [27]; contribute to reducing the workload on courts [39]; help lawyers assess their clients' claims in a timely and objective manner [6]; finally, contribute to reducing the workload on lawyers and help more clients receive legal advice more quickly, cheaply and efficiently, which can trigger positive transformations in the practice of the legal profession [6].

1.1. Related Works

As mentioned above, artificial intelligence is used to predict the outcomes of court decisions. In a very prescient article, Lawlor [40] stated that in the future, computers would be able to analyze judicial decisions and predict their outcomes [40]. Today, more than 50 years after his work, natural language processing and machine learning technologies offer the possibility to analyze legal texts and, through this analysis, to successfully predict court decisions [25].

Especially in recent years, a significant number of studies have been published on predicting the judgments of various national and international courts by using the aforementioned techniques. For example, in a study by Aletras et al. [25] on the judgments of the European Court of Human Rights (ECtHR), a Support Vector Machine classifier was used to predict whether Articles 3, 6 and 8 of the European Convention on Human Rights were violated or not (binary classification) based on 584 judgments, with a success rate of 79% [25]. In another study, which also focused on ECtHR judgments and followed a similar methodology, a more comprehensive (3,132 judgments) and balanced data set was used. Unlike the previous study, the "law" heading in the judgments, which includes the legal arguments of the court related to the relevant case, was not taught to the machine. As a result, a 77% success rate was achieved. The researchers stated that their study was more representative than the previous study because it used a larger data set and that the system was less "biased" because they did not teach the system the "law" heading in the judgments [8].

Studies on the prediction of judicial decisions are not limited to the ECtHR. For example, Katz et al. [17] used more than 28,000 decisions of the US Supreme Court and attempted to predict both the judgment as a whole and the votes of each judge. As a result, this study achieved 71.9% success in predicting the judges' vote and 70.2% success in predicting the court decision as a whole [17]. Lage-Freitas et al. [21] tried to predict the decisions of the Brazilian appellate court with a dataset of 4,403 decisions and achieved 79% success [21].

The highest success rate we have witnessed in the previous studies belongs to the study of Şulea et al. [46]. Taking more than 126,000 decisions of the French Supreme Court since the 1800s as a dataset, this study, unlike other studies, worked on two separate classification tasks with six and eight components, rather than two components, and achieved a success rate of up to 97% [46]. It is possible to say that the number and quality of the decisions in the data sets played a role in the high success of this study. In addition, the fact that the NLP method yields more successful results in inflected languages such as French than in agglutinative languages such as Turkish can be counted among the reasons for this result. On the other hand, Virtucio et al. [19], who studied the Philippine Supreme Court, obtained 59%, one of the lowest results in the previous studies, despite having a dataset of more than 27,000 decisions. The authors believe that this is due to the fact that the decisions in their dataset are structurally weaker than the decisions of the supreme courts in other countries, that the decisions are related to a wide variety of areas of law, and that there is no platform where they can obtain the decisions in a more organized manner [19].

It is necessary to mention two studies that are closely related to our study in terms of utilizing the decisions of the CCT as a data set. In a paper published in May 2021, a study was conducted on a total of 480 judgments on "public morality" (92 judgments) and "freedom of expression" (388 judgments) and tested whether the system created could successfully fulfill the two-component classification task (violation or no violation). The authors also included "inadmissible" judgments in the class of no violation of rights. It was stated that the experiment achieved an average success rate of 90% [33]. Another study published in July 2021 was not limited to the Constitutional Court, but also attempted to predict the decisions of many other high courts in Türkiye. In relation to the subject of our work, Mumcuoğlu et al. used a dataset of 1290 Constitutional Court decisions (149 no violations and 1141 violations) and achieved 91.8% success [7].

In addition to these studies, it has been attempted to make decision predictions based on the previous decisions of both higher courts and lower courts in areas such as criminal law, private law, family law, etc., and satisfactory results have been reached in a majority of the studies [26-29, 31, 32, 34].

1.2. Constitutional Court of The Republic of Turkiye

Constitutional Courts in the world came to the agenda after it was realized that the legislative power could make unconstitutional acts. As a result, constitutional courts in Europe were established independently from other judicial bodies, and thus, the model of constitutional jurisdiction based on a special court established for this purpose developed in Continental Europe, in addition to the example of constitutional jurisdiction in the USA. Although independent constitutional courts were first established in countries such as Austria, Czechoslovakia, Spain and Ireland following the First World War, with the spread of constitutionalism movements, especially after the Second World War the number of constitutional courts in the world increased rapidly and constitutional courts were established in countries such as Italy, Germany and France in Continental Europe [35]. The Republic of Türkiye was also included in the constitutionalism wave of this period and the "Constitutional Court of the Republic of Türkiye" (CCT) was established with the 1961 Constitution.

The main task of the constitutional courts is constitutionality review. In this context, constitutional courts review the constitutionality of laws and other legislative acts through abstract reviews and concrete control of norms. In addition to these duties, constitutional courts also protect constitutional values and fundamental rights and freedoms regulated in constitutions. Concordantly, a review mechanism called the individual

application procedure has also been developed to ensure the protection of individuals who believe that their constitutional rights and obligations have been violated by the public power. This mechanism is currently enshrined in the constitutions of Germany, Hungary, Portugal, Poland, the Czech Republic and Slovakia [36]. The first examples of the individual application procedure in the world were implemented in Latin countries before Europe [37]. In Türkiye, on the other hand, the individual application procedure is generally inspired by examples from continental Europe.

In the CCT, there was no such review mechanism prior to 2011. The 1921, 1924 and 1961 Constitutions and the first version of the 1982 Constitution did not regulate the individual application procedure. However, following the 2010 amendment to the Constitution, with the addition made to Article 148 of the 1982 Constitution of the Republic of Türkiye (CRT), the individual application procedure was added to the duties of the CCT. Following the constitutional amendment, the individual application procedure entered into force on September 23, 2012.

In Türkiye, the scope, proceeding, and consequences of the individual application procedure are regulated in Article 148 of the CRT and Law No. 6216. According to the CRT, anyone who believes that one of his/her fundamental rights and freedoms regulated in the Constitution and the European Convention on Human Rights (ECHR) has been violated by the public power may file an individual application to the CCT after exhausting the legal remedies. Other issues regarding the individual application procedure are regulated by Law No. 6216 on the Establishment and Trial Procedures of the Constitutional Court[12]. According to the relevant article of the CRT and the articles of the Law No. 6216 on individual application, anyone in Türkiye - real persons as well as private legal entities – whose one of the fundamental rights and freedoms enshrined in the CRT and the ECHR has been violated by public power can request the elimination of the consequences of this violation through an application to the CCT. However, the scope of the individual application procedure is limited both in terms of the subject matter of the application, the applicant and the period of time required for the application. With the individual application procedure, the Republic of Türkiye mainly aims to prevent the violation of the fundamental rights and freedoms of individuals protected by the CRT by public power, but it also aims to reduce the large number of applications against Türkiye to the European Court of Human Rights (ECtHR) and to create an effective judicial remedy to review these applications within the country before applying to the ECtHR [38]. Therefore, the scope of the individual application is limited to the fundamental rights and freedoms regulated in the ECHR among the fundamental rights and freedoms enshrined in the CRT.

Following an individual application, CCT conducts a two-stage examination. At the admissibility stage, it is evaluated whether the application fulfills the conditions stipulated in the law. At this stage, CCT examines the application in terms of person, place, time and subject matter, and decides; whether the ordinary remedies in domestic law are exhausted, an apparent violation in the application is existed and concrete evidence therein is included, the right of application is abused, the application has constitutional relevance/weight, and the damage caused by the violation of rights is significant [41]. This examination is carried out by the Commissions established within the Court and composed of two members of CCT, and a unanimous decision has to be taken as to whether the application meets the requirements. The Commission sends the applications that are deemed "admissible" to the Sections of the CCT, which are composed of a president and six CCT judges. The second stage of the examination of the applications, the examination on the merits, is carried out by the Sections. If the Sections are to render a decision that contradicts a previous decision or if they believe that the matter is important due to its nature, they may send the application to the Plenary Assembly, which is composed of all members of the CCT, and the Plenary Assembly shall decide on the application. If the Sections or the Plenary Assembly are of the opinion that a fundamental right and freedom has been violated, the relevant unit decides that the right has been violated, otherwise it decides that there has been no violation.

In reaching the above-mentioned decisions, CCT makes use of its rapporteur judges, as set out in Law No. 6216 and the Rules of Procedure of the Constitutional Court (Rules of Procedure)[13]. The rapporteurs prepare draft decisions on the relevant application and submit them to the Committees, Sections or the Plenary Assembly. The rapporteurs prepare these draft decisions in accordance with the format set out in the Rules of Procedure. In addition, the Research and Jurisprudence Unit established within the CCT examines the draft judgments in terms of consistency and development of case law, legal terminology, and spelling rules before they are discussed in the Plenary Session and the Sections. As a result, each decision of the CCT has a systematic style and literary structure in accordance with a certain format.

If there is an admissible application, the CCT first decides whether there is a violation of a right, and then, if there is a violation, whether there is a way to eliminate the consequences of this violation [42]. As a result, generally, the CCT awards pecuniary and/or non-pecuniary compensation for the damages caused by the violation of rights after the CCT renders a decision on the existence of a violation of rights. However, there is no limitation in the constitution or the law regarding the nature of the reparations that the CCT may rule. On the other hand, if the violation stems from a court decision - although it cannot retry the case itself - it sends the dispute that led to

[12] For the Turkish text of the law, see: https://www.resmigazete.gov.tr/eskiler/2011/04/20110403-1.htm, accessed on 29.03.2023.

[13] For the Turkish text of the law, see: https://www.resmigazete.gov.tr/eskiler/2012/07/20120712-18.htm, accessed on 29.03.2023.

the violation to the court that issued the decision for retrial; thus, it eliminates the consequences of the violation. Violation judgments are notified to the Ministry of Justice of the Republic of Türkiye together with those concerned and published on the Court's website. In addition, important judgments of the Court on individual applications are published in the Official Gazette. Thus, it is aimed that the legislative, executive, and judicial bodies are informed about the issues that cause violations of rights and develop policies to eliminate similar violations in future cases.

Since 2012, when it entered into force in Türkiye, the individual application procedure has had a significant impact on the protection of fundamental human rights, the reduction of human rights violations by the public power and the formulation of human rights-centered policies. At this point, individual applications have both direct effects by means of reparation of the harm of the person whose right is violated, and also have indirect effects [43]. When the CCT finds a violation in an individual application, if the violation stems from a law or an administrative regulatory act, it informs the relevant institutions about the normative regulation that led to the violation; if the violation stems from a judicial decision, it requests the court that issued the decision to conduct a retrial in accordance with the CCT 's violation decision. In the case of a violation of rights arising from a law or legislative act, the CCT also sends the violation decision to the Grand National Assembly of Türkiye ("GNAT") and draws the attention of it to the norm that caused the violation. Although this notification of the CCT is not a directive to the GNAT to amend or repeal the norm, it constitutes a contribution to the legislature towards the improvement of fundamental rights and freedoms and has a positive impact on the quality of the legislative function [44]. Thus, it increases the awareness of the administration, the legislature and the judiciary on fundamental rights and freedoms while fulfilling their duties. On the other hand, the CCT 's evaluations on fundamental rights and freedoms through individual application enables CCT to have a rights-centered approach in both abstract reviews and concrete control of norms [43].

While the individual application procedure fulfills the above-mentioned functions in terms of the protection of fundamental rights and freedoms, it also encounters some problems. At this point, it is noteworthy that the number of individual applications to CCT is increasing day by day. On the other hand, the fact that the applications do not have the fundamental rights and freedoms-oriented perspective required by the individual application procedure, the fact that the applicants consider the individual application procedure as an appeal to the higher court as a continuation of the judicial process, and the lack of knowledge of both individuals and lawyers as to which cases involve a violation of fundamental rights and freedoms and whether this violation can be remedied through the individual application procedure increase the workload of the Court and thus make it difficult to conclude the applications within a reasonable time and reduce the efficiency of the individual application procedure [45]. The Individual Application Statistics published by the CCT every year clearly reflect this problem.

According to the CCT's Statistics on Individual Applications dated 2022, a total of 470,938 individual applications were made to the CCT between 2012 and 2022. 23.3% of these applications were made only in 2022. It is also observed that the CCT's workload has been on a general upward trend and has increased significantly, especially in the last two years [72]. Numbers according to years are given in Table 1. In parallel, the number of applications pending before the Court has been steadily increasing, from 17,046 to 72,278 in 2022 [72]. At this point, although it is seen that the CCT's workload has increased significantly, it is possible to draw inferences regarding the source of this increase when the statistics of the CCT's decisions rendered as a result of the applications are analyzed. According to 2022 data, CCT ruled inadmissibility in 298,059 of the 375,017 individual applications it has finalized to date. This number corresponds to 79.5% of the adjudicated applications [73].

Table 1. Number of Received and Adjudicated Individual Applications by Years

Year	Received	Ratio (%)	Adjudicated	Ratio (%)
2012	1342	0.28	4	0.00
2013	9897	2.10	4924	1.31
2014	20578	4.37	10926	2.91
2015	20376	4.33	15368	4.10
2016	80756	17.15	16089	4.29
2017	40530	8.61	89651	23.91
2018	38186	8.11	35357	9.43
2019	42971	9.12	39238	10.46
2020	40402	8.58	45197	12.05
2021	66121	14.04	45227	12.06
2022	109779	23.31	73036	19.48
Total	470938		375017	

Inadmissibility decisions are rendered in the case of individual applications that have not been filed in accordance with the procedure prescribed by the CCT and the law. In addition, the CCT may decide on the inadmissibility of applications that are not of importance for the application and interpretation of the CRT or for the determination of the scope and limits of fundamental rights and where the applicant has not suffered any significant damage, as well as applications that are manifestly ill-founded. In these cases, while seeking the existence of both elements together, the CCT may not decide on inadmissibility even in cases where it does not consider constitutional importance and at the same time considers that the applicant does not suffer significant damage [47] . In this instance, the Court has a margin of appreciation. The majority of the inadmissibility decisions are cases where the facts and circumstances of the violation of rights cannot be clearly concretized in the application, which is expressed as "manifestly ill-founded". Adjudicated applications by judgment type are below in Figure 1.

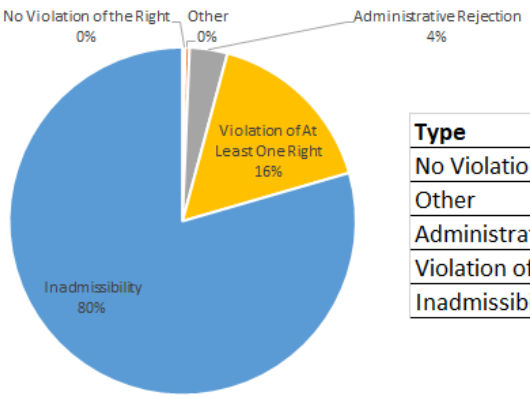

Type	Number	Ratio
No Violation of the Right	960	0,26
Other	1524	0,41
Administrative Rejection	13210	3,52
Violation of At Least One Ri	61264	16,34
Inadmissibility	298059	79,48

Figure 1. Adjudicated Applications by Judgment Type

These data on the individual application procedure show that both the applicants and the lawyers, who are the legal experts filing the applications, fail to correctly apply the format prescribed by the CCT in their applications[14], fail to correctly judge which events and facts show that fundamental rights and freedoms have been violated, thus causing the workload of the CCT to increase, reducing the efficiency of the individual application procedure and making it difficult for the CCT to finalize individual applications within a reasonable time. At this point, when annual statistics are analyzed, although the performance of the CCT can be considered satisfactory in terms of coping with the workload [48], looking at the 2021 and 2022 statistics, this performance of the CCT does not seem to be sustainable in the long term, given the increasing number of pending cases. These problems negatively affect the realization of the CCT's objectives of preventing violations of fundamental rights and freedoms by the public power and reducing the number of applications from Türkiye to the ECtHR. Failure to finalize the applications within reasonable periods of time will cause the CCT to be unable to fulfill its function as a "domestic law filter" in front of the applications to the ECtHR, and will also lead to the risk that the CCT will issue low quality decisions in order to meet the large number of applications while establishing the jurisprudence that will ensure the protection of fundamental rights and freedoms due to the increasing workload. Ultimately, the status of the individual application procedure as an effective remedy before the ECtHR will be jeopardized [38].

In order to make the workload of the CCT sustainable, it is necessary to reduce the number of individual applications and to improve the decision-making capacity of the CCT [49]. Problems similar to the above-mentioned problems of the CCT also exist at the ECtHR. Artificial intelligence-based systems are one of the means that the ECtHR is working on to cope with these workload problems. In the "Symposium on Workload in Individual Application and Solution Proposals" held by the CCT on March 1, 2022, to determine the strategies to deal with these problems, it was brought to the agenda whether artificial intelligence is planned to be used in handling this workload, along with many solution proposals put forward. CCT officials stated that studies are being carried out in this direction and that the issue is on the Court's agenda (*Bireysel Başvuruda İş Yükü ve Çözüm Önerileri Sempozyumu*, 2022, p. 77).

2. MATERIAL AND METHOD

The ability to analyze data in unstructured form can provide researchers with new perspectives, especially in the field of social sciences. In this sense, text mining methods are needed in order to process texts written in natural language properly. Text mining is an information-supported semi-automatic process that enables the extraction of implicit and useful information from unstructured data [50].

Most of the content that is the subject of text mining is texts produced in natural language. Natural Language Processing (NLP) is a set of special techniques based on Syntax (Syntax), linguistics (Morphology) and semantics (Semantics) that enable the analysis of such content [51]. Although NLP approaches provide significant benefits in many languages, the performance of the analyzes is affected due to the additive and rich formal language structure of Turkish [52]. In this study, it is aimed to establish a model that can predict the probability of acceptance of possible applications to the constitutional court, in terms of content and form, by processing the text mining methods of decision texts in semi-structured form produced in natural language. The process of the model to be constructed for this purpose is given in Figure 2.

[14] The CCT prescribes the format of individual applications with the help of a pre-prepared form that meets the requirements of the law and explains how to fill out the form in its guidelines (CCT, n.d.)

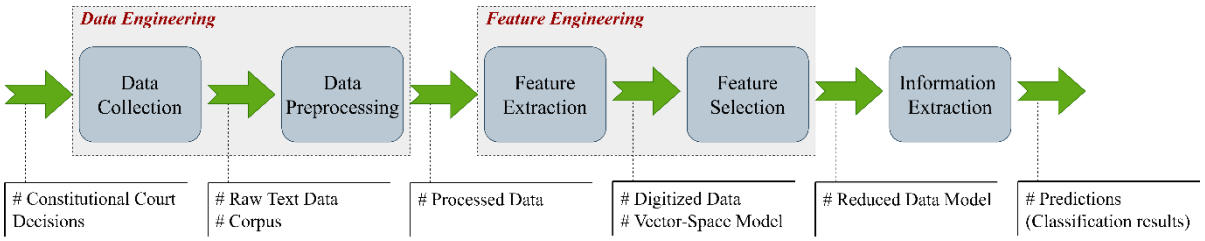

Figure 2. The process of the text mining approach in the study

Data engineering, with its most basic definition, is obtaining the data set and processing it to make it quality. Afterwards, the data set is digitized, and the necessary features are selected to make it ready for analysis from the feature engineering stage. In the last stage, information extraction is carried out with the estimation (classification) model.

2.1. Data Collection

Similar to other mining processes, the first step in text mining applications is to obtain data. The main data source is generally open access in the web environment and data is extracted with special techniques called scraping. The main output of the data collection phase is a collection of documents called corpus.

2.2. Data Preprocessing

The performance of analysis processes in text mining is directly related to the quality of the corpus. If the data set in the corpus is not properly formatted, in other words, if the data quality is not obtained, a situation known as the "Garbage-in, Garbage-out" phenomenon may be encountered. In this sense, data preprocessing steps are critical [53, 54].

The first step in the preprocessing processes is tokenazing, in which texts are broken down into their smallest units. During this process, each word, punctuation mark, symbol, etc. is converted into tokens. Optionally, the unit list can be extended by creating word groups with n-gram techniques [55, 56]. The second stage is the standardization of the list of tokens. For this purpose, numbers, punctuation marks, symbols, abbreviations, white spaces are removed first. Capital letters are converted to lowercase letters. Thus, a list of only lowercase words is obtained [56]. With the standardized list filtering stage, it takes its final form before linguistic preprocessing. During the filtering step, stop words are removed [55, 56]. For this process, the Turkish stop word list consisting of 179 words in the NLTK library in Python was used. In addition, words lower than a certain frequency should be removed and the matrix size should be reduced to a controllable level. In the last stage, words are cleaned from their suffixes and reduced to their roots. In addition, the function of these words in the sentence, the types of words and phrases are also performed at this stage with the sentence part-of-speech tagging method [56-59]. At the end of this stage, different attributes are added to each word and phrase.

After the data preprocessing stage, the data set, which has been processed and improved in quality, is transferred to the feature engineering process with the term document matrix structure.

2.3. Feature Extraction

The term document matrix obtained as a result of the preprocessing process must be digitized with a special transformation called vector-space model before the information extraction step. This process actually consists of rearranging the texts with some numerical conversion functions. At this stage, which is called feature extraction, there are different levels of vector space models.

Term Frequency – Inverse Document Frequency (TF-IDF) method, which performs numerical conversion at character and word level, is one of the most preferred methods [55]. TF-IDF calculates a value depending on the proportional frequency of the number of a word in the document and in the total corpus, together with the calculated value, how much information that word carries, or how important the world, is determined.

The Word2Vec method, which transforms at the word level, is the word embedding technique that has been preferred in academic studies in recent years with its high performance. The method, which is a prediction-based unsupervised learning approach, was invented in 2013 [60]. In matrix-based transformation, digitization according to the difference in operation of inputs and outputs is performed by Continous Bag of Words (cBOW) and SkipGram methods [61].

While the importance of the word in the document is taken into account in the TF-IDF method, it is independent of the semantic relationship [63]. In the Word2Vec method, the semantic relationship is provided to a certain extent by the window_size parameter [62]. The Doc2Vec method, which is a Document-Level embedding technique, is a special artificial neural network-based method that transforms the document as a whole into a numerical matrix, taking into account the semantic relationship. The difference of the method, which works with the Distributed Memory Model Of Paragraph Vectors (PV-DM) and Paragraph Vector With A Distributed Bag Of Words (PVDBOW) learning methods, from the Word embeddings methods is that it uses documents as input [64].

After the features at different levels are extracted, the newly formed matrix is directed to the feature selection stage.

2.4. Feature Selection

The high size of the matrix obtained after feature extraction necessitates reducing it to controllable dimensions before the information extraction stage. In this context, the process of identifying features that will potentially contribute to the analysis is called feature selection. Extra trees, which are an ensemble expansion of the random forest approach, are often preferred when the datasets are very large, especially in terms of bias, high variance and computational ease [65]. In this approach, different from the random forest approach, different decision trees are derived by considering the entire data set and learning is performed by combining them with an ensemble approach.

2.5. Information Extractaion

The information extraction stage is basically the fulfillment of data mining tasks such as classification, clustering, etc. on the matrix from the feature selection stage. In this study, the ensemble model, in which two different binary classification approaches are integrated, is organized as follows.

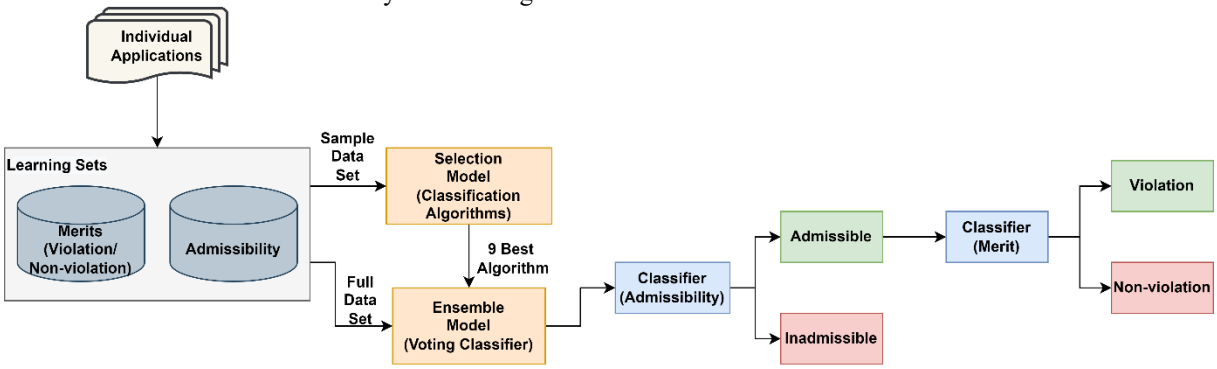

Figure 3. Two-stage classification-based integrated information extraction model

One of the important problems in machine learning approaches is overfitting and various methods are used to avoid this situation [66]. In this study, cross validation (k=10) was preferred to reduce the effect of heterogeneous learning sets on the learning process [67]. In addition, considering the excessive learning tendency of some classification models, the ensemble model was established in which the learning of different numbers of models was evaluated together [68]. Thanks to this model, it has been tried to reduce the effects of overift models on total performance with integrated evaluation instead of making a single model's learning performance-oriented estimation [69, 70]. In this two-stage classification model, first of all, predictions are made with a large number of classification models in a part of the data set. Afterwards, a pretrained model is created by integrating the algorithms with the best performance in an ensemble approach in order to make a prediction across the whole data set.

3. RESULTS

The information to be interpreted in the study was obtained in 5 stages, as depicted in Figure 4 below, depending on the the process given in the methodology section.

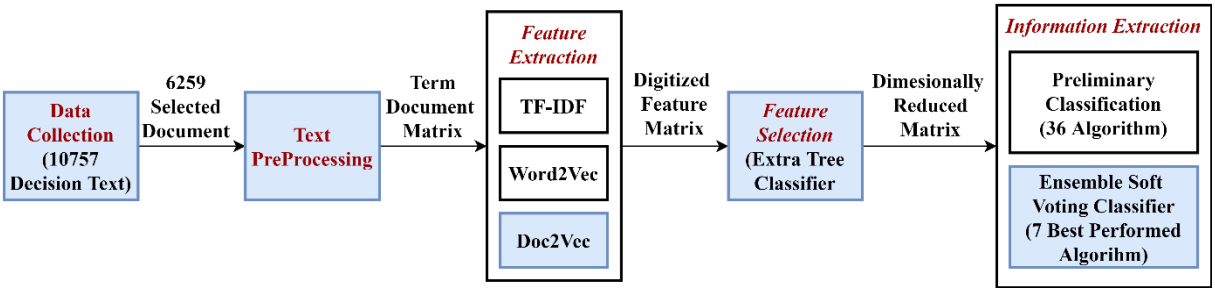

Figure 4. Text mining application process of the study

First, the data collection process was carried out. In this sense, CCT's individual application judgments, which are shared openly on https://kararlarbilgibankasi.anayasa.gov.tr, have been extracted to form a document corpus. The "Facts" heading, which summarizes the events that the applicant went through and the stages that the legal matter subject to the application went through before coming before the CCT, was extracted from the total of 10757 decision texts obtained. In order to eliminate the possible negative impact of very long and short documents on vector transformations, the size of the model data can be reduced by removing relevant documents [71]. Afterwards, in order not to affect the performance of the learning process, very short (less than 2500 characters) and very long (more than 20000 characters) documents were excluded from the corpus and the size was reduced to 6259 documents. In addition, 24 Rights/Liberties, 259 Intervention Claims and 38 Reparation categories for each decision text were drawn and added to the model as attributes. General summary information about the data set is given in table 2.

Table 2. Overview of the corpus

Decision Type	Number of Decision	Character Count			Word Count		
		Min.	Avg.	Max.	Min.	Avg.	Max.
Merit (Violation)	5786 (2955*)	119	5644	117319	25	717	16498
Merit (Non-Violation)	705 (532*)	414	13780	416526	49	1766	53436
Inadmissable	4266 (2732*)	112	6410	156215	18	816	20476
Total	10757 (6259*)	112	6485	416526	18	825	53436

* Number of decision texts with more than 2500 characters and less than 20000 characters

In the data preprocessing processes, after uniting, standardization and filtering processes, low-frequency words (96820 words that occur less than 10 times) were eliminated and the data set was finalized [74]. For the digitization of the processed data set, three different methods, which are frequently preferred in the literature, were used. The methods were evaluated with their classification process performances. The Doc2Vec document-level digitizing vector space model gave better results than the other models in both merit and admissibility evaluations in terms of four different classification performance criteria.

Table 3. Performance of Feature Extraction methods in different classification models

	Merit (Violation / Non-Violation)				Admissibility			
	Accuracy	Recall	Precision	F1 Score	Accuracy	Recall	Precision	F1 Score
TF-IDF	0.6716	0.6717	0.6751	0.6685	0.7597	0.7597	0.7664	0.7577
Word2Vec	0.8117	0.8117	0.8179	0.8099	0.8411	0.8411	0.8430	0.8408
Doc2Vec	0.8183	0.8183	0.8203	0.8178	0.8522	0.8523	0.8535	0.8521

Although the Doc2Vec model achieved high performances in the merits and admissibility classification models with 0.8183 and 0.8522, respectively, it was evaluated that these values may have potential to be improved. The fact that the size of the vector space model can be very large in document level models brings feature selection approaches to the fore. In this sense, the feature selection model was run with the extra tree classifier method in order to improve the analysis results. The confusion matrix and performance indicators for the feature selection model run separately for both classification sets are given in Tables 4 and 5.

Table 4. Classification Set 1 (Merit) model performances with extra tree classifier feature selection algorithms

		Actually		Model Performances	
		Positive (1)	Negative (0)		
Predicted	Positive (1)	(True Positive) 496	(False Positive) 35	Accuracy	0.8832
				Recall	0.8833
	Negative (0)	(False Negative) 89	(True Negative) 442	Precision	0.8907
				F1 Score	0.8827

Table 5. Classification Set 2 (Admissibility) model performances with extra tree classifier feature selection algorithms

		Actually		Model Performances	
		Positive (1)	Negative (0)		
Predicted	Positive (1)	(True Positive) 2294	(False Positive) 437	Accuracy	0.9030
				Recall	0.9030
	Negative (0)	(False Negative) 93	(True Negative) 2638	Precision	0.9098
				F1 Score	0.9025

It has been observed that the performance of the classification model established for the estimation of the substantive examination (merit) increased significantly in terms of all four performance criteria, and the accuracy value increased up to 0.8832. Similarly, it is seen that the classification performances of the admissibility evaluation have also increased, and the accuracy value has been increased from 0.8522 to 0.9030.

Random forest was used as the main estimator in all trials during the feature engineering process. After this stage, it is aimed to increase the overall performance by using different classification models. In the classification model, which was constructed in two stages from the information extraction stage, 36 different classification algorithms, which have been successfully used in text classification in the literature, were trained with a sample data set and the 7 most successful ones were selected for use in the ensemble model. Selected models and accuracy values are given in Table 6.

Table 6. Performance evaluation of top performed algorithms for ensemble model

	Merit	Admissibility
Histogram-Based Gradient Boosting Classification Tree	0.9633	0.9162
Linear Discriminant Analysis	0.9821	0.9154
Ridge Classifier	0.9821	0.9154
Gradient Boosting	0.9869	0.9130
Random Forest	0.8832	0.9030
Logistic Regression	0.8446	0.8940
AdaBoost Classifier	0.9840	0.8936

In the ensemble model, it was preferred to integrate the soft vote/majority vote classifier method. Therefore, an odd number of (7) high performance algorithms is included in the integrated model. Confusion matrices and performance values for the generated ensemble model are given in Tables 7 and 8.

Table 7. Ensemble learning model performance results for Classification Set 1 (Merit)

		Actually		Model Performances	
		Positive (1)	Negative (0)		
Predicted	Positive (1)	(True Positive) 531	(False Positive) 0	Accuracy	0.9718
				Recall	0.9718
	Negative (0)	(False Negative) 30	(True Negative) 501	Precision	0.9737
				F1 Score	0.9717

Table 8. Ensemble learning model performance results for Classification Set 2 (Admissibility)

		Actually		Model Performances	
		Positive (1)	Negative (0)		
Predicted	Positive (1)	(True Positive) 2271	(False Positive) 460	Accuracy	0.9156
				Recall	0.9155
	Negative (0)	(False Negative) 1	(True Negative) 2730	Precision	0.9277
				F1 Score	0.9149

4. DISCUSSION AND CONCLUSION

Our study is the first systematic study that attempts to predict the admissibility and merits of the Constitutional Court's individual application decisions (two-stage binary classification task) by processing the heading of “Facts” of these decisions using machine learning and NLP techniques, and our model achieved 97.18% success rate. In two studies with the CCT’s datasets, Sert et al. [33] 0.90 and Mumcuoğlu et al. [7] achieved 0.918 success rates. It is worth explaining the similarities and differences between our study and the two studies [7, 33], which are important in terms of the methodology used and utilizing the CCT’s decisions in order to shed light on the innovative aspect of our work. First of all, it should be underlined that, unlike the aforementioned study by Sert et al. [33], our study aims to teach court decisions to artificial intelligence in aggregate by using all available data without categorizing a certain right (not only public morality and freedom of expression) and to measure the overall success of the system by randomly selecting court decisions to be used for testing. Moreover, unlike Sert et al. [33] and Mumcuoğlu et al. [7], this study first aims to predict whether the application is admissible or not and then to predict whether a right has potentially been violated on the merits. Therefore, in this study, there is a two-stage process, each consisting of a binary classification task. In this respect, this study is more inclusive in that it aims to develop a system capable of predicting the Constitutional Court's decisions on both admissibility and merits and is more representative in that it aims to use a more comprehensive data set. On the other hand, to the best of our knowledge, such a study, which conducts a two-stage prediction in terms of admissibility and merits, has been conducted before, neither in Turkey nor in other countries. In this respect, this study sets a unique example in this area.

On the other hand, in Sert et al.'s [33] study, the machine was taught the "the subject of the application" and "the evaluation" headings of the Constitutional Court judgments. In particular, the evaluation heading is the heading where the Constitutional Court explains its opinion on the case in detail. Teaching the machine, the evaluation and law headings in court decisions has been criticized in the literature for increasing the potential of the machine to be "biased" [8]. In this study, in line with the preference of Mumcuoğlu et al. [7], we aim to teach the machine the "Facts" heading of the judgments and predict whether there is a possible violation of rights. Finally, Sert et al. [33] used the "data augmentation" method for the decisions in the category of "general morality" and Mumcuoğlu et al. [7] used the "data augmentation" method for all decisions of the Constitutional Court since the dataset they used was unbalanced. Coulombe [72] stated that there are methods for data augmentation in texts such as adding noise to the text, inserting spelling errors, replacing words with synonyms, annotating with regular expressions, annotating with syntax trees, and annotating with back translation. It is not specified which of these methods were used in this study. All of these methods try to preserve the basic statistics and distribution of the data. If data augmentation is done only on a sample with features extracted, this can easily mean generating data from which classification algorithms can learn [72]. In our study, such a method is not preferred, and the dataset is created in a balanced manner based on the available data from the beginning, in order to create a model that is appropriate for producing predictions that are closer to reality. Working on ECHR decisions in similar studies, Aletras et al. [25] 0.79 and Medvedeva et al. [8] reached 0.77 accuracy values. In our study, both different methods were used, and a very high decision was examined compared to these two studies. Therefore, our study here has shown very high success compared to these two studies.

In the future studies, decisions such as political party closure cases, constitutionality audit and administrative cases, which fall within the jurisdictive scope of the Constitutional Court, can also be predicted. Although the model presented in the study works on the draft decisions of the constitutional court rapporteur, it can be expanded to support other court decisions by making the necessary adjustments. In addition, the methods used here can be compared by applying to the European Court of Human Rights or court decisions of other countries. Furthermore, it is possible to apply our method to decisions written in other languages because our method is language independent. Finally, with the "active learning" approach that supports the active participation of decision makers in the machine learning process, potential problems that may arise due to technical legal language can be avoided.

Acknowledgement

This study was supported by the Scientific and Technological Research Council of Turkey (TUBITAK) through the Scientific and Technological Research Projects Support Program (3005) with the project number 122G019.

REFERENCES

[1] Davies G. The Relationship between Empirical Legal Studies and Doctrinal Legal Research. Erasmus Law Review. 2020;13(2):3–12. doi:10.5553/ELR.000141.

[2] Frankenreiter J, Livermore MA. Computational Methods in Legal Analysis. Annual Review of Law and Social Science. 2020;16(1):39–57. doi:10.1146/annurev-lawsocsci-052720-121843.

[3] Hutchinson T, Duncan N. Defining and Describing What We Do: Doctrinal Legal Research. Deakin Law Review. 2012;17(1):83–120.

[4] Kazmierski V. How Much "Law" in Legal Studies? Approaches to Teaching Legal Research and Doctrinal Analysis in a Legal Studies Program. Canadian Journal of Law and Society. 2014;29(3):297–310.

[5] Taekema S. Methodologies of Rule of Law Research: Why Legal Philosophy Needs Empirical and Doctrinal Scholarship. Law and Philosophy. 2021;40(1):33–66. doi:10.1007/s10982-020-09388-1.

[6] Alarie B, Niblett A, Yoon AH. How artificial intelligence will affect the practice of law. University of Toronto Law Journal. 2018;68(Suppl 1):106–24. doi:10.3138/utlj.2017-0052.

[7] Mumcuoğlu E, Öztürk CE, Ozaktas HM, Koç A. Natural Language Processing in Law: Prediction of Outcomes in the Higher Courts of Turkey. Information Processing & Management. 2021;58(5):102684. doi:10.1016/j.ipm.2021.102684.

[8] Medvedeva M, Vols M, Wieling M. Using Machine Learning to Predict Decisions of the European Court of Human Rights. Artificial Intelligence and Law. 2020;28(2):237–66. doi:10.1007/s10506-019-09255-y.

[9] Surden H. Machine Learning and Law. Washington Law Review. 2014;89(1):87–115.

[10] Agrawal K. Legal Case Summarization: An Application for Text Summarization. 2020 International Conference on Computer Communication and Informatics (ICCCI). 2020:1–6. doi:10.1109/ICCCI48352.2020.9104093.

[11] Hachey B, Grover C. Extractive summarisation of legal texts. Artificial Intelligence and Law. 2007;14(4):305–45. doi:10.1007/s10506-007-9039-z.

[12] Sheik R, Nirmala SJ. Deep Learning Techniques for Legal Text Summarization. 2021 IEEE 8th Uttar Pradesh Section International Conference on Electrical, Electronics and Computer Engineering (UPCON). 2021:1–5.

[13] Sil R, Alpana, Roy A, Dasmahapatra M, Dhali D. An Intelligent Approach for Automated Argument-Based Legal Text Recognition and Summarization Using Machine Learning. Journal of Intelligent & Fuzzy Systems. 2021;41(5):5457–66. doi:10.3233/JIFS-189867.

[14] Dixon JHB. What Judges and Lawyers Should Understand About Artificial Intelligence Technology. Judges' Journal. 2020;59(1):36–8.

[15] Reiling AD. Courts and Artificial Intelligence. International Journal for Court Administration. 2020;11(2):8. doi:10.36745/ijca.343.

[16] Wang N. "Black Box Justice": Robot Judges and AI-Based Judgment Processes in China's Court System. 2020 IEEE International Symposium on Technology and Society (ISTAS). 2020:58–65. doi:10.1109/ISTAS50296.2020.9462216.

[17] Katz DM. Quantitative Legal Prediction—Or—How I Learned to Stop Worrying and Start Preparing for the Data-Driven Future of the Legal Services Industry. Emory Law Journal. 2013;62(4):909–66.

[18] Kızrak MA, Buluz B, Özparlak BO, Ünsal B, Durlu Gürzümar D, Deniz Atalar G, et al. Law in the Era of Artificial Intelligence [Joint Workshop]. The Bar of Istanbul, Ankara and İzmir; 2019. Available from: https://www.istanbulbarosu.org.tr/files/docs/Yapay_Zeka_Caginda_Hukuk2019.pdf

[19] Virtucio MBL, Aborot JA, Abonita JKC, Avinante RS, Copino RJB, Neverida MP, et al. Predicting Decisions of the Philippine Supreme Court Using Natural Language Processing and Machine Learning. 2018 IEEE 42nd Annual Computer Software and Applications Conference (COMPSAC). 2018:130–5. doi:10.1109/COMPSAC.2018.10348.

[20] Wu T. Will Artificial Intelligence Eat the Law: The Rise of Hybrid Social-Ordering Systems. Columbia Law Review. 2019;119(7):2001–28.

[21] Lage-Freitas A, Allende-Cid H, Santana O, de Oliveira-Lage L. Predicting Brazilian Court Decisions. arXiv:1905.10348 [Cs]. 2019. Available from: http://arxiv.org/abs/1905.10348

[22] Ruger TW, Kim PT, Martin AD, Quinn KM. The Supreme Court Forecasting Project: Legal and Political Science Approaches to Predicting Supreme Court Decisionmaking. Columbia Law Review. 2004;104(4):1150. doi:10.2307/4099370.

[23] Shaikh RA, Sahu TP, Anand V. Predicting Outcomes of Legal Cases Based on Legal Factors Using Classifiers. Procedia Computer Science. 2020;167:2393–402. doi:10.1016/j.procs.2020.03.292.

[24] Osbeck MK, Gilliland M. Outcome Prediction in the Practice of Law. Foresight: The International Journal of Applied Forecasting. 2018;50:42–8.

[25] Aletras N, Tsarapatsanis D, Preoţiuc-Pietro D, Lampos V. Predicting judicial decisions of the European Court of Human Rights: A Natural Language Processing perspective. PeerJ Computer Science. 2016;2:e93. doi:10.7717/peerj-cs.93.

[26] Goel S, Roshan S, Tyagi R, Agarwal S. Augur Justice: A Supervised Machine Learning Technique To Predict Outcomes Of Divorce Court Cases. 2019

Fifth International Conference on Image Information Processing (ICIIP). 2019:280–5.
[27] Li J, Zhang G, Yan H, Yu L, Meng T. A Markov Logic Networks Based Method to Predict Judicial Decisions of Divorce Cases. 2018 IEEE International Conference on Smart Cloud (SmartCloud). 2018:129–32. doi:10.1109/SmartCloud.2018.00029.
[28] Kowsrihawat K, Vateekul P, Boonkwan P. Predicting Judicial Decisions of Criminal Cases from Thai Supreme Court Using Bi-directional GRU with Attention Mechanism. 2018 5th Asian Conference on Defense Technology (ACDT). 2018:50–5. doi:10.1109/ACDT.2018.8592948.
[29] Chen B, Li Y, Zhang S, Lian H, He T. A Deep Learning Method for Judicial Decision Support. 2019 IEEE 19th International Conference on Software Quality, Reliability and Security Companion (QRS-C). 2019:145–9. doi:10.1109/QRS-C.2019.00040.
[30] Contini F. Artificial Intelligence and the Transformation of Humans, Law and Technology Interactions in Judicial Proceedings. Law, Technology and Humans. 2020;2(1):4–18. doi:10.5204/lthj.v2i1.1478.
[31] Yuan D. Case Study of Criminal Law Based on Multi-Task Learning. 2020 International Conference on Artificial Intelligence and Computer Engineering (ICAICE). 2020:98–103. doi:10.1109/ICAICE51518.2020.00025.
[32] Long S, Tu C, Liu Z, Sun M. Automatic Judgment Prediction via Legal Reading Comprehension. arXiv:1809.06537 [Cs]. 2018. Available from: http://arxiv.org/abs/1809.06537
[33] Sert MF, Yıldırım E, Haşlak İ. Using Artificial Intelligence to Predict Decisions of the Turkish Constitutional Court. Social Science Computer Review. 2021;089443932110103. doi:10.1177/08944393211010398.
[34] O'Sullivan C, Beel J. Predicting the Outcome of Judicial Decisions Made by the European Court of Human Rights. arXiv:1912.10819 [Cs, Stat]. 2019. Available from: http://arxiv.org/abs/1912.10819
[35] Fendoğlu HT. Anayasa Yargısı. 4th ed. Yetkin Yayınları; 2020.
[36] Gözler K. Anayasa Hukukunun Genel Esasları. 12th ed. Ekin Yayıncılık; 2020.
[37] İnceoğlu S. Anayasa Mahkemesi'ne Bireysel Başvuru: Türkiye ve Latin Modelleri. 1st ed. Oniki Levha Yayınları; 2017.
[38] Göztepe E. Türkiye'de Anayasa Mahkemesi'ne Bireysel Başvuru Hakkının (Anayasa Şikâyeti) 6216 Sayılı Kanun Kapsamında Değerlendirilmesi. Türkiye Barolar Birliği Dergisi. 2011;95.
[39] Fagan F. Natural Language Processing for Lawyers and Judges. SSRN Electronic Journal. 2020. doi:10.2139/ssrn.3564966.
[40] Lawlor RC. What Computers Can Do: Analysis and Prediction of Judicial Decisions. American Bar Association Journal. 1963;49(4):337–44.
[41] Ekinci H. Anayasa Mahkemesine Bireysel Başvuruda Kabul Edilebilirlik Kriterleri ve İnceleme Yöntemi. Anayasa Yargısı. 2013;30.
[42] Şirin T. Türkiye'de Anayasa Şikayeti (Bireysel Başvuru). 1st ed. Oniki Levha Yayınları; 2013.
[43] Akyel R. Bireysel Başvuru Yolu: Misyonu, Vizyonu Ve Uygulanması. Adalet Dergisi. 2022;68(1):53–92.
[44] Kılıç A. Anayasa Mahkemesinin Bireysel Başvuru Kararlarının Türkiye Büyük Millet Meclisine Bildirilmesi. Anayasa Dergisi. 2021;38(1).
[45] Azaklı M. Bireysel Başvuru Usulü, Süre ve Temellendirilmemiş Şikâyet. Bireysel Başvuruda İş Yükü ve Çözüm Önerileri Sempozyumu. 2022. p.17–32.
[46] Şulea OM, Zampieri M, Vela M, van Genabith J. Predicting the Law Area and Decisions of French Supreme Court Cases. RANLP 2017—Recent Advances in Natural Language Processing Meet Deep Learning. 2017:716–22. doi:10.26615/978-954-452-049-6_092.
[47] Aydin ÖD. Türk Anayasa Yargısında Yeni Bir Mekanizma: Anayasa Mahkemesi'ne Bireysel Başvuru. Gazi Üniversitesi Hukuk Fakültesi Dergisi. 2011;15(4).
[48] Tekbaş DA. Anayasa Mahkemesi Bireysel Başvuru İstatistiklerinin Değerlendirilmesi. Anayasa Dergisi. 2018;35.
[49] Ekinci H. Anayasa Mahkemesinin Bireysel Başvuru İş Yükü, Çözüme Yönelik Mahkeme Pratiği ve Öneriler. Uyuşmazlık Mahkemesi Dergisi. 2015;5(5). doi:10.18771/umd.58105.
[50] Sharda R, Delen D, Turban E. Analytics, Data Science, & Artificial Intelligence: Systems for Decision Support. Pearson Education, Inc; 2020.
[51] Zhai C, Massung S. Text Data Management and Analysis: A Practical Introduction to Information Retrieval and Text Mining. Association for Computing Machinery and Morgan & Claypool; 2016.
[52] Çetin FS, Eryiğit G. Türkçe Hedef Tabanlı Duygu Analizi İçin Alt Görevlerin İncelenmesi–Hedef Terim, Hedef Kategori ve Duygu Sınıfı Belirleme. Bilişim Teknolojileri Dergisi. 2018;11(1):43–56.
[53] Vidgen B, Derczynski L. Directions in Abusive Language Training Data, A Systematic Review: Garbage in, Garbage Out. PLOS One. 2020;15(12):e0243300.
[54] Geiger RS, Yu K, Yang Y, Dai M, Qiu J, Tang R, Huang J. Garbage in, garbage out? Do machine learning application papers in social computing report where human-labeled training data comes from? Proceedings of the 2020 Conference on Fairness, Accountability, and Transparency. 2020:325–36.
[55] Jo T. Text Mining: Concepts, Implementation, and Big Data Challenge. Studies in Big Data. Springer International Publishing; 2018.
[56] Anandarajan M, Hill C, Nolan T. Practical text analytics. Maximizing the Value of Text Data. Springer; 2019.
[57] Aravi G. Metin Madenciliği ile Sosyal Medya Analizi [Yüksek Lisans Tezi]. İstanbul: İstanbul Aydın Üniversitesi; 2014.
[58] Weiss SM, Indurkhya N, Zhang T, Damerau F. Text Mining: Predictive Methods for Analyzing

Unstructured Information. Springer, New York; 2005.
[59] Cady F. The data science handbook. John Wiley & Sons; 2017.
[60] Mikolov T, Chen K, Corrado G, Dean J. Efficient Estimation of Word Representations in Vector Space. Proceedings of Workshop at ICLR. 2013.
[61] Jang B, Kim I, Kim JW. Word2vec Convolutional Neural Networks for Classification of News Articles and Tweets. PloS One. 2019;14(8):e0220976.
[62] Goldberg Y, Levy O. word2vec Explained: Deriving Mikolov et al.'s Negative-Sampling Word-Embedding Method. arXiv preprint arXiv:1402.3722. 2014.
[63] De Boom C, Van Canneyt S, Bohez S, Demeester T, Dhoedt B. Learning semantic similarity for very short texts. 2015 IEEE International Conference on Data Mining Workshop (ICDMW). 2015:1229–34.
[64] Le Q, Mikolov T. Distributed Representations of Sentences and Documents. In: International Conference on Machine Learning; 2014. p. 1188–96.
[65] Geurts P, Ernst D, Wehenkel L. Extremely randomized trees. Machine Learning. 2006;63:3–42.
[66] Dietterich T. Overfitting and undercomputing in machine learning. ACM Computing Surveys. 1995;27(3):326–7.
[67] Moore AW. Cross-Validation for Detecting and Preventing Overfitting. School of Computer Science, Carnegie Mellon University; 2001.
[68] Polikar R. Ensemble Learning. In: Zhang C, Ma Y, editors. Ensemble Machine Learning. Springer, Boston, MA; 2012. p. 1–34.
[69] Kim MJ, Kang DK. Ensemble with Neural Networks for Bankruptcy Prediction. Expert Systems with Applications. 2010;37(4):3373–9.
[70] Brownlee J. Better deep learning: train faster, reduce overfitting, and make better predictions. Machine Learning Mastery; 2018.
[71] Schütze, H., Manning, C. D., & Raghavan, P. (2008). Introduction to information retrieval. Cambridge: Cambridge University Press. p.129-130
[72] Coulombe C. Text Data Augmentation Made Simple By Leveraging NLP Cloud APIs. ArXiv:1812.04718 [Cs]. 2018. Available from: http://arxiv.org/abs/1812.04718
[73] Constitutional Court Of The Republic Of Turkey. Individual Application Statistics (23/9/2012—31/12/2022). 2022.
[74] Mikolov, T., Kopecky, J., Burget, L., & Glembek, O. (2009, April). Neural network based language models for highly inflective languages. In 2009 IEEE international conference on acoustics, speech and signal processing (pp. 4725-4728). IEEE.

Volume 14, Issue 2, Page 240-246, 2025 https://doi.org/10.46810/tdfd.1661900 Research Article

BİNGÖL UNIVERSITY

Türk Doğa ve Fen Dergisi
Turkish Journal of Nature and Science
www.dergipark.gov.tr/tdfd

A Residual Neural Network with a Novel Orthogonal Regularization for Covid-19 Diagnosis using X-ray images

Kazım FIRILDAK[1*], Gaffari ÇELİK[2], Muhammed Fatih TALU[3]

[1] Fırat University, Department of Computer Technology, Elazığ, Türkiye
[2] Ağri Ibrahim Çeçen University, Department of Computer Technology, Ağrı, Türkiye
[3] İnönü University, Department of Computer Science, Malatya, Türkiye
Kazım FIRILDAK ORCID No: 0000-0002-1958-3627
Gaffari ÇELİK ORCID No: 0000-0001-5658-9529
Muhammed Fatih TALU ORCID No: 0000-0003-1166-8404

**Corresponding author: kfirildak@firat.edu.tr*

(Received: 20.03.2025, Accepted: 04.06.2025, Online Publication: 27.06.2025)

Keywords
Deep learning, Residual network, Orthogonal regularization, Covid-19

Abstract: Covid-19 is a viral infection that affects the respiratory tract and causes serious health problems on a global scale. Due to the high contagiousness of the disease, early detection and accurate classification are of great importance. In this study, a novel orthogonal regularization method is proposed to improve the detection accuracy of Covid-19 disease from X-ray images. The proposed regularization method, evaluated using ResNet110, improves the classification accuracy compared to traditional Orthogonal regularization approaches. In the experimental studies, the proposed method is compared with various regularization techniques and the highest classification success rate is achieved by increasing the test accuracy rate to 96.52%. In addition, it is observed that the proposed method optimizes the learning curve of the model, especially in the later stages of the training process, and increasing the test accuracy. In addition, compared to the existing orthogonal regularization methods for Covid-19 detection, the proposed approach improved the test classification performance by approximately 1% in accuracy, F1-score, sensitivity, recall and specificity metrics.

Yeni bir Orthogonal Düzgünleştirme Kullanan Artık Yapay Sinir Ağı ile X-Ray Görüntülerinden Covid-19 Tespiti

Anahtar Kelimeler
Derin öğrenme, Artık ağ, Ortagonal düzgünleştirme, Covid-19

Öz: Covid-19, solunum yollarını etkileyen ve küresel ölçekte ciddi sağlık sorunlarına neden olan viral bir enfeksiyondur. Bulaşıcılığı nedeniyle hastalığın erken teşhis ve doğru sınıflandırılması büyük önem taşımaktadır. Bu çalışmada, X-ışını görüntülerinden Covid-19 hastalığının tespit doğruluğunu artırmak için yeni bir ortogonal düzgünleştirme yöntemi önerilmiştir. ResNet110 ağına uygulanan yöntem, geleneksel ortogonal düzgünleştirme yaklaşımlarına kıyasla sınıflandırma doğruluğunu artırılmaktadır. Deneysel çalışmalarda, önerilen yöntem çeşitli düzgünleştirme teknikleriyle karşılaştırılmış ve test doğruluk oranını %96,52'ye çıkarılarak en yüksek sınıflandırma doğruluğu elde edilmiştir. Önerilen yöntemin özellikle eğitim sürecinin sonraki aşamalarında modelin öğrenme eğrisini optimize ettiği ve test doğruluğunu artırdığı da görülmüştür. Ayrıca, Covid-19 tespiti için mevcut ortogonal düzgünleştirme yöntemleriyle karşılaştırıldığında, önerilen yaklaşım test sınıflandırma performansını doğruluk, F1 puanı, duyarlılık, keskinlik ve özgüllük metriklerinde yaklaşık %1 oranında iyileşme sağlanmıştır.

1. INTRODUCTION

Covid-19 is a new mutated form of coronaviruses, a ribonucleic virus [1]. It, which has affected many countries of the world in recent years, spreads rapidly by human-to-human transmission [2]. According to the report published by the World Health Organization, 776.8 million confirmed cases and more than 7 million deaths have been reported [3]. Patients infected with this new coronavirus have symptoms such as fever, fatigue,

headache, shortness of breath [4]. The rapid spread and progression of the disease increases the importance of early diagnosis. In advanced stages, it can lead to serious complications up to pneumonia in the lungs.
Covid-19 is primarily diagnosed using Reverse Transcription Polymerase Chain Reaction (RT-PCR) test. However, the PCR test has an accuracy rate of approximately 70% in correctly identifying the disease [5]. Therefore, in addition to the RT-PCR test, X-ray and computed tomography (CT) imaging are commonly utilized by physicians [6]. CT is a widely used technique for disease detection; however, obtaining CT images is an expensive procedure. Given the rapid global spread of the disease, particularly in underdeveloped countries, the implementation of a more cost-effective diagnostic method is crucial. Although the sensitivity of detecting COVID-19 from chest X-ray images is below 70%, its affordability makes it a valuable tool in disease diagnosis when further developed and optimized [7,8].

Artificial intelligence applications are widely utilized in the medical field. Narin et al. implemented a hybrid deep learning approach on X-ray images to detect pneumonia caused by the Covid-19 [9]. In their study, COVID-19 pneumonia was identified with an accuracy of 98.0% using the InceptionV3 convolutional neural network, alongside ResNet50. Another study conducted by Wang et al. achieved a sensitivity of 91% in detecting COVID-19 using their proposed deep learning architecture [10]. Similarly, Horry et al. employed CT, X-ray, and ultrasound imaging for COVID-19 detection. They applied VGG19, a deep learning architecture, to these images, achieving a sensitivity of 86% for X-ray images, 100% for ultrasound images, and 84% for CT images [11]. Loey et al. utilized CT images to detect COVID-19. To enhance the performance of the deep learning architecture, the dataset containing a limited number of samples was augmented using a Convolutional Generative Adversarial Network (CGAN). Subsequently, the architectures were trained on both classical and CGAN-based augmented data using AlexNet, VGG16, VGG19, GoogleNet, and ResNet50 networks. Among these, the ResNet50 architecture achieved the highest accuracy of 82% with classical data augmentation [12].

In this study, a novel orthogonal regularization (OR) method is proposed. This method is subsequently applied to the ResNet110 network for the detection of COVID-19. The second section of the study outlines the materials and methods. The third section presents the experimental results and compares the performance of the proposed method with existing approaches. Finally, the fourth section discusses the obtained results and provides suggestions for future research.

2. MATERIAL AND METHOD

2.1. Covid-19 Dataset

The dataset consists of chest X-ray images of pneumonia caused by the COVID-19 virus, which has significantly impacted the world in recent years. It includes a total of three classes: normal, other pneumonia, and COVID-19 pneumonia [13,14]. The dataset contains 1,200 COVID-19, 1,341 normal, and 1,345 other pneumonia X-ray images. A total of 80% of the data was used for training, while the remaining 20% was allocated for testing. Figure 1 shows sample images of the Covid-19 dataset.

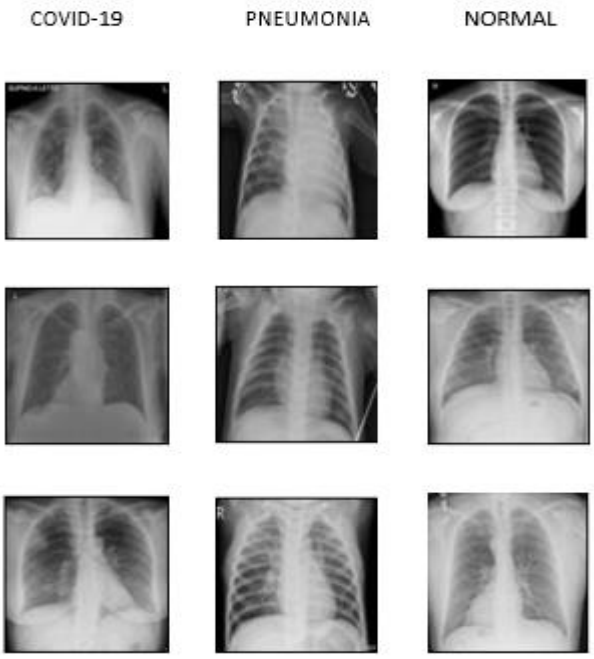

Figure 1. Covid-19 dataset X-ray images.

2.2. Residual Neural Network

Residual Neural Network (ResNet) is an architecture proposed to address the gradient vanishing problem [15]. Residual layers (residual blocks) enhance training efficiency by utilizing the output of a previous layer as an input to subsequent layers. The architecture of a residual layer is illustrated in Figure 2(a). The literature contains ResNet architectures with varying depths and widths. In this study, ResNet110 (Figure 2(b)) is used. This architecture incorporates bottleneck residual layers, and its depth is given by the formula p = 9n + 2, where n represents the total number of convolutions and p denotes the total depth. Thus, ResNet110 consists of 1.7 million parameters.

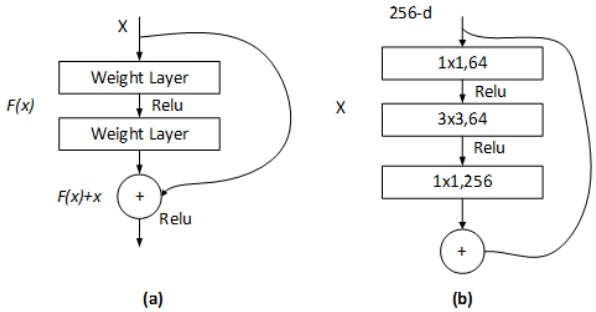

Figure 2. ResNet architectures. (a) Basic residual block, (b) Residual block used for ResNet110.

2.3. Orthogonal Regularization

Regularization is one of the key elements of deep learning, a subfield of machine learning. Regularization is

usually applied as a penalty function added to the loss function [16]. The penalty function is defined as a method that aims to reduce the test error in the learning model but does not reduce the training error [17]. This definition is a restrictive statement for deep architectures. Because methods such as weight both training and test error [18]. As a result, all techniques used for better generalization and test accuracy of the neural network are called regularization.

One of the most significant challenges in artificial neural networks (ANN) is the vanishing or exploding gradients as the depth of the network increases. To address this issue, it has been proposed that the parameter matrix should approximate the Gram matrix [19]. While the stability of forward propagation is achieved through batch normalization, the uniform distribution of the error cannot be ensured in the backpropagation process [20]. An alternative approach to address this issue is the OR method [21–23]. OR methods in the literature have been proposed as an alternative to the classical weight decay regularization approach.

Orthogonality is defined as x, y being two vectors, $x, y \in R^n$ for $x \cdot y = 0 \rightarrow x \perp y$. Unit orthogonality (orthonormality) forces the vector norms to be equal to one: $\|x\| = 1 \quad and \ \|y\| = 1$. After this a priori information, it is necessary to mention how orthogonality is used in the ANN training process. In the feed-forward algorithm of ANN, kth layer output vector x is transformed $y = W^T x$ while moving to the $(k+1)th$ layer input.

where W is called the linear transformation matrix (Equation 1). The condition that the norms of x and y are equal to each other during this transformation is called Norm-Preservation and is shown in Equations 1 and 2.

$$W = \begin{bmatrix} | & | & | \\ w_1 & \dots & w_n \\ | & | & | \end{bmatrix}_{mxn} \tag{1}$$

$$\|y\| = \sqrt{y^T y} = \sqrt{x^T W W^T x} = \sqrt{x^T x} = \|x\|, \quad eğer \ WW^T = I \tag{2}$$

Orthogonal vectors are needed to preserve vector norm values. Therefore, the distance of the WW^T result to the unit matrix is obtained as the cost value. Bansal et al. proposed to classify four different categories of methods for regularization this cost value [21]. These are Soft Orthogonal (SO), Double Soft Orthogonal (DSO), Mutual Coherence (MC) and Spectral Restricted Isometry Property (SRIP) orthogonal regularization [20,24–27].

SO, the column vectors of the matrix W are required to be perpendicular to each other and have unit length. Accordingly, the regularization cost (R) is calculated by multiplying the distance of the result $W^T W \in R^{nxn}$ from the unit matrix $[I]_{nxn}$ by a coefficient λ .The mathematical form of the SO method is given in Equation 3.

$$D(W) = \lambda \|W^T W - I\|_F^2 \tag{3}$$

The cost gradient is calculated as $4\lambda W(W^T W - I)$ and is used in the back propagation algorithm to update the parameters. W a matrix with rows m and columns n. The rank of the matrix is m if it is greater than or equal to m, n. This situation is called under complete matrix. In such cases, an orthogonality relation can be established. However, if it is greater than or equal to n, m, even if the rank of the matrix is m, this is called an over complete matrix. $W^T W \in R^{nxn}$ may not be identified from these matrices. To overcome these shortcomings, approaches have been developed that divide the weight matrix W into subspaces such as Stiefel manifold or Jakobi. These approaches reduce the columns of the over complete W matrix to lower dimensional subspaces, making the matrix easier to process and analyze [24].

DSO, the column vectors of the matrix W are required to be perpendicular to each other in two different vector spaces ($W^T W \in R^{nxn}$ ve $WW^T \in R^{mxm}$) and to be of unit length [21]. Accordingly, the cost function is defined as follows:

$$D(W) = (\|W^T W - I\|_F^2 + \|WW^T - I\|_F^2) \tag{4}$$

where W is weight matrix and has m rows and n columns. m is greater than n, the regularization loss is calculated according to the formula $\lambda\|W^T W - I\|_F^2$, n is greater than or equal to m, the formula $\lambda\|WW^T - I\|_F^2$ is used.

Another OR method is MC. W the MC value between the column vectors of the parameter matrix is calculated as shown in Equation 5 [26].

$$\mu_W = max_{i \neq j} = \frac{|\langle w_i, w_j \rangle|}{\|w_i\| + \|w_j\|} \tag{5}$$

For the MC method, w_i is the column vector ith of W. μ_W, is seen that in the range [0,1] and in the case of ortagonality, it approaches 0, and in other cases it approaches 1. The use of L_∞ is preferred because it is the vector element with the highest absolute value and plays the biggest role in increasing the consistency value [26]:

$$D(W) = \lambda\|W^t W - I\|_\infty \tag{6}$$

For MC L_∞ returns the largest value in the vector elements.

Regularization methods developed using spectral restricted isometry property (SRIP) give better results in statistical metrics and execution time than other methods[27,28].The regularization cost function used in this approach is as shown in Equation 7.

$$D(W) = \lambda \cdot \sigma(W^T W - I) \tag{7}$$

where λ is the regularization coefficient. $\sigma(W^T W - I)$ function returns the spectral norm of the $W^T W - I$ matrix and is calculated as shown in Equation 8.

$$u \leftarrow (W^t W - I)v$$
$$v \leftarrow (W^t W - I)u \quad (7)$$
$$\sigma(W^t W - I) \leftarrow \frac{\|v\|}{\|u\|}$$

where v is a vector starting with random values in R^n space. Then the vector u and again v are computed iteratively. The spectral norm is obtained by the ratio of both vector norms.

2.4. Proposed Orthogonal Regularization Method

Orthogonal regularization approaches generally aim to approximate the weight matrix W as a Gram matrix. However, this approach weakens the regularization effect in overcomplete cases and negatively impacts the performance of the network. Furthermore, enforcing all weights to be orthogonal vectors hinders the model's convergence towards an optimal learning curve [27]. The proposed OR approach is based on enforcing column vectors to be binary while modulating orthogonality transitions.

In this context, Figure 3 presents the parameter images (filter/mask images) in the layers of three different CNN architectures (AlexNet [29], VGG16 [30], and ResNet50 [15]) trained on the ImageNet dataset. A careful analysis of the figure reveals that numerous binary images within the layers are nearly orthogonal to each other. This observation supports the hypothesis that the training process inherently seeks orthogonal pairs of binary images [31].

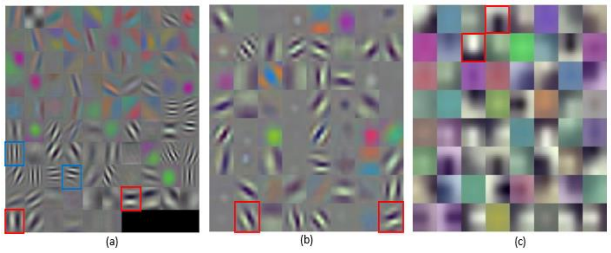

Figure 3. Hidden layer weight visualization (a) AlexNet,(b) ResNet50, (c) VGG16.

While classical regularization approaches force all parameter vectors in the layer to be orthogonal to each other by $W^T W - I$ operation, in the proposed approach, only binary vector pairs are forced to be orthogonal. The cost function of the proposed regularization approach is given below:

$$D(W) = \lambda \sum_{i \in \{1,3,5 \ldots\}} ({w_i}^T w_{i+1} - 1), \quad (9)$$

where λ is the regularization rate and w_i is the column vector i of W. The total loss function observed in the training/testing activities of the datasets is calculated as shown in Equation 10.

$$H(W) = \alpha * K(W) + (1 - \alpha) * D(W) \quad (10)$$

K is the loss function and the cross entropy error value. D is the regularization loss. In the experiments D cost varies and the effect of regularization is analyzed. $H(W)$ is the total loss function. The total loss function of the proposed algorithm contains loop and condition expressions. This process forces the weights of the network to perform OR in binary layers, not in general. The main reason for this is to avoid the overcomplete situation. For these reasons, the derivative of the proposed method and the loss function are calculated by automatic derivative methods [32].

2.5. Performance Evaluation Metrics

In this study, the metrics Acc, Pre, Recall, F1-score and Spe and the confusion matrix are used to measure the experimental performance of the proposed models. In the confusion matrix, TP and TN values indicate the number of correctly classified samples, FP and FN indicate the number of incorrect predictions of the model. These metrics are given mathematically below [33,34].

$$Acc = (TP + TN)/(TP + TN + FP + FN) * 100 \quad (11)$$
$$Pre = TP/(TP + FP) \quad (12)$$
$$Recall = TP/(TP + FN) \quad (13)$$
$$F1 - score = (2 * Pre * Recall)/(Pre + Recall) \quad (14)$$
$$Spe = TN/(TN + FP) * 100 \quad (15)$$

where Acc, Pre, Recall, Spe and F1-score are derived from the confusion matrix. Acc is the ratio of the number of correctly predicted images for each class to the total number of images. Pre and Recall are the precision and sensitivity values of class detection, respectively. The higher these values are, the better the images belonging to the class are detected. F1-score is the harmonic mean of Pre and Recall.

The confusion matrix gives information about the actual and predicted classes in a classifier. The class performance of a model is evaluated using the matrix values in Figure 4 [33,35].

		Predicted Class	
		Positive Class	Negative Class
Actual Class	Positive Class	True Positive (TP)	False Negative (FN)
	Negative Class	False Positive (FP)	True Negative (TN)

Figure 4. Confusion matrix.

3. EXPERIMENTAL RESULTS

In this section, the effect of regularization on training and testing using the COVID-19 dataset with the ResNet110 architecture is analyzed. The training parameters utilized for ResNet110 are presented in Table 1. The Adam optimizer is employed, with the learning rate set to $10^{-2}$and the number of epochs set to 200. The obtained results are presented in Table 2.

Additionally, Figure 5 presents the accuracy curve of the proposed approach (ResNet110+OR) and the ResNet110 architecture during training.

Table 1. Training parameters of ResNet110

Parameters	ResNet110
Input layer	32x32x3
Intermediate layer	12 residual blocks and fully connected classifier
Output layer	10
Activation	ReLU
Optimization	Adam
Package size	128
Epoch	200
Learning rate	0.01

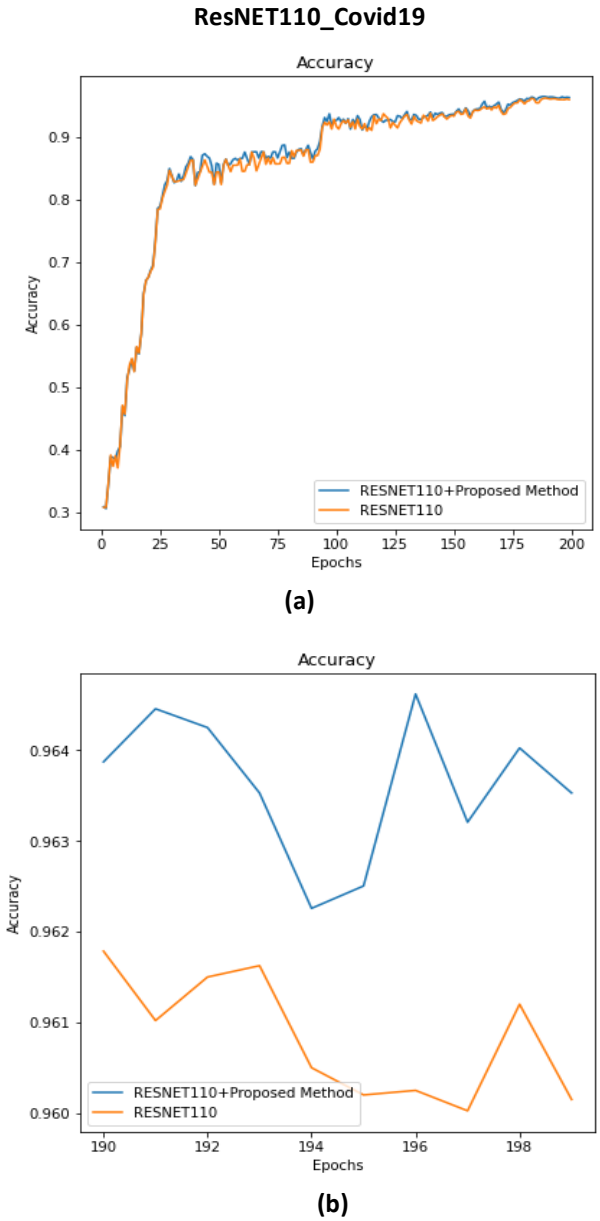

Figure 5. ResNet110 accuracy/epoch for Covid-19 dataset.

In Table 2, when the proposed OR method is compared with orthogonal regularization methods in the literature, the results indicate that the proposed method demonstrates an improvement in statistical metrics. While the accuracy of ResNet110 (a model without regularization) is reported as 96.01%, this increases to 96.54% with the proposed OR method. Precision (Pre) and Recall are measured at 96.52% and 96.51%, respectively, indicating that the proposed approach achieves better class discrimination compared to other methods. Furthermore, a specificity (Spe) of 98.27% was achieved with the proposed approach, demonstrating improved performance in reducing false positives.

Table 2. Test results obtained with ResNet110 architecture using different OR techniques

Method	Dog (%)	Pre (%)	Recall (%)	Spe (%)	F1 (%)
ResNet110	96.01	95.98	95.97	98.01	95.97
ResNet110+SO	96.24	96.25	96.22	98.13	96.24
ResNet110+DSO	96.14	96.12	96.09	98.07	96.10
ResNet110+MC	96.24	96.25	96.22	98.13	96.24
ResNet110+SRIP	96.41	96.38	96.36	98.20	96.37
Proposed OR	**96.54**	**96.52**	**96.51**	**98.27**	**96.51**

The proposed OR method provides a significant improvement in both classification accuracy and other key performance metrics. Specifically, the test accuracy improves by approximately 1%.

As shown in Figure 5, the effect of regularization is limited during the initial 25 iterations. However, after the 50th iteration, the effect of regularization becomes more pronounced in the model's test performance. These findings confirm that the proposed approach enhances classification accuracy by approximately 1%.

4. DISCUSSION AND CONCLUSION

In this study, the effectiveness of a new orthogonal regularization method developed for COVID-19 detection is investigated. The proposed OR method, which is added to the loss function of the ResNet110 architecture, aims to optimize the hidden layer weights as binary orthogonal vectors. Experimental results indicate that the regularization effect is limited during the first 25 iterations of training, but a significant performance gain is observed after the 50th iteration. In addition, the proposed method achieves 96.52% classification accuracy in detecting COVID-19 from X-ray images, demonstrating superior performance compared to orthogonal regularization approaches such as SO, DSO, MC, and SRIP. It is shown that the unified regularization approach improves learning efficiency by enhancing the classification performance of neural networks and can be utilized in detecting critical diseases such as COVID-19.

In future studies, the applicability of the method for detecting other diseases will be investigated by testing it on different deep learning architectures and larger datasets. Furthermore, by evaluating its performance in real-time applications within clinical environments, this study aims to contribute to the broader and more effective adoption of AI-driven medical imaging technologies for disease detection.

REFERENCES

[1] Zhu N, Zhang D, Wang W, Li X, Yang B, Song J, et al. A Novel Coronavirus from Patients with Pneumonia in China, 2019. N Engl J Med [Internet]. 2020 Feb 20;382(8):727–33. Available from: http://www.nejm.org/doi/10.1056/NEJMoa2001017

[2] Lewis D. COVID-19 rarely spreads through surfaces. So why are we still deep cleaning? Nature [Internet]. 2021 Feb 4;590(7844):26–8. Available from: https://www.nature.com/articles/d41586-021-00251-4.

[3] WHO. COVID-19 Epidemiological Update [Internet]. 2024. Available from: https://www.who.int/publications/m/item/covid-19-epidemiological-update---24-december-2024.

[4] Tuncer T, Ozyurt F, Dogan S, Subasi A. A novel Covid-19 and pneumonia classification method based on F-transform. Chemom Intell Lab Syst [Internet]. 2021 Mar;210:104256. Available from: https://linkinghub.elsevier.com/retrieve/pii/S0169743921000241.

[5] Fang Y, Zhang H, Xie J, Lin M, Ying L, Pang P, et al. Sensitivity of Chest CT for COVID-19: Comparison to RT-PCR. Radiology [Internet]. 2020 Aug;296(2):E115–7. Available from: http://pubs.rsna.org/doi/10.1148/radiol.2020200432

[6] Xie X, Zhong Z, Zhao W, Zheng C, Wang F, Liu J. Chest CT for Typical Coronavirus Disease 2019 (COVID-19) Pneumonia: Relationship to Negative RT-PCR Testing. Radiology [Internet]. 2020 Aug;296(2):E41–5. Available from: http://pubs.rsna.org/doi/10.1148/radiol.2020200343

[7] Quan H, Xu X, Zheng T, Li Z, Zhao M, Cui X. DenseCapsNet: Detection of COVID-19 from X-ray images using a capsule neural network. Comput Biol Med [Internet]. 2021 Jun;133:104399. Available from: https://linkinghub.elsevier.com/retrieve/pii/S0010482521001931

[8] Wong HYF, Lam HYS, Fong AHT, Leung ST, Chin TWY, Lo CSY, et al. Frequency and Distribution of Chest Radiographic Findings in Patients Positive for COVID-19. Radiology [Internet]. 2020 Aug;296(2):E72–8. Available from: http://pubs.rsna.org/doi/10.1148/radiol.2020201160

[9] Narin A, Kaya C, Pamuk Z. Automatic detection of coronavirus disease (COVID-19) using X-ray images and deep convolutional neural networks. Pattern Anal Appl [Internet]. 2021 Aug 9;24(3):1207–20. Available from: https://link.springer.com/10.1007/s10044-021-00984-y

[10] Wang L, Wong A. COVID-Net: A Tailored Deep Convolutional Neural Network Design for Detection of COVID-19 Cases from Chest X-Ray Images. 2020 Mar 22; Available from: http://arxiv.org/abs/2003.09871

[11] Horry MJ, Chakraborty S, Paul M, Ulhaq A, Pradhan B, Saha M, et al. COVID-19 Detection Through Transfer Learning Using Multimodal Imaging Data. IEEE Access [Internet]. 2020;8:149808–24. Available from: https://ieeexplore.ieee.org/document/9167243/

[12] Loey M, Manogaran G, Khalifa NEM. A deep transfer learning model with classical data augmentation and CGAN to detect COVID-19 from chest CT radiography digital images. Neural Comput Appl [Internet]. 2020 Oct 26; Available from: https://link.springer.com/10.1007/s00521-020-05437-x

[13] Chowdhury MEH, Rahman T, Khandakar A, Mazhar R, Kadir MA, Mahbub Z Bin, et al. Can AI Help in Screening Viral and COVID-19 Pneumonia? IEEE Access [Internet]. 2020;8:132665–76. Available from: https://ieeexplore.ieee.org/document/9144185/

[14] Rahman T, Khandakar A, Qiblawey Y, Tahir A, Kiranyaz S, Abul Kashem S Bin, et al. Exploring the effect of image enhancement techniques on COVID-19 detection using chest X-ray images. Comput Biol Med [Internet]. 2021 May;132:104319. Available from: https://linkinghub.elsevier.com/retrieve/pii/S001048252100113X

[15] He K, Zhang X, Ren S, Sun J. Deep Residual Learning for Image Recognition. In: 2016 IEEE Conference on Computer Vision and Pattern Recognition (CVPR) [Internet]. IEEE; 2016. p. 770–8. Available from: http://ieeexplore.ieee.org/document/7780459/

[16] Bishop CM. Neural networks for pattern recognition. Oxford; 1995.

[17] Goodfellow IJ, Bengio Y, Courville A. Deep Learning. Cambridge, MA, USA: MIT Press; 2016.

[18] Krizhevsky A, Sutskever I, Hinton GE. ImageNet classification with deep convolutional neural networks. Commun ACM [Internet]. 2017 May 24;60(6):84–90. Available from: https://dl.acm.org/doi/10.1145/3065386

[19] Szu H, Scheff K. Gram-Schmidt Orthogonalization Neural Nets for. 2018.

[20] Zhang L, Li D, Guo Q. Deep Learning From Spatio-Temporal Data Using Orthogonal Regularizaion Residual CNN for Air Prediction. IEEE Access [Internet]. 2020;8:66037–47. Available from: https://ieeexplore.ieee.org/document/9056826/

[21] Bansal N, Chen X, Wang Z. Can We Gain More from Orthogonality Regularizations in Training Deep CNNs? 2018 Oct 22; Available from: http://arxiv.org/abs/1810.09102

[22] Xie D, Xiong J, Pu S. All You Need is Beyond a Good Init: Exploring Better Solution for Training Extremely Deep Convolutional Neural Networks with Orthonormality and Modulation. In: 2017 IEEE Conference on Computer Vision and Pattern Recognition (CVPR) [Internet]. IEEE; 2017. p. 5075–84. Available from: http://ieeexplore.ieee.org/document/8100022/

[23] Rodríguez P, Gonzàlez J, Cucurull G, Gonfaus JM, Roca X. Regularizing CNNs with Locally Constrained Decorrelations. 2016 Nov 7; Available from: http://arxiv.org/abs/1611.01967

[24] Huang L, Liu X, Lang B, Yu A, Wang Y, Li B. Orthogonal weight normalization: Solution to

optimization over multiple dependent stiefel manifolds in deep neural networks. In: Proceedings of the AAAI Conference on Artificial Intelligence. 2018.

[25] Donoho DL. Compressed sensing. IEEE Trans Inf Theory [Internet]. 2006 Apr;52(4):1289–306. Available from: http://ieeexplore.ieee.org/document/1614066/

[26] Lu C, Li H, Lin Z. Optimized projections for compressed sensing via direct mutual coherence minimization. Signal Processing [Internet]. 2018 Oct;151:45–55. Available from: https://linkinghub.elsevier.com/retrieve/pii/S0165168418301464

[27] Zhang Z, Ma W, Wu Y, Wang G. Self-Orthogonality Module: A Network Architecture Plug-in for Learning Orthogonal Filters. In: 2020 IEEE Winter Conference on Applications of Computer Vision (WACV) [Internet]. IEEE; 2020. p. 1044–8. Available from: https://ieeexplore.ieee.org/document/9093466/

[28] Zhang L, Li D, Guo Q. Deep Learning From Spatio-Temporal Data Using Orthogonal Regularizaion Residual CNN for Air Prediction. IEEE Access. 2020;8:66037–47.

[29] Krizhevsky A, Sutskever I, Hinton GE. ImageNet classification with deep convolutional neural networks. Commun ACM. 2017;60(6):84–90.

[30] Simonyan K, Zisserman A. Very deep convolutional networks for large-scale image recognition. In: 3rd International Conference on Learning Representations (ICLR 2015). Computational and Biological Learning Society; 2015. p. 1–14.

[31] Fırıldak K, Çelik G, Talu MF. Derin Ağlar İçin Yeni Bir Birimdik Düzgünleştirme Yaklaşımı. Adıyaman Üniversitesi Mühendislik Bilim Derg [Internet]. 2024 Apr 30;11(22):18–34. Available from: http://dergipark.org.tr/tr/doi/10.54365/adyumbd.1390894

[32] Griewank A, Walther A. Evaluating derivatives: principles and techniques of algorithmic differentiation. SIAM; 2008.

[33] Powers DMW. Evaluation: from precision, recall and F-measure to ROC, informedness, markedness and correlation. 2020 Oct 10; Available from: http://arxiv.org/abs/2010.16061

[34] Celik G. Detection of Covid-19 and other pneumonia cases from CT and X-ray chest images using deep learning based on feature reuse residual block and depthwise dilated convolutions neural network. Appl Soft Comput [Internet]. 2023 Jan;133:109906. Available from: https://linkinghub.elsevier.com/retrieve/pii/S1568494622009553

[35] Dodia S, B. A, Mahesh PA. Recent advancements in deep learning based lung cancer detection: A systematic review. Eng Appl Artif Intell [Internet]. 2022 Nov;116:105490. Available from: https://linkinghub.elsevier.com/retrieve/pii/S0952197622004808

Volume 14, Issue 2, Page 247-258, 2025 https://doi.org/10.46810/tdfd.1639446 Research Article

BİNGÖL UNIVERSITY

Türk Doğa ve Fen Dergisi
Turkish Journal of Nature and Science
www.dergipark.gov.tr/tdfd

Enhancing Geometry Education through Deep Learning Models: Addressing Challenges in Three-Dimensional Shape Visualization

Abdullah ŞENER[1*], Serdal POÇAN[2], Burhan ERGEN[3]

[1] Fırat University, Faculty of Economics and Administrative Sciences, Department of Management Information Systems, Elazığ, Türkiye
[2] Bingöl University, Genç Vocational School, Department of Computer Technologies, Bingöl, Türkiye
[3]Fırat University, Faculty of Engineering, Department of Computer Engineering, Elazığ, Türkiye
Abdullah ŞENER ORCID No: 0000-0002-8927-5638
Serdal POÇAN ORCID No: 0000-0001-6901-0889
Burhan ERGEN ORCID No: 0000-0003-3244-2615

**Corresponding author: asener@firat.edu.tr*

(Received: 13.02.2025, Accepted: 04.06.2025, Online Publication: 27.06.2025)

Keywords
Artificial intelligence, Deep learning, Mathematics education, Three-dimensional shapes

Abstract: Integrating technology into mathematics education is crucial for enhancing the understanding of mathematical concepts and skills, as well as increasing motivation. This is particularly applicable in geometry classes, where technology can facilitate the detection of geometric shapes, impacting both the learning and teaching processes. In this context, emerging concepts of artificial intelligence and deep learning can be utilized as tools to overcome such limitations. This study addresses the challenges that teachers face when drawing three-dimensional geometric shapes in digital environments. Shapes drawn manually in digital environments can often be complex, making it difficult for teachers to create accurate and precise drawings. Deep learning models can assist teachers in correcting drawing errors, thereby providing students with clearer and more comprehensible visuals to facilitate the learning of geometric concepts. The study emphasizes the high accuracy rates achieved using various deep learning models, highlighting their impressive capabilities in accurately classifying geometric shapes.

Derin Öğrenme Modelleriyle Geometri Eğitiminin Geliştirilmesi: Üç Boyutlu Şekil Görselleştirmesindeki Zorlukların Ele Alınması

Anahtar Kelimeler
Yapay zaka, Derin öğrenme, Matematik eğitimi, Üç boyutlu şekiller

Öz: Matematik eğitimine teknolojinin entegrasyonu, hem matematiksel kavram ve becerilerin anlaşılmasını geliştirmek hem de motivasyonu artırmak açısından büyük önem taşımaktadır. Bu durum özellikle geometri derslerinde geçerlidir; zira teknoloji, geometrik şekillerin algılanmasını kolaylaştırarak öğrenme ve öğretme süreçlerini olumlu yönde etkileyebilmektedir. Bu bağlamda, yapay zekâ ve derin öğrenme gibi gelişmekte olan kavramlar, mevcut sınırlılıkların aşılmasında birer araç olarak kullanılabilir. Bu çalışma, öğretmenlerin dijital ortamlarda üç boyutlu geometrik şekilleri çizerken karşılaştıkları zorlukları ele almaktadır. Dijital ortamlarda elle çizilen şekiller çoğu zaman karmaşık olabilmekte ve bu durum, öğretmenlerin doğru ve hassas çizimler yapmalarını güçleştirmektedir. Derin öğrenme modelleri, öğretmenlere çizim hatalarını düzeltmede yardımcı olarak, öğrencilerin geometrik kavramları daha açık ve anlaşılır görseller üzerinden öğrenmelerini sağlayabilir. Çalışma, çeşitli derin öğrenme modelleri kullanılarak elde edilen yüksek doğruluk oranlarına vurgu yaparak, bu modellerin geometrik şekilleri doğru şekilde sınıflandırmadaki etkileyici yeteneklerini ön plana çıkarmaktadır.

1. INTRODUCTION

Mathematics is a learning content that uses a symbolic language that refers to numbers, quantity, space and structure [1,2]. It is imperative to ensure that as many members of the society as possible have a solid grasp of the basics of mathematics and can learn and understand it effectively [3], but many students experience anxiety thinking that mathematics is difficult and that they are likely to fail, and consequently develop a negative attitude towards mathematics. The teaching methods that lead to this problem should be reconsidered [4], and it is important to provide suitable conditions for easy learning to occur [5].

When literature is considered, it is possible to see that technology, which is a part of our daily life, is heavily integrated with education. Many institutions supported adapting cognitive technologies to education, and stated the importance of teachers and students using technology in class actively [6]. Developments in technology also transform the perception of the classroom, and concepts such as flipped classrooms affect learning styles. In this context, virtual classroom environments created through online learning tools inevitably stretch [7]. Mathematics lessons and technology are getting more and more integrated, and the importance of digital technologies in improving learning experiences is being emphasized [1]. The integration of technology into education, especially mathematics learning, is considered important and is becoming a trend [8]. Recent studies (e.g., Chen et al [9]; Park & Kwon [10]) emphasize the increasing relevance of AI-enhanced learning platforms, highlighting the need for adaptive and intelligent systems in mathematics education.

Interest in how to use mobile devices to support learning and teaching, increases as technology becomes widespread [11]. Technology is integrated into daily life, and it plays an important role in education [12]. Technology, a part of daily life, affects knowledge-seeking behaviors, communication, and behaviors. Consequently, educational environments started to change, and digital culture in educational environments started to be cited in curricula [13]. These changes caused educational technologies with different interactions to become widespread, in addition to affecting education curricula. Students started using tablets instead of notebooks, and teachers are using different teaching tools, such as Google Classroom, Edmodo, PowerSchool, and Moodle. In addition, different online studying environments paved their way into education. The increasing number of active users of such courses show that distance learning methodologies are appreciated [13]. As a result, the role of technology is important in the development of mathematical concepts and skills in students [14].

Computer technologies can be integrated in every aspect of a classroom. Teaching specialized techniques become more interesting, and students can learn new concepts faster and easier [15]. Although there are differences in research questions or methodologies, we need to build bridges between different communities and learn from each other without having to reinvent the wheel [16]. At the same time, we think that in addition to different cultures learning from each other, the cooperation between different disciplines will contribute to each other in the context of teaching and learning.

Many studies in mathematics education show that artificial objects and especially technological objects are important in mediating mathematical issues [17]. It is stated that this contributes to the satisfaction levels of teachers since in-class participation and interest of students increase [18]. On the other hand, especially during online lessons, expending more energy to deliver a subject may cause teachers to be stressed, and students may need to work harder to understand the lesson [19]. This shows that more work should be done on what should be done to reduce stress for teachers in online courses and to facilitate learning for students [9].

Artificial intelligence (AI), which is a tool to support and even further develop human skills, is a hot topic in public debates as in many sciences [20]. AI, which is entrusted to futuristic societies, previously created in the imagination of science fiction writers and filmmakers, is now a reality of everyday life in our modern high-tech societies. There are many definitions of AI, and each of these definitions has been revised over time [21]. It is stated that the term AI was first used in 1956 at a conference held at Dartmouth University on how machines simulate the intelligent activities of humans [22]. Wang et al [23] define AI as "to make a computer work like a human mind" (p. 2), Rapaport [24] defines AI as "…a scientific study of what problems can be solved, what tasks can be accomplished, and what features of the world can be understood computationally (i.e., using the language of Turing Machines), and then to provide algorithms to show how this can be done efficiently, practically, physically, and ethically" (p. 54).

Important developments were experienced in artificial intelligence in education (AIED). Artificial intelligence technologies, one of the popular technology topics in some developed countries, have begun to be included in the training [10]. Two main questions are asked when thinking about the past and shaping the future: What are our strongest aspects, and what are the opportunities of the future [16]? Positive aspects of AI are expressed at the point of increasing the quality of education [25]. For example, AI can lift limitations such as time and place for teachers and offer unique learning environments such as collaborative learning environments to students [16]. AI, which offers innovative and creative opportunities in many science fields, became popular in mathematics education as well [26]. The relationship between mathematics and artificial intelligence is not one-sided. Artificial intelligence has an important place in the development of computer-based tools in the learning and teaching of mathematics, as well as the contribution of mathematics to artificial intelligence becoming a science field [27].

Geometry is a branch of mathematics that is difficult and feared by students [28]. In addition, the complexity of geometry compared to numerical operations and algebra causes major difficulties while trying to overcome problems experienced while learning [29]. Especially, representing a 3D shape as a 2D shape may affect students' reasoning [30] and this causes them to shy away from geometry. Spatial thinking, which is also expressed as the ability to establish the relationship between 2D and 3D representations, is considered important not only in mathematics but also in other branches of science [31]. The lattices formed with shapes in the geometry lessons may cause students to not be able to visualize the visual in their minds, and this causes the students to not be able to visualize spatial objects fully. These problems arising from the characteristics of geometric shapes appear as problems in distinguishing some shapes from each other [32].

Teaching geometric shapes is crucial in shaping children's thoughts. However, sufficient training material to do so is limited [33]. Although it is easier to draw on paper using drawing tools such as pencils in geometry, we have recently seen that many computer aided auxiliary tools are used in distance education [34]. The development of technology has also affected the teaching and learning process [35].

Online learning becomes more popular as the curricula in education institutes become digitized. The global pandemic, as well as the increasing number of students are stated as the causes, and consequently the need to use automated techniques in learning and teaching is highlighted [36]. Over a decade, advances in digital technologies have created new learning opportunities for rural and distance learners to provide distance education [37]. It has been incredibly challenging, especially in developing countries where teachers and organizations do not have the appropriate tools for effective teaching through distance learning [26]. Deficiencies or mistakes in the visualization of geometric concepts can cause students to fail learning knowledge they need to acquire about a concept [38]. Algorithms regarding machine learning in geometric shapes have become popular recently [39]. The emphasis on the combination of analytical and visual thinking, especially in animating a 3D shape in the mind or coping with the problems of plane and solid geometry [40], explains the reason for the emerging need. The visual and logical-structural foundation of a geometric concept are correlated. Logical-structural foundations refer to the correlations between properties and shape [38]. In addition, students' drawing skills, hence their spatial visualization and spatial orientation skills should be developed to draw and interpret shapes correctly [41]. Therefore, technological developments become popular in making geometric drawings easy, appealing to the eye, expressing ideas and understanding subjects more easily.

The spatial imagination plays a significant role in the cognitive development of individuals undergoing training within the educational system. Cognitive development, encompassing general intelligence, problem-solving skills, and 3D modeling, is influenced by various factors [42]. Distance learning has gained increasing popularity for various reasons, necessitating the exploration of challenges encountered in teaching mathematics within distance education environments. Specifically, limitations in drawing 3D shapes as 2D representations directly impact the process of learning and teaching. Furthermore, the imperative integration of Artificial Intelligence (AI) into education has become evident. The study underscores the growing trend of technology integration in mathematics education, with a particular emphasis on the pivotal role of digital technologies in enriching learning experiences. Within this framework, the objective is to predict and classify 3D drawings, a task that teachers often find challenging in digital environments. This endeavor, facilitated by deep learning models, is expected to directly influence the learning process.

Upon reviewing the literature, it becomes apparent that studies utilizing deep learning methods in mathematics as a component of AI are relatively limited. This scarcity may be attributed to the insufficient collaboration among different disciplines. Consequently, this study is deemed significant, and it is anticipated to serve as a pioneering effort for future research endeavors.

2. MATERIAL AND METHOD

2.1. Dataset

In this study, a custom dataset was constructed to evaluate the performance of the proposed deep learning models in classifying geometric shapes. The dataset comprises a total of 1,249 black-and-white images created manually in a digital environment. All images were drawn by twelve voluntary participants, including pre-service mathematics teachers and high school students, using drawing tablets and stylus pens. The drawings were created using basic digital drawing software, simulating a natural hand-drawing experience within a controlled digital setting.

To ensure standardization and consistency, participants were provided with predefined shape guidelines, including examples and basic dimensional constraints. Each drawing was evaluated based on visual clarity, geometric accuracy, and adherence to shape criteria before inclusion in the dataset. The finalized dataset includes three main geometric categories: spheres (142 images), pyramids (464 images: 120 square pyramids, 156 cones, and 188 triangular pyramids), and prisms (643 images: 175 rectangular prisms, 182 cubes, 142 cylinders, and 144 triangular prisms). All images vary in resolution and scale, then were normalized into grayscale format for compatibility with image processing algorithms. A sample of the image collection is presented in Figure 1, illustrating the diversity and structure of the dataset used in this research.

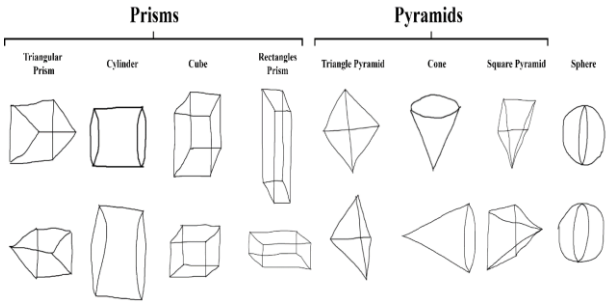

Figure 1. Example Images from the Dataset used in the Research

2.2. Deep Learning

Deep learning is a machine learning technique that predicts or generates results based on a dataset containing multiple layers. The primary objective of deep learning is to extract new information from the data it processes using the artificial neural network it employs. Among various deep learning methods, the Convolutional Neural Network (CNN) architecture is the most widely used [43]. CNNs recognize images with shared features and classify them by grouping them based on similarities, akin to the human brain's functioning [44]. The CNN architecture is composed of a series of layers, including the convolutional layer, non-linearity layer, pooling layer, flattening layer, and fully-connected layer [45]. The convolutional layer serves as the core of the CNN architecture, where the majority of computationally intensive operations occur. This layer detects both low-level and high-level features by applying filters to the input images. The non-linearity layer captures non-linear patterns by introducing transformations to the data. In the pooling layer, the size of the feature maps is reduced, which decreases the number of parameters and weights in the network. This reduction is typically achieved through max pooling, which selects the highest value within n×n regions, or average pooling, which computes the mean value of these regions. The flattening layer converts the data into a one-dimensional matrix, preparing it for the fully connected layer, which is the final stage of the CNN architecture. The fully connected layer establishes the relationship between the input and output layers [46, 47].

2.3. Visual Geometry Group-19

The Visual Geometry Group (VGG)-19 is a convolutional neural network with a depth of 24 layers. Its architecture consists of 16 convolutional layers, 5 pooling layers, and 3 fully connected layers. The network was pre-trained on more than one million images from the ImageNet database. VGG-19 accepts image inputs of 224 x 224 pixels and contains approximately 138 million parameters [48]. It utilizes 3x3 pixel filters in the convolutional layer to reduce the number of parameters in the architecture.

2.4. Xception

GoogLeNET (Inception V1), is created by Google engineers inspired by "Network-In-Network" [49]. Inception V2 and Inception V3 versions were developed later [50]. The Xception architecture is an extension of Inception architecture that replaces standard Inception modules with deeply separable convolution [51]. The Xception network was pre-trained on over one million images from the ImageNet database and processes image inputs of 224 x 224 pixels. Rather than dividing the input data into compressed chunks, the network independently maps spatial correlations for each output channel and employs 1 x 1 depthwise convolutions to capture inter-channel correlations.

2.5. The proposed approach

In the study, two new models are proposed based on VGG-19 and Xception architectures. A dataset containing geometric shapes created by drawing in a computer environment was used to evaluate the performances of the models. 70% of the images in the dataset were used for training and 30% for validation. The first step of the study involves adjusting the images in the dataset, which have varying resolutions and sizes, to a fixed resolution of 224 x 224 pixels, the input size required by the VGG-19 and Xception models. This step aims to optimize classification speed and minimize memory usage on the computer. During resizing, all images are scaled to this predetermined size. Care is taken to ensure that the dimensions are not excessively reduced, preserving as much image quality as possible. If the images are resized too much, it may become difficult to retain the necessary information for accurate image classification. In the next part of the study, the dataset images brought to fixed resolution and size were classified separately on the developed VGG-19 and Xception models. Classification processes were primarily carried out on prisms and pyramid classes. Then, classification was carried out by combining all classes. Based on the results obtained, the performances of the developed models were compared. Figure 2 illustrates the overall design of the VGG-19 model developed in the study.

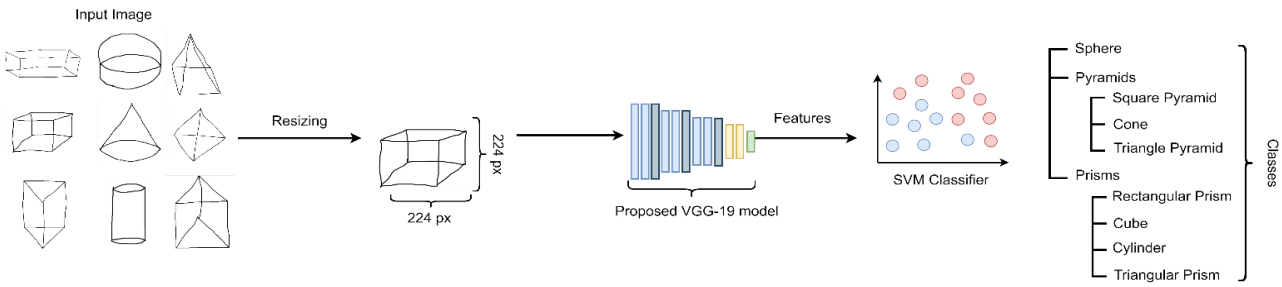

Figure 2. General Design of the Recommended VGG-19 Model

The model illustrated in Figure 2 comprises 25 layers in total. These include 13 convolutional layers, 5 max-pooling layers, 2 dropout layers, 2 batch normalization layers, 2 fully connected layers, and 1 softmax layer. In the developed VGG-19 model, 13 convolutional and 5 max-pooling layers are applied to the gray-scale computer-generated geometric shape images inputted into the model. After completing the convolution and pooling layers, the data is passed through the flattening and fully connected (FC1) layers, followed by the first batch normalization layer. A dropout operation is then applied with a rate between 0.3 and 0.5 to prevent overfitting by reducing the risk of the network memorizing the training data. Subsequently, the second fully connected layer and batch normalization layer are applied, followed by another dropout process with the same drop rate. The final classification output is generated using the softmax optimization algorithm. Additionally, the ReLU activation function is used in the convolutional layers of the model. Figure 3 illustrates the architecture of the Xception model, which is the second model developed in this study.

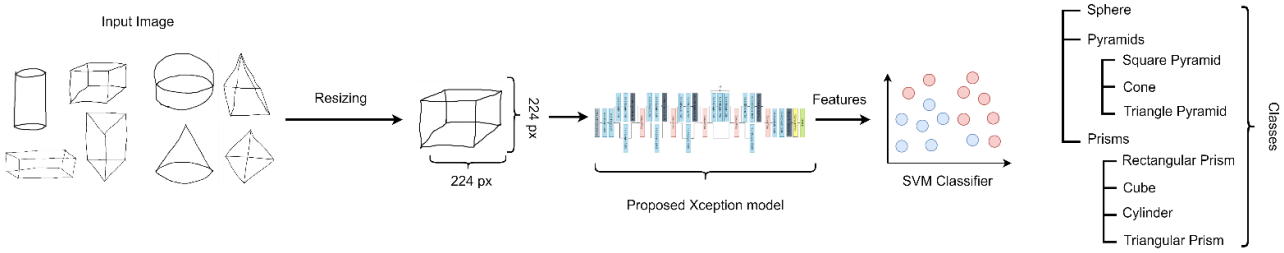

Figure 3. General Design of the Recommended Xception Model

The Xception model shown in Figure 3 consists of a total of 31 layers. These include 19 convolutional layers, 5 max-pooling layers, 2 dropout layers, 2 batch normalization layers, 2 fully connected layers, and 1 output (softmax) layer. The same parameters used in the VGG-19 model were also applied to the Xception model to enable a fair comparison between the models developed in the study.

2.6. Media and Libraries

The training and validation processes of the models developed based on VGG-19 and Xception are carried out using PyCharm 2021. Python 3.6 and OpenCV, Keras, Sklearn, Matplotlib, Imageio, NumPy, PIL and Os libraries were used to process the dataset used in models. The computer operating system used in the study is 64-bit Windows 11. The hardware specifications include an NVIDIA GeForce® RTX™ 3060 6GB graphics card, an 11th Gen Intel® Core™ i7 processor (2.3GHz, 24M Cache, up to 4.6GHz, 8 cores), and 16GB of memory.

3. RESULTS AND DISCUSSION

In the study, 70% of the dataset was used for training and 30% for validation processes in the evaluation of the performances of both models. A total of 464 images, 326 training and 138 validation images, were used in the classification of the pyramids. 643 images, 452 training and 191 validation, were used while classifying prisms. During general classification, 1249 images were used, of which 878 were for training and 371 for validation. Table 1 presents the training parameters of the developed models. The dropout rates between 0.3 and 0.5 were chosen to prevent overfitting while maintaining generalization. The number of epochs (10) was selected to ensure convergence without excessive computation. A mini-batch size of 16 was found optimal during preliminary testing to balance performance and training stability.

Table 1. Training Parameters of the Developed Model

Parameter	Value
Epoch	10
Mini Batch Size	16
Dropout	0,3-0,5
Activation Function	ReLu
Optimization Algorithm	Softmax

In the first stage of the study, the classification of pyramid images, which are divided into 3 subgroups, was performed using the VGG-19-based model. Figure 4 shows the accuracy and loss values obtained during the model's training and testing phases as a result of the classification. When the graphics are examined, it can be seen that the developed model learns quickly. It can be seen that the network continues to learn, as evident from the ups and downs until the 10th iteration. After the training of the model was completed, an accuracy rate of 81% was obtained.

Figure 4. Accuracy and Loss Graphics of the VGG-19 Model Developed to Classify Pyramid Images

A confusion matrix is a table that summarizes the prediction results in a classification process. It is used to provide an idea about the error rate of a model developed through the classification process. Confusion matrix is

frequently used in the literature to define the performance of models in classification problems. If we evaluate it for binary classification models, the confusion matrix is depicted as shown in Figure 5.

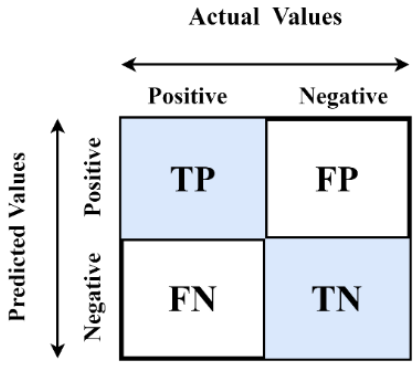

Figure 5. Confusion Matrix

The confusion matrix was used to evaluate the performance of the models whose classification operations were performed. Terms used while constructing the confusion matrix: TP: True Positive, FP: False Positive, TN: True Negative, and FN: False Negative. Precision, Recall, Accuracy and F1-Score values of the model can also be calculated using these values. The mathematical operations given in equations 1, 2, 3 and 4 are used to calculate these values.

$$Precision = \frac{TP}{TP + FP} \quad (1)$$

$$Recall = \frac{TP}{TP + FN} \quad (2)$$

$$Accuracy = \frac{TP + TN}{TP + TN + FP + FN} \quad (3)$$

$$F1 - Score = \frac{2 * precision * recall}{precision + recall} \quad (4)$$

Table 2 presents the analysis results of the classification conducted using the test data from the proposed VGG-19 model.

Table 2. Analysis Results of Classification

Classes	Rec.%	Prc. %	F1-Scr. %	Acc. %
Square pyramid	100	68	81	81
Cone	100	75	86	
Triangle pyramid	64	100	78	

Figure 6 presents the confusion matrix of the VGG-19 model based on the results obtained from classification. This matrix provides a detailed view of the model's classification ability by showing the correct and incorrect predictions across the pyramid categories, offering insights into where misclassifications are most likely to occur.

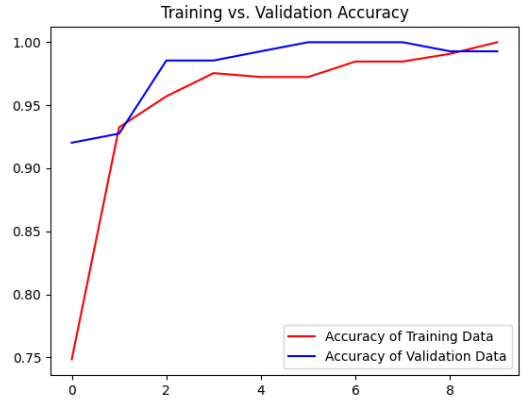

Figure 6. Confusion Matrix of VGG-19 Model Developed for Classifying Pyramid Images

In the second stage of the study, the classification of the pyramid images consisting of 3 subgroups was carried out using the Xception based model. Figure 7 presents the accuracy and loss values of the model after training and training after using test data.

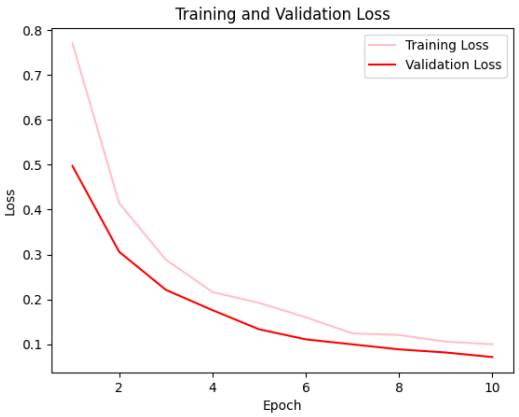

Figure 7. Accuracy and Loss Graphics of Xception Model Developed for Classification of Pyramid Images

When the graphics are examined, it can be seen that the developed model learns quickly. It can be seen that the network continues to learn, as evident from the ups and downs until the 10th iteration. After the training of the model was completed, an accuracy rate of 100% was obtained. Table 3 presents the analysis results of the Xception model using test data.

Table 3. Analysis Results of Classification

Classes	Rec. %	Prc. %	F1-Scr. %	Acc. %
Square pyramid	100	100	100	100
Cone	100	100	100	
Triangle pyramid	100	100	100	

Figure 8 presents the confusion matrix of the recommended Xception model based on the results obtained after classification.

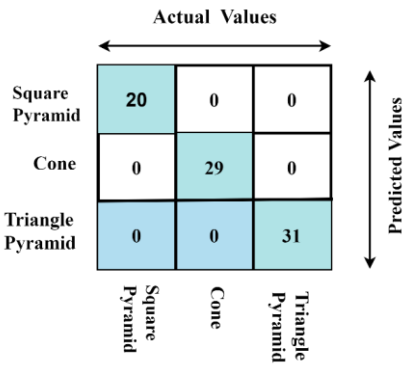

Figure 8. Confusion Matrix of Xception Model Developed to Classify Pyramid Images

In the third stage of the study, the classification of prism images, divided into four subgroups, was performed using the VGG-19-based model. Figure 9 presents the accuracy and loss rates as a result of training after classification and training using test dataset. When the graphics are examined, it can be seen that the developed model learns quickly. It can be seen that the network continues to learn, as evident from the ups and downs until the 10th iteration. After the training of the model was completed, an accuracy rate of 81% was obtained.

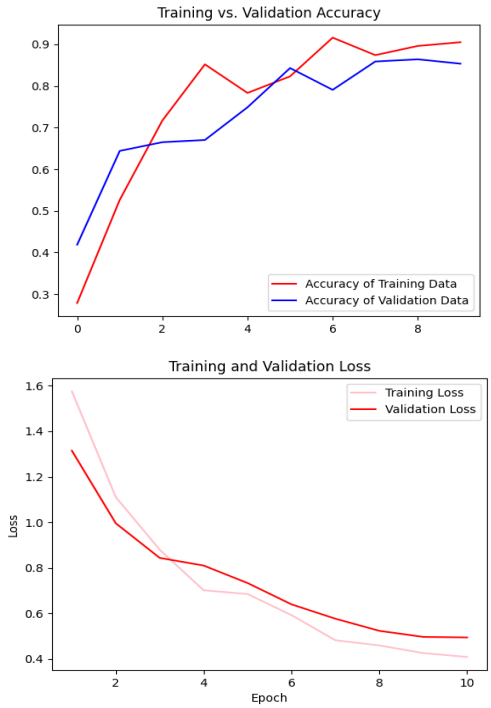

Figure 9. Accuracy and Loss Graphics of the VGG-19 Model Developed to Classify Prism Images

Table 4 shows the analysis results of the classification using the test data from the proposed VGG-19 model.

Table 4. Classification Analysis Results

Classes	Rec.%	Prc. %	F1-Scr. %	Acc. %
Rectangular prism	59	91	71	81
Cube	94	50	65	
Cylinder	90	100	95	
Triangular prism	100	94	97	

Figure 10 presents the confusion matrix of the recommended VGG-19 model based on the classification results.

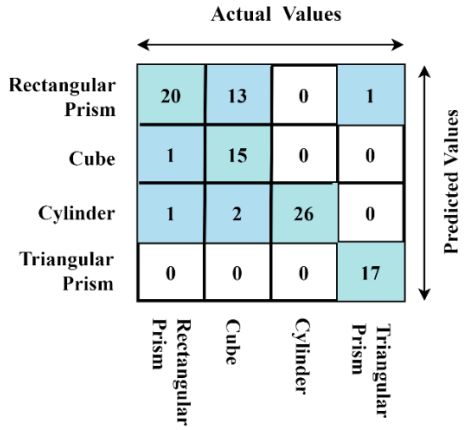

Figure 10. Confusion Matrix of the Developed VGG-19 Model to Classify Prism Images

In the fourth stage of the study, the classification of prism images consisting of 4 subgroups was carried out using the Xception based model. Figure 11 presents the accuracy and loss rates as a result of training after classification and training using test dataset. When the graphics
are examined, it can be seen that the developed model learns quickly. It can be seen that the network continues to learn, as evident from the ups and downs until the 10th iteration. After the training of the model was completed, an accuracy rate of 92% was obtained.

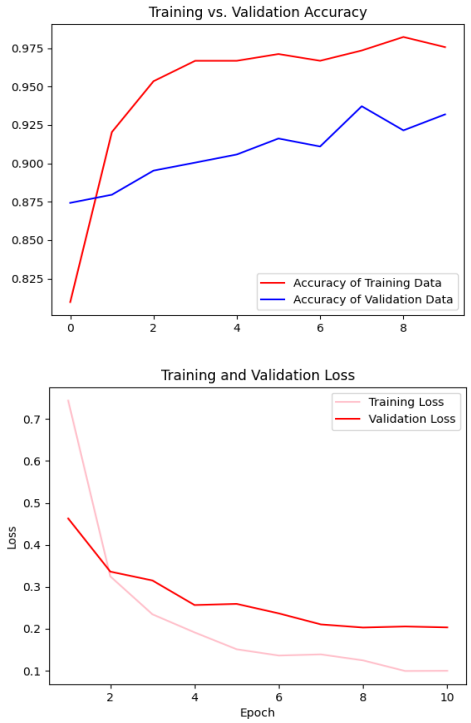

Figure 11. Accuracy and Loss Graphics of the VGG-19 Model Developed to Classify Prism Images

Table 5 shows the analysis results of the classification using the test data from the proposed Xception model.

Table 5. Analysis Results of Classification

Classes	Rec.%	Prec. %	F1-Scr.%	Acc.%
Rectangular prism	75	100	86	92
Cube	100	79	88	
Cylinder	100	100	100	
Triangle prism	100	91	95	

Figure 12 presents the confusion matrix of the recommended Xception model based on the classification results.

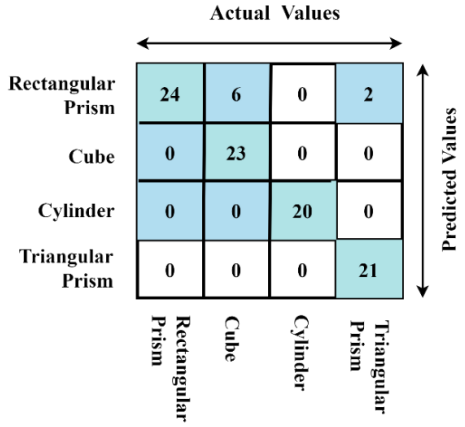

Figure 12. Confusion Matrix of the Recommended Xception Model Developed to Classify Prism Images

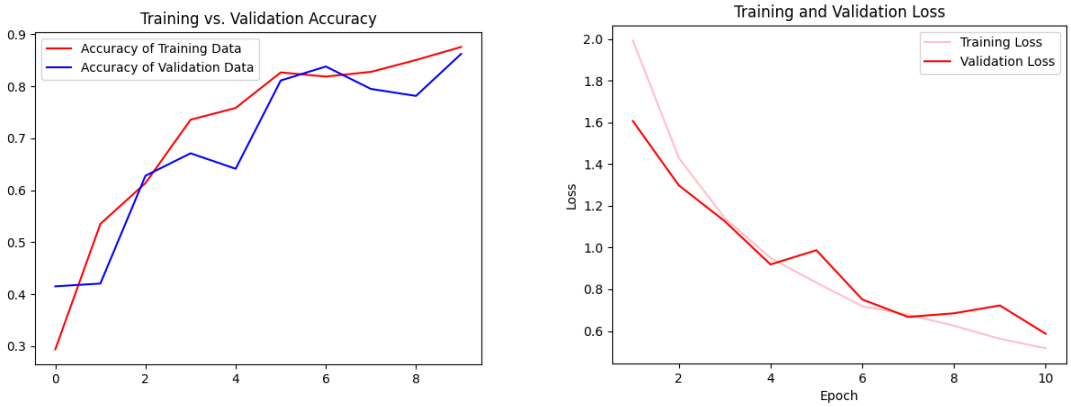

Figure 13. Accuracy and Loss Graphics of the Developed VGG-19 Model to Classify All Images in the Dataset

In the fifth stage of the study, the classification of images consisting of 8 subgroups was carried out using the VGG-19 based model. Figure 13 presents the accuracy and loss rates as a result of training after classification and training using test dataset. When the graphics are examined, it can be seen that the developed model learns quickly. It can be seen that the network continues to learn, as evident from the ups and downs until the 10th iteration. After the training of the model was completed, an accuracy rate of 84% was obtained.

Table 6 presents the classification results obtained using the test data from the proposed VGG-19 model.

Table 6. Classification Results Analysis

Classes	Rec.%	Prc. %	F1-Scr. %	Acc. %
Rectangular prism	71	89	79	84
Square pyramid	83	94	88	
Cone	96	100	98	
Cube	82	62	71	
Sphere	100	100	100	
Cylinder	95	91	93	
Triangle pyramid	100	55	71	
Triangular prism	64	95	76	

Figure 14 presents the confusion matrix of the recommended VGG-19 model according to the classification results.

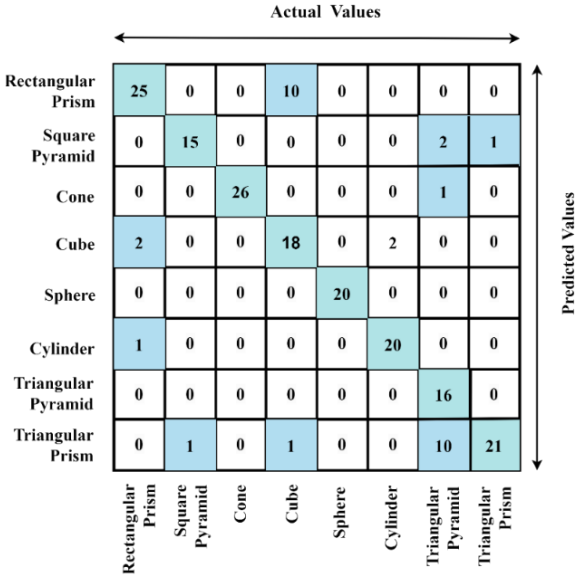

Figure 14. Confusion Matrix of VGG-19 Model Developed to Classify All Images in Dataset

In the last stage of the study, the classification of images consisting of 8 subgroups was carried out using the Xception based model. Figure 15 presents the accuracy and loss rates as a result of training after classification and training using test dataset. When the graphics are examined, it can be seen that the developed model learns

quickly. It can be seen that the network continues to learn, as evident from the ups and downs until the 10th iteration. After the training of the model was completed, an accuracy rate of 95% was obtained.

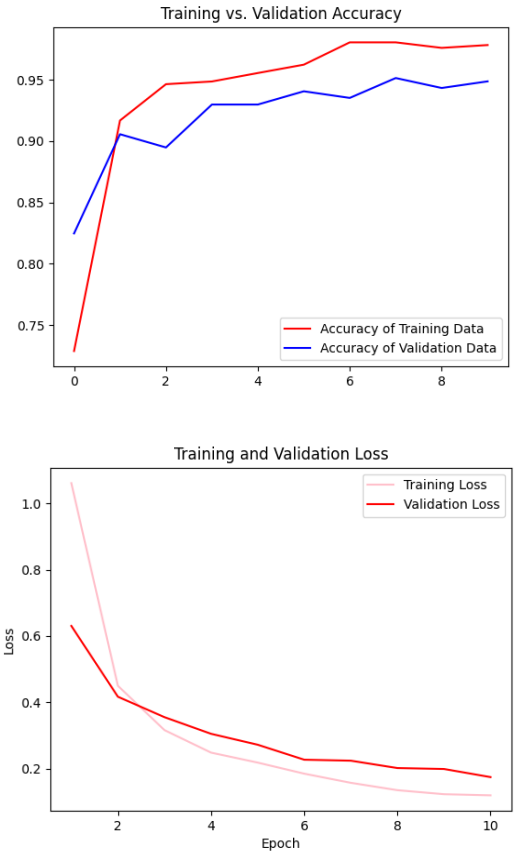

Figure 15. Accuracy and Loss Graphics of Xception Model Developed to Classify All Images in Dataset

Table 7 presents the analysis results obtained from the test data of the proposed Xception model.

Table 7. Analysis results of classification

Classes	Rec. %	Prc. %	F1-Scr. %	Acc. %
Rectangular prism	76	100	86	95
Square pyramid	92	96	94	
Cone	100	100	100	
Cube	100	73	84	
Sphere	100	100	100	
Cylinder	100	100	100	
Triangle pyramid	100	100	100	
Triangular prism	94	89	92	

Figure 16 presents the confusion matrix of the recommended Xception model according to the classification results.

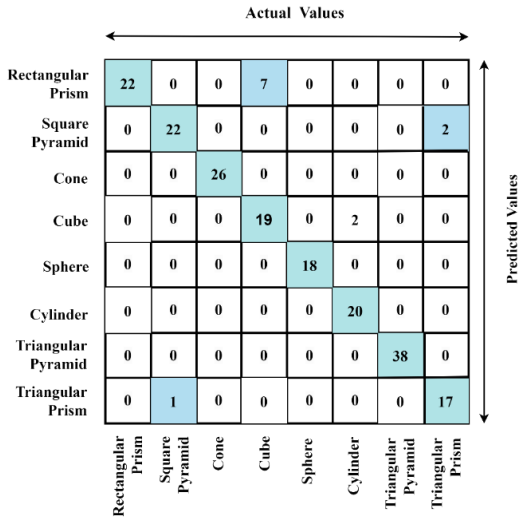

Figure 16. Confusion Matrix of Xception Model Developed to Classify All Images in Dataset

The performance of the VGG-19 and Xception models developed in this study was evaluated using a custom dataset of hand-drawn geometric figures. In the initial phase, classification was conducted on images categorized under pyramids. The VGG-19 model achieved an accuracy of 81%, whereas the Xception model reached a perfect accuracy of 100% in this category. In the second phase, classification was extended to prism images, where VGG-19 yielded 81% accuracy and Xception achieved 92%. Finally, when the models were tested across the complete dataset comprising spheres, pyramids, and prisms, VGG-19 recorded 84% accuracy, while Xception attained 95%. These results consistently highlight the superior performance of the Xception architecture.

When comparing these outcomes to existing studies in the field, varying conclusions can be observed. Patil and Golellu [52], for instance, found VGG-16 to outperform VGG-19 and Xception, while Özdemir and Arslan [53] reported higher performance with InceptionV3. Similarly, Humayun et al. [54] identified VGG-16 as the most effective model in their comparative analysis. These discrepancies underscore the influence of dataset characteristics and hardware configurations on model performance, highlighting the importance of contextual evaluation.

In terms of practical applications, the integration of these models into educational environments holds promising potential. Teachers can utilize simplified versions of such models through mobile applications or browser-based platforms to instantly assess and provide feedback on students' geometric drawings. These tools could be used during in-class activities by allowing students to sketch shapes digitally and receive automated evaluations, thus reinforcing spatial reasoning skills in real-time. In remote learning contexts, students can upload images of their drawings to receive instant classification and feedback, which may enhance engagement and comprehension outside traditional classroom settings. Moreover, these AI-powered systems can be integrated into digital whiteboards or geometry learning platforms, enabling

teachers to demonstrate correct shape construction and offer error-correction suggestions interactively. By embedding deep learning into formative assessment practices, educators can create a more inclusive and adaptive learning experience tailored to individual student needs.

The utility of hand-drawn image datasets, such as MNIST, has been widely acknowledged in the literature for similar tasks. Studies by Garin & Tauzin [55], Grover & Toghi [56], Iyer [57], Kadam et al. [58], and Prabhu [59] illustrate the effectiveness of convolutional neural networks (CNNs) in classifying handwritten figures. Audibert and Maschio [60] introduced a CNN-based system named FINNger to identify mathematical hand signs in children, achieving an accuracy of 92%. They emphasized challenges related to background noise and spatial separation in image data but nonetheless demonstrated the pedagogical value of AI systems in mathematics education. Such findings further validate the current study's emphasis on the educational utility of AI-enhanced tools in geometry instruction. Table 8 presents a comparative analysis of the results obtained in this study with those reported in the literature using similar datasets.

Table 8. Comparative analysis of the results

Authors	Method	Accuracy %
Zhang L. [61]	Dual-channel CNN	%73
Hayat et al. [62]	Deep convolutional neural network-based (DCNN)	%94
Ali et al. [63]	Sketch-DeepNet	%95
This Study	**VGG19**	**%84**
This Study	**Xception**	**%95**

As shown in Table 7, the Xception model developed in this study achieved an accuracy rate comparable to the highest reported in the literature. While the VGG-19 model yielded slightly lower performance, it still demonstrated competitive results. These findings highlight the effectiveness of deep learning architectures, particularly Xception, in the classification of hand-drawn geometric figures, and underscore the potential of integrating such models into educational technologies.

The number of images in the dataset plays a crucial role in the training of deep learning models. To evaluate the performance of the models developed in this study, the researchers created a custom dataset. However, the relatively small number of images in the dataset is considered a limitation. Hand-drawn images by different people were used in the study to overcome this issue. In addition, it is thought that the study will contribute to the literature by sharing the datasets created from this and similar studies on different digital platforms. Due to the universal nature of geometry, it is possible to further improve the model developed by using the hand-drawn images by students and teachers in different countries, together. In addition, studies similar to this can be carried out in different learning areas apart from the geometry learning area. Similar studies can be conducted using different deep learning models and the results can be compared. In line with the results obtained, this study and similar studies can provide great benefits to students and learning in mathematics lessons in computer environments and mobile devices through applications.

4. CONCLUSION

Distance education is becoming widespread today. In this context, efforts to find solutions to problems encountered in mathematics lessons in distance education are increasing. In particular, drawing 3D objects in a computer environment creates problems related to spatial thinking for the learner. It is possible to come across different solutions in the literature to overcome these limitations. The study aimed to determine the geometric shapes using deep learning models by using the dataset containing the 3D hand-drawn geometric shapes in the computer environment. In this context, two models have been developed based on VGG-19 and Xception architectures, which are popular deep learning models today. The performances of the developed models were measured using the dataset in the study, and the two models were compared based on the obtained values, and it was determined that the Xception model provided better results. The Xception model classified geometric objects with 95% accuracy in general classification. Considering the results obtained, deep learning methods can be used to solve problems encountered in distance education.

Considering the obtained results, deep learning methods can be employed to address the challenges encountered in distance education. Consequently, the use of artificial intelligence, especially deep learning models, in geometry classes serves as a robust solution to the difficulties faced in drawing and visualizing geometric shapes in digital environments. As demonstrated in the study, the high accuracy rates achieved by these models underscore their potential to revolutionize mathematics education, making it more accessible, engaging, and effective for students. Teachers can leverage these technologies not only to enhance instructional methods but also to alleviate the stress associated with online
courses and ultimately create a conducive environment for effective learning.

REFERENCES

[1] Bray A., Tangney B. Technology usage in mathematics education research–A systematic review of recent trends. Computers & Education. 2017;114;255-273.

[2] Chao W. H., Yang C. Y., Chang R. C. A study of the interactive mathematics mobile application development. 1st IEEE International Conference on Knowledge Innovation and Invention (ICKII). 2018. p.248-249

[3] Daly I., Bourgaize J., Vernitski A. Mathematical mindsets increase student motivation: Evidence from the EEG. Trends in Neuroscience and Education. 2019;15; 18–28.

[4] Baykul Y. İlkokulda matematik öğretimi [Teaching mathematics in primary school].12th ed. Pegem Akademi; 2014.

[5] Altun M. Eğitim fakülteleri ve sınıf öğretmenleri için matematik öğretimi [Teaching mathematics for education faculties and primary teachers]. 19th ed.

Aktüel Alfa Akademi; 2015.
[6] Sevimli E., Kul Ü. Evaluation of the contents of mathematics textbooks in terms of compliance to technology: Case of secondary school. Necatibey Faculty of Education Electronic Journal of Science and Mathematics Education. 2015. 9(1), 308-331.
[7] Engelbrecht J., Llinares S., Borba M. C. Transformation of the mathematics classroom with the internet. ZDM Mathematics Education. 2020. 52(5), 825-841.
[8] Azizul S. M. J., Din R. Teaching and learning geometry using GeoGebra software via MOOC. Journal of Personalized Learning. 2016. 2(1), 39-50.
[9] Chen B., Bao L., Zhang R., Zhang J., Liu F., Wang S., Li M. A Multi-Strategy Computer-Assisted EFL Writing Learning System With Deep Learning Incorporated and Its Effects on Learning: A Writing Feedback Perspective. Journal of Educational Computing Research. 2023. 61(8), 60-102.
[10] Park W., Kwon H. Implementing artificial intelligence education for middle school technology education in Republic of Korea. International Journal of Technology and Design Education. 2023. p.1-27.
[11] Kearney M., Maher D. Mobile learning in pre-service teacher education: Examining the use of professional learning networks. Australasian Journal of Educational Technology. 2019. 35(1), 135-148.
[12] Aksu H. H. Mathematics teachers' opinions on distance education using the Educational Informatics Network (EBA). Turkish Online Journal of Educational Technology. 2021. 20(2), 88-97.
[13] Chassignol M., Khoroshavin A., Klimova A., Bilyatdinova A. Artificial Intelligence trends in education: a narrative overview. Procedia Computer Science. 2018. 136, 16-24.
[14] Shumway J. F., Welch L. E., Kozlowski J. S., Clarke-Midura J., Lee V. R. Kindergarten students' mathematics knowledge at work: the mathematics forprogramming robot toys. Mathematical Thinking and Learning. 2021. p.1-29.
[15] Iskrenovic-Momcilovic O. Improving geometry teaching with scratch. International Electronic Journal of Mathematics Education. 2020. 15(2), 5-8.
[16] Roll I., Wylie R. Evolution and revolution in artificial intelligence in education. International Journal of Artificial Intelligence in Education. 2016. 26(2), 582-599.
[17] Bussi M. B., Mariotti M. A. Semiotic mediation in the mathematics classroom: Artifacts and signs after a Vygotskian perspective. Handbook of international research in mathematics education. 2nd ed., 2008. pp. 746–805.
[18] Bolliger D. U., Wasilik O. (Factors influencing faculty satisfaction with online teaching and learning in higher education. Distance Education. 2009. 30(1), 103-116.
[19] Jumadi A., Nasrudin F. S. M., Arunah N. S. K., Mohammad S. A., Abd Ghafar N., Zainuddin N. A. Students' and lecturers' perceptions of students' difficulties in geometry courses. International Journal of Advanced Research in Education and Society. 2022. 4(2), 50-64.
[20] Neubauer A. C. The future of intelligence research in the coming age of artificial intelligence–With a special consideration of the philosophical movements of trans-and posthumanism. Intelligence. 2021. 87, 101563.
[21] Goralski M. A., Tan T. K. Artificial intelligence and sustainable development. The International Journal of Management Education. 2020. 18(1), 100330.
[22] Zhang C., Lu Y. Study on artificial intelligence: The state of the art and future prospects. Journal of Industrial Information Integration. 2021.23, 100224.
[23] Wang P., Liu K., Dougherty Q. Conceptions of artificial intelligence and singularity. Information. 2018. 9.4: 79.
[24] Rapaport W. J. What is artificial intelligence? Journal of Artificial General Intelligence. 2020. 11(2), 52–56.
[25] Bundy A. Preparing for the future of Artificial Intelligence. AI & Soc. 2017. 32, 285–287.
[26] Mohamad Nasri N., Husnin H., Mahmud S. N. D., Halim L. Mitigating the COVID-19 pandemic: a snapshot from Malaysia into the coping strategies for pre-service teachers' education. Journal of Education for Teaching. 2020. 46(4), 546-553.
[27] Van Vaerenbergh, Steven; Pérez-Suay, Adrián. A classification of artificial intelligence systems for mathematics education. In: Mathematics education in the age of artificial intelligence: How artificial intelligence can serve mathematical human learning. Cham: Springer International Publishing. 2022. p. 89-106.
[28] Sulistiowati D. L., Herman T., Jupri A. Student difficulties in solving geometry problem based on Van Hiele thinking level. In: Journal of Physics: Conference Series. IOP Publishing. 2019. p. 042118.
[29] Wong W. K., Yin S. K., Yang H. H., Cheng Y. H. Using computer-assisted multiple representations in learning geometry proofs. Journal of Educational Technology & Society. 2011. 14(3), 43-54.
[30] Fujita T., Kondo Y., Kumakura H., Kunimune S., Jones K. Spatial reasoning skills about 2D representations of 3D geometrical shapes in grades 4 to 9. Mathematics Education Research Journal. 2020. 32(2), 235-255.
[31] Cohen C. A., Hegarty M. Sources of difficulty in imagining cross sections of 3D objects. In Proceedings of the Annual Meeting of the Cognitive Science Society. Vol. 29. No. 29. 2007.
[32] Parmanov A. A., Mamatov J. A., Kahhorov M. J., Fayzullaev S. U. Main tasks of teaching geometry at the secondary school. Eastern European Scientific Journal. 2020. 1(2).57-59.
[33] Sarama, J., Clements, D. H.. Clements. Early childhood mathematics education research: Learning trajectories for young children. Routledge, 2009.
[34] Wojtowicz A., Wojtowicz B., Kopec K. Descriptive geometry in the time of COVID-19: Preliminary assessment of distance education during pandemic social isolation. Advances in Engineering Education. 2020. 8(4), 1-10.
[35] Yurniwati Y., Utomo E. Problem-based learning flipped classroom design for developing higher-

order thinking skills during the COVID-19 pandemic in geometry domain. In: Journal of Physics: Conference Series. IOP Publishing. 2020. p. 012057.
[36] Carter Jr R. A., Rice M., Yang S., Jackson H. A. Self-regulated learning in online learning environments: strategies for remote learning. Information and Learning Sciences.2020. 121 (5/6), 321-329.
[37] Lowrie T., Jorgensen R. Teaching mathematics remotely: Changed practices in distance education. Mathematics Education Research Journal, 24(3).2012. 371-383.
[38] Haj-Yahya A. Do prototypical constructions and self-attributes of presented drawings affect the construction and validation of proofs? Mathematics Education Research Journal. 2020. 32(4), 685-718.
[39] Murugan A., Tadesse F. W., Wondirad E. N., Bizuneh M. T., Firew A. Machine learning in identification of polygon shapes for recognition of mechanical engineering drawings. International Journal of Mechanical Engineering. 2022. 7(2), 2282-2288.
[40] Patkin D., Plaksin O. Procedural and relational understanding of pre-service mathematics teachers regarding spatial perception of angles in pyramids. International Journal of Mathematical Education in Science and Technology. 2019. 50(1), 121-140.
[41] Kepceoglu, I. Effect of dynamic geometry software on 3-dimensional geometric shape drawing skills. Journal of Education and Training Studies. 2018. 6(10), 98-106.
[42] Šafhalter A., Glodež S., Šorgo A., Ploj Virtič M. Development of spatial thinking abilities in engineering 3D modeling course aimed at lower secondary students. International Journal of Technology and Design Education. 2022. 32, 167-184.
[43] Gu J., Wang Z., Kuen J., Ma L., Shahroudy A., Shuai B., Liu T., Wang X., Wang G., Cai J., Chen T. Recent advances in convolutional neural networks. Pattern Recognition. 2018. 77, 354-377.
[44] Min S., Lee B., Yoon S. Deep learning in bioinformatics. Briefings in Bioinformatics. 2017. 18(5), 851-869.
[45] Hanbay K. Hyperspectral image classification using convolutional neural network and two-dimensional complex Gabor transform. Journal of the Faculty of Engineering and Architecture of Gazi University. 2020. 35(1), 443-456.
[46] Kurt F. Analysis of the effects of hyperparameters in convolutıonal neural networks. (Publication No. 519157) Master's thesis, Hacettepe University; 2018.
[47] Niepert M., Ahmed M., Kutzkov K. Learning convolutional neural networks for graphs. In Proceedings of the 33rd international conference on machine learning. 2016. p. 2014-2023
[48] Mateen M., Wen J., Nasrullah Song S., Huang Z. Fundus image classification using VGG-19 architecture with PCA and SVD. Symmetry. 2018. 11(1), 1-12.
[49] Lin Min, Chen Qiang, Yan Shuicheng. Network in network. arXiv preprint arXiv:1312.4400.2013.
[50] Szegedy C., Vanhoucke V., Ioffe S., Shlens J., Wojna Z. Rethinking the inception architecture for computer vision. In Proceedings of the IEEE Conference on Computer Vision and Pattern Recognition. 2016. p.2818–2826.
[51] Chollet F. Xception: Deep learning with depthwise separable convolutions, In Proceedings of the IEEE Conference on Computer Vision and Pattern Recognition. 2017. p. 1251-1258.
[52] Patil S., Golellu A. Classification of COVID-19 CT Images using transfer learning models. In 2021 International Conference on Emerging Smart Computing and Informatics (ESCI). 2021. p. 116-119.
[53] Özdemir D., Arslan N. N. Analysis of deep transfer learning methods for early diagnosis of the Covid-19 disease with chest X-ray images. Düzce University Journal of Science & Technology. 2022. 10(2), 628-640.
[54] Humayun M., Sujatha R., Almuayqil S. N., Jhanjhi N. Z. A transfer learning approach with a convolutional neural network for the classification of lung carcinoma. In: Healthcare. MDPI, 2022. p. 1058.
[55] Garin A., Tauzin G. A topological" reading" lesson: Classification of MNIST using TDA. In 2019 18th IEEE International Conference On Machine Learning And Applications (ICMLA). 2019. p. 1551-1556.
[56] Grover D., Toghi B. MNIST dataset classification utilizing k-NN classifier with modified sliding-window metric. In Science and Information Conference. 2019. p. 583-591
[57] Iyer L. R., Chua Y., Li, H. Is neuromorphic mnist neuromorphic? Analyzing the discriminative power of neuromorphic datasets in the time domain. Frontiers in Neuroscience. 2021. 15, 1-21.
[58] Kadam S. S., Adamuthe A. C., Patil A. B. CNN model for image classification on MNIST and fashion-MNIST dataset. Journal of Scientific Research. 2020. 64(2), 374-384.
[59] Prabhu V. U. Kannada-MNIST: A new handwritten digits dataset for the Kannada language. arXiv preprintarXiv:1908.01242, 2019.
[60] Audibert R. B., Maschio V. M. FINNger--Applying artificial intelligence to ease math learning for children. arXiv preprint arXiv:2105.12281, 2021.
[61] Zhang L. Hand-drawn sketch recognition with a double-channel convolutional neural network. EURASIP Journal on Advances in Signal Processing. 2021.1: 73.
[62] Hayat S., She K., Yu Y., Mateen M. Deep cnn-based features for hand-drawn sketch recognition via transfer learning approach. Editorial Preface From the Desk of Managing Editor, 2019, 10.9.
[63] Ali S., Aslam N., Kim D., Abbas A., Tufail S., Azhar B.Context awareness based Sketch-DeepNet architecture for hand-drawn sketches classification and recognition in AIoT. PeerJ Computer Science, 2023, 9: e1186.

Volume 14, Issue 2, Page 259-269, 2025 https://doi.org/10.46810/tdfd.1667574 Research Article

BİNGÖL UNIVERSITY

Türk Doğa ve Fen Dergisi
Turkish Journal of Nature and Science
www.dergipark.gov.tr/tdfd

Spatial Patterns of Species Diversity in the Saline Vegetation of Central Anatolia, Türkiye

Didem AMBARLI[1*]

[1]Middle East Technical University, Department of Biological Sciences, Laboratory of Terrestrial Ecology, Ankara, Türkiye
Didem AMBARLI ORCID No: 0000-0001-5589-9373

**Corresponding author: dambarli@metu.edu.tr*

(Received: 28.03.2025, Accepted: 16.06.2025, Online Publication: 27.06.2025)

Keywords
Beta diversity, Biodiversity, Halophyte, Steppe, Marsh

Abstract: Vegetation on saline soils thrives under extreme conditions. The saline vegetation of Central Anatolia is a key component of the Irano-Anatolian Biodiversity Hotspot, notable for its high habitat and species diversity. However, there has been a lack of quantitative assessments of plant diversity in these areas. To address this gap, this study aims to calculate and compare: 1) local species diversity (alpha diversity) across five vegetation alliances, 2) regional diversity (gamma diversity) for each alliance, and 3) the spatial variation in species diversity within alliances (beta diversity). Data from 101 plots representing five alliances, collected from Burdur Lake, Acıgöl, Salt Lake, Seyfe Lake, and Sultansazlığı were compiled from relevant publications. The results showed high species diversity in areas with high variation in salinity or humidity due to ecotone characteristics at all spatial scales. Notably, diversity was highest in salt steppes (*Achilleo wilhelmsii-Artemision santonici*) and in slightly saline, summer-dry marshes (*Lepidio caespitosi-Limonion iconici* and *Inulo aucheranae-Elymion salsi*). Conversely, diversity was lower in non-saline steppes typical of gypsum soils (*Astragalo karamasici-Gypsophilion eriocalycis*) and in communities found on hypersaline soils (*Salicornion fruticosae*). Overall, beta diversity was high, reflecting significant species turnover. These findings numerically support existing literature, which suggests that plant community composition can change drastically over short distances in saline areas. The results highlight the conservation priority of saline areas with ecotone characteristics.

Türkiye'nin İç Anadolu Bölgesi'ndeki Tuzlu Bitki Topluluklarının Tür Çeşitliliğinin Mekansal Desenleri

Anahtar Kelimeler
Beta çeşitlilik, Biyolojik çeşitlilik, Bozkır, Halofit, Sazlık

Öz: Tuzlu alanlardaki bitki örtüsü ekstrem koşullar altında gelişir. İç Anadolu'nun tuzlu bitki örtüsü, yüksek habitat ve tür çeşitliliği ile İran-Anadolu Biyoçeşitlilik Sıcak Noktası' nın öne çıkan habitatlarını barındırır. Ancak, bu alanların tür çeşitliliğine yönelik nicel çalışma yapılmamıştır. Bu çalışmada 1) tuzlu alanlarda gelişen beş alyansın yerel tür çeşitliliği (alfa çeşitlilik), 2) her alyansın bölgesel çeşitliliği (gama çeşitlilik) ve 3) her alyansa ait parsellerde çeşitlilik farkları (beta çeşitlilik) hesaplanmıştır. Bu amaçla, bugüne kadar Burdur Gölü, Acıgöl, Tuz Gölü, Seyfe Gölü ve Sultan Sazlığı' nda yapılan çalışmalarda tespit edilen beş alyansa ait 101 parselin verileri kullanılmıştır. Her alansal ölçekte tür çeşitliliğinin yüksek çıktığı alyanslar tuz oranı ya da nemlilik açısından geçiş özelliğindeki yerlerde gözlenir. Çeşitlilik tuza dayanıklı bozkırlar (*Achilleo wilhelmsii-Artemision santonici*) ve tuzluluk oranı düşük, yazın kuruyan bataklıklarda (*Lepidio caespitosi-Limonion iconici* ve *Inulo aucheranae-Elymion salsi*) yüksek çıkmıştır. Tuzcul alan temsiliyeti düşük, jipsli bozkırları temsil eden kurak bozkırlarda (*Astragalo karamasici-Gypsophilion eriocalycis*) ve tuz oranı yüksek topraklarda gelişen topululuklarda (*Salicornion fruticosae*) çeşitlilik düşük çıkmıştır. Genel anlamda beta çeşitlilik değerleri yüksektir ve bunun nedeni yüksek tür devridir. Bu bulgu, tuzlu alanlarda bitki örtüsünün kısa mesafelerde ciddi değişimler gösterdiğini belirten literatür bilgisini sayısal olarak desteklemektedir. Bulgular toprak özellikleri açısından geçiş özelliğinde, ekoton oluşturan tuzcul alanların koruma açısından öncelikli olduğunu ortaya koymaktadır.

1. INTRODUCTION

Saline vegetation covers large areas around inland lakes in arid lands [1]. Many of Türkiye's saline areas are assigned as conservation priority sites with many endemic plants, migrant or resident bird populations [2]. They are also worth attention in terms of interesting and unique adaptations developed under high-stress conditions [3, 4]. Sadly, those precious areas have been either destroyed or degraded because of climate change, uncontrolled groundwater use in agriculture, cropland expansion, salt extraction, and tourism developments [2]. Therefore, it is crucial to understand biodiversity patterns of saline areas and guide conservation activities with ecological evidence. This would contribute to keep saline areas on the agenda of nature conservation.

There are several saline areas in Central Anatolia [5]. The flora and plant community composition have been under research since 1960s [6]. Studies on vegetation have been carried out since 1970s with a classical phytosociological approach, aiming classification in which expert evaluations play a substantial role. As a result of those studies, the following vegetation hierarchy was proposed: two vegetation alliances and their associations under the ASTRAGALO-BROMETEA Quézel, 1973 steppe class, and seven alliances and several associations under SALICORNIETEA Br.-Bl. & Tüxen 1931 class [5]. In none of those studies, hovewer, an objective and qualitative evaluation of biodiversity patterns was provided, which remains a gap in saline biodiversity studies. Notwithstanding, the commonest measure of biodiversity is the species diversity and there are many methods available to measure it [7, 8]. The only study which applied quantitative methods to saline vegetation in Türkiye was conducted in Çukurova Plain, Adana, and analyzed alpha and beta diversity along humidity and salinity gradients [9]. Yet, to date, there have been no such quantitative studies targeting saline areas in Central Anatolia, which is at the heart of the Irano-Anatolian biodiversity hotspot [10]. This research gap results in shortcomings related to providing quantitative evidence for nature conservation value of the saline vegetation.

Species diversity can be measured and evaluated at three different spatial scales: alpha, beta and gamma [11]. Alpha diversity represents the local species diversity on a single site and it is the most commonly used scale of the species diversity [12]. The common measures of the alpha diversity are the species richness, i.e., the number of different species in a site, Shannon's and Simpson's indices which account for both species richness and abundances [13]. Gamma diversity represents the regional diversity of a community resulting from synthesis of local diversities sampled in several sites [8]. Beta diversity is expressed as the difference or proportion of alpha and gamma diversities and can be calculated with various approaches and formula [14]. The patterns of those three species diversity measures can be different as a result of different drivers. For example, a community can have high alpha but low beta diversity. The reason of that may be that the compositions of species-rich communities in all sites are very similar due to limited environmental variation which would otherwise support different species at different sites. On the contrary, in sites with high levels of environmental stress and variation one can expect low alpha diversity but high beta diversity. In the first case it may be sufficient to conserve a few representative sites to conserve communities but in the second case it is essential to conserve many sites within the distribution range of communities. Consequently, to guide conservation activities, it is of vital importance to measure species diversity at different spatial scales.

In this study, alpha, beta and gamma diversities of plant communities along humidity and aridity gradients in saline areas were calculated and compared. The study tested four hypotheses: 1) On hypersaline soils, low levels of alpha diversity were expected because extremely saline soils prevent growth of many plant species but allow only few ones well-adapted to those conditions. 2) In humid areas, by contrast, lack of aridity and salt stress would enable a high level of alpha diversity. 3) In ecotone areas -transitions of different habitat types or soil attributes (i.e., sub-humid or slightly-saline environments)- high levels of beta diversity were expected as environmental heterogeneity supports many different species. 4) Gamma diversity is highest in plant communities covering largest areas because species turnover would be high and there is high probability of including a many species in a large area.

2. MATERIAL AND METHOD

2.1. Materials

In this study the datasets collected in 25 m^2 or 40 m^2-sized plots sampled in central Anatolia, published in four articles [15-18], were compiled for analysis. The five vegetation alliances previously identified by those studies were accepted as target plant communities (Table 1). Three other studies that did not include a phytosociological classification were excluded [19-21]. Alpha, beta and gamma diversities of each alliance were calculated for each alliance based on the corresponding dataset and subsequently compared. Some alliances were identified in more than one study area; therefore, a regional comparison was not conducted.

Plot size can influence the alpha, beta and gamma diversity results [22]. Using data from plots of widely varying sizes may lead to inconsistencies. To avoid this, plots with very small or large areas were excluded, and only data from plots sized 25 m^2 or 40 m^2—commonly used and moderate sizes in phytosociological studies [15–18]—were retained. Specifically, 24 plots with sizes of 4, 8, 16, or 100 m^2 representing *Thero-Salicornion* Br.-Bl. 1933 in Yurdakulol et al. 1996 [15] were excluded. The data of a non-saline but adjacent steppe alliance, *Astragalo karamasici-Gypsophilion eriocalycis* Ketenoğlu et al. 1983, were included as a reference outlier group to support better interpretation of results. In total, data of 101 plots representing five vegetation alliances were used in the analyses:

Table 1. Vegetation alliances included in the study. Only data from plots of 25 m^2 or 40 m^2 sizes were used. For class and ordo names, syntaxonomic names in the source publications were used. Some names and higher-level classifications differ in Mucina et al. 2016 and FloraVeg. EU. * In Aydoğdu et al. 2002, no alliance was defined for one association.

Vegetation type and location	Class and ordo	Alliance, associations, plot number and size	Source
Steppes Burdur Lake and Acıgöl	ASTRAGALO-BROMETEA Quézel 1973, ONOBRYCHIDO ARMENI-THYMETALIA LEUCOSTOMI Akman, Ketenoğlu, Quézel 1985	***Astragalo karamasici-Gypsophilion eriocalycis*** Ketenoğlu, Quezel, Akman, Aydoğdu 1983: *Artemisetum santonici* Çetik 1981, 7 plots, 25 m^2	[15]
Salt steppes Salt Lake and Seyfe Lake	ASTRAGALO-BROMETEA Quézel 1973, ONOBRYCHIDO ARMENI-THYMETALIA LEUCOSTOMI Akman, Ketenoğlu, Quézel 1985	***Achilleo wilhelmsii- Artemision santonici*** Aydoğdu, Hamzaoğlu, Kurt 2004: *Achilleo wilhelmsii-Artemisietum santonici* Aydoğdu, Hamzaoğlu, Kurt 2004, *Artemisio scopariae-Peganetum harmalae* Aydoğdu, Hamzaoğlu, Kurt 2004, 25 plots, 25 m^2 and 40 m^2	[17]
Salt marshes Burdur Lake and Acıgöl	Salicornietea Br.-Bl. Ex Tx (Puccinellio-Salicornietea Topa 1938), JUNCETALIA MARITIMI Braun-Blanq. ex Horvatić 1934	***Salicornion fruticosae*** Br.-Bl. 1933: *Cresso creticae-Halocnemetum strobilacei* Yurdakulol Öcel, Demirörs, Yıldız, Keleş 1996, 4 plots, 25 m^2*	[15]
Salt marshes Salt Lake and Seyfe Lake	Salicornietea Br.-Bl. Ex Tx (Puccinellio-Salicornietea Topa 1938), HALOSTACHETALIA (Grossheim) E.Topa. 1938	***Lepidio caespitosi-Limonion iconici*** Aydoğdu, Hamzaoğlu, Kurt 2002: *Lepidio caespitosi-Limonietum iconici, Limonio tamaricoidis-Puccinellietum convolutae, Sphenopodo divaricati-Halocnemetum strobilacei, Suaedo anatolicae-Salsoletum nitrariae,* 27 plots, 25 m^2	[16]
Salt marshes Salt Lake and Seyfe Lake	Salicornietea Br.-Bl. Ex Tx (Puccinellio-Salicornietea Topa 1938), JUNCETALIA MARITIMI Braun-Blanq. ex Horvatić 1934	***Inulo aucheranae-Elymion salsi*** Aydoğdu, Hamzaoğlu, Kurt 2002: *Inulo aucheranae-Elymetum salsi*, *Eragrostio collinae-Puccinellietum anatolicae,* 19 plots, 40 m^2	[16]
Salt marshes Sultansazlığı, Kayseri	SALICORNIETEA FRUTICOSAE Br.-Bl. 1931, HALOSTACHETALIA (Grossheim) E.Topa. 1938	***Lepidio caespitosi-Limonion iconici*** Aydoğdu, Hamzaoğlu & Kurt 2002*: Halocnemetum strobilacei* (B.Keller) Topa 1938, *Lepidio caespitosi-Limonietum iconici* Aydoğdu, Hamzaoğlu ve Kurt 2002, *Halocnemetum strobilacei* (B.Keller) Topa 1938, 9 plots, 25 m^2	[18]
Salt marshes Sultansazlığı, Kayseri	SALICORNIETEA FRUTICOSAE Br.-Bl. 1931, JUNCETALIA MARITIMI Braun-Blanq. ex Horvatić 1934	***Inulo aucheranae-Elymion salsi*** Aydoğdu, Hamzaoğlu ve Kurt 2002: *Inulo aucheranae-Elymetum salsi* Aydoğdu, Hamzaoğlu ve Kurt 2002, *Tamaricetum parviflorae-tetrandrae* Hamzaoğlu ve Aksoy 2006, 11 plots, 25 m^2	[18]

Achilleo wilhelmsii-Artemision santonici Aydoğdu, Kurt, Hamzaoglu, Ketenoglu & Cansaran 2004, *Astragalo karamasici-Gypsophilion eriocalycis* Ketenoğlu, Quezel, Akman, Aydoğdu 1983, *Inulo aucheranae-Elymion salsi* Aydoğdu, Hamzaoğlu, Kurt 2002, *Lepidio caespitosi-Limonion iconici* Aydoğdu, Hamzaoğlu, Kurt 2002, and *Salicornion fruticosae* Br.-Bl. 1933. These alliances were included in the most recent synthesis of Türkiye's vegetation [23], although some names and higher-level classifications differ in Mucina's list of European vegetation [24] and in the Database of European Vegetation, Habitats and Flora (FloraVeg.eu). Saline vegetation changes along the gradients of aridity and salinity from center towards periphery of each saline lake, resulting in environmental, not regional, differentiation of vegetation types [23]. Consequently, similar vegetation zonation is observed around each lake [25]. Since salt marshes and salt steppes across central Anatolia share comparable floristic and environmental characteristics, the compiled dataset represents the region's saline vegetation overall [5].

Astragalo karamasici-Gypsophilion eriocalycis, a non-saline steppe alliance, was first described on the gypsum bedrocks around Çankırı [26]. A sub-alliance was later identified on gypsiferous soils between Sivas and Erzincan [27]. It is mainly found on gypsum-rich soils with many endemic and gypsophile species. Characteristic species include *Astragalus karamasicus, A. aduncus, Thymus leucostomus*, *Linum mucronatum* subsp. *gypsicola*, *Gypsophila eriocalyx, G.parva, Lappula barbata, Ziziphora tenuior* and *Z. taurica, Centaurea patula, Allium flavum* subsp. *tauricum* var. *pilosum* (*Allium flavum* var. *pilosum* in the original publication), *Bupleurum boissieri, Silene supina* subsp. *pruinosa* [28]. In the dataset from Burdur Lake, *Artemisia santonicum* was the dominant species, while the frequency and cover values of the alliance's diagnostic species were relatively low [15].

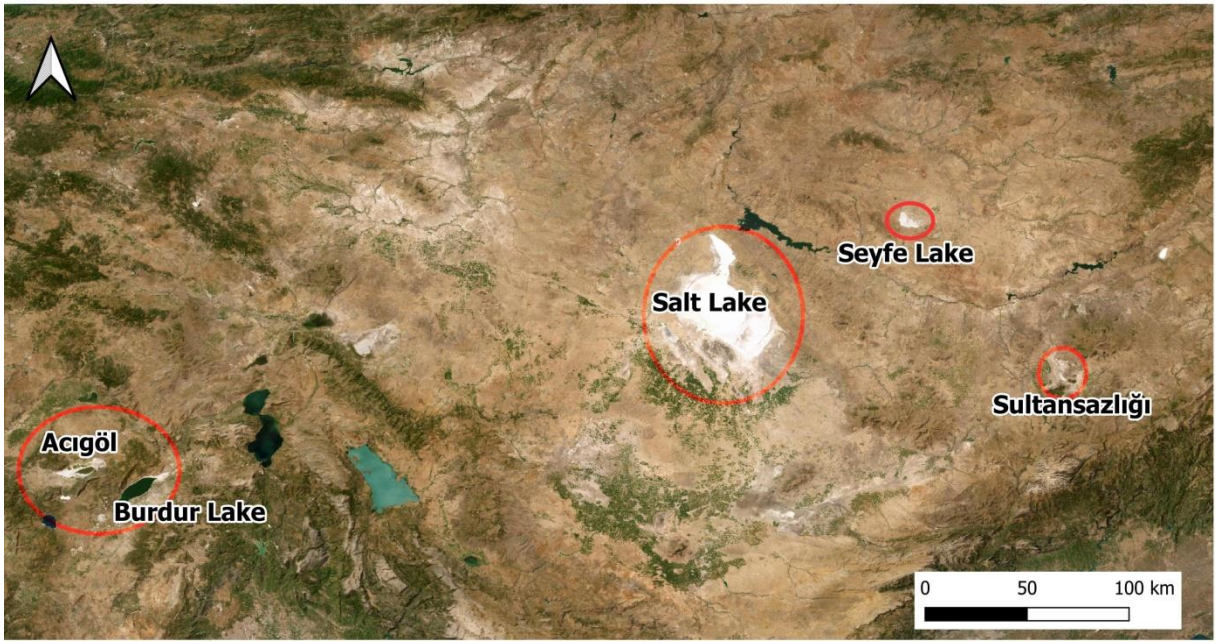

Figure 1. Map of the study area. Google Earth layer is the base of the map [35]. Saline areas appear white. The studied areas are labeled and shown in red ellipses. The map was prepared using the QGIS program [36].

Achilleo wilhelmsii-Artemision santonici alliance represents salt steppes around Salt Lake and Seyfe Lake in the Konya basin and intertwoven with hypersaline vegetation [17]. Dominant species include *Artemisia santonicum* and *Achillea santolinoides* subsp. *wilhemsii*. Other common species of the alliance are *Allium pseudoflavum* and *Noaea mucronata*. Halophytes are frequently found.

Lepidio caespitosi-Limonion iconici is a salt marsh alliance occurring at ecotones between *Artemisia* steppes and submerged *Juncus* spp. swamps. The alliance is found on strongly-saline soils that remain wet except the driest summer months in Konya Basin [23]. Dominant species are *Halocnemum strobilaceum, Frankenia hirsuta, Petrosimonia brachiata, Limonium iconicum* and *Lepidium cartilagineum* subsp. *caespitosum* (published as *Lepidium caespitosum*).

Cresso creticae-Halocnemetum strobilacei plant association was identified in salt marshes around Burdur Lake and Acıgöl [15]. It shows the characteristics of two alliances, i.e. *Thero-Salicornion* Br.-Bl. 1933 and *Salicornion fruticosae* Br.-Bl. 1933. The former consists of annual succulent plants in tidal flats and irregularly inundated inland depressions in the Mediterranean and warm Atlantic zone, while the latter comprises dwarf chenopod shrubs under similar conditions [24]. In this study, the dataset was evaluated under the *Salicornion fruticosae* alliance, as the plant community composition was more consistent with this alliance. Dominant and common species included *Halocnemum strobilaceum, Cressa cretica* and *Salicornia perennans (*published as *Salicornia europea* subsp. *prostate*).

Inulo aucheranae-Elymion salsi salt marshes are found on south of Salt Lake in areas that dry between August and October but remain otherwise wet [16]. Soil salinity is relatively low. Most characteristic species are endemics. The common or dominant species included *Elymus elongatus* subsp. *salsus*, *Inula aucherana* and *Juncus maritimus*.

2.2. Study Sites

The data for this study were collected from four different sites within Konya Basin, located in Central Anatolia Region of Türkiye: i) Saline soils around Salt Lake (Tuz Gölü), spanning the provinces of Ankara, Konya and Aksaray, ii) saline areas around Seyfe Lake in Kırşehir province, iii) the Sultansazlığı marshes in Kayseri province, and iv) saline areas around Denizli Acıgöl and Burdur Lake (Figure 1). Although Burdur Lake and Acıgöl are not officially included in Central Anatolia, they were included in the study due to their proximity to the regional boundary and the similarity of their saline vegetation to that of the Central Anatolia. Environmental data from the original publications [15–18] indicate the following characteristics for these sites: Elevation ranges from 930 to 1140 meters above sea level, annual precipitation varies between 308 and 370 mm, and the highest average temperature during the warmest months can reach 33.3 °C. According to Emberger's classification system, two bioclimate types are present: the semi-arid lower very cold Mediterranean climate and the arid upper very cold Mediterranean climate.

All study areas feature saline hydromorphic alluvial soils, with salinity influenced by proximity to water bodies, salt accumulation, and humidity. In the salt marshes of Salt Lake and Seyfe Lake, pH ranges from 8.2 to 8.6, sodium ion (Na^+) concentrations from 38.1 to 853.1 me/L, and chloride ion (Cl^-) concentrations from 3 to 32.5 me/L. In the surrounding saline steppes, values are lower: pH 7.5–7.7, Na^+ 3–10.8 me/L, and Cl^- 11.0–11.2 me/L.

Sultansazlığı marshes are sodic, with pH values between 8.8 and 9.4, Na^+ concentrations from 2825 to 4475 ppm, and Cl^- concentrations from 1.1 to 9.4 ppm. In the steppes around Burdur Lake and Acıgöl, the pH is approximately 7.8, with Na^+ ranging from 12 to 20 me/L and Cl^- from 5.8 to 10.1 me/L; in salt marshes, these values are Na^+ 15–25 me/L and Cl^- 6.9–8.3 me/L, with a pH of 7.8

2.3. Data Processing, Calculations and Tests

Plant nomenclature followed the List of Plants of Turkey: Vascular Plants [29]. Taxonomic updates made since the publication of the original data sources were incorporated; synonymized names were replaced with currently accepted names, and any typographical errors in taxon names were corrected. Duplicate entries of the same species within syntaxonomic tables were consolidated. Species were used as the taxonomic unit for three reasons: (1) the study aimed to assess species-level diversity, (2) subspecies were not consistently identified or reported, and (3) retaining both species and subspecies data could distort species diversity calculations. Consequently, subspecies and varietal data were aggregated at the species level, and a few entries recorded only at the genus level were excluded. The final dataset comprised a species-by-site matrix of 191 species across 101 plots.

Many studies targeting alpha and gamma diversity in plants have only used species richness and not used cover or abundance data [30]. However, abundance data are needed to calculate different measures of alpha diversity. In the vegetation datasets used in this study, species abundance was recorded using the Braun-Blanquet's cover-abundance scale [31], using one of seven categories: - (absent), r (cover < 5%, one individual or rare), + (cover < 5%, very few individuals), 1 (cover < 5%, individuals abundant with very low cover or not abundant but with higher cover), 2 (cover < 25%), 3 (cover 25% - 50%), 4 (cover 50% - 75%) and 5 (cover > 75%). Furthermore, categories of 1 and 2 were divided into subcategories [32]. To use these ordinal categories in diversity calculations, numerical transformations are required. According to Wildi [33], the Braun-Blanquet scale can be converted using rank values and the formula $x'=x^y$, where x is the rank and y is an exponent selected by the researcher. For instance, using y=0.25yields values between 1 and 1.7 for the entire scale, minimizing distinctions between rare and dominant species, which is unsuitable for this study's goals. Alternatively, using y=2.5 produces values more representative of actual cover (e.g., a "5" becomes 88.18), but this inflates gamma diversity. As a compromise, the study used y=1.5, producing the following transformation: – = 0; r = 1; + = 1.84; 1 = 2.83; 2 = 5.20; 3 = 8.00; 4 = 11.18; 5 = 14.7. A sensitivity analysis showed that alpha diversity values calculated using y=0.25 and y=2.5 showed no significant differences from the calculation with y=1.5. Therefore y=1.5 was chosen for its balance. Data were digitized using the JUICE software [34].

Hill numbers were used to quantify species diversity on both alpha and gamma scales [37], allowing for weighting based on species abundance [37, 38]. The following were calculated: species richness (qD = 0, equal weighting), Shannon diversity (qD = 1, abundance-weighted), inverse Simpson (qD = 2, greater weight to dominant species). Alpha diversity was calculated using the renyi function of the *vegan* package in R software [39]. Comparisons of diversity between alliances were conducted using the nonparametric Kruskal-Wallis test, followed by Wilcoxon pairwise comparisons. Statistical significance was set at $p < 0.05$, and results were visualized using the *ggpubr* package [40].

In the study, gamma diversity was calculated at the level of alliances, the lowest regional unit in the vegetation classification [41]. It groups associations with shared regional patterns but local differences and meets the gamma diversity level [42]. Gamma diversity was estimated using incidence-based rarefaction and extrapolation [43], with 95% coverage-based standardization [44]. This method can interpolate or extrapolate biodiversity using species accumulation curves. Bootstrap confidence intervals were used to assess statistical differences, where non-overlapping intervals indicate significance [7]. Incidence was adopted as the data type because cover-abundance scales converted to abundance data gave unreliable results in this calculation.

Beta diversity was assessed using three abundance-based metrics, i.e., Bray-Curtis dissimilarity index, balanced variation in species abundances and unidirectional abundance gradients. Analogous to species turnover [45], balanced variation in species abundances (beta.bray.bal) computes how much a decline of a species' abundance from one site to another is balanced with an increase in abundance of another species. Analogous to nestedness [45], unidirectional abundance gradients (beta.bray.gra) are calculated to measure how much sites are subsets of other sites with high abundances of each species. The widely used Bray-Curtis dissimilarity index is derived from the sum of these two sources of dissimilarity. Beta diversity calculations were performed using the *betapart* package in R software [46]. The data set was divided into alliances and for each alliance, abundance-based pair-wise dissimilarities of all plots were calculated. All calculations were performed with R software [48] in the R Studio environment [49].

3. RESULTS

3.1. Alpha Diversity

The mean species richness of saline vegetation based on data from 101 plots with 25 m^2 or 40 m^2 sizes, was 17.0 (standard error ± 0.464) with species richness ranging from 6 to 27. The average Shannon diversity was 14.5 (±0.438), and the inverse Simpson diversity was 12.0 (±0.414).

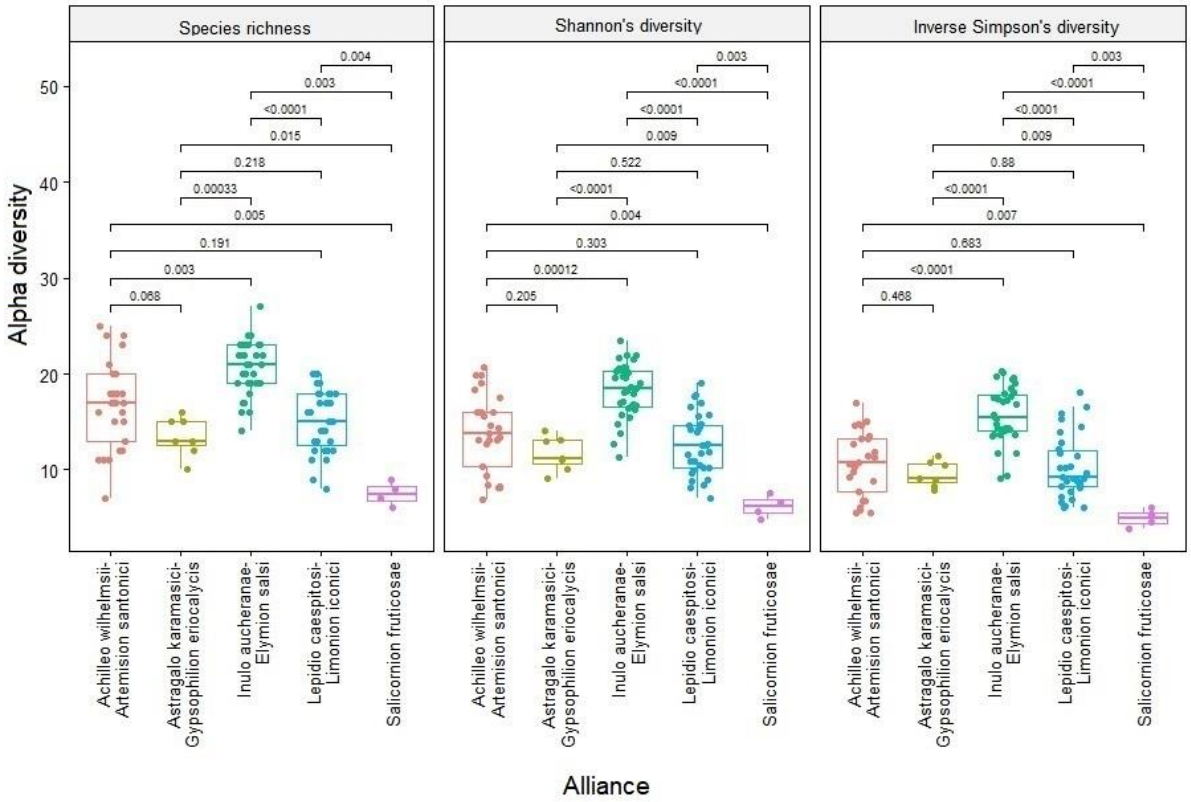

Figure 2. Boxplots showing the alpha level diversity of five alliances representing Central Anatolian saline vegetation. The alliances are shown in different colors. The graph was generated using the *ggpubr* package in R Studio [40]. The alpha diversity value of each plot is indicated with a dot using the "jitter" feature. Statistical significances between the alliances were indicated using *p* values of Wilcoxon tests.

Statistically significant differences in alpha diversity were observed among the alliances, according to the nonparametric Kruskal-Wallis test ($p < 0.0001$). Pairwise comparisons using the Wilcoxon test revealed significant differences between several alliances (Figure 2). The *Inulo aucheranae–Elymion salsi alliance*, representing slightly saline, summer-dry marshes, exhibited the highest species richness. This was followed by the *Achilleo wilhelmsii–Artemision santonici* salt steppes and the *Lepidio caespitosi–Limonion iconici* transitional salt marshes. Conversely, the alliances with the lowest species richness were the *Astragalo karamasici–Gypsophilion eriocalycis* steppes and the *Salicornion fruticosae* hypersaline vegetation with succulent Chenopods. Notably, these two alliances were represented by a small number of plots in the dataset.

The patterns observed for Shannon and inverse Simpson diversity indices mirrored those of species richness in terms of statistical significance and diversity ranking. Importantly, using different transformation values (y = 0.25 and y = 2.5) for Braun-Blanquet cover categories did not alter the results in terms of statistical significance or the order of diversity rankings—only the p-values of the Wilcoxon tests varied slightly.

3.2. Beta Diversity

Bray-Curtis dissimilarity index (beta.bray) results indicated that within most alliances, plots were either highly similar or very dissimilar in species composition. The *Achilleo wilhelmsii–Artemision santonici* salt steppes exhibited relatively high beta diversity, whereas the *Astragalo karamasici–Gypsophilion eriocalycis* steppes displayed relatively low Bray-Curtis values (Figure 3). The median dissimilarity values for the remaining three alliances were close to each other and to the overall mean. Despite being represented by only four plots, the *Salicornion fruticosae* alliance showed a wide range of Bray-Curtis values.

In contrast to alpha diversity, beta diversity comparisons revealed fewer statistically significant differences among alliances. Specifically, the *Lepidio caespitosi–Limonion iconici* transitional salt marshes exhibited significantly lower dissimilarity values than the *Achilleo wilhelmsii–Artemision santonici* salt steppes, while the *Inulo aucheranae–Elymion salsi* alliance had significantly higher values compared to other salt marshes. Species turnover values (beta.bray.bal) were similar to the Bray-Curtis index and reflected comparable patterns in inter-alliance differences. In contrast, values for nestedness (beta.bray.gra) were generally low across alliances (Figure 3). Nonetheless, based on this metric, most alliances were significantly different from each other.

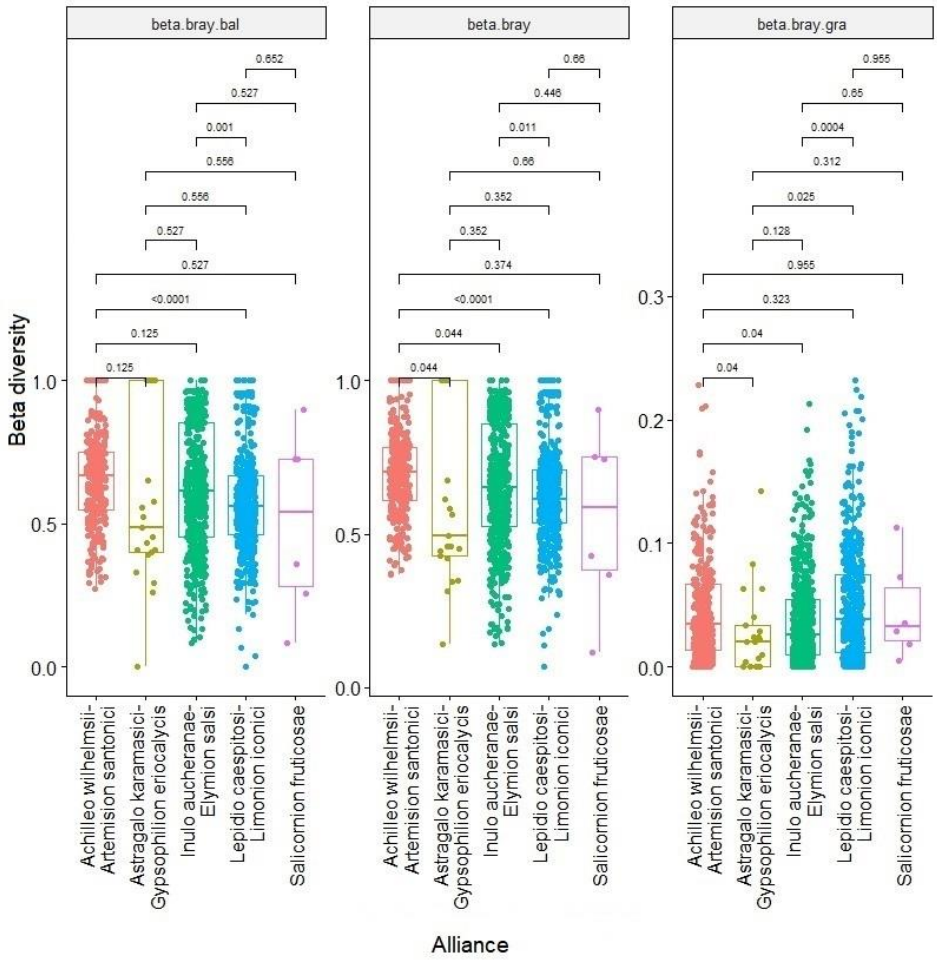

Figure 3. Boxplots showing the beta diversity of five alliances representing Central Anatolian saline vegetation with three different measures. The alliances are shown in different colors. Each point indicates the dissimilarity value of two different plots within an alliance. For clarity, overlapping points were shifted slightly using the "jitter" feature. Values for the first two measures of beta diversity ranged from 0 to 1, while the beta.bray.gra axis ranged from 0 to 0.5.

3.3. Gamma Diversity

The average species richness at the gamma (regional) level was estimated at 70.1±17.1. Significant differences in gamma diversity were observed among the alliances (Figure 4). The highest species richness was recorded in two salt marsh alliances: *Lepidio caespitosi–Limonion iconici* and *Inulo aucheranae–Elymion salsi*, followed by the salt steppes of *Achilleo wilhelmsii–Artemision santonici*. The lowest values were found in the *Astragalo karamasici–Gypsophilion eriocalycis* steppes and the hypersaline *Salicornion fruticosae* vegetation. However, this ranking changed when species frequency was considered using Shannon and inverse Simpson diversity indices. In particular, the diversity of *Lepidio caespitosi–Limonion iconici* decreased relative to other highly diverse alliances, approaching the values of the *Astragalo karamasici–Gypsophilion eriocalycis* steppes. By contrast, the *Inulo aucheranae–Elymion salsi* and *Achilleo wilhelmsii–Artemision santonici* alliances maintained high values, indicating more even distribution of species.

4. DISCUSSION AND CONCLUSION

Saline habitats are typically considered species-poor [5]. However, this study found an average of 17 species per 25 or 40 m² plot, which is relatively high given the stressful conditions associated with salinity. For comparison, the European Grassland Database reports an average of 35 species per 100 m² plot for *Astragalo-Brometea* steppes (n = 3) and 10 species for *Juncetea maritimi* marshes (n = 78) [50]. The Central Anatolian saline plots demonstrate comparable species richness, especially considering their smaller size.

Among the alliances, *Inulo aucheranae–Elymion salsi* slightly saline, summer-dry marshes had the highest alpha diversity. These habitats feature moderate salinity and humidity levels—conditions that are neither as harsh as hypersaline environments nor as dry as typical steppes. This finding supports the second hypothesis: intermediate environmental stress fosters higher species richness [51, 52]. A similar pattern was observed in Mongolian grasslands, where diversity increased with humidity [53]. On the other hand, the lowest alpha diversity was observed in the *Salicornion fruticosae* hypersaline vegetation, in line with the first hypothesis and existing literature indicating that extreme conditions (e.g. hypersalinity) significantly limit species establishment [54]. Previous research from Çukurova similarly showed increased alpha and beta diversity with decreasing salinity and increasing humidity [9], further supporting these results.

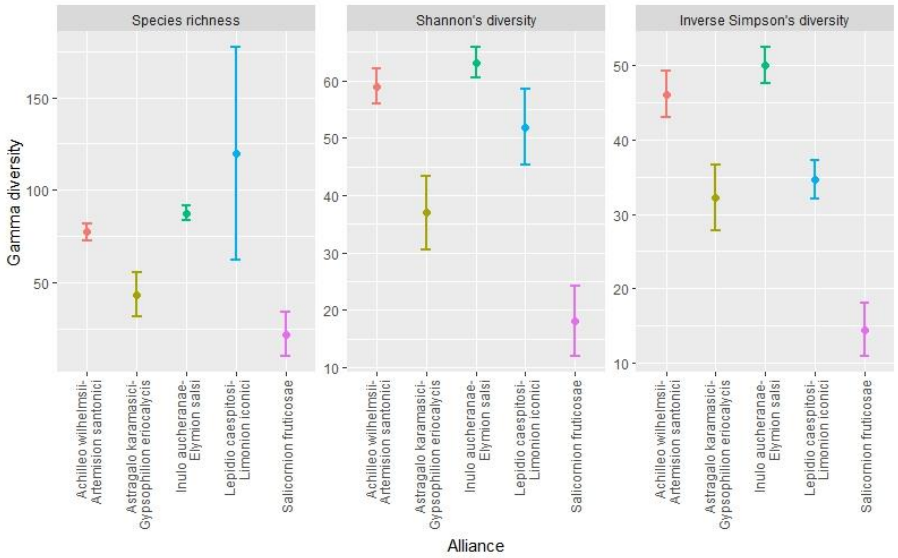

Figure 4. Gamma diversity of five alliances representing Central Anatolian saline vegetation. The alliances are shown in different colors. Diversity estimates are shown with dots and confidence intervals with lines.

The beta diversity across alliances was generally high. This suggests that plots within the same alliance can be markedly different in species composition. The high dissimilarity was largely driven by species turnover (beta.bray.bal), rather than nestedness (beta.bray.gra). In Central Anatolia, microhabitat variability is high—even across short distances—leading to complete species replacement in nearby plots. These findings are consistent with the presence of beta diversity values approaching 1 in Figure 3 and confirm substantial small-scale compositional changes [42]. This supports the argument that regional diversity in saline habitats, though modest at the plot level, is significantly enhanced by spatial heterogeneity. Conservation efforts should therefore prioritize multiple representative sites rather than focusing on single locations.

The *Achilleo wilhelmsii–Artemision santonici* salt steppes exhibited the highest beta diversity and were also among the most diverse in terms of alpha and gamma diversity. These communities occur at the transition between steppe and saline zones and may be classified as ecotones [17]. Similar findings have shown ecotones to be high in beta diversity and critical in conservation prioritization [55]. Additionally, their high gamma diversity likely results from combining species pools from two different ecosystems [5, 56]. These transitional areas should therefore be focal points for biodiversity conservation in Central Anatolia.

Salt marsh communities also demonstrated high beta diversity, second only to salt steppes. This may be attributed to two additional factors: (i) salt marsh plots were located in two distinct regions (Salt Lake and Sultansazlığı), separated by over 100 km, and (ii) a greater number of plots were included. This wide geographic range and larger sampling effort naturally lead to higher species turnover and thus elevated beta diversity [57].

The highest gamma diversity was observed in *Achilleo wilhelmsii–Artemision santonici* salt steppes and *Inulo aucheranae–Elymion salsi* low-saline marshes. These results reaffirm the value of ecotones and moderately saline habitats for conserving regional species richness, partially supporting the fourth hypothesis. In contrast, the *Astragalo karamasici–Gypsophilion eriocalycis* steppes had low diversity at both alpha and gamma levels. The data used for this alliance originated from plots around Lake Burdur, where the habitat is both saline and arid—non-optimal for this community type, which typically occurs on gypsiferous soils such as those in Çankırı, Ankara, and Erzincan [15, 26, 27]. Including plots from those core regions in future studies would likely improve gamma diversity estimates for the alliance. Currently, these data suggest that gypsophilous vegetation is not a major component of Central Anatolia's saline habitats. The *Salicornion fruticosae* alliance also showed low alpha and gamma diversity, in line with its ecological characteristics. Hypersaline environments support only a few specialized species [5], but even within this limited group, there was some variation, as indicated by a few plots with high beta high beta diversity values.

This study relied on vegetation data collected between 1996 and 2006. Since then, saline ecosystems in Central Anatolia have been increasingly impacted by climate change and anthropogenic activities. Saline lakes have contracted due to reduced precipitation, groundwater depletion, and agricultural expansion [58–60]. These changes likely influence both the composition and extent of saline vegetation, making updated fieldwork essential.

The data sources of this study had different plot sizes calculated with minimal area method. Very small and very large plots were excluded from the analysis as numerical comparison of the species data from those plots may lead to erroneous results. But two commonest and closer sizes were kept to make maximum use of available data. In future studies, if standardized data can be collected from each plant community with equal size and number of plots, comparisons can be made with smaller confidence interval estimates. With a similar approach, studies with nested plots are thought to provide the most useful data in terms of numerical analysis [61].

Conducting new vegetation studies in the same areas but with standardized methods will provide up-to-date and precise results.

Studies of syntaxonomic classification have advanced with new quantitative and objective methods in delimitation of the syntaxonomic units [62]. As a result, vegetation classifications of different regions around world have been revised and new classifications were proposed (e.g. see [63] for forests of Japan). Syntaxonomic classification of the saline steppes requires such quantitative analyses and revisions. Before that, collecting data from under-represented parts of central Anatolia such as Palas Lake in Kayseri is a must. I hope this study will be a motivation for such further studies. After a comprehensive revision, similar analyses of biodiversity patterns can provide the complete picture of the spatial biodiversity patterns.

This study provides the first quantitative comparison of species diversity in saline habitats across Central Anatolia, analyzing five major vegetation alliances across alpha, beta, and gamma levels. Each diversity component revealed a different pattern, emphasizing the need for multi-scalar approaches in biodiversity assessments. Alliances thriving under moderate conditions (e.g., ecotones) are crucial for conserving high local and regional diversity. However, low-diversity habitats, including those with extreme conditions or limited sampling, may still host rare or endemic species and warrant conservation.

In conclusion, conserving the biodiversity of Central Anatolian saline ecosystems requires a dual strategy: protecting both moderately stressful ecotone habitats and preserving the unique, harsh environments that support specialized flora. This work underscores the ecological complexity of these habitats and the importance of updated, standardized research for effective conservation planning.

Acknowledgements

I am sincerely thankful to Prof. Dr. Mecit Vural for supporting my work. I am thankful to all vegetation scientists involved in data collection.

REFERENCES

[1] Atalay İ. Türkiye'nin Ekolojik Bölgeleri - Ecoregions of Turkey. 2nd Ed. Ankara: Palme Yayıncılık; 2014.
[2] Eken G, Bozdoğan M, İsfendiyaroğlu S, Kılıç DT, Lise Y. (ed.). Türkiye'nin Önemli Doğa Alanları. Ankara: Doğa Derneği; 2007.
[3] Yildiztugay E, Ozfidan-Konakci C, Kucukoduk M. The role of antioxidant responses on the tolerance range of extreme halophyte *Salsola crassa* grown under toxic salt concentrations. Ecotoxicol Environ Saf. 2014; 110:21-30.
[4] Uzilday B, Özgür R, Sekmen AH, Yildiztugay E, Turkan İ. Changes in the alternative electron sinks and antioxidant defence in chloroplasts of the extreme halophyte *Eutrema parvulum* (*Thellungiella parvula*) under salinity. *Ann Bot*. 2015; 115(3):449–463.
[5] Tuğ GN, Yaprak AE, Vural M. The floristical, ecological, and syntaxonomical characteristics of salt marshes and salt steppes in Turkey. In: Sabkha Ecosystems, vol VI: Asia/Pacific, Switzerland,: Springer; 2019. p. 413-446.
[6] Şahin B. Vejetasyon Kaynakları. In: Güner A, editor. Resimli Türkiye Florası. Cilt 1. İstanbul: Nezahat Gökyiğit Botanik Bahçesi; 2014. p. 225-243.
[7] Colwell RK, Coddington JA Estimating terrestrial biodiversity through extrapolation. Philos Trans R Soc Lond B Biol Sci. 1994;345(1311):101-118.
[8] Beck J, Schwanghart W. Comparing measures of species diversity from incomplete inventories: an update. Methods Ecol Evol. 2010;1(1):38-44.
[9] Yilmaz KT, Akca E, Cakan H, Ünlükaplan Y, Kapur S. Relation between soil salinity and species composition of halophytic plant communities: A baseline data inventory for wetland monitoring. Turk J Bot. 2020;44(5):493-508.
[10] Mittermeier RA, Turner WR, Larsen FW, Brooks TM, Gascon C. Global biodiversity conservation: the critical role of hotspots. In: Zachos FE, Habel JC, editors. Biodiversity hotspots—distribution and protection of conservation priority areas. Berlin: Springer; 2011. p. 3–22.
[11] Chiarucci A, Bacaro G, Scheiner SM. Old and new challenges in using species diversity for assessing biodiversity. Philos Trans R Soc Lond B Biol Sci. 2011; 366(1576): 2426-2437.
[12] Magurran AE, McGill BJ. Biological diversity: frontiers in measurement and assessment. Oxford: OUP; 2010.
[13] Roswell M, Dushoff J, Winfree R. A conceptual guide to measuring species diversity. Oikos. 2021; 130(3):321-338.
[14] Tuomisto H. A diversity of beta diversities: straightening up a concept gone awry. Part 1. Defining beta diversity as a function of alpha and gamma diversity. Ecography, 2010;33(1): 2-22.
[15] Yurdakulol E, Öcel I, Demirörs M, Yıldız A, Keleş Y. Ecological and syntaxonomic investigation of salt marshes vegetation in the vicinity of Burdur and Acıgöl (Denizli/Turkey). Ecol Mediterr. 1996; XXII(1/2):51-61.
[16] Aydoğdu M, Hamzaoğlu E, Kurt L. New halophytic syntaxa from Central Anatolia (Turkey). Isr J Plant Sci. 2002;50:313-323.
[17] Aydoğdu M, Kurt L, Hamzaoğlu E, Ketenoğlu O, Cansaran A. Phytosociological studies on salty steppe communities of Central Anatolia, Turkey. Isr J Plant Sci. 2004;52:71-79.
[18] Hamzaoğlu E, Aksoy A. Sultansazlığı Bataklığı halofitik toplulukları üzerine fitososyolojik bir çalışma (İç Anadolu-Kayseri). Ekoloji. 2006;15(60):8-15.
[19] Birand H. Orta Anadolu bozkırında vejetasyon incelemelerinin ilk sonuçları: 1. Tuz Gölü Çorakçıl Bitki Bitlikleri. Konya: Selçuk Üniversitesi Yayınları; 1962.

[20] Birand H. Die verwüstung der Artemisia-Steppe bei Karapınar in zentralanatolien. Vegetati. 1970; 20:21-47.
[21] Serteser A, Acar H . Acıgöl (Afyonkarahisar) çevresinin halofitik vejetasyonu ve toprak ilişkisi. AKÜ FEMÜBİD. 2016; 16:495-506.
[22] Meier ES, Hofer G. Effects of plot size and their spatial arrangement on estimates of alpha, beta and gamma diversity of plants in alpine grassland. Alp Bot. 2016;126(2): 167-176.
[23] Ketenoğlu O, Vural M, Kurt L, Körüklü T. Vejetasyon. In: Güner A. editor. Resimli Türkiye Florası. Volume 1. İstanbul: Nezahat Gökyiğit Botanik Bahçesi; 2014.
[24] Mucina L, Bültmann H, Dierßen K, Theurillat JP, Raus T, Čarni A, et al. Vegetation of Europe: hierarchical floristic classification system of vascular plant, bryophyte, lichen, and algal communities. Appl Veg Sci. 2016:19:3-264.
[25] Aksoy A, Hamzaoğlu E. Vegetation zones in the salty marshes of Central Anatolia and natural borders of agricultural usage. In: Öztürk M, Waisel Y, Ajmal Khan M, Görk G, editors. Biosaline Agriculture and Salinity Tolerance in Plants. Basel: Birkhäuser Verlag; 2006.
[26] Ketenoğlu O, Güzel P, Akman Y, Aydoğdu M. New syntaxa on the gypsaceous formations in the Central Anatolia. Ecol Mediterr. 1983; Tome IX, Fascicule 3-4.
[27] Ketenoğlu O, Aydoğdu M, Kurt L, Akman Y, Hamzaoğlu E. Syntaxonomic research on the gypsicole vegetation in Cappadocia, Turkey. Isr J Plant Sci.2000;48:121–128.
[28] Akman Y, Ketenoğlu O, Kurt L, Vural M. İç Anadolu Step Vejetasyonu. Ankara: Palme Yayıncılık; 2014.
[29] Güner A, Aslan S, Ekim T, Vural M, Babaç MT. Türkiye Bitkileri Listesi (Damarlı Bitkiler). İstanbul: Nezahat Gökyiğit Bahçesi ve Flora Araştırmaları Derneği Yayını; 2012.
[30] Večeřa M, Divíšek J, Lenoir J, Jiménez-Alfaro B, Biurrun I, Knollová I, et al. Alpha diversity of vascular plants in European forests. J Biogeogr. 2019;46(9):1919-1935.
[31] Braun-Blanquet J. Pflanzensoziologie-Grundzüge der Vegetationskunde. Wien and New York: Springer Verlag; 1964.
[32] Barkman JJ, Doing H, Segal S. Kritische Bemerkungen und vorschläge zur quantitativen Vegetationsanalyse. Acta Bot Neerl. 1964:13:394-419.
[33] Wildi O. Data analysis in vegetation ecology. London: Wiley-Blackwell; 2017.
[34] Tichý L. JUICE, software for vegetation classification. J Veg Sci. 2002;13:451–453.
[35] Google Earth Version: 7.3.6.9796 [Internet] 2024. [cited in October 2024] Available from https://earth.google.com/web/
[36] QGIS.org (2024). QGIS Geographic Information System. Open Source Geospatial Foundation Project. Available from http://qgis.org
[37] Hill MO. Diversity and evenness: a unifying notation and its consequences. Ecology. 1973;54(2): 427-432.
[38] Jost L. Entropy and diversity. Oikos. 2006;113(2): 363-375.
[39] Oksanen J, Blanchet FG, Kindt R, Legendre P, O'hara R, Simpson GL, et al. Vegan: community ecology package. R package version 1.17-4 2010
[40] Kassambara, A. 2023. *ggpubr: 'ggplot2' Based Publication Ready Plots*. R package version 0.6.0.
[41] Willner W. What is an alliance? VCS. 2020;1: 139-144.
[42] Kurt L, Nilhan TG, Ketenoglu O. Synoptic view of the steppe vegetation of Central Anatolia, Turkey. Asian J Plant Sci. 2006; 5(4): 733-739.
[43] Chao A, Gotelli NJ, Hsieh TC, Sander EL, Ma KH, Colwell RK, et al. Rarefaction and extrapolation with Hill numbers: a framework for sampling and estimation in species diversity studies. Ecol Monogr. 2014;84(1):45-67.
[44] Chao A, Jost L. Coverage-based rarefaction and extrapolation: standardizing samples by completeness rather than size. Ecology. 2012;93(12):2533-2547.
[45] Baselga A. Partitioning the turnover and nestedness components of beta diversity. Glob Ecol Biogeogr. 2010;19(1):134-143.
[46] Baselga A, Orme CDL. Betapart: an R package for the study of beta diversity. Methods Ecol. Evol. 2012;3(5):808-812.
[47] Baselga A. Separating the two components of abundance-based dissimilarity: balanced changes in abundance vs. abundance gradients. Methods Ecol. Evol. 2013;4:552–557.
[48] R Core Team. R: A language and environment for statistical computing. Vienna: R Foundation for Statistical Computing [Internet]. 2024 [cited in March 2024] Available from https://www.R-project.org/
[49] Posit team. RStudio: Integrated Development Environment for R. [Internet]. 2024. [cited in March 2024] Available from http://www.posit.co/.
[50] Biurrun I, Burrascano S, Dembicz I, Guarino R, Kapfer J, Pielech R, et al. GrassPlot v. 2.00 – first update on the database of multi-scale plant diversity in Palaearctic grasslands. PG, 2019;44:26–47.
[51] Sarr DA, Hibbs DE, Huston MA A Hierarchical perspective of plant diversity. Q Rev Biol. 2005;80(2):187-212.
[52] De Bello F, Lepš J, Sebastià M-T. Variations in species and functional plant diversity along climatic and grazing gradients. Ecography. 2006;29:801-810.
[53] Zhang Q, Hou X, Li FY, Niu, J, Zhou Y. Ding Y, et al. Alpha, beta and gamma diversity differ in response to precipitation in the Inner Mongolia grassland. PLoS One. 2014;9(3): e93518.
[54] Eliáš Jr P, Sopotlieva D, Dítě D, Hájková P, Apostolova I, Senko D,et al. Vegetation diversity of salt-rich grasslands in Southeast Europe. Appl Veg Sci. 2013;16(3):521-537.
[55] Gaston KJ, Rodrigues ASL, van Rensburg, BJ, Koleff P, Chown SL. Complementary representation and zones of ecological transition. Ecol Lett. 2001;4:4-9.
[56] Ambarlı D, Zeydanlı US, Balkız Ö, Aslan S, Karaçetin E, Sözen M. An overview of biodiversity

and conservation status of steppes of the Anatolian Biogeographical Region. Biodivers Conserv. 2016; 25: 2491-2519.

[57] Dengler J. Pitfalls in small-scale species-area sampling and analysis. Folia Geobot, 2008;43:269-287.

[58] Cunillera-Montcus D, Beklioğlu M, Cañedo-Argüelles M, Jeppesen E, Ptacnik R, Amorim CA, et al. Freshwater salinisation: a research agenda for a saltier world. TREE.2022; 37(5):440-453.

[59] Yılmaz G, Çolak MA, Özgencil İK, Metin M, Korkmaz M, Ertuğrul S, et al. Decadal changes in size, salinity, waterbirds, and fish in lakes of the Konya Closed Basin, Turkey, associated with climate change and increasing water abstraction for agriculture. Inland Waters. 2021;11(4):538-555.

[60] Dönmez AA, Uğurlu Aydın Z; Yüzbaşıoğlu İS. On the border of extinction and speciation, Polygala seyfegoluensis (Polygalaceae), a new species from marshy habitat, Central Türkiye: Under the threat of climate change, water retreat, and subsequent degradation. Turk J Bot. 2024;48(1):44–56.

[61] Dengler J, Boch S, Filibeck G, Chiarucci A, Dembicz I, Guarino R, et al. Assessing plant diversity and composition in grasslands across spatial scales: the standardised EDGG sampling methodology. *PG.* 2016;32,13−30.

[62] De Cáceres M, Franklin SB, Hunter JT, Landucci F, Dengler J, Roberts DW. Global overview of plot-based vegetation classification approaches. Phytocoenologia. 2018;48(2).

[63] Noriyuki M, Kondo H, Shitara T, Yoshikawa M, Hoshino Y. A new formal classification for Japanese forest vegetation based on traditional phytosociological concepts. Appl Veg Sci. 2021;24:e12611.